ELSEVIER OCEANOGRAPHY SERIES 73

GLOBAL CLIMATE CHANGE AND RESPONSE OF CARBON CYCLE IN THE EQUATORIAL PACIFIC AND INDIAN OCEANS AND ADJACENT LANDMASSES

Edited by
H. KAWAHATA and Y. AWAYA

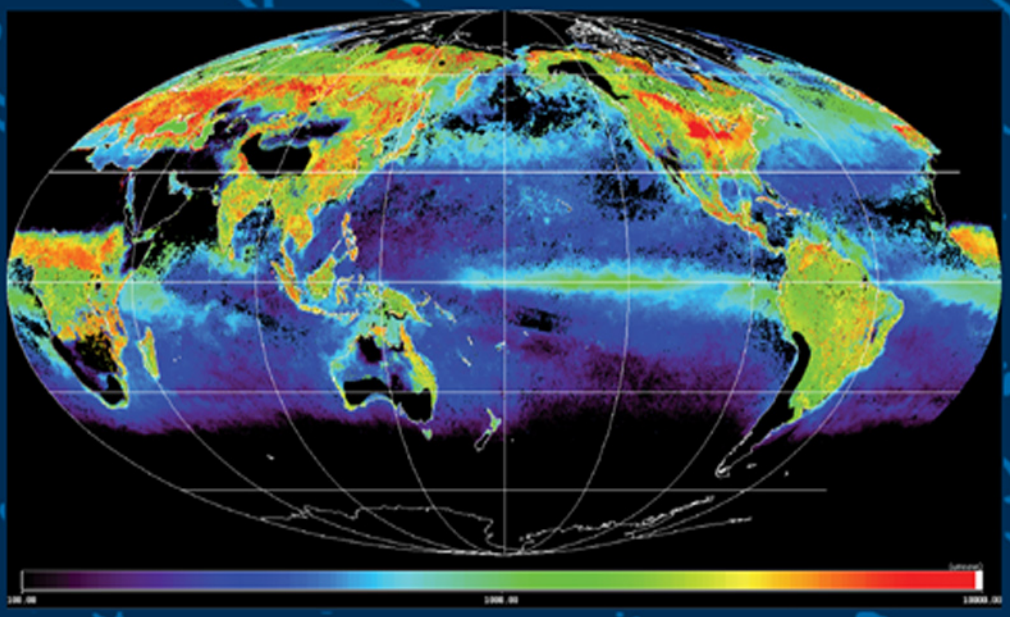

Series Editor: David Halpern

GLOBAL CLIMATE CHANGE AND RESPONSE OF CARBON CYCLE IN THE EQUATORIAL PACIFIC AND INDIAN OCEANS AND ADJACENT LANDMASSES

Elsevier Oceanography Series
Series Editor: David Halpern(1993-)

FURTHER TITLES IN THIS SERIES

For more information see our website: http://www.elsevier.com/locate/eos

37. W. Langeraar
Surveying and Charting of the Seas
40. J.C.J. Nihoul (Editor)
Coupled Ocean-Atmosphere Models
46. J.C.J. Nihoul (Editor)
Small scale Turbulence and Mixing in the Ocean
48. S.R. Massel
Hydrodynamics of Coastal Zones
49. V.C. Lakhan and A.S. Trenhaile (Editors)
Applications in Ocean Modeling
53. J. Dera (Editor)
Marine Physics
54. K. Takano (Editor)
Oceanography of Asian Marginal Seas
55. Tan Weiyan
Shallow Water Hydrodynamics
56. R.H. Charlier and J.R. Justus
Ocean Energies, Environmental, Economic and Technological Aspects of Alternative Power Sources
57. P.C. Chu and J.C. Gascard (Editors)
Deep convection and Deep Water Formation in Oceans
58. P.A. Pirazzoli, J. Pluet
World Atlas of Holocene Sea-Level Changes
59. T. Teramoto (Editor)
Deep Ocean Circulation – Physical and Chemical Aspects
60. B. Kjerfve (Editor)
Coastal Lagoon Proceses
61. P. Malanotte-Rizzoli (Editor)
Modern Approaches to Data Assismilation in Ocean Modeling
62. J.H. Stel, H.W.A. Behrens, J.C. Borst, L.J. Droppert and J.P. van der Meulen (Editors)
Operational Oceanography
63. D. Halpern (Editor)
Satellites, Oceanography and Society
64. P. Boccotti
Wave Mechanics for Ocean Engineering
65. Richard E. Zeebe and Dieter Wolf-Gladrow
CO2 in Seawater: Equilibrium, Kinetics, Isotopes
66. N.C. Flemming(Editor-in-Chief)
Operational Oceanography: Implementation at the European and Regional Scales
67. V. C. Lakhan (Editor)
Advances in Coastal Modeling
68. G.J. Goni and P. Malanotte-Rizzoli (Editors)
Interhemispheric Water Exchange in the Atlantic Ocean
69. H. Dahlin, N.C. Flemming, K. Nittis and S.E. Petersson (Editors)
Building the European Capacity in Operational Oceanography
70. Á.Borja and M. Collins (Editors)
Oceanography and Marine Environment of the Basque Country
71. A.G.Kostianoy, J.C.J. Nihoul and V.B. Rodionov
Physical Oceanography of Frontal Zones in the Subarctic Seas
72. W. Fennel and T. Neumann
Introduction to the Modelling of Marine Ecosystems

Elsevier Oceanography Series, 73

GLOBAL CLIMATE CHANGE AND RESPONSE OF CARBON CYCLE IN THE EQUATORIAL PACIFIC AND INDIAN OCEANS AND ADJACENT LANDMASSES

Edited by

H. KAWAHATA
Ocean Research Institute, University of Tokyo, Nakano-ku, Tokyo, Japan

and

Y. AWAYA
Forestry and Forest Products Research Institute, Tsukuba, Iberaki, Japan

ELSEVIER
Amsterdam – Boston – Heidelberg – London – New York – Oxford
Paris – San Diego – San Francisco – Singapore – Sydney – Tokyo

Elsevier
Radarweg 29, PO Box 211, 1000 AE Amsterdam, The Netherlands
The Boulevard, Langford Lane, Kidlington, Oxford OX5 1GB, UK

First edition 2006

Library of Congress Cataloging-in-Publication Data
A catalog record for this book is available from the Library of Congress

British Library Cataloguing in Publication Data
A catalogue record for this book is available from the British Library

ISBN-13: 978-0-444-52948-0
ISBN-10: 0-444-52948-9
ISSN: 0422-9894 (series)

Printed and bound in The Netherlands

06 07 08 09 10 10 9 8 7 6 5 4 3 2 1

List of Contributors

John R. Moisan (27)
Kei Muneyama (255)
Hiroyuki Muraoka (417)
Akihiko Murata (1)
Shoichiro Nakamoto (255)
Kisaburo Nakata (255)
Douglas J. Neilson (27)
Josef M. Oberhuber (255)
Yusuke Oe (445)
Toshiyuki Ohtsuka (395)
Takehisa Oikawa (335)
Albert Olioso (295)
David W. Pierce (27)
S. Prasanna Kumar (255)
Stéphanie Reynaud (239)
Tim Rixen (157)
Claire Rollion-Bard (239)
Hironori Sako (395)
Andreas Schiller (175)
Haruhisa Shimoda (383)
Fernando P. Siringan (210)
Janet Sprintall (175)
Bulusu Subrahmanyam (255)
Atsushi Suzuki (210)
Atsushi Tsuda (65)
Masaki Uchida (395)
Kyozo Ueyoshi (255)
Rik Wanninkhof (1)
Tsuyoshi Watanabe (239)
Susan E. Wijffels (175)
Katsumi Yokouchi (65)
Minoru Yoneda (210)
Dafang Zhuang (361)

Contents

This page intentionally left blank

Chapter 1

Long-Term Trend of the Partial Pressure of CO_2 in Surface Waters and Sea–Air CO_2 Flux in the Equatorial Pacific

Hisayuki Y. Inoue[1,5,*], Richard A. Feely[2], Masao Ishii[1], Takeshi Kawano[3], Akihiko Murata[3] and Rik Wanninkhof[4]

[1]*Geochemical Research Department, Meteorological Research Institute, Tsukuba, Ibaraki 305-0052, Japan*
[2]*Pacific Marine Environmental Laboratory, National Oceanic and Atmospheric Administration, Seattle, WA 98115-0070, USA*
[3]*Ocean Research Department, Japan Marine Science and Technology Center, Yokosuka, Kanagawa 237-0061, Japan*
[4]*Atlantic Oceanographic and Meteorological Laboratory, National Oceanic and Atmospheric Administration, Miami, FL 33149, USA*
[5]*Laboratory of Marine and Atmospheric Geochemistry, Graduate School of Environmental Earth Sciences, Hokkaido University, Kita-ku, Sapporo 060-0810, Japan*

Abstract

Measurements of partial pressure of CO_2 in surface waters (pCO_2^{sw}) and overlying air (pCO_2^{air}) were made intermittently in the central and western equatorial Pacific from January 1987 to January 2003. We estimated the long-term trend of the pCO_2^{sw} in the high nutrient low chlorophyll (HNLC) region and the western Pacific warm pool. The spatial distribution of pCO_2^{sw} in the HNLC region could be expressed as a linear function of sea surface temperature (SST) and concentration of macronutrients ($[NO_2^-]+[NO_3^-]$), and in the western Pacific warm pool as a function of SST and sea surface salinity (SSS). By using an average SST (27.4 °C) and concentration of nitrate and nitrite (3.9 μmol/kg) in the HNLC

*Corresponding author.
E-mail address: hyoshika@ees.hokudai.ac.jp (H.Y. Inoue).

Elsevier Oceanography Series 73
Edited by H. Kawahata and Y. Awaya
ISBN: 0-444-52948-9

region and the average SST (29.6 °C) and SSS (34.29) in the western Pacific warm pool between 1987 and 2003, we obtained pCO_2^{sw} values for respective cruises. The growth rate of pCO_2^{sw} due to increases in atmospheric CO_2 was calculated to be 1.4 ± 0.5 μatm/yr in the HNLC region and 1.3 ± 0.3 μatm/yr in the western Pacific warm pool. The sea−air CO_2 flux in the equatorial Pacific since 1998 was evaluated by using underway pCO_2^{sw} data measured by Japan Meteorological Agency, Meteorological Research Institute (JMA/MRI), National Oceanic and Atmospheric Administration, Pacific Marine Environmental Laboratory (NOAA/PMEL), and NOAA, Atlantic Oceanographic and Meteorological Laboratory (NOAA/AOML). From 1998 to 2003 the sea−air CO_2 flux in the equatorial Pacific (5°N–10°S, 140°E–90°W) showed lowest flux in January/February 1998 (0.1 ± 0.1 Pg C/yr, 1997/98 El Niño), and highest (0.9 ± 0.4 Pg C/yr) in January/February 2001, suggesting significant interannual variations in sea−air CO_2 flux in the equatorial Pacific. In October 2002−January 2003, which was within a weak El Niño period, the CO_2 flux in the equatorial Pacific was 0.5 ± 0.3 Pg C/yr, almost same as that of the non-El Niño period. In this period, sea−air CO_2 flux in the central and western equatorial Pacific decreased considerably to the same level of January/February 1998, but that in the eastern equatorial Pacific remained fairly constant.

Keywords: partial pressure of CO_2; sea−air CO_2 flux; Oceanic carbon cycle; Equatorial Pacific; Long-term trend

1 Introduction

By exchanging CO_2 with the atmosphere, ocean plays an important role in determining the atmospheric CO_2 level that has been increasing due to human activities (IPCC, 2001). The CO_2 flux between the sea and the overlying air (F) can be estimated by the product of the gas transfer velocity expressed as a function of wind speed (k; Wanninkhof, 1992; Wanninkhof and McGillis, 1999), the solubility of CO_2 (s; Weiss, 1974), and the difference in partial pressure (or fugacity) of CO_2 between the sea surface water and the air ($\Delta pCO_2 = pCO_2^{sw} - pCO_2^{air}$):

$$F = k \cdot s\left(pCO_2^{sw} - pCO_2^{air}\right) \tag{1}$$

The pCO_2^{sw} actually determines whether the ocean acts as a source for atmospheric CO_2 or a sink, because it varies significantly as compared with that of air (see e.g., Takahashi et al., 2002).

The equatorial Pacific is a well-documented source for atmospheric CO_2 in which the sea−air CO_2 flux has been estimated to vary between 0.02 and 0.96 Pg–C/yr, depending on changes in physical and biological processes driven by the El Niño−southern oscillation (ENSO) phenomena (Feely et al., 2002). As described by Le Borgne et al. (2002), the equatorial Pacific consists of two regions that have distinct carbon system dynamics: the high nutrient

low chlorophyll (HNLC) region and the western Pacific warm pool. The HNLC region extends from the eastern edge of the western Pacific warm pool to the coast of south America. Since the 1980s temporal and spatial variations in pCO_2^{sw} in the equatorial Pacific have been examined (see e.g., Feely et al., 2002; Takahashi et al., 2003). According to Feely et al. (2002), the prominent feature of pCO_2^{sw} in the eastern equatorial Pacific can be described as follows. Shoaling thermocline to the east and local upwelling and the Peruvian upwelling bring waters containing high CO_2 concentration to the surface. The northward-flowing Peru Current entrains water with high pCO_2^{sw} into the south equatorial current (SEC). These lead to the highest pCO_2^{sw} in the eastern equatorial Pacific HNLC region. A steep gradient of pCO_2^{sw} occurs between the SEC and the north equatorial counter-current (NECC) with pCO_2^{sw} nearly equal to that of air. The boundary between the SEC and NECC ranges from 0.5° or less from the equator in the east to 5°N at 140°W. The boundaries of the regions vary due to the phase of the ENSO cycle and the presence of the tropical instability waves.

The pCO_2^{sw} in the western Pacific warm pool, characterized by high sea surface temperature (SST $>$ 28.5 °C), low sea surface salinity (SSS $<$ 34.5), and low concentration of macronutrients, tend to be slightly supersaturated with respect to that of atmospheric CO_2 (Inoue et al., 1996, 2001; Feely et al., 2002; Le Borgne et al., 2002). In the central and western equatorial Pacific, the longitudinal distributions of pCO_2^{sw}/SSS vary depending on the geographical position of the boundary between the HNLC region and western Pacific warm pool. Inoue et al. (1996) reported that the longitude with high gradient of pCO_2^{sw}/SSS (the eastern edge of warm pool) was related to the southern oscillation index (SOI; Le Borgne et al., 2002; Ishii et al., 2003). The western Pacific warm pool migrates eastward during the El Niño event (Picaut et al., 1996; Delcroix et al., 1998; Johnson et al., 2000), which leads to a decrease in pCO_2^{sw} to near equilibrium with respect to the air. Boutin et al. (1999) reported that western Pacific warm pool moving east–west exerts strong control on the sea–air CO_2 flux in the equatorial Pacific.

By using atmospheric inversions and ocean models, Le Quéré et al. (2003) report that ocean and land sinks are estimated to be, respectively, 0.3 (0.1–0.6) and 0.7 (0.4–0.9) Pg C/yr larger in the 1990s than in the 1980s. Oceanic regions where long-term variations in sea–air CO_2 flux occur should be determined in order to understand the changing global carbon cycle; examining spatial distributions of pCO_2^{sw} over decades is of particular importance in order to elucidate the long-term variations in oceanic uptake of anthropogenic CO_2. In the equatorial Pacific, there have been a few studies of the long-term trend of pCO_2^{sw}, which is mainly caused by the large interannual variations in pCO_2^{sw} described above. In the eastern equatorial Pacific, Feely et al. (1999) estimated the long-term trend of pCO_2^{sw} in the center of upwelling area near the equator (1.27 ± 0.18 μatm/yr). In the

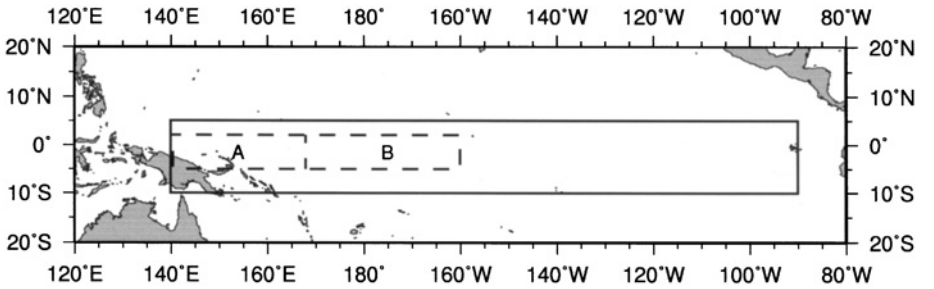

Figure 1: Equatorial Pacific where air−sea CO_2 flux was examined (5°N–10°S, 140°E–80°W, surrounded by solid line). The long-term trend of pCO_2^{sw} (dashed line) was examined in the western Pacific warm pool (A) and the HNLC region (B).

southern subtropical zone along 150°W, Feely et al. (2002) reported the growth rate of pCO_2^{sw} of 1.0 ± 0.3 μatm/yr, similar to that found by Feely et al. (1999) in the center of upwelling area. In the subtropics of the western North and South Pacific, however, the long-term trend of pCO_2^{sw} (Inoue et al., 1995, 1999) is similar. Recently, Takahashi et al. (2003) determined a change in the pCO_2^{sw} growth rate in the central and western equatorial Pacific between 1980s and 1990s attributed it to the changes in the phase of the Pacific decadal oscillation (PDO) that occurred between 1988 and 1992. They reported that before the PDO phase shift the *in situ* pCO_2^{sw} changed at a mean rate of 5 ± 3 μatm per decade in the western Pacific warm pool and -9 ± 13 μatm per decade in the central equatorial Pacific and after the PDO phase shift 34 ± 4 μatm per decade in the western Pacific warm pool and 18 ± 7 μatm per decade in the central equatorial Pacific.

In this work, first we will examine the long-term trend of pCO_2^{sw} in the central and western equatorial Pacific (Fig. 1) by using the data measured by the MRI/JMA group over the period from January 1987 to March 2003 (Table 1), and then variations in sea−air CO_2 flux in the equatorial Pacific (Fig. 1, 5°N–10°S, 140°E–90°W) by combining data taken after 1998 with underway pCO_2^{sw} (fCO_2^{sw}) data (http://www.pmel.noaa.gov/uwpco2/, http://www.aoml.noaa.gov/ocd/oaces/mastermap.html) taken by the CO_2 groups of the National Oceanic and Atmospheric Administration, the Pacific Marine Environmental Laboratory (NOAA/PMEL) and the Atlantic Oceanographic and Meteorological Laboratory (NOAA/AOML).

2 Observations

Japan Meteorological Agency, Meteorological Research Institute (JMA/MRI) measurements of pCO_2^{sw} and pCO_2^{air} used in this work were made in the

Table 1: Cruise list in the equatorial Pacific (5°N−10°S) used in this work

Cruise name	Time of observation	Latitude	Longitude	SOI[1]	Ship
JENEX-87	Jan.–Feb. 1987	5°N–5°S	160°E–160°W	−1.4	Natsushima
JAPACS-89	Jan.–Feb. 1989	5°N–5°S	160°E–160°W	1.4	Natsushima
JAPACS-90	Jan.–Feb. 1990	5°N–5°S	147°E–160°W	−1.3	Natsushima
KH90-2&3	Sept.–Dec. 1990	5°N–10°S	148°E–150°W	−0.5	Hakuho-maru
JAPACS-91	Jan.–Feb. 1991	5°N–5°S	147°E–160°W	0.3	Natsushima
KY9401	Jan.–Feb. 1994	5°N–4°S	135°E–165°W	−0.2	Kaiyo
KY9411	Nov.–Dec. 1994	5°N–0°	146°E–165°W	−1.2	Kaiyo
KY9512	Dec. 1995–Feb. 1996	5°N–3°S	137°E–165°W	0.0	Kaiyo
KY9701	Dec. 1996–Feb. 1997	5°N–5°S	132°E–167°W	1.0	Kaiyo
RY9709	October 1997	5°N–2°S	145°E–165°E	−1.9	Ryofu-maru
KY9712	Dec. 1997–Jan. 1998	5°N–5°S	136°E–180°	−2.3	Kaiyo
MR97K2	Feb. 1998	5°N–0°	176°E–164°W	−2.7	Mirai
Ka'imimoana TAO	Feb.–May 1998	8°N–8°S	95°W–110°W	−2.0	Ka'imimoana
MR98K2	Jan. 1999	5°N–0°	135°E–167°W	2.0	Mirai
KY9901	Jan.–Feb. 1999	5°N–1°S	137°E–168°E	1.4	Kaiyo
Ka'imimoana TAO	Jan.–Feb. 1999	5°N–10°S	125°W–140°W	1.4	Ka'imimoana
MR99K6&7	Oct.–Dec. 1999	5°N–5°S	135°E–167°W	1.2	Mirai
Ron Brown TAO	Nov.–Dec. 1999	5°N–10°S	95°W–110°W	1.3	Ron Brown
MR00K8	Jan. 2001	5°N–0°	145°E–160°W	1.1	Mirai
GasEx 2001	Jan.–Mar. 2001	5°N–10°S	92°W–140°W	1.0	Ron Brown
MR01K1	Feb.–Mar. 2001	5°N–5°S	147°E–156°E	1.0	Mirai
Ron Brown TAO	Nov. –Dec. 2001	5°N–10°S	90°W–110°W	−0.3	Ron Brown
MR02K1&2	Jan.–Mar. 2002	5°N–5°S	145°E–160°W	0.1	Mirai
Ron Brown TAO	Oct. –Nov. 2002	5°N–8°S	95°W–114°W	−0.7	Ron Brown
MR02K6	Nov. 2002–Mar. 2003	5°N–5°S	138°E–160°W	−0.9	Mirai

[1]The monthly SOI values are taken from the Climate Prediction Centre (http://www.cpc.ncep.noaa.gov).

equatorial Pacific from January 1987 to February 2003. Underway measurements of pCO_2^{sw} and pCO_2^{air} for these cruises were carried out with systems reported earlier (Inoue, 2000; Körtzinger et al., 2000). The underway system consists of a nondispersive infrared gas analyzer, a shower-head-type equilibrator, diaphragm pumps, and a unit for removal of water vapor in sample air. Uncontaminated water from the inlet of sample seawater about 4–5 m below the surface was continuously pumped at flow rates >50 L/min to the laboratory and introduced into the equilibrator at approximately 10 L/min. CO_2 in the water equilibrates with recirculated air in the shower-head-type equilibrator. The CO_2 mole fraction in the dry air equilibrated with seawater was determined by using working reference gases traceable to the WMO mole fraction scale.

The underway measurements of fCO_2^{sw} and fCO_2^{air} were made aboard the NOAA ships *Malcolm Aldridge*, the *Discoverer*, the *Ka'imimoana* and *Ron Brown* by using similar systems as described above and detailed in Wanninkhof and Thoning (1993) and Feely et al. (1998). In this work, the precision and accuracy of the xCO_2^{sw}, CO_2 mixing ratio in the dry air equilibrated with surface seawater, was estimated to be within 1–2 ppm. Results of an intercomparison held aboard the FS Meteor in the North Atlantic in June 1996, which included the JMA/MRI system but not the NOAA systems, generally agree with about 2 ppm (Körtzinger et al., 2000).

3 Results and Discussion

3.1 Long-Term Trend of pCO_2^{SW} in the HNLC Region

As compared with pCO_2^{sw} distribution in the subtropics showing basically the same pattern in the same time (month) of the year (Inoue et al., 1995), the pCO_2^{sw} distribution in the equatorial Pacific varied considerably especially associated with the ENSO phenomena (Fig. 2). In the equatorial Pacific, therefore, it is extremely difficult to detect the long-term trend of pCO_2^{sw} by simply comparing pCO_2^{sw} data taken several years apart (Goyet and Peltzer, 1994).

Thermodynamics, ocean dynamics (lateral flow, vertical mixing, and upwelling of water), and biological activities are considered to be major processes (Poisson et al., 1993; Lee et al., 1998) affecting pCO_2^{sw} via changes in total dissolved inorganic carbon (DIC), total alkalinity, pH, temperature, and salinity. One of the approaches for evaluating the long-term trend is to compare the pCO_2^{sw} data taken at the same thermodynamic, oceanographic and biological conditions. Feely et al. (1999) have reported the long-term trend of pCO_2^{sw} for the core of upwelled water in the region of temperature minimum near the equator between 140 and 160°W using temperature

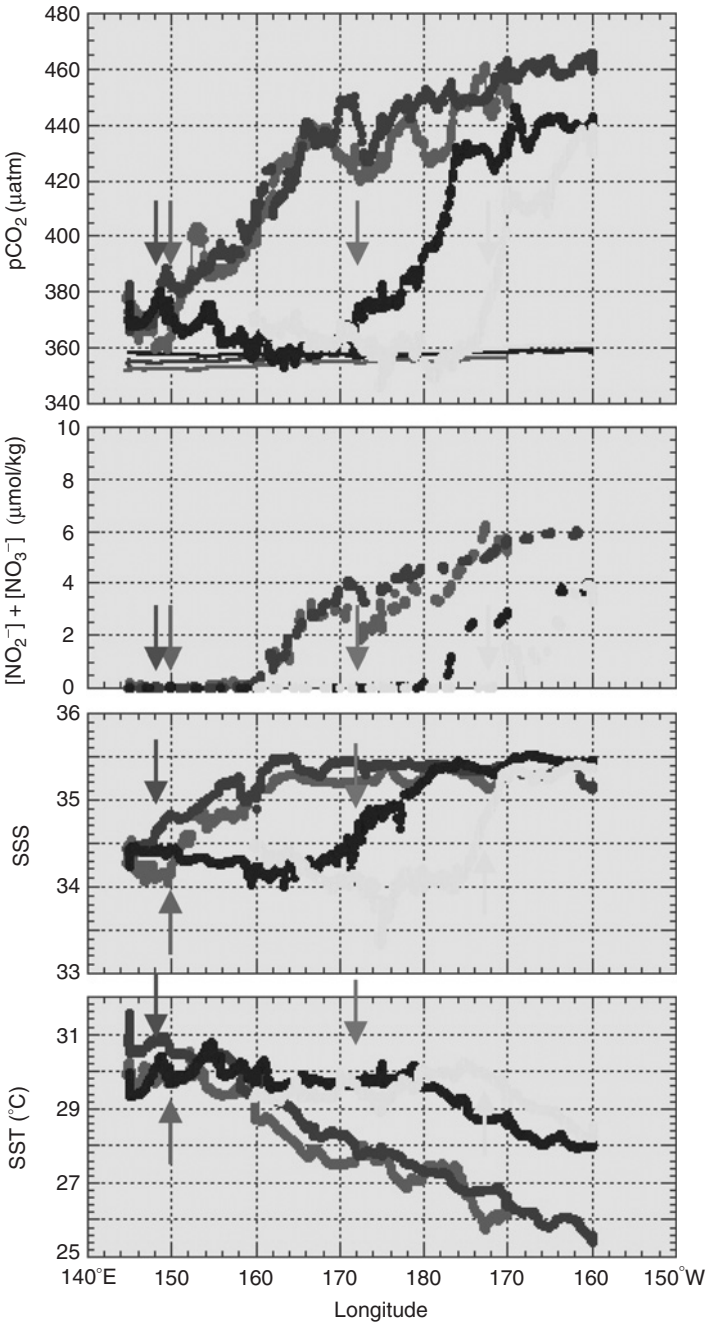

Figure 2: Longitudinal distributions of pCO_2^{sw}, pCO_2^{air}, $[NO_2^-]$+$[NO_3^-]$, SSS and SST along the equator in October/December 1999 (red), January/March 2001 (blue), January/March 2002 (green) and November 2002/March 2003 (yellow). In the upper panel, the thick line shows pCO_2^{sw} and the thin line pCO_2^{air}. Arrows show the boundary between the HNLC region and western Pacific warm pool (For colour version, see Colour Plate Section).

normalized pCO_2^{sw} values. Feely et al. (2002) also discussed the long-term trend of pCO_2^{sw} along 150°W between 1979 and 1990s by using a pCO_2^{sw}−SST relationship.

As pointed out by Wanninkhof et al. (1996), SST by itself is not a robust predictor of pCO_2^{sw} in the HNLC region. Dandonneau (1995) concluded that most of the variations of pCO_2^{sw} in the eastern equatorial Pacific were coherent in parallel with nitrate concentration and fluorescence, and inversely with SST. Wanninkhof et al. (1996) reported that the pCO_2^{sw} showed the best correlation with a combination of NO_3^- and SST:

$$pCO_2^{sw} = A_c + B_c(\mathrm{SST}) + C_c([NO_2^-] + [NO_3^-]) \quad (2)$$

where A, B, and C are coefficients determined empirically and subscript c means the HNLC region. In this work, we assumed that calculating the pCO_2^{sw} normalized to the same SST and concentration of nitrate and nitrite ($[NO_2^-]$+$[NO_3^-]$, hereafter expressed as NO_3) is the best approach to determine the pCO_2^{sw} value at the same conditions of thermodynamics, ocean dynamics and biological activities in the HNLC region. The spatial distribution of pCO_2^{sw} in the HNLC region was generally approximated well using equation (2) (Table 2). An example of the least squares fit of equation (2) to the data in January 2001 is shown in Fig. 3, in which the pCO_2^{sw} has been calculated with a root-mean-squares deviation (rms) of 2 μatm. However, the coefficients for this relationship cannot be applied to the data during other phases of the ENSO cycle with the same amount of accuracy (Wanninkhof et al., 1996). For example, the relationship of pCO_2^{sw} with SST and NO_3 in January 2001 gave a deviation (bias) of about 13 μatm for the pCO_2^{sw} in January/February 1999 (Table 2).

In order to evaluate the long-term trend, we determined the coefficients and the intercept of equation (2) for respective cruises (Table 2) and then calculated the pCO_2^{sw} normalized to the average SST and NO_3. The average SST (27.4 °C) and NO_3 (3.9 μmol/kg) observed from 1989 to 2003 minimize any effects of changes in thermodynamics, ocean dynamics, and biological activity on the pCO_2^{sw}. By assuming the linear long-term trend, the growth rate of pCO_2^{sw} at the average SST and NO_3 was estimated to be 1.4 ± 0.5 μatm/yr (Fig. 4) in the HNLC region, which is very similar to the increase in atmospheric CO_2. Figure 5 represents the growth rate of pCO_2^{sw} expressed as a function of SST and NO_3, which varied from 0.6 to 2.1 μatm/yr. If the pCO_2^{sw} were determined at exactly the same condition of thermodynamics, ocean dynamics, and biological activity, the calculated growth rate of pCO_2^{sw} would be the same irrespective of changes in SST and NO_3. NO_3 increases with decrease in SST (Chavez et al., 1996). In this context, the fairly constant growth rate of pCO_2^{sw} with conditions between low SST−high NO_3 and high SST−low NO_3 as indicated by an arrow in Fig. 5,

Table 2: Multiple linear regressions to estimate the spatial distribution of pCO_2^{sw} in the HNLC region in 1989−2003

Time of observation	Longitude	Equation	n	r
Jan.–Feb. 1989	160°E–160°W	$pCO_2^{sw}(\pm 3.8) = 263.9(\pm 78.3)+4.36(\pm 2.59)SST+9.44(\pm 2.08)NO_3$	9	0.948
Sep.–Oct. 1990	180°–150°W	$pCO_2^{sw}(\pm 5.9) = 807.9(\pm 84.9)-14.65(\pm 2.88)SST+2.37(\pm 1.45)NO_3$	23	0.952
Jan. 1994	175°E–165°W	$pCO_2^{sw}(\pm 3.8) = 1060.9(\pm 267.0)-22.35(\pm 8.92)SST-2.37(\pm 5.75)\ NO_3$	7	0.989
Jan. 1996	176°E–165°W	$pCO_2^{sw}(\pm 3.6) = -137.2(\pm 183.5)+18.07(\pm 6.14)SST+20.16(\pm 4.66)NO_3$	8	0.948
Jan. 1997	173°E–167°W	$pCO_2^{sw}(\pm 2.7) = 372.2(\pm 56.7)+0.87(\pm 1.90)SST+11.86(\pm 1.19)NO_3$	32	0.984
Jan. 1999	171°E–171°W	$pCO_2^{sw}(\pm 3.4) = 168.5(\pm 90.6)+7.29(\pm 3.17)SST+16.58(\pm 2.18)NO_3$	68	0.969
Dec. 1999	162°E–170°W	$pCO_2^{sw}(\pm 3.9) = 412.0(\pm 41.9)-0.07(\pm 1.44)SST+7.58(\pm 0.77)NO_3$	175	0.941
Jan. 2001	162°E–162°W	$pCO_2^{sw}(\pm 2.6) = 272.1(\pm 25.1)+4.42(\pm 0.82)SST+12.42(\pm 0.60)NO_3$	194	0.978
Jan. 2002	177°W–160°W	$pCO_2^{sw}(\pm 2.1) = 478.3(\pm 70.1)-2.41(\pm 2.34)SST+8.04(\pm 1.25)NO_3$	59	0.957
Jan. 2003	170°W–160°W	$pCO_2^{sw}(\pm 1.7) = 239.1(\pm 41.9)+5.28(\pm 1.40)SST+12.33(\pm 0.62)NO_3$	94	0.987

Note: The standard error of analysis (in μatm) is listed in parentheses after pCO_2^{sw}, the standard error for the coefficient and intercept are in parenthesis after coefficient and intercept, n is the number of data, and r is the correlation coefficient. Macronutrients in surface seawater were monitored continuously for cruises conducted after 1999.

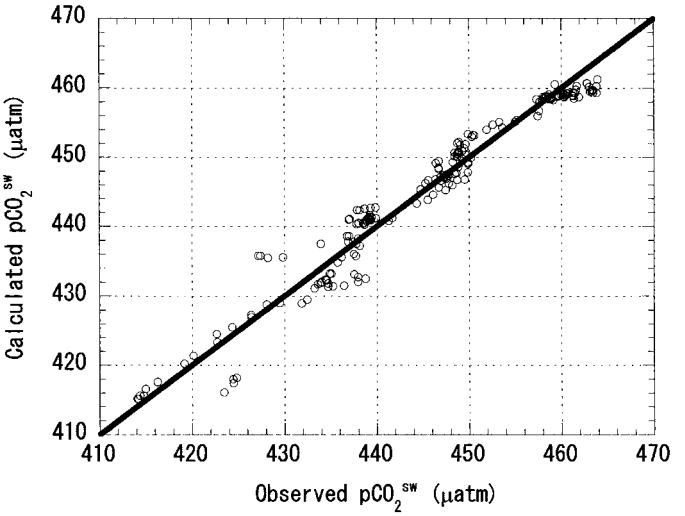

Figure 3: The pCO_2^{sw} calculated as the function of SST and NO_3 against observed pCO_2^{sw} in January/February 2001.

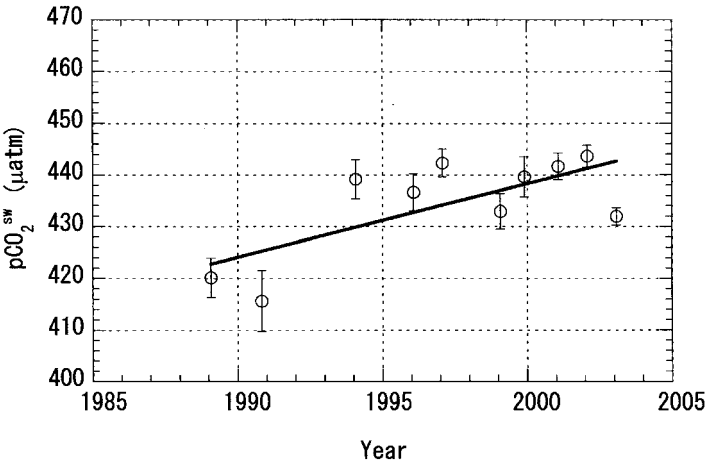

Figure 4: The pCO_2^{sw} at average SST (27.4 °C) and NO_3 (3.9 μmol/kg) in the HNLC region west of 150°W in 1989–2003. The solid line shows the linear long-term trend of $pCO_2^{sw}(t) = 1.4(t–1985)+418.0$, where t is the elapsed time (year) since January 1985. The standard error of analysis was 7.4 μatm, and the standard error for the coefficient was 0.5 μatm/yr, intercept 6.7 μatm and the correlation coefficient was 0.68.

could suggest the validity of the present approach for estimating the long-term trend of pCO_2^{sw}.

Our results obtained in the HNLC region also agreed well with the increase of pCO_2^{sw} in the core of upwelled water, where the entrained

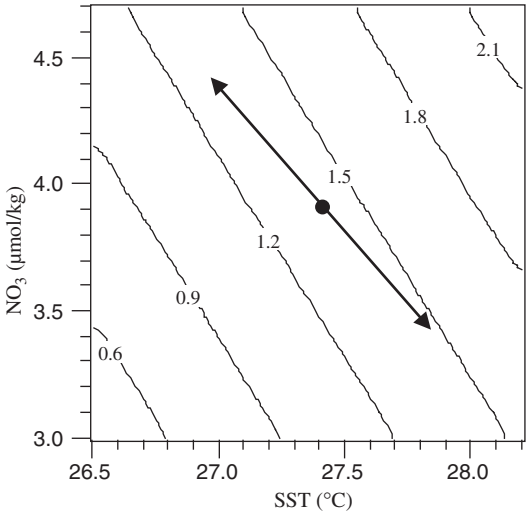

Figure 5: The growth rate of pCO_2^{sw} that was calculated using SST and NO_3 via equation (2). Solid circle shows the growth rate of pCO_2^{sw} at average SST and NO_3. An arrow shows apparent SST dependence of NO_3^- observed in the HNLC region.

subtropical water is injected into the upwelled water at the equator. This suggests that the upwelled water has been recently exposed to, and equilibrated with, the atmosphere (Feely et al., 1999). After upwelling of water, the current atmospheric CO_2 level does not largely affect the growth rate of pCO_2^{sw} in the HNLC region, suggesting a relatively small uptake of anthropogenic CO_2 in the HNLC region. The apparent growth rate of total DIC in the HNLC region inferred from pCO_2^{sw} and buffer (Revelle) factor is estimated to be $\sim$0.8 μmol/kg/yr. This agrees well with the DIC increase of 0.91 ± 0.09 mol/kg/yr that Ishii et al. (2003) deduced from the apparent temperature dependence of normalized DIC and total alkalinity.

3.2 Long-Term Trend of pCO_2^{sw} in the Western Pacific Warm Pool

The western Pacific warm pool migrates eastward following the occurrence of El Niño. In this warm pool, high pCO_2^{sw} is absent due to a deep thermocline and nutricline, combined with a barrier layer produced by shallow haloclines (Le Borgne et al., 2002). A barrier layer between a shallow halocline and the top of the thermocline prevents entrainment of cold water, rich in CO_2 and nutrients, across the bottom of the mixed layer, indicating the importance of surface salinity field in the warm pool on modulating pCO_2^{sw} levels. The distribution of pCO_2^{sw} in the western Pacific warm pool can be approximated well by a linear function of SST and SSS

(Inoue et al., 2001):

$$pCO_2^{w} = A_w + B_w(SST) + C_w(SSS) \quad (3)$$

where A, B, and C are coefficients determined empirically and subscript w means western Pacific warm pool. The relationship of pCO_2^{sw} with SST and SSS in January/February 2002 is shown as an example in Fig. 6. This relationship of pCO_2^{sw} with SST and SSS cannot be applied to the data recorded during other periods (Table 3), as is the case for equation (2) in the HNLC region. The growth rate of pCO_2^{sw} at the average SST and SSS observed in 1987−2003 is calculated to be 1.3 ± 0.3 µatm/yr in the western Pacific warm pool (Fig. 7). Within the range of a standard deviation from the average for SST and SSS, the long-term trend of pCO_2^{sw} ranged from 1.0 to 1.6 µatm/yr (Fig. 8). With respect to changes in SST and SSS in the western Pacific warm pool, Ando and Kuroda (2002) reported two dominant modes: a positive correlation mode in which the density field is not affected and a negative correlation mode having substantial impact on the density field. The fairly constant growth rate of pCO_2^{sw} occurred under conditions of increasing SST and SSS and thus a negligible change in the density field. A stable density field provides favorable conditions for determining the long-term trend of pCO_2^{sw}. The growth rate of pCO_2^{sw} determined for average SST and SSS in the western Pacific warm pool is equal to that given by the average SST and NO_3 in the HNLC region.

In order to evaluate the long-term trend of pCO_2^{sw} in the HNLC region and western Pacific warm pool, we used a multiple linear regression

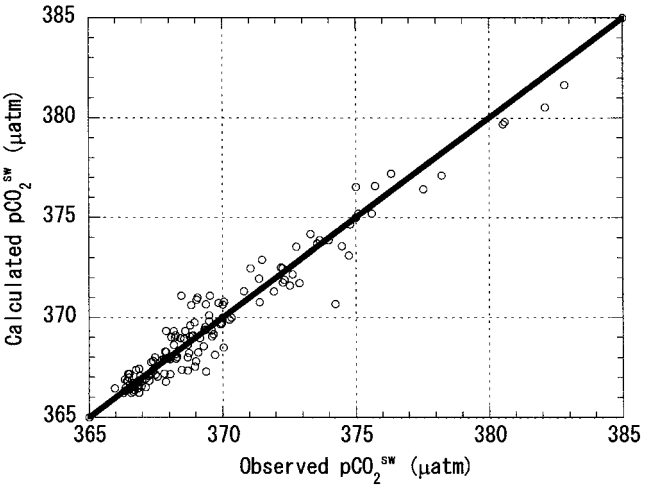

Figure 6: The pCO_2^{sw} calculated as a function of SST and SSS against observed pCO_2^{sw} in January/February 2001.

Table 3: Multiple linear regressions to estimate the spatial distribution of pCO_2^{sw} in the western Pacific warm pool in 1987−2003

Time of observation	Longitude	Equation	n	r
Jan.–Feb. 1987	160°E–180°	$pCO_2^{sw}(\pm 2.4) = -717.6(\pm 242.7)+10.66(\pm 2.82)SST+21.90(\pm 5.45)SSS$	19	0.743
Jan.–Feb. 1990	147°E–170°E	$pCO_2^{sw}(\pm 0.9) = -619.9(\pm 242.7)+8.54(\pm 3.46)SST+21.08(\pm 2.59)SSS$	8	0.972
Nov. 1990	160°E–170°E	$pCO_2^{sw}(\pm 1.8) = 88.8(\pm 124.9)-1.36(\pm 2.37)SST+8.71(\pm 2.62)SSS$	10	0.800
Feb. 1991	147°E–165°E	$pCO_2^{sw}(\pm 3.1) = -605.8(\pm 204.4)+7.47(\pm 6.37)SST+21.24(\pm 7.96)SSS$	11	0.859
Jan.–Feb. 1994	138°E–160°E	$pCO_2^{sw}(\pm 6.5) = -20.2(\pm 155.3)-7.57(\pm 1.58)SST+17.42(\pm 3.75)SSS$	192	0.555
Nov.–Dec. 1994	147°E–170°W	$pCO_2^{sw}(\pm 3.1) = -82.0(\pm 32.8)+13.2(\pm 0.88)SST+1.36(\pm 1.16)SSS$	363	0.710
Dec. 1995	147°E–157°E	$pCO_2^{sw}(\pm 3.0) = -325.1(\pm 93.6)+5.83(\pm 2.48)SST+14.87(\pm 2.48)SSS$	68	0.680
Jan.–Feb. 1997	137°E–165°E	$pCO_2^{sw}(\pm 3.6) = -249.2(\pm 94.6)-1.44(\pm 1.42)SST+19.19(\pm 3.46)SSS$	43	0.736
Oct. 1997	147°E–165°E	$pCO_2^{sw}(\pm 2.3) = -579.0(\pm 38.3)+10.43(\pm 0.67)SST+18.60(\pm 0.89)SSS$	162	0.890
Dec. 1997	143°E–178°E	$pCO_2^{sw}(\pm 2.8) = -536.2(\pm 22.2)+9.46(\pm 0.42)SST+18.21(\pm 0.85)SSS$	774	0.904
Feb. 1998	180°–163°W	$pCO_2^{sw}(\pm 2.6) = -439.5(\pm 42.6)–2.44(\pm 0.64)SST+25.27(\pm 0.97)SSS$	184	0.863
Jan. 1999	142°E–152°E	$pCO_2^{sw}(\pm 1.9) = -575.1(\pm 66.9)+7.66(\pm 1.14)SST+20.60(\pm 1.91)SSS$	177	0.733
Nov. 1999	143°E–151°E	$pCO_2^{sw}(\pm 1.7) = -1344.6(\pm 39.8)+9.89(\pm 0.89)SST+41.37(\pm 1.00)SSS$	182	0.959
Jan.–Feb. 2002	145°E–170°E	$pCO_2^{sw}(\pm 2.5) = -1665.1(\pm 50.0)+9.23(\pm 0.48)SST+51.15(\pm 1.38)SSS$	374	0.905
Mar. 2002	145°E–156°E	$pCO_2^{sw}(\pm 2.5) = -525.5(\pm 58.5)–15.27(\pm 0.77)SST+38.91(\pm 1.53)SSS$	364	0.871
Jan. 2003	160°E–180°E	$pCO_2^{sw}(\pm 1.4) = -485.9(\pm 10.1)+4.89(\pm 0.36)SST+20.67(\pm 0.25)SSS$	382	0.982

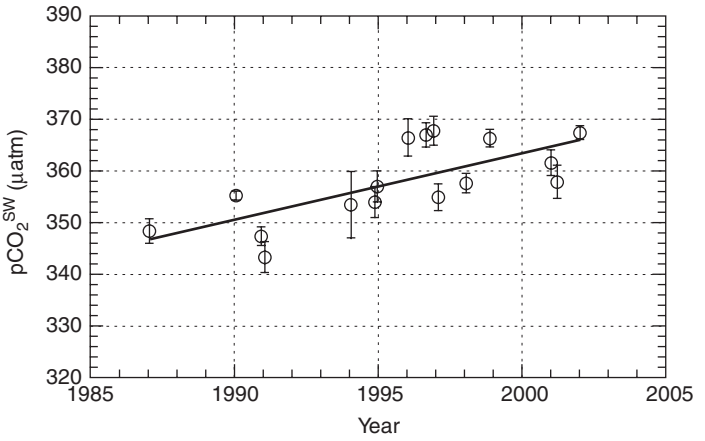

Figure 7: The pCO_2^{sw} at average SST (29.5 °C) and SSS (34.29) in the western Pacific warm pool in 1987–2003. The solid line shows the linear long-term trend of $pCO_2^{sw}(t) = 1.3(t-1985)+344.0$, where t is the elapsed time (year) since January 1985. The standard error of analysis was 5.6 µatm, and the standard error for the coefficient was 0.3 µatm/yr, intercept 5.6 µatm and the correlation coefficient was 0.71.

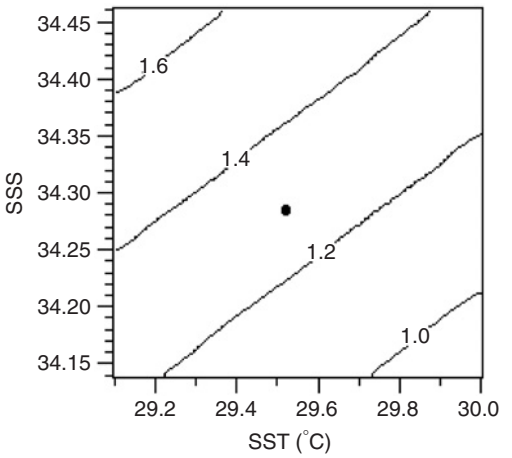

Figure 8: The growth rate of pCO_2^{sw} that was calculated using SST and SSS via equation (3). Solid circle shows the growth rate of pCO_2^{sw} at average SST and SSS.

analysis given by equations (2) and (3). With respect to spatial distributions, the pCO_2^{sw} can be calculated well with rms of 2–3 µatm for the HNLC and the western Pacific warm pool. In this work, we examined the long-term trend of pCO_2^{sw} at given SST and NO_3 in the HNLC region and SST and SSS

in the western Pacific warm pool, which might provide the pCO_2^{sw} at the same conditions of thermodynamics, ocean dynamics and biological activity. At average values of SST and NO_3 in the HNLC region and SST and SSS in the western equatorial Pacific warm pool observed from 1987 to 2003, the long-term trend of pCO_2^{sw} was calculated to be 1.4 ± 0.5 µatm/yr in the HNLC region and 1.3 ± 0.3 µatm/yr in the western Pacific warm pool. The growth rates of pCO_2^{sw} for both regions were close to that in the core of upwelled water between 140 and 160°W (Feely et al., 1999; Feely et al., 2002) and pCO_2^{air} (1.6 ± 0.4 µatm/yr). The growth rates of pCO_2^{air} was calculated from the atmospheric data from Christmas Island (1°42′N, 157°10′W) and container ships by NOAA/CMDL (Conway et al., 1994). The growth rate of pCO_2^{sw} in the central and western equatorial Pacific and that of the core of upwelled water suggests a somewhat smaller uptake of anthropogenic CO_2 after upwelling than other portions of the North Pacific (Sabine et al., 2004). Takahashi et al. (2003) showed that the pCO_2^{sw} over the Pacific equatorial zone appears to have changed substantially during the past two decades in coincidence with the PDO phase shift that occurred between 1988 and 1992. They reported that after the PDO phase shift ΔpCO_2 increased by 19 µatm in the western area by the year 2001. This includes changes in carbonate system other than uptake of anthropogenic CO_2, that is, ocean dynamics and/or biological activity. The extremely high growth rate of pCO_2^{sw} (2.5 ± 0.3 µatm/yr) was reported at the time-series station ALOHA in the North Pacific subtropical gyre (Dore et al., 2003). Keeling et al. (2004) proposed that the large increase in pCO_2^{sw} resulted mainly from the increased flow from northwestern waters with greater pCO_2^{sw} and salinity related to a large-scale reorganization of the climate system over the North Pacific. Our data sets are mostly taken after the PDO phase shift (Takahashi et al., 2003) and include data from 5°S to 2°N, 137°E to 170°W in the western Pacific warm pool. In order to examine temporal and spatial variations in growth rate of pCO_2^{sw} in the equatorial Pacific, it is further necessary to conduct precise and repeated measurements at least over a few decades.

3.3 Air–Sea CO_2 Flux in the Equatorial Pacific

If the parameters SST, SSS, and NO_3 are measured widely and remotely like SST and chlorophyll, we could easily interpolate/extrapolate the observed pCO_2^{sw} data in the equatorial Pacific, which would allow us to evaluate the sea–air CO_2 flux more precisely. Historically, the pCO_2^{sw}–SST or DIC–SST relationship has been used in order to estimate temporal and spatial variations in pCO_2^{sw} in the equatorial Pacific (Lee et al., 1998; Boutin et al., 1999; Loukos et al., 2000; Cosca et al., 2003; Ishii et al., 2003). For example,

on the basis of the assumption that, either directly or indirectly, the thermodynamic, transport, and biological effects are correlated with temperature, Lee et al. (1998) examined the interannual variability of pCO_2^{sw} using the pCO_2^{sw}–SST relationship. Wanninkhof et al. (1996) and Feely et al. (1999, 2002) calculated CO_2 flux along the cruise track by using observed pCO_2^{sw} and extrapolated it to the equatorial Pacific for specific latitude and longitude regions.

As discussed above, the pCO_2^{sw}–SST relationship determined for a certain cruise cannot be applied for long-term changes in pCO_2^{sw} (Dandonneau, 1995; Wanninkhof et al. 1996). The pCO_2^{sw}–SST relationship determined by compiling data taken over several years gives us a spatial average estimate of pCO_2^{sw} variations as a function of SST, because it is determined based on the concept that the observed pCO_2^{sw} included a "random error." With respect to the global carbon cycle, what we would like to know is if the pCO_2^{sw} field including the "random error" varied on time scale of ENSO cycle. The approach by Wanninkhof et al. (1996) and Feely et al. (1999, 2002) is to evaluate this pCO_2^{sw} field, though the pCO_2^{sw} is extrapolated without using parameters that relate to the carbon system.

In this work, we determined pCO_2^{sw}–SST relationships on the basis of data collected within a few months to obtain pCO_2^{sw} distribution on the basis of MRI/JMA, NOAA/PMEL and NOAA/AOML data (Table 3). We divided the equatorial Pacific rather arbitrarily into regions in which a single pCO_2^{sw}–SST relationship was applied (see Appendix). We obtained a pCO_2^{sw} map (Fig. 9) by applying average SST during the observation period (ftp://ftp.ncep.noaa.gov/pub/cmb/sst/oimonth). The CO_2 transfer velocity was calculated by Wanninkhof (1992):

$$k = 0.39 U_{av}^2 (Sc_{20}/Sc)^{1/2} \tag{4}$$

where U_{av} is the averaged wind speed during the observation, and Sc_{20} and Sc are the Schmidt number for CO_2 at 20 °C and at SST. Data of averaged wind speed were acquired from the Japan Meteorological Agency (GANAL data sets).

Boutin et al. (1999) provided a time series of sea–air CO_2 flux of 0.18 Pg C/yr between the equator and 5°S using pCO_2^{sw}–SST and pCO_2^{sw}–SST anomaly relationships, which agreed well with that of Cosca et al. (2003), who gave the mean flux of 0.3 ± 0.1 Pg/yr for an area that covers approximately half of the Pacific equatorial belt (90°W–165°E, 5°N–10°S) during 1985–2001. Loukos et al. (2000) found an average CO_2 flux of 0.5 Pg C/yr for 1982–1993, while recently Ishii et al. (2003) found 0.4 Pg C/yr for 1990–2000.

Table 4 lists the air–sea CO_2 flux obtained in this work. A large sea–air CO_2 flux of 0.9 ± 0.4 Pg C/yr was observed in January/February 2001, and

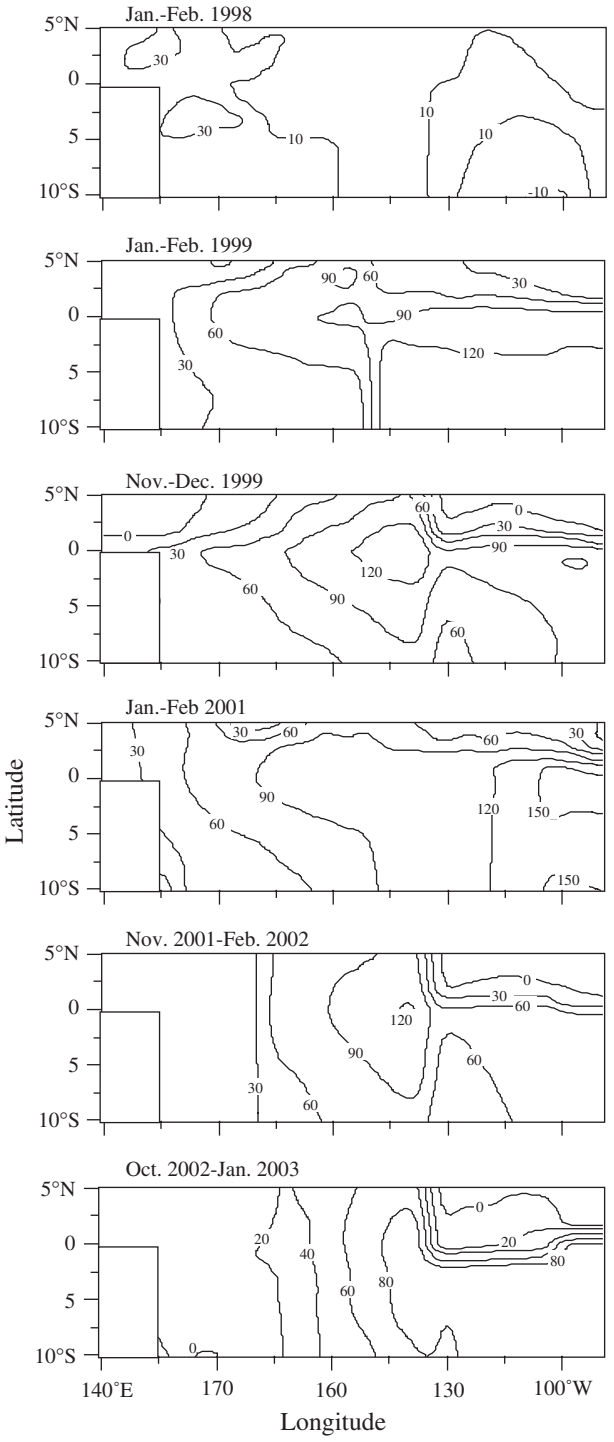

Figure 9: The distribution of ΔpCO_2 in the equatorial Pacific in January/February 1998, January/February 1999, November/December 1999, January/February 2001, November 2001/February 2002, and October 2002/January 2003.

Table 4: Estimated sea-to-air CO_2 flux in the equatorial Pacific during the last 5 years

Year	Month	SOI	Region of interest	Area ($\times 10^6$ km^2)	ΔpCO_2^{sw} (μatm)	Annual flux (Pg C/yr)	Reference
1997/98	Spring–spring		10°N–10°S, 135°E–80°W	35		0.2 ± 0.14	Feely et al., 2002
1998			10°N–10°S, 135°E–80°W	35	30	0.4 ± 0.2	Feely et al., 2002
1998	Jan.–Feb.	−3.0	5°N–10°S, 140°E–90°W	24	12(18)	$0.1 \pm 0.1 (0.08 \pm 0.05)$	This work
1999	Jan.–Feb.	1.4	5°N–10°S, 140°E–90°W	24	71(39)	$0.6 \pm 0.3 (0.2 \pm 0.1)$	This work
1999	Nov.–Dec.	1.3	5°N–10°S, 140°E–90°W	24	64(43)	$0.6 \pm 0.3 (0.2 \pm 0.1)$	This work
2001	Jan.–Feb.	1.3	5°N–10°S, 140°E–90°W	24	88(58)	$0.9 \pm 0.4 (0.3 \pm 0.1)$	This work
2001−2002	Nov.–Feb.	0.2	5°N–10°S, 140°E–90°W	24	50(31)	$0.5 \pm 0.3 (0.1 \pm 0.1)$	This work
2002−2003	Oct.–Jan.	−0.8	5°N–10°S, 140°E–90°W	24	42(18)	$0.5 \pm 0.3 (0.05 \pm 0.03)$	This work

Note: ΔpCO_2 and CO_2 flux west of 160°W (central and western equatorial Pacific) are in parentheses after those of equatorial Pacific.

relatively low CO_2 flux ($\sim$0.5 Pg C/yr) in November 2001/February 2002 and October 2002/January 2003. The lowest CO_2 flux of 0.1 Pg C/yr was estimated for the period of January/February 1998, during the period of 1997/98 El Niño. Feely et al. (2002) estimated the sea−air CO_2 flux of 0.2 ± 0.14 Pg C/yr for the 1-year period from spring 1997 to spring 1998. The bimonthly sea−air CO_2 flux listed in Table 3 varied more than those estimated by using a $pCO_2^{sw}(TCO_2)$–SST relationship over the same period. During 1997−1998, the growth rate of atmospheric CO_2 increased steeply and reached a level larger than 3 ppm/yr in the first half of 1998 and then decreased (http://www.cmdl.noaa.gov/ccg/index.html). It is thus of particular importance to examine the CO_2 flux on time scales of ENSO phenomena (probably shorter than a few months) to figure out the role of the equatorial Pacific in the current global carbon cycle. During the 2002/03 El Niño event (October 2002/January 2003), the pCO_2^{sw} in the central and western equatorial Pacific decreased considerably, but in the eastern equatorial Pacific remained almost at the same level as during the previous non-El Niño period of November 2001/February 2002 (Fig. 10). This led to the relatively lower sea−air CO_2 flux in the central and western equatorial Pacific (west of 160°W) during the 2002/03 El Niño period, which was comparable to that of 1997/98 El Niño. The remarkable contrast between the western and eastern Pacific is attributed to a deeper thermocline and weaker winds in the western Pacific, which causes pCO_2^{sw} values to be nearly in equilibrium with the atmosphere and, hence, the lower sea-to-air CO_2 fluxes. In a remarkable contrast, the eastern Pacific had much higher CO_2 fluxes because the thermocline was almost as shallow as during non-El Niño periods, resulting in very high pCO_2^{sw} values due to upwelling of relatively cold CO_2-enriched waters from the equatorial undercurrent. Coupled with strong southeasterly winds, the resulting CO_2 fluxes during the 2002/03 El Niño in the eastern equatorial Pacific were very similar to the fluxes observed during a non-El Niño period. The central and western equatorial Pacific (west of 160°W) showed relatively large variability of sea−air CO_2 flux as pointed out by Inoue et al. (2002), though changes in sea−air CO_2 flux would only affect the growth rate of atmospheric CO_2 by about $\sim$0.2 ppm/yr. These results suggest the recent phase shift of the 1990s (Chavez et al., 2003; Takahashi et al., 2003) may have resulted in a net increase in the outgasing of CO_2 at the equator, causing an enhancement of the global warming impacts of CO_2 on the atmosphere.

Acknowledgements

We thank officers and crew of R/V Natsushima, R/V Kaiyo, and R/V Mirai belonging to the Japan Marine Science and Technology Center (JAMSTEC),

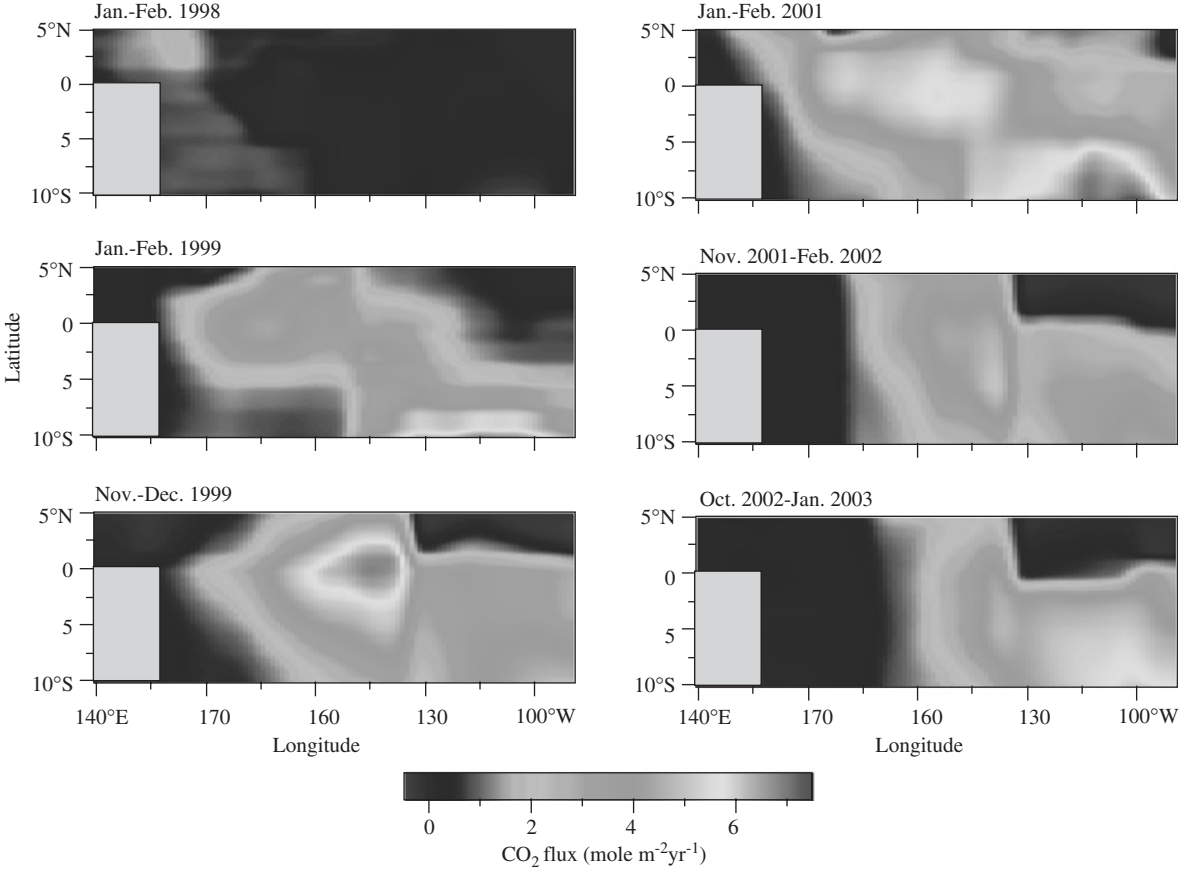

Figure 10: The distribution of CO_2 flux in the equatorial Pacific in January/February 1998, January/February 1999, November/December 1999, January/February 2001, November 2001/February 2002, and October 2002/January 2003 (For colour version, see Colour Plate Section).

of R/V Hakuho-maru belonging to the Ocean Research Institute/University of Tokyo, of R/V Ryofu-maru belonging to the Japan Meteorological Agency and of the ships *Malcolm Aldridge*, the *Discoverer*, and the *Ka'imimoana* and *Ron Brown* of the National Oceanic and Atmospheric Administration (NOAA) of USA. RAF and RW also thank the officers and crew of the NOAA ships *Ronald H. Brown* and *Ka'imimoana* for logistics support. HYI, MI, TK, and AM appreciate the staff of Marine Work Japan Ltd., Nippon Marine Enterprise Ltd., Global Ocean Development Inc., and Kansai Environmental Engineering Center Co. for their technical support on board and providing hydrographic and meteorological data sets. Hydrographic and meteorological data observed aboard the R/V Mirai are/will be available from Data Management Office of JAMSTEC and Japan Oceanographic Data Center. This work was supported by the grant from the "Global Carbon Cycle and Related Mapping based on Satellite Imaginary Program (GCMAPS)" of Ministry of Education, Culture, Sports, Science and Technology, Japan. The Office of National Oceanic and Atmospheric Research of NOAA supported RAF and RW with project support from the Global Carbon Cycle Program under the leadership of Dr. Kathy Tedesco and Dr. Mike Johnson.

Appendix

In order to evaluate the sea−air CO_2 flux in the equatorial Pacific, we divided the equatorial Pacific into regions (Fig. A.1) on the basis of the current system and carbonate chemistry in the equatorial Pacific. In the eastern equatorial Pacific, we evaluated the pCO_2^{sw}–SST relationships in the NECC and SEC by examining the latitudinal distribution of pCO_2^{sw}. The pCO_2^{sw} in the SEC is remarkably larger than pCO_2^{air} and the pCO_2^{sw} in the NECC nearly equal to pCO_2^{air}. If we could not obtain a good pCO_2^{sw}–SST relationship, we divided the SEC and NECC of the eastern Pacific longitudinally into a few regions where a good pCO_2^{sw}–SST relationship was shown. The longitudinal boundary in the eastern and central equatorial Pacific was a mid-point between two meridional transects of shipboard observations. In the central equatorial Pacific, if we observe the pCO_2^{sw}–SST relationship for the NECC, we divided the central Pacific into two regions. Longitudinally we estimated the eastern edge of western Pacific warm pool (western equatorial Pacific) by examining pCO_2^{sw}/SSS change against longitude. If we could not obtain a good pCO_2^{sw}–SST relationship, we divided western equatorial Pacific warm pool into two regions where a good pCO_2^{sw}–SST relationship was shown. The equations used to estimate the pCO_2^{sw} on the basis of SST field are given in the Table A.1.

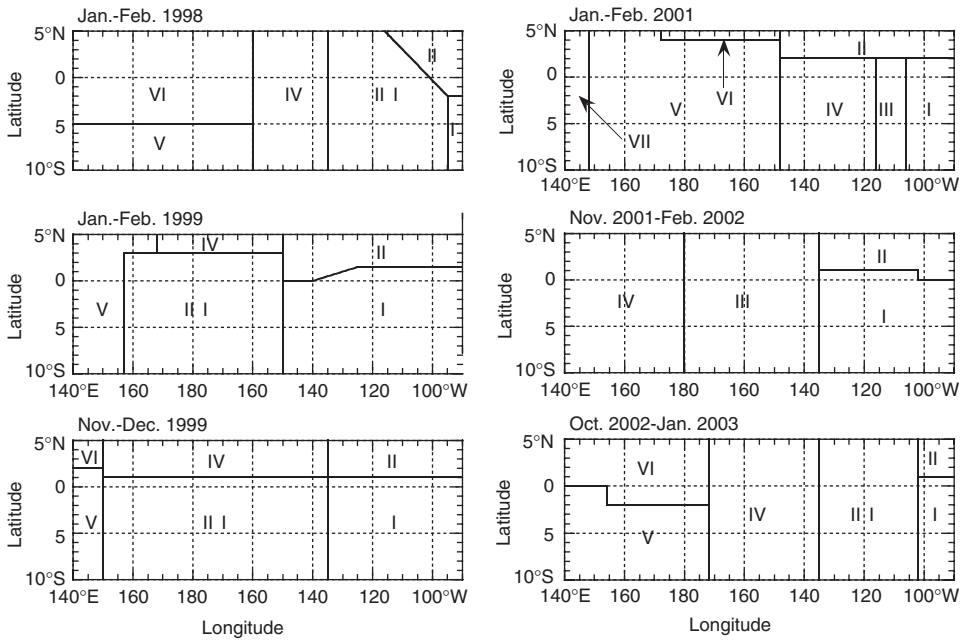

Figure A.1: The equatorial Pacific was divided, rather arbitrarily, into areas that provided a good pCO_2^{sw}–SST relationship. The equations used in the respective areas are given in Table A.1.

Table A.1: pCO_2^{sw}–SST relationship in the equatorial Pacific used in this work.

	January/February 1998	*n*	*r*
Region I	$pCO_2^{sw}(3.5) = 50.7(11.6)+10.73(0.39)SST$ $(SST > 29\,^{\circ}C)$	891	0.678
Region I	$pCO_2^{sw}(4.8) = 363.1$ $(SST \leq 29\,^{\circ}C)$	833	
Region II	$pCO_2^{sw}(8.6) = 354.5$	510	
	$pCO_2^{air} = 347.8(0.9)$	891	
Region III	Inoue et al. (2002)[a]		
Region IV	Inoue et al. (2002)[a]		
Region V	Inoue et al. (2002)[a]		
	January/February 1999		
Region I	$pCO_2^{sw}(6.1) = 269.7(4.7)+8.17(0.19)SST$	498	0.888
Region I	$pCO_2^{sw}(6.7) = 1019.3(6.5)-24.49(0.25)SST$	782	0.961
Region III	$pCO_2^{sw}(5.3) = 758.3(3.7)-12.77(0.14)SST$	661	0.964
Region IV	$pCO_2^{sw}(2.4) = 1678.0(41.8)-47.69(1.53)SST$	24	0.989
Region V	$pCO_2^{sw} = 362.1(7.5)$	447	
	$pCO_2^{air} = 354.4(2.9)$	1280	

Table A.1 (*Continued*)

	January/February 1998	*n*	*r*
	November/December 1999		
Region I	$pCO_2^{sw}(14.6) = 726.2(6.1) - 12.17(0.28)SST$	2268	0.678
Region II	$pCO_2^{sw}(8.4) = 777.6(7.1) - 16.95(0.28)SST$	666	0.918
Region III	$pCO_2^{sw}(6.6) = 932.7(8.3) - 18.20(0.29)SST$	556	0.936
Region IV	$pCO_2^{sw}(4.9) = 1182.5(42.5) - 28.45(1.58)SST$	48	0.936
Region V	$pCO_2^{sw}(4.4) = -180.1(67.8) + 18.42(2.27)SST$	178	0.522
Region VI	$pCO_2^{sw}(3.4) = -503.6(74.4) + 28.50(2.51)SST$	95	0.762
	$pCO_2^{air} = 355.9(1.3)$	3426	
	January/February 2001		
Region I	$pCO_2^{sw}(20.2) = 1202.4(46.2) - 27.56(1.83)SST$	517	0.552
Region II	$pCO_2^{sw}(7.9) = 1904.8(68.5) - 56.48(2.59)SST$	252	0.809
Region III	$pCO_2^{sw}(2.7) = 264.2(13.3) + 9.17(0.52)SST$	469	0.635
Region IV	$pCO_2^{sw} = 472.3(3.9)$	3566	
Region V	$pCO_2^{sw}(5.3) = -727.9(54.9) + 98.35(3.93)SST - 2.03(0.07)SST^2$	985	0.980
Region VI	$pCO_2^{sw}(2.5) = 1886.0(87.4) - 54.18(3.17)SST$	16	0.977
Region VII	$pCO_2^{sw} = 371.1(4.0)$	182	
	$pCO_2^{air} = 356.0(1.3)$	5259	
	November 2001/February 2002		
Region I	$pCO_2^{sw}(19.1) = 742.3(9.0) - 12.92(0.41)SST$	3025	0.498
Region II	$pCO_2^{sw}(9.8) = 570.6(5.3) - 8.43(0.21)SST$	1156	0.767
Region III	$pCO_2^{sw}(7.7) = 910.8(20.5) - 16.82(0.72)SST$	408	0.757
Region IV	$pCO_2^{sw} = 368.5(8.6)$	596	
	$pCO_2^{air} = 358.5(1.7)$	4643	
	October 2002/January 2003		
Region I	$pCO_2^{sw} = 450.4(14.1)$	2211	
Region II	$pCO_2^{sw} = 352.5(2.8)$	359	
Region III	$pCO_2^{sw}(4.5) = 651.4(6.9) - 10.79(0.26)SST$	549	0.869
Region IV	$pCO_2^{sw}(4.0) = 1041.3(13.7) - 21.50(0.48)SST$	355	0.923
Region V	$pCO_2^{sw}(2.9) = -211.2(6.5) + 19.41(0.22)SST$	592	0.965
Region VI	$pCO_2^{sw}(3.3) = 9.9(9.3) + 12.36(0.32)SST$	905	0.793
	$pCO_2^{air} = 359.8(1.4)$	4077	

pCO_2^{sw}–SST relationship: The standard error of analysis (in μatm) is listed in parentheses after each pCO_2^{sw}, the standard error for the coefficient and intercept are in parentheses after coefficient and intercept, *n* is the number of data, and *r* is the correlation coefficient.
pCO_2^{air}: Average value during the cruise and standard deviation from the average are listed in parentheses. Some pCO_2^{sw} are listed in the same manner.
[a] pCO_2^{sw} data were estimated on the basis of Table 1 by Inoue et al. (2002).

References

Ando, K., Kuroda, Y., 2002. Two modes of salinity and temperature variation in the surface layer of the Pacific warm pool. Journal of Oceanography 58, 599–609.

Boutin, J., Etcheto, J., Dandonneau, Y., Bakker, D. C. E., Feely, R. A., Inoue, H. Y., Ishii, M., Ling, R. D., Nightingale, P. D., Metzl, N., Wanninkhof, R., 1999. Satellite sea surface temperature: a useful tool for interpreting *in situ* pCO_2 measurements in the equatorial Pacific Ocean. Tellus 51B, 490–508.

Chavez, F. P., Ryan, J., Lluch-Cota, S. E., Miguel, N. C., 2003. From anchioves to sardines and back: Multidecadal change in the Pacific Ocean. Science 299, 217–221.

Chavez, F., Service, S. K., Buttrey, S. E., 1996. Temperature-nitrate relationships in the central and eastern tropical Pacific. Journal of Geophysical Research 101 (C9), 20553–20563.

Conway, T. J., Tans, P. P., Waterman, L. S., Thoning, K. W., Kitzis, D. W., Masarie, K. A., Zhang, N., 1994. Evidence for interannual variability of the carbon cycle from the National Oceanic and Atmospheric Administration/Climate Monitoring and Diagnostics Laboratory global air sampling network. Journal of Geophysical Research 99, 22831–22856.

Cosca, C. E., Feely, R. A., Boutin, J., Etcheto, J., McPhaden, M. J., Chavez, F. P., Strutton, P. G., 2003. Seasonal and interannual CO_2 flux for the central and eastern equatorial Pacific Ocean as determined from fCO_2–SST relationships. Journal of Geophysical Research 108(C8), 3278, doi:10.1029/2000JC000677.

Dandonneau, Y., 1995. Sea-surface partial pressure of carbon dioxide in the eastern equatorial Pacific (August 1991 to October 1992): A multivariate analysis of physical and biological factors. Deep-Sea Research II 42, 349–364.

Delcroix, T., Gourdeau, L., Hénin, C., 1998. Sea surface salinity change along the Fiji-Japan shipping track during the 1996 La Niña and 1997 El Niño period. Geophysical Research Letters 25, 3169–3172.

Dore, J. E., Lukas, R., Sadler, D. W., Karl, D. M., 2003. Climate-driven changes to the atmospheric CO_2 sink in the subtropical North Pacific Ocean. Nature 424, 754–757.

Feely, R. A., Boutin, J., Cosca, C. E., Dandonneau, Y., Etcheto, J., Inoue, H. Y., Ishii, M., Le Quéré, C., Mackey, D. J., McPhaden, M., Metzl, N., Poisson, A., Wanninkhof, R., 2002. Seasonal and interannual variability of CO_2 in the equatorial Pacific. Deep-Sea Research II 49, 2443–2470.

Feely, R. A., Wanninkhof, R., Milburn, H. B., Cosca, C. E., Stapp, M., Murphy, P. P., 1998. A new automated underway system for making high precision pCO_2 measurements onboard research ships. Analytical Chimica Acta 377, 185–191.

Feely, R. A., Wanninkhof, R., Takahashi, T., Tans, P. P., 1999. Influence of El Niño on the equatorial Pacific contribution to atmospheric CO_2 accumulation. Nature 398, 597–601.

Goyet, C., Peltzer, E. T., 1994. Comparison of the August–September 1991 and 1979 surface partial pressure of CO_2 distribution in the equatorial Pacific ocean near 150°W. Marine Chemistry 45, 257–266.

Inoue, H. Y., 2000. CO_2 exchange between the atmosphere and the ocean: Carbon cycle studies of the Meteorological Research Institute since 1968. In: Handa, N., Tanoue, E., Hama, T. (Eds.), Dynamics and Characterization of Marine Organic Matter. TerraPub/Kluwer, Tokyo, pp. 509–531.

Inoue, H. Y., Ishii, M., Matsueda, H., Aoyama, M., Asanuma, I., 1996. Changes in longitudinal distribution of the partial pressure of CO_2(pCO_2) in the central and western equatorial Pacific, west of 160°W. Geophysical Research Letters 23, 1781–1784.

Inoue, H. Y., Ishii, M., Matsueda, H., Saito, S., Aoyama, M., Tokieda, T., Midorikawa, T., Nemoto, K., Kawano, T., Asanuma, I., Ando, K., Yano, T., Murata, A., 2001. Distributions and variations in the partial pressure of CO_2 in surface waters (pCO_2^{sw}) of the central and western equatorial Pacific during the 1997/98 El Niño event. Marine Chemistry 76, 59–75.

Inoue, H. Y., Ishii, M., Matsueda, H., Saito, S., Midorikawa, T., Nemoto, K., 1999. MRI measurements of partial pressure of CO_2 in surface waters of the Pacific during 1968 to 1970: Re-evaluation and comparison of data with those of 1980s and 1990s. Tellus 51B, 830–848.

Inoue, H. Y., Matsueda, H., Ishii, M., Fushimi, K., Hirota, M., Asanuma, I., Takasugi, Y., 1995. Long-term trend of the partial pressure of carbon dioxide (pCO_2) in surface waters of the western North Pacific, 1984–1993. Tellus 47B, 391–413.

IPCC. 2001. Houghton, J. T., Ding, Y., Griggs, D. J., Noguer, M., van der Linden, P. J., Dai, X., Maskell, K., Johnson, C. A. (Eds.), The Carbon Cycle and Atmospheric Carbon Dioxide, In: Climate Change 2001: The Scientific Basis. Cambridge University Press, Cambridge, UK and New York, USA, pp. 881.

Ishii, M., Saito, S., Tokieda, T., Kawano, T., Matsumoto, K., Inoue, H. Y., 2004. Variability of surface layer CO_2 parameters in the western and central Equatorial Pacific. In: Shiyomi, M., Kawahata, H., Koizumi, H., Tsuda, A., Awaya, Y. (Eds.), Global Environmental Change in the Ocean and Land. TERRAPUB, Tokyo, pp. 59–94.

Johnson, G. C., McPhaden, M. J., Rowe, G. D., McTaggart, K. E., 2000. Upper equatorial Pacific Ocean current and salinity variability during the 1996–98 El Niño-La Niña cycle. Journal of Geophysical Research 105, 1037–1053.

Keeling, C. D., Brix, H., Gruber, N., 2004. Seasonal and long-term dynamics of the upper ocean carbon cycle at station ALOHA near Hawaii. Global Biogeochemical Cycles 18, GB4006, doi:10.1029/2004GB002227.

Kőrtzinger, A., Mintrop, L., Wallace, D. W. R., Johnson, K. M., Neill, C., Tilbrook, B., Towler, P., Inoue, H. Y., Ishii, M., Shaffer, G., Torres Saavedra, R. F., Ohotaki, E., Yamashita, E., Poisson, A., Brunet, C., Schauer, B., Goyet, C., Eischeid, G., 2000. The international at-sea intercomparison of fCO_2 systems during the R/V Meteor Cruise 36/1 in the North Atlantic Ocean. Marine Chemistry 72, 171–192.

Le Borgne, R., Barber, R. T., Delcroix, T., Inoue, H. Y., Mackey, D. J., Rodier, M., 2002. Pacific warm pool and divergence: temporal and zonal variations on the equator and their effects on the biological pump. Deep-Sea Research II 49, 2471–2512.

Lee, K., Wanninkhof, R., Takahashi, T., Doney, S. C., Feely, R. A., 1998. Low interannual variability in recent oceanic uptake of atmospheric carbon dioxide. Nature 396, 155–159.

Le Quéré, C., Aumont, O., Bopp, L., Bousquet, P., Ciais, P., Francey, R., Heimann, M., Keeling, C. D., Keeling, R. F., Kheshgi, H., Peylin, P., Piper, S. C., Prentice, I. C., Rayner, P. J., 2003. Two decades of ocean CO_2 sink and variability. Tellus 55B, 649–656.

Loukos, H., Vivier, F., Murphy, P. P., Harrison, D. E., Le Quéré, C., 2000. Interannual variability of equatorial Pacific CO_2 fluxes estimated from temperature and salinity data. Geophysical Research Letters 27, 1735–1738.

Picaut, J., Ioualalen, M., Menkes, C., Delcroix, T., McPhaden, M., 1996. Mechanism of the zonal displacements of the Pacific Warm Pool, implications for ENSO. Science 274, 1486–1489.

Poisson, A., Metzl, N., Brunet, C., Schauer, B., Bres, B., Ruiz-Pino, D., Louanchi, F., 1993. Variability of sources and sinks of CO_2 in the western Indian and Southern Oceans during the year 1991. Journal of Geophysical Research 98, 22759–22778.

Sabine, C. L., Feely, R. A., Watanabe, Y. W., Lamb, M. F., 2004. Temporal evolution of the north Pacific CO_2 uptake rate. Journal of Oceanography 60 (1), 5–15.

Takahashi, T., Sutherland, S. C., Feely, R. A., Cosca, C. E., 2003. Decadal variation of the surface water PCO_2 in the western and central equatorial Pacific. Science 302, 852–856.

Takahashi, T., Sutherland, S. C., Sweeney, C., Poisson, A., Metzl, N., Tilbrook, B., Bates, N., Wanninkhof, R., Feely, R. A., Olafsson, J., Nojiri, Y., 2002. Global sea-air CO_2 flux based on climatological surface ocean pCO_2, and seasonal biological and temperature effects. Deep-Sea Research II 49, 1601–1622.

Wanninkhof, R., 1992. Relationship between wind speed and gas exchange over the ocean. Journal of Geophysical Research 97, 7373–7382.

Wanninkhof, R., Feely, R. A., Chen, H., Cosca, C., Murphy, P. P., 1996. Surface water fCO_2 in the eastern equatorial Pacific during the 1992–1993 El Niño. Journal of Geophysical Research 101, 16333–16343.

Wanninkhof, R., McGillis, W. R., 1999. A cubic relationship between air-sea CO_2 exchange and wind speed. Geophysical Research Letters 26, 1889–1993.

Wanninkhof, R., Thoning, K., 1993. Measurement of fugacity of CO_2 in surface water using continuous and discrete sampling methods. Marine Chemistry 44, 189–204.

Weiss, R. F., 1974. Carbon dioxide in water and seawater: the solubility of a non-ideal gas. Marine Chemistry 2, 203–215.

Chapter 2

Global Change and Oceanic Primary Productivity: Effects of Ocean–Atmosphere–Biological Feedbacks

Arthur J. Miller[1,*], Albert J. Gabric[2], John R. Moisan[3], Fei Chai[4], Douglas J. Neilson[1], David W. Pierce[1] and Emanuele Di Lorenzo[5]

[1]*Scripps Institution of Oceanography, La Jolla, CA 92093-0224, USA*
[2]*Griffith University, Nathan, 4111, Australia*
[3]*NASA/GSFC Wallops Flight Facility, Wallops Island, VA 23337, USA*
[4]*School of Marine Sciences, University of Maine, Orono, ME 04469, USA*
[5]*Georgia Institute of Technology, Atlanta, GA 30332, USA*

Abstract

Our current understanding of how climate change due to increasing greenhouse gases is expected to affect oceanic biology and of how the physical–biological feedbacks may influence the evolving physical climate system is summarized. The primary effects of ocean biology on physical climate include its influence on the carbon cycle, the influence of oceanic phytoplankton on upper-ocean absorption, and the influence of DMS production by phytoplankton on atmospheric aerosols. The primary influences of physical climate on the ocean biology are the influence of aoelian dust deposition and the multitude of ways that community structure can be altered. The focus is on the tropical and midlatitude Pacific Ocean, with results from other ocean basins also noted.

Keywords: global change; climate feedbacks; ocean ecosystem; Pacific ocean; physical–biological interactions

*Corresponding author
E-mail address: ajmiller@ucsd.edu (A.J. Miller).

Elsevier Oceanography Series 73
Edited by H. Kawahata and Y. Awaya
ISBN: 0-444-52948-9

1 Introduction

As greenhouse gases continue to increase in the global atmosphere, the coupled climate system will continue to adjust to these changes in radiative forcing in many ways. Among these coupled adjustment processes are possible changes in the physical–biological coupling of the ocean-atmosphere climate and the oceanic ecosystem. In what ways can ocean biology affect changes in physical climate? How might these coupling processes affect the future climate state?

We aim here to summarize the feedback processes among the ocean, the atmosphere, and oceanic biology in the context of how these feedbacks will affect or be altered by global warming scenarios in the Pacific sector. We draw on modeling studies and available observations in key regions of the world ocean, including the tropical Pacific and the midlatitude regions of the northern and southern hemispheres.

2 Ocean Biotic Feedbacks with Centennial Climate Change

Our ability to predict the impacts of global warming is limited by a number of key uncertainties, significant among which is the role of biotic feedbacks (IPCC, 2001). The response of biota in the surface ocean is particularly pertinent and still not well understood. However, the potential for multiple feedbacks between climate, ocean circulation and mixing, and photosynthetic primary production has been manifestly evident for some time (Falkowski et al., 2000; Gildor and Follows, 2002). Indeed, the oceans are estimated to have taken up approximately 30% (with great uncertainty) of CO_2 emissions arising from fossil-fuel use and tropical deforestation between 1980 and 1989, thereby slowing down the rate of greenhouse global warming (Ittekkot et al., 1996).

Although the ocean biota compartment is estimated to contain only around 3 Gt C, the flux from the dissolved inorganic reservoir to the particulate organic phase (carbon uptake through primary production) is around $10\,\mathrm{Gt\,C\,yr^{-1}}$ (Siegenthaler and Sarmiento, 1993). Thus the size of marine biota carbon reservoir is much smaller than the fluxes in and out the reservoir. Elsewhere in the global carbon cycle, the reservoirs are much larger than the fluxes. This implies that any changes in the activity of this reservoir can mean substantial changes in the fluxes to related reservoirs. An especially important flux in the oceans is the burial of particulate organic carbon in marine sediments, which removes atmospheric CO_2 for prolonged time periods. Fig. 1 schematizes the major carbon reservoirs and flux directions in the global carbon cycle.

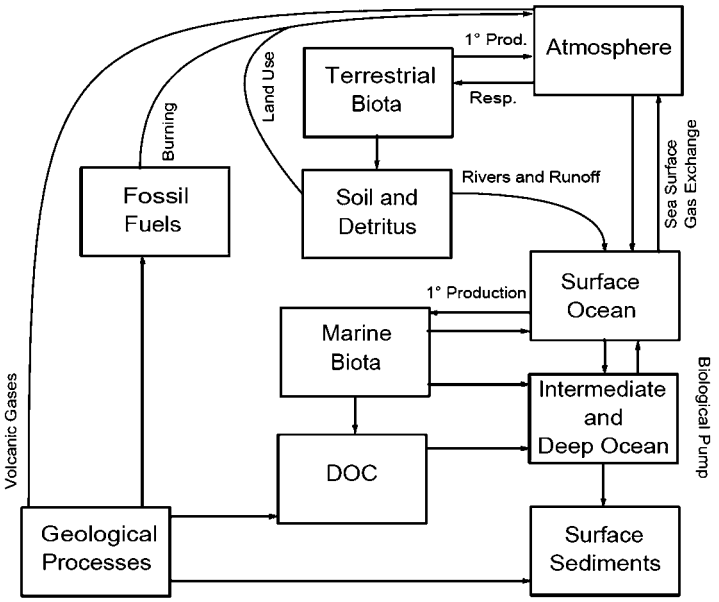

Figure 1: Schematic diagram of the major reservoirs and flux directions of the global carbon cycle.

Photosynthesis, the major process by which marine biota sequester CO_2, is largely controlled by the availability of macronutrients and trace elements such as iron (de Baar et al., 1995; Behrenfeld et al., 1996; Coale et al., 1996; Falkowski et al., 1998). Changes in freshwater runoff or increases in aeolian dust transport resulting from climate warming could change the inputs of nutrients and iron to the ocean, thereby affecting CO_2 sequestration.

Climate change can also cause shifts in the structure of biological communities in the upper ocean – for example, between coccoliths and diatoms. In the Ross Sea, diatoms (primarily *Nitzshia subcurvata*) dominate in highly stratified waters, whereas *Phaeocystis antarctic*a dominate when waters are more deeply mixed (Arrigo et al., 1999). Changes to ocean stratification could impact species composition and alter the downward fluxes of organic carbon and consequently the efficiency of the biological pump.

Several coupled atmosphere-ocean models have been used to project the effect of climate change on marine biota (Sarmiento et al., 1998; Joos et al., 1999; Gabric et al., 2003; Pierce, 2003). These models include some or all of the processes associated with carbonate chemistry and gas exchange, physical and biological uptake of CO_2, and changes in temperature, salinity, wind speed, and ice cover. They account for simple changes in biological productivity, but not for changes in external nutrient supply, or changes in the biogeography of planktonic species, which is a major deficiency as they thus cannot simulate more complex biological feedbacks (Gabric et al., 2003).

The range of model estimates of the climate change impact is dependent on the choice of scenario for atmospheric CO_2 and on assumptions concerning marine biology. At high CO_2 concentrations, marine biology can have a greater impact on atmospheric CO_2 than at low concentrations because the buffering capacity of the ocean is reduced (Sarmiento and Quéré, 1996). Although the impact of changes in marine biology is highly uncertain and many key processes are not included in current models, sensitivity studies can provide approximate upper and lower bounds for the potential impact of marine biology on future ocean CO_2 uptake. A sensitivity study of two extreme scenarios for nutrient supply to marine biology gave a range of 8–25% for the reduction of CO_2 uptake by mid-21st century (Sarmiento et al., 1998). This range is comparable to other uncertainties, including those stemming from physical transport.

3 Ocean–Atmosphere–Ecosystem Feedback Processes

Climate feedback processes can be broadly divided into two categories: geophysically mediated, where only the physical climate system is important, and biogeochemically mediated, where various biospheric and geochemical components become important as well (Lashof, 1989). Examples of the first category include water vapor feedback, the sea-ice/solar albedo feedback and various cloud feedbacks. Examples of the second category include changes in upper-ocean absorption due to phytoplankton and changes in community structures that affect CO_2 cycling and storage. The biogeochemical feedbacks that affect changes in temperature, radiation, and moisture are the most important since they have the most direct link to the physical climate system (Woodwell et al., 1998).

Currently, most global climate models do not include biogeochemically mediated feedback processes explicitly, such as the role of ocean ecosystems and its impact on carbon cycle and climate variability. Important new advances, however, have allowed new progress in this direction as summarized recently by Miller et al. (2003). We next explain the key processes by which ocean biology may influence the physical climate system over timescales relevant to global warming. Besides the effect of oceanic biology on altering carbon cycling and sequestration (Boyd and Doney, 2003), these processes include the effects of phytoplankton on upper-ocean absorption of radiation and the production of DMS aerosols by certain types of phytoplankton. Physical forcing also affects the ecosystem in important ways. These include changing the deposition of aeolian dust, which affects the limiting nutrient iron in the ocean and changing community composition by altering the environment in the ocean. The next sections will summarize these issues, including a final section on the local response of the North Pacific Ocean.

4 Absorption of Radiation by Phytoplankton in the Upper Ocean

The effect of the absorption of solar energy by phytoplankton on upper-ocean thermal properties has been the subject of research for the past 20 years. While absorption of solar energy is dominated by absorption from seawater itself in many open ocean regions, the variability in the absorption and distribution of solar energy into the upper layers of the open ocean is controlled primarily by phytoplankton pigment concentrations (Platt, 1969; Smith and Baker, 1978). Lewis et al. (1983) were the first to demonstrate that nonuniform vertical distributions of phytoplankton pigments cause variations in local heating, and, under certain vertical chlorophyll profile conditions, could support the development of a thermal instability within the water column.

Initial attempts (Paulson and Simpson, 1977) at addressing the effects of varying water quality types [as described by Jerlov (1968)] on the attenuation of irradiance in the ocean lead to a simple parameterization that characterizes absorption between the longwave and shortwave (visible) bands of solar energy using different e-folding scales, and set the e-folding scale of the shortwave band dependent on the water quality type. This parameterization has commonly been used to provide buoyancy forcing in one-dimensional, ocean surface mixed-layer models (Price et al., 1986; Schudlich and Price, 1992). More sophisticated methods to estimate the solar energy flux into the ocean resolve the depth- and wavelength-dependent spectral diffuse attenuation coefficients (Siegel and Dickey, 1987; Morel and Antoine, 1994), and Siegel and Dickey (1987) have shown that this method greatly improves the ability to compare observed irradiance fields to model estimates.

The first work to directly address the link between ocean thermodynamics and bio-optical processes (Simonot et al., 1988) coupled the bulk mixed-layer model of Gaspar (1985, 1988) to a simple, nonspectral, diffuse attenuation model for solar energy attenuation and a six-component ecosystem model (Agoumi et al., 1985). Results on simulations of the seasonal cycles at Ocean Weather Station Romeo show that the phytoplankton seasonal cycle has a significant impact on sea surface temperature evolution.

While early modeling studies all agreed that chlorophyll attenuation plays an important role in ocean physics, few direct observations had been available to confirm this. However, during the coastal transition zone field study along the California coast, Ramp et al. (1991) interpreted observations of a surface warming feature during a wind relaxation event to be caused by patchiness in the near surface chlorophyll distribution. The first notion that this biological–physical process acted on equatorial ocean regions was presented by Sathyendranath et al. (1991), who argued that chlorophyll patches were important driving mechanisms for variations in sea surface temperature. Such sea surface temperatures (SST) anomalies have been

shown (Kershaw, 1985) to influence the evolution of Arabian Sea monsoons. Additionally, Kahru et al. (1993) presented evidence from AVHRR satellite analysis and *in situ* observation to show that cyanobacteria blooms in the Baltic Sea were responsible for elevating the SST to 1.5°C. Global analysis of the ocean color fields in the tropical Pacific Ocean (McClain et al., 2002) also verified that enhanced chlorophyll regions were linked with enhanced surface-layer heating. Further evidence of the impact of phytoplankton on the evolution of mixed layers is presented by Stramska and Dickey (1993), who used bio-optical observations from a mooring off Iceland in conjunction with a version of the Mellor-Yamada two-and-a-half layer mixed layer model (Mellor and Yamada, 1982) to show that the importance of this coupling is most significant in regions of high chlorophyll and weak vertical mixing. One such region is the equatorial region of the ocean, where high solar fluxes are collocated with low wind speed "doldrums" (Fig. 2a) and high chlorophyll equatorial upwelling regions (Fig. 2b).

In the western warm pool (WWP) region of the Pacific Ocean, Siegel et al. (1995) demonstrated that the amount of solar radiation penetrating through the bottom of the mixed layer ($\sim$23 W m^{-2} at 30 m) is a large fraction of the net air–sea heat flux ($\sim$40 W m^{-2}). Following a period of sustained westerly wind burst and a corresponding near 300% increase in mixed-layer chlorophyll concentrations, the resulting biologically mediated increase in solar energy attenuation created a decrease in energy flux across the mixed layer (5.6 W m^{-2} at 30 m) and supported a mixed-layer heating rate of 0.13 °C per month. In the same year, Ramanathan et al. (1995) believed that a discrepancy occurred within the computed heat balance of the ocean-atmosphere energy budget in the western equatorial Pacific and that this discrepancy was due to "A Missing Physics" which would modify the manner and importance of cloud absorption of solar energy. Arguments were presented that this Missing Physics was in fact related to the manner in which solar radiation penetrates through the bottom of the mixed layer in this clear water region (M. R. Lewis, private communication). Further evidence has largely dismissed the claims of Ramanathan et al. (1995), and the importance of properly attenuating solar energy into the water column is now widely accepted.

The importance of characterizing the penetrative fluxes of solar energy through the upper-ocean mixed layer and into the permanent pycnocline prompted Ohlmann et al. (1996) to carry out a global analysis of the magnitude of this flux. The global map of these fluxes (Fig. 3) shows high net solar fluxes (10–25 W m^{-2}) in the equatorial Pacific and Indian Oceans regions. The values are highest at the eastern regions of the equatorial Pacific Ocean, where heat below the pycnocline is transported west to the Pacific arm pool regions. How variations in these fluxes are linked to El Niño southern oscillations (ENSO) dynamics is still unknown, but storage of heat below the mixed layer can tie up heat energy until winter ventilation/mixing

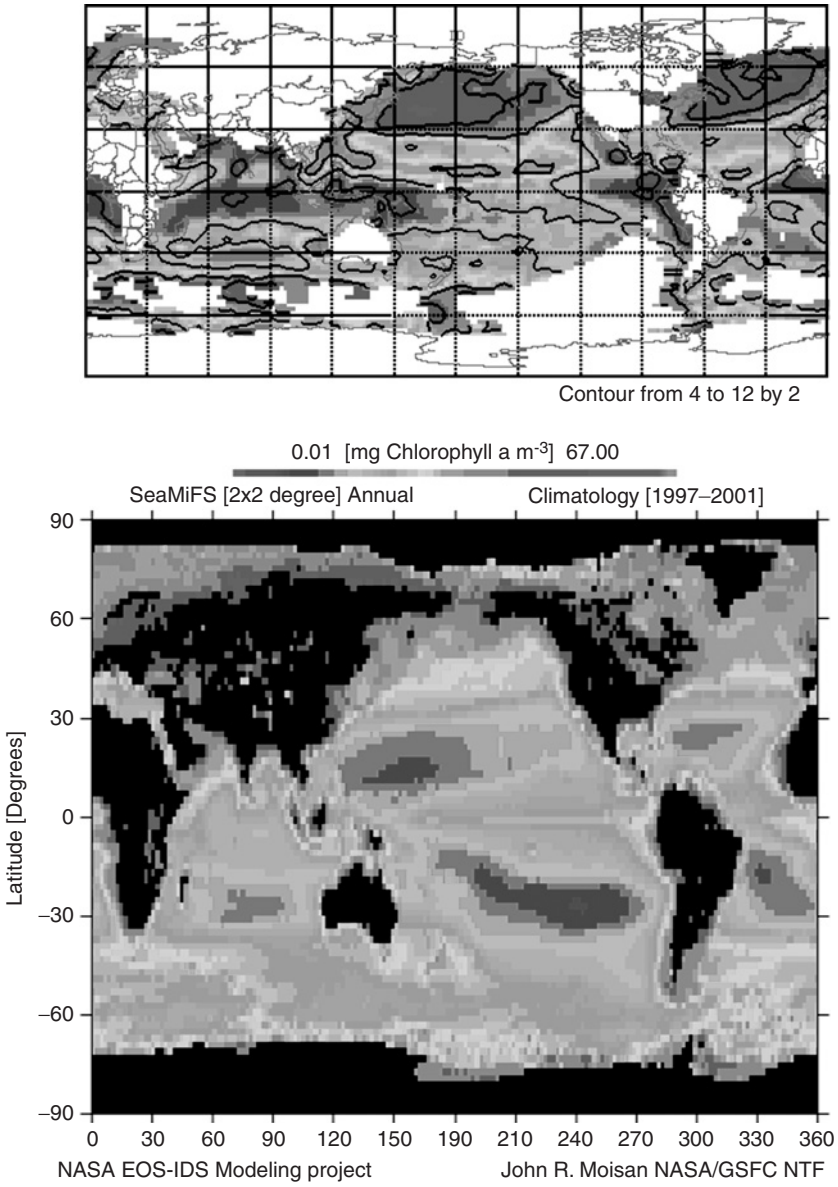

Figure 2: (a) January mean of Oberhuber atlas surface wind field. Note the low wind speeds near the equatorial Pacific and Indian Ocean regions. (b) SeaWiFS annual mean 2 $\times$ 2 degree binned climatology. Note the high chlorophyll values in the eastern equatorial Pacific (For colour version, see Colour Plate Section).

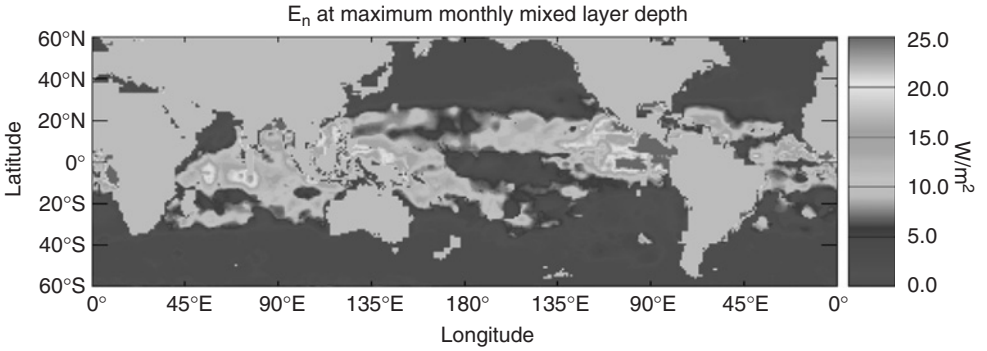

Figure 3: Modeled climatological values of the net solar flux at the base of the deepest monthly mixed layer (W m^{-1} m^{-1}). Values correspond to solar fluxes entering the permanent pycnocline. Largest values exist where the deepest monthly mixed layer and chlorophyll concentration are low and solar flux is high. From Ohlmann et al. (1996) (For colour version, see Colour Plate Section).

processes entrain it back into the mixed layer. Further demonstrations of the importance of bio-optical forcing (Ohlmann et al., 1998), using data collected from the western Pacific warm pool during TOGA-COARE and mixed-layer model simulations, noted also that increases in the penetrative heat loss to below the mixed layer resulted in a destabilization of the thermocline and a deepening of the mixed layer – creating a feedback mechanism for ocean heat flux and mixed-layer depths (MLDs) that are modified through chlorophyll concentrations.

An additional link was made between clouds and ocean heat flux processes by Siegel et al. (1999) who show that under cloudy sky conditions the near UV to green fraction of the solar spectrum is less absorbed than the rest of the solar energy spectrum. This allows a greater fraction of the total energy to penetrate further into the water column. At 0.1 m depth, this relative increase can be as high as a factor of 2 and likely influences the diurnal heat balance by altering the upper most ocean layer daily heat balances, and could alter the local heat budgets on longer timescales when taking into account the effects on the ocean-atmosphere latent, sensible and back radiation terms. A more recent effort using observations from the hyperspectral ocean dynamics experiment (HYCODE) and a radiative transfer model shows that the rate of heating in a coastal region water column can increase by $\sim$0.2 °C $(13\,\mathrm{h})^{-1}$ during high chlorophyll conditions (Chang and Dickey, 2004).

The majority of the research in the 1990s focused on demonstrating the importance of bio-optics in modifying the vertical flux of heat in the upper ocean. Links between bio-optical forcing of the upper-ocean thermal structure and horizontal momentum forcing only began to appear in the early part of this millennium. Edwards et al. (2001, 2004) used steady-state forms of the

momentum equation in conjunction with an analytical description of a high concentration band of phytoplankton biomass (chlorophyll) to ascertain the effect of chlorophyll on ocean circulation patterns. The results demonstrated that the presence of chlorophyll in the water has an impact on ocean circulation, creating both horizontal currents and bands of upwelling and downwelling in regions near the chlorophyll/biomass front. Gildor et al. (2003), in another modeling study, used a simple atmospheric model for climate coupled to a nitrogen–phytoplankton–zooplankton (NPZ) model (Edwards and Brindley, 1999) to demonstrate that intraseasonal variations in SST and precipitation could be forced by inherent oscillations of an ecosystem.

Recent results from coupled circulation/bio-optical models have demonstrated the significance of biological feedbacks with the ocean climate. Phytoplankton pigment concentrations derived from the coastal zone color scanner (CZCS) were used by Nakamoto et al. (2000) to force an isopycnal ocean circulation model coupled to a mixed-layer model to show that the higher chlorophyll concentrations in October versus May increased the amount of solar energy absorption and the rate of heating in the upper ocean. These changes lead to a decrease in MLDs, a decrease in water temperatures beneath the mixed layer, and an increase in surface mixed-layer temperature. Comparison simulations of the equatorial Pacific (Nakamoto et al., 2001) using a similar coupled isopycnal-mixed layer ocean circulation model and forced with and without chlorophyll (CZCS-derived pigments) demonstrated that the presence of the chlorophyll leads to shallower mixed layer in the equatorial Pacific, which generates anomalous westward geostrophic currents north and south of the equator. In the western equatorial Pacific, the anomalous currents enhance the equatorial undercurrent (EUC). The biologically enhanced EUC leads to anomalous upwelling in the eastern equatorial Pacific, while the spatially averaged SST over the Pacific increases due to heat trapped by phytoplankton in the upper ocean. Using sea-viewing wide field-of-view sensor (SeaWiFS)-derived chlorophyll pigment data in the MIT global ocean model, Ueyoshi et al. (2003) confirmed the process described by Nakamoto et al. (2001) whereby chlorophyll modulates oceanic heat uptake by radiation and subsequently generates biologically induced currents in the equatorial Pacific.

Shell et al. (2003) forced an atmospheric general circulation models (GCM) with the SST pattern that arises from this phytoplankton effect and showed that the amplitude of the global surface-layer atmospheric temperature seasonal cycle increases by roughly 0.5°C. Frouin and Iacobellis (2002) estimated that phytoplankton serves to warm the global atmosphere by up to 0.25 °C, supporting the idea that phytoplankton exerts a significant influence on large-scale climate variability. Oschlies (2004) showed that surface heat fluxes act as a negative feedback to reduce the absorptive warming effects of phytoplankton in the upper ocean of a fully interactive physical–biological

model. Manizza et al. (2005) used a fully coupled physical–biological ocean model to show that phytoplankton biomass amplifies the seasonal cycles of SST, MLDs, and ice cover by roughly 10%.

Attenuation of solar energy into the ocean using diffuse attenuation coefficients has been used for a variety of ocean modeling studies. Rochford et al. (2001) developed a global field for the diffuse attenuation $k_{\mathrm{PAR}}$of photosynthetically available radiation (PAR) – the visible portion of the solar energy spectrum that is not absorbed in the first several centimeter of water column – using data from the SeaWiFS. The diffuse attenuation field was used in the finite depth version of the NLOM global ocean circulation model with an embedded mixed layer to determine the sensitivity of the model solutions to the diffuse attenuation fields. The results demonstrated that using the derived SST prediction improved in the low latitude regions but the MLD predictions showed no significant improvement. In addition, using a constant clear ocean k_{PAR}value of $0.06\,\mathrm{m}^{-1}$ produces reasonable results for much of the global ocean regions.

In a similar study using a primitive equation, global ocean circulation/mixed layer model forced with spatially varying radiation attenuation coefficients derived from CZCS data, Murtugudde et al. (2003) show that the results from such coupled models can be counterintuitive. For instance, in the eastern equatorial Pacific, where the presence of high chlorophyll leads to strong attenuation of solar energy, realistic solar energy attenuation leads to increased subsurface loss of solar energy, increased SST, deeper mixed layers, reduced stratification, and horizontal divergence (upwelling/downwelling). Timmermann and Jin (2002), using a dynamic ENSO model, point out that eastern equatorial Pacific ocean chlorophyll blooms during La Nina periods create a temperature regulating negative feedback that redistributes heat into the surface layer and the associated results from the air–sea coupling dampens the La Nina conditions. This mechanism is thought to counter the positive Bjerknes atmosphere-ocean feedback that links La Nina events with stronger trade winds that force stronger upwelling leading to the intensification of La Nina conditions.

More sophisticated attempts to link the role of ocean biological feedback mechanisms are just beginning to emerge and support the notion that biological effects enhance ENSO variability. Marzeion et al. (2005) used a primitive equation ocean model with a dynamic ocean mixed layer and a nine-component ecosystem model coupled to an atmospheric mixed-layer model and a statistical atmospheric model to investigate the feedback between chlorophyll concentrations and the ocean heat budget in the tropical Pacific. The results from this study supported the earlier conclusions by Timmermann and Jin (2002) of a bioclimate feedback mechanism and earlier results describing the possible effects on the surface ocean currents (Murtugudde et al., 2003). The results present a scenario where subsurface

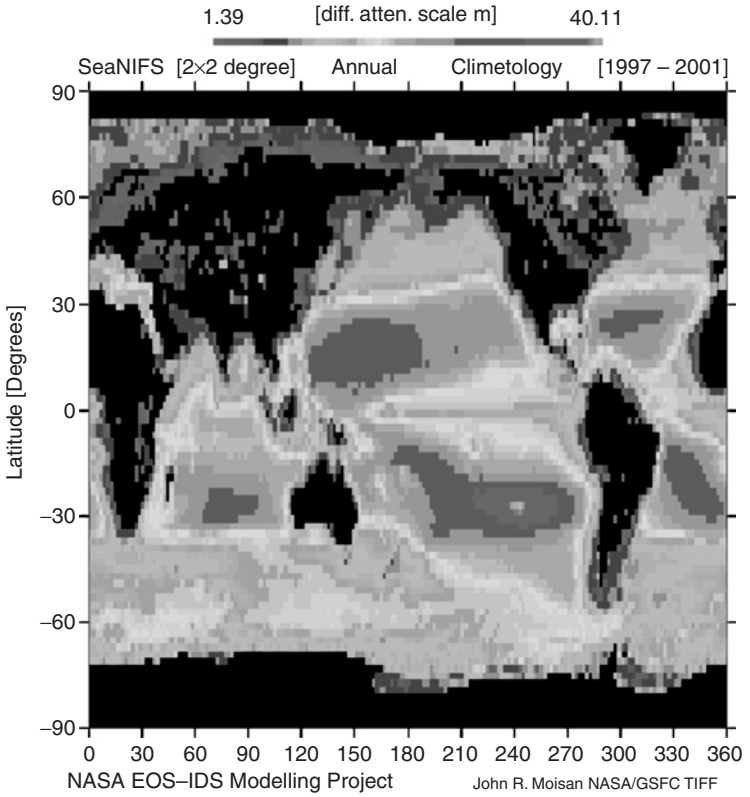

Figure 4: The 2×2 degree annual mean SeaWiFS-derived diffuse attenuation coefficient [m-1] field for PAR (For colour version, see Colour Plate Section).

chlorophyll concentrations force changes in subsurface heating rates and leading to changes in subsurface heating, mixed-layer deepening, alterations in surface ocean currents, and ultimately supporting an eastern Pacific surface warming.

The most recent version of the community climate system model under development at NCAR and the NASA MOM4 model is making use of the observed spatially varying diffuse attenuation obtained from ocean color estimates (Fig. 4). Future global climate simulations will be taking this physical–biological feedback mechanism into account (Ohlmann, 2003).

5 Production of Atmospheric DMS by Oceanic Phytoplankton

Dimethylsulfide (DMS) is the most abundant form of volatile sulfur (S) in the ocean and is the main source of biogenic reduced S to the global atmosphere

(Andreae and Crutzen, 1997). The sea-to-air flux of S due to DMS is currently estimated to be in the range (15–33) Tg S yr^{-1}, constituting about 40% of the total atmospheric sulfate burden (Chin and Jacob, 1996). At the hemispheric scale (Gondwe et al., 2003) estimate that seawater DMS contributes 43% of the mean annual column burden of non-sea-salt sulfate (nss-SO_4^{2-}) in the relatively pristine southern hemisphere, but only 9% in the northern hemisphere, where anthropogenic sulfur sources are overwhelming.

During its synthesis and cycling in the upper ocean, DMS is ventilated to the atmosphere, where it is rapidly oxidized to form nss-SO_4^{2-} and methanesulfonate (MSA) aerosols. Sulfate aerosols (of both biogenic and anthropogenic origin) play an important role in the earth's radiation balance both directly through scattering, absorption, and reflection of solar and terrestrial radiation, and indirectly, by modifying cloud microphysical properties (Charlson et al., 1992). The flux of DMS from the ocean to the atmosphere is an important concern for atmospheric modelers since the net effect of DMS is believed to be a cooling effect for the global climate (Kiene, 1999). While wind forcing is known to control the piston pumping velocity of DMS gas across the air–sea interface (Liss and Slater, 1974), the percent yield of DMS from DMSP ($100 \times DMS_{\text{Production Rate}}/DMSP_{\text{Consumption Rate}}$) is well correlated to MLDs (Simó and Pedrós-Alló, 1999). Combining this relationship with the global climatologies of MLDs produces a map demonstrating the seasonal and global variability of this efficiency (Fig. 5). Combining these estimates with estimates of the air–sea flux of DMS (Bates et al., 1987a) may have some potential for gaining additional insight in the level of net DMS production in the ocean. In addition to seasonal variations in DMS production, ecosystem changes in the Pacific equatorial regions are now known to undergo spatial and temporal variations that are linked to larger scale climate variations such as ENSO (Karl et al., 1995). Such variability should also impact the production level of DMS and its associated air–sea flux.

Various phytoplankton species synthesize differing amounts of dimethylsulfoniopropionate (DMSP), the precursor to DMS. The function of DMSP in algal physiology seems to be varied, and it is thought to act as an osmolyte, a cryoprotectant, and also relieve oxidative stress in the algal cell (Kirst et al., 1991; Liss et al., 1993; Stefels, 2000; Sunda et al., 2002). In general, coccolithophorids and small flagellates have higher intracellular concentrations of DMSP.

It is well established that the oceans are highly supersaturated in DMS with respect to atmospheric concentrations (Barnard et al., 1982; Liss et al., 1993). In fact, DMS is so supersaturated that recent field experiments on air–sea CO_2 gas flux have used the flux of DMS as a proxy signal to sparameterize the physical process of air–sea gas transfer (Dacey, private communication, 2003). Vertical profiles of DMS in the Sargasso Sea (Dacey

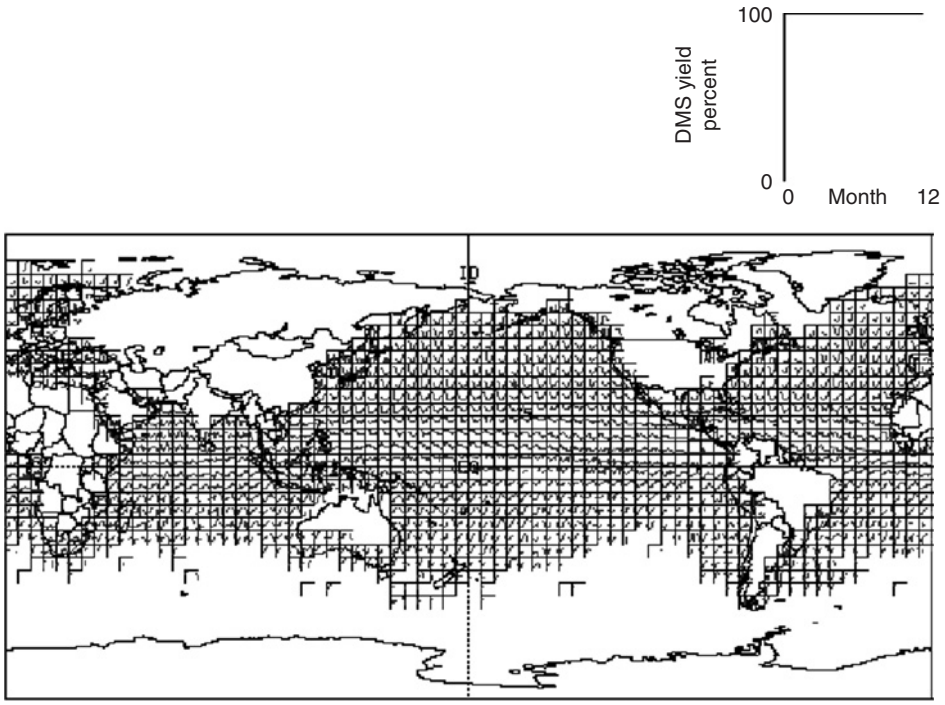

Figure 5: DMS percent yield climatologies estimated using observed MLD climatologies from the NODC XBT data set and the Simo and Pedrós-Alló (1999) DMS yield relationship (For colour version, see Colour Plate Section).

et al., 1998) show a marked subsurface 10 m maximum. A comparison of the depth-integrated annual cycle of DMS, chlorophyll, and primary production rates in this region shows that DMS concentrations peak in late summer (August) when both chlorophyll and primary production rates are lower than their earlier spring maximum values – suggesting that DMS production by phytoplankton is not directly linked to photosynthetic processes and may be due to release from grazing by zooplankton (Leck et al., 1990). However, correlations between algal biomass and DMS concentrations have been found for dinoflagellate and coccolithophore blooms (Leck et al., 1990). Because of these obvious complexities, attempts to model the production of DMS (Gabric et al., 1993) in ecosystem models have included both direct (primary production) and indirect (grazing) sources. Refer to Lee et al. (1999) for a recent review of DMS in aquatic environments.

Shaw (1983) and then Charlson et al. (1987) [notably called the "CLAW Hypothesis," derived from the first letters of the author's last names], postulated links between DMS, atmospheric sulfate aerosols, and global climate. It was hypothesized that global warming would be accompanied

by an increase in primary production, and biogenic production of DMS-derived sulfate aerosols leading to increased scattering, more cloud condensation nuclei (CCN), and brighter clouds. Such changes in the atmosphere's radiative budget would cool the earth's surface and thus stabilize climate against perturbations due to greenhouse warming. While phytoplankton is the protagonists in this feedback loop, recent advances in understanding the complex cycle of DMS suggest that it is the entire marine food web (Fig. 6) that determines net DMS production and not just algal taxonomy (Simó, 2001).

The emission of DMS and aerosol particle concentrations is well correlated across varying latitudes and seasons (Bates et al., 1987b). However, Schwartz (1988), in a comparison between southern (SH) and northern hemisphere (NH) cloud albedo records, argues that the CLAW hypothesis is not valid since the anthropogenically introduced sulfur aerosols in the NH should have created a noted increase in cloud albedo over the past century and none were observed. The debate on the CLAW hypothesis continues to date (Sherwood and Idso, 2003).

The DMS-climate feedback hypothesis has stimulated a very significant research effort. Several large-scale studies inspired by the International Global Atmospheric Chemistry program (IGAC) have addressed aspects

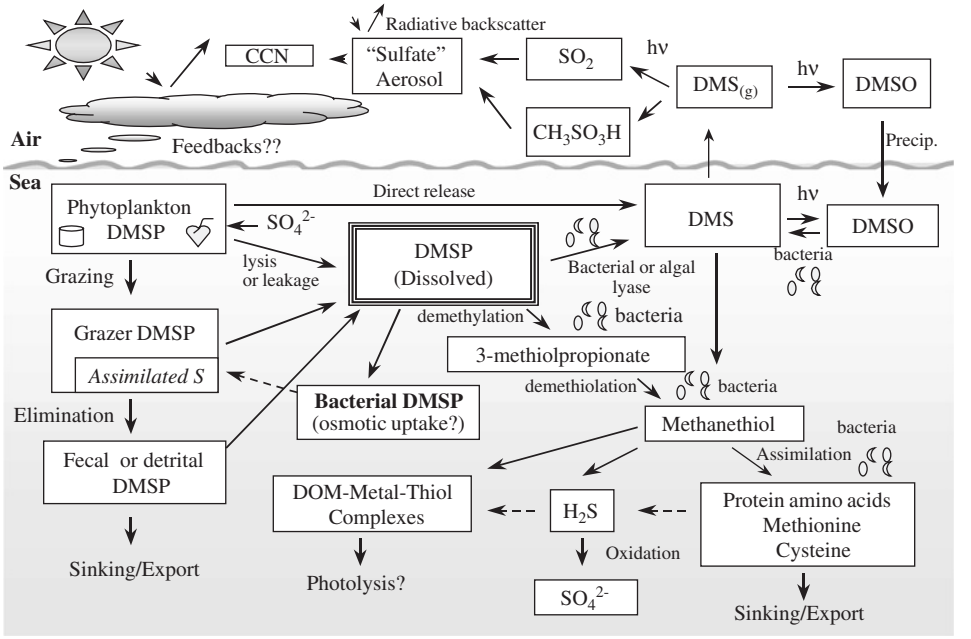

Figure 6: Conceptual model of the cycling of DMSP and DMS in the upper ocean.

of the DMS–aerosol–climate connection, including ASTEX/MAGE (Huebert et al., 1996), ACE-1 (Bates et al., 1998), and AOE-91 (Leck et al., 1996). A global database of DMS seawater concentrations and fluxes has been compiled (Kettle et al., 1999; Kettle and Andreae, 2000), and more recently, a simple empirical algorithm relating DMS seawater concentration to the oceanic MLD and surface chlorophyll concentration has also been derived (Simó and Dachs, 2002).

Notwithstanding this progress, the quantitative evaluation of the DMS-climate hypothesis remains a daunting challenge. This is due in part to the need to integrate knowledge across the traditional disciplinary boundaries of ecology, oceanography, and atmospheric science but also due to our incomplete understanding of the DMS marine production cycle.

General circulation models predict the planet's mean temperature will increase under the "business as usual" scenario (Houghton et al., 1996). The most recent estimate of average warming for a doubling of CO_2 is $3.3 \pm 0.8\,^{\circ}K$ (Grassl, 2000). However, there is strong spatial variation in this perturbation, with large temperature and salinity changes predicted to occur in the polar oceans (e.g., Hirst, 1999). The associated warming and salinity reduction is generally accompanied by a shallowing of the oceanic mixed layer, and stronger illumination of the upper water column, both of which can affect the food-web dynamics and consequently DMS production (Gabric et al., 2001a). It is pertinent to note that the Simó and Dachs' algorithm employs an inverse relation between MLD and DMS concentration, suggesting that DMS seawater concentration is likely to increase under global warming.

Attempts to assess the direction and magnitude of the DMS-climate feedback (Foley et al., 1991; Lawrence, 1993; Gabric et al., 2001b) indicate a small-to-moderate negative feedback on climate (stabilizing), with magnitude of order 10–30%, and considerable regional variability. The results of the use of GCM data to force a DMS model in the Antarctic Ocean under a global warming scenario suggests that significant perturbation to the DMS flux will occur at high latitudes (Gabric et al., 2003). Fully coupled climate and biogeochemistry models (Joos et al., 1999; Cox et al., 2000) are the next step in further unraveling the DMS-climate link.

6 Deposition of Aeolian Dust on the Ocean by the Atmosphere

Aeolian dust deposition over the oceans provides a biogeochemical link between climate change and terrestrial and marine ecosystems (Ridgwell, 2002). A major natural source of new iron to open ocean surface waters is continentally derived aeolian dust, which supplies about three times the

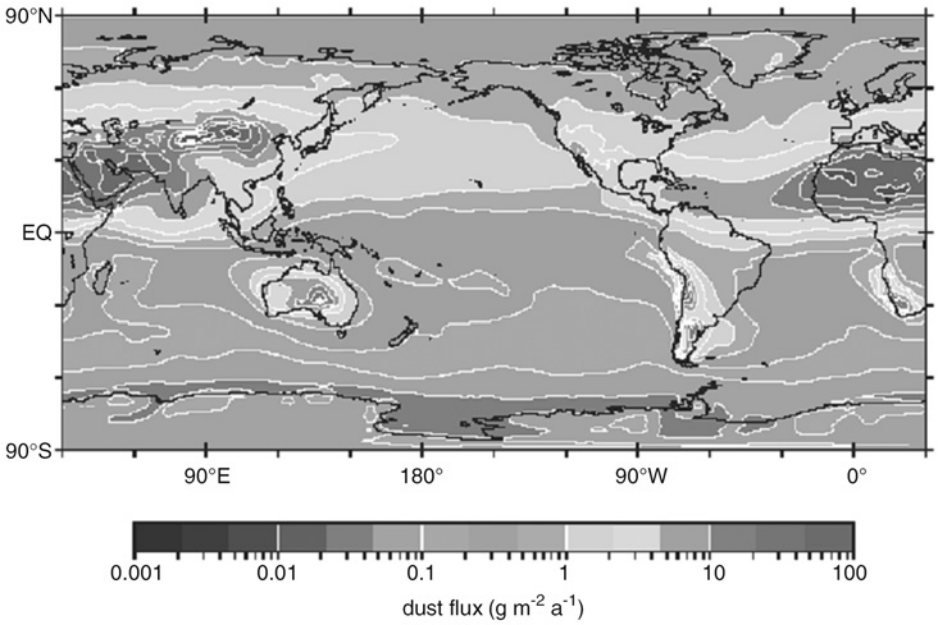

Figure 7: Contemporary annual mean dust deposition rate (Ginoux et al., 2001 (For colour version, see Colour Plate Section)).

fluvial input (Duce and Tindale, 1991). *In situ* iron-fertilization experiments have been conducted in both the equatorial Pacific [IronEx I (Martin et al., 1994) and IronEx II (Coale et al., 1996) and Southern Ocean (SOIREE (Boyd and Law, 2001))]. On all three occasions, raising the iron level in the water by a few nanomoles per liter produced a significant increase in phytoplankton biomass. During IronEx II, the increase was at least an order of magnitude. Iron-limited high nutrient low chlorophyll (HNLC) regions comprise approximately 30% of the world ocean and include the Southern Ocean (de Baar et al., 1995). The majority of iron deposition to the ocean occurs in the NH and is principally associated with dust export from the major arid zones such as the Sahara and Taklamakan Deserts (Fig. 7). The North Atlantic and North Pacific Oceans receive 48% and 22% of global iron deposition to the oceans, while the Indian Ocean (principally in the Arabian Sea) receives 18% and the Mediterranean Sea 4%. The South Atlantic and South Pacific Oceans receive only 4% and 2%, respectively, while the polar regions in both hemispheres also receive very low iron inputs, with the Arctic receiving only 0.9% and the Antarctic 0.5% (Gao et al., 2001).

The subantarctic Southern Ocean is an HNLC region, and it has been suggested that deep mixing and the availability of iron limit primary production. Australian mineral dust is high in iron content and can be transported

over the Australian sector of the subantarctic Southern Ocean, particularly during the austral spring and summer when dust storm frequency in southern Australia is maximal. Recently, Gabric et al. (2002) reported evidence for a coupling between satellite-derived (SeaWiFS) aerosol optical thickness and chlorophyll concentration in the upper ocean. The coupling was evident at monthly, weekly, and daily timescales. The shorter timescale coupling supports the hypothesis that episodic atmospheric delivery of iron is stimulating phytoplankton growth in this region.

Long-term climate variability may also be related to variation in dust deposition rates. Evidence for a possible influence on the glacial–interglacial variability of atmospheric CO_2 comes from the observed changes in dust deposition, recorded in the 420 kyr Vostok Antarctic ice core (Petit et al., 1999). The concentration of dust contained within the ice exhibits a series of striking peaks against a background of relatively low values. Intriguingly, the occurrence of these peaks correlates with periods of particularly low atmospheric CO_2 values. It has been hypothesized that enhanced dust supply to this region during the last glacial could have driven a more vigorous oceanic biological pump with consequent draw-down of atmospheric CO_2 (Martin, 1990).

Numerical models of the global carbon cycle have since demonstrated that realistic increases in the strength of the biological pump in the Southern Ocean are unable to explain glacial atmospheric CO_2 mixing ratios as low as ~190 ppm. However, of the total ~90 ppm deglacial rise in atmospheric CO_2, the initial 40–50 ppm occurs extremely rapidly (within just ~3 kyr) and up to 10 kyr before the collapse of the NH ice sheets. Predictions of a carbon cycle model that explicitly accounts for the biogeochemical cycling of Fe in the ocean, confirm that changes in the aeolian supply of Fe to the Southern Ocean may be at least partly responsible for these particular features of the CO_2 record (Watson et al., 2000).

Interestingly, it has also been proposed that aeolian delivery of iron can also influence the oceanic sulfur cycle and the oxidation of DMS in the remote marine atmosphere. Zhuang et al. (1992) report that over 50% of the total iron present in remote marine aerosols is in the soluble Fe(II) form, which is readily available to phytoplankton. The photoreduction reaction that produces Fe(II) in aerosols also produces the hydroxyl radical, which is required for the oxidation of atmospheric DMS to MSA, and ultimately the formation of CCN.

The fact that atmospheric Fe fluxes appear to play an important role in ecosystem dynamics in many locations underscores the interwoven nature of the links between climate change, the biogeochemical cycles of carbon, nitrogen, and sulfur, and the potential for the oceans to sequester carbon.

7 Changes in Oceanic Community Composition by Climate Changes

Much of the literature on future climate change has ignored the possible ecological shifts and changes in the pelagic food web that may occur as the oceans warm. These changes may have a strong and significant impact on the feedbacks between ocean biology and the physical climate system. Because much of the expected change is dictated by what community is present and where in the world the community is located, there are few universal answers (Kennedy et al., 2002; Poff et al., 2002). The most important climate forcings are direct thermal effects (e.g., temperature-induced changes in metabolism), and indirect, thermal effects (e.g., changes caused by thermally induced changes to the environment such as decreased upwelling).

Paleoecological studies can give us a clue to the potential for future climate-change-induced ecological shifts. For example, the glacial iron hypothesis conjectures that an increase in aeolian Fe deposition to the Southern Ocean during the last glacial maximum (LGM) stimulated primary and export production (Kumar et al., 1995) resulting in a decrease in atmospheric pCO_2 (Martin, 1990). Evidence suggests that diatoms and coccolithophorids did not play a prominent role in this increased production (Howard and Prell, 1994; De La Rocha et al., 1998). One hypothesis that can explain the increased production, as well as evidence for higher levels of DMS-derived MSA, in ice cores during glacial times (Legrand et al., 1991), is that the algal bloom-forming species responsible for the atmospheric pCO_2 drawdown was a high DMSP-producing organism that has left no sedimentary record (DiTullio et al., 2000; Moore et al., 2000). Increased abundance of the colonial haptophyte *P. antarctica* (a high DMSP producer) during the LGM would be consistent with the accumulated evidence.

Expectations that current temperature levels will rise in the coming decades can be detrimental or favorable to specific members of the ocean's communities. Since there is a limit to the temperature rise in tropical waters (based on limitations imposed by evaporative cooling), larger organismal responses will occur in temperate and higher latitude regions. Temperature changes will directly affect an organism's metabolism, growth, and fecundity (among other things) and can be considered stressful as the temperature moves outside the "normal" range for the organism. If the temperature change is slow, it is possible that the organisms can shift their distributional patterns to accommodate. In the case of dramatic changes in temperature or where organisms cannot relocate to more acceptable climes, the result can be reduced numbers or localized extinctions. Kennedy and Mihursky (1971) demonstrated this in the laboratory using estuarine invertebrates subjected to a short-term increase of 1 °C. In their experiments, mortality increased from 0%, at the lower temperature, to 100% at the higher.

Temperature increases can have positive effects related to increased fecundity with temperature. In this case, some organisms will experience a muting of seasonal declines in fecundity/abundance or year-round fecundity/abundance increases. In both cases, the result will be a general annual mean increase in numbers (assuming the temperature increase is sublethal). Of course, changes in abundance of specific species, caused by migration or increased fecundity/mortality, can fundamentally change the trophic interdependencies in a particular region, leading to a change in the composition of the underlying community. Terming the increase in abundance "positive" may only make sense in a practical way for commercially important species.

The temperature tolerance range of many species may delimit their geographical distribution, with populations shifting latitudinally in response to shifting climatic zones. For example, recent large-scale changes in the biogeography of zooplankton (specifically, calanoid copepods) have been detected in the northeastern North Atlantic Ocean (Beaugrand et al., 2002; Beaugrand and Reid, 2003). Strong biogeographical shifts in all copepod assemblages were found with a northward extension of more than 10° in latitude of warm-water species associated with a decrease in the number of cold-water species. These changes were attributed to regional increase in sea surface temperature.

Open ocean regions may be affected by changes in the thermohaline pump, in which temperature-induced changes in density lead to mixing via overturning of cold dense surface waters with less dense subsurface waters. This mechanism is responsible for transport of oxygen and nutrients to the deep ocean and would adversely impact organisms and communities in the deep ocean. Carbon dioxide is also transported to the deep ocean, but a slowdown would not affect deep-ocean organisms directly because there is no light for CO_2 photosynthesis and the pressures at depth disallow formation of carbonate structures. However, some suggest that decreasing transport to depth would increase the amount of CO_2 at the surface, decrease CO_2 uptake by the ocean from the atmosphere, and exacerbate CO_2 buildup in the atmosphere. This is offset by those who believe that global warming will lead to increased stratification of the surface waters, which would trap more autotrophs at the surface causing an increase in photosynthesis and uptake of CO_2, which in turn would lead to uptake by the ocean of atmospheric CO_2, and a decrease in atmospheric CO_2.

Several lines of evidence from the Hawaii Ocean Time Series and the limited historical data suggest that N_2 fixation is an important source of new nitrogen for the open ocean ecosystems of the North Pacific Ocean (Karl et al., 2001). These independent measurements and estimates during the past couple of decades reveal increases in *Trichodesmium* (the dominate N_2 fixer) population abundances, increases in the molar N:P ratio above the

thermocline, and DIC drawdown in absence of nitrate and other forms of fixed nitrogen. The nitrogen budget based on the data estimates and a one-dimensional model calculation suggest that N_2 fixation presently supplies up to half of the nitrogen required to sustain particulate material export from the euphotic zone, but this source of new nitrogen from the N_2 fixation process was much smaller before the 1980s. The increase in *Trichodesmium* abundances and the high percentage of N_2-supported primary production indicate that the ocean ecosystems are not in steady state. The changing ocean ecosystems are influenced by either oceanic variability, or a new quasi-steady state established in response to the Pacific decadal variability (Karl, 1999).

Changes in ocean circulation affects many aspects of ecosystems, including such things as nutrient distribution patterns (via upwelling and horizontal transport) and the transport of larvae and juveniles by currents. If the location of flow changes or the timing of that location changes then species may not arrive at spawning or nurturing grounds at optimal times and losses can occur to the species itself or to grazer/predator populations relying on that species. Seasonal timings between predator and prey species can also be affected. Many zooplanktons spend winter at depth and rise to the surface waters in the spring. Depending on the community the phytoplankton may bloom at altered times, changing the conditions which lead to zooplankton growth when they reach the surface waters.

Contemporary ecological data indicate that planktonic populations can respond extremely sensitively and quickly to ocean variability. Long-term climate–plankton connections have been detected in the Pacific in the CalCOFI program (e.g., Roemmich and McGowan, 1995) and in the North Atlantic in the continuous plankton recorder (CPR) program (Colebrook, 1979). Phenological (seasonal) changes are also evident in the North Atlantic CPR data, with some species reaching their seasonal peak up to 2 months earlier in the 1990s compared to the long-term seasonal mean. The effects of climate on plankton can take place on a worldwide scale and may be transferred from plankton to higher trophic levels; for example, by fish or bird populations (Aebischer et al., 1990; Veit et al., 1996).

Analysis of long-term changes in phytoplankton, zooplankton, and salmon in relation to hydrometeorological forcing in the northeast Atlantic Ocean revealed significant relationships between (1) long-term changes in all three trophic levels, (2) sea surface temperature in the northeastern Atlantic, (3) NH temperature, and (4) the North Atlantic oscillation. The similarities detected between plankton, salmon, temperature, and other climatic parameters are also seen in their cyclical variability and in a stepwise shift that started after a pronounced increase in NH temperature anomalies at the end of the 1970s. Importantly, the changes flowed through

the entire food web, with all biological variables showing a pronounced change over a relatively short time. These changes started after *circa* 1982 with a decline in euphausiids, followed by an increase in total abundance of small copepods, an increase in phytoplankton biomass (1984), a decrease in the large zooplankter *Calanus finmarchicus*, and by 1988, a decrease in salmon. It is interesting to note that such a scenario of a decline in herbivores and top predators has also been found in laboratory microcosm experiments which simulated the impact of global warming on an aquatic ecosystem (Petchey et al., 1999.).

Coastal regions are affected by warming in a number of ways including changes in precipitation/runoff, flooding, changes in salinity and oxygen content, and changes in circulation patterns. Precipitation changes affect runoff, which directly affects nutrient concentrations in the estuarine and nearshore coastal areas. In addition, runoff is also a primary source of pollutants in these regions. Increased runoff can inoculate coastal runoffs leading to increased blooms of phytoplankton. These blooms, in turn can affect the communities by removing needed nutrients, upsetting the oxygen balance, introducing toxins, and affecting the depth that light penetrates to. Not all species are capable of taking advantage of a sudden influx of nutrients and these events tend to favor the larger phytoplankton whose large surface area can absorb proportionally more nutrients. Because of this, unexpected inputs of nutrients can lead to localized changes in the community composition in short order. Timing and seasonality of community cycles can consequently be disrupted.

Coral reefs exist in a balance between water clarity and light penetration and occur at depths where the light penetration is optimal for growth of the coral's zooxanthellae symbionts. Should any climate-related change translate to a decrease in light penetration then the coral, and their reefs, will be jeopardized. Increases in CO_2 can change the carbonate chemistry in the ocean, which can lead to decreases in the amount of carbonate dissolved in the water. Since carbonate is the principal component in "hard" corals, an increase in CO_2 will, and already has, lead to destruction of the coral reefs. The coral reef community then is destroyed not only by loss of the organisms but by loss of habitat in the form of the reefs laid down by those organisms.

Changes in biodiversity, physiology, phenology, and geographic distributions of plankton will likely alter competitive interactions between species and trophic levels and may radically affect the marine food web, sea-to-atmosphere carbon fluxes, and nutrient recycling processes. However, as pointed out by Falkowski et al. (1998), our present lack of mechanistic understanding of the multiple feedbacks between marine ecosystems and climate limits our ability to make quantitative predictions.

8 Primary Productivity Response to Climate Change in the North Pacific

The North Pacific is of special interest because of its societal importance in supporting fisheries and because of the consequent effect of the downstream response over North America to possible feedbacks involving the oceanic biology. Changes in the physical environment of the North Pacific driven by global climate change can be expected to have an important effect on the primary productivity and the entire local ecosystems.

North Pacific primary productivity changes in response to global warming have been examined by driving a diagnostic NPZ model by the environmental changes predicted by a global ocean-atmosphere-coupled general circulation model (O-A GCM), as described in detail by Pierce (2003). The physical environment parameters that affect the biological model are MLD, solar insolation, water temperature, and Ekman upwelling at the base of the mixed layer. Although feedbacks to the physical climate are not included in this run, it provides a remarkable view of how the ocean biology may change in the globally warmed world.

The physical parameters that drive the ecosystem model were obtained from a climate change projection run of the parallel climate model (PCM) (Washington et al., 2000). This uses the CCM3 global atmospheric general circulation model run at T42 resolution (approximately 2.8° in latitude and longitude), coupled to the parallel ocean program (POP) ocean model run at 2/3° resolution. The coupled model includes land surface, runoff, and sea ice components, and is forced by a so-called "business as usual" (IS92a) scenario of future CO_2 and sulfur aerosol emissions. The PCM is relatively insensitive to CO_2 forcing (e.g., Allen et al., 2001); most other major coupled climate models show larger global temperature increases by the year 2100 than does PCM.

A result of this simulation is illustrated in Fig. 8, which shows the ratio of primary productivity in the decade of the 2090s over the decade of the 2000s. Growing season values (March through June) are used here (but see below). The main effect of the changes in physical environment is to decrease the primary productivity in the shaded regions of Fig. 8. Detailed analysis (Pierce, 2003) shows that these changes are forced primarily by increased stratification (a consequence of the warmer surface temperatures) leading to a decline in MLDs during the winter. The shallower MLDs keep the NPZ system closer to equilibrium, with a consequent reduction in the amplitude of the spring bloom. In other words, in the shaded regions of Fig. 8, the decade of the 2000s has deep wintertime-mixed layers that are associated with a sharp wintertime drop in phytoplankton (and consequently zooplankton) concentrations. This is partly due to mixing a given quantity of phytoplankton over a deeper layer and partly due to the lower

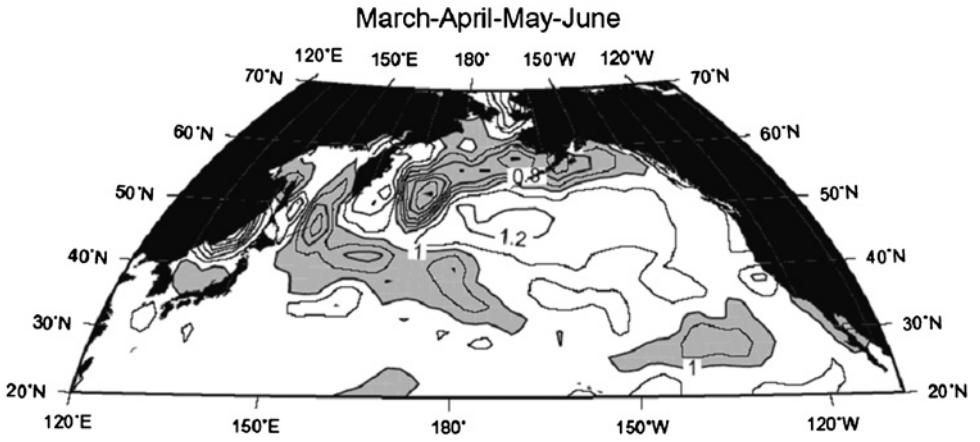

Figure 8: Ratio of primary productivity in the decade of the 2090s over the decade of the 2000s for the March through June growing season (Pierce, 2003).

average illumination levels in a deeper mixed layer. The rapid restratification of the water column in spring holds the phytoplankton near the surface in a well-illuminated region, and the depleted zooplankton cannot graze sufficiently quickly to prevent a spring phytoplankton bloom.

In the 2090s, the shallower mixed layers keep the phytoplankton and zooplankton populations more evenly populated year round, with, as a result, less of a spring bloom. It follows that productivity during the rest of the year is somewhat higher in the shaded regions during the 2090s as compared to the 2000s, but this is generally not enough to overcome the loss of the spring bloom, resulting in a net yearly reduction of productivity over the majority of the shaded region in Fig. 8. In the nonshaded regions of Fig. 8, the general increase in temperature by the 2090s tends to increase primary productivity. The overall result, then, is a combination of a modest, near-uniform increase in productivity due to the warmer water combined with a sharp loss of springtime productivity in the regions where warmer surface waters cap the wintertime mixed layer in the future.

It should be kept in mind that this line of analysis does not include other effects that will likely be important in the North Pacific, such as changes in the relative number of species, some of which might be better adapted than others to the changing environmental conditions. Also, future changes in the biogeochemical environment (such as increased iron deposition from industrial activity in east Asia) could have a strong effect as well.

This type of coarse resolution climate model is unable to resolve the dynamics of ocean boundary current systems. Yet primary production in these boundary currents, e.g., in the eastern boundary upwelling system of the North Pacific, is an important contributor to the earth's carbon budget.

Bakun (1990) suggested, based on observational evidence, that the warming of ocean temperatures associated with greenhouse conditions would lead to an inhibition of nighttime cooling and enhancement of daytime heating near the coast. This leads to an intensification of the continental thermal lows adjacent to the upwelling systems. The increase in onshore–offshore atmospheric pressure gradient would then be translated into an intensification of the coastal upwelling winds. More recently this idea has gained observational and modeling support. Schwing and Mendelssohn (1997) report a strengthening of upwelling favorable winds along the North Pacific eastern boundary current. Snyder et al. (2003) find a significant increase in upwelling favorable winds in a high-resolution regional climate model simulation forced by greenhouse gases.

In contrast to these observations of increased upwelling favorable winds, coastal observations over the last 50 years in the California Current System reveal a transition towards conditions that are more typical of reduced upwelling, such as a freshening of the surface waters in the coastal upwelling boundary (Bograd and Lynn, 2003; Di Lorenzo et al., 2005) and a decline in macrozooplankton abundance (Roemmich and McGowan, 1995). A possible explanation for these seemingly contradictory lines of evidence involves the observed increase in upper ocean stratification associated with warmer temperatures. In this scenario, the stratification exerts a stronger control than the winds on the ability of upwelling to supply subsurface nutrient-rich water at the coast (McGowan et al., 2003). This hypothesis has been tested with an eddy-resolving model of the coastal ocean driving a prognostic NPZ ecosystem model (Fig. 9). Di Lorenzo et al. (2005) performed model experiments that included as forcing conditions both the observed strengthening of the upwelling winds and the warming trend over the last 50 years. The effect of the increased stratification is strong enough in these experiments to inhibit the otherwise upwelling favorable conditions. The model chlorophyll response indicated a reduction in primary production in response to the combined effects of upper-ocean heating and increased upwelling favorable winds (Fig. 9).

Chai et al. (2003) used a coarse-resolution ocean model hindcast to determine that decadal climate variability has the largest impact on oceanic biological variability in the central North Pacific, a region bounded by two oceanographic fronts at approximately 30–32° N (Subtropical Front) and 42–45° N (Subarctic Front) in the central Pacific. This was based upon their analysis of the response of the MLD and the Ekman pumping to Pacific decadal variability. To extend this analysis and depict the possible changes in the carbon budget, Fig. 10 shows the spatially averaged modeled TCO_2 concentration for the central North Pacific (defined as follow: 35° N–45° N, 170° E–150° W).

The modeled monthly averaged TCO_2 concentration in the central North Pacific shows several scales of temporal variability between 1950 and 1993

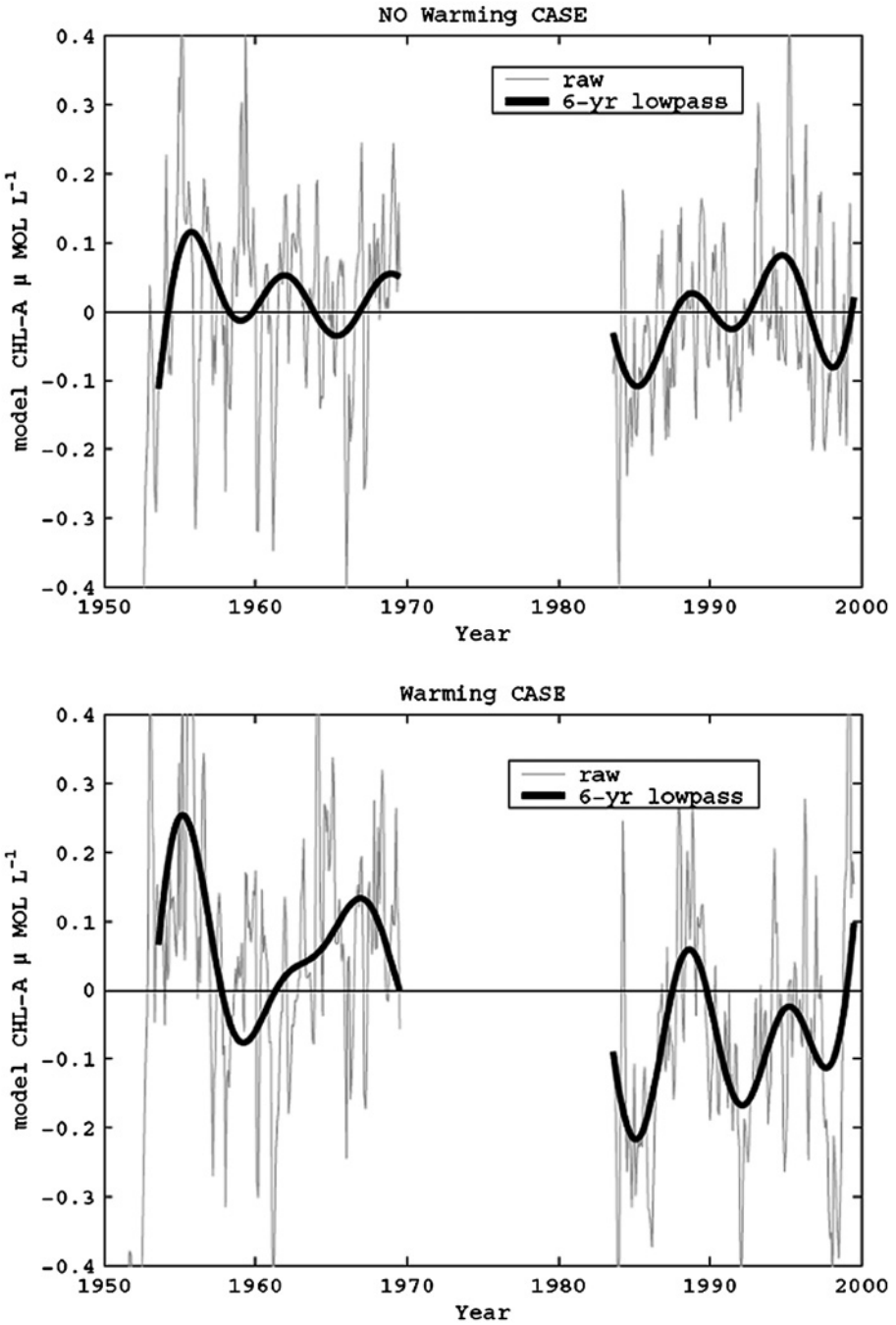

Figure 9: Time series of model surface Chl-a averaged over the eddy-resolving California Current model coastal boundary within 50 km from the coast. (a) Model experiment that include the strengthening of the upwelling winds but no warming conditions. (b) Same as (a) but the warming conditions are also included as forcing. See Di Lorenzo et al. (2005) for details of the physical model experiments.

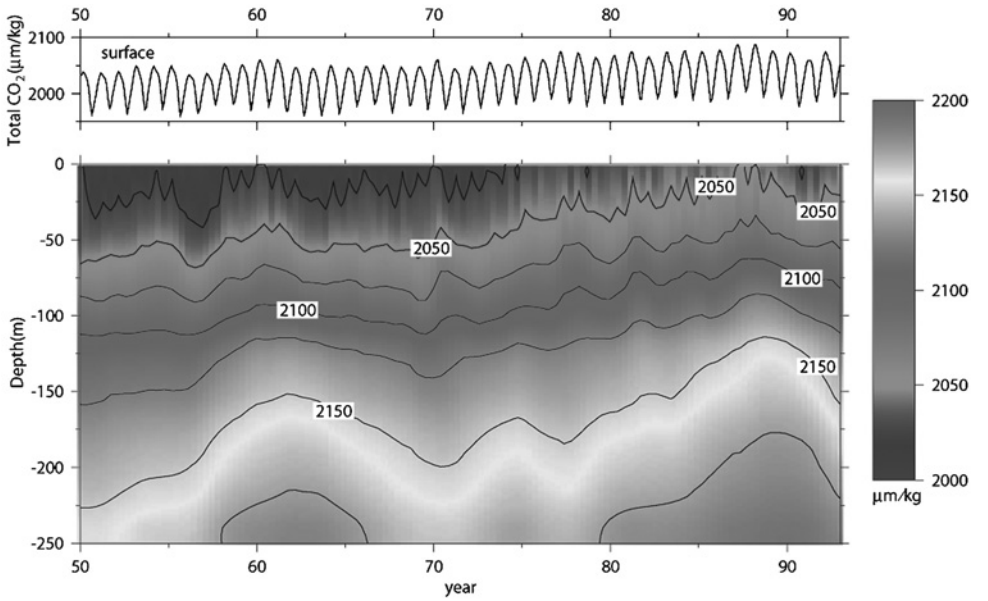

Figure 10: Time series of TCO_2 (unit: $\mu mol\,kg^{-1}$) in central north Pacific (35°–45° N, 170°–150° W). Top panel shows the time series of surface TCO_2 concentration. The lower panel shows the vertical profile of modeled TCO_2 concentration from the surface to 250 m. The contour interval is 25 $\mu mol\,kg^{-1}$ (For colour version, see Colour Plate Section).

(Fig. 10). First, the TCO_2 has a strong seasonal cycle in the central North Pacific, which is due to the seasonal cycle of upper-ocean physical conditions and biological uptake. The second most pronounced temporal variability between 1950 and 1993 is the influence of Pacific decadal variability. For example, the modeled TCO_2 concentration is higher during the 1980s and early 1960s, and the values are lower during 1970s and late 1960s. One of the reasons for the increase in modeled TCO_2 concentration during the 1980s is the change in ocean circulation and MLD in response to the wind pattern changes in the central North Pacific. Chai et al. (2003) found that the modeled winter MLD shows the largest increase between 30° N and 40° N in the central North Pacific (150° to 180° E), with a value 40–60% higher (deeper mixed layer) during 1979–1990 relative to 1964–1975 values. They also found that the winter and annual mean Ekman pumping velocity difference between 1979–1990 and 1964–1975 shows the largest increase located between 30° N and 45° N in the central and eastern North Pacific (180° to 150° W).

Beside the impact of decadal climate variability on the modeled TCO_2 concentration, there is another temporal trend (increasing from 1950 to 1993) in the modeled TCO_2 concentration in the central North Pacific. This increase is due to anthropogenic effects because the model is forced with the

observed atmospheric pCO_2 from 1950 to 1993, which increased significantly during this period. In order to separate the anthropogenic uptake and storage of CO_2 from the natural cycle of climate impact, Chai et al. (private communication, 2006) conducted a second experiment in which the atmospheric pCO_2 is fixed at 1950 values and other surface forcing are unchanged. By comparing the results from this twin experiments, Chai et al. (2005) estimated the anthropogenic uptake and storage of CO_2 in the Pacific Ocean solely due to the changing of atmospheric pCO_2, eliminating the effects of changing upper ocean circulation and mixing. The modeled anthropogenic CO_2 has a linear trend since 1950 with a surface-increasing rate of $0.57\,\mu molkg^{-1}y^{-1}$, which agrees with several independent estimates based on the observations (Sabine et al., 2004).

9 Conclusion

We have summarized many aspects of our current understanding of how climate change due to increasing greenhouse gases will affect oceanic biology and how the physical–biological feedbacks may influence the evolving physical climate system. The primary effects of ocean biology on physical climate were its influence on the carbon cycle, the influence of oceanic phytoplankton on upper-ocean absorption, and the influence of DMS production by phytoplankton on atmospheric aerosols. The primary influences of the physical climate on the ocean biology were the influence of aoelian dust deposition and the multitude of ways that community structure can be altered. Our focus was on the tropical and midlatitude Pacific Ocean, although results from other ocean basins were also noted.

The greatest need for building on our current understanding of these processes is long-term physical and biological observations in the ocean-atmosphere system. Modeling efforts must be constrained and instigated by these observational programs, and the observational strategies must be motivated by the model results as well. Since we still lack an adequate depiction of present-day oceanic community structures, it is very difficult to determine how they will change over time and how the climate feedbacks will be affected. Physical–biological modeling efforts should be directed to those few oceanic regions where we currently have a fair understanding of what species are present and how they vary naturally over time, such as the southern California Current System (CalCOFI region). We can then assess our skills at and prediction based on data gathered in the coming months or years. This will provide a fair assessment of our skills of predicting the responses of oceanic biology and the physical climate feedbacks on the centennial timescale of global warming.

Acknowledgements

Financial support for Miller, Neilson, Pierce, and Di Lorenzo was provided by the National Aeronautics and Space Administration (NAG5-9788), the National Oceanic and Atmospheric Administration (NA17RJ1231 through ECPC and CORC), the Department of Energy (DE-FG03-01ER63255), and the National Science Foundation (OCE-00-82543). Financial support for Chai was provided by the National Aeronautics and Space Administration (NASA-1043) and the National Science Foundation (OCE-01-37272). Financial support for Moisan was provided by NASA. The views herein are those of the authors and do not necessarily reflect the views of NOAA, NASA, or any of their subagencies.

References

Aebischer, N. J., Coulson, J. C., Colebrook, J. M., 1990. Parallel long-term trends across four marine trophic levels and weather. Nature 347, 753–755.

Agoumi, A., Gosse, P., Khalanski, M., 1985. Numerical modeling of the influence of vertical thermal structure on phytoplanktonic growth in the English Channel. Proceedings European Symposium on Marine Biology 19, 23–38.

Allen, M., Raper, S., Mitchell, J., 2001. Climate change – uncertainty in the IPCC's third assessment report. Science 293, 430–440.

Andreae, M. O., Crutzen, P. J., 1997. Atmospheric Aerosols: biogeochemical sources and role in atmospheric chemistry. Science 276, 1052–1058.

Arrigo, K. R., Robinson, D. H., Dunbar, R. B., Tullo, G. R. D., v. Woert, M., Lizotte, M. P., 1999. Phytoplankton community structure and the drawdown of nutrients and CO_2 in the Southern Ocean. Science 283, 365–367.

Bakun, A., 1990. Global climate change and intensification of coastal ocean upwelling. Science 247, 198–201.

Barnard, W. R., Andreae, M. O., Watkins, W. E., 1982. The flux of dimethylsulfide from the oceans to the atmosphere. Journal of Geophysical Research 87, 8787–8793.

Bates, T. S., Charlson, R. J., Gammon, R. H., 1987a. Evidence for the climatic role of marine biogenic sulfur. Nature 329, 319–321.

Bates, T. S., Cline, J. D., Gammon, R. H., Kelly-Hansen, S. R., 1987b. Regional and seasonal variations in the flux of oceanic dimethylsulfide to the atmosphere. Journal of Geophysical Research 92, 2930–2938.

Bates, T. S., Huebert, B. J., Gras, J. L., Griffiths, F. B., Durkee, P. A., 1998. International global atmospheric chemistry (IGAC) project's first aerosol characterization experiment (ACE-1): Overview. Journal of Geophysical Research 103, 16297–16318.

Beaugrand, G., Reid, P. C., 2003. Long-term changes in phytoplankton, zooplankton and salmon related to climate. Global Change Biology 9, 801–817.

Beaugrand, G., Reid, P. C., Ibanez, F., Lindley, A. J., Edwards, M., 2002. Reorganization of North Atlantic marine copepod biodiversity and climate. Science 296, 1692–1694.

Behrenfeld, M. J., Bale, A. J., Kolber, Z. S., Aiken, J., Falkowski, P. G., 1996. Confirmation of iron limitation of phytoplankton photosynthesis in the equatorial Pacific Ocean. Nature 383, 508–516.

Bograd, S. J., Lynn, R. J., 2003. Long-term variability in the Southern California current system. Deep-Sea Research Part II 50, 2355–2370.

Boyd, P. W., Doney, S. C., 2003. The impact of climate change and feedback processes on the ocean carbon cycle. In: Fasham, M. J. R. (Ed.), Ocean Biogeochemistry: The Role of the Ocean Carbon Cycle in Global Change. Springer-Verlag, Berlin, Heidelberg, New York, pp. 157–193.

Boyd, P. W., Law, C. S., 2001. The southern ocean iron release experiment (SOIREE)-introduction and summary. Deep Sea Research Part II 48, 2425–2438.

Chai, F., Jiang, M. S., Barber, R. T., Dugdale, R. C., Chao, Y., 2003. Interdecadal variation of the transition zone chlorophyll front: A physical-biological model simulation between 1960 and 1990. Journal of Oceanography 59, 461–475.

Chang, G. C., Dickey, T. D., 2004. Coastal ocean optical influences on solar transmission and radiant heating rate. Journal of Geophysical Research 109, Art. No. C01020.

Charlson, R. J., Lovelock, J. E., Andreae, M. O., Warren, S. G., 1987. Oceanic phytoplankton, atmospheric sulphur, cloud albedo and climate. Nature 326, 655–661.

Charlson, R. J., Schwartz, S. E., Hales, J. M., Cess, R. D., Coakley, J. A., Hansen, J. E., Hofmann, D. J., 1992. Climate forcing by anthropogenic aerosols. Science 255, 423–430.

Chin, M., Jacob, D. J., 1996. Anthropogenic and natural contributions to tropospheric sulfate: a global model analysis. Journal of Geophysical Research 101, 18691–18699.

Coale, K. H., et al., 1996. A massive phytoplankton bloom induced by an ecosystem-scale iron fertilization experiment in the equatorial Pacific Ocean. Nature 383, 495–501.

Colebrook, J. M., 1979. Continuous plankton records: Seasonal cycles of phytoplankton and copepods in the North Atlantic Ocean and the North Sea. Marine Biology 51, 23–32.

Cox, P. M., Betts, R. A., Jones, C. D., Spall, S. A., Totterdell, I. J., 2000. Acceleration of global warming due to carbon-cycle feedbacks in a coupled climate model. Nature 408, 184–187.

Dacey, J. W. H., Howse, F. A., Michaels, A. F., Wakeham, S. G., 1998. Temporal variability of dimethylsulfide and dimethylsulfoniopropionate in the Sargasso Sea. Deep-Sea Research Part I 45, 2085–2104.

de Baar, H. J. W., de Jong, J. T. M., Bakker, D. C. E., Loscher, B. M., Veth, C., Bathmann, U., Smetacek, V., 1995. Importance of iron for plankton blooms and carbon dioxide drawdown in the Southern Ocean. Nature 373, 412–415.

De La Rocha, C. L., Brzezinski, M. A., DeNiro, M. J., Shemesh, A., 1998. Silicon isotope composition of diatoms as an indicator of past oceanic change. Nature 395, 680–683.

Di Lorenzo, E., Miller, A. J., Schneider, N., McWilliams, J. C., 2005. The warming of the California current: Dynamics, thermodynamics and ecosystem implications. Journal of Physical Oceanography 35, 336–362.

DiTullio, G. R., Grebmeir, J., Lizzote, M. P., Arrigo, K. R., Robinson, D. H., Leventer, A., Barry, J., Van Woert, M., Dunbar, R. B., 2000. Rapid and early export of *Phaeocystis antarctica* blooms to deep water and sediments of the Ross Sea. Antarctica. Nature 404, 595–598.

Duce, R. A., Tindale, N. W., 1991. Atmospheric transport of iron and its deposition in the ocean. Limnology and Oceanography 36, 1715–1726.

Edwards, A. M., Brindley, J., 1999. Zooplankton mortality and the dynamical behaviour of plankton population models. Bulletin of Mathematical Biology 61, 303–339.

Edwards, A. M., Platt, T., Wright, D. G., 2001. Biologically-induced circulation at fronts. Journal of Geophysical Research 106, 7081–7095.

Edwards, A. M., Wright, D. G., Platt, T., 2004. Biological heating effect of a band of phytoplankton. Journal of Marine Systems 49, 89–103.

Falkowski, P. G., Barber, R. T., Smetacek, V., 1998. Biogeochemical controls and feedbacks on ocean primary production. Science 281, 200–206.

Falkowski, P., Scholes, R. J., Boyle, E., Canadell, J., Canfield, D., Elser, J., Gruber, N., Hibbard, K., Hogberg, P., Linder, S., Mackenzie, F. T., Moore, B., Pedersen, T., Rosenthal, Y., Seitzinger, S., Smetacek, V., Steffen, W., 2000. The global carbon cycle: A test of our knowledge of earth as a system. Science 290, 291–296.

Foley, J. A., Taylor, K. E., Ghan, S. J., 1991. Planktonic dimethylsulfide and cloud albedo: an estimate of the feedback response. Climatic Change 18, 1–15.

Frouin, R., Iacobellis, S., 2002. Influence of phytoplankton on the global radiation budget. Journal of Geophysical Research 107, Art No. 4377.

Gabric, A. J., Cropp, R., Ayers, G. P., McTainsh, G., Braddock, R., 2002. Coupling between cycles of phytoplankton biomass and aerosol optical depth as derived from SeaWiFS time series in the Subantarctic Southern Ocean. Geophysical Research Letters 29, Art. No. 1112.

Gabric, A. J., Cropp, R., Hirst, A., Marchant, H., 2003. The sensitivity of dimethylsulphide production to simulated climate change in the eastern Antarctic Southern Ocean. Tellus B 55, 966–981.

Gabric, A. J., Gregg, W., Najjar, R., Erickson, D., Matrai, P., 2001a. Modelling the biogeochemical cycle of dimethylsulphide in the upper ocean. Chemosphere: Global Change Science 3, 377–392.

Gabric, A., Murray, C. N., Stone, L., Kohl, M., 1993. A model of dimethylsulphide production during a phytoplankton bloom. In: Restelli, G., Angeletti, G. (Eds.), Dimethylsulfide: Oceans, Atmosphere and Climate. Kluwer Academic, Netherlands, pp. 63–81.

Gabric, A. J., Whetton, P., Cropp, R., 2001b. Dimethylsulphide production in the subantarctic Southern Ocean under enhanced greenhouse conditions. Tellus B 53, 273–287.

Gao, Y., Kaufman, Y. J., Tanre, D., Kolber, D., Falkowski, P. G., 2001. Seasonal distributions of aeolian iron fluxes to the global ocean. Geophysical Research Letters 28, 29–32.

Gaspar, P., 1985. Modéles de la couche active de l'océan pour des simulations climatiques. Ph.D. Thesis, 154 pp., Universite Catholique de Louvain, Louvain, Belgium, unpublished.

Gaspar, P., 1988. Modeling the seasonal cycle of the upper ocean. Journal of Physical Oceanography 18, 161–180.

Gildor, H., Follows, M. J., 2002. Two-way interactions between ocean biota and climate mediated by biogeochemical cycles. Israel Journal of Chemistry 42, 15–27.

Gildor, H., Sobel, A. H., Cane, M. A., Sambrotto, R. N., 2003. A role for ocean biota in tropical intraseasonal atmospheric variability. Geophysical Research Letters 30. Art. No. 1460.

Ginoux, P., Chin, M., Tegen, I., Prospero, J., Holben, B., Dubovik, O., L. S.-J., 2001. Global simulation of dust in the troposphere: Model description and assessment. Journal of Geophysical Research 106, 20,255–20,273.

Gondwe, M., Krol, M., Gieskes, W., Klaassen, W., de Baar, H., 2003. The contribution of ocean-leaving DMS to the global atmospheric burdens of DMS, MSA, SO_2, and NSS SO_4^{2-}. Global Biogeochemical Cycles 17. Art. No. 1056.

Grassl, H., 2000. Status and improvements of coupled general circulation models. Science 288, 1991–1997.

Hirst, A. C., 1999. The Southern Ocean response to global warming in the CSIRO coupled ocean atmosphere model. Environmental Modelling and Software 14, 227–241.

Houghton, J. T., Meira Filho, L. G., Callander, B. A., Harris, N., Kattenberg, A., Varney, S. K., 1996. Climate change 1995: Contribution of Working Group 1 to the Second Assessment Report of the IPCC. Cambridge University Press, Cambridge, p. 572.

Howard, W. R., Prell, W. L., 1994. Late quaternary $CaCO_3$ production and preservation in the Southern Ocean: Implications for oceanic and atmospheric carbon cycling. Paleooceanography 9, 453–482.

Huebert, B. J., Pszenny, A., Blomquist, B., 1996. The ASTEX/MAGE experiment. Journal of Geophysical Research 101, 4319–4329.

IPCC, 2001. Climate Change 2001. Cambridge University Press, New York.

Ittekkot, V., Jilan, S., Miles, E., Desa, E., Desai, B. N., Everett, J. T., Magnuson, J. J., Tsyban, A., Zuta, S., 1996. Oceans. In: Watson, R. T., Zinyowera, M. C., Moss, R. H. (Eds.), Climate Change 1995: Impacts, Adaptations, and Mitigation of Climate Change: Scientific-Technical Analyses. Contribution of Working Group II to the Second Assessment Report of the Intergovernmental Panel on Climate Change. Cambridge University Press, Cambridge, United Kingdom and New York, NY, USA, pp. 267–288.

Jerlov, N. G., 1968. Optical Oceanography. Amsterdam: Elsevier, p. 194.
Joos, F., Plattner, G., Stocker, T. F., Marchal, O., Schmittner, A., 1999. Global warming and the marine carbon cycle feedbacks on future atmospheric CO_2. Science 284, 464–467.
Kahru, M., Leppänen, J.-M., Rud, O., 1993. Cyanobacteria blooms cause heating of the sea surface. Marine Ecology Progress Series 101, 1–7.
Karl, D. M., 1999. A sea of change: Biogeochemical variability in the North Pacific Subtropical Gyre. Ecosystems 2, 181–214.
Karl, D. M., Bjorkman, K. M., Dore, J. E., Fujieki, L., Hebel, D. V., Houlihan, T., Letelier, R. M., Tupas, L. M., 2001. Ecological nitrogen-to-phosphorus stoichiometry at station ALOHA. Deep-Sea Research 48, 1529–1566.
Karl, D. M., Letelier, R., Hebel, D., Tupas, L., Dore, J., Christian, J., Winn, C., 1995. Ecosystem changes in the North Pacific subtropical gyre attributed to the 1991–1992 El Niño. Nature 373, 230–234.
Kennedy, V. S., Mihursky, J. A., 1971. Upper temperature tolerances of some estuarine bivalves. Chesapeake Science 12, 193–204.
Kennedy, V. S., Twilley, R. R., Kleypas, J. A., Cowan, J. H., Hare, S. R., 2002. Coastal and Marine Ecosystem and Global Climate Change. Pew Center for Global Climate Change, Arlington, VA, p. 51.
Kershaw, R., 1985. Onset of the southwest monsoon and sea-surface temperature anomalies in the Arabian Sea. Nature 315, 561–563.
Kettle, A., Andreae, M. O., 2000. Flux of dimethylsulphide from the oceans: a comparison of updates data sets and flux models. Journal of Geophysical Research 105, 26793–26808.
Kettle, A. J., et al., 1999. A global database of sea surface dimethylsulfide (DMS) measurements and a procedure to predict sea surface DMS as a function of latitude, longitude and month. Global Biogeochemical Cycles 13, 399–444.
Kiene, R. P., 1999. Sulfur in the mix. Nature 402, 363–365.
Kirst, G. O., Thiel, C., Wolff, H., Nothnagel, J., Wanzek, M., 1991. Dimethylsulfoniopropionate (DMSP) in ice algae and its possible biological role. Marine Chemistry 35, 381–388.
Kumar, N., Anderson, R. F., Mortlock, R. A., Froelich, P. N., Kublik, P., Dittrich-Hannen, B., Suer, M., 1995. Increased biological activity and export production in the glacial Southern Ocean. Nature 378, 675–680.
Lashof, D. A., 1989. The dynamic greenhouse: Feedback processes that may influence future concentrations of atmospheric trace gases and climate change. Climatic Change 14, 213–242.
Lawrence, M. G., 1993. An empirical analysis of the strength of the phytoplankton-dimethylsulfide-cloud-climate feedback cycle. Journal of Geophysical Research 98, 20663–20673.
Leck, C., Bigg, E. K., Covert, D. S., Heintzenberg, J., Maenhaut, W., Nilsson, E. D., Wiedensohler, A., 1996. Overview of the atmospheric research programme during the International Arctic Ocean Expedition of 1991 (IAOE–91) and its scientific results. Tellus B 48, 136–155.

Leck, C., Larsson, U., Bagander, L. E., Johansson, S., Hajdu, S., 1990. Dimethyl sulfide in the Baltic Sea: Annual variability in relation to biological activity. Journal of Geophysical Research 95, 3353–3363.

Lee, P. A., de Mora, S. J., Levasseur, M., 1999. A review of dimethylsulfoxide in aquatic environments. Atmosphere-Ocean 37, 439–456.

Legrand, M., Feniet-Saigne, C., Saltzman, E., Germain, C., Barkov, N., Petrov, V., 1991. Ice-core record of oceanic emissions of dimethylsulfide during the last climate cycle. Nature 350, 144–146.

Lewis, M. R., Cullen, J. J., Platt, T., 1983. Phytoplankton and thermal structure in the upper ocean: Consequences of nonuniformity in chlorophyll profile. Journal of Geophysical Research 88, 2565–2570.

Liss, P. S., Malin, G., Turner, S. M., 1993. Production of DMS by phytoplankton. In: Restelli, G., Angeletti, G. (Eds.), Dimethylsulfide: Oceans, Atmosphere and Climate. Kluwer Academic, The Netherlands, pp. 1–14.

Liss, P. S., Slater, P. G., 1974. Fluxes of gases across the air-sea interface. Nature 247, 181–184.

Manizza, M., Le Quere, C., Watson, A. J., Buitenhuis, E. T., 2005. Bio-optical feedbacks among phytoplankton, upper ocean physics and sea-ice in a global model. Geophysical Research Letters 32 doi:10.1029/2004GL020778.

Martin, J. H., 1990. Glacial-interglacial CO_2 change: The iron hypothesis. Paleooceanography 5, 1–13.

Martin, J. H., Coale, K. H., Johnson, K. S., 1994. Testing the iron hypothesis in ecosystems of the equatorial Pacific Ocean. Nature 371, 123–129.

Marzeion, B., Timmermann, A., Murtugudde, R., Jin, F.-F., 2005. Bio-physical feedbacks in the tropical Pacific. Journal of Climate 18, 58–70.

McClain, C. R., Christian, J. R., Signorini, S. R., Lewis, M. R., Asanuma, I., Turk, D., Dupouy-Douchement, C., 2002. Satellite ocean-color observations of the tropical Pacific Ocean. Deep-Sea Research Part II 49, 2533–2560.

McGowan, J. A., Bograd, S. J., Lyn, R. J., Miller, A. J., 2003. The biological response to the 1977 regime shift in the California Current. Deep-Sea Research Part II 50, 2567–2582.

Mellor, G. L., Yamada, T., 1982. Development of a turbulence closure model for geophysical fluid problems. Reviews of Geophysics 20, 851–875.

Miller, A. J., Alexander, M. A., Boer, G. J., Chai, F., Denman, K., Erickson, D. J., Frouin, R., Gabric, A. J., Laws, E. A., Lewis, M. R., Liu, Z., Murtgudde, R., Nakamoto, S., Neilson, D. J., Norris, J. R., Ohlmann, J. C., Perry, R. I., Schneider, N., Shell, K. M., Timmermann, A., 2003. Potential feedbacks between Pacific Ocean ecosystems and interdecadal climate variations. Bulletin of the American Meteorological Society 84, 617–633.

Moore, J. K., Abbott, M. R., Richman, J. R., Nelson, D. M., 2000. The Southern Ocean at the last glacial maximum: A strong sink for atmospheric carbon dioxide. Global Biogeochemical Cycles 14, 455–475.

Morel, A., Antoine, D., 1994. Heating rate within the upper ocean in relation to its bio-optical state. Journal of Physical Oceanography 24, 1652–1665.

Murtugudde, R., Beauchamp, J., McClain, C. R., Lewis, M., Busalacchi, A. J., 2003. Effects of penetrative radiation on the upper tropical ocean circulation. Journal of Climate 15, 470–476.

Nakamoto, S., Prasanna Kumar, S., Oberhuber, J. M., Ishizaka, J., Muneyama, K., Frouin, R., 2001. Response of the equatorial Pacific to chlorophyll pigment in a mixed layer isopycnal ocean general circulation model. Geophysical Research Letters 28, 2021–2024.

Nakamoto, S., Prasanna Kumar, S., Oberhuber, J. M., Muneyama, K., Frouin, R., 2000. Chlorophyll modulation of sea surface temperature in the Arabian Sea in a mixed layer-isopycnal general circulation model. Geophysical Research Letters 27, 747–756.

Ohlmann, J. C., 2003. Ocean radiant heating in climate models. Journal of Climate 16, 1337–1351.

Ohlmann, J. C., Siegel, D. A., Gauthier, C., 1996. Ocean mixed layer radiant heating and solar penetration: A global analysis. Journal of Climate 9, 2265–2280.

Ohlmann, J. C., Siegel, D. A., Washburn, L., 1998. Radiant heating of the western equatorial Pacific during TOGA-COARE. Journal of Geophysical Research 103, 5379–5395.

Oschlies, A., 2004. Feedbacks of biotically induced radiative heating on upper-ocean heat budget, circulation, and biological production in a coupled ecosystem-circulation model. Journal of Geophysical Research 109 doi:10.1029/2004JC002430.

Paulson, C. A., Simpson, J. J., 1977. Irradiance measurements in the upper ocean. Journal of Physical Oceanography 7, 953–956.

Petchey, O. L., McPhearson, P. T., Casey, T. M., Morin, P. J., 1999. Environmental warming alters food-web structure and ecosystem function. Nature 402, 69–72.

Petit, J. R., et al., 1999. Climate and atmospheric history of the past 420,000 years from the Vostok ice core, Antarctica. Nature 399, 429–436.

Pierce, D. W., 2003. Future changes in biological activity in the North Pacific due to anthropogenic forcing of the physical environment. Climatic Change 62, 45–74.

Platt, T., 1969. The concept of energy efficiency in primary production. Limnololgy and Oceanography 14, 653–659.

Poff, N. E., Brinson, M. M., Day, J. W., 2002. Aquatic Ecosystems and Global Climate Change. Pew Center on Global Climate Change, Arlington, VA, p. 44.

Price, J. F., Weller, R. A., Pinkel, R., 1986. Diurnal cycling: Observations and models of the upper ocean response to diurnal heating, cooling, and wind mixing. Journal of Geophysical Research 91, 8411–8427.

Ramanathan, V., Subasilar, B., Zhang, G., Conant, W., Cess, R., Kiehl, J., Grassl, H., Shi, L., 1995. Warm pool heat budget and shortwave cloud forcing: A missing physics?. Science 267, 499–503.

Ramp, S. R., Garwood, R. W., Davis, C. O., Snow, R. L., 1991. Surface heating and patchiness in the coastal ocean of central California during a wind relaxation event. Journal of Geophysical Research 96, 14,947–14,957.

Ridgwell, A. J., 2002. Dust in the Earth system: The biogeochemical linking of land, air, and sea. Philosophical Transactions of the Royal Society A 360, 2905–2924.

Rochford, P. A., Kara, A. B., Wallcraft, A. J., Arnone, R. A., 2001. Importance of solar subsurface heating in ocean general circulation models. Journal of Geophysical Research 106, 30,923–30,938.

Roemmich, D., McGowan, J., 1995. Climatic warming and the decline of zooplankton in the California current. Science 256, 1311–1313.

Sabine, C. L., Feely, R. A., Watanabe, Y. W., Lamb, M. F., 2004. Temporal evolution of the North Pacific Ocean CO_2 uptake. Journal of Oceanography 60, 5–15.

Sarmiento, J. L., Hughes, T. M. C., Stouffer, R. J., Manabe, S., 1998. Simulated response of the ocean carbon cycle to anthropogenic climate warming. Nature 393, 245–249.

Sarmiento, J. L., Quéré, C. L., 1996. Oceanic carbon dioxide uptake in a model of century scale global warming. Science 274, 1346–1350.

Sathyendranath, S., Gouveia, A. D., Shetye, S. R., Ravindran, P., Platt, T., 1991. Biological control of surface temperature in the Arabian Sea. Nature 349, 54–56.

Schudlich, R. R., Price, J. F., 1992. Diurnal cycles of current, temperature, and turbulent dissipation in a model of the equatorial upper ocean. Journal of Geophysical Research 97, 5409–5422.

Schwartz, S. E., 1988. Are global cloud albedo and climate controlled by marine phytoplankton. Nature 336, 441–445.

Schwing, F. B., Mendelssohn, R., 1997. Increased coastal upwelling in the California Current System. Journal of Geophysical Research 102, 3421–3438.

Shaw, G. E., 1983. Bio-controlled thermostasis involving the sulphur cycle. Climatic Change 5, 297–303.

Shell, K. M., Frouin, R., Nakamoto, S., Somerville, R. C. J., 2003. Atmospheric response to solar radiation absorbed by phytoplankton. Journal of Geophysical Research 108, 4445 doi:10.1029/2003JD003440.

Sherwood, K., Idso, C., 2003. Demise of "The CLAW" greatly exaggerated. CO_2 Science Magazine 6, Editorial.

Siegel, D. A., Dickey, T. D., 1987. On the parameterization of irradiance for open ocean photoprocesses. Journal of Geophysical Research 92, 14,648–14,662.

Siegel, D. A., Ohlmann, J. C., Washburn, L., 1995. Solar radiation, phytoplankton pigments and the radiant heating of the equatorial Pacific warm pool. Journal of Geophysical Research 100, 4885–4891.

Siegel, D. A., Westberry, T. K., Ohlmann, J. C., 1999. On ocean color and ocean radiant heating. Journal of Climate 12, 1101–1116.

Siegenthaler, U., Sarmiento, J. L., 1993. Atmospheric carbon dioxide and the ocean. Nature 365, 119–125.

Simó, R., 2001. Production of atmospheric sulfur by oceanic plankton: Biogeochemical, ecological and evolutionary links. Trends in Ecology and Evolution 16, 287–294.

Simó, R., Dachs, J., 2002. Global ocean emission of dimethylsulfide predicted from biogeophysical data. Global Biogeochemical Cycles 16 Art. No. 1078.

Simó, R., Pedrós-Alló, C., 1999. Role of vertical mixing in controlling the oceanic production of dimethyl sulphide. Nature 402, 396–399.

Simonot, J.-Y., Dollinger, E., Le Treut, H., 1988. Thermodynamic-biological-optical coupling in the oceanic mixed layer. Journal of Geophysical Research 93, 8193–8202.

Smith, R. C., Baker, K. S., 1978. The bio-optical state of ocean waters and remote sensing. Limnology and Oceanography 23, 247–259.

Snyder, M. A., Sloan, L. C., Diffenbaugh, N. S., Bell, J. L., 2003. Future climate change and upwelling in the California Current. Geophysical Research Letters 30 Art. No. 1823.

Stefels, J., 2000. Physiological aspects of the production and conversion of DMSP in marine algae and higher plants. Journal of Sea Research 43, 183–197.

Stramska, M., Dickey, T. D., 1993. Phytoplankton bloom and the vertical thermal structure of the upper ocean. Journal of Marine Research 51, 819–842.

Sunda, W., Kieber, D. J., Kiene, R. P., Huntsman, S., 2002. An antioxidant function for DMSP and DMS in marine algae. Nature 418, 317–320.

Timmermann, A., Jin, F.-F., 2002. Phytoplankton influences on tropical climate. Geophysical Research Letters 29, 2104 doi:10.1029/2002GL015434.

Ueyoshi, K., Stammer, D., Nakamoto, S., Subrahamanyam, B. Prasanna-Kumar, S., Muneyama, K., 2003. Sensitivity of the equatorial Pacific Ocean circulation to chlorophyll modulation of penetrative solar radiation in a GCM. XXII General Assembly of the International Union of Geodesy and Geophysics, IUGG 2003 Scientific Program and Abstracts, Sapporo, Japan. JSP09/11P/B20-002, page B.103.

Veit, R. R., Pyle, P., McGowan, J. A., 1996. Ocean warming and long-term change in pelagic bird abundance within the California current system. Marine Ecology Progress Series 139, 11–18.

Washington, W. M., Weatherly, J. W., Meehl, G. A., Semtner, A. J., Bettge, T. W., Craig, A. P., Strand, W. G., Arblaster, J., Wayland, V. B., James, R., Zhang, Y., 2000. Parallel Climate Model (PCM) control and transient simulations. Climate Dynamics 16, 755–774.

Watson, A. J., Bakker, D. C. E., Ridgwell, A. J., Boyd, P. W., Law, C. S., 2000. Effect of iron supply on Southern Ocean CO_2 uptake and implications for glacial atmospheric CO_2. Nature 407, 730–733.

Woodwell, G. M., Mackenzie, F. T., Houghton, R. A., Apps, M., Gorham, E., Davidson, E., 1998. Biotic feedbacks in the warming of the earth. Climatic Change 40, 495–518.

Zhuang, G. S., Yi, Z., Duce, R. A., Brown, P. R., 1992. Link between iron and sulfur cycles suggested by detection of Fe(II) in remote marine aerosols. Nature 355, 537–539.

This page intentionally left blank

Chapter 3

Simulated *In Situ* Measurements of Primary Production in Japanese Waters

Katsumi Yokouchi[1,*], Atsushi Tsuda[2], Akira Kuwata[3], Hiromi Kasai[4], Tadafumi Ichikawa[5], Yuichi Hirota[5], Kumiko Adachi[6], Ichio Asanuma[7] and Hiroshi Ishida[8]

[1]*Seikai National Fisheries Research Institute, Fisheries Research Agency, 1551-8 Taira-machi, Nagasaki 851-2213, Japan*
[2]*Ocean Research Institute, University of Tokyo, 1-15-1 Minamidai, Tokyo 164-8639, Japan*
[3]*Tohoku National Fisheries Research Institute, Fisheries Research Agency, 3-27-5 Shinhama-cho, Shiogama, Miyagi 985-0001, Japan*
[4]*Hokkaido National Fisheries Research Institute, Fisheries Research Agency, 116 Katsuragoi, Kushiro, Hokkaido 085-0802, Japan*
[5]*National Research Institute of Fisheries Science, Fisheries Research Agency, 6-1-21 Sanbashidori, Kochi 780-8010, Japan*
[6]*National Research Institute of Fisheries Engineering, Fisheries Research Agency, Ebidai, Hasaki, Kashima 314-0421, Japan*
[7]*Frontier Research Promotion Department, JAMSTEC, 2173-25 Showa, Kanazawa, Yokohama, Kanagawa 236-0001, Japan*
[8]*General Environmental Technos Co., Ltd., 1-3-5 Ando-cho, Chuo-ku, Osaka 541-0052, Japan*

Abstract

In the global carbon cycle and related mapping based on satellite imagery program (GCMAPS), daily primary production, integrated over the euphotic zone (IPP), was measured around Japan for the validation of algorithms to estimate primary productivity derived from satellite observations. A total of 176 measurements were made by simulated *in situ* deck-incubations and a small number of *in situ* incubations, with inoculation of stable isotope ^{13}C-bicarbonate, essentially according to the JGOFS protocol. IPP ranged from 30 mgC/m^2/day

*Corresponding author.
E-mail address: yokouchi@affrc.go.jp (K. Yokouchi).

Elsevier Oceanography Series 73
Edited by H. Kawahata and Y. Awaya
ISBN: 0-444-52948-9

in March in Oyashio-transition waters (subarctic) to 3,980 mgC/m^2/day in May in continental shelf waters of the East China Sea (ECS, subtropic Case II). IPP varied seasonally in Oyashio-transition waters, with high values from April to August, and very low values from September to March. In contrast, seasonal variations in IPP in other areas were not marked, with a slight increase in May in Kuroshio waters (subtropic) and Tosa Bay (subtropic inshore), and in both May and August in ECS continental shelf waters. We estimated annual primary production (gC/m^2/year) to be 340 in ECS continental shelf waters, 280 in Tosa Bay, 200 in Oyashio-transition waters, and 110 in Kuroshio waters. Maximum primary production per unit of chlorophyll *a* (P^B_{opt}) tended to increase with temperature where sea surface temperature (SST) was between 0 and 30°C, but varied largely above about 16°C in the subtropics including Kuroshio waters, Tosa Bay, and ECS continental shelf waters. The water-column light-utilization efficiency index increased as photosynthetically available radiation (PAR) on the surface decreased in Oyashio-transition waters, Kuroshio waters, and ECS continental shelf waters. We propose preliminary empirical relationships for estimating IPP from standing stock of chlorophyll *a* (IPP) and surface PAR (integrated over a day), for these three waters around Japan.

Keywords: primary production; simulated *in situ* method; ^{13}C-spiked incubations; seasonal variations; validation

1 Introduction

Primary production by phytoplankton supports biological processes and fisheries production in the ocean (Ryther, 1969; Nixon, 1988). Carbon fixation by photosynthesis in the euphotic zone acts as a biological pump to transport CO_2 from air to deeper layers, and is a key process in understanding global warming (Sarmiento and Toggweider, 1984; Duarte and Cebrian, 1996). Ocean color observation by satellites is an effective tool for exploring temporal and spatial variations in primary production at basin and global scales (Geider and Osborne, 1992). Using the data derived from the ocean color satellite sensor, Sea-viewing Wide Field-of-view Sensor (SeaWiFS), Behrenfeld and Falkowski (1997) estimated the primary productivity in the ocean, which was revealed to be equivalent to that of terrestrial forests. However, the dataset used for this estimation did not include data from the western North Pacific and waters around Japan. It is necessary to develop specialized algorithms for Japanese waters in order to more accurately evaluate global primary productivity from satellite images (Asanuma et al., 2000, 2001a, b; Kameda and Ishizaka, 2003).

Following the development of the ^{14}C method by Steemann-Nielsen (1952), measurement of primary production became routine for oceanographic observations worldwide (Behrenfeld et al., 2002). In Japan, however, legal restriction regarding the use of radioactive carbon ^{14}C resulted in very few measurements being made (e.g., Aruga and Monsi, 1962; Matsudaira,

1964). After Hama et al. (1983) established a stable isotope ^{13}C method, *in situ* measurements of primary production have increased around Japan (e.g., Shiomoto, 2000; Imai et al., 2002). However, the accumulated *in situ* measurement data are still insufficient for validation of algorithms around Japan.

This study aims to: (1) construct a dataset of primary production by *in situ* or simulated *in situ* measurements for algorithm validation for data from SeaWiFS operational periods, and (2) extract seasonal variations in primary production using basin-scale comparisons around Japan. This study was supported by the Japanese Ministry of Education, Culture, Sports, Science and Technology (MEXT) as part of the Global Carbon Cycle and Related Mapping based on Satellite Imagery Program (GCMAPS). All data are available in the JGOFS North Pacific Process Study data set distributed by Japan Oceanographic Data Center.

2 Materials and Methods

2.1 Dataset of Primary Production Around Japan

The GCMAPS project constructed a dataset of primary production by ^{13}C-spiked incubations in a wide range of Pacific Ocean environments, ranging from equatorial to subarctic waters. Data collected included sampling location, date, daily photosynthetically available radiation (PAR), euphotic zone depth (from the surface to a depth where light levels equal 1% of surface light), and temperature, relative irradiance, and chlorophyll *a* at each sampling depth within the euphotic zone. This study used 176 measurements from that dataset; these measurements are based on 24-h incubations using an *in situ* or simulated *in situ* method, collected from April 1999 to March 2003, from subtropic to subarctic waters around Japan (Fig. 1).

2.2 Definition of Waters

Oyashio waters (subarctic), the Oyashio-Kuroshio transition, and Kuroshio waters (subtropic) were distinguished according to Kawai's (1972) definition, using the temperature at a depth of 100 or 200 m. This study uses the term "Oyashio-transition waters" to describe the area including Oyashio waters and the Kuroshio-Oyashio transition. A fixed station (lat 33°12'54"N, long 133°23'36"E) in Tosa Bay with a bottom depth of 100 m was located inshore northwest of Kuroshio waters. The East China Sea (ECS, subtropic) was divided into two regions (continental shelf waters and Kuroshio waters) using a definition based on the temperature at a depth of 200 m (Kawai, 1972). The term "Kuroshio waters" as used in this study includes the Kuroshio waters, the ECS, and Pacific inshore areas. ECS continental shelf waters are a typical Case II, a group of water with higher chlorophyll *a* and

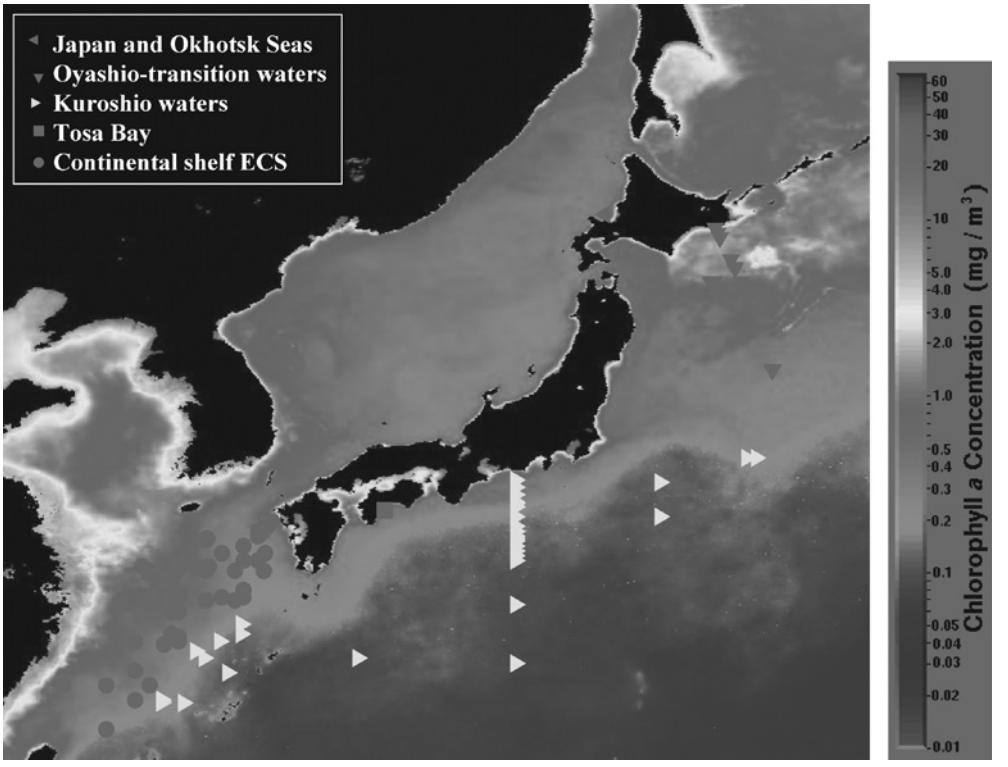

Figure 1: Measuring sites for primary production using a ^{13}C spiked incubation for 24 hours in Japan and Okhotsk Seas, Oyashio-transition waters, Kuroshio waters, Tosa Bay, and continental shelf waters in the East China Sea overlaid on an annual mean of chlorophyll *a* in 2002 derived from SeaWiFS (http://www.seawifs.gsfc.nasa.gov/cgi/level3.pl/) (For colour version, see Colour Plate Section).

suspended matters(Morel and Prieur, 1977) under the influence of Chinese Coastal waters and the effluent from the Changjiang River. The dataset consists of 48 measurements in Oyashio-transition waters, 46 in Kuroshio waters, 18 in Tosa Bay, 58 in ECS continental shelf waters, and 6 in the Japan and Okhotsk Seas (Table 1).

2.3 ^{13}C-Spiked Incubations and Calculations for Primary Production

Primary production was measured via the *in situ* or simulated *in situ* incubation method, essentially according to the Joint Global Ocean Flux Study (JGOFS) protocol (Knap et al., 1996). Vertical profile of relative PAR in the euphotic zone was estimated using transparency measured by Secchi disk (Poole and Atkins, 1929) or directly measured with a PRR-600 Profiling

Table 1: Primary production and related parameters observed around Japan

Number	Cruise	Date	Latitude (°N)	Longitude (°E)	1% light depth (m)	Surface temperature (°C)	Total daily incident PAR (E/m^2/d)	Surface chlorophyll a (μg/l)	Standing stock of chlorophyll a (mg/m^2)	P^B_{opt} (mgC/mgChl/d)	Primary production		Method	Starting time	Region
											Surface (mgC/m^3/d)	Integrated over euphotic zone (mgC/m^2/d)			
1	TK9908	Aug. 8, 1999	43°18.1′N	140°55.3′E	44	22.4	64.5	1.94	36.61	57.68	112.07	725	Simulated	14:10	JSOKH
2	TK0004	Apr. 22, 2000	44°29.9′N	144°19.9′E	50	0.0	12.4	2.05	55.63	9.44	18.01	380	Simulated	12:45	JSOKH
3	TK0005	May 27, 2000	45°29.9′N	145°10.0′E	25	4.2	15.1	0.91	24.19	16.61	15.06	184	Simulated	13:35	JSOKH
4	HK0010	Oct. 10, 2000	45°00.0′N	144°44.9′E	48	13.1	nd	0.45	42.30	31.37	14.21	462	Simulated	13:45	JSOKH
5	TK0107B	Jul. 22, 2001	45°13.3′N	143°05.4′E	40	16.5	nd	0.40	50.89	43.07	17.31	378	Simulated	9:40	JSOKH
6	TK0110	Oct. 7, 2001	45°00.0′N	144°44.9′E	40	12.5	24.0	0.73	34.83	22.89	16.75	361	Simulated	14:45	JSOKH
7	TK9904	Apr. 16, 1999	41°45.0′N	145°22.4′E	28	2.0	32.1	7.42	172.48	21.66	90.37	1,708	Simulated	10:00	O
8	TK9904	Apr. 19, 1999	42°29.9′N	145°00.0′E	60	2.6	54.9	0.42	26.26	10.52	4.46	140	Simulated	7:50	O
9	TK9908	Aug. 3, 1999	42°49.9′N	144°49.9′E	15	12.7	47.1	4.86	159.23	44.14	214.57	1,529	Simulated	14:40	O
10	HK9910	Oct. 10, 1999	40°00.0′N	146°15.0′E	45	16.0	22.8	0.81	33.71	37.13	29.95	491	Simulated	10:55	O
11	TK0004	Apr. 20, 2000	41°00.0′N	145°44.9′E	15	2.6	41.5	15.00	264.62	11.72	175.89	1,610	Simulated	10:45	O
12	TK0004	Apr. 21, 2000	42°40.0′N	144°55.0′E	24	3.8	21.8	9.57	137.76	7.82	45.23	570	Simulated	12:25	O
13	TK0005	May 31, 2000	42°40.0′N	144°55.0′E	46	9.2	22.3	0.44	25.54	63.39	28.14	564	Simulated	14:35	O
14	HK0010	Oct. 6, 2000	41°29.9′N	145°30.0′E	36	17.5	nd	0.39	27.32	38.36	12.37	353	Simulated	10:40	O
15	HK0101	Jan. 15, 2001	41°00.0′N	145°44.9′E	40	2.8	nd	0.11	4.59	51.92	5.61	76	Simulated	11:10	O
16	WK0101	Jan. 24, 2001	40°29.9′N	145°04.2′E	57	6.5	20.4	0.31	19.91	16.02	4.98	120	*in-situ*	8:03	O
17	WK0101	Jan. 24, 2001	40°29.9′N	145°04.2′E	57	6.5	20.4	0.31	20.22	21.44	6.67	234	Simulated	11:00	O
18	WK0104	Apr. 16, 2001	40°30.0′N	145°04.2′E	16	3.5	45.4	15.42	271.92	17.06	258.94	2,116	*in-situ*	8:10	O
19	WK0104	Apr. 16, 2001	40°30.0′N	145°04.2′E	16	3.5	41.4	15.42	277.07	22.41	345.62	3,385	Simulated	13:15	O
20	WK0104	Apr. 23, 2001	40°46.8′N	144°50.9′E	27	4.0	39.5	3.69	97.97	16.21	42.47	860	*In-situ*	6:00	O
21	WK0104	Apr. 23, 2001	40°46.8′N	144°50.9′E	27	4.0	22.1	3.69	99.63	26.03	96.11	1,233	Simulated	11:15	O
22	WK0104	May 2, 2001	40°58.8′N	144°40.8′E	13.5	1.9	33.1	9.53	136.22	14.97	142.60	1,165	*In-situ*	8:00	O
23	WK0104	May 2, 2001	40°58.8′N	144°40.8′E	13.5	1.9	30.7	9.53	137.41	26.01	247.79	1,710	Simulated	11:45	O
24	HK0105	May 13, 2001	40°29.9′N	146°00.0′E	48	8.0	53.6	0.91	39.58	35.00	31.81	642	Simulated	16:10	O
25	WK0106	Jun. 28, 2001	41°00.0′N	144°41.9′E	52	15.6	48.3	1.00	79.92	34.87	29.84	601	*In-situ*	8:05	O
26	WK0106	Jun. 28, 2001	41°00.0′N	144°41.9′E	52	15.6	40.3	1.00	92.23	42.01	22.67	1,261	Simulated	12:00	O
27	Tr0108	Sep. 1, 2001	41°00.0′N	144°41.9′E	32	17.3	35.6	1.05	37.37	14.88	13.97	355	Simulated	5:00	O
28	WK0111	Nov. 10, 2001	41°00.0′N	144°41.9′E	46	15.7	15.2	1.10	48.07	17.23	18.99	398	Simulated	10:55	O
29	WK0201	Jan. 25, 2002	41°00.6′N	144°47.4′E	49	1.3	13.4	0.41	20.30	9.42	3.02	98	*In-situ*	11:00	O
30	WK0201	Jan. 25, 2002	41°00.6′N	144°47.4′E	49	1.3	12.3	0.41	20.22	15.01	6.17	167	Simulated	13:30	O
31	WK0204	Apr. 15, 2002	41°00.0′N	144°42.0′E	13.5	1.7	37.6	13.87	197.65	35.49	492.37	2,671	*In-situ*	8:00	O
32	WK0204	Apr. 15, 2002	41°00.0′N	144°42.0′E	13.5	1.7	31.7	13.87	198.24	37.18	515.81	3,680	Simulated	11:50	O
33	TK0203	Mar. 17, 2002	41°29.9′N	145°30.0′E	nd	1.6	15.3	0.72	35.51	7.89	5.71	nd	Simulated	10:15	O
34	WK0206	June 15, 2002	40°59.4′N	144°42.6′E	33	13.7	17.4	0.90	33.80	39.30	34.15	483	*In-situ*	8:05	O
35	WK0206	June 15, 2002	40°59.4′N	144°42.6′E	33	13.7	13.5	0.90	39.28	45.86	40.31	598	Simulated	11:40	O
36	HK9910	Oct. 11, 1999	41°28.0′N	145°31.3′E	46	18.0	12.1	0.69	43.34	24.50	17.00	304	Simulated	12:15	O-K
37	TK0003	Mar. 11, 2000	40°00.0′N	146°15.0′E	59	6.5	27.8	0.21	13.08	22.15	4.17	126	Simulated	10:55	O-K

Table 1 (*Continued*)

Number	Cruise	Date	Latitude (°N)	Longitude (°E)	1% light depth (m)	Surface temperature (°C)	Total daily incident PAR (E/m^2/d)	Surface chlorophyll *a* (μg/l)	Standing stock of chlorophyll *a* (mg/m^2)	P^B_{opt} (mgC/mgChl/d)	Primary production		Method	Starting time	Region
											Surface (mgC/m^3/d)	Integrated over euphotic zone (mgC/m^2/d)			
38	TK0003	Mar. 12, 2000	41°29.9′N	145°30.0′E	86	8.0	14.0	0.22	20.56	2.26	0.50	31	Simulated	12:45	O-K
39	WK0101	Jan. 30, 2001	38°00.0′N	146°49.1′E	49	13.3	37.3	0.22	10.61	18.15	3.68	131	*In-situ*	8:35	O-K
40	WK0101	Jan. 30, 2001	38°00.0′N	146°49.1′E	49	13.3	29.1	0.22	10.69	28.33	6.26	148	Simulated	13:30	O-K
41	WK0104	Apr. 20, 2001	3800.0′N	146°49.1′E	43	14.9	32.5	0.68	26.45	43.52	27.72	606	*In-situ*	9:30	O-K
42	WK0104	Apr. 20, 2001	38°00.0′N	146°49.1′E	43	14.9	19.5	0.68	25.76	48.48	30.25	667	Simulated	14:30	O-K
43	WK0104	Apr. 30, 2001	38°00.0′N	146°49.1′E	41	13.9	10.7	1.24	42.35	41.79	51.74	782	Simulated	6:20	O-K
44	WK0106	Jul. 2, 2001	38°00.0′N	146°49.1′E	43	22.6	50.1	1.15	74.43	29.02	32.88	1,294	*In-situ*	12:00	O-K
45	WK0106	Jul. 2, 2001	38°00.0′N	146°49.1′E	43	22.6	49.4	1.15	75.14	31.65	36.15	1,040	Simulated	15:00	O-K
46	TK0107	Jul. 5, 2001	41°29.9′N	145°30.0′E	46	18.0	15.1	0.74	29.69	25.85	19.00	270	Simulated	14:50	O-K
47	Tr0108	Aug. 29, 2001	38°00.0′N	146°49.1′E	70	27.1	34.1	0.28	32.36	19.13	5.29	263	Simulated	7:30	O-K
48	Wk0111	Nov. 15, 2001	38°01.2′N	146°49.1′E	54	17.3	10.9	0.59	30.37	16.69	9.85	217	*In-situ*	8:15	O-K
49	Wk0111	Nov. 15, 2001	38°01.2′N	146°49.1′E	54	17.3	11.0	0.59	30.76	12.65	7.47	214	Simulated	10:50	O-K
50	WK0201	Feb. 1, 2002	37°59.4′N	146°48.6′E	60	11.3	11.5	0.46	28.04	23.51	10.89	289	Simulated	13:30	O-K
51	WK0204	Apr. 20, 2002	38°00.6′N	146°49.2′E	51	13.3	47.3	0.807	39.69	34.02	21.06	614	*In-situ*	8:00	O-K
52	WK0204	Apr. 20, 2002	38°00.6′N	146°49.2′E	51	13.3	44.3	0.807	39.71	38.20	20.43	781	Simulated	11:20	O-K
53	WK0206	June 20, 2002	38°00.0′N	146°48.66′E	35	18.6	53.8	0.63	21.38	30.26	16.29	443	*In-situ*	6:00	O-K
54	WK0206	June 20, 2002	38°00.0′N	146°48.66′E	35	18.6	43.7	0.63	21.32	29.93	18.92	403	Simulated	9:20	O-K
55	9905syunyo	May 15, 1999	33°19.8′N	138°00.0′E	43	19.8	nd	0.36	22.50	90.80	32.32	586	Simulated	3:35	K
56	9905syunyo	May 16, 1999	32°29.9′N	138°00.0′E	94	23.6	nd	0.15	21.07	60.30	6.74	272	Simulated	3:05	K
57	DK9907	Jul. 8, 1999	28°10.9′N	132°31.9′E	46	28.7	51.9	0.13	5.56	34.42	3.63	151	Simulated	2:30	K
58	9911syunyo	Nov. 15, 1999	33°19.8′N	138°00.0′E	41	22.9	25.7	0.96	39.98	19.50	14.30	418	Simulated	16:45	K
59	9911syunyo	Nov. 17, 1999	32°00.0′N	138°00.0′E	60	23.6	23.1	0.56	32.97	18.40	10.09	297	Simulated	12:35	K
60	0002syunyo	Feb. 4, 2000	34°00.0′N	138°00.0′E	64	19.5	4.7	0.44	28.01	15.80	6.89	289	Simulated	4:15	K
61	0002syunyo	Feb. 5, 2000	32°14.9′N	138°00.0′E	73	19.3	6.8	0.28	20.61	9.80	2.56	156	Simulated	4:00	K
62	0005syunyo	May 13, 2000	31°49.7′N	138°00.0′E	82	24.0	nd	0.15	23.06	36.06	5.07	403	Simulated	3:00	K
63	0005syunyo	May 14, 2000	31°30.0′N	138°00.0′E	78	24.0	nd	0.12	13.11	13.47	1.02	116	Simulated	3:00	K
64	0007syunyo	Jul. 15, 2000	32°29.9′N	138°00.0′E	75	27.7	nd	0.40	30.24	25.05	10.07	412	Simulated	3:30	K
65	0007syunyo	Jul. 16, 2000	31°49.7′N	138°00.0′E	109	26.8	nd	0.09	16.41	26.62	2.50	136	Simulated	3:00	K
66	0010syunyo	Oct. 14, 2000	32°19.8′N	138°00.0′E	63	25.7	26.6	0.21	9.15	18.21	3.88	140	Simulated	3:45	K
67	0010syunyo	Oct. 15, 2000	31°40.2′N	138°00.0′E	95	26.5	24.1	0.10	15.11	13.00	1.32	67	Simulated	3:50	K
68	0104soyo	Apr. 16, 2001	31°49.7′N	138°00.0′E	56	21.7	41.9	0.40	21.82	18.11	6.78	242	Simulated	3:50	K
69	0104soyo	Apr. 17, 2001	31°30.0′N	138°00.0′E	58	20.1	21.7	0.26	16.80	16.26	3.87	135	Simulated	3:50	K
70	0104soyo	Apr. 20, 2001	33°00.0′N	143°00.0′E	72	19.2	50.9	0.31	19.74	18.84	5.53	289	Simulated	4:00	K
71	0104soyo	Apr. 21, 2001	34°10.2′N	143°00.0′E	67	20.7	26.1	0.31	20.93	18.24	4.75	215	Simulated	4:10	K
72	0104soyo	Apr. 24, 2001	35°00.0′N	146°19.8′E	68	19.5	40.2	0.54	28.47	11.75	6.28	291	Simulated	3:45	K
73	0104soyo	Apr. 25, 2001	35°00.0′N	146°00.0′E	53	17.8	19.4	0.83	40.72	11.36	9.45	224	Simulated	3:40	K

74	0107Hokko	Jul. 31, 2001	32°40.2′N	138°00.0′E	78	29.1	53.4	0.08	14.16	50.52	4.16	221	Simulated	3:30	K
75	0107Hokko	Aug. 1, 2001	32°10.2′N	138°00.0′E	94	28.6	50.9	0.08	13.85	41.71	2.77	203	Simulated	3:30	K
76	0111soyo	Nov. 25, 2001	33°00.0′N	138°00.0′E	82	Nd	19.7	0.29	24.47	17.04	3.93	218	Simulated	2:50	K
77	0201Hokko	Jan. 26, 2002	33°20.0′N	138°00.0′E	78	18.8	9.7	0.39	17.72	8.64	2.68	117	Simulated	3:45	K
78	0205soyo	May 12, 2002	33°00.0′N	138°00.0′E	77	22.9	19.3	0.81	37.92	16.91	13.68	428	Simulated	4:00	K
79	0205soyo	May 15, 2002	28°00.0′N	138°00.0′E	98	22.9	25.4	0.13	20.04	30.65	4.08	189	Simulated	3:00	K
80	0205soyo	May 17, 2002	30°00.0′N	138°00.0′E	93	22.5	26.6	0.14	19.61	30.74	4.18	208	Simulated	2:40	K
81	0207soyo	Jul. 5, 2002	30°00.0′N	138°00.0′E	105	27.5	44.2	0.05	14.56	37.80	1.81	143	Simulated	2:10	K
82	0207soyo	Jul. 8, 2002	34°15.0′N	138°00.0′E	37	24.1	39.2	0.61	135.22	36.70	22.50	399	Simulated	3:35	K
83	0207soyo	Jul. 9, 2002	33°45.0′N	138°00.0′E	91	27.2	47.5	0.10	26.35	21.79	2.27	215	Simulated	3:20	K
84	0211soyo	Nov. 12, 2002	33°30.0′N	138°00.0′E	85	23.7	1.5	0.43	26.36	7.92	3.44	88	Simulated	4:20	K
85	0211soyo	Nov. 13, 2002	34°00.0′N	138°00.0′E	47	18.4	16.9	2.06	109.01	11.49	23.69	639	Simulated	4:20	K
86	0301soyo	Jan. 11, 2003	34°00.0′N	138°00.0′E	65	17.6	16.7	0.60	23.13	25.08	9.43	360	Simulated	4:50	K
87	0301soyo	Jan. 12, 2003	33°45.0′N	138°00.0′E	98	19.9	20.6	0.48	42.67	18.06	4.86	450	Simulated	4:50	K
88	0301soyo	Jan. 14, 2003	30°00.0′N	138°00.0′E	98	20.9	19.7	0.32	36.05	12.97	3.10	229	Simulated	2:15	K
89	Kotaka	Dec. 16, 1999	33°12.9′N	133°23.6′E	39	20.3	nd	0.32	13.26	78.00	25.10	531	*In-situ*	12:40	TB
90	Kotaka	Jan. 26, 2000	33°12.9′N	133°23.6′E	48	16.3	nd	0.32	14.46	26.00	7.80	205	*In-situ*	11:15	TB
91	Kotaka	Jul. 17, 2000	33°12.9′N	133°23.6′E	65	27.2	nd	0.08	17.78	82.00	6.40	975	*In-situ*	10:50	TB
92	Kotaka	Aug. 4, 2000	33°12.9′N	133°23.6′E	63	24.5	nd	0.37	51.92	61.00	22.60	535	*In-situ*	10:50	TB
93	Kotaka	Sep. 19, 2000	33°12.9′N	133°23.6′E	56	26.5	nd	0.41	12.77	79.00	32.20	270	*In-situ*	11:25	TB
94	Kotaka	Oct. 11, 2000	33°12.9′N	133°23.6′E	61	25.3	nd	0.21	12.07	90.00	16.40	644	*In-situ*	11:00	TB
95	Kotaka	Nov. 16, 2000	33°12.9′N	133°23.6′E	60	23.2	nd	0.42	21.86	61.00	25.50	641	*In-situ*	10:45	TB
96	Kotaka	Dec.. 5, 2000	33°12.9′N	133°23.6′E	52	20.8	nd	0.39	19.82	46.00	16.90	493	*In-situ*	6:30	TB
97	Kotaka	Jan. 16, 2001	33°12.9′N	133°23.6′E	43	15.5	nd	0.42	18.99	32.00	9.30	401	*In-situ*	11:20	TB
98	Kotaka	Feb. 14, 2001	33°12.9′N	133°23.6′E	55	16.8	nd	0.55	33.18	31.00	14.20	601	*In-situ*	10:55	TB
99	Kotaka	Apr. 11, 2001	33°12.9′N	133°23.6′E	43	19.7	nd	0.55	20.90	75.50	41.20	765	*In-situ*	11:25	TB
100	Kotaka	May 11, 2001	33°12.9′N	133°23.6′E	69	21.6	nd	0.36	21.60	94.70	34.00	1,390	*In-situ*	10:50	TB
101	Kotaka	Jul. 13, 2001	33°12.9′N	133°23.6′E	50	27.0	nd	0.24	10.35	208.00	35.60	918	*In-situ*	11:00	TB
102	Kotaka	Aug. 7, 2001	33°12.9′N	133°23.6′E	41	28.8	nd	0.13	28.59	240.00	29.70	1,191	*In-situ*	11:35	TB
103	Kotaka	Sep. 15, 2001	33°12.9′N	133°23.6′E	67	27.8	nd	0.17	15.59	71.20	12.20	437	*In-situ*	10:55	TB
104	Kotaka	Oct. 5, 2001	33°12.9′N	133°23.6′E	67	26.6	nd	0.17	14.12	80.70	13.60	563	*In-situ*	11:20	TB
105	Kotaka	Nov. 21, 2001	33°12.9′N	133°23.6′E	50	22.6	nd	0.59	23.01	64.00	36.80	1,034	*In-situ*	11:20	TB
106	Kotaka	Dec. 19, 2001	33°12.9′N	133°23.6′E	63	19.6	nd	0.39	18.93	50.00	18.00	710	*In-situ*	11:30	TB
107	DK9907	Jul. 10, 1999	27°40.9′N	128°01.9′E	58	27.3	38.8	0.16	11.43	41.57	4.89	249	Simulated	1:50	ECS-K
108	DK9907	Jul. 11, 1999	28°10.9′N	127°13.0′E	51	28.9	51.1	0.17	8.11	88.12	7.22	270	Simulated	1:00	ECS-K
109	DK9907	Jul. 12, 1999	26°39.0′N	126°29.9′E	65	28.9	41.6	0.10	10.16	51.42	4.98	212	Simulated	0:15	ECS-K
110	YK9907	Oct. 27, 1999	29°20.1′N	128°30.1′E	65	25.8	29.8	0.16	11.71	62.65	5.83	473	*In-situ*	5:10	ECS-K
111	YK9907	Oct. 27, 1999	29°20.1′N	128°30.1′E	65	25.8	29.8	0.16	11.71	58.53	3.10	454	Simulated	6:12	ECS-K
112	KY0001	May 14, 2000	26°40.0′N	125°45.1′E	89	25.0	67.3	0.36	32.82	68.27	19.23	1,654	Simulated	3:50	ECS-K
113	KY0001	May 14, 2000	26°40.0′N	125°45.0′E	89	25.0	67.3	0.36	32.82	50.66	18.24	992	*In-situ*	4:15	ECS-K
114	DK00-07	Jul. 21, 2000	27°40.9′N	128°01.9′E	95	29.4	52.9	0.07	16.36	45.30	3.20	358	Simulated	1:40	ECS-K
115	DK00-07	Jul. 22, 2000	28°25.0′N	126°55.0′E	81	29.4	55.2	0.20	16.71	39.50	6.50	489	Simulated	3:50	ECS-K
116	YK0007	Oct. 13, 2000	29°00.0′N	128°30.0′E	57	26.8	27.1	0.19	10.04	62.75	7.83	367	Simulated	5:30	ECS-K
117	KY0204	Mar. 3, 2003	28°45.1′N	127°45.1′E	80	23.2	8.1	0.33	16.61	32.75	5.03	317	Simulated	4:30	ECS-K
118	KY0204	Mar. 7, 2003	26°45.2′N	125°45.1′E	73	23.3	3.3	0.27	15.19	45.79	12.17	291	Simulated	4:10	ECS-K
119	YK9907	Oct. 24, 1999	30°37.6′N	126°01.8′E	38	22.9	35.1	1.45	54.93	71.99	65.09	2,416	Simulated	8:15	ECS-C
120	YK9907	Oct. 24, 1999	30°37.8′N	126°01.8′E	38	22.9	35.1	1.45	54.93	106.22	148.14	2,654	*In-situ*	6:56	ECS-C
121	YK9907	Nov. 3, 1999	28°38.4′N	125°45.0′E	41	24.9	22.1	0.40	15.17	63.66	12.98	648	Simulated	6:15	ECS-C

Table 1 (*Continued*)

Number	Cruise	Date	Latitude (°N)	Longitude (°E)	1% light depth (m)	Surface temperature (°C)	Total daily incident PAR (E/m^2/d)	Surface chlorophyll *a* (μg/l)	Standing stock of chlorophyll *a* (mg/m^2)	P^B_{opt} (mgC/mgChl/d)	Primary production		Method	Starting time	Region
											Surface (mgC/m^3/d)	Integrated over euphotic zone (mgC/m^2/d)			
122	YK9908	Feb. 10, 2000	32°49.9′N	129°30.0′E	33	14.5	26.0	1.10	37.18	31.41	20.56	697	Simulated	6:10	ECS-C
123	YK9908	Feb. 11, 2000	32°40.0′N	129°19.8′E	65	16.4	19.4	0.35	20.23	33.89	8.58	447	Simulated	6:15	ECS-C
124	YK9908	Feb. 12, 2000	32°29.8′N	129°10.2′E	49	15.9	26.5	0.36	17.23	33.96	7.25	407	Simulated	6:00	ECS-C
125	YK9908	Feb. 13, 2000	32°19.9′N	129°00.0′E	70	17.0	28.1	0.36	21.57	41.91	8.41	640	Simulated	6:00	ECS-C
126	KY0001	Apr. 25, 2000	32°29.9′N	128°59.8′E	35	18.1	30.5	0.85	25.48	43.59	33.19	753	Simulated	4:40	ECS-C
127	KY0001	Apr. 27, 2000	31°30.0′N	129°00.0′E	43	16.0	nd	1.01	32.77	44.55	38.93	1,159	Simulated	5:00	ECS-C
128	KY0001	Apr. 28, 2000	31°29.7′N	126°29.3′E	33	13.8	30.5	0.59	21.08	62.14	36.66	840	Simulated	5:52	ECS-C
129	KY0001	Apr. 28, 2000	31°29.7′N	126°29.3′E	33	13.8	30.5	0.59	21.08	44.06	26.00	541	*In-situ*	4:00	ECS-C
130	KY0001	Apr. 30, 2000	31°14.8′N	126°59.8′E	33	18.4	29.1	0.30	18.58	106.73	32.02	501	Simulated	3:15	ECS-C
131	KY0001	May 1, 2000	30°45.1′N	125°59.8′E	30	14.7	37.8	0.58	27.05	49.91	28.95	482	Simulated	3:00	ECS-C
132	KY0001	May 2, 2000	30°30.0′N	128°30.0′E	54	20.6	35.6	0.28	17.74	145.76	40.81	1,430	Simulated	4:30	ECS-C
133	KY0001	May 3, 2000	30°29.5′N	126°00.4′E	27	14.8	46.9	0.71	27.71	54.64	34.91	906	Simulated	4:00	ECS-C
134	KY0001	May 4, 2000	30°15.1′N	128°29.8′E	43	20.4	48.5	0.26	9.10	214.90	31.65	1,087	Simulated	4:10	ECS-C
135	KY0001	May 5, 2000	29°44.9′N	126°00.9′E	30	17.9	40.7	0.42	28.83	175.89	35.24	2,598	Simulated	3:50	ECS-C
136	KY0001	May 5, 2000	29°44.9′N	126°00.9′E	30	17.9	40.7	0.42	28.83	241.30	33.08	3,983	*In-situ*	4:10	ECS-C
137	DK00-07	Jul. 23, 2000	29°00.0′N	126°00.0′E	65	29.1	58.1	0.12	13.24	55.70	6.60	334	Simulated	0:40	ECS-C
138	YK0007	Oct. 3, 2000	28°54.4′N	126°15.0′E	49	26.1	20.6	0.16	21.68	90.67	14.51	569	Simulated	5:30	ECS-C
139	YK0007	Oct. 4, 2000	28°54.4′N	126°15.0′E	41	26.1	31.5	0.35	18.47	78.48	18.12	645	Simulated	5:20	ECS-C
140	YK0007	Oct. 5, 2000	28°54.4′N	126°15.0′E	49	25.6	13.4	0.19	17.18	75.86	14.41	374	Simulated	5:05	ECS-C
141	YK0007	Oct. 6, 2000	28°54.5′N	126°15.0′E	46	25.6	6.8	0.31	18.47	65.80	17.70	338	Simulated	5:05	ECS-C
142	YK0007	Oct. 8, 2000	28°54.4′N	126°15.0′E	35	25.0	30.0	0.62	21.09	62.82	25.95	833	Simulated	5:20	ECS-C
143	YK0007	Oct. 14, 2000	30°30.0′N	128°30.0′E	41	25.5	29.8	0.20	9.44	105.23	15.61	511	Simulated	5:00	ECS-C
144	YK0007	Oct. 15, 2000	32°00.0′N	128°30.0′E	51	25.7	31.3	0.18	11.46	89.31	13.04	588	Simulated	4:30	ECS-C
145	YK0007	Oct. 16, 2000	31°30.0′N	126°29.9′E	51	24.4	29.1	0.34	14.57	96.37	15.73	877	Simulated	4:40	ECS-C
146	YK0007	Oct. 17, 2000	31°30.0′N	128°30.0′E	51	25.4	15.0	0.44	19.78	46.28	20.36	468	Simulated	4:15	ECS-C
147	YK0106	Jul. 21, 2001	30°18.0′N	126°18.0′E	54	28.5	nd	0.19	19.50	114.05	16.35	1,060	Simulated	4:40	ECS-C
148	YK0106	Jul. 22, 2001	30°18.0′N	125°18.0′E	41	28.9	nd	0.20	15.65	146.76	17.65	975	Simulated	3:30	ECS-C
149	YK0106	Jul. 23, 2001	31°18.0′N	125°00.0′E	27	28.2	nd	0.55	24.93	91.00	30.35	1,017	Simulated	3:30	ECS-C
150	YK0106	Jul. 24, 2001	31°05.9′N	126°06.0′E	35	29.0	nd	0.21	21.63	141.56	18.69	1,217	Simulated	3:30	ECS-C
151	YK0106	Jul. 25, 2001	32°11.9′N	127°12.0′E	84	29.7	nd	0.08	16.30	145.21	9.66	677	Simulated	3:30	ECS-C
152	YK0106	Jul. 26, 2001	31°18.0′N	127°18.0′E	57	30.3	nd	0.11	16.15	241.35	26.55	1,311	Simulated	3:30	ECS-C
153	KY0104	Aug. 29, 2001	31°08.9′N	125°12.0′E	41	28.6	24.9	0.28	25.75	147.06	41.18	1,392	Simulated	5:20	ECS-C
154	KY0104	Aug. 30, 2001	30°00.0′N	124°12.0′E	51	28.2	30.6	0.50	29.97	111.01	55.50	1,765	Simulated	4:15	ECS-C
155	KY0104	Aug. 31, 2001	30°00.0′N	125°12.0′E	57	28.3	41.1	0.35	24.32	89.77	22.97	1,533	Simulated	4:15	ECS-C
156	KY0104	Sep. 1, 2001	31°08.9′N	126°12.0′E	43	27.3	30.4	0.28	24.93	144.32	30.94	1,271	Simulated	5:00	ECS-C
157	KY0104	Sep. 2, 2001	30°08.9′N	126°12.0′E	62	28.3	14.3	0.23	26.72	99.16	19.88	824	Simulated	5:35	ECS-C
158	KY0104	Sep. 3, 2001	31°08.9′N	127°12.0′E	76	28.3	29.8	0.29	25.41	112.98	29.56	1,477	Simulated	4:15	ECS-C

159	KY0104	Sep. 4, 2001	30°08.9′N	127°12.0′E	70	27.8	17.4	0.19	23.32	95.07	18.06	845	Simulated	4:15	ECS-C
160	KY0104	Sep. 5, 2001	31°08.9′N	128°12.0′E	68	28.0	39.0	0.22	18.24	98.63	11.57	1,039	Simulated	5:50	ECS-C
161	KY0104	Sep. 6, 2001	30°08.9′N	128°12.1′E	62	28.1	6.2	0.14	15.46	86.58	12.12	299	Simulated	5:50	ECS-C
162	KY0104	Sep. 7, 2001	31°08.9′N	129°12.0′E	70	28.3	32.5	0.31	23.58	78.64	21.02	1,219	Simulated	5:45	ECS-C
163	YK0204	Jun. 12, 2002	31°44.9′N	129°15.0′E	51	24.2	41.8	0.22	12.72	131.88	20.62	822	Simulated	4:30	ECS-C
164	YK0204	Jun. 14, 2002	31°44.9′N	127°45.0′E	68	23.9	48.7	0.10	16.43	170.09	10.16	969	Simulated	4:20	ECS-C
165	YK0204	Jun. 15, 2002	32°15.2′N	127°14.8′E	60	24.3	46.3	0.14	15.15	87.66	9.38	595	Simulated	4:00	ECS-C
166	YK0204	Jun. 16, 2002	30°45.1′N	125°44.8′E	43	23.2	42.9	0.21	16.95	117.75	21.57	1,034	Simulated	4:10	ECS-C
167	KY0204	Mar. 2, 2003	30°14.9′N	127°45.0′E	69	18.1	24.4	0.21	14.99	92.42	8.50	830	Simulated	4:30	ECS-C
168	KY0204	Mar. 4, 2003	28°45.0′N	126°15.0′E	30	20.1	12.2	0.84	22.99	49.11	18.93	591	Simulated	4:20	ECS-C
169	KY0204	Mar. 5, 2003	27°44.8′N	124°45.0′E	57	17.4	4.7	0.25	12.93	68.58	17.04	362	Simulated	4:05	ECS-C
170	KY0204	Mar. 6, 2003	27°14.9′N	125°15.0′E	57	20.6	12.1	0.43	25.19	58.94	20.33	830	Simulated	4:10	ECS-C
171	KY0204	Mar. 8, 2003	25°44.9′N	123°44.9′E	64	23.3	13.5	0.36	14.49	78.95	11.25	586	Simulated	4:20	ECS-C
172	KY0204	Mar. 9, 2003	27°14.9′N	122°15.0′E	46	16.7	30.5	0.36	16.12	100.10	13.65	955	Simulated	4:10	ECS-C
173	KY0204	Mar. 10, 2003	26°44.9′N	124°44.9′E	43	22.6	27.2	0.42	15.56	139.81	31.81	1,322	Simulated	4:20	ECS-C
174	KY0204	Mar. 11, 2003	27°14.9′N	123°44.9′E	43	17.8	40.7	0.48	16.41	109.21	11.10	1,191	Simulated	4:20	ECS-C
175	KY0204	Mar. 12, 2003	28°44.9′N	124°45.0′E	41	15.1	9.9	2.04	27.37	64.64	22.47	674	Simulated	4:00	ECS-C
176	KY0204	Mar. 13, 2003	29°45.0′N	126°15.0′E	43	14.4	19.5	0.41	19.09	66.99	7.23	754	Simulated	4:10	ECS-C

Note:

A term nd indicates no datum was available.
Depth-integrated primary production and the standing stock of chlorophyll a were obtained by integrating over the euphotic zone (1% light depth).
Primary production was measured by *in-situ* incubations and/or simulated *in-situ* deck incubations.
JSOKH: Japan and Okhotsk Seas, O: Oyashio, O-K: Oyashio-Kuroshio transition, K: Kuroshio, TB: Tosa Bay, ECS-K: Kuroshio in the East China Sea, ECS-C: continental shelf waters in the East China Sea.

Reflectance Radiometer (Biospherical Instruments Inc, San Diego, CA, USA.). Seawater samples were collected prior to sunrise, from four to eight depths, using Niskin or Go-Flo samplers (General Oceanics Inc., Miami, FL, USA) (Fitzwater et al., 1982). The water samples were immediately sieved through a 100- or 200-μm mesh plankton net to remove large-sized zooplankton, whose body size in dominant species was reffered to select which mesh size to use. The pre-screened seawater was transferred into three or four 500- to 2,500-ml polycarbonate bottles, which had previously been acid cleaned. The seawater in the bottles was spiked with $NaH^{13}CO_3$ solution (Shoko Co., Ltd., Tokyo, Japan) to a final concentration of about 10% total carbonate. One bottle was immediately used for the zero time blank and two or three bottles were incubated for about 24 h in a deck incubator at a range of irradiances corresponding to the depths at which the samples were taken, using neutral density and marine-blue filters (ACRYLITE, Mitsubishi Rayon Co., Ltd., Tokyo, Japan). Temperature during incubation was maintained at the sea surface temperature (SST) using continuous flowing surface seawater or cooling devices. Just after incubation, particulate matter was filtered onto a Whatman GF/F filter (Whatman International Ltd., Maidstone, England) that had been precombusted at 450°C for 4 h. The filters were rinsed with ^{13}C-free prefiltered seawater to remove dissolved inorganic carbon. After storage at a temperature below –20°C the filters were treated with HCl fumes or without ones according to Kanda et al. (1998). Particulate organic carbon and ^{13}C atom% were determined using a ^{13}C analyzer EX-130S (JASCO, Hachioji, Japan), a mass spectrometer ANCA-SL (Europa Scientific, Crewe, UK) or DELTA-plus (Finnigan MAT, Bremen, Germany). Total carbonate in the seawater was measured or estimated from salinity (Parsons et al., 1984). The particulate organic carbon fixation rate (mgC/m^3/day) was calculated according to Hama et al. (1983). The details of the methods used by each institution and vessel varied slightly and are summarized in Table 2. Trapezoidal integration was adopted for calculation of the depth-integrated primary production over the euphotic zone (IPP, mgC/m^2/day) and annual primary production (gC/m^2/year) based upon monthly means in different waters.

2.4 Observation of Environmental Factors

Temperature and salinity were measured using a thermometer and Auto Sal (Guildline Instruments Ltd., Smiths Falls, Canada) for sea surface water, respectively and using a conductivity-temperature-depth recorder SBE 9plus (Sea Bird Electronics Inc., Bellevue, WA, USA) for deeper waters. The upper mixed-layer depth was defined as the depth at a temperature 1°C lower than that at the surface. Chlorophyll *a* was measured using a fluorometer (Turner Designs Inc., Sunnyvale, CA, USA) after 50 to 300 ml of seawater was filtered

Table 2: Summary of the methods for primary production measurements in different organizations

Institute	Hokkaido National Fisheries Research Institute	Tohoku National Fisheries Research Institute	National Research Institute of Fisheries Engineering	National Research Institute of Fisheries Science	Seikai National Fisheries Research Institute	General Environmental Technos Co., Ltd.
Region	Oyashio, Okhotsk Sea, Japan Sea	Oyashio, Kuroshio-Oyashio transition	Kuroshio	Tosa Bay	Continental shelf of East China Sea, Kuroshio	Continental shelf of East China Sea, Kuroshio, western North Pacific
Determination of light depths	Vertical profile of PAR measured by PRR-600	Transparency or vertical profile of PAR measured by a PAR sensor	Vertical profile of PAR measured by PRR-600	Vertical profile of PAR measured by PRR-600	Transparency	Transparency
Number of sampling depths	4–7	5 (*in-situ*), 6 (simulated)	5–6	5	8	7
Light depths of sampling depths	100, 45, 20, 9, 4, 2, 1%	100, 50, 10, 5, 2.5, 1%	100, 50, 25, 10, 1 (5, 2.5, 0.5)%	100, 60, 20, 10, 1%	100, 50, 25, 10, 5, 2.5, 1, 0.5%	100, 50, 25, 10, 5, 2.5, 1%
Water sampler	Go-Flo	Go-Flo, X-Niskin	Go-Flo	Go-Flo	Go-Flo	Lever action water sampler
Clean sampling		Kevlar line, teflon coated messenger			Nylon coated wire, teflon coated messenger	Kevlar line, teflon coated messenger
Mass spectrometer	ANCA-SL, ^{13}C-analyzer	ANCA-SL	ANCA-SL	EA1110-DELTAplus Advantage ConFloSystem	ANCA-SL, FlashEA-DELTAplus ConFloSystem	ANCA-SL
Removal of inorganic carbon by an acid treatment in a HCl vapor	No	No	Yes	Yes	No	No
Sensor for total daily incident PAR	Li-Cor 2pi sensor	2pi sensorSUD033/PAR/W	Li-Cor 2pi sensor	None	Li-Cor 2pi sensor	Li-Cor 2pi sensor
Starting time of incubation	Around noon	Between sunrise and noon	Before sunrise	Around noon	Before sunrise	Before sunrise
Incubation methods	Simulated *in-situ*	*In-situ,* simulated *in-situ*	Simulated *in-situ*	*In-situ*	*In-situ,* simulated *in-situ*	Simulated *in-situ*
Note			2-L of water incubated		0.3 to 1-L of water incubated	1-L of water incubated

using a Whatman GF/F filter. The pigments on the filter were extracted in *N*,*N*-dimethylformamide (Suzuki and Ishimaru, 1990) or 90% acetone with sonic destruction of the phytoplankton cells (Parsons et al., 1984). The standing stock of chlorophyll *a* (mgChl/m^2) was calculated in a trapezoidal integration over the euphotic zone. Total daily incident PAR was measured using a PAR sensor LI-190 (Li-Cor Inc, Lincoln, NE, USA) installed on the ship.

2.5 Comparison between *in-situ* and Simulated *in-situ* Incubations

Results from *in situ* and simulated *in situ* incubations were compared at 19 stations in Oyashio-transition waters and ECS. IPP measured by simulated *in situ* incubation ranged from 65 to 210% of the IPP measured by *in situ* incubation, with a mean of 131%. Surface primary production by simulated *in situ* incubation ranged from 44 to 226% of the value by *in situ* incubation, with a mean of 121%. The means of both IPP and surface primary production by simulated *in situ* incubation were not significantly different from those recorded by *in situ* incubation.

3 Results and Discussion

3.1 Seasonal Variations in Euphotic Zone and Upper Mixed Layer

Values of PAR (Fig. 2A) ranged from 3.3 to 67.3 E/m^2/day with large variations among stations. PAR in Oyashio-transition waters was lower than that in the other areas throughout the year. PAR was high in May but low from October to March in all waters. The depth of the euphotic zone (Fig. 2B) ranged from 15 to 109 m with large differences among stations. A common feature of the seasonal variation among different waters was a decrease in the depth of the euphotic zone during April and May.

SST (Fig. 2C) varied widely, from 0.0°C in the Okhotsk Sea to 30.3°C in Kuroshio waters. The monthly mean temperatures in the Oyashio-transition waters were 5.3 to 20.2°C, showing both the lowest absolute SST and the largest seasonal variations we observed. Higher temperatures and smaller seasonal variations were recorded in Kuroshio waters, Tosa Bay, and ECS continental shelf waters, where temperatures ranged from 14 to 30°C. The depth of the upper mixed layer shoaled into the euphotic zone in all waters from April to October (Fig. 2D). In summer, the upper mixed layer reached less than 10% light depth in Oyashio-transition waters, and about 20% light depth in the other waters.

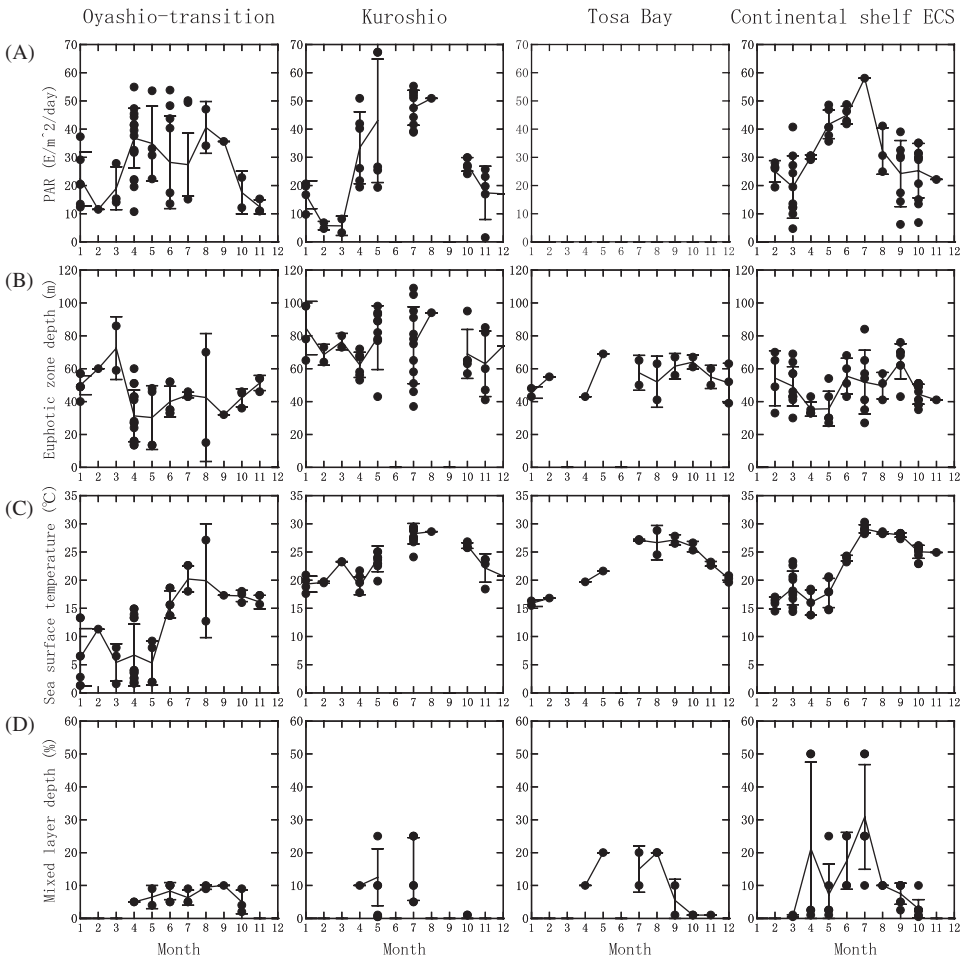

Figure 2: Seasonal change in (A) total daily incident photosynthetically available radiation (PAR, E/m^2/day), (B) euphotic zone depth in 1% light depth (m), (C) sea surface temperature (°C), (D) upper mixed layer depth in relative light (%) in the euphotic zone of Oyashio-transition waters, Kuroshio waters, Tosa Bay, and continental shelf waters of the East China Sea. Solid lines connect monthly means with standard deviations.

3.2 Seasonal Variations in Phytoplankton Biomass and Primary Production

Sea surface chlorophyll *a* (Fig. 3A) reached a maximum of 15.0 μg/L in Oyashio-transition waters, with a large peak from April to May, and a small increase in August. In contrast, in other waters it was sparse throughout the year, with small seasonal variations (e.g., a slight increase during spring and autumn). Standing stock of chlorophyll *a* in the euphotic zone (Fig. 3B)

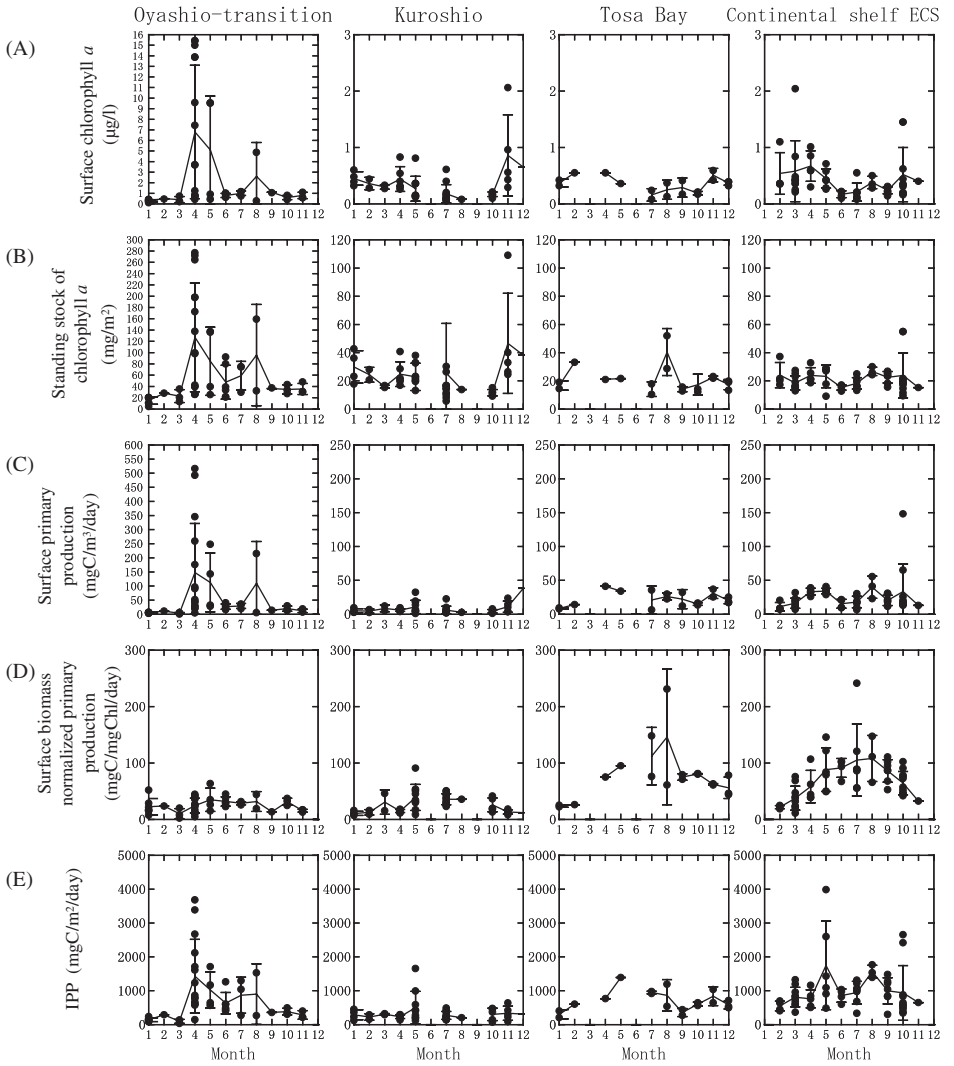

Figure 3: Seasonal change in (A) surface chlorophyll *a* (μg/l), (B) standing stock of chlorophyll *a* in the euphotic zone (mg/m^2), (C) daily carbon fixation rate at the sea surface(mgC/m^3/day), (D) biomass normalized primary production at sea surface (mgC/mgChl/day), (E) daily primary production integrated over the euphotic zone (IPP, mgC/m^2/day) of Oyashio waters, Kuroshio waters, Tosa Bay, and continental shelf waters of the East China Sea. Solid lines connect monthly means with standard deviations.

reached a maximum of 265 mg/m^2 in Oyashio-transition waters, where it markedly increased during spring and summer; in other waters the mean was about 20 mg/m^2, with no remarkable variations during the course of the year.

Primary production at the sea surface (Fig. 3C) reached a maximum of 520 mgC/m^3/day in Oyashio-transition waters, displaying large seasonal variations with peaks from April to May and in August. In other areas the variations were small, with a slight increase from April to May. Chlorophyll *a* normalized primary production at the sea surface (Fig. 3D) peaked in Oyashio-transition waters and Kuroshio waters in May, and in Tosa Bay and ECS continental shelf waters in August. IPP (Fig. 3E) ranged from 30 mgC/m^2/day in March in Oyashio-transition waters to 3,980 mgC/m^2/day in May in ECS continental shelf waters. IPP varied seasonally in Oyashio-transition waters, with high production from April to August and very low production from September to March. In contrast, seasonal variations in IPP in other areas were not remarkable, with a slight increase in May in Kuroshio waters and Tosa Bay, and increases in both May and August in ECS continental shelf waters. Annual primary production (gC/m^2/year) was estimated to be 340 in ECS continental shelf waters, 280 in Tosa Bay, 200 in Oyashio-transition waters, and 110 in Kuroshio waters.

3.3 Vertical Distribution and Depth-Integration of Phytoplankton Biomass and Primary Production

Chlorophyll *a* concentrations and primary production generally increased in the surface layer in the spring, when the depth of the upper mixed layer decreased to less than that of the euphotic zone (Fig. 2D). Subsurface maxima of chlorophyll *a* and primary production in Kuroshio waters, Tosa Bay, and ECS continental shelf waters were observed in the summer, when the water column was stratified; however, no marked subsurface maxima were recorded in Oyashio-transition waters (Fig. 4A). Chlorophyll *a* normalized primary production decreased with depth mainly due to the exponential extinction of light with depth (Fig. 4B). The subsurface maximum of primary production was not as marked as that of chlorophyll *a* (Fig. 4C).

The best correlation between IPP and the standing stock of chlorophyll *a* (Fig. 5A) was found in Oyashio-transition waters. The presence of subsurface maxima in other areas may be responsible for the worsened correlation found in those areas. The correlation (r^2) between IPP and surface PAR ranged from 0.550 to 0.701 (Fig. 5B).

3.4 Relationship Between Primary Production and Environmental Factors

Behrenfeld and Falkowski (1997) expressed the maximum carbon-fixation rate per unit of chlorophyll *a*, P^B_{opt} (mgC/mgChl/h) as a function of SST to estimate IPP from chlorophyll *a*, PAR, and temperature data derived by satellite. The present study encompassed a wide range of SSTs (0 to 30°C).

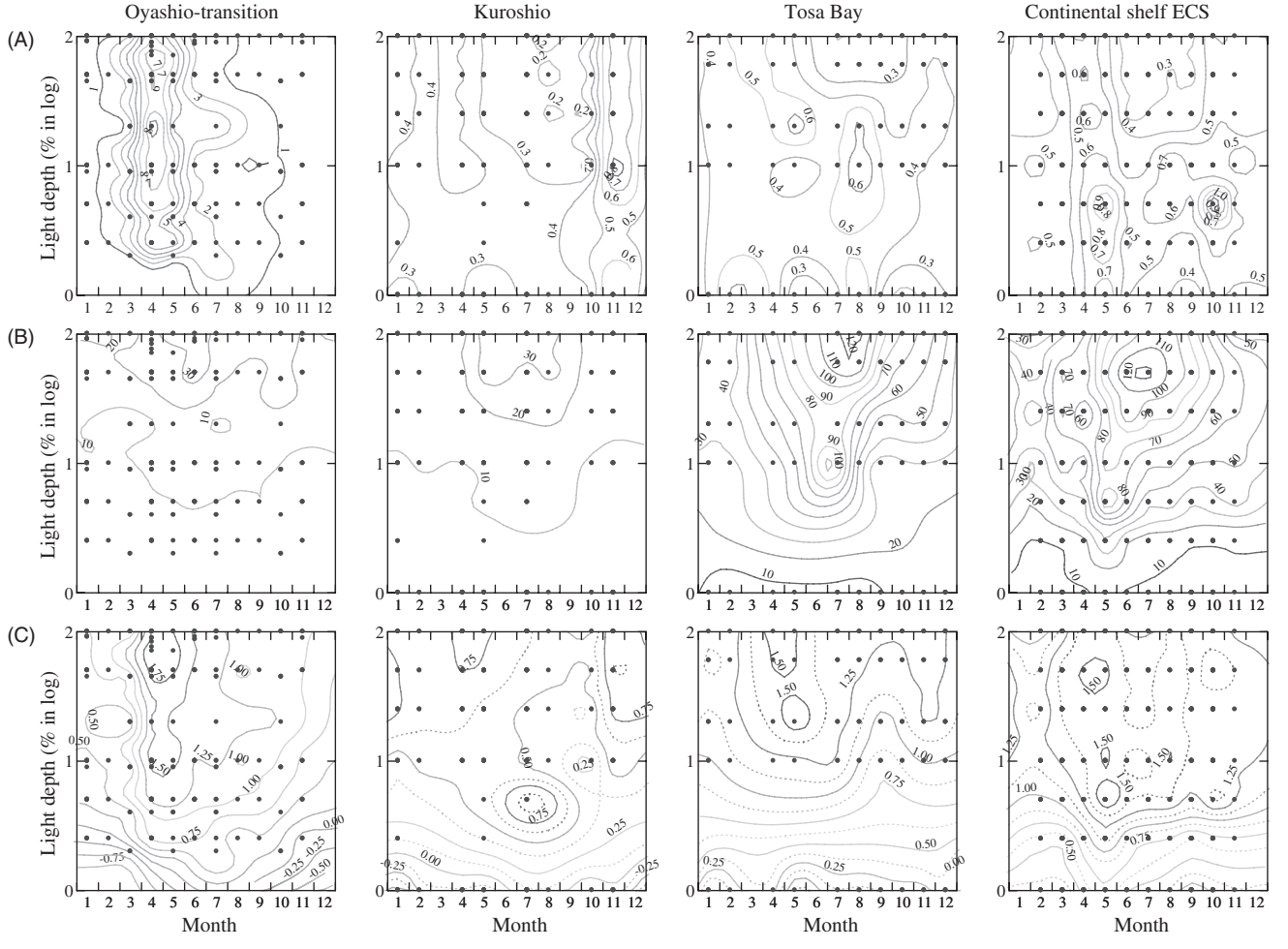

Figure 4: Seasonal change in vertical profile of (A) chlorophyll *a* concentration in μg/l, (B) biomass normalized primary production in mgC/mgChl/day, and (C) primary production in $\log_{10}$ (mgC/m^3/day) in the euphotic zone of light depth (% in $\log_{10}$) of Oyashio-transition waters, Kuroshio waters, Tosa Bay, and continental shelf waters of the East China Sea (For colour version, see Colour Plate Section).

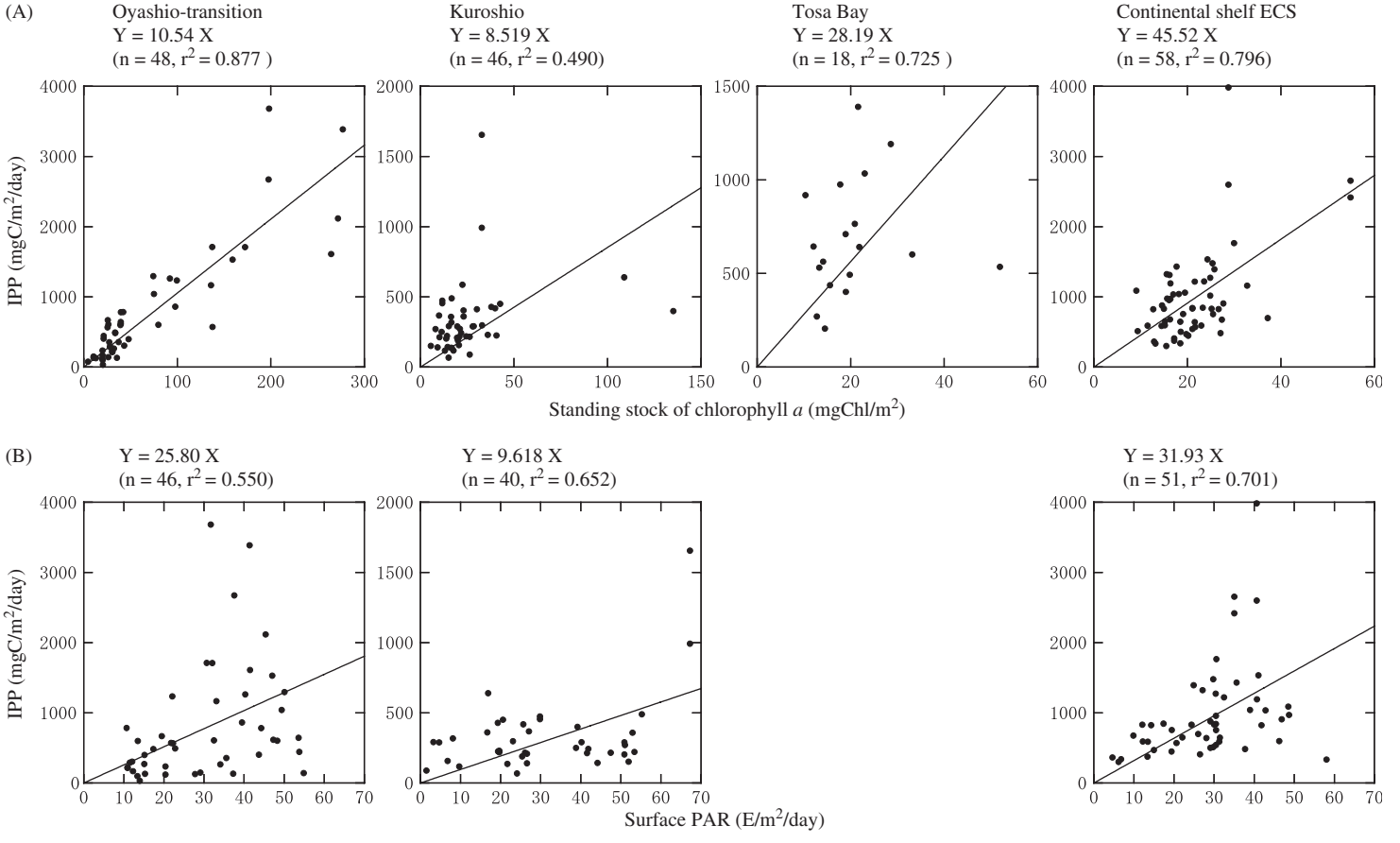

Figure 5: Plot of depth-integrated primary production (IPP) to (A) standing stock of chlorophyll *a* and (B) photosynthetically available radiation (PAR) on the surface in Oyashio-transition waters, Kuroshio waters, Tosa Bay, and continental shelf waters of the East China Sea.

The relationship between P^B_{opt} (mgC/mgChl/day) and SST (T), expressed in exponential form as equation (1) (n = 175, $r^2 = 0.218$), is similar to the theoretical maximum specific growth rate described by Eppley (1972); the high-order polynomial in equation (2) (n = 175, $r^2 = 0.227$), parameterized using a nonlinear regression analysis of SYSTAT ver.10 (SPSS Inc, Chicago, IL, USA), is similar to a preliminary empirical model by Behrenfeld and Falkowski (1997).

$$\log 10 P^B_{\mathrm{opt}} = 0.0249T + 1.23. \tag{1}$$

$$\begin{aligned} P^B_{\mathrm{opt}} = & -1.267 \times 10^{-6} T^7 + 1.319 \times 10^{-4} T^6 - 5.3237 \times 10^{-3} T^5 \\ & + 0.10457 T^4 - 1.025 T^3 + 4.6278 T^2 - 6.3898 T + 19.096. \end{aligned} \tag{2}$$

P^B_{opt} tended to increase with SST at temperatures between 0 and 30°C, with large variations above about 16°C (Fig. 6). Kuroshio waters, Tosa Bay, and ECS continental shelf waters had the same temperature regime, with P^B_{opt} values that varied by a factor of more than three. The use of factors other than

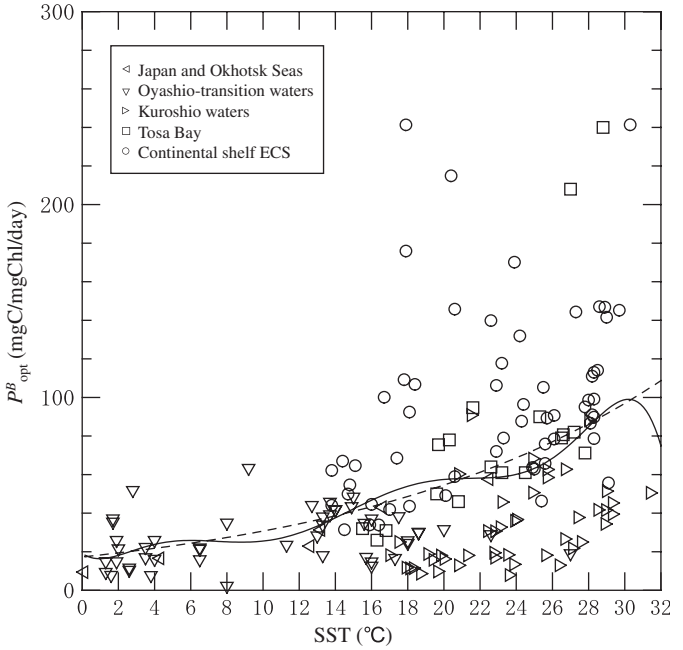

Figure 6: Relationship between sea surface temperature (SST) and maximum biomass normalized primary production (P^B_{opt}) around Japan. A solid line indicates an empirical function with high-order polynomial and a dashed line with exponential.

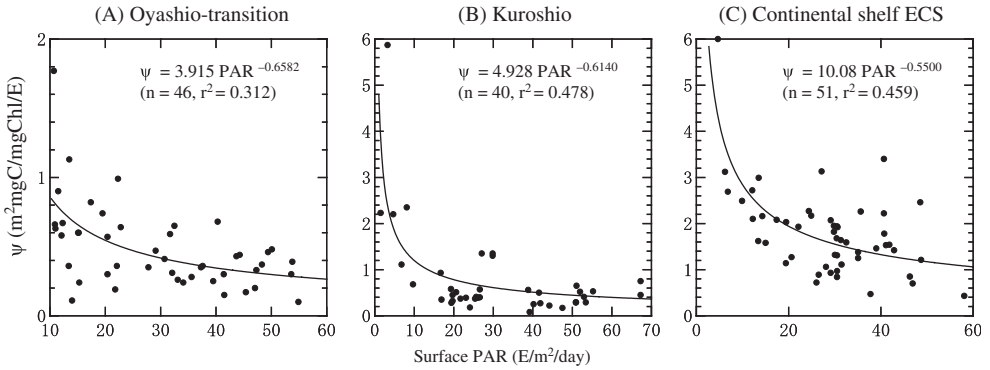

Figure 7: Relationship of water-column light utilization index ψ to total daily incident PAR in Oyashio-transition waters (A), Kuroshio waters (B), and continental shelf waters of the East China Sea (C).

SST is expected to improve algorithms to estimate primary productivity using P^B_{opt} values.

Falkowski (1981) proposed a water-column light-utilization efficiency index, ψ (m^2 mgC/mgChl/E), defined as:

$$\psi = \text{IPP}/\text{IB}/\text{IE}_0, \tag{3}$$

where IPP is primary production integrated from the surface to the base of the euphotic zone over a day, IB is the chlorophyll-based biomass integrated from the surface to the base of the euphotic zone, and IE_0 is PAR incident on the surface integrated over a day. Falkowski and Raven (1997) mentioned that ψ increased as PAR decreased on the basis of analysis of data for hundreds of stations in the world's oceans. We proposed empirical relationships between ψ and PAR for estimating IPP in Oyashio-transition waters, Kuroshio waters, and ECS continental shelf waters (Fig. 7), based on the standing stock of chlorophyll *a* (integrated from the surface to the base of the euphotic zone) and sea surface PAR (integrated over a day).

3.5 Improving Algorithms for Primary Production Estimation

Estimates of IPP in Tosa Bay and ECS continental shelf waters were about three times higher than estimates for Kuroshio waters with a similar temperature regime (14–30°C). Nutrients may prove to be promising parameters for improvement of algorithms for primary production estimation (Berger et al., 1989; Behrenfeld et al., 2002). Differences in IPP may result from the level of nutrient supply, which may be influenced, for example, by the

Changjiang River, by resuspension on the continental shelf, and by local upwelling in the shelf break under the Kuroshio front (Yanagi et al., 1998). High productivity in Tosa Bay seems to have been induced by a new nutrient supply associated with upwelling into the subsurface layers, due to the influence of the Kuroshio meander, the intrusion of warm water, and coastal upwelling during the summer when the water column is stratified (Ichikawa and Hirota, 2004). On the other hand, because primary production in Oyashio-transition waters was concentrated in the surface layers during spring and summer, without a subsurface maximum, satellite observation at the sea surface is an effective means to estimate primary production integrated over the euphotic zone (IPP) (Kasai et al., 1998). However, iron-limited offshore areas east of Oyashio waters (Tsuda et al., 2003) will require different algorithms to estimate primary production (Behrenfeld et al., 2002).

Asanuma (2006) established a depth- and time-resolved primary productivity model using SST, sea surface chlorophyll *a*, and daily PAR derived from satellite observations, and recorded good agreement when the model was validated with this GCMAPS dataset. Maps of annual primary production from 1998 to 2002 (Fig. 8), produced according to Asanuma (2006), show high-productivity areas around the mouth of the Changjiang River and an intrusion of Oyashio waters, with low-productivity areas in the Kuroshio meander and in a warm core ring east of mainland Japan. Ning et al. (1995) reported that annual primary production ($gC/m^2/y$) was 104 in the Bohai Sea, 155 in the Yellow Sea, and 252 off the mouth of the Changjiang River. The annual primary production figures that Ning et al. (1995) recorded for these coastal waters were lower than those measured for ECS continental shelf waters during the present study, possibly due to the light limitation by suspended matter in the coastal waters. However, algorithms estimating primary production in Chinese coastal waters as typical Case II should be validated using *in situ* primary production data, associated with chlorophyll *a*, suspended matter, and colored dissolved organic matter (C-DOM).

Furthermore, year-to-year variations in annual primary production in highly productive waters (Fig. 8) such as Oyashio waters and ECS continental shelf waters should contribute to global variations in primary production. In the GCMAPS project, we constructed a dataset of up to 176 measurements of primary production around Japan (Table 1) for validation of the algorithm that converts SeaWiFS data to primary production. Through validation and improvement of the algorithm with *in situ* data, satellite ocean color observation will become a more effective tool to monitor primary production, with fine spatial and temporal resolution on global scales. Satellite-derived estimates of organic production in food webs and carbon fixation in the surface layer may contribute to better understanding of variations in fisheries production and global-warming processes.

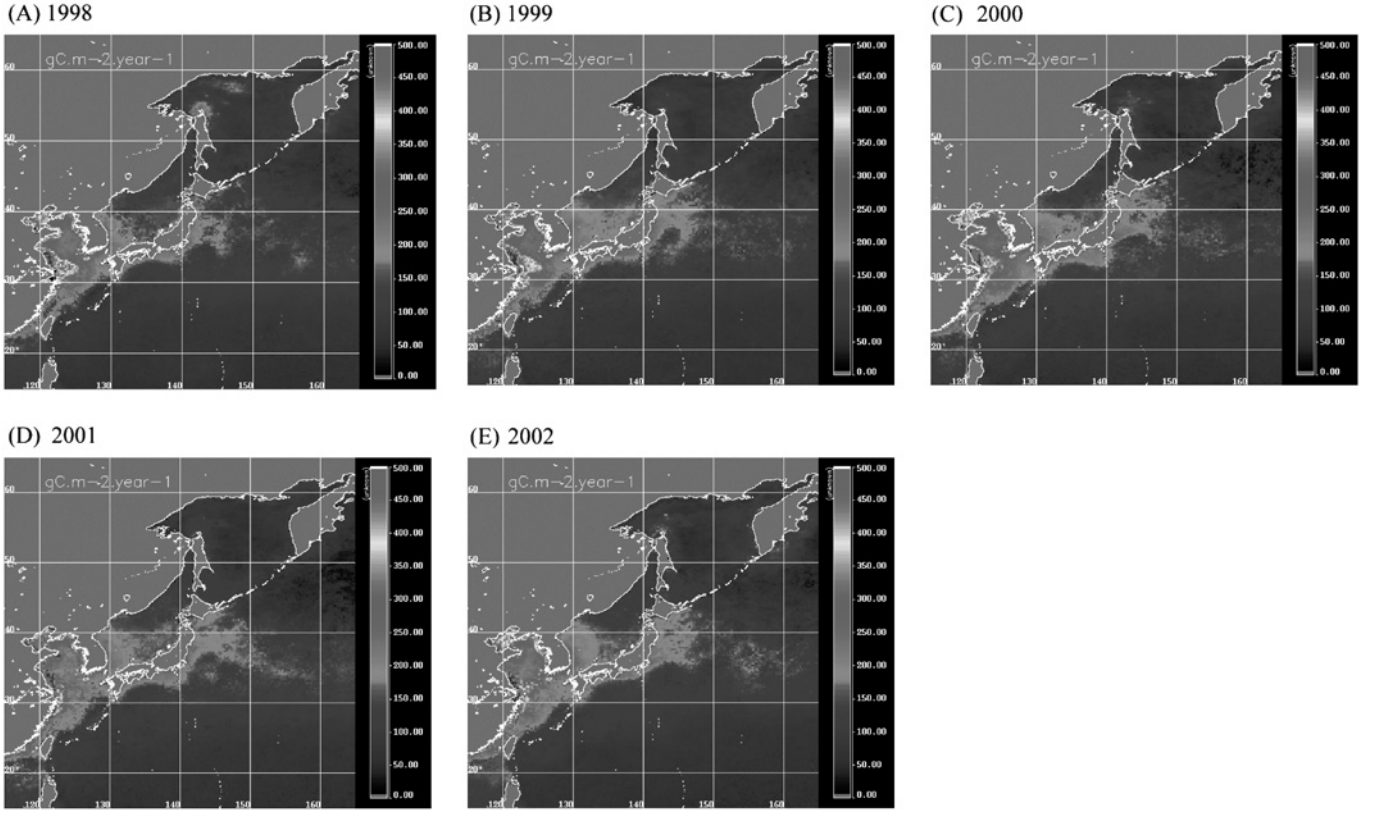

Figure 8: Maps of annual primary production (gC/m^2/year) from 1998 to 2002 produced according to Asanuma (2006) (For colour version, see Colour Plate Section).

Acknowledgements

The authors are grateful to Professor Toshiro Saino and Professor Satoru Taguchi for their helpful discussion and encouragement, Dr. Takahiko Kameda and Dr. Joji Ishizaka for their helpful suggestions regarding data formats, Dr. Masao Ishii and Dr. Tsuneo Ono for measurement of total carbonate in seawater, Dr. Akihiro Shiomoto and Dr. Yutaka Matsuo for improvement of methods, and Ms. Yoko Kiyomoto and Mr. Kazumaro Okamura for their cooperation in sample collection and analysis. The authors express their gratitude to Dr. Hodaka Kawahata for his promotion of this study as leader of the GCMAPS project.

References

Aruga, Y., Monsi, M., 1962. Primary production in the northwestern part of the Pacific off Honshu, Japan. Journal of the Oceanographic Society of Japan 18, 37–46.

Asanuma, I., 2006. Depth and Time Resolved Primary Productivity Model Examined for Optical Properties of Water. In: Kawahata, H., Awaya, Y. (Eds.), Global Climate Change and Response of Carbon Cycle in the Equatorial Pacific and Indian Oceans and Adjacent Landmasses. Elsevier Oceanography Series (73), pp. 91–110.

Asanuma, I., Matsumoto, K., Kawano, T., 2001a. Validation of photosynthetically available radiation estimated from satellite data for primary productivity model. Proceedings of the CEReS International Symposium on Remote Sensing of the Atmosphere and Validation of Satellite Data, pp. 62–67.

Asanuma, I., Matsumoto, K., Kawano, T., Kawahata, H., 2001b. Satellite estimated primary productivity and carbon flux. Sixth International Carbon Dioxide Conference, pp. 505–508.

Asanuma, I., Tanaka, T., Matsumoto, K., Kawano, T., 2000. Primary productivity model based on photosynthetically available radiation. Hyperspectral remote sensing of the ocean. Proceedings of SPIE V4154, 153–158.

Behrenfeld, M. J., Falkowski, P. G., 1997. Photosynthetic rates derived from satellite-based chlorophyll concentration. Limnology and Oceanography 42 (1), 1–20.

Behrenfeld, M. J., Maranon, E., Siegel, D. A., Hooker, S. B., 2002. Photoacclimation and nutrient-based model of light-saturated photosynthesis for quantifying oceanic primary production. Marine Ecology Progress Series 228, 103–117.

Berger, W. H., V. S. Smetacek, G. Wefer (Eds.), 1989, Productivity of the Ocean: Present and Past. Wiley, New York.

Duarte, C. M., Cebrian, J., 1996. The fate of marine autotrophic production. Limnology and Oceanography 41 (8), 1758–1766.

Eppley, R. W., 1972. Temperature and phytoplankton growth in the sea. Fisheries Bulletin 70 (4), 1063–1084.

Falkowski, P. G., 1981. Light-shade adaptation and assimilation numbers. Journal of Plankton Research 3, 203–216.

Falkowski, P. G., Raven, J. A., 1997. Aquatic Photosynthesis. Blackwell Science, p. 375.

Fitzwater, S. E., Knauer, G. A., Martin, J. H., 1982. Metal contamination and primary production: field and laboratory methods of control. Limnology and Oceanography 27, 544–551.

Geider, R. J., Osborne, B. A., 1992. Algal Photosynthesis: The Measurement of Algal Gas Exchange. Routledge, Chapman and Hall, New York, p. 256.

Hama, T., Miyazaki, T., Ogawa, Y., Iwakuma, T., Takahashi, M., Otsuki, A., Ichimura, S., 1983. Measurement of photosynthetic production of a marine phytoplankton population using a stable ^{13}C isotope. Marine Biology 73, 31–36.

Ichikawa, T., Hirota, Y., 2004. Seasonal changes of primary productivity in the Tosa Bay, Japan. Oceanography in Japan 13 (3), 259–269 (in Japanese with English abstract).

Imai, K., Nojiri, Y., Tsurushima, N., Saino, T., 2002. Time series of seasonal variation of primary productivity at station KNOT (44°N, 155°E) in the sub-arctic western North Pacific. Deep-Sea Research II 49, 5395–5408.

Kameda, T., Ishizaka, J., 2003. Studies on oceanic primary production using ocean color remote sensing data. Bulletin of Fisheries Research Agency (9), 118–148 (in Japanese with English abstract).

Kanda, J., Sada, K., Koike, I., Yokouchi, K., 1998. Application of an automated carbon-nitrogen analyzer for elemental and isotopic analysis of samples retained on glass-fiber filters. International Journal of Environment Analytical Chemistry 72 (3), 163–171.

Kasai, H., Saito, H., Tsuda, A., 1998. Estimation of standing stock of chlorophyll *a* and primary production from remote-sensed ocean color in the Oyashio region, the western subarctic Pacific, during the spring bloom in 1997. Journal of Oceanography 54, 527–537.

Kawai, H., 1972. Hydrography of the Kuroshio Extension. In: Stommel, H., Yoshida, K. (Eds.), Kuroshio Its Physical Aspects. Tokyo, University of Tokyo Press, pp. 235–352.

Knap, A., Michaels, A., Close, A., Ducklow, H., Dickson, A. (Eds.), 1996. Protocols for the Joint Global Ocean Flux Study (JGOFS) Core Measurements. JGOFS Report Nr. 19, vi+170 pp. Reprint of the IOC Manuals and Guides No. 29, UNESCO 1994.

Matsudaira, Y., 1964. Cooperative studies on primary productivities in the coastal waters of Japan. Informatics Bulletin for Planktonology in Japan 11, 24–73 (in Japanese).

Morel, A., Prieur, L., 1977. Analysis of variations in ocean color. Limnology and Oceanography 22, 709–722.

Ning, X., Liu, Z., Shi, J., 1995. Primary production and potential fisheries production in the Bohai Sea, the Yellow Sea and the East China Sea. Acta Oceanology Sinica 17 (3), 72–84 (in Chinese).

Nixon, S. W., 1988. Physical energy inputs and the comparative ecology of lake and marine ecosystems. Limnology and Oceanography 33 (4, part 2), 1005–1025.

Parsons, T. R., Maita, Y., Lalli, C. M., 1984. A Manual of Chemical and Biology Methods for Seawater Analysis. Pergamon Press, Oxford, p. 173.

Poole, H. H., Atkins, W. R. G., 1929. Photoelectric measurements of submarine illumination throughout the year. Journal of Marine Biology Association of the United Kingdom 16, 297–324.

Ryther, J. H., 1969. Photosynthesis and fish production in the sea. Science 166, 72–76.

Sarmiento, J. L., Toggweider, J. R., 1984. A new model for the role of the ocean in determining atmospheric pCO_2. Nature 308, 621–624.

Shiomoto, A., 2000. Chlorophyll-*a* and primary production during spring in the oceanic region of the Oyashio Water, the north-western Pacific. Journal of Marine Biology Association of the United Kingdom 80, 343–354.

Steemann-Nielsen, E., 1952. The use of radioactive carbon ^{14}C for measuring organic production in the sea. Journal du Conseil International pour l'Exploration de la Mer 18, 117–140.

Suzuki, R., Ishimaru, T., 1990. An improved method for the determination of phytoplankton chlorophyll using *N*,*N*-dimethylformamide. Journal of the Oceanographic Society of Japan 46, 190–194.

Tsuda, A., Takeda, S., Saito, H., Nishioka, J., Nojiri, Y., Kudo, I., Kiyosawa, H., Shiomoto, A., Imai, K., Ono, T., Shimamoto, A., Tsumune, D., Yoshimura, T., Aono, T., Hinuma, A., Kinugasa, M., Suzuki, K., Sohrin, Y., Noiri, Y., Tani, H., Deguchi, Y., Tsurushima, N., Ogawa, H., Fukami, K., Kuma, K., Saino, T., 2003. A mesoscale iron enrichment in the western subarctic Pacific induces a large centric diatom bloom. Science 300, 958–961.

Yanagi, T., Shimizu, T., Lie, H. J., 1998. Detailed structure of the Kuroshio frontal eddy along the shelf edge of the East China Sea. Continental Shelf Research 18, 1039–1056.

Chapter 4

Depth and Time Resolved Primary Productivity Model Examined for Optical Properties of Water

Ichio Asanuma*

Tokyo University of Information Sciences, 1200-2, Yato, Wakaba, Chiba, 265–8501, Japan

Abstract

A depth and time resolved primary productivity model is proposed and validated with *in situ* and simulated *in situ* incubations using ^{13}C in the western Pacific Ocean. In this model, a vertical distribution of photosynthetically available radiation (PAR) is modeled based on the chlorophyll *a* concentration in the surface layer, where the assumption is that the surface chlorophyll *a* concentration determines the light field. A vertical distribution of chlorophyll *a* concentration is modeled with an empirical equation, in which a chlorophyll maximum is observed along the vertical distribution of PAR. A carbon fixation rate is modeled as a function of PAR and temperature, in contrast to previous studies, in which a temperature-dependent function is significantly improved. By finding an optimum vertical distribution of PAR for various combinations of chlorophyll *a* concentration and diffused attenuation coefficient, our depth and time resolved primary productivity model exhibited a good correlation with *in situ* and simulated *in situ* incubation.

Keywords: primary productivity; ocean color; chlorophyll *a*; diffused attenuation coefficient; remote sensing

1 Introduction

A contribution of biota to global warming in a long timescale is of a strong interest to human beings as storage of carbon dioxide. In addition, it is

*Corresponding author.
E-mail address: asanuma@rsch.tuis.ac.jp (I. Asanuma).

Elsevier Oceanography Series 73
Edited by H. Kawahata and Y. Awaya
ISBN: 0-444-52948-9

expected that biota will exhibit its variation of standing stock as a response to climate change. Bengtsson et al. (1999) studied perceived inconsistencies between global temperature observations over the last two decades and results from climate simulations with some hypothesis for the slower global warming. The biosphere may have a certain contribution and a response to the global warming. The terrestrial biosphere has been essentially in balance with implying compensating growth of the biosphere (Houghton et al.,1997), but oceanic biota has not been studied well because of difficulties of expeditions. Langenfelds et al. (1999) pointed a temporal variation of oceanic biota response to the carbon flux between the ocean and the atmosphere. Christian et al. (1997) estimated the net flux of carbon across particular depth and pointed the biological pump being a sink for atmospheric CO_2 in the north Pacific subtropical gyre.

Now, satellite-based ocean color sensing systems provide chlorophyll *a* distribution continuously since 1996. The Ocean Color Temperature Scanner (OCTS) provided a global coverage of chlorophyll *a* distribution from November 1976 to June 1997 (Simada et al., 1999). The Sea-Viewing Wide Field-of-View Sensor (SeaWiFS) continues its observation since September 1997 (McClain et al., 1992). This series of ocean color observation has a possibility to study contribution of phytoplankton to climatological change for these 10 years, although there is a discontinuity of 2 months between the two programs. The OCTS and SeaWiFS provide a similar specification with bands, full-width half-maximum of wavelength, maximum radiance, and signal-to-noise ratio, which are based on some experience in the Coastal Zone Color Scanner (CZCS). In contrast, the Moderate Resolution Imaging Spectrometer (MODIS) and the Global Imager (GLI) have a narrow bandwidth with 36 bands, to establish multipurpose missions on ocean, land, atmosphere, and cryosphere. It is an urgent mission for space agencies to exhibit a consistency in geophysical values among different sensors indicating different characteristics. The consistency is necessary to analyze a long-term observation. If there is even a small inconsistency among systems, a combination of remote sensing parameters may exhibit amplified inconsistency in the final geophysical value in time.

Estimates of global primary productivity from the ocean color measurement are one approach to discuss a contribution of the oceanic biota to global warming or climate change. Morel (1991) discussed the light field in the water relative to photosynthesis, which is extended to a wavelength-resolved primary productivity model. Behrenfeld et al. (1997) and Falkowski et al. (1998) proposed a light- and temperature-dependent primary productivity model based on the satellite measurement. Arrigo et al. (1998) implied a possibility of a primary productivity model in southern ocean waters. Those models worked to some extent, but some failures were also observed, in which an overestimate was observed in the middle latitude and an

underestimate was observed in the lower latitude. Photosynthetically available radiation (PAR) dependent depth and time resolved primary productivity model was proposed to recover from those failures (Asanuma et al., 2000, 2001a, b). A vertical distribution of PAR is defined by an empirical equation as a function of the chlorophyll *a* concentration in the surface, which is observed by ocean color sensors. A vertical distribution of chlorophyll *a* concentration is also defined by an empirical equation as a function of the vertical distribution of PAR. A carbon fixation rate is defined as a function of PAR and temperature. Through the validation process of the primary productivity model in this study, this model exhibited overestimates relative to *in situ* measurement on the water with higher chlorophyll *a* concentration. In this chapter, a new algorithm is proposed to represent a vertical distribution of PAR as a function of chlorophyll *a* concentration in the surface. A new depth and time resolved primary productivity model is validated with *in situ* measurement using ^{13}C as a tracer around the equatorial Pacific, in subtropic waters including the East China Sea, and in subarctic waters including coastal waters off Hokkaido.

2 Depth and Time Resolved Primary Productivity Model

2.1 Carbon Fixation Rate

A depth and time resolved primary productivity model was proposed to estimate primary productivity from satellite measurement (Asanuma et al., 2000, 2001a, b). A vertical distribution of PAR is defined by an empirical equation as a function of the chlorophyll *a* concentration in the surface. A vertical distribution of chlorophyll *a* concentration is also defined by an empirical equation as a function of the vertical distribution of PAR. A carbon fixation rate is defined as a function of PAR and temperature. This depth resolved primary productivity model was proposed because of an insufficient estimate of primary productivity by a single layer model, in which it is difficult to represent a vertical contribution of primary productivity from a subsurface or deep chlorophyll *a* maximum. The model suggested in this chapter combines vertical parameters and integrates for 24 h to estimate a primary productivity as follows:

$$PPeu = \int_t \int_z C(z) P^B\{z, PAR(z), T\} \; PAR(0,t)/PAR(0,noon) \; \mathrm{d}z \; \mathrm{d}t \tag{1}$$

where $PPeu$ is primary productivity ($\mathrm{mgC\,m^{-2}\,day^{-1}}$), P^B is carbon fixation rate ($\mathrm{mgC\,mgChl\text{-}a^{-1}\,m^{-3}\,h^{-1}}$), PAR is photosynthetically available

radiation (Ein m^{-2} day^{-1} for $PAR(z)$, and Ein m^{-2} h^{-1} for $PAR(0,t)$ and $PAR(0,noon)$, C is chlorophyll a concentration (mg m^{-3}), T is water temperature (°C), z is depth (m), and t is time from 0 to 24 h. The carbon fixation rate, P^B, is proposed as a function of daily PAR, temperature, and depth from the dataset opened through the homepage of the ocean primary productivity working group (http://marine.rutgers.edu/opp/database/database2.html). In this database, carbon fixation rate (mgC mgChl^{-1} m^{-3} h^{-1}) is given for seawater temperature (°C), daily PAR (Ein m^{-2} day^{-1}), and depth (m). The dataset was clustered into some temperature ranges and plotted as a function of the carbon fixation rate and PAR. Figs. 1a, b, c show plots of the empirically fitted carbon fixation rate, (P^B), as a function of PAR and temperature of 10, 20, and 27°C. Each thin solid line is a measure of carbon fixation rate along the water column for each temperature range at various stations. Each thin solid line shows an increase of carbon fixation rate from lower PAR to higher PAR, and low carbon fixation rate with a photoinhibition at the highest PAR, which is corresponding to the surface. Carbon fixation rate along the water column is proportional to PAR in the surface. To represent a group of carbon fixation rate at a certain temperature range, an empirical equation of carbon fixation rate is proposed with regression lines as a function of PAR and temperature as in the equation (2). The first exponent term of equation (2) controls a slope in lower PAR region and the second exponent term controls a depression in higher RAR region.

$$P^B(z) = c\{1 - \exp(-a\ PAR(z)/PAR(0))\}\ \exp(-b\ PAR(z)/PAR(0)) \tag{2}$$

where, $PAR(z)$ and $PAR(0)$ are daily PAR (Ein m^{-2} day^{-1}) at certain depth and the surface, and P^B is the carbon fixation rate for unit volume and per hour (mgC mgChl^{-1} m^{-3} h^{-1}). In this study, $P^B(z)$ is assumed as the carbon fixation rate at noon. Parameters, a, b, and c were empirically determined from previous measurement of the carbon fixation rate for unit volume and per hour with the daily PAR at the surface and with the various sea-surface temperatures as follows:

$$a = 0.04\ (0.1\ m\ PAR_{(0)} + n) \tag{3}$$

$$m = -0.0001\ T^3 + 0.0036T^2 - 0.0007T + 0.2557 \tag{3-1}$$

$$n = 0.00024T^3 - 0.0113T^2 + 0.0868T - 0.1042 \tag{3-2}$$

$$b = 0.3(0.00048T^3 - 0.019T^2 + 0.1T + 3.1214) \tag{4}$$

$$c = 17 \tag{5}$$

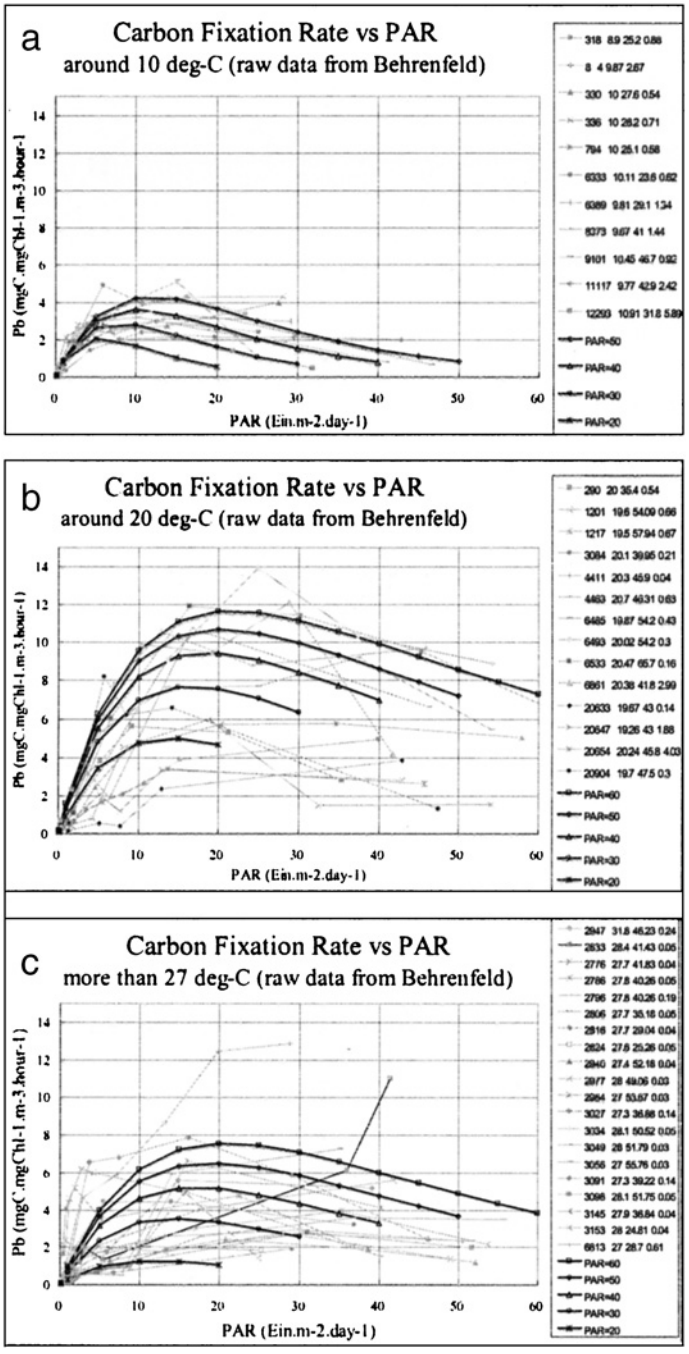

Figure 1: Empirically filled carbon fixation rate (P^H) as a function of Photosynthetically Available Radiation (PAR) and temperatures of 10, 20, and 17°C.

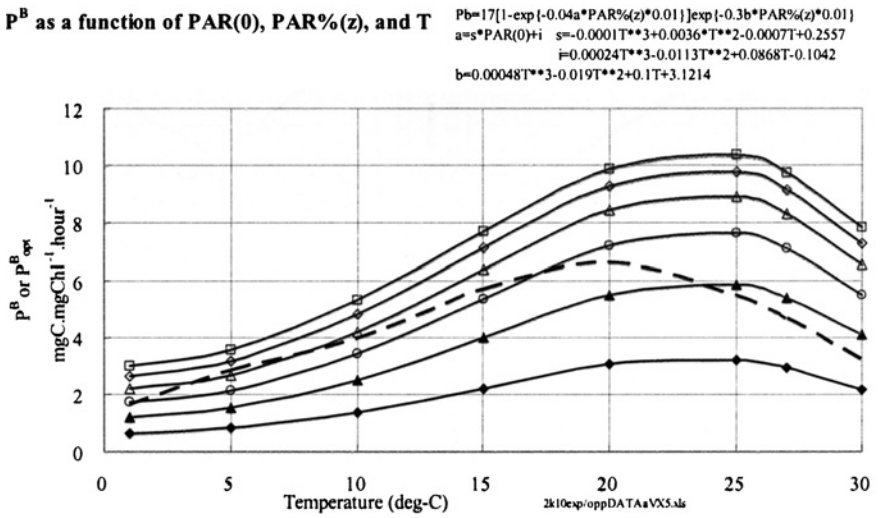

Figure 2: Carbon fixation rate (P^{H}) as a function of Photosynthetically Available Radiation (PAR) and sea-surface temperature. Solid lines show P^{B} is a function of sea-surface temperature for different PAR intensities, 10(◆), 20(▲), 30(○), 40(Δ), 50(◇), and 60(□) Ein $\mathrm{m}^{-2}\,\mathrm{day}^{-1}$. A dashed line exhibits the maximum carbon fixation rate within a water column ($P^{\mathrm{B}}_{\mathrm{opt}}$) proposed by Behrenfeld and Falkowski (1997) and is given as the seventh-order polynomial or temperature.

The carbon fixation rate is plotted in Fig. 2 as a function of sea-surface temperature for PAR of 10, 20, 30, 40, 50, and 50 Ein $\mathrm{m}^{-2}\,\mathrm{day}^{-1}$ with the carbon fixation proposed by Behrenfeld and Falkowski (1997). The carbon fixation rate proposed in this study covers variation of carbon fixation rate for each temperature, which was difficult to represent with one empirical equation proposed by the previous studies. In addition, the carbon fixation rate proposed in this study is quite different from an exponent increase of carbon fixation rate for temperature, which is proposed by Eppley (1972) and is often applied to the general circulation model (GCM).

2.2 Photosynthetically Available Radiation Along the Water Column

An attenuation process of the light penetrating the water is explained by a diffused attenuation coefficient as follows:

$$Ed_{\lambda}(z2) = \exp\{-Kd_{\lambda}(z2 - z1)\}\ Ed_{\lambda}(z1), \tag{6}$$

where $Ed_{\lambda}(z1)$ is the initial downwelling diffused spectrum irradiance at depth $z1$ m and at the wavelength λ nm, $Ed_{\lambda}(z2)$ is the final downwelling

diffused spectrum irradiance at depth z2 m and Kd_λ is the downward diffused attenuation coefficient m^{-1} at the wavelength λ nm. In ocean color remote sensing, chlorophyll a concentration and diffused attenuation coefficient at 490 nm are estimated from multichannel observation in visible bands. Empirical equations for chlorophyll a concentrations and diffuse attenuation coefficient are proposed independently. O'Reilly et al. (2000) proposed four bands ratio for three ranges of chlorophyll a concentration, where ratios of 510–555 nm, 490–555 nm, and 443–555 nm are used from low to high chlorophyll a concentration, but there remains uncertainty of the algorithm for high chlorophyll a concentration because of inadequate number of *in situ* data. Muller (2000) proposed two bands ratio of 490–555 nm to estimate diffused attenuation coefficient at 490 nm, and also reported the uncertainty of the algorithm of diffused attenuation coefficient $> 0.25\,m^{-1}$. Both empirical equations are used for standard products of SeaWiFS project. Unfortunately, the algorithms for chlorophyll a concentration and diffused attenuation coefficient are not insufficient to cover a coastal region, where high chlorophyll a concentration and high diffused attenuation coefficient are expected.

In the first approach for this chapter, an empirical equation (7) was proposed to retrieve a vertical distribution of PAR along the water column, which was suggested from *in situ* measurement of downwelling spectrum irradiance and chlorophyll a concentrations. In the measurement from the research vessel on the western equatorial Pacific and the Kuroshio region, a spectrum irradiance radiometer was deployed to measure a vertical distribution of downwelling irradiance for a full depth of euphotic zone. PAR was computed by integrating spectrum responses of downwelling irradiance between 400 and 700 nm. As PAR near the surface exhibits variation because of unstable wave motion, PAR from 2 or 3 m to 10 or 15 m were plotted in a log scale and its regression line was used to determine PAR at the surface with an assumption that the surface water shows a uniform diffused attenuation coefficient.

$$PAR(z) = \exp\{2.3(-0.025\ C_0 - 0.017)\ z\}\ PAR(0) \tag{7}$$

where C_0 is chlorophyll a concentration on the surface, $PAR(z)$ is PAR at depth z m, and $PAR(0)$ is PAR at the surface. Equation (7) worked to represent a relationship between chlorophyll a concentration and PAR in the water, which exhibits a low chlorophyll a concentration with an oligotrophic water.

2.3 Vertical Distribution of Chlorophyll *a* Along the Water Column

Platt et al. (1988a) and Platt and Sathyendranath (1988b) proposed an empirical equation to represent a vertical distribution of chlorophyll a concen-

tration with the Gaussian distribution. In contrast to these empirical equations, a vertical distribution of chlorophyll *a* concentration is proposed by the following empirical equation as a function of a vertical distribution of PAR and chlorophyll *a* concentration in the surface.

$$C(z) = [1 - (0.9 + 0.7C_0)\exp\{-0.8PAR\%(z, C_0)\}] \quad \exp\{-0.8PAR\%(z, \ C_0)\} + C_0 \tag{8}$$

The equation (8) reproduces a constant concentration of chlorophyll *a* from the surface to the just above of the chlorophyll maximum. The chlorophyll maximum and following vertical distribution of chlorophyll *a* are observed just on the slant line of the vertical distribution of PAR. Fig. 3 shows vertical

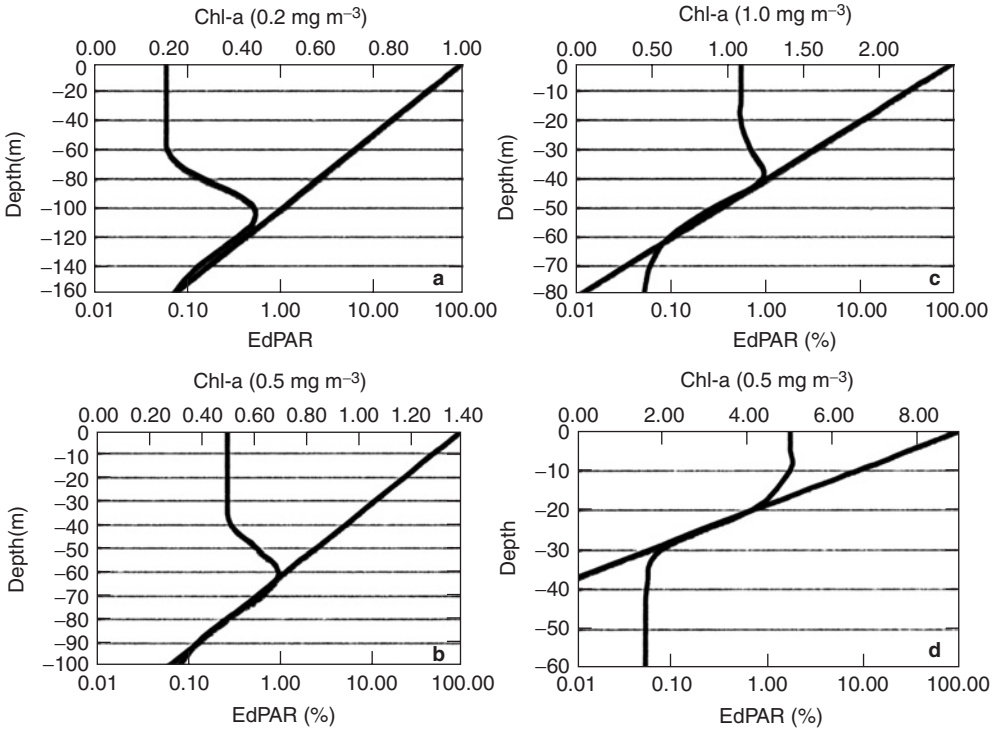

Figure 3: Vertical distribution of chlorophyll *a* concentration based on vertical distribution of photosynthetically available radiation (PAR). The PAR along the water column is given by the equation (7). Then the equation (8) estimates the vertical distribution of chlorophyll *a* concentration (a) for $0.2\,\mathrm{mg\,m^{-3}}$, (b) for $0.5\,\mathrm{mg\,m^{-3}}$, (c) for $1.0\,\mathrm{mg\,m^{-3}}$, and (d) for $5.0\,\mathrm{mg\,m^{-3}}$ chlorophyll *a* concentration on the surface. Second *X*-axis of each figure varies to keep an overlap between vertical distribution lines of PAR and chlorophyll *a* concentration around the chlorophyll maximum.

distributions of chlorophyll *a* concentration based on vertical distributions of PAR for a different full scale of chlorophyll *a* concentration on the second *X*-axis. The full scale of chlorophyll *a* concentration on the second *X*-axis is empirically adjusted to match a slant line of PAR with a slant line of chlorophyll *a* concentration for the depth deeper than chlorophyll maximum. Two bold lines on Fig. 3a represent vertical distributions of PAR and chlorophyll *a* in case of the surface chlorophyll *a* concentration being $0.2\,\mathrm{mg\,m^{-3}}$ with a full scale of chlorophyll *a* concentration for $1.0\,\mathrm{mg\,m^{-3}}$ on the second *X*-axis. Fig. 3a shows a deep chlorophyll maximum around 100 m and chlorophyll *a* concentration decreases to 150 m along a vertical distribution of PAR. Two bold lines in Fig. 3b are in case of the surface chlorophyll *a* concentration being $0.5\,\mathrm{mg\,m^{-3}}$ with a full scale of chlorophyll *a* concentration for $1.4\,\mathrm{mg\,m^{-3}}$. Fig. 3b shows a deep chlorophyll maximum around 60 m. Two bold lines on Fig. 3c are in case of the surface chlorophyll *a* concentration being $1.0\,\mathrm{mg\,m^{-3}}$ with a full scale of chlorophyll *a* concentration for $2.5\,\mathrm{mg\,m^{-3}}$. Fig. 3c shows a subsurface chlorophyll maximum around 40 m. Chlorophyll *a* concentration decreases along a vertical distribution of PAR and a valid range of chlorophyll *a* concentration is limited to around 60 m, where PAR percentage to the surface is about 0.1%. Two bold lines on Fig. 3d are in case of the surface chlorophyll *a* concentration being $5.0\,\mathrm{mg\,m^{-3}}$ with a full scale of chlorophyll *a* concentration for $9.0\,\mathrm{mg\,m^{-3}}$. Fig. 3d shows a surface chlorophyll maximum. A valid range of chlorophyll *a* concentration is limited to around 30 m where PAR percentage to the surface is about 0.1%, although chlorophyll *a* concentration is plotted to 80 m.

The vertical distributions of chlorophyll *a* concentration are determined by equations (7) and (8) as a function of chlorophyll *a* concentration in the surface. Equation (7) determines light penetration field. Equation (8) determines vertical distribution of chlorophyll *a* along the light penetration field. In this hypothesis, a diffused attenuation coefficient of water is determined by chlorophyll *a* concentration only and there is a possibility of error to estimate vertical distribution of chlorophyll *a* concentration in the case of water, where suspended sediment's phytoplankton exists in addition to phytoplankton.

2.4 Photosynthetically Available Radiation

PAR on the surface is one inevitable parameter to estimate the primary productivity. Frouin (2000) proposed a research product for PAR from SeaWiFS measurement with a model for PAR at the surface in the day ($\mathrm{Ein\,m^{-2}\,day^{-1}}$) using parameters of remote sensing reflectance of clouds and possibility of cloud presence. Frouin discussed a possibility of the sun glint region in the missing data, which reduces the accuracy of PAR estimate. Although some uncertainties remain for PAR products, the SeaWiFS

project provides PAR data in the global scale routinely for end users. In this study, PAR products for the monthly mean (Ein m^{-2} day^{-1}) are accepted to compute a daily averaged primary productivity for the month.

The time resolved primary productivity model in this study ingests the difference of PAR within a day. Hourly PARs for a cloud free and ideal atmospheric condition of the globe for each month were calculated with the help of MODerate spectral resolution atmospheric TRANSmittance algorithm and computer model (MODTRAN) in the version 4.3. MODTRAN was developed by the Air Force Research Laboratories (AFRL) in collaboration with Spectral Sciences, Inc. (http://www.vs.afrl.af.mil/Division/VSBYB/modtran4.html). MODTRAN was operated with the mid-latitude summer atmospheric model with the aerosol model, in which the boundary layer of 0–2 km is selected to the maritime aerosol type with 23 km visibility at the sea level. Spectrum radiance of a white target with a reflectance of 1.0 for all spectrums on the sea surface was calculated from 400 to 700 nm with 10 nm intervals with MODTRAN. The PAR is the spectrum integration from 400 to 700 nm and the solid angle integration for the hemisphere with an assumption of Lambertian reflectance of the white target. PAR was calculated for every 10° of latitude for every hour on one day in the middle of each month from January to December. The monthly mean hourly PAR for a day (Ein m^{-2} h^{-1}) is the maximum temporal resolution for the current primary productivity model.

The hourly carbon fixation rate for the noon on the day, $P^B(z,noon)$, is given by the daily-observed PAR in equation (2). Then the hourly carbon fixation rate is estimated with the model computed hourly PAR and will be ingested into the depth and time integration in equation (1).

$$P^B(z,\ t) = P^B(z,\ noon)\ \ PAR_M(0,\ t)/PAR_M(0,\ noon) \tag{9}$$

where $PAR_M(0,t)$ is the model estimated hourly PAR at the hour, t, in the day at the surface, and $PAR_M(0,noon)$ is the model estimated PAR at noon in the day at the surface. This estimate of carbon fixation rate for the time in a day has an assumption that a carbon fixation rate is proportional to intensity of PAR and the carbon fixation rate does not reflect a nonlinear response of physiological activity of phytoplankton. This time-resolved concept of primary productivity can integrate hourly primary productivity from sunrise to sunset or for 24 h in the summer time of the high-latitude region according to time-dependent PAR as a function of latitude and month. In contrast, a time-integrated primary productivity model generally multiples a carbon fixation rate per hour and day length in hour, which does not have a sufficient time resolution from latitude to latitude or month to month.

2.5 Examination of Primary Productivity Model from the Point of Optical Property

Monthly primary productivity was estimated over the globe using chlorophyll *a* dataset provided by the NASA Goddard Space Flight Center (GSFC) based on SeaWiFS observation, the Multichannel Sea-Surface Temperature (MCSST) dataset provided by the Jet Propulsion Laboratory (JPL) based on NOAA/AVHRR observation, and PAR datasets provided by GSFC based on SeaWiFS observation. The results of the primary productivity are verified with the *in situ* measurement along the equatorial Pacific, the northwestern Pacific, and the East China Sea.

In situ primary productivity was measured by *in situ* incubation or on-deck simulated *in situ* incubation using ^{13}C solvent as a tracer. Niskin bottles were applied to take seawater from sampling depths before the sunrise. A prefilter of 100-μm pore size was applied to intake the seawater to an incubation bottle of polycarbonate, to avoid the involvement of zooplanktons for incubation. The incubation bottles were deployed into the sampling depths for the *in situ* incubation before sunrise. The incubation bottles were set into an incubation pool before sunrise, where several blue filters were combined to simulate PAR of sampling depths and the water temperature of the incubation pool was maintained constant with the surface water or a chilling unit. The incubation period was selected to 12 h from sunrise to sunset or 24 h from sunrise to the next sunrise for incubation, because of the lower sensitivity of ^{13}C relative to ^{14}C, the averaging physiological activities of phytoplankton within a day. The incubated sample water was filtered by the glass fiber filter, GF/F, to capture phytoplankton. The phytoplankton on the filter was processed by a mass spectrometer to analyze carbon uptake by phytoplankton based on the method proposed by Hama et al. (1987).

Fig. 4 shows a scatter diagram between the primary productivity estimated by the model in this study and *in situ* measurement. Model estimated and measured primary productivities along the equatorial Pacific (○) and the subarctic water including the northwestern Pacific (□) indicated a good agreement. In contrast, some model-estimated primary productivities on the subtropic water including the East China Sea (Δ) indicated an overestimate against measured primary productivities. This overestimation suggests (i) comparisons of measurement on the different water mass between the model and *in situ* data, where satellite data are spatially averaged for 9 km and temporally averaged for 1 month and (ii) a possibility of overestimation of primary productivity depending on the PAR vertical distribution, which was determined by chlorophyll *a* concentration.

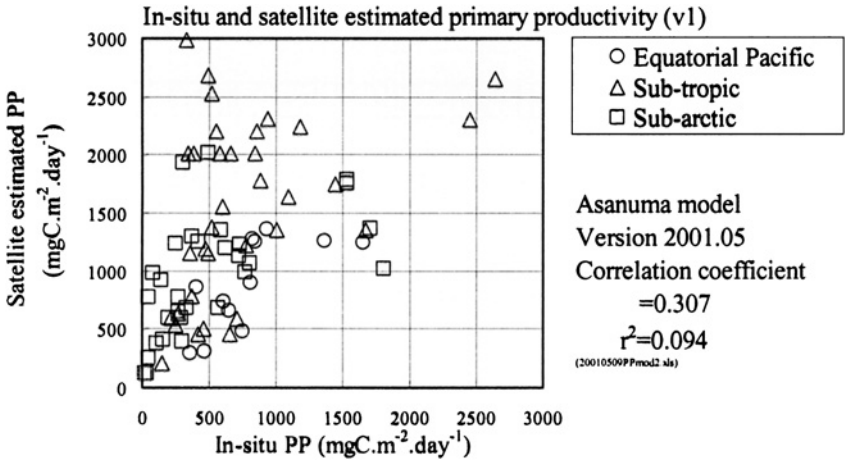

Figure 4: Scatter diagram of primary productivity between the model estimated and *in situ* and/or simulated *in situ* measured primary productivity based on the vertical distribution of PAR in equation (7). The correlation coefficient between the model estimated and the *in situ* primary productivity was 0.307.

2.6 A New Model for Vertical Distribution of PAR

Unfortunately, the primary productivity using the empirical equation (8) exhibited overestimates of primary productivity in the East China Sea and in the water off the Sanriku. On the East China Sea, the Seikai-ku Fishery Research Laboratory conducted *in situ* and simulated *in situ* incubations to estimate primary productivities for the water located on the eastern end of the continental shelf. The water on the eastern end of the continental shelf was the case-I water, where the concentration of suspended particles or colored dissolved organic matter is low and is different from the continental shelf case-II water. Off the Sanriku, the Hokkaido-ku Fishery Research Laboratory conducted *in situ* and simulated *in situ* incubations to estimate primary productivities for the Kuroshio originated water, the Oyashio, and the mixing region between two waters. The water off the Sanriku exhibits a variation in primary productivity with a variation in chlorophyll *a* concentration, of which water is also classified as the case-I water with a low concentration of suspended particles and colored dissolved organic matter. Although the water for *in situ* measurements was case-I water, the primary productivity was estimated higher than *in situ* measurement with higher chlorophyll *a* concentration.

A distribution of diffused attenuation coefficient at 490 nm (Kd_{490}) and chlorophyll *a* concentration were surveyed from the satellite observation data, to check validity of the unique empirical equation for PAR by

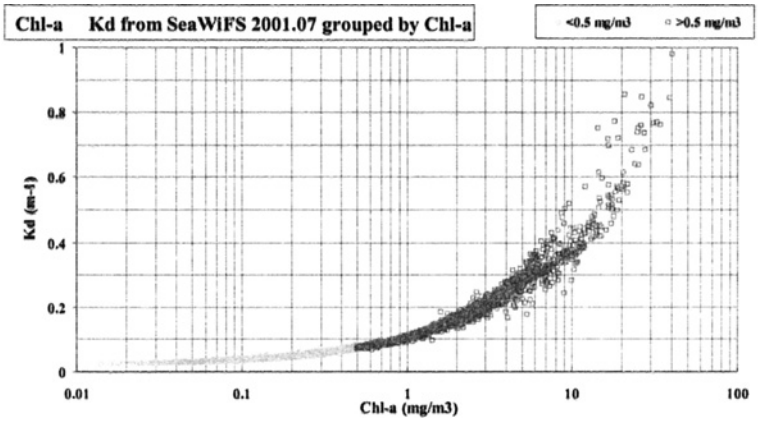

Figure 5: Plots of chlorophyll a concentration and diffused attenuation coefficient at 490 nm (Kd_{490}) for each pixels observed by SeaWiFS around Japan in July 2001. Data were selected from the monthly mean of level-3 products of SeaWiFS project. Plots of chlorophyll a concentration less than $0.5\,\mathrm{mg\,m^{-3}}$ exhibits a deep chlorophyll maximum more than 50 m and is corresponding to the case-I water. Kd_{490} exhibits a larger divergence in a higher chlorophyll a concentration.

chlorophyll a concentration on the surface. Fig. 5 indicates a scatter diagram between Kd_{490} and chlorophyll a concentration for the monthly composite data of SeaWiFS in July 2001 on the northwestern Pacific waters including the East China Sea, the Kuroshio along the Japan Islands, and water off Sanriku. Points are classified into two groups by a chlorophyll a concentration of $0.5\,\mathrm{mg\,m^{-3}}$, which is a threshold of chlorophyll a concentration giving a deep chlorophyll maximum more than 50 m. Kd_{490} at chlorophyll a concentration of $1.0\,\mathrm{mg\,m^{-3}}$ shows a variation of $\pm 0.02\,\mathrm{m^{-1}}$. Similarly, Kd_{490} exhibits variation of $\pm 0.05\,\mathrm{m^{-1}}$ at $5.0\,\mathrm{mg\,m^{-3}}$, $\pm 0.12\,\mathrm{m^{-1}}$ at $10.0\,\mathrm{mg\,m^{-3}}$, and $\pm 0.15\,\mathrm{m^{-1}}$ at $20.0\,\mathrm{mg\,m^{-3}}$. A less variation of Kd_{490} at lower chlorophyll a concentration suggests that optical properties in the open water, like the case-I water, could be represented by a unique equation between chlorophyll a concentration and Kd_{490}. In contrast, a large variation of Kd_{490} at higher chlorophyll a concentration, which is corresponding to the coastal water, suggests a difficulty in representing a relationship between Kd_{490} and chlorophyll a concentration with a unique equation. A combination of phytoplankton, suspended particles, and colored dissolved organic matter are cause of variations in Kd_{490} and chlorophyll a concentration using multispectrum remote sensing data at the current algorithm.

Figs. 6a and b show vertical distributions of PAR estimated by equations (7) and (10), respectively.

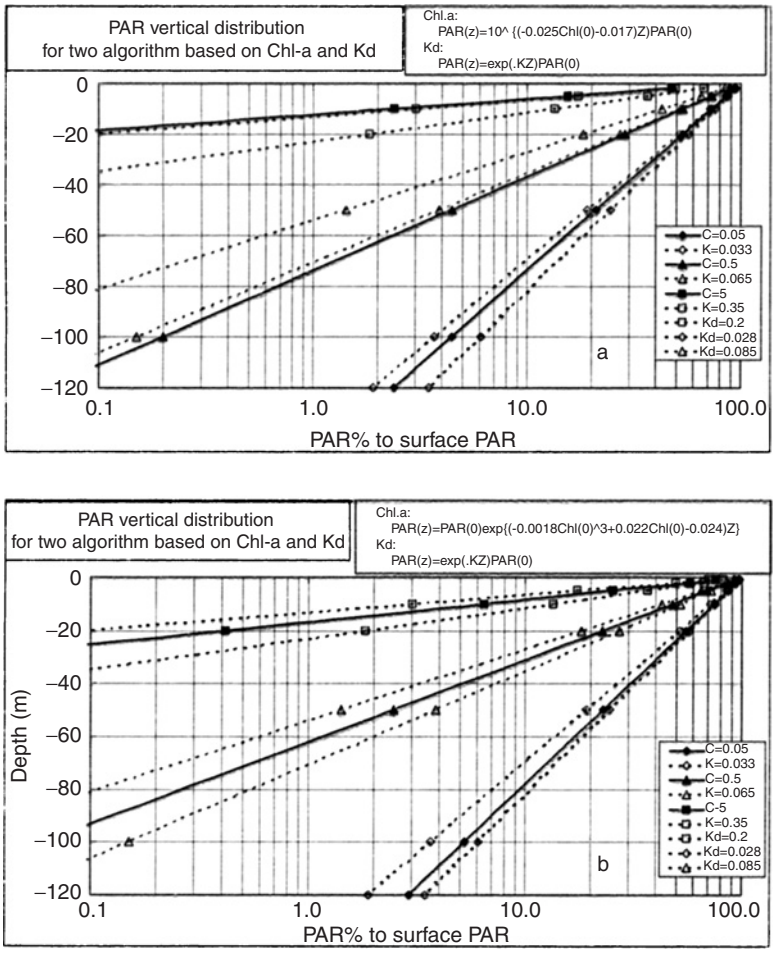

Figure 6: Vertical distributions of PAR. Solid lines show vertical distributions of PAR for three different chlorophyll *a* concentrations in the surface. The solid lines in Fig. 6a were computed by equation (7). The solid lines on Fig. 6b were computed by equation (10). For both figures, possible pairs of diffused attenuation coefficients at 490 nm (Kd_{490}) for three different chlorophyll *a* concentrations are plotted by dashed lines based on equation (6). Kd490 was selected from Fig. 5 for 0.028 and 0.033 m^{-1}, 0.065 and 0.085 m^{-1}, and 0.2 and 0.35 m^{-1} for 0.05, 0.065, and 5.0 mg m^{-3} of chlorophyll *a* concentration, respectively. Equation (10) gives the vertical distributions of PAR within the variation of Kd_{490}s for corresponding chlorophyll *a* concentration.

According to Fig. 6a, the equation (7) exhibits an underestimate of PAR for chlorophyll *a* concentration of 0.05 and 5.0 mg m^{-3}, where PAR did not penetrate deeper relative to PARs estimated by Kd_{490}. In addition, an

overestimate of PAR was observed for a chlorophyll *a* concentration of $0.5\,\mathrm{mg\,m^{-3}}$, where the PAR penetrates into deeper waters.

So as to avoid those over- and underestimates of vertical distributions of PAR on Fig. 6a, a new empirical equation was proposed to estimate vertical distributions of PAR based on chlorophyll *a* concentration to minimize errors in the previous equation (7) and to find an optimum distribution of PAR as follows:

$$PAR\%_{(z)} = \exp\{(-0.0018\ C_0^3 + 0.022\ C_0^2\ - 0.11\ C_0\ - 0.024)Z\}\ PAR\%_{(0)} \tag{10}$$

where C_0 is chlorophyll *a* concentration in the surface, $\mathrm{mg\,m^{-3}}$, Z is the depth in m. Fig. 6b shows vertical distributions of PAR estimated by equation (10) with solid lines. The solid lines are observed within a pair of two Kd_{490}s of dashed lines for each combination. The proposed equation (10) provides the optimum vertical distributions of PAR with a unique solution for each chlorophyll *a* concentration.

Fig. 7 shows a scatter diagram between *in situ* and model-estimated primary productivities. The correlation coefficient was 0.768, which was a significant improvement of the correlation coefficient from 0.307 in Fig. 4. Although there are some underestimates at some stations, Fig. 7 exhibits a good correlation between *in situ* and model-estimated primary productivities. The underestimates of primary productivity were observed at three

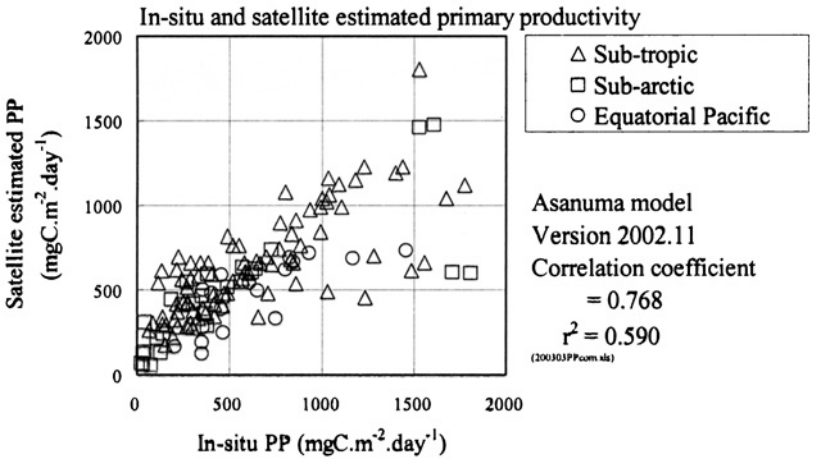

Figure 7: Scatter diagram of primary productivity between the model-estimated and *in situ* measured primary productivity based on the vertical distribution of PAR in equation (10). The correlation coefficient between the model-estimated and the *in situ* primary productivity was 0.768.

different regions, especially at stations exhibiting higher primary productivity. As the major group of measurement exhibited a good correlation, the primary productivity model proposed in this study is working in a good manner.

But, the spatial and temporal difference between *in situ* measurement and model calculation could be one reason for the error. *In situ* measurement is given for one station, where a limited amount of water mass is a subject for measurement. There is a difficulty of repeated measurement to get a mean value because of an incubation period of 12 or 24 h. *In situ* measurement will be conducted on the day with the PAR for the day, which could not be a mean PAR for a month or some period because of a weather condition for the day. In contrast, the model is applied to chlorophyll *a* distribution, sea-surface temperature, and PAR, which are temporally averaged for 1 month and spatially averaged for $9 \times 9\,\mathrm{km}^2$. The major error was observed in high primary productivity region, which is corresponding to a high chlorophyll *a* concentration. There are uncertainties of representing the water mass for $9 \times 9\,\mathrm{km}^2$ in space, because of a small possibility of equally distribution of high chlorophyll *a* concentration on the corresponding area. There are also uncertainties of continuous presence of high chlorophyll *a* concentration for the period corresponding to *in situ* measurement and monthly average of satellite observation. For these reasons, the spatial and temporal average by satellite observation may be the significant error for this validation using *in situ* measurement.

It is ideal to use simultaneous satellite observation with *in situ* measurement including chlorophyll *a* distribution, sea-surface temperature, and PAR. Unfortunately, chlorophyll *a* distribution observed by a polar orbit satellite has a possibility of cloud presence within a pass over the *in situ* measurement station, which covers the region once a day. Because of this less opportunity of chlorophyll *a* observation by polar orbit satellites, weekly or monthly composite for chlorophyll *a* concentration is applied, although a daily composite dataset is provided. In contrast, sea-surface temperature observation by polar orbit satellite has several opportunities within a day by a few NOAA polar orbit satellites and high opportunity of observation. The daily composite sea-surface temperature dataset is not available globally, but locally. A global sea-surface temperature dataset is provided on a weekly or monthly composite because of cloud presence. PAR is also provided on a weekly or monthly basis because of reducing uncertainties of error.

3 Summary

The depth and time resolved primary productivity model using chlorophyll *a* concentration and sea-surface temperature was proposed. Through the

validation process of the model based on *in situ* measurement on the equatorial Pacific, the northwestern Pacific, and the East China Sea, the model exhibited the overestimates in some waters. It was suggested that the optical properties of water is the major reason for the overestimates.

Then, the optical property of the water around Japan was studied as a function of chlorophyll *a* concentration and diffused attenuation coefficient based on SeaWiFS data. The water with high chlorophyll *a* concentration exhibited the wide range of diffused attenuation coefficient at 490 nm (Kd_{490}). The variation in Kd_{490} suggested the error in estimating a vertical distribution of PAR and chlorophyll *a* concentration as a function of chlorophyll *a* concentration in the surface water. Our previous empirical equation (7) for the vertical distribution of PAR is modified to fit the variation of Kd_{490} at given chlorophyll *a* concentration as indicated by equation (10).

As a result, the optically optimized PAR-dependent depth and time resolved primary productivity model indicated a good correlation between the model estimates and *in situ* primary productivity measurement.

Acknowledgements

This study is supported by the special coordination fund of the Ministry of Education, Culture, Sports, Science and Technology, Global Carbon Mapping (GCMAP) from 1998 to 2002.

References

Arrigo, K. R., Worthen, D., Schnell, A., Lizotte, M. P., 1998. Primary production in southern ocean waters. Journal of Geophysical Research 103 (C8), 15587–15600.

Asanuma, I., Matsumoto, K., Kawano, T., Kawahata, H., 2001a. Satellite estimated primary productivity and carbon flux. Sixth International Carbon Dioxide Conference, pp. 505–508.

Asanuma, I., Matsumoto, K., Kawano, T., 2001b. Validation of photosynthetically available radiation estimated from satellite data for primary productivity model. Procedures of the CEReS International Symposium on Remote Sensing of the Atmosphere and Validation of Satellite Data, pp. 62–67.

Asanuma, I., Tanaka, T., Matsumoto, K., Kawano,T., 2000. Primary productivity model based on photosynthetically available radiation. Hyperspectral remote sensing of the ocean. Procedures of SPIE V4154, pp. 153–158.

Behrenfeld, M., Falkowski, P. G., 1997. Photosynthetic rates derived from satellite-based chlorophyll concentration. Limnology and Oceanography 42 (1), 1–20.

Bengtsson, L., Roeckner, E., Stendel, M., 1999. Why is the global warming proceeding much slower than expected?. Journal of Geophysical. Research 104 (D4), 3865–3876.

Christian, J. R., Lewis, M. R., Karl, D. M., 1997. Vertical fluxes of carbon, nitrogen, and phosphorus in the north Pacific subtropical gyre near Hawaii. Journal of Geophysical. Research 102 (C7), 15667–15677.

Eppley, R. W., 1972. Temperature and phytoplankton growth in the sea. Fishery Bulletin 70, 1063–1085.

Falkowski, P. G., Behrenfeld, M. J., Balch, W., Campbell, J. W., Iverson, R. L., Kiefer, D. A., Morel, A., Yoder, J. A., 1998. Satellite primary productivity data and algorithm development: A science plan for Mission to Planet Earth. SeaWiFS Technical Report Series, Vol. 42, p. 37.

Frouin, R., 2000. http://orca.gsfc.nasa.gov/seawifs/par/doc/seawifs_par_wfigs.pdf.

Hama, T., Handa, N., Hama, J., 1987. Determination of amino acid production rate of a marine phytoplankton population with ^{13}C and gas chromatography-mass spectrometry. Limnology and Oceanography 32, 1144–1153.

Houghton, R. A., Davidson, E. A., Woodwell, G. M., 1997. Missing sinks, feedbacks and understanding the role of terrestrial ecosystems in the global carbon balance. Global Biogeochemical Cycles 12, 25–34.

Langenfelds, R. L., Francey, R. J., Steel, L. P., Battle, M., Keeling, R. F., Budd, W. F., 1999. Partitioning of the global fossil CO_2 sink using a 19-year trend in atmospheric O_2. Geophysical Research Letters 26 (13), 1897–1900.

McClain, C., Esaias, W. E., Barnes, W., Guenther, B., Endres, D., Hooker, S. B., Mitchell, B. G., Barnes, R., 1992. SeaWiFS calibration and validation plan. NASA Technical Memorandum 104566, Vol. 3, p. 43.

Morel, A., 1991. Light and marine photosynthesis: A spectral model with geochemical and climatological implications. Progressive Oceanography 26, 263–306.

Muller, J. L., 2000. SeaWiFS algorithm for the diffuse attenuation coefficient, K(490), using water-leaving radiances at 490 and 555 nm. Vol.11 SeaWiFS Postlaunch Calibration and Validation Analyses, Part 3, pp. 24–27.

O'Reilly, J. E. et al., 2000: Ocean color chlorophyll *a* algorithms for SeaWiFS, OC^2, and OC^4: version 4. In: Hooker, S. B., Firestone, E. R. (Eds.) SeaWiFS Postlaunch Calibration and Validation Analyses, Part 3. NASA Technical Memorandum 2000–206892, Vol. 11, pp. 9–23.

Platt, T., Sathyendranath, S., Caverhill, C. M., Lewis, M. R., 1988a. Ocean primary production and available light: Further algorithms for remote sensing. Deep Sea Research 35, 855–879.

Platt, T., Sathyendranath, S., 1988b. Oceanic primary production: Estimation by remote sensing at local and regional scales. Science 241, 1613–1620.

Simada, M., Oaku, H., Mitomi, Y., Murakami, H., Kawamura, H., 1999. Calibration of the ocean color and temperature scanner. IEEE Trans. Geoscience and Remote Sensing 37 (3), 1484–1495.

Chapter 5

Settling Particles in the Central North Pacific

Hodaka Kawahata[1,2,*]

[1]*Graduate School of Frontier Sciences and Ocean Research Institute, University of Tokyo, 1-15-1 Minamidai, Nakano-ku, Tokyo 164-8639, Japan*
[2]*Geological Survey of Japan, National Institute of Advanced Industrial Science and Technology, 1-1-1 Higashi, Tsukuba, Ibaraki 305-8567, Japan*

Abstract

Sediment-trap experiments were conducted in the central North Pacific from the subtropical to the subarctic water mass (30°N–46°N) in order to understand the characteristics of settling particles as they relate to the biological pump. Fluxes of total mass, organic matter (OM), carbonate, biogenic opal, and lithogenics showed definite seasonal changes. In particular, there was a steep gradient in export production from June to December 1993 at the studied sites along a transect at 175°E, while the gradient was quite uniform from January to April 1994. Annual mean total mass flux varied from 47.4 mg m^{-2} day^{-1} at the southernmost station (Site 6; 30°N) in subtropical waters to 207.7 mg m^{-2} day^{-1} at the subarctic station (Site 8; 46°N). The transition zone showed intermediate fluxes of 41.1 and 94.6 mg m^{-2} day^{-1} (Sites 5 and 7; 34°N and 37°N, respectively). Correlations between OM, carbonate, and biogenic opal fluxes suggest that siliceous plankton was mainly responsible for the OM flux via settling particles at the subarctic station (Site 8), while carbonaceous plankton was responsible at the subtropical station (Site 6). Compared with the mean particle flux at mid-latitudes in the Atlantic, the Pacific showed significantly high biogenic opal flux due to nutrient enrichment in Pacific surface waters. The injection of aerosol-derived iron from the Asian continent may play a role in enhancing primary and export production in this area. An interesting feature observed in this study area is that a significant time lag was present between the dust storm peaks in the Asian continent source region and peaks of lithogenic flux at Site 7. This time lag suggests that eolian dust is being transported in the following

*Corresponding author.
E-mail address: kawahata@ori.u-tokyo.ac.jp (H. Kawahata).

Elsevier Oceanography Series 73
Edited by H. Kawahata and Y. Awaya
ISBN: 0-444-52948-9

manner: atmospheric transport brings dust from the source region to the ocean, where it remains suspended in the upper layer of the Kuroshio Current and Kuroshio Extension for up to 2 months; the dust is then removed by incorporation into biogenic pellets or amorphous aggregates when primary production is active in the upper layers.

Keywords: seasonality; settling particle fluxes; dust; Central North Pacific; Westerly wind; Kuroshio; Carbon cycle

1 Introduction

The mid-latitude central Pacific is sensitive to climatic change, because its location corresponds to the position of the Northern Hemisphere westerly wind system, in a transition zone between subtropical and subarctic waters (e.g., Thompson, 1981; Thunell and Mortyn, 1995). The central North Pacific is characterized by two major water masses (the subarctic and subtropical water masses) and a transition zone (the Kuroshio Current and Kuroshio Extension; Tchernia, 1980). The subarctic region extends from the Bering Sea to approximately 40°N, where it borders the Kuroshio Current and Kuroshio Extension along a complex oceanographic front. The subarctic water mass is characterized by the presence of a permanent halocline at 100–200 m. The subtropical region is located between 31°N and 10°N. The northern boundary of this region is determined by the position of the Kuroshio Current and Kuroshio Extension, which together form a narrow transition region with a biological composition distinct from that found to the north or south. The subtropical region is characterized by a permanent thermocline, in contrast to the permanent halocline of the subarctic region (Tchernia, 1980). The thermal contrast between the subarctic and subtropical water masses is so large that a latitudinal shift of the Kuroshio Current and Kuroshio Extension can affect the climate in the Japanese islands and North America (Kennett and Ingram, 1995; Behl and Kennett, 1996; Ujiie and Ujiie, 1999) (Fig. 1).

The differing physical parameters of the subarctic and subtropical water masses result in differences in primary productivity and biological components. The subarctic water mass shows high primary productivity, which may reduce the partial pressure of carbon dioxide (pCO_2) in surface water during the late spring (Kawahata et al., 1998a). In contrast, the subtropical water mass is characterized by oligotrophic conditions, with low primary productivity due to the surface water's permanent thermocline. A study of pigments and picoplankton groups in the central North Pacific along a transection at 175°E showed definite gradients in the meridional distribution of

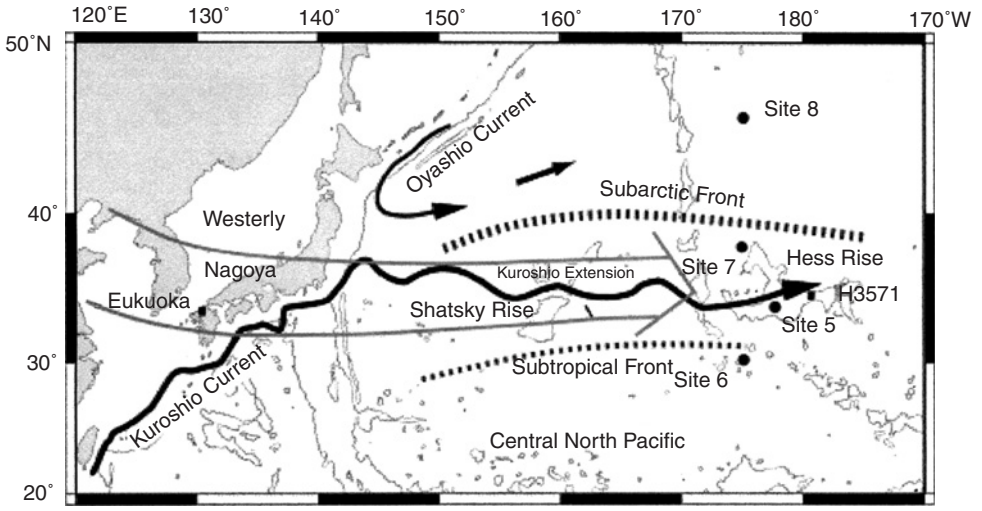

Figure 1: Locations of the four sediment-trap mooring sites for this study. Surface hydrography of the central North Pacific is also presented. The subtropical and subarctic fronts showed seasonal latitudinal shift. Sites 6, 5, 7, and 8 were located at 30°00.1′N, 174°59.7′E; 34°25.3′N, 177°44.2′E; 37°24.2′N, 174°56.7′E and 46°07.2′N, 175°01.9′E, respectively.

divinyl chlorophyll-*a* and autotrophic picoplankton, in terms of carbon biomass reflecting water masses (Ishizaka et al., 1994; Suzuki et al., 1995). In spite of the significance of biological effects on the ocean carbon cycle, the downward flux and settling particle composition has been studied in the mid-latitude central North Atlantic, but not in the central North Pacific (Honjo and Manganini, 1993).

In order to understand the chemical properties of settling particles and carbon cycles in the central North Pacific, four sediment trap moorings were deployed from 1993 to 1994 (Table 1). The studied sites were located in the subtropical water mass (Site 6), the transition zone (Sites 5 and 7), and the subarctic water mass (Site 8). This paper documents carbonate, organic matter (OM), biogenic opal, and lithogenic fluxes of settling particles in order to characterize biological pump activity at various locations in the central North Pacific. Iron-addition experiments carried out in recent years showed substantial increases in chlorophyll-*a* and primary production and a reduction in pCO_2 in the North-Pacific subarctic gyre (Tsuda et al., 2003; Boyd et al., 2004). Moreover, the mid-latitude central Pacific is potentially a receiving area for eolian dust from the Asian continent (Duce et al., 1991). Consequently, the contribution of eolian dust to primary production and lithogenic flux is also discussed in this paper.

Table 1: Locations of the mooring sites, deployment times, trap, and water depths as well as the durations of the sampling intervals

Trap name	Position		Seafloor depth (m)	Trap depth (m)	Sampling duration
Station 6	30°00.1′N	174°59.7′E	5,390	3,873	16-Jun-93 to 1-Jun-94
Station 5, shallow	34°25.3′N	177°44.2′E	3,365	1,342	16-Jun-93 to 16-Apr-94
Station 5, deep	”	”	”	2,848	16-Jun-93 to 1-Jun-94
Station 7, shallow	37°24.2′N	174°56.7′E	5,105	1,482	1-Jun-93 to 9-Apr-94
Station 7, deep	”	”	”	4,588	1-Jun-93 to 9-Apr-94
Station 8	46°07.2′N	175°01.9′E	5,435	1,412	16-Jun-93 to 16-Apr-94

2 Material and Analytical Methods

Trap locations, deployment dates, and sampling interval durations are given in Table 1. Cone-shaped traps with 21-cup collectors and a collection area of 0.5 m^2 (SMD21-6000: Nichiyu-giken-kogyou Ltd.®, Tokyo, Japan; PARFLUX Mark 7G-21: McLane®, Woods Hole, MA, USA) were attached to moored arrays. The same cone shapes were adopted in order to attain the same collection efficiency. The procedures for deploying sediment traps and analyzing organic carbon (OC), carbonate, biogenic silica, and lithogenics are described in detail by Kawahata et al. (1998a,b) and Kawahata et al. (2000). The filtered samples were dried at 60°C, and the dried particles were weighed (SD = 0.01% for 15–175 mg weight), crushed, and homogenized. Residues of selected samples were examined under an optical microscope to verify complete dissolution of the siliceous micro-organisms, especially in the case of biogenic opal. Several samples gave unusual values and were analyzed three times, yielding a precision of ±3% for the measured opal values. Other analytical errors are as follows: OC and carbonate, ±2%; TN, ±3%. The contribution of lithogenic matter was calculated as:

$$\text{Lithogenics} = \text{Total} - \text{Carbonate} - \text{OM} - \text{Opal},$$

where $\text{OM} = \text{OC} \times 1.8$.

The relative standard deviations of lithogenics are 5 and 25% for lithogenic contents of 22 and 5 wt.%, respectively.

3 Results

Six records from different areas and water depths are available (Tables 2–5). Records from two water depths are available from Site 5 (1,342 and 2,848 m) and from Site 7 (1,482 and 4,588 m). Total flux data for all sites investigated are depicted in Fig. 2. The flux data all refer to the <1 mm size fraction, which clearly dominated particle flux, because the >1 mm size fraction is generally dominated by zooplankton remains. Seasonal fluctuation in seawater temperature through the 300-m-thick water column was estimated by linear interpolation of World Ocean Atlas 1994 grid data for each site (Figs. 3–6) (Levitus and Boyer, 1994).

3.1 Site 6

The total flux record at Site 6 exhibited one broad maximum, with intermediate values (116 mg m^{-2} day^{-1}) from January through March (Fig. 2 and Table 2). The mean fluxes and relative contributions of carbonate, OM, biogenic opal, and lithogenics were 30.2 (63.7%), 4.8 (10.1%), 4.2 (8.9%), and 8.2 (17.3%) mg m^{-2} day^{-1}, respectively, and followed the total flux. Carbonate was the dominant constituent and was composed of coccolithophores and planktonic foraminifera. Percentages of OM were in the range of 7.5–13.2%. The biogenic opal content varied from 4.5 to 12.0%. Lithogenic material, which was mostly clay-sized, ranged from 13.6 to 25.4% of the total mass.

3.2 Sites 5 and 7

The total mass, carbonate, OM, biogenic opal, and lithogenic fluxes at the shallow and deep traps at Sites 5 and 7 exhibited similar seasonality, although the deep traps occasionally exhibited higher fluxes than the shallow traps, indicating that vertical transport of settling particles was predominant in the transition zone (Figs. 2, 4, and 5; Tables 3 and 4). Two flux maxima (in June 1993 and late March 1997) were observed in these four traps. A relatively stratified water structure from July to September 1993 resulted in low biogenic-material production at both sites. The mean fluxes and relative abundance of carbonate, OM, biogenic opal, and lithogenics in the shallow traps were 23.3 (56.7%), 5.2 (12.8%), 3.7 (8.9%), and 8.9 (21.6%) mg m^{-2} day^{-1} at Site 5 and 41.4 (43.8%), 11.6 (12.3%), 17.5 (18.5%), and 24.0 (25.4%) mg m^{-2} day^{-1} at Site 7, respectively. Coccolithophores and planktonic foraminifera contributed much more than diatoms at both sites.

3.3 Site 8

The highest total-mass fluxes among all the traps deployed along the 175°E transect were measured at the northernmost site, where two peaks were

Table 2: Sampling dates, flux rates, percentage and various ratios ($C_{Organic}$/N, opal/carbonate and $C_{Organic}$/$C_{Carbonate}$) of material collected at Site 6

Sample number	Trap cup		Duration (days)	Total	%				Carbonate	Organic matter	% of Total Biogenic opal	Lithogenics	$C_{Organic}$/N atom	Opal/carbonate (wt./wt.)	$C_{Organic}$/$C_{Carbonate}$ atom
	Open	Close			Carbonate	Organic matter	Biogenic opal	Lithogenics							
Site 6															
1	16-Jun-93	1-Jul-93	15	29.5	16.8	2.6	2.5	7.5	57.2	8.9	8.6	25.4	8.3	0.15	0.72
2	1-Jul-93	1-Aug-93	31	31.8	19.4	2.4	2.9	7.1	61.1	7.5	9.2	22.3	8.3	0.15	0.56
3	1-Aug-93	1-Sep-93	31	34.7	21.3	3.0	4.2	6.2	61.4	8.6	12.0	18.0	8.9	0.20	0.65
4	1-Sep-93	1-Oct-93	30	24.4	15.0	1.9	2.8	4.6	61.7	7.8	11.6	19.0	8.5	0.19	0.58
5	1-Oct-93	1-Nov-93	31	20.5	13.1	1.6	2.2	3.6	64.0	7.6	10.8	17.6	8.7	0.17	0.55
6	1-Nov-93	1-Dec-93	30	18.9	12.1	1.5	1.7	3.5	64.1	8.2	9.2	18.6	8.7	0.14	0.59
7	1-Dec-93	16-Dec-93	15	26.9	16.7	2.5	2.6	5.1	62.2	9.2	9.8	18.8	8.9	0.16	0.68
8	16-Dec-93	1-Jan-94	16	32.7	19.2	3.1	3.9	6.5	58.9	9.3	11.9	19.8	8.9	0.20	0.73
9	1-Jan-94	16-Jan-94	15	35.9	21.7	3.8	3.9	6.6	60.3	10.5	10.7	18.5	9.0	0.18	0.80
10	16-Jan-94	1-Feb-94	16	84.8	53.0	8.3	7.5	16.0	62.5	9.8	8.8	18.9	9.0	0.14	0.73
11	1-Feb-94	16-Feb-94	15	91.1	58.6	9.0	7.6	16.0	64.2	9.8	8.3	17.6	8.6	0.13	0.71
12	16-Feb-94	1-Mar-94	13	84.1	55.8	8.4	7.3	12.6	66.3	10.0	8.7	15.0	8.6	0.13	0.70
13	1-Mar-94	16-Mar-94	15	88.6	59.7	9.2	7.6	12.0	67.4	10.4	8.6	13.6	8.7	0.13	0.72
14	16-Mar-94	1-Apr-94	16	116.0	80.1	13.5	5.2	17.2	69.1	11.6	4.5	14.8	8.4	0.06	0.78
15	1-Apr-94	16-Apr-94	15	108.0	67.9	14.2	10.0	15.9	62.8	13.2	9.3	14.7	8.7	0.15	0.97
16	16-Apr-94	1-May-94	15	64.9	41.0	7.5	5.7	10.7	63.2	11.6	8.8	16.5	8.6	0.14	0.85
17	1-May-94	16-May-94	15	22.4	13.7	2.8	1.7	4.2	61.4	12.5	7.4	18.7	8.8	0.12	0.94
18	16-May-94	1-Jun-94	16	10.8											

Note: All data refer to the <1 mm size fraction.

Table 3: Sampling dates, flux rates, percentage and various ratios ($C_{Organic}$/N, opal/carbonate and $C_{Organic}$/$C_{Carbonate}$) of material collected at Site 5

Sample number	Trap cup		Duration (days)	Total	%				Carbonate	Organic matter	% of Total Biogenic opal	Lithogenics	$C_{Organic}$/N atom	Opal/ Carbonate (wt./wt.)	$C_{Organic}$/ $C_{Carbonate}$ atom
	Open	Close			Carbonate	Organic matter	Biogenic opal	Lithogenics							
Site 5 shallow															
1	16-June-93	1-July-93	15	140.9	50.3	19.4	18.9	52.3	35.7	13.8	13.4	37.1	8.0	0.38	1.79
2	1-Jul-93	1-Aug-93	31	31.4	13.1	4.2	2.0	12.2	41.7	13.2	6.4	38.7	8.5	0.15	1.47
3	1-Aug-93	1-Sep-93	31	26.9	15.5	3.3	2.1	6.0	57.6	12.2	7.9	22.3	8.3	0.14	0.98
4	1-Sep-93	1-Oct-93	30	9.0	5.6	1.0	0.8	1.6	62.0	11.1	9.2	17.7	7.5	0.15	0.83
5	1-Oct-93	1-Nov-93	31	6.5	4.9	0.6	0.2	0.7	76.2	10.0	2.7	11.0	7.3	0.04	0.60
6	1-Nov-93	1-Dec-93	30	27.7	17.5	3.7	1.7	4.8	63.3	13.4	6.0	17.3	8.4	0.09	0.98
7	1-Dec-93	16-Dec-93	15	42.5	27.5	6.3	2.7	6.0	64.7	14.8	6.4	14.1	8.0	0.10	1.06
8	16-Dec-93	1-Jan-94	16	40.9	25.3	5.5	3.5	6.6	62.0	13.4	8.5	16.1	8.2	0.14	1.00
9	1-Jan-94	16-Jan-94	15	30.0	17.4	3.9	2.3	6.4	58.0	13.1	7.6	21.3	8.0	0.13	1.05
10	16-Jan-94	1-Feb-94	16	38.5	23.4	4.2	3.0	7.8	60.9	10.9	7.9	20.2	8.0	0.13	0.83
11	1-Feb-94	16-Feb-94	15	70.2	43.9	6.8	9.9	9.6	62.5	9.7	14.1	13.7	8.0	0.23	0.72
12	16-Feb-94	1-Mar-94	13	53.4	35.8	4.7	3.8	9.1	67.0	8.9	7.2	17.0	7.6	0.11	0.61
13	1-Mar-94	16-Mar-94	15	52.4	34.7	5.1	6.2	6.4	66.2	9.7	11.8	12.2	7.8	0.18	0.68
14	16-Mar-94	1-Apr-94	16	121.2	76.1	18.3	7.4	19.4	62.8	15.1	6.1	16.0	7.4	0.10	1.11
15	1-Apr-94	16-Apr-94	15	28.9	18.6	4.5	2.3	3.5	64.4	15.6	7.9	12.1	7.4	0.12	1.12
Deep															
1	16-Jun-93	1-Jul-93	15	140.0	58.0	16.5	19.3	46.3	41.4	11.8	13.8	33.1	8.0	0.33	1.31
2	1-Jul-93	1-Aug-93	31	92.4	41.9	7.8	13.3	29.4	45.3	8.5	14.3	31.8	7.8	0.32	0.87
3	1-Aug-93	1-Sep-93	31	58.6	30.9	4.6	6.3	16.7	52.8	7.8	10.8	28.6	8.1	0.20	0.69
4	1-Sep-93	1-Oct-93	30	53.8	28.6	4.1	5.9	15.2	53.2	7.6	11.0	28.2	8.1	0.21	0.66
5	1-Oct-93	1-Nov-93	31	46.5	25.8	3.9	6.7	10.0	55.6	8.4	14.5	21.5	8.4	0.26	0.70
6	1-Nov-93	1-Dec-93	30	51.8	29.7	4.3	4.7	13.2	57.2	8.2	9.1	25.5	8.2	0.16	0.66
7	1-Dec-93	16-Dec-93	15	69.9	40.6	6.6	7.9	14.9	58.1	9.4	11.3	21.3	8.6	0.19	0.75
8	16-Dec-93	1-Jan-94	16	67.0	40.0	5.5	8.9	12.5	59.7	8.2	13.3	18.7	8.5	0.22	0.64
9	1-Jun-94	16-Jan-94	15	44.8	23.5	4.1	4.4	12.8	52.4	9.1	9.8	28.7	8.2	0.19	0.80
10	16-Jun-94	1-Feb-94	16	62.8	37.9	5.2	4.5	15.2	60.3	8.3	7.2	24.2	8.4	0.12	0.63
11	1-Feb-94	16-Feb-94	15	63.6	39.5	4.7	6.9	12.5	62.1	7.4	10.9	19.6	8.2	0.18	0.55
12	16-Feb-94	1-Mar-94	13	79.2	51.9	5.5	7.0	14.7	65.6	7.0	8.9	18.6	8.1	0.14	0.49
13	1-Mar-94	16-Mar-94	15	77.8	50.1	6.0	6.2	15.6	64.4	7.7	7.9	20.0	8.0	0.12	0.55
14	16-Mar-94	1-Apr-94	16	156.8	100.8	19.5	11.6	24.8	64.3	12.5	7.4	15.8	7.4	0.11	0.90
15	1-Apr-94	16-Apr-94	15	107.0	68.5	12.8	8.3	17.4	64.0	12.0	7.8	16.3	7.6	0.12	0.86
16	16-Apr-94	1-May-94	15	105.9	67.1	14.5	6.8	17.5	63.3	13.7	6.4	16.5	7.6	0.10	1.00
17	1-May-94	16-May-94	15	40.3	25.6	4.1	3.7	6.9	63.6	10.2	9.1	17.1	6.9	0.14	0.74
18	16-May-94	1-Jun-94	16	159.0	63.6	21.0	29.5	44.9	40.0	13.2	18.6	28.2	7.9	0.46	1.53

Note: All data refer to the <1 mm size fraction.

Table 4: Sampling dates, flux rates, percentage and various ratios ($C_{Organic}$/N, opal/carbonate and $C_{Organic}$/$C_{Carbonate}$) of material collected at Site 7

Sample number	Trap cup		Duration (days)	Total	%				Carbonate	Organic matter	% of Total Biogenic opal	Lithogenics	$C_{Organic}$/N atom	Opal/ Carbonate (wt./wt)	$C_{Organic}$/ $C_{Carbonate}$ atom
	Open	Close			Carbonate	Organic matter	Biogenic opal	Lithogenics							
Site 7 shallow															
1	1-Jun-93	16-Jun-93	15	218.2	76.0	36.4	46.3	59.5	34.8	16.7	21.2	27.3	7.5	0.61	2.22
2	16-Jun-93	1-Jul-93	15	319.6	115.6	41.3	67.2	95.5	36.2	12.9	21.0	29.9	7.6	0.58	1.65
3	1-Jul-93	16-Jul-93	15	147.6	57.9	15.9	31.4	42.3	39.2	10.8	21.3	28.7	7.6	0.54	1.27
4	16-Jul-93	1-Aug-93	16	75.5	32.7	8.4	14.1	20.3	43.2	11.2	18.7	26.9	8.0	0.43	1.19
5	1-Aug-93	16-Aug-93	15	68.7	30.0	7.6	12.9	18.2	43.7	11.0	18.8	26.5	8.4	0.43	1.17
6	16-Aug-93	1-Sep-93	16	100.8	26.7	10.9	28.3	35.0	26.5	10.8	28.0	34.7	7.7	1.06	1.88
7	1-Sep-93	16-Sep-93	15	89.6	25.5	8.3	25.1	30.7	28.5	9.2	28.0	34.3	7.6	0.98	1.50
8	16-Sep-93	1-Oct-93	15	37.2	13.5	3.8	8.8	11.1	36.3	10.2	23.6	29.9	7.5	0.65	1.30
9	1-Oct-93	16-Oct-93	15	45.5	14.9	5.0	11.5	14.2	32.7	11.0	25.2	31.2	7.4	0.77	1.55
10	16-Oct-93	1-Nov-93	16	62.9	24.8	7.8	13.8	16.4	39.4	12.5	22.0	26.1	7.5	0.56	1.46
11	1-Nov-93	16-Nov-93	15	103.3	54.3	12.1	16.8	20.2	52.5	11.7	16.3	19.5	7.9	0.31	1.03
12	16-Nov-93	1-Dec-93	15	61.5	33.0	7.7	9.1	11.7	53.7	12.5	14.9	19.0	7.2	0.28	1.08
13	1-Dec-93	16-Dec-93	15	72.0	41.5	9.3	8.7	12.5	57.7	12.9	12.1	17.4	7.7	0.21	1.04
14	16-Dec-93	1-Jan-94	16	48.7	27.4	6.0	6.2	9.1	56.2	12.2	12.8	18.7	7.6	0.23	1.01
15	1-Jan-4	16-Jan-94	15	17.5	8.9	2.2	2.6	3.7	51.0	12.6	15.0	21.4	7.5	0.29	1.14
16	16-Jan-94	1-Feb-94	16	24.2	10.5	3.4	4.1	6.2	43.4	14.1	17.0	25.5	7.7	0.39	1.50
17	1-Feb-94	16-Feb-94	15	48.9	27.2	4.5	7.0	10.3	55.5	9.1	14.4	21.0	7.3	0.26	0.76
18	16-Feb-94	1-Mar-94	13	56.4	29.9	5.5	8.6	12.3	53.1	9.7	15.3	21.9	7.3	0.29	0.85
19	1-Mar-94	16-Mar-94	15	104.3	63.8	12.8	9.9	17.9	61.2	12.2	9.5	17.1	7.2	0.15	0.93
20	16-Mar-94	1-Apr-94	16	185.2	103.5	22.9	22.0	36.7	55.9	12.4	11.9	19.8	7.4	0.21	1.02
21	1-Apr-94	9-Apr-94	8	99.9	61.2	11.5	10.1	17.1	61.2	11.5	10.1	17.2	7.0	0.16	0.87
Deep															
1	1-Jun-93	16-Jun-93	15	71.5	25.0	9.6	15.0	22.0	35.0	13.4	20.9	30.7	7.7	0.60	1.77
2	16-Jun-93	1-Jul-93	15	217.8	81.1	24.1	46.8	65.7	37.2	11.1	21.5	30.2	8.0	0.58	1.37
3	1-Jul-93	16-Jul-93	15	84.4	37.8	6.1	16.2	24.3	44.7	7.3	19.2	28.8	7.7	0.43	0.75

4	16-Jul-93	1-Aug-93	16	54.8	25.4	3.2	9.3	17.0	46.3	5.8	16.9	31.0	7.8	0.37	0.58
5	1-Aug-93	16-Aug-93	15	50.2	22.6	3.0	9.3	15.3	45.0	6.0	18.6	30.4	7.9	0.41	0.62
6	16-Aug-93	1-Sep-93	16	51.0	22.0	3.1	8.1	17.8	43.1	6.1	15.9	34.9	7.7	0.37	0.65
7	1-Sep-93	16-Sep-93	15	51.2	20.4	3.0	10.7	17.1	39.8	5.9	20.8	33.5	7.8	0.52	0.68
8	16-Sep-93	1-Oct-93	15	52.9	19.4	3.4	11.4	18.8	36.6	6.4	21.5	35.6	7.7	0.59	0.81
9	1-Oct-93	16-Oct-93	15	46.5	17.6	2.7	10.7	15.5	37.8	5.7	23.0	33.5	7.6	0.61	0.70
10	16-Oct-93	1-Nov-93	16	66.7	26.4	3.4	15.1	21.8	39.6	5.1	22.6	32.6	7.6	0.57	0.60
11	1-Nov-93	16-Nov-93	15	60.9	26.7	3.1	12.4	18.6	43.9	5.1	20.4	30.6	7.6	0.46	0.54
12	16-Nov-93	1-Dec-93	15	65.4	25.6	4.5	14.2	21.0	39.2	6.9	21.7	32.2	7.9	0.55	0.82
13	1-Dec-93	16-Dec-93	15	71.1	31.8	4.3	14.6	20.4	44.7	6.0	20.5	28.8	7.6	0.46	0.62
14	16-Dec-93	1-Jan-94	16	69.8	29.9	4.2	15.2	20.5	42.8	6.1	21.8	29.4	7.7	0.51	0.66
15	1-Jan-94	16-Jan-94	15	51.8	20.9	3.2	11.0	16.8	40.2	6.2	21.2	32.4	7.6	0.53	0.71
16	16-Jan-94	1-Feb-94	16	28.3	11.5	1.9	5.7	9.3	40.7	6.6	20.0	32.8	7.9	0.49	0.75
17	1-Feb-94	16-Feb-94	15	51.7	19.6	3.5	10.9	17.7	37.9	6.7	21.1	34.3	7.8	0.56	0.82
18	16-Feb-94	1-Mar-94	13	51.6	20.5	3.4	10.4	17.3	39.7	6.7	20.1	33.5	7.7	0.51	0.78
19	1-Mar-94	16-Mar-94	15	84.6	36.4	5.9	15.7	26.5	43.1	7.0	18.6	31.4	7.7	0.43	0.75
20	16-Mar-94	1-Apr-94	16	138.8	72.1	13.2	20.3	33.1	52.0	9.5	14.6	23.9	7.5	0.28	0.85
21	1-Apr-94	9-Apr-94	8	82.2	45.7	7.6	11.3	17.6	55.6	9.2	13.8	21.5	7.5	0.25	0.77

Note: All data refer to the <1 mm size fraction.

Table 5: Sampling dates, flux rates, percentage and various ratios ($C_{Organic}$/N, opal/carbonate and $C_{Organic}$/$C_{Carbonate}$) of material collected at Site 8

Sample number	Trap cup		Duration (days)	Total	%				Carbonate	Organic matter	% of Total Biogenic opal	Lithogenics	$C_{Organic}$/N atom	Opal/ Carbonate (wt./wt.)	$C_{Organic}$/ $C_{Carbonate}$ atom
	Open	Close			Carbonate	Organic matter	Biogenic opal	Lithogenics							
Site 8															
1	16-Jun-93	1-Jul-93	15	79.0	26.9	7.0	40.1	4.9	34.1	8.9	50.8	6.3	7.3	1.49	1.21
2	1-Jul-93	1-Aug-93	31	363.6	38.5	37.3	255.6	32.2	10.6	10.3	70.3	8.8	8.4	6.64	4.48
3	1-Aug-93	1-Sep-93	31	325.2	50.1	26.0	220.9	28.2	15.4	8.0	67.9	8.7	7.4	4.41	2.40
4	1-Sep-93	1-Oct-93	30	273.9	47.7	17.5	198.6	10.1	17.4	6.4	72.5	3.7	7.3	4.16	1.70
5	1-Oct-93	1-Nov-93	31	321.8	56.3	18.2	236.3	11.0	17.5	5.7	73.4	3.4	7.2	4.20	1.49
6	1-Nov-93	1-Dec-93	30	294.1	90.4	17.6	178.5	7.6	30.7	6.0	60.7	2.6	7.3	1.97	0.90
7	1-Dec-93	16-Dec-93	15	219.1	58.1	11.4	139.6	10.0	26.5	5.2	63.7	4.6	7.5	2.40	0.91
8	16-Dec-93	1-Jan-94	16	100.5	25.0	5.6	66.2	3.8	24.8	5.6	65.9	3.7	7.1	2.65	1.04
9	1-Jan-94	16-Jan-94	15	64.7	13.7	5.1	44.7	1.1	21.2	8.0	69.1	1.7	6.9	3.27	1.74
10	16-Jan-94	1-Feb-94	16	45.1	9.3	3.2	30.9	1.8	20.5	7.0	68.4	4.1	7.1	3.34	1.58
11	1-Feb-94	16-Feb-94	15	51.2	9.5	4.3	34.9	2.6	18.5	8.3	68.1	5.1	6.6	3.68	2.08
12	16-Feb-94	1-Mar-94	13	59.3	8.9	3.6	44.5	2.2	15.1	6.0	75.2	3.7	7.1	4.98	1.84
13	1-Mar-94	16-Mar-94	15	105.3	14.2	5.0	80.2	5.9	13.5	4.7	76.2	5.6	7.1	5.64	1.62
14	16-Mar-94	1-Apr-94	16	62.6	12.5	3.6	43.2	3.4	19.9	5.8	69.0	5.4	6.3	3.46	1.34
15	1-Apr-94	16-Apr-94	15	191.8	25.3	7.7	151.3	7.6	13.2	4.0	78.9	3.9	6.4	5.99	1.42

Note: All data refer to the <1 mm size fraction.

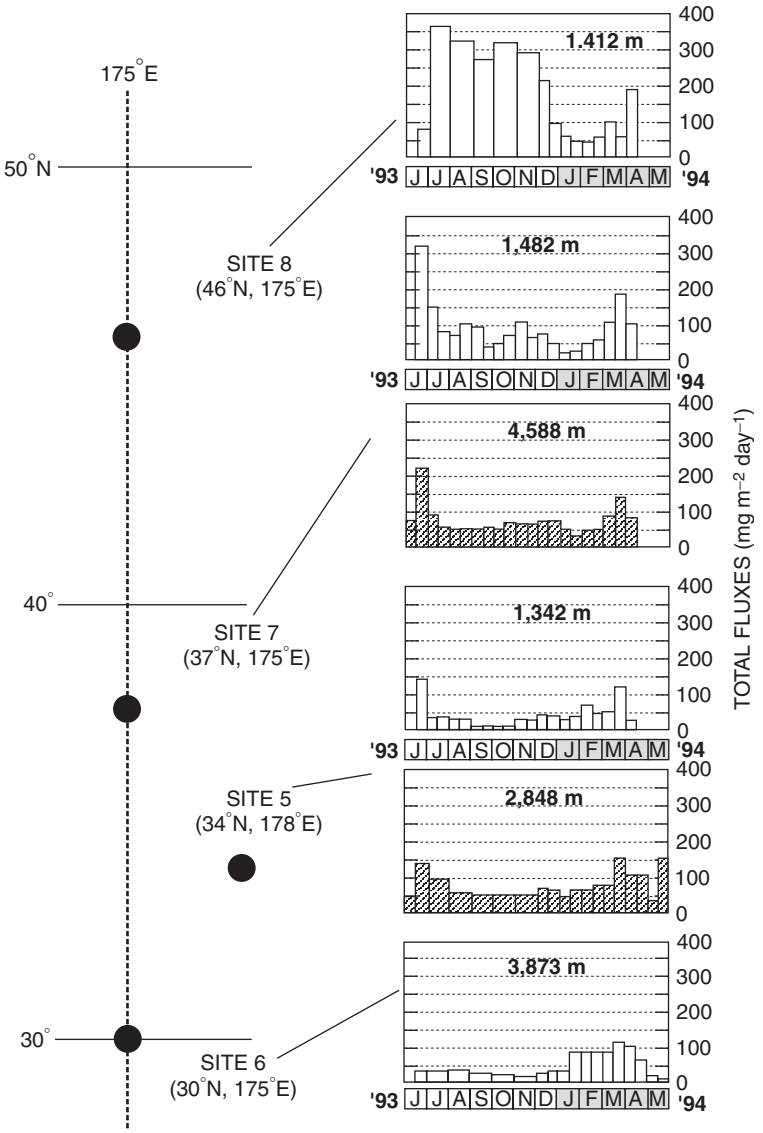

Figure 2: Total mass fluxes (mg m^{-2} day^{-1}) at Sites 5, 6, 7, and 8 in the central North Pacific Ocean.

identified (one large distinct peak in July to December 1993 and a smaller peak in April 1994; see Fig. 2 and Table 5). Total fluxes varied between 45.2 and 363.6 mg m^{-2} day^{-1} with a mean value of 207.7 mg m^{-2} day^{-1}. The carbonate flux pattern followed that of total flux, whereas the biogenic opal, OM, and lithogenic fluxes peaked in July 1993 and decreased thereafter (Fig. 6). Settling particles at Site 8 were characterized by a high flux of

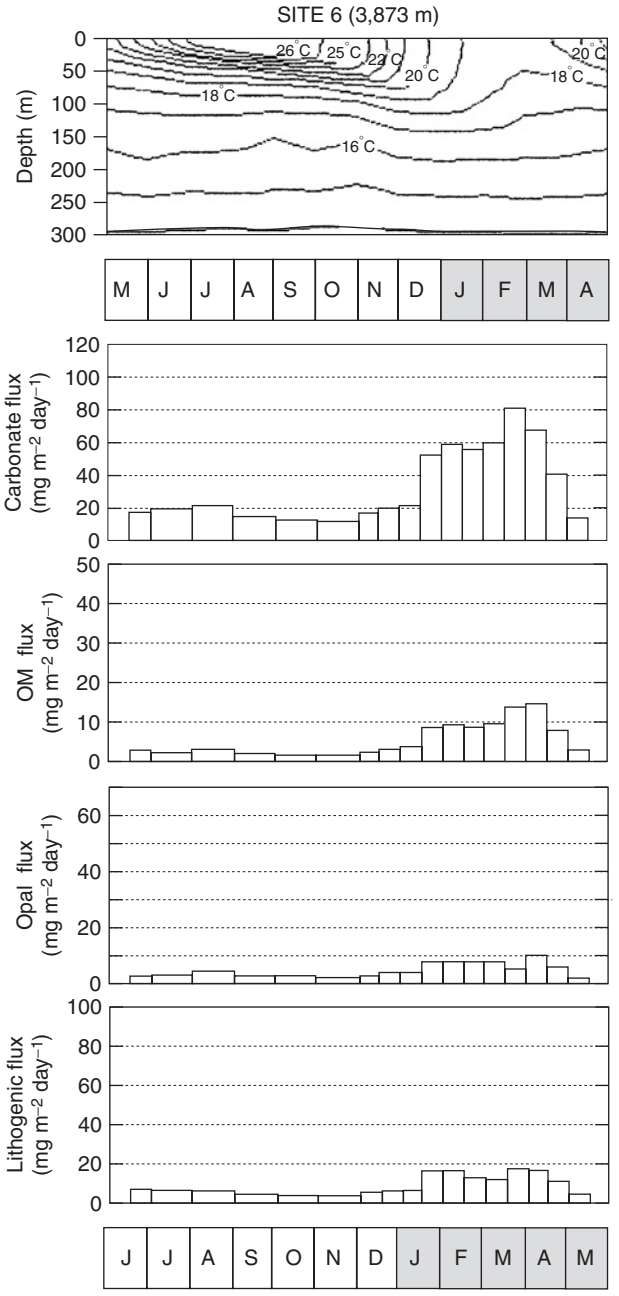

Figure 3: Temperature cross section from linear interpolation of (29.5°N, 174.5°E), (29.5°N, 175.5°E), (30.5°N, 174.5°E), and (30.5°N, 175.5°E) grid data of World Ocean Atlas 1994 at Site 6 (Levitus and Boyer, 1994). Fluxes of carbonate, organic matter (OM), biogenic opal, and lithogenic matter from June 1993 to May 1994 at Site 6. OM is estimated by multiplying OC by a factor of 1.8.

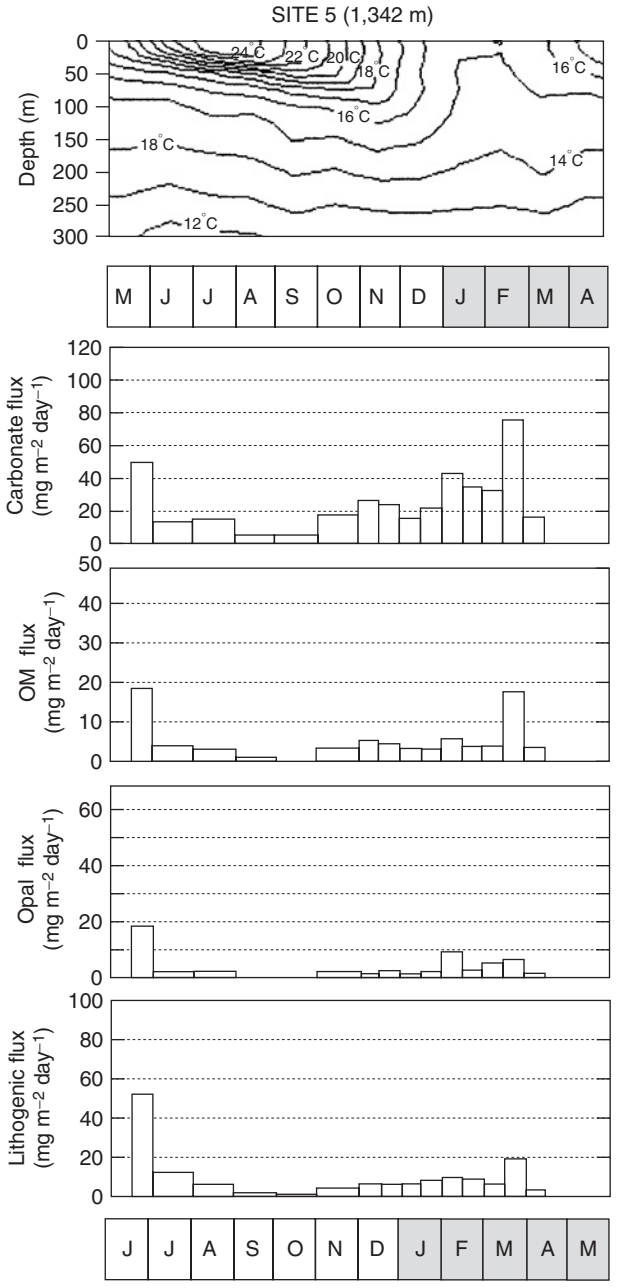

Figure 4: Temperature cross section at 34.5°N, 174.5°E grid data of World Ocean Atlas 1994 at Site 5 (Levitus and Boyer, 1994). Fluxes of carbonate, OM, biogenic opal, and lithogenic matter from June 1993 to April 1994 at the shallow trap.

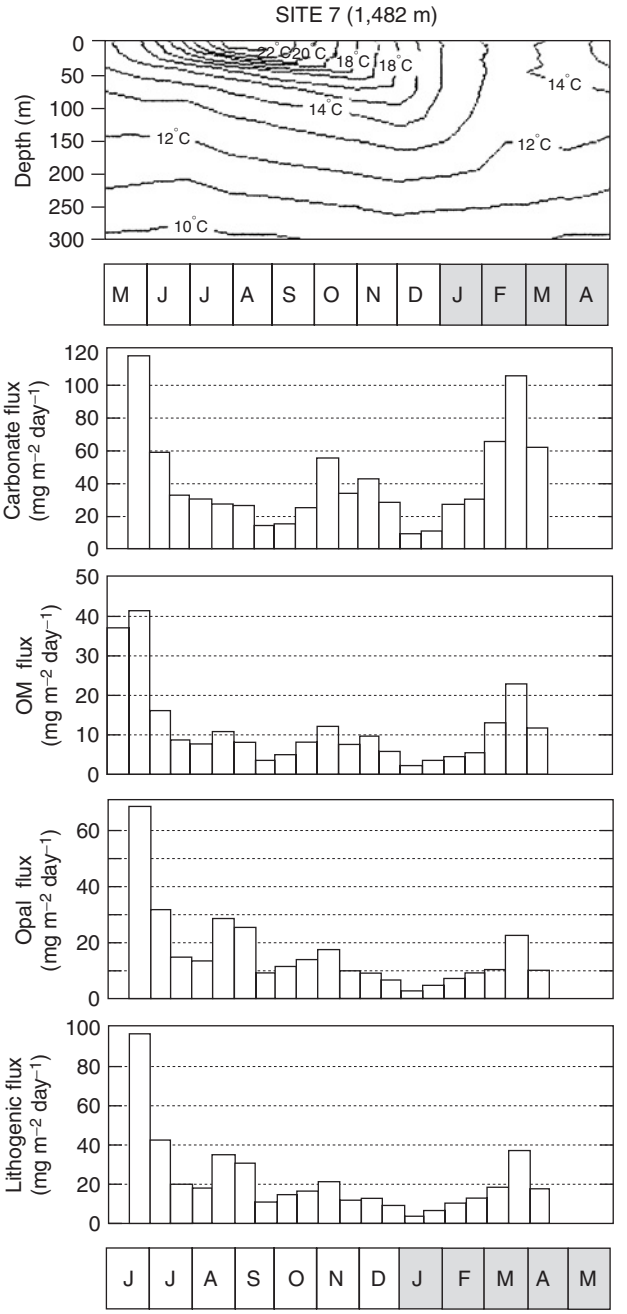

Figure 5: Temperature cross section from linear interpolation of (37.5°N, 174.5°E) and (37.5°N, 175.5°E) grid data of World Ocean Atlas 1994 at Site 7 (Levitus and Boyer, 1994). Fluxes of carbonate, OM, biogenic opal, and lithogenic matter from June 1993 to April 1994 at the shallow trap.

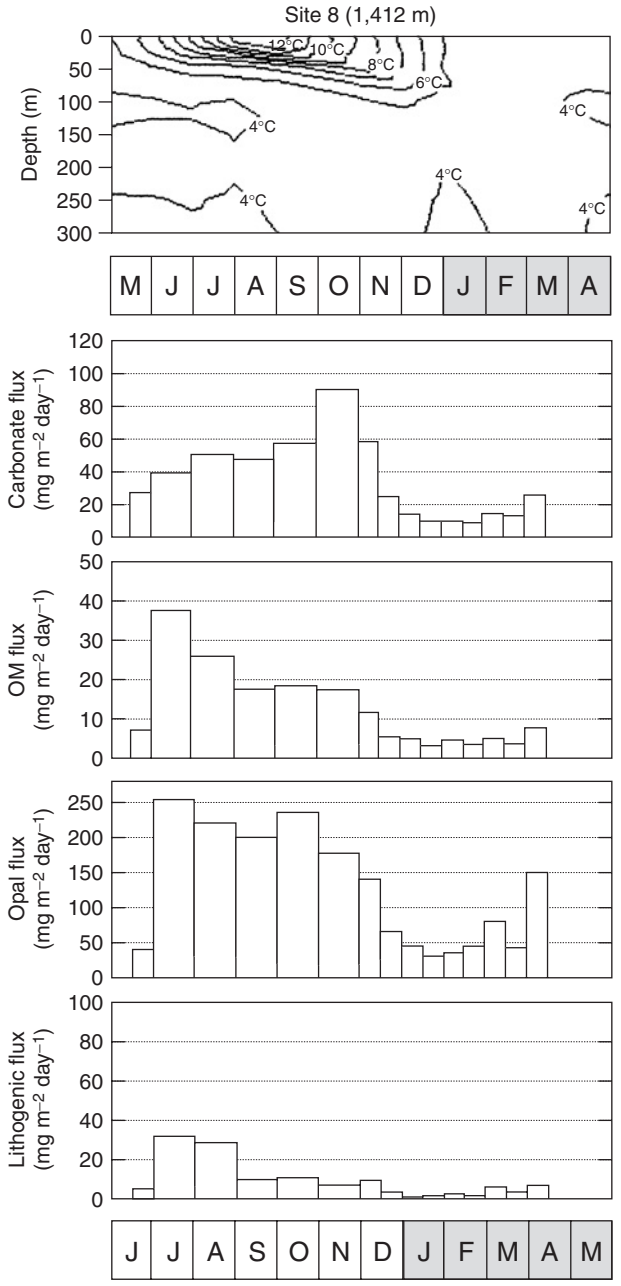

Figure 6: Temperature cross section from linear interpolation of (45.5°N, 174.5°E), (45.5°N, 175.5°E), (46.5°N, 174.5°E), and (46.5°N, 175.5°E) grid data of World Ocean Atlas 1994 at Site 8 (Levitus and Boyer, 1994). Fluxes of carbonate, OM, biogenic opal and lithogenic matter from June 1993 to April 1994 at Site 8.

biogenic opal. The biogenic opal flux ranged from 30.9 to 255.6, averaging 143.4 mg m^{-2} day^{-1}, which accounted for 69.0% of total flux. Therefore, mean ratios of biogenic opal/carbonate and $C_{Organic}/C_{Carbonate}$ (OC/carbonate carbon) were high (3.9 and 1.7, respectively). Values of biogenic opal/carbonate and $C_{Organic}/C_{Carbonate}$ at specific sites were as follows: Site 6, 0.15 and 0.72; Site 5, 0.14 and 0.99; Site 8, 0.45 and 1.26, respectively (Tables 2–5).

4 Discussion

4.1 General Features of the Settling Particle Flux in The Central North Pacific

Although Site 6 exhibited one total mass flux maximum in spring 1994, the site was seasonally influenced by two different water masses (Figs. 1 and 2): the subtropical water mass (June–December 1993), when relatively stratified surface ocean conditions resulted in a low mean OM flux (2.3 mg m^{-2} day^{-1}), and the transition water mass (January–April 1994), when well-developed mixing of the surface ocean led to moderate OM flux (8.5 mg m^{-2} day^{-1}) (Fig. 3 and Table 2). During the latter period, Sites 5 and 7 showed comparable mean OM fluxes of 6.8 and 9.0 mg m^{-2} day^{-1}, respectively (Figs. 4 and 5; Tables 3 and 4). These values were also consistent with the mean OM flux (4.6 mg m^{-2} day^{-1}) at Site 8, owing to the low temperature and low light intensity in the subarctic gyre (Fig. 6 and Table 5). This observation suggests that primary and export production were quite uniform in a large area from the northern subtropical gyre to the subarctic gyre in the North Pacific during the winter and early spring of 1994.

Mean OM fluxes from June to December, 1993 were 5.5, 12.9, and 17.7 mg m^{-2} day^{-1} at Sites 5, 7, and 8, respectively. The subarctic site (Site 8) had OM flux >7 times that of the subtropical site (Site 6), indicating the presence of a steep gradient in export production along the transect of 175°E. This gradient is reflected in an increase in annual mean OM flux from south to north, consistent with estimates of primary production from SeaWiFS satellite imagery (http://www.oceancolor.gsfc.nasa.gov/SeaWiFS/).

Although the seasonal profile of biogenic opal flux was generally similar to that of OM flux in the studied sites, the latitudinal gradient was much steeper. Biogenic opal fluxes from June to December were 2.9, 4.0, 21.5, and 167.0 mg m^{-2} day^{-1} at Sites 6, 5, 7, and 8, respectively. In spite of the low gradient, biogenic opal fluxes from January to April, 1994 were 5–9 mg m^{-2} day^{-1} at Sites 6, 5, and 7 and 61 mg m^{-2} day^{-1} at Site 8. Site 8, located in the subarctic gyre, was characterized by a particularly significant contribution of biogenic opal to total mass flux (69%); carbonate flux was predominant in the subtropical and transitional water masses. Mean carbonate

fluxes were relatively uniform from the subtropical to the subarctic water masses (30.2 mg m^{-2} day^{-1} at Site 6, 41.5 mg m^{-2} day^{-1} at Site 7, and 38.5 mg m^{-2} day^{-1} at Site 8), in spite of seasonal variability in carbonate production. This suggests that the annual mean carbonate production rate was relatively uniform in the central North Pacific, regardless of water mass, and that the biogenic opal/carbonate ratio increased from the subtropical to the subarctic water masses. This distribution essentially reflects the prevalent plankton community structure in the upper ocean (Eguchi et al., 2003), where diatoms predominate over carbonate and calcareous nannoplankton (high opal/carbonate ratio) at higher latitudes. It is also consistent with results obtained in one-day floating trap experiments (Bernstein et al., 1990).

OM export production was generally associated with biogenic opal- and carbonate-producing plankton communities. Good correlation between biogenic opal and OM fluxes was observed at Sites 8 ($r = 0.90$) and 7 ($r = 0.91$), indicating that diatoms were mainly responsible for the OM flux in the settling particles. On the other hand, the carbonate flux was highly correlated with the OM flux at Site 6 ($r = 0.98$), indicating that foraminifers and calcareous nannoplankton played an important role in vertical transport of OM by the settling particles. As the OM flux increased, the $C_{\mathrm{Organic}}/C_{\mathrm{Carbonate}}$ ratio showed a tendency to increase. A similar tendency has also been observed in the western equatorial Pacific (Kawahata et al., 1998b) and on a global scale (Francois et al., 2002). Diatom blooms tend to enhance the export flux, with higher $C_{\mathrm{Organic}}/C_{\mathrm{Carbonate}}$ ratios of the settling particles, leading to a reduction in pCO_2 in the upper ocean (Kawahata et al., 1998b).

These observations were confirmed by detailed sampling of the upper 250 m of the water column during May 1993, when sediment traps were deployed (NEDO, 1994) (Fig. 7). Phosphate, silica, nitrate, and nitrite concentrations were low in stratified surface waters at Site 6. In contrast, nutrients were abundant in the surface ocean at Site 8. These results are in agreement with the observation that subarctic water has a greater potential to enhance biological activity, compared to the subtropical water mass. In addition, appreciable amounts of these macronutrients were detected in the surface water at Sites 5 and 7 (located in the transition zone). Although this zone is not within a high-nutrient low-chlorophyll (HNLC) region, some nutrients input by eolian dust may affect surface-water primary production.

4.2 Comparison of Annual Mean Particle Fluxes between Pacific and Atlantic Mid-Latitude Sites

The annual mean export flux of settling particles estimated in this study was compared with values from mid-latitude sites in the Atlantic. The mean total mass fluxes at 1 km water depth measured by the North Atlantic

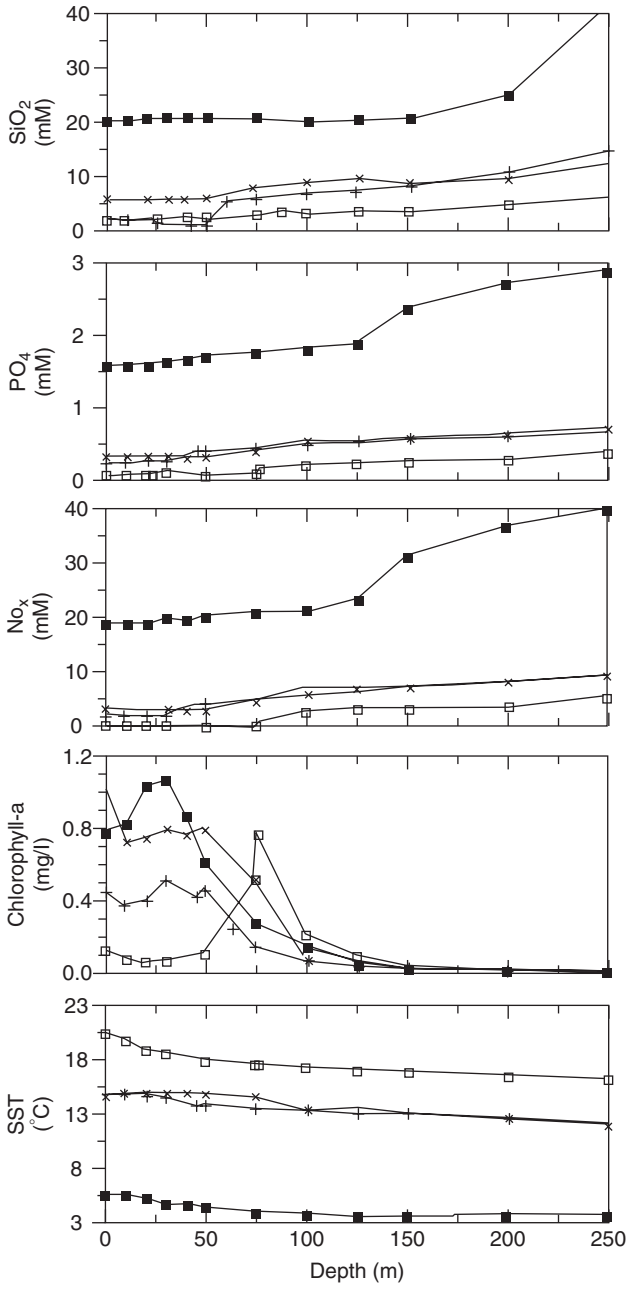

Figure 7: Sea surface temperature (SST), Chlorophyll-*a*, phosphate, and dissolved silica versus water depth at Sites 6, 7, and 8 along a transect of 175°E. Data are cited from NEDO (1994).

Bloom Experiment (NABE) for 1 year from 4 April 1989 to 17 April 1990 at approximately 34°N (NABE 34°N, located at 33°49.3'N, 21°00'5W) and 48°N (NABE 48°N, located at 47°42.9'N, 20°51'5W) were 53.2 and 56.7 mg m^{-2} day^{-1}, respectively (Fig. 8). The NABE 34°N value is comparable to that at Site 5 but lower than that at Site 7, while the NABE 48°N value is about one-quarter of that at Site 8. Mean carbonate fluxes were relatively uniform from subtropical to subarctic water masses in the Pacific, and were comparable to those at the NABE sites (approximately 30 mg m^{-2} day^{-1}). As has already been shown by Berger et al. (1989), the mid-latitude region in the

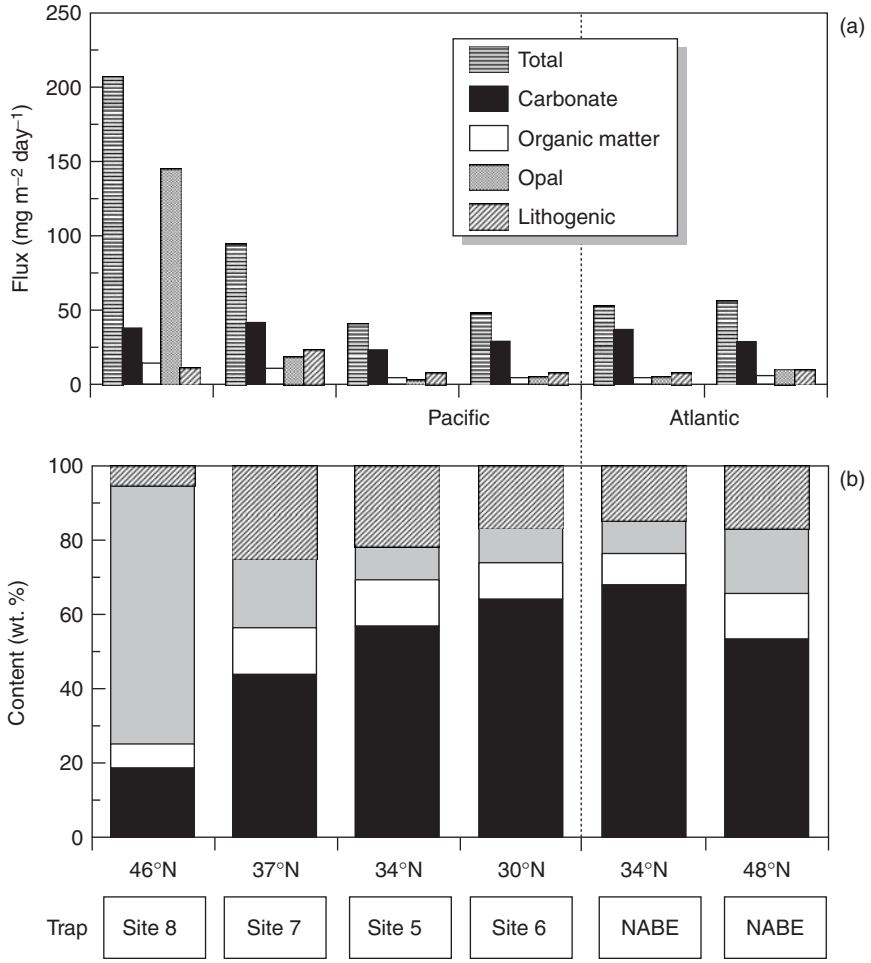

Figure 8: Mean daily fluxes (a) and contents (b) of carbonate, OM, opal, and lithogenic matter at Sites 8, 7, 5, and 6 as well as at Atlantic mid-latitude sites. Results from NABE 34°N and 48°N are at 1 km water depth of 33°49.3′N, 21°00′5W, and 47°42.9′N, 20°51′5W, respectively.

central North Pacific is more productive than that in the central North Atlantic. The OM flux at Site 5 was about 1.5 times that at NABE 34°N, while that at Site 8 was about 3.5 times that at NABE 48°N. The most important contrast between the Pacific and Atlantic was noticed in the biogenic opal flux. The mean biogenic opal fluxes from NABE 34°N and 48°N were 4.5 and 9.7 mg m^{-2} day^{-1}, respectively, indicating a gradual increase in biogenic opal production from south to north. In contrast, mean biogenic opal fluxes at Sites 5, 7, and 8 were 3.7, 17.5, and 143.4 mg m^{-2} day^{-1}, respectively, indicate a sharp increase in biogenic opal production from the northern transition zone to the subarctic water mass. In general, the deep water of the North Pacific is enriched with more nutrients such as phosphate and silica than is the deep water of the North Atlantic, because the former has accumulated nutrients and carbon dioxide (through degradation of settling OM) for a longer period of time (Honjo, 1996). These substances are also present in upwelled seawater, leading to higher OM and biogenic opal production rates in the North Pacific. A relatively low flux of biogenic components was observed in pre- and post-bloom episodes in the Atlantic sites. Total mass flux averaged 2.5 mg m^{-2} day^{-1} during a post-bloom episode at NABE 34°N, suggesting that biogenic production is limited only during bloom episodes at mid-latitude Atlantic sites.

4.3 Origin of Lithogenics in the Mid-Latitude Central Pacific

The mean annual flux of lithogenic particles was highest at Site 7 (24 mg m^{-2} day^{-1}). The mean annual lithogenic fluxes were 8.2 mg m^{-2} day^{-1} at Site 6, 8.9 mg m^{-2} day^{-1} at Site 5, and 11.2 mg m^{-2} day^{-1} at Site 8. The position of Site 7 (located at approximately 37°N, 175°E) corresponds to the latitude at which strong mid-latitude westerly winds are found over the Pacific (maximum high-altitude wind velocities in modern climatic zones have been observed at about 30°N–40°N) (Rex and Goldberg, 1958).

The lithogenic fraction was mainly composed of fine clay minerals with a very small amount of quartz. It is difficult to analyze chemical and isotopic properties of the quartz in the settling particles because of sample size limitations. Two types of quartz grains (type 1, relatively round quartz grains with diameters between 0.1 and 8 μm; and type 2, relatively large, angular quartz grains >8 μm in diameter) have been identified in the sediments of core H3571, recovered from 3,571 m water depth at the Hess Rise (34°54.25'N and 179°42.18'E, Fig. 1) (Kawahata et al., 2000).

The oxygen isotopic composition ($\delta^{18}O$) of quartz provides direct evidence for the provenance of soils and sediments. Oxygen isotopic composition values of 16.4‰–17.7‰ of the type 1 quartz are comparable to those of loess from China and dust from Japan (+16.2‰ and +16.3‰; Syers et al., 1972; Mizota and Matsuhisa, 1985), but differ from those of quartz dust from

the mid-continental United States (+19‰ to +20‰), volcanic ash quartz (usually <+10‰), and quartz transformed from biogenic opal during early diagenesis (>+30‰). In addition, the type 1 quartz was similar with respect to grain size and shape to quartz in Chinese loess. We therefore concluded that the type 1 quartz was of Asian continental origin and was transported through the atmosphere, whereas the type 2 quartz was determined to be of volcanic ash origin (Kawahata et al., 2000). The distribution of the aerosol quartz correlates well with that of total Al, indicating that the alumino-silicate minerals such as feldspars and clay minerals may also have been transported from the Asian continent as an aerosol.

4.4 Relationship between Lithogenics and Primary Production in the Mid-Latitude Central Pacific

Based on surface-layer water properties, phosphorus (P) and nitrate do not appear to be significant limiting nutrients to phytoplankton growth in the transition zone. The injection of aerosol-derived iron from Asian dust storms (Martin et al., 1987), which is known to cause significant short-term increases in subtropical productivity in central regions of the North Pacific Central Gyre (Ditullio and Laws, 1991) is probably of greater relevance.

To estimate the flux of iron in association with mineral aerosol particles, we used the value of 1.6 wt.% for the abundance of Fe in mineral aerosols (Maeda et al., 2002). The solubility (in seawater) of elements attached to mineral aerosols is important in determining their impact on oceanic biogeochemical cycles. Solubility is dependent primarily on pH, sources, and particle size. Although it is impossible to give definite solubility values, the solubility in seawater of P attached to aerosol particles is estimated to be <1%–50% (Wollast and Chou, 1985; Duce et al., 1991).

The fixation rate of OC ($\text{Fixation}_{\text{Organic}}$) can be estimated as follows:

$$\text{Fixation}_{\text{Organic}} = a \times \frac{1.6 \times 10^{-2} \times \text{FLUX}_{\text{Aerosol}}}{b}$$

where a is the solubility in seawater of an element attached to aerosol particles and b is the Fe:C ratio of particulate OM. If it is assumed that $\text{FLUX}_{\text{Aerosol}}$ is equal to the lithogenic flux, than the minimum value of a is 1%, and that of $b = 7.9 \times 10^{-5}$ (Boyd et al., 2004), respectively. $\text{Fixation}_{\text{Organic}}$ fluctuates between 1 and 106 (mean 21) mg m^{-2} day^{-1} at Site 5, between 8 and 193 (mean 48) mg m^{-2} day^{-1} at Site 7, and between 2 and 65 (mean 18) mg m^{-2} day^{-1} at Site 8, respectively. Since we adopted a solubility of 1% here, these values should be minima. The higher $\text{Fixation}_{\text{Organic}}$ values suggest that iron input may play an important role in enhancing primary and export production in this area, unless other nutrients become limiting.

Dust-storm activity, which is responsible for releasing mineral dust to the atmosphere in eastern Asia (e.g., the Gobi and Takla Makan deserts), is greatest in spring (March–May) as a result of the combined effects of low rainfall, increased occurrence of high winds associated with cold fronts, and freshly ploughed soil for spring planting (e.g., Watts, 1969; Uematsu et al., 1983) (Fig. 9). There is no meteorological station on mid-latitude central

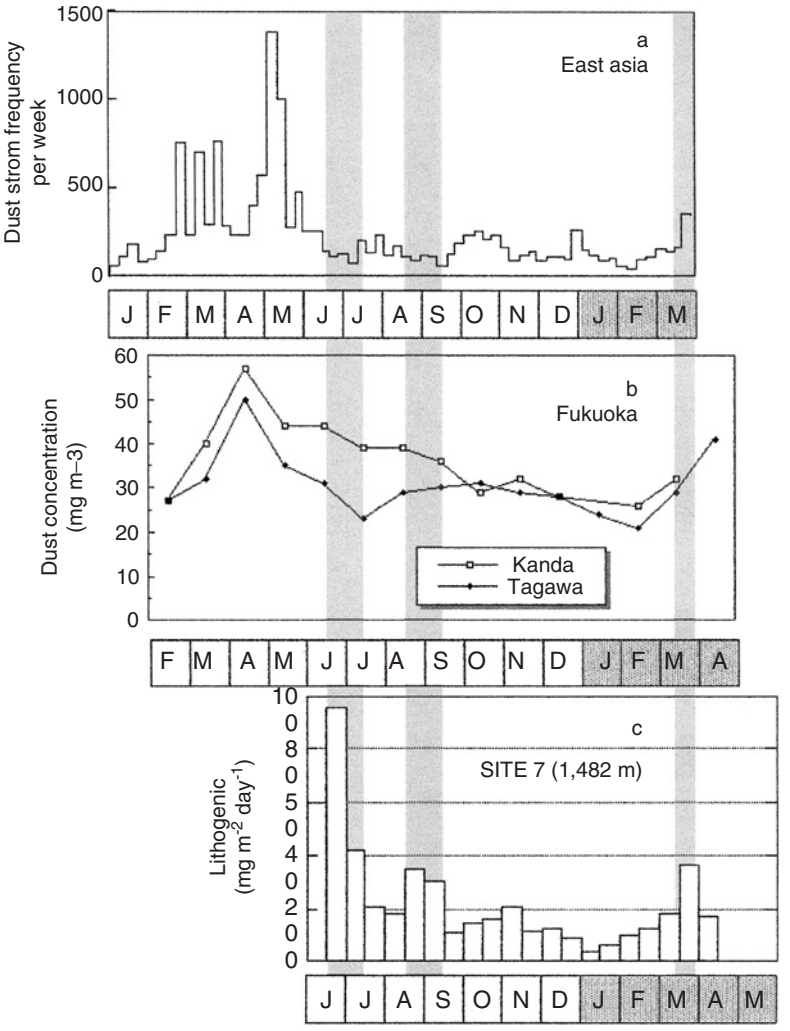

Figure 9: (a) Frequency of dust storm reports in the eastern part of Asia in 1981 and early 1982 (Uematsu et al., 1983). (b) Temporal variation of the atmospheric dust concentration records observed at Tagawa and Karita-wakahisa cities in the Fukuoka (33°N, 131°E), the western part of Japan in 1998 (Environmental section of Fukuoka local government, personal communication). (c) Lithogenic flux observed at the shallow trap of Site 7.

North Pacific oceanic islands for monitoring eolian dust. Two stations (at Tagawa and Kanda in Fukuoka, 33°N, 131°E, western Japan) have accumulated dust concentration records for the last 5 years. The dust flux is low during summer, autumn, and winter, with the highest levels recorded from February through May (Environmental section of Fukuoka local government, personal communication). Another data set was provided by the University of Nagoya, which has analyzed seasonal variation of vertically integrated aerosol backscatter at 532 nm at Nagoya City (35°N, 137°E) since March 1994. No data were available covering the period of the sediment-trap experiments, but 3-year measurements at Nagoya present general seasonal trends regarding the amount of dust in the upper atmosphere (4–8 km); the dust was transported more extensively over the Pacific in this layer than in the lower layer. Aerosol concentrations were very high each year from April to May in spite of large, sporadic short-term (<1 week) fluctuations from September to early October and December to January. However, lithogenic fluxes at Site 7 showed relatively low values during these periods. In contrast, low aerosol concentration was always observed from June to August, late October to November, and February to early March, when large lithogenic fluxes were observed at Site 7. Therefore, it is evident that the maximum lithogenic flux of the settling particles into the ocean's interior lagged behind the maximum aerosol concentration in the atmospheric column.

The time lag was partly due to transport time from the Japanese islands to Site 7 and settling time from the surface ocean to the sediment trap. Although Site 7 is approximately 2,500 km downwind from the Japanese islands, the high speed of the jet stream (often >500 km day^{-1}) quickly transports dust to the site (Duce et al., 1980). Biogenic aggregates (such as diatom and coccolithophores) cause accelerated sinking of small non-biogenic particles with settling speeds of 160–200 m day^{-1}; thus, it takes <10 days for particles to sink from the upper water column to the shallow trap depth (e.g., Takahashi, 1986). Because the actual time lag could be between 15 days and 2 months, it is unlikely that eolian dust was transported directly from the source area to the trap site through the atmosphere.

For a single floating particle of dust, the small particle size (<8 μm) prevents it from being removed rapidly from the ocean surface. This suggests that the eolian dust was transported from the source region to the ocean by the wind, and that it then remained suspended in the upper water layer of the Kuroshio Current and Kuroshio Extension for up to 2 months; the dust was then removed by incorporation into biogenic pellets or amorphous aggregates when primary production was activated. In other words, transport of lithogenic matter in the transition zone was by both westerly winds and the Kuroshio Extension. Although phytoplankton primary

production has now been demonstrated to be iron-limited in some areas of the oceans (e.g., Boyd et al., 2000, 2004; Tsuda et al., 2003), recent studies emphasize that there are more complex interactions within the ocean than simple iron limitation or sufficiency, with evidence of co-limitation by iron along with light and other macro- and micronutrients (e.g., Si, N, P, Co, and Zn). Aerosol particles are so enriched in heavy metals that these micronutrients provide more constraints for primary and export production in the transition zone in the North Pacific (Fig. 9).

5 Summary and Conclusions

1. Although fluxes of total mass, OM, carbonate, biogenic opal, and lithogenics showed definite seasonal change, the annual mean fluxes generally increased from south to north. Diatoms played a significant role in OM and biogenic opal fluxes at the subarctic station (Site 8), while coccolith and foraminifera were important at the subtropical station. In general, an increase in OM flux was associated with higher opal/carbonate and $C_{Organic}/C_{Carbonate}$ ratios in the central North Pacific.
2. Dust particles originating from the Asian continent contributed to lithogenic flux in the central North Pacific. The injection of aerosol-derived iron from Asia has a potential role in enhancing primary and export production in this area, unless other nutrients such as phosphate and nitrate become limiting. The maximum lithogenic flux of the settling particles into the ocean's interior lagged behind the maximum aerosol concentration in the atmospheric column. A plausible explanation for the time lag could be that eolian dust was transported from the source region to the sea through the atmosphere, remained suspended in the upper water column of the Kuroshio Current and/or Kuroshio Extension for some time, and was then removed by incorporation into biogenic pellets or amorphous aggregates when primary production became enhanced.
3. The significantly higher biogenic opal flux measured in the Pacific as compared with the Atlantic can be ascribed to higher concentrations of nutrients in central North Pacific surface waters.

Acknowledgements

The author expresses his appreciation to Professor V. Ittekkot (University of Bremen), Dr. L. P. Gupta (Geological Survey of Japan), and two anonymous reviewers for valuable suggestions to improve the manuscript. The author also thanks Professor H. Tsubota, Dr. A. Nishimura, Dr. Y. Tanaka, Dr. K. Ikehara, and the crew of the R.V. *Hakurei-maru* for help in sample

collection, and Ms. K. Nagayoshi for drawing figures. This study was supported by the following research programs: 'Northwest Pacific Carbon Cycle study' and 'Study on paleoceanography', funded by the GSJ, AIST.

References

Behl, R. J., Kennett, J. P., 1996. Brief interstadial events in the Santa Barbara basin, NE Pacific, during the past 60 kyr. Nature 379, 243–246.

Berger, W. H., Smetacek, V. S., Wefer, G., 1989. Ocean productivity and paleoproductivity – an overview. In: Berger, W. H., Smetacek, V. S., Wefer, G. (Eds.), Productivity of the Ocean: Present and Past. Wiley, Chichester, pp. 1–34.

Bernstein, R. E., Betzer, P. R., Takahashi, K., 1990. Radiolarians from the western North Pacific Ocean: A latitudinal study of their distributions and fluxes. Deep-Sea Research I 37, 1677–1696.

Boyd, P. W., Law, C. S., Wong, C. S., Nojiri, Y., Tsuda, A., Levasseur, M., Takeda, S., Rivkin, R., Harrison, P. J., Strzepek, R., Gower, J., Makay, R. M., Abraham, E., Arychuk, M., Barwell-Clarke, J., Crawford, W., Crawford, D., Hale, M., Harada, K., Johnson, K., Kiyosawa, H., Kudo, I., Marchetti, A., Miller, W., Needoba, J., Nishioka, J., Ogawa, H., Page, J., Robert, M., Saito, H., Sastri, A., Sherry, N., Soutar, T., Sutherland, N., Taira, Y., Whitney, F., Wong, S. K. E., Yoshimura, T., 2004. The decline and fate of an iron-induced subarctic phytoplankton bloom. Nature 428, 549–553.

Boyd, P. W., Watson, A. J., Law, C. S., Abraham, E. R., Trull, T., Murdoch, R., Bakker, D. C. E., Bowie, A. R., Buesseler, K. O., Chang, H., Charette, M., Croot, P., Downing, K., Frew, R., Gall, M., Hadfield, M., Hall, J., Harvey, M., Jameson, G., LaRoche, J., Liddicoat, M., Ling, R., Maldonado, M. T., McKay, R. M., Nodder, S., Pickmere, S., Pridmore, R., Rintoul, S., Safi, K., Sutton, P., Strzepek, R., Tanneberger, K., Turner, S., Waite, A., Zeldis, J., 2000. A mesoscale phytoplankton bloom in the polar Southern Ocean stimulated by iron fertilization. Nature 407, 695–702.

Ditullio, G. R., Laws, E. A., 1991. Impact of an atmospheric oceanic disturbance on phytoplankton community dynamics in the North Pacific Central Gyre. Deep Sea Research I 38, 1305–1329.

Duce, R. A., Liss, P. S., Merrill, J. T., Atlas, E. L., Buat-Menard, P., Hicks, B. B., Miller, J. M., Prospero, J. M., Arimoto, R., Church, T. M., Ellis, W., Galloway, J. N., Hansen, L., Jickells, T. D., Knap, A. H., Reinhardt, K. H., Schneider, B., Soudine, A., Tokos, J. J., Tsunogai, S., Wollats, R., Zhou, M., 1991. The atmospheric input of trace species to the world ocean. Global Biogeochemical Cycles 5, 193–259.

Duce, R. A., Unni, C. K., Ray, B. J., Prospero, J. M., Merrill, J. T., 1980. Long-range atmospheric transport of soil dust from Asia to the tropical North Pacific: Temporal variability. Science 209, 1522–1524.

Eguchi, N. O., Ujiie, H., Kawahata, H., 2003. Seasonal variations in planktonic foraminifera at three sediment traps in the Subarctic, Transition and Subtropical zones of the central North Pacific Ocean. Marine Micropaleontology 48, 149–163.

Francois, R., Honjo, S., Krishfield, R., Manganini, S., 2002. Factors controlling the flux of organic carbon to the bathypelagic zone of the ocean. Global Biogeochemical Cycles 16, No. 1087.

Honjo, S., 1996. Fluxes of particles to the interior of the open oceans. In: Ittekkot, V., Schafer, P., Honjo, S., Depetris, P. J. (Eds.), Particle Flux in the Ocean. SCOPE John Wiley and Sons Ltd., New York, pp. 91–154.

Honjo, S., Manganini, S. J., 1993. Annual biogenic particle fluxes to the interior of the North Atlantic Ocean; studied at 34°N 21°W and 48°N 21°W. Deep-Sea Research II 40, 587–607.

Ishizaka, J., Kiyosawa, H., Ishida, K., Ishikawa, K., Takahashi, M., 1994. Meridional distribution and carbon biomass of autotrophic picoplankton in the central North Pacific Ocean during late northern summer 1990. Deep-Sea Research I 41, 1745–1766.

Kawahata, H., Okamoto, T., Matsumoto, E., Ujiie, H., 2000. Fluctuations of eolian flux and ocean productivity in the mid-latitude north Pacific during the last 200 kyr. Quaternary Science and Reviews 19, 1279–1291.

Kawahata, H., Suzuki, A., Ohta, H., 1998a. Sinking particles between the equatorial and subarctic regions (0°N–46°N) in the central Pacific. Geochemistry Journal 32, 125–133.

Kawahata, H., Suzuki, A., Ohta, H., 2000. Export fluxes in the western Pacific warm pool. Deep-Sea Research I 47, 2061–2091.

Kawahata, H., Yamamuro, M., Ohta, H., 1998b. Seasonal and vertical variations of sinking particle fluxes in the West Caroline Basin. Oceanologica Acta 21, 521–532.

Kennett, J. P., Ingram, B. L., 1995. A 20-000-year record of ocean circulation and climate change from the Santa Barbara basin. Nature 377, 510–513.

Levitus, S., Boyer, T., 1994. World Ocean Atlas 1994 Volume 4: Temperature. NOAA Atlas NESDIS 4, U.S. Department of Commerce, Washington, D.C. (available at: http://www.ingrid.ldeo.columbia.edu/SOURCES/LEVITUS94/).

Maeda, R., Kawahata, H., Nohara, M., 2002. Fluctuation of biogenic and abiogenic sedimentation on the Shatsky Rise in the western North Pacific during the late Quaternary. Marine Geology 189, 197–214.

Martin, J. H., Knauer, G. A., Karl, D. M., Broenkow, W. W., 1987. VERTEX: Carbon cycling in the northeast pacific. Deep-Sea Research I 34, 267–285.

Mizota, C., Matsuhisa, Y., 1985. Eolian additions to soil and sediments of Japan. Soil Science and Plant Nutrition 31, 369–382.

NEDO, 1994. Reports on North Pacific Carbon Cycle Study during NH93. In: Tsubota (Ed.), New Energy and Industrial Technology Development Organization, Ministry of International Trade and Industry, pp. 1–284 (in Japanese).

Rex, R. W., Goldberg, E. D., 1958. Quartz contents of pelagic sediments of the Pacific Ocean. Tellus 10, 153–159.

Suzuki, K., Handa, N., Kiyosawa, H., Ishizaka, J., 1995. Distribution of the prochlorophyte Prochlorococcus in the central Pacific Ocean as measured by HPLC. Limnology and Oceanography 113, 116–123.

Syers, J. K., Mokma, D. L., Jackson, M. L., Dolcater, D. L., Rex, R. W., 1972. Mineralogical composition and cesium-137 retention properties of continental aerosolic dust. Soil Science 113, 116–123.

Takahashi, K., 1986. Seasonal fluxes of pelagic diatoms in the subarctic Pacific, 1982–1983. Deep-Sea Research I 33, 1225–1251.

Tchernia, P., 1980. Descriptive Regional Oceanography. Pergamon Press, Oxford, p. 248.

Thompson, P. R., 1981. Planktonic foraminifera in the western North Pacific during the past 150 000 years: Comparison of modern and fossil assemblages. Palaeogeography, Palaeoclimatology, Palaeoecology 35, 241–279.

Thunell, R. C., Mortyn, P. G., 1995. Glacial climate instability in the Northeast Pacific Ocean. Nature 376, 504–506.

Tsuda, A., Takeda, S., Saito, H., Nishioka, J., Nojiri, Y., Kudo, I., Kiyosawa, H., Shiomoto, A., Imai, K., Ono, T., Shimamoto, A., Tsumune, D., Yoshimura, T., Aono, T., Hinuma, A., Kinugasa, M., Suzuki, K., Sohrin, Y., Noiri, Y., Tani, H., Deguchi, Y., Tsurushima, N., Ogawa, H., Fukami, K., Kuma, K., Saino, T., 2003. A mesoscale iron enrichment in the western subarctic Pacific induces a large centric diatom bloom. Science 300, 958–961.

Uematsu, M., Duce, R. A., Prospero, J. M., Chen, L., Merrill, J. T., McDonald, R. L., 1983. Transport of mineral aerosol from Asia over the North Pacific Ocean. Journal of Geophysics Research 88, 5343–5352.

Ujiie, H., Ujiie, Y., 1999. Late quaternary course changes of the Kuroshio current in the Ryukyu arc region, northwestern Pacific Ocean. Marine Micropaleontology 37, 23–40.

Watts, I. E. M., 1969. Climates of China and Korea. In: Arakawa, H. (Ed.), Climates of Northern and Eastern Asia, World Survey of Climatology. Elsevier, New York, Vol. 8, pp. 1–118.

Wollast, R., Chou, L., 1985. Kinetic study of the dissolution of albite with a continuous flow-through fluidized bed reactor. In: Drever, J. I. (Ed.), The Chemistry of Weathering. D. Reidel, Norwell, MA, pp. 75–96.

This page intentionally left blank

Chapter 6

Understanding Biogeochemical Processes in the Pacific Ocean on the Basis of Labile Components of Settling Particles

Lallan P. Gupta[1,*] and Hodaka Kawahata[2]

[1]*National Institute of Advanced Industrial Science and Technology, 1-1-1 Higashi, Tsukuba-shi 305-8567, Japan*
[2]*Ocean Research Institute, Tokyo University, 1-15-1 Minamidai, Tokyo 164-8639, Japan*

Abstract

Settling particles collected by sediment traps deployed intermittently for about 1 year at various locations in the Pacific Ocean showed spatial, sporadic and sometimes seasonal variations in flux and labile composition of the particles. The samples from the western Pacific warm pool (WPWP) provided clear evidence of El Niño–Southern Oscillation (ENSO)-related changes in the composition of particulate labile components (amino acids (AA) and hexosamines (HAs)) and in the flux of settling particles. The particle flux in the western WPWP was higher during El Niño, whereas in the eastern WPWP it was higher during La Niña. Settling particles in the WPWP were more labile during a La Niña event than during El Niño. On the other hand, settling particles collected from the Tasman Sea during La Niña showed the highest concentration of AAs, HAs and particulate organic carbon-normalised AAs, which is consistent with higher primary productivity in this part of the Pacific Ocean. Settling particles at deeper depths in the ocean are more deficient in labile components than those at shallow depths because of ongoing microbial decomposition of organic matter. Occasionally higher particle fluxes were also observed at deeper depths relative to those at shallow depths,

*Corresponding author.
E-mail address: gupta.lp@aist.go.jp (L.P. Gupta).

Elsevier Oceanography Series 73
Edited by H. Kawahata and Y. Awaya
ISBN: 0-444-52948-9

probably as a result of lateral advection and re-suspension of highly degraded particulate organic matter in the deep ocean.

Keywords: settling particles; particle flux; amino acid; hexosamine; biogeochemistry; Tasman Sea; Coral Sea; Pacific Ocean

1 Introduction

Primary production (PP) in the open ocean is the major process supplying nutrients and energy to organisms living in deep waters and on the sea floor. However, this supply is influenced by climatic phenomena on local, regional and global scales. One such phenomenon is the El Niño–Southern Oscillation (ENSO) event, whose first signs of initiation become evident in the equatorial Pacific Ocean. Under normal conditions, the central and eastern equatorial Pacific are characterised by upwelling, which supports moderate primary productivity. In contrast, in the western Pacific around the Indonesian maritime continent, the supply of nutrients through the Mindanao-dome upwelling and terrestrial inputs due to tropical rainfall on the continent support a relatively high primary productivity (Kawahata, 1999). The equatorial waters between these two regions, including the western Pacific warm pool (WPWP), show the lowest primary productivity (Mackey et al., 1995, 1997; Antoine et al., 1996; Radenac and Rodier, 1996). As an El Niño (the warm phase of ENSO) event sets in, this pattern of upwelling and productivity changes, depending upon the intensity of the event. Owing to weak easterlies, upwelling of cold equatorial water ceases in central and eastern parts of the Pacific and the warm water and rainfall zone usually found around the Indonesian maritime continent shifts eastwards. The shift of the rainfall zone probably decreases the supply of nutrients from surface runoff in the Indonesian maritime region, while shoaling of the nutricline by 20–40 m would enhance primary productivity in the surface water, as reported for the 1987 El Niño by Radenac and Rodier (1996). Strong westerly wind bursts produce strong mixing events in the Indonesian maritime region (Godfrey and Lindstrom, 1989). During a typical El Niño event, the WPWP extends farther to the east and reaches or overpasses the international dateline (180°E/W). The onset of a La Niña (the cool phase of ENSO) event coincides with strong easterlies, which drive an intense upwelling in the eastern equatorial Pacific, causing the cold water 'tongue' to extend well beyond the international dateline, where primary productivity increases to levels higher than those typical for the WPWP (Glantz, 1996).

ENSO-related changes are thus closely associated with changes in upwelling patterns and nutrient availability in surface waters of the equatorial Pacific. These changes influence plankton distribution and PP across the

equatorial Pacific (McCarthy et al., 1996; Welling and Pisias, 1998). The western equatorial Pacific appears to experience marked temporal variations related to zonal displacements of both the WPWP and the upwelling regions (Le Borgne et al., 2002). Changes in the western Pacific caused by these displacements and influencing various aspects of the oceanography, climatology and biogeochemistry of the region, have attracted a lot of attention (e.g. Dunne et al., 2000; Gupta and Kawahata, 2000; Higgins and Mackey, 2000; Gupta and Kawahata, 2002). Primary production and the subsequent sinking of particulate organic matter (POM) in the form of fecal pellets and aggregates in this region may be fundamental for understanding the global carbon cycle, because about 80% of the net community production in the equatorial Pacific is estimated to sink to the sea floor in the form of POM annually (Hansell et al., 1997a, b).

The relative abundance of individual amino acids (AAs) and hexosamines (HAs) in settling particles in the ocean indicates the degree of degradation of the POM and its potential for further degradation by heterotrophs as it descends through the water column. Estimation of these relatively labile (easy to metabolise) compounds, and various parameters based on them, has been used extensively to understand biogeochemical processes operating in various oceans (e.g. Cowie and Hedges, 1994; Wakeham et al., 1997; Dauwe and Middelburg, 1998; Gupta and Kawahata, 2002, 2003a; Ingalls et al., 2003). Since ENSO-related variability implies dramatic changes in oceanographic properties, biological activities and nutrient availability in the equatorial Pacific, a consequent change in the labile composition of the settling POM is expected. Sediment traps have been used extensively to estimate particle flux in oceans and have provided new information on the composition of settling particles. Major components of the settling particles in the low- to mid-latitude austral western Pacific show carbonate dominance and opal depletion (Kawahata and Ohta, 2000). Because of its low particle flux, the southern Coral Sea has been reported to be oligotrophic, and POM here is more recycled than that further south in the Tasman Sea, where high levels of new production lead to a higher particle flux (Kawahata and Ohta, 2000).

In this article, we discuss sediment-trap data obtained from the western equatorial Pacific, Coral Sea and Tasman Sea in order to investigate the impact of ENSO variability on the export flux and biogeochemistry of settling POM. Export flux of POM implies the amount of particles settling through a unit area in water column in a unit time. The 1991–1999 period, which includes both an El Niño and a La Niña event, is examined. The 1990–1995 El Niño is thought to be the longest warming event on record since 1882 (Trenberth and Hoar, 1996), and the 1999–2001 La Niña phase actually started in the middle of 1998 (Garrett, 2000). The sediment-trap data sets from the Coral Sea and Tasman Sea provide an opportunity to

study latitudinal changes in the AA and HA flux and composition. Moreover, the sampling plan was designed so that seasonal and vertical changes in the flux and composition of settling particles in these parts of the Pacific Ocean could be explored.

2 Study Area

Two series (M and N) of sediment traps were deployed along the equator in the western Pacific (Fig. 1). Trap sites M1 and N2 were located in the hemipelagic zone, where the Mindanao and Halmahera eddies are prominent features (Godfrey, 1996). The other trap sites in these series were located either in the WPWP or in the equatorial upwelling area. Except at site N10, the ENSO condition did not change for the entire duration of each trap's deployment, i.e., either El Niño or La Niña (Fig. 2) conditions prevailed during trap deployment. The north equatorial current (NEC), equatorial

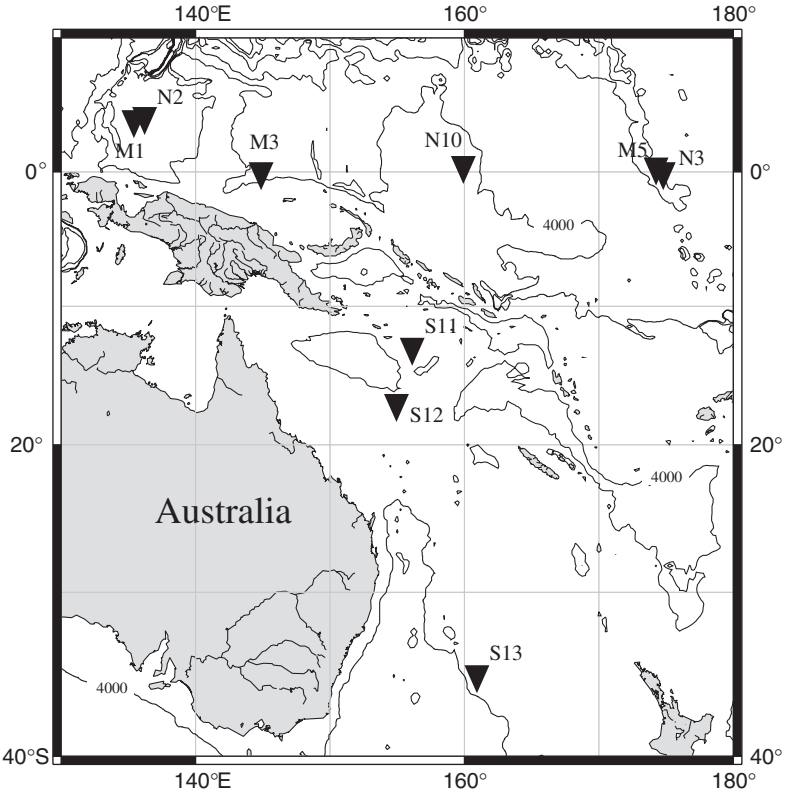

Figure 1: Location of sediment traps in the western equatorial and southeastern Pacific Ocean. Bathymetric contours correspond to 4,000 m water depth.

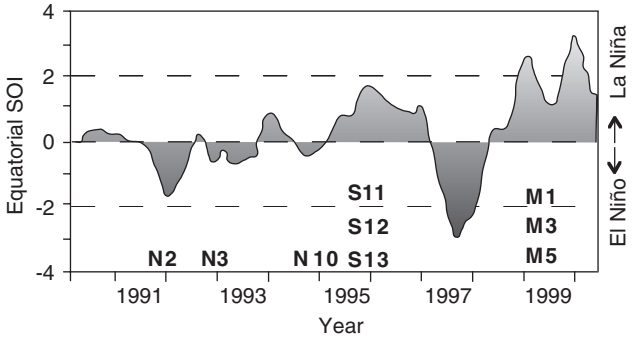

Figure 2: Variations in the equatorial southern oscillation index (SOI) during the sediment trap experiments and approximate duration of sampling, shown by the positions of the trap site names (see details in Table 1).

counter current (ECC) and south equatorial current (SEC) are the three major surface ocean currents in this area. West-bound equatorial currents (NEC and SEC) are the major forces causing the accumulation of warm water in the WPWP (Gordon and Fine, 1996). Also important is the equatorial undercurrent (EUC), an east-bound flow having the potential to affect the settling-particle flux along the equator (Hansell et al., 1997a). Sea surface temperature (SST) is usually higher than 28 °C throughout the WPWP, but thermal and spatial variations may occur owing to changes in solar irradiation, ENSO events and global warming or cooling (Yan et al., 1992).

Another series of traps was deployed in the south-west Pacific near the Australian continent. Important hydrographical features in this region are the tropical convergence and Tasman front. The subtropical east Australian current (EAC) merges with the temperate Tasman current at about 30°S and forms the Tasman front, which diverts towards the central Pacific (Mulhearn, 1987). The merger results in a complicated pattern of eddies (Tate et al., 1989), whose deep structure extends from the sea surface to abyssal depths (Mulhearn et al., 1986). Sites S11 and S12 were located north of the tropical convergence in the Coral Sea, while site S13 was located south of the Tasman front in the Tasman Sea. The average monthly SST varies between 26.5 °C and 30.2 °C around S11 and between 24.7 °C and 29.0 °C around S12. The Tasman Sea is characterised by seasonal SST changes with larger variation (between 16.2 °C and 21.9 °C), caused by latitudinal fluctuation of the Tasman front.

3 Methodology

Bottom-tethered sediment-trap moorings were deployed in the western equatorial Pacific and south-west Pacific Ocean. The locations of moorings

and other details are provided in Table 1. In general, N-series trap moorings were deployed during El Niño, while M- and S-series moorings were deployed during La Niña (Fig. 2). Two cone-shaped sediment traps were deployed at different depths at each mooring, except at sites N10, S11 and S13, each of which had only one, shallow trap. Each trap had a 0.5-m^2 aperture and 21 to 26 sampling bottles attached to its rotary plate. Prior to deployment, the sampling bottles were filled with filtered (membrane filter, 0.45 μm pore size) seawater, which was mixed with sodium borate/boric acid-buffered 3% formalin solution to retard microbial degradation of the collected samples. After trap recovery, the samples were stored under refrigeration at 2–4 °C until analysis in a land-based laboratory. Recognisable zooplankton 'swimmers' were picked out with forceps, and then the samples were filtered through a 1-mm-mesh screen. After filtration, the samples were split into aliquots using a high-precision sample splitter. One aliquot of each sample was filtered through a 0.45-μm (pore size) polycarbonate filter. The sample on the filter was then rinsed with 2–3 mL Milli-Q water and dried at 40 °C in an oven. The dried sample was removed from the filter and homogenised manually using an agate mortar (Kawahata et al., 1998a, b).

The analysis of AAs and HAs has been described in detail by Gupta and Kawahata (2000). In brief, 5–10 mg of sample was hydrolysed with 6 N HCl at 110 °C under an argon atmosphere in a sealed glass ampoule for 22 h. Fifty microlitres of internal standard (2 mM L-norleucine) was added to each ampoule prior to hydrolysis. The hydrolysed sample was filtered through a 0.45-μm (pore size) filter and then dried in a rotary evaporator at 40 °C. The residue was dissolved into about 2 mL Milli-Q water and dried again to remove HCl. The residue was then dissolved in 1000 μL of a buffer solution (pH 2.2). Ten microlitres of this solution was injected by an autosampler into a Shimadzu AA analyser (LC-9A). Post-column derivatisation of eluted species was carried out with *o*-phthaldialdehyde (OPA) and then detected by a fluorescence detector. Ten microlitres of an AA and HA standard solution of known composition was also injected after every fifth sample, and the resulting peak areas were compared to estimate AA and HA concentrations in the samples. The method produces results with a relative standard deviation (RSD) of less than 10%. Carbon and nitrogen were analysed in dried homogenised samples with a Yanaco MT-5 CHN analyser. The RSD with this technique is 2% for organic carbon (OC) and 3% for total nitrogen (TN). In duplicate analyses of OC and TN, RSD was equal to 2.0 and 0.2 wt.%, respectively.

Amino acids are among the easily degradable constituents of POM and are quickly metabolised while settling through the water column (Handa and Tominaga, 1969; Lee and Cronin, 1984). Wakeham et al. (1984) reported that decreases in aspartic and glutamic acids relative to non-protein AAs (β-alanine and γ-aminobutyric acid) might result from preferential decomposition of

Table 1: Details of sediment-trap location, deployment depth and sample collection period

Site	Location		Trap	Trap depth (m)	Seafloor depth (m)	Sampling duration		Sample interval (days)	Trap type
						Begin	End		
N2	4°07.5′N	136°16.6′E	Shallow	1,769	4,888	4-Jun-91	15-Apr-92	12–16	a
			Deep	4,574		4-Jun-91	15-Apr-92	12–16	a
M1	4°02.9′N	135°00.0′E	Shallow	970	4,762	1-Jan-99	21-Nov-99	15	b
			Deep	2,940		1-Jan-99	21-Nov-99	15	b
M3	0°00.8′N	145°01.6′E	Shallow	1,020	3,680	5-Jan-99	21-Nov-99	15	b
			Deep	2,060		5-Jan-99	21-Nov-99	15	b
N10	1°13.2′N	160°33.9′E	Shallow	1,164	3,181	1-Oct-94	16-Apr-95	13–15	a
N3	0°00.2′N	175°09.7′E	Shallow	1,357	4,880	1-Jun-92	16-Apr-93	13–16	c
			Deep	4,363		1-Jun-92	16-Apr-93	13–16	c
M5	0°02.3′N	174°56.4′E	Shallow	1,040	4,828	13-Jan-99	21-Nov-99	15	b
			Deep	3,000		13-Jan-99	21-Nov-99	15	b
S11	12°59.6′S	155°59.6′E	Shallow	1,315	1,832	16-May-95	1-Apr-96	14–16	c
S12	17°45.7′S	154°49.5′E	Shallow	1,298	2,821	16-May-95	16-Jan-96	14–16	c
			Deep	2,304		16-May-95	16-Mar-96	14–16	c
S13	35°31.0′S	161°00.0′E	Shallow	1,161	3,174	1-Jun-95	1-Mar-96	14–16	c

Note: Trap types – (a) 21 sample cup trap, MARK7G-21, McLane Ltd., Woods Hole; (b) 26 sample cup trap, SMD26S-6000, Nichiyu-giken-kogyou Ltd., Tokyo; (c) 21 sample cup trap, SMD21-6000, Nichiyu-giken-kogyou Ltd., Tokyo.

protein AAs. Molar ratios of aspartic acid/β-alanine (Asp/β-Ala) and glutamic acid/γ–aminobutyric acid (Glu/γ-Aba) have been used as indicators of microbial degradation of POM, with low ratios indicating relatively more degraded POM (Ittekkot et al., 1984b). The molar ratio between total AAs and HAs (AA/HA) indicates the relative degree of microbial reworking and phyto- and zooplanktonic sources of POM (Degens and Mopper, 1976; Degens and Ittekkot, 1984). Low AA/HA ratios with the HA being mostly glucosamine (Glc-NH_2) indicate large amounts of chitinous material. In many bacterial cell walls, both Glc-NH_2 and galactosamine (Gal-NH_2) are present (Walla et al., 1984), and a Glc-NH_2/Gal-NH_2 ratio <4 has been measured in various bacterial species (Kandler, 1979). The Glc-NH_2/Gal-NH_2 ratio is therefore often used to differentiate chitinous zooplankton from microbial biomass (Haake et al., 1992). These diagenetic indicator ratios are qualitative or semi-quantitative in nature, especially the Asp/β-Ala and Glu/γ-Aba ratios, owing to multiple possible origins of β-Ala and γ-Aba (Lee and Cronin, 1982). Nevertheless, β-Ala and γ-Aba contents of settling POM increase with increasing depth. The Glc-NH_2/Gal-NH_2 and AA/HA ratios are more definitive (quantitative).

4 Results and Discussion

4.1 Variations in Total Mass and AA Fluxes

In the hemipelagic zone, average total mass flux (TMF) at site N2 was higher than that at site M1, and the vertical decrease in the average TMF at both sites was negligible (Fig. 3). Comparison of data from individual samples revealed that the deep trap sometimes recorded a lower TMF of settling particulate matter but at other times, higher ones. In contrast, at site M3 in the warm pool and M5 in the equatorial-upwelling zone, the deep traps recorded a higher TMF than the shallow traps throughout the sampling period. In addition, the traps at these sites recorded higher fluxes relative to those deployed at sites N10 and N3. AA fluxes in the hemipelagic zone were much lower at site M1 than at site N2. The range of variation in the M-series traps was much larger than that in the N-series traps (Gupta and Kawahata, 2002). The shallow trap at site M3 in the warm pool zone occasionally recorded a near-zero flux during September–October 1999 (Fig. 4). At site S11 in the Coral Sea, TMF varied from 4.2 to 58.7 mg m^{-2} d^{-1}, with higher fluxes during the austral spring (August–September 1995) and at the beginning of the austral summer (October 1995) (Gupta and Kawahata, 2003a). TMF at site S12 in the Coral Sea varied from 6.8 to 17.7 mg m^{-2} d^{-1}, with no particular seasonal trends. However, in the deep trap at site 12, TMF was occasionally higher than the corresponding sample in the shallow

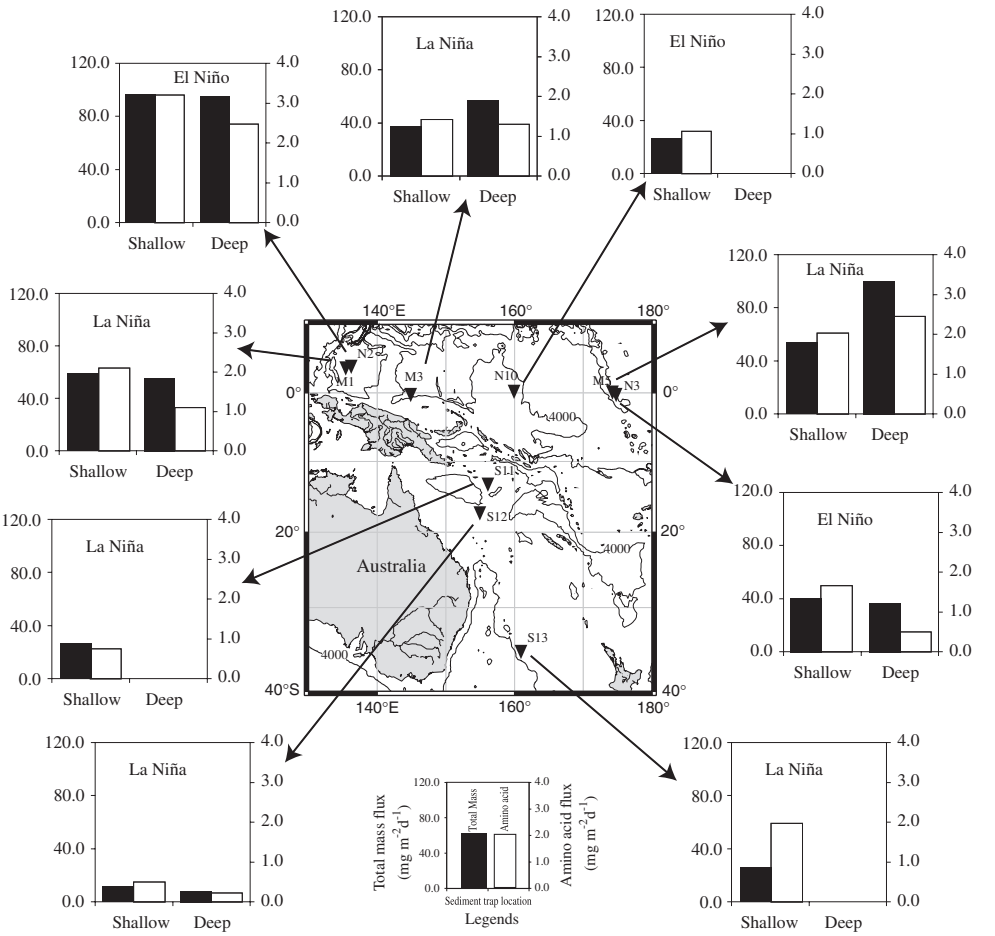

Figure 3: Regional variations in average values of settling particle mass and amino acid fluxes in the western equatorial and south-eastern Pacific Ocean.

trap. Nonetheless, the average TMF in the deep trap was lower than that in the shallow trap (Fig. 3) and varied from 2.8 to 11.7 mg m^{-2} d^{-1}. TMF at site S13 varied from 6.3 to 68.4 mg m^{-2} d^{-1}, with a strong seasonal signal in late spring (September–October 1995).

Higher TMF in deep traps, relative to shallow traps, has been observed by a number of other studies, and various explanations have been offered to account for the increase in particle flux with increasing water depth. Chemolithotrophic new production (Karl and Knauer, 1984; Roth and Dymond, 1989), aggregate formation due to zooplanktonic activity in deep waters (Walsh et al., 1988a), lateral advection from a nearby more productive region (Siegel et al., 1990) and contribution of re-suspended particles

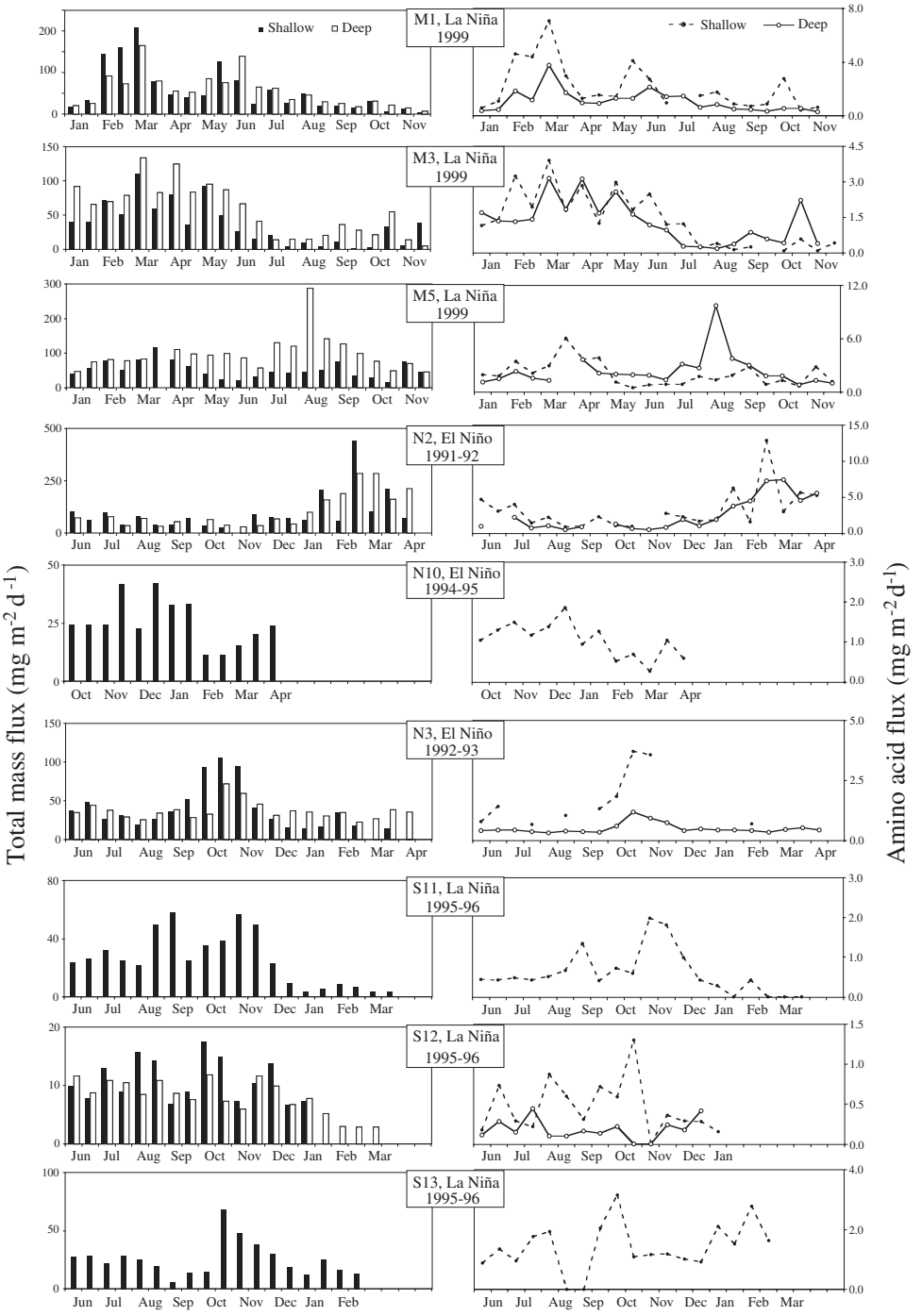

Figure 4: Seasonal changes in settling particle mass and amino acid fluxes in the western equatorial and south-eastern Pacific Ocean. The scales in each sub-figure have been deliberately chosen to enhance the seasonal variation of data at a site.

from nepheloid layer (Walsh et al., 1988b; Gupta and Kawahata, 2000) are possible explanations for the increase in the fluxes with increasing water depth.

4.2 Variations in Biogeochemical Parameters

Settling POM was enriched in AAs in M-series traps compared with in N-series traps. In all cases, AA content decreased from the shallow trap to the deep trap at the same site. This vertical decrease is commonly interpreted as a greater loss of labile AAs relative to other metabolites because of ongoing microbial degradation of settling POM. The deep traps at all sites clearly recorded higher β-Ala+γ-Aba contents relative to the shallow traps. In the hemipelagic zone, the average β-Ala+γ-Aba content was higher in the M1 traps than in the N2 traps. The shallow traps at sites M3 and N10 in the warm pool zone had nearly equal β-Ala+γ-Aba concentrations, while at the eastern end of the pool (site N3) β-Ala+γ-Aba content was relatively low in the shallow trap. In the equatorial upwelling zone, the shallow trap at site M5 recorded a β-Ala+γ-Aba content comparable to that recorded in the shallow traps at the other sites.

Amino acid carbon and nitrogen contents relative to OC and TN (AA-C and AA-N, respectively) showed a vertical decrease between the shallow and deep traps at all sites (Fig. 5). Also, the M-series traps recorded considerably higher AA-C and AA-N contents than the N-series traps. In all three zones, the ratios Asp/β-Ala, Glu/γ-Aba and Glc-NH_2/Gal-NH_2 showed a vertical decrease between the shallow and deep traps at the same site. The site M1 traps in the hemipelagic zone recorded lower Asp/β-Ala ratios than the N2 traps in the same zone. In the warm pool zone, the M3 trap recorded a slightly higher Asp/β-Ala ratio than the N10 trap, but the N3 traps in this zone recorded the highest values. In the warm pool and equatorial upwelling zones, the Glc-NH_2/Gal-NH_2 ratio was much larger in the M-series traps than in the N-series traps, but in the hemipelagic zone, the difference between the M1 and N2 traps was relatively small. The M-series traps recorded slightly higher values for the AA/HA ratio than the N-series traps.

At site S11, samples from the end of December 1995 and the beginning of January 1996 showed the highest Glc-NH_2/Gal-NH_2 ratios, which were associated with relatively low AA/HA ratios. These ratios indicate that zooplanktonic debris and faecal pellets were a major vehicle for POM transport to the deep ocean during the austral summer. At site S12, the Asp/β-Ala, Glu/γ-Aba and AA/HA ratios suggest that higher fluxes of AA and HA brought microbially less-degraded POM to the trap depth. The indicator ratios Asp/β-Ala and Glu/γ-Aba in the deep trap suggest that the samples with lower AA contents had microbially more-degraded POM compared with those with higher AA content. The site S12 deep trap was located near the Queensland Plateau, which might be a source of laterally advected material,

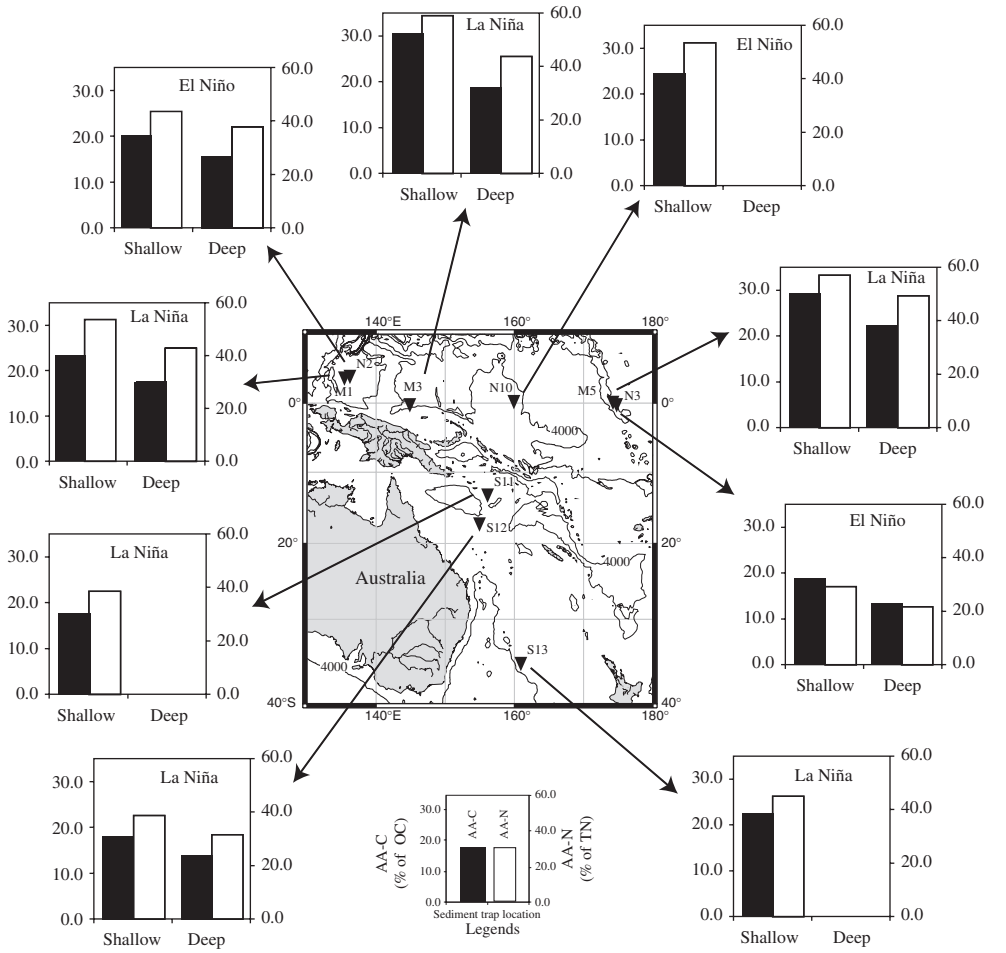

Figure 5: Regional variations in average values of amino acid carbon and nitrogen with respect to total organic carbon and total nitrogen, respectively, in particles settling in the western equatorial and south-eastern Pacific Ocean.

especially under the influence of the EAC. Moreover, mid-depth circulation may re-suspend sediments lying on the sea floor (Davis, 1998). Re-suspended POM is generally depleted in labile components and therefore has a high C/N_{atomic} ratio. The samples collected during the second half of June 1995 showed a sharp increase in the C/N_{atomic} ratio between the shallow (6.3) and deep trap (8.6), while the AA and HA contents decreased from 92.5 and 5.2 mg g^{-1} to 32.7 and 3.5 mg g^{-1}, respectively. Although these changes are to some degree expected because of the ongoing degradation of settling POM, their abruptness indicates mixing of resuspended POM with settling POM. The samples collected by the deep trap towards the end of July and in

December 1995 had much higher indicator ratios compared with the shallow trap samples corresponding to the same period. The higher values indicate a possible contribution of relatively fresh POM laterally advected from more productive surface waters.

Arrival of relatively fresh POM at trap depth is possible through the formation of large, rapidly settling aggregates of phytoplankton, which have been observed to exist under low zooplanktonic grazing pressure (Peinert et al., 1989). Modelling and experimental studies by Sarnelle (1999) have also shown that herbivorous zooplankton tend to reduce the vertical flux of phytoplanktonic biomass in lakes and possibly in other aquatic systems. In addition, rapid settling of particles during periods of high primary productivity in surface waters of the north-eastern subarctic Pacific Ocean (site OSP) has been observed to reduce loss of organic components into the water column (Wong et al., 1999). In contrast, the low C/N_{atomic} ratio at site S13 during September 1995 was associated with high Glc-NH_2/Gal-NH_2 and low AA/HA ratios, indicating considerable influence of zooplanktonic debris; thus, POM became enriched in proteinaceous material, bringing the ratio down to 5.9. The C/N_{atomic} ratio at site S13 was, in general, slightly lower than that at sites S11 and S12. The lower ratios (implying fresh POM) at site S13 may be attributed to rapid settling or to a reduced rate of microbial degradation of POM. In the mesopelagic environment, free-living bacteria are the principal mediators of particle decomposition (Cho and Azam, 1988), achieved by extracellular enzymatic hydrolysis exceeding the growth requirements of the bacteria (Smith et al., 1992). The enzymatic degradation is dependent on ambient temperature, which leads to enhanced export of relatively unhydrolysed POM in low-temperature waters (Vetter and Deming, 1994), e.g., at site S13. In addition, SST has been shown to influence primary productivity (Prasanna Kumar et al., 2001), which in turn influences particle flux to the deep ocean (Pace et al., 1987). Mulhearn et al. (1986) have reported the presence of eddies in the Tasman Sea whose influence extends to abyssal depths. Such eddies can redistribute suspended particles in the mid-ocean and consequently lead to higher particle fluxes, such as those recorded by the site S13 trap.

4.3 Comparison with Other Trap Sites

Flux and composition data in this study show a wide range of temporal and spatial variations; this spread is comparable to observations made in similar experiments in the equatorial Pacific. Average TMF varied from a minimum of 25.7 mg m^{-2} d^{-1} at site N10 to a maximum of 100.0 mg m^{-2} d^{-1} at site M5 (deep trap). The minimum flux at site N10 was the lowest reported for the equatorial Pacific and reflected the oligotrophic character of this site. In contrast, the highest TMF values in the equatorial ocean (265–350 mg m^{-2} d^{-1})

were recorded during 1979–1980 in the Panama Basin. In this study, the average AA flux was the lowest (0.5 mg m^{-2} d^{-1}) at the site N3 deep trap. The trap depth difference of about 3,200 m at this site may account for the lower AA flux at site N3, but site M3 traps did not show any significant decrease in the AA flux (1.4–1.3 mg m^{-2} d^{-1}) with increasing depth (1,020–2,060 m). Ittekkot et al. (1984a) reported a relatively small decrease in AA flux (3.6–3.4 mg m^{-2} d^{-1}) with increasing depth in the Panama Basin, while at site N3, the AA flux decreased by a factor of 3 between the shallow and deep traps. Lee et al. (2000) observed a similar decrease in the AA flux in the eastern equatorial Pacific. In the central Bay of Bengal (CBBT site), TMF varied between 69.7 and 232.1 mg m^{-2} d^{-1} at 950 m (shallow trap) and between 83.3 and 340.5 mg m^{-2} d^{-1} at 2286 m (deep trap) (Schäfer et al., 1998). AA-N% accounted for 36.7–52.3% and 29.9–45.5% of TN in the shallow and deep traps, respectively. Attributed to large sediment delivery by the Ganges and Brahmaputra rivers, the TMF values at CBBT were much higher than those recorded at sites S11 and S12. However, AA-N contents were within a range comparable to values recorded at sites S11 and S12. Haake et al. (1996) reported AA concentrations of 36.4 mg g^{-1} at 850 m (shallow) and 22.5 mg g^{-1} at 2,900 m (deep) in the central Arabian Sea (CAST site). AA-C accounted for 19.9% and 15.6% of OC at the shallow and deep traps, respectively. These values from the CAST site are within the range recorded at sites S11 and S12 in this study.

All the traps showed a general order of dominance of grouped AAs: neutral > acidic > basic > aromatic AAs. On average, their relative molar concentrations varied within a very short range at all the trap sites. However, shallow traps recorded a larger amplitude of variation than deep traps. It seems that POM at the depths of shallow traps was more heterogeneous in its chemical composition, but at the depths of deep traps, it was degraded to the extent that the seasonal differences among the samples became difficult to distinguish in terms of their AA composition. At site S13, higher particle fluxes resulted in a higher supply of labile carbon and nitrogen to the benthic community, assuming that approximately half of the POM flux at ca. 1,000 m depth reaches the sea floor (Jahnke, 1996). A similar trend of high flux of relatively more labile POM settling in higher latitudes has been noted in the central North Pacific (Gupta and Kawahata, 2003b).

4.4 ENSO and Zonal Variations in Observed Parameters

In the hemipelagic zone, an El Niño event brought a relatively higher TMF and AA flux compared with those during La Niña (Table 2). These higher fluxes resulted from enhanced PP due to westerly wind-induced shoaling of the nutricline (Lindstrom et al., 1987; Radenac and Rodier, 1996). Despite high fluxes, labile components of settling POM were low, as indicated by low

values of OC-normalised AA and AA/HA ratios. A low non-protein AA content and high Asp/β-Ala ratio could result from slow degradation rates of quickly settling POM. Low Glc-NH_2/Gal-NH_2 ratios indicate depletion of zooplanktonic debris in the settling POM. In contrast, the La Niña event resulted in labile content-enriched POM but reduced TMF and AA flux. The settling POM, however, underwent enhanced degradation, as indicated by high non-protein AA contents and low Asp/β-Ala ratios. The lower fluxes during La Niña probably resulted from lower primary productivity associated with deepening of the nutricline in the hemipelagic zone. Higher values of OC-normalised AAs, AA-C%, AA-N% and AA/HA and Glc-NH_2/Gal-NH_2 ratios indicate that the settling POM was more labile during La Niña than during El Niño.

The warm pool zone contrasted sharply with the hemipelagic zone in terms of TMF and AA flux. El Niño events reduced the fluxes in the warm pool zone. These lower fluxes were associated with lower labile content of the settling POM, as indicated by low values of OC-normalised AA, AA-C%, AA-N%, Glc-NH_2/Gal-NH_2 and AA/HA. Low β-Ala+γ-Aba content indicated reduced degradation of the settling POM during an El Niño event. Although low, the eastern region of the warm pool recorded higher fluxes than the central region. Total mass and AA fluxes were higher, as were the other parameters, except Glu/γ-Aba, during a La Niña event, but they were comparable to those recorded in the eastern region of the warm pool during an El Niño event. In this case, the higher flux of AAs increased the labile content of settling POM. Higher β-Ala+γ-Aba and low Glu/γ-Aba ratios suggest enhanced degradation of settling POM during La Niña. Although located in the warm pool, the considerable distance (ca. 1,600 km) between the trap sites (M3, N10 and N3) could account for some variations in the studied parameters. Furthermore, a closer look at the equatorial southern oscillation index (SOI; Fig. 2) indicates that the 1994–1995 El Niño was relatively weak (small negative deviation from the mean) and short in duration. Across the warm pool zone, this weak El Niño might have caused little change in the biogeochemical properties of settling POM.

In the equatorial upwelling region, higher PP led to higher fluxes of total mass and AAs. The average values recorded in the shallow trap were somewhat higher than those in the warm pool zone but comparable to those in the hemipelagic zone during the 1999 La Niña. As was the case in the hemipelagic zone, labile components of the settling POM appeared to be degraded at a faster rate, also in the equatorial upwelling zone, during the La Niña event. In the eastern equatorial Pacific (site C; 1°N, 139°W), Dymond and Collier (1988) also observed biogenic particle fluxes during the 1984 La Niña 2–3 times those observed during the 1983 El Niño, when the particle flux diminished owing to decreased PP in the surface water.

Table 2: Average values of fluxes and various biogeochemical parameters observed at various sites in this study

Sediment-trap site		N2, M1	N10, N3, M3	M5	S11	S12	S13
Parameters	ENSO phase	Regions in the equatorial Pacific Ocean			Coral Sea		Tasman Sea
		Hemipelagic	Warm pool	Eq. Upwelling			
Total mass flux (mg m^{-2} d^{-1})	El Niño	95.9 (94.9)	25.7, 40.1 (36.2)	–	–	–	–
	La Niña	58.6 (55.3)	37.1 (56.6)	53.7 (100.0)	25.8	11.0 (7.9)	25.5
Amino acid flux (mg m^{-2} d^{-1})	El Niño	3.2 (2.5)	1.1, 1.7 (0.5)	–	–	–	–
	La Niña	2.1 (1.1)	1.4 (1.3)	2.0 (2.4)	0.7	0.5 (0.2)	2.0
Amino acid (mg (100 mg OC)$^{-1}$)	El Niño	45.9 (36.0)	56.1, 43.5 (30.8)	–	–	–	–
	La Niña	53.3 (40.4)	69.6 (43.6)	67.4 (51.0)	40.0	41.0 (31.8)	51.8
Amino acid carbon (% of OC)	El Niño	19.9 (15.6)	24.4, 18.7 (13.2)	–	–	–	–
	La Niña	23.2 (17.4)	30.4 (18.7)	29.3 (22.1)	17.5	17.9 (13.8)	22.4
Amino acid nitrogen (% of TN)	El Niño	43.3 (37.8)	53.3, 29.2 (21.6)	–	–	–	–
	La Niña	53.5 (42.8)	59.0 (43.7)	56.9 (49.2)	38.5	38.7 (31.4)	44.9
β-Ala+γ-Aba (mole%)	El Niño	0.6 (1.1)	0.7, 0.5 (1.1)	–	–	–	–
	La Niña	0.8 (1.4)	0.7 (1.3)	0.7 (1.1)	0.7	0.8 (1.1)	0.7
Asp/β-Ala (mole ratio)	El Niño	41.0 (29.0)	27.0, 45.6 (18.8)	–	–	–	–
	La Niña	26.9 (14.9)	29.8 (15.6)	30.2 (18.9)	37.9	37.8 (22.1)	38.2
Glu/γ-Aba (mole ratio)	El Niño	28.0 (12.9)	45.2, 44.8 (24.2)	–	–	–	–
	La Niña	28.2 (13.7)	42.0 (17.2)	39.7 (19.5)	40.2	34.7 (22.4)	54.8
Glc-NH_2/Gal-NH_2 (mole ratio)	El Niño	5.9 (5.1)	6.5, 5.8 (4.2)	–	–	–	–
	La Niña	7.8 (7.2)	11.3 (7.7)	15.0 (13.2)	5.4	3.7 (3.7)	10.1
AA/HA (mole ratio)	El Niño	10.3 (10.3)	20.3, 14.6 (9.7)	–	–	–	–
	La Niña	14.4 (16.0)	22.4 (15.1)	16.3 (13.5)	10.7	20.6 (12.8)	16.9

Note: AA, amino acid; OC, organic carbon; TN, total nitrogen; β-Ala, beta alanine; γ-Aba, gama aminobutyric acid; Asp, aspartic acid; Glu, glutamic acid; HA, hexosamine; Glc-NH2, glucosamine; Gal-NH2, galactosamine; Eq., equatorial; –, no data. Values in brackets refer to deep trap data.

4.5 Biogeochemical Indicators and the Plankton Community

Asp/β-Ala and Glu/γ-Aba ratios showed irregular variations in all three zones across the equatorial Pacific during El Niño and La Niña changes. However, β-Ala+γ-Aba content was uniformly higher in La Niña samples, and was responsible for the lower Asp/β-Ala and Glu/γ-Aba ratios. As has been observed by Goddard and Graham (1997) and Stoens et al. (1999), the 1991–1995 El Niño occurred in discrete periods (i.e. a discontinuous event) and was a weak warming event. It is possible that the Asp/β-Ala and Glu/γ-Aba ratios represent borderline values for El Niño and La Niña changes. A more detailed examination of the data (Table 2) shows that average Glu/γ-Aba ratios were nearly unchanged during El Niño and La Niña phases. However, average Asp/β-Ala values in both shallow and deep traps at M1 and N2 and in shallow traps at M5 and N3 differed considerably between El Niño and La Niña events. The AA-based parameters, including β-Ala+γ-Aba content, showed a certain uniformity in the labile nature of the samples collected at all sites during La Niña, and this uniformity is in contrast to that observed during El Niño events. Based on their study of radiolarians in the equatorial Pacific during warm (El Niño) and cold (La Niña) phases of the 1992 ENSO, Welling and Pisias (1998) suggested that environmental forcing can determine plankton community composition. By taking this finding into consideration, the above-observed uniformity in AA parameters might be explained by the presence of a planktonic community with a particular type of species composition in surface waters during an El Niño event. This particular community contributed to production of settling POM, whose AA-based parameters differed from those based on settling POM produced by a different plankton community that existed thereduring La Niña.

5 Conclusions

Photosynthetic activity of phytoplankton is a major factor determining whether the equatorial Pacific Ocean acts as a source or sink of carbon dioxide. The observations made in this study suggest that POM flux to the deep ocean is also considerably influenced by ENSO variability. El Niño conditions lead to a considerable increase in settling particle and AA fluxes in the hemipelagic region of the western equatorial Pacific Ocean. Although the fluxes are high, settling POM is fairly degraded, as suggested by AA-based biogeochemical parameters. The warm pool region, on the other hand, shows moderate to little change in particle flux and associated parameters, probably because primary productivity is quite low in this part of the Pacific (oligotrophic region). However, settling POM is less degraded than that in the hemipelagic and equatorial upwelling regions. The sediment-trap data

from the south-west Pacific, on the other hand, show that TMF and AA and HA fluxes are higher in the Tasman Sea than in the Coral Sea, apparently because of low SST and high PP in the Tasman Sea. In contrast to the usual decrease in particle flux with depth, some deep traps occasionally showed higher TMF and AA flux; however, POM in deep traps was more degraded than that in the corresponding shallow traps. The C/N_{atomic} ratio coupled with AA- and HA-based indicator ratios clearly indicate a contribution of resuspended as well as of laterally advected POM to the deep traps.

Acknowledgements

The authors are grateful to two anonymous reviewers whose comments substantially improved this manuscript. This study was supported by the following research programmes: 'NOPACCS' consigned to the Kansai Environmental Engineering Center Col. Ltd. by the New Energy and Industrial Technology Development Organization (NEDO), and 'GCMAPS' by the Ministry of Education, Culture, Sports, Science and Technology (MEXT).

References

Antoine, D., Andre, J. M., Morel, A., 1996. Oceanic primary production. 2. Estimation at global scale from satellite (coastal zone color scanner) chlorophyll. Global Biogeochemical Cycles 10 (1), 57–69.

Cho, B. C., Azam, F., 1988. Major role of bacteria in biogeochemical fluxes in the ocean's interior. Nature 332, 441–443.

Cowie, G. L., Hedges, J. I., 1994. Biochemical indicators of diagenetic alteration in natural organic matter mixtures. Nature 369, 304–307.

Dauwe, B., Middelburg, J. J., 1998. Amino acids and hexosamines as indicators of organic matter degradation state in North Sea sediments. Limnology and Oceanography 43 (5), 782–798.

Davis, R. E., 1998. Preliminary results from directly measuring middepth circulation in the tropical and South Pacific. Journal of Geophysical Research 103 (C11), 24619–24639.

Degens, E. T., Ittekkot, V., 1984. A new look at clay-organic interaction. Mitteilungen aus dem Geologisches Palaeontologisches Institut der Universitaet Hamburg, SCOPE/UNEP sonderband, 56, pp. 229–248.

Degens, E. T., Mopper, K., 1976. Factors controlling the distribution and early diagenesis of organic material in marine sediments. In: Wiley, J. P., Chester, R. (Eds.), Chemical Oceanography. Academic Press, San Diego, pp. 59–113.

Dunne, J. P., Murray, J. W., Rodier, M., Hansell, D. A., 2000. Export flux in the western and central equatorial Pacific: Zonal and temporal variability. Deep-Sea Research 47, 901–936.

Dymond, J., Collier, R., 1988. Biogenic particle fluxes in the equatorial Pacific: Evidence for both high and low productivity during the 1982–1983 El-Niño. Global Biogeochemical Cycles 2, 129–137.

Garrett, D., 2000. Climate Prediction Centre, NOAA (available at: http// :www.cpc.ncep.noaa.gov/products/analysis_monitoring/bulletin/figt2.gif).

Glantz, M. H., 1996. Currents of change: El Niño's impact on climate and society. University Press, Cambridge, p. 194.

Goddard, L., Graham, N. E., 1997. El Niño in the 1990s. Journal of Geophysical Research 102 (C5), 10423–10436.

Godfrey, J. S., 1996. The effect of the Indonesian throughflow on the ocean circulation and heat exchange with the atmosphere: A review. Journal of Geophysical Research 101 (C5), 12217–12237.

Godfrey, J. S., Lindstrom, E. J., 1989. The heat budget of the equatorial western Pacific surface mixed layer. Journal of Geophysical Research 94 (C6), 8007–8017.

Gordon, A. L., Fine, R. A., 1996. Pathways of water between the Pacific and Indian oceans in the Indonesian seas. Nature 379, 146–149.

Gupta, L. P., Kawahata, H., 2000. Amino acid and hexosamine compositions and flux of sinking particulate matter into the equatorial Pacific at 175°E longitude. Deep-Sea Research 47 (10), 1937–1960.

Gupta, L. P., Kawahata, H., 2002. Impact of ENSO variability on the flux and composition of sinking POM in the western equatorial Pacific Ocean: Amino acids and hexosamines. Deep-Sea Research II 49 (13–14), 2769–2782.

Gupta, L. P., Kawahata, H., 2003a. Biogeochemical processes and labile composition of settling particulate organic matter in the south-west Pacific Ocean. Marine and Freshwater Research 54, 259–270.

Gupta, L. P., Kawahata, H., 2003b. Vertical and latitudinal variations in amino acid fluxes and compositions of settling particles along 175°E in the North Pacific Ocean. Tellus 55B, 445–455.

Haake, B., Ittekkot, V., Ramaswamy, V., Nair, R. R., Honjo, S., 1992. Fluxes of amino acids and hexosamines to the deep Arabian Sea. Marine Chemistry 40, 291–314.

Haake, B., Rixen, T., Reemtsma, T., Ramaswamy, V., Ittekkot, V., 1996. Processes determining seasonality and interannual variability of settling particle fluxes of the deep Arabian Sea. In: Ittekkot, V., Schäfer, P., Honjo, S., Depetris, P. J. (Eds.), Particle Flux in the Ocean. John Wiley, Chichester, pp. 251–270.

Handa, N., Tominaga, H., 1969. A detailed analysis of carbohydrates in marine particulate matter. Marine Biology 2, 228–235.

Hansell, D. A., Bates, N. R., Carlson, C. A., 1997a. Predominance of vertical loss of carbon from surface waters of the equatorial Pacific Ocean. Nature 386, 59–61.

Hansell, D. A., Carlson, C. A., Bates, N. R., Poisson, A., 1997b. Horizontal and vertical removal of organic carbon in the equatorial Pacific Ocean: A mass balance assessment. Deep-Sea Research II 44 (9–10), 2115–2130.

Higgins, H. W., Mackey, D. J., 2000. Algal class abundances, estimated from chlorophyll and carotenoid pigments, in the western Equatorial Pacific under El Niño and non-El Niño conditions. Deep-Sea Research 47, 1461–1483.
Ingalls, A. E., Lee, C., Wakeham, S. G., Hedges, J. I., 2003. The role of biominerals in the sinking flux and preservation of amino acids in the Southern Ocean along 170°W. Deep-Sea Research II 50 (3–4), 713–738.
Ittekkot, V., Degens, E. T., Honjo, S., 1984a. Seasonality in the fluxes of sugars, amino acids, and amino sugars to the deep ocean: Panama Basin. Deep-Sea Research 31, 1071–1083.
Ittekkot, V., Deuser, W. G., Degens, E. T., 1984b. Seasonality in the fluxes of sugars, amino acids, and amino sugars to the deep ocean: Sargasso Sea. Deep-Sea Research 31, 1057–1069.
Jahnke, R. A., 1996. The global ocean flux of particulate organic carbon: Areal distribution and magnitude. Global Biogeochemical Cycles 10 (1), 71–88.
Kandler, O., 1979. Zellwandstrukturen bei Methan-Bakterien. Naturwissenschaften 66, 95–105.
Karl, D. M., Knauer, G. A., 1984. Vertical distribution, transport, and exchange of carbon in the northeast Pacific Ocean: Evidence for multiple zones of biological activity. Deep-Sea Research 31, 221–243.
Kawahata, H., 1999. Fluctuation in the ocean environment within the western Pacific warm pool during Late Pleistocene. Paleoceanography 14 (5), 639–652.
Kawahata, H., Ohta, H., 2000. Sinking and suspended particles in the south-west Pacific. Marine and Freshwater Research 51, 113–126.
Kawahata, H., Suzuki, A., Ohta, H., 1998a. Sinking particles between the equatorial and subarctic regions (0°N–46°N) in the central Pacific. Geochemical Journal 32, 125–133.
Kawahata, H., Yamamuro, M., Ohta, H., 1998b. Seasonal and vertical variations of sinking particle fluxes in the West Caroline Basin. Oceanologica Acta 21 (4), 521–532.
Le Borgne, R., Barber, R. T., Delcroix, T., Inoue, H. Y., Mackey, D. J., Rodier, M., 2002. Pacific warm pool and divergence: Temporal and zonal variations on the equator and their effects on the biological pump. Deep-Sea Research II 49 (13–14), 2471–2512.
Lee, C., Cronin, C., 1982. The vertical flux of particulate organic nitrogen in the sea: Decomposition of amino acids in the Peru upwelling area and the equatorial Atlantic. Journal of Marine Research 40, 227–251.
Lee, C., Cronin, C., 1984. Particulate amino acids in the sea: Effects of primary productivity and biological decomposition. Journal of Marine Research 42, 1075–1097.
Lee, C., Wakeham, S. G., Hedges, J. I., 2000. Composition and flux of particulate amino acids and chloropigments in equatorial Pacific seawater and sediments. Deep-Sea Research 47, 1535–1568.
Lindstrom, E., Lukas, R., Fine, R., Firing, E., Godfrey, S., Meyers, G., Tsuchiya, M., 1987. The western equatorial Pacific Ocean circulation study. Nature 330, 533–537.

Mackey, D. J., Parslow, J., Griffiths, F. B., Higgins, H. W., Tilbrook, B., 1997. Phytoplankton productivity and the carbon cycle in the western Equatorial Pacific under El Niño and non-El Niño conditions. Deep-Sea Research II 44 (9–10), 1951–1978.

Mackey, D. J., Parslow, J., Higgins, H. W., Griffiths, F. B., O'Sullivan, J. E., 1995. Plankton productivity and biomass in the western equatorial Pacific: Biological and physical controls. Deep-Sea Research II 42 (2–3), 499–533.

McCarthy, J. J., Garside, C., Nevins, J. L., Barber, R. T., 1996. New production along 140°W in the equatorial Pacific during and following the 1992 El Niño event. Deep-Sea Research II 43 (4–6), 1065–1093.

Mulhearn, P. J., 1987. The Tasman front: A study using satellite infrared imagery. Journal of Physical Oceanography 17, 1148–1155.

Mulhearn, P. J., Filloux, J. H., Lilley, F. E. M., Bindoff, N. L., Ferguson, I. J., 1986. Abyssal currents during the formation and passage of a warm-core ring in the East Australian Current. Deep-Sea Research 33 (11/12), 1563–1576.

Pace, M. L., Knauer, G. A., Karl, D. M., Martin, J. H., 1987. Primary production, new production and vertical flux in the eastern Pacific Ocean. Nature 325, 803–804.

Peinert, R., von Bodungen, B., Smetacek, V. S., 1989. Food web structure and loss rate. In: Berger, W. H., Smetacek, V. S., Wefer, G. (Eds.), Productivity of the ocean: Present and past. John Wiley and Sons, New York, pp. 35–48.

Prasanna Kumar, S., Ramaiah, N., Gauns, M., Sarma, V. V. S. S., Muraleedharan, P. M., Raghukumar, S., Dileep Kumar, M., Madhupratap, M., 2001. Physical forcing of biological productivity in the Northern Arabian Sea during the Northeast Monsoon. Deep-Sea Research II 48, 1115–1126.

Radenac, M. H., Rodier, M., 1996. Nitrate and chlorophyll distributions in relation to thermohaline and current structures in the western tropical Pacific during 1985–1989. Deep-Sea Research II 43 (4–6), 725–752.

Roth, S. E., Dymond, J., 1989. Transport and settling of organic material in a deep-sea hydrothermal plume: Evidence from particle flux measurement. Deep-Sea Research 36, 1237–1254.

Sarnelle, O., 1999. Zooplankton effects on vertical particulate flux: Testable models and experimental results. Limnology and Oceanography 44 (2), 357–370.

Schäfer, P., Ittekkot, V., Gravenhorst, G., Langel, R., Reineking, A., 1998. Variations of δ^{15}N-values and hydrolysable amino acids in settling particles in the ocean. Isotopes in Environmental and Health Studies 34, 191–199.

Siegel, D. A., Granata, T. C., Michaels, A. F., Dickey, T. D., 1990. Mesoscale eddy diffusion, particle sinking, and the interpretation of sediment trap data. Journal of Geophysical Research 95, 5305–5311.

Smith, D. C., Simon, M., Alldredge, A. L., Azam, F., 1992. Intense hydrolytic enzyme activity on marine aggregates and implications for rapid particle dissolution. Nature 359, 139–142.

Stoens, A., Menkes, C., Radenac, M. H., Dandonneau, Y., Grima, N., Eldin, G., Memery, L., Navarette, C., Andre, J. M., Moutin, T., Raimbault, P., 1999. The coupled physical-new production system in the equatorial Pacific during the 1992–1995 El Niño. Journal of Geophysical Research 104 (C2), 3323–3339.

Tate, P. M., Jones, I. S. F., Hamon, B. V., 1989. Time and space scales of surface temperatures in the Tasman Sea, from satellite data. Deep-Sea Research 36 (3), 419–430.

Trenberth, K. E., Hoar, T. J., 1996. The 1990–1995 El Niño-Southern Oscillation event: Longest on record. Geophysical Research Letters 23 (1), 57–60.

Vetter, Y. A., Deming, J. W., 1994. Extracellular enzyme activity in the Arctic Northeast Water polynya. Marine Ecology Progress Series 114, 23–34.

Wakeham, S. G., Lee, C., Farrington, J. W., Gagosian, R. B., 1984. Biogeochemistry of particulate organic matter in the oceans: Results from sediment trap experiments. Deep-Sea Research 31 (5), 509–528.

Wakeham, S. G., Lee, C., Hedges, J. I., Hernes, P. J., Peterson, M. L., 1997. Molecular indicators of diagenetic status in marine organic matter. Geochimica et Cosmochimica Acta 61, 5363–5369.

Walla, M. D., Lau, P. Y., Morgan, S. L., Fox, A., Brown, A., 1984. Capillary gas chromatography-mass spectrometry of carbohydrate components of Legionelle and other bacteria. Journal of Chromatography A 288, 399–413.

Walsh, I., Dymond, J., Collier, R., 1988a. Rates of recycling of biogenic components of settling particles in the ocean derived from sediment trap experiments. Deep-Sea Research 35 (1), 43–58.

Walsh, I., Fischer, K., Murray, D., Dymond, J., 1988b. Evidence for resuspension of rebound particles from near-bottom sediment traps. Deep-Sea Research 35 (1), 59–70.

Welling, L. A., Pisias, N. G., 1998. Radiolarian fluxes, stocks, and population residence times in surface waters of the central equatorial Pacific. Deep-Sea Research 45, 639–671.

Wong, C. S., Whitney, F. A., Crawford, D. W., Iseki, K., Matear, R. J., Johnson, W. K., Page, J. S., Timothy, D., 1999. Seasonal and interannual variability in particle fluxes of carbon, nitrogen and silicon from time series of sediment traps at Ocean Station P, 1982–1993: Relationship to changes in subarctic primary productivity. Deep-Sea Research II 46, 2735–2760.

Yan, X. H., Ho, C. R., Zheng, Q., Klemas, V., 1992. Temperature and size variabilities of the Western Pacific Warm Pool. Science 258, 1643–1645.

Chapter 7

Monsoonal Impacts on the Biological Pump in the Northern Indian Ocean as Discerned from Sediment Trap Experiments

Tim Rixen* **and Venupopalan Ittekkot**

Centre for Tropical Marine Ecology, Fahrenheitstr. 6, D-28359, Bremen, Germany

Abstract

Sediment trap data obtained from the western Arabian Sea have been used to characterize monsoon-induced environmental conditions driving the export of material from the surface ocean into the deep sea. The ratio between particulate organic carbon (POC) and particulate inorganic carbon (PIC) of exported material was taken as an indicator of the impact of the biological pump on the oceanic uptake of atmospheric CO_2. The results indicate that the biological pump is most effective in nitrogen-limited systems in which the availability of dissolved silica allows diatoms to play an important but not necessarily a dominant role within the plankton community. Accordingly, the biological pump can even be more efficient in oligotrophic systems than in eutrophic upwelling areas. A comparison with results obtained from other sediment trap experiments in the northern Indian Ocean reveals the highest annual mean POC/PIC ratios in the northern Bay of Bengal. The high POC/PIC ratios have been attributed to the impact of river discharges on the plankton community structure. The climate anomaly El Niño Southern Oscillation (ENSO) seems to influence the efficiency of the biological pump in the northern Bay of Bengal via its impact on the precipitation rates and consequently on the river discharge.

*Corresponding author.
E-mail address: trixen@uni-bremen.de (T. Rixen).

Elsevier Oceanography Series 73
Edited by H. Kawahata and Y. Awaya
ISBN: 0-444-52948-9

Keywords: biological pump; sediment trap experiments; POC/PIC ratios; Bay of Bengal

1 Introduction

Marine organisms influence the exchange of CO_2 between the ocean and the atmosphere via photosynthesis and precipitation of carbonates. These processes affect the fugacity of CO_2 (fCO_2) in the surface water by changing the concentration of total dissolved inorganic carbon (DIC) and the total alkalinity (TA) (Zeebe and Wolf-Gladrow, 2001). A decrease in surface water fCO_2 favouring the CO_2 uptake from the atmosphere is caused by a reduced DIC concentration and an enhanced TA. During the precipitation of carbonate, DIC and TA are consumed resulting in a net increase of fCO_2 in surface water. Accordingly, the precipitation of carbonates is referred to as the 'carbonate counter pump' (Heinze et al., 1991). In contrast, the photosynthetic production of organic matter lowers the fCO_2 by the direct consumption of DIC and nutrients and their subsequent export into the deep sea. The net effect of the so-called organic carbon pump and the carbonate counter pump on the fCO_2 comprises the biological pump (Volk and Hoffert, 1985). Owing to counteracting effects of the two pumps on the fCO_2, the ratio between particulate organic carbon and particulate inorganic carbon in the material exported into the deep sea is suggested as an indicator for the CO_2 uptake efficiency of the biological pump (Berger and Keir, 1984). Model studies have shown that an increase of the global mean POC/PIC (rain) ratio by a factor of 2 and ~3 can reduce the atmospheric CO_2 concentration by 28.5 and 70 ppm, respectively (Heinze et al., 1991; Archer et al., 2000). The 70-ppm decrease was achieved by assuming that the export production is driven by siliceous diatoms growing at the expense of carbonate-producing coccolithophorids. Since diatoms depend on the availability of silica, changes of their relevance in the plankton community are believed to result from reorganisation of the marine silica cycle or enhanced silica inputs from terrestrial sources (Froelich et al., 1992; Harrison, 2000; Conley, 2002; Matsumoto and Sarmiento, 2002).

In the framework of a joint Indo/German project and the Joint Global Ocean Flux Studies (JGOFS), PIC and POC exported from the surface ocean have been collected continuously by deep-moored sediment traps deployed at several sites in the northern Indian Ocean (Nair et al., 1989; Haake et al., 1993; Rixen et al., 1996; Lee et al., 1998; Honjo et al., 1999; Rixen et al., 2002; Unger et al., 2003; Fig. 1). The western Arabian Sea (WAST) was one of the main JGOFS study sites where in addition to sediment trap studies comprehensive field experiments were performed in 1994 and 1995. This

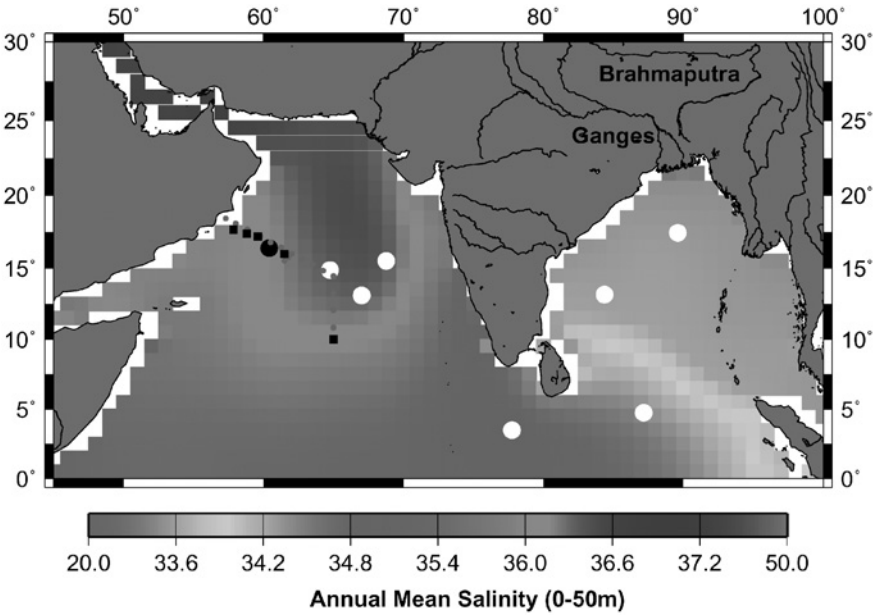

Figure 1: Map of the northern Indian Ocean showing the mean annual salinity averaged for the upper 50 m of the water column (Data: World Ocean Atlas, 1998, http://www.cdc.noaa.gov/cdc/data.woa98.html). Black circles show the long-term sediment trap site in the western Arabian Sea (WAST). White circles and black squares indicate the other joint Indo/German and the US JGOFS sediment trap sites, respectively. US JGOFS water sampling sites are shown by the red circles (For colour version, see Colour Plate Section).

work combines results obtained by the Indo/German sediment trap experiment program and JGOFS and aims at improving our understanding of processes controlling the POC/PIC ratios in settling particles.

2 Study Area

The Arabian Sea and the Bay of Bengal are strongly influenced by the Asian monsoon. The monsoon is driven by sea-level pressure difference between the Asian landmass and the Indian Ocean (Ramage, 1971, 1987). During the boreal winter, the sea-level pressure over Asia exceeds that over the Indian Ocean due to a stronger cooling of the landmass. Following the pressure gradient and being deflected by the Coriolis force, the wind blows from the NE over the Arabian Sea and the Bay of Bengal between December and February (NE monsoon; Currie et al., 1973). During summer (June–September), the heating of the Asian landmass leads to the formation of a strong atmospheric

low that attracts the SE trade winds which blow as SW winds (SW monsoon) over the Arabian Sea after crossing the equator due to the associated change of the Coriolis force. During their passage over the central Indian Ocean and the Arabian Sea, the SW monsoon winds gather water vapour sustaining the heavy rainfall over the Indian subcontinent (Ramesh Kumar and Prasad, 1997; Ramesh Kumar and Schlüssel, 1998). The monsoon rain feeds one of the world's largest river systems (Ganges–Brahamaputra) that originates in the Himalayas and discharges into the Bay of Bengal (Milliman and Meade, 1983; Milliman et al., 1984; Subramanian et al., 1985; Ludwig and Probst, 1996).

In the Arabian Sea, the SW winds forming a low-level jet (Findlater jet) enforce upwelling of cold and nutrient-enriched subsurface water that leads to high primary productivity and consequently high export rates of organic matter from the euphotic zone into the deep ocean (Findlater, 1977; Nair et al., 1989; Antoine et al., 1996; Rixen et al., 2005). The inter-annual variability of upwelling-driven organic carbon fluxes corresponds to changes in the strength of the Findlater jet, whereas a stronger Findlater jet results in stronger upwelling and higher organic carbon fluxes into the deep sea (Rixen et al., 2000b). In the absence of upwelling, the marine productivity and the associated particle export from the surface ocean is linked to the interplay between the light penetration depth (euphotic zone) and vertical mixing regulating the availability of nutrients (Prahl et al., 2000; Rixen et al., 2002). Nutrient inputs via vertical mixing are considered to be the prime factor driving the organic carbon flux in the Bay of Bengal except during the late spring inter-monsoon and the late SW monsoon when upwelling along the Indian coast and riverine nutrient inputs increase the organic carbon fluxes into the deep Bay of Bengal (Ittekkot et al., 1991; Schäfer et al., 1996; Unger et al., 2003).

3 Methods

3.1 Sediment Trap

Since 1986, mark 6 and mark 7 sediment traps (Honjo and Doherty, 1988) have been deployed at water depths of approximately 3,000 m in the WAST (15°31′N 68°43′E; Fig. 1; Table 1). Sampling intervals were set between 12 and 26 days. Prior to the deployment, the sampling cups were filled with sea water collected at the mooring depth and enriched with sodium chloride ($35\,g\,l^{-1}$) and mercury (II) chloride ($3.3\,g\,l^{-1}$) to prevent degradation of trapped material (Lee et al., 1992). After recovery, the samples were sieved into greater and smaller than 1-mm fractions in order to separte large swimmers. The wet sample material was filtered on pre-weighed nuclepore filter (0.4 μm) and dried at 40°C. The dry weights of the smaller than 1 mm fraction were used for calculating the total fluxes and the material itself was

Table 1: Sampling period (SP), position, trap depth, water depth, deployment periods and mean sampling intervals

SP	Latitude (°N)	Longitude (°E)	Trap depth (m)	Water depth (m)	Deployment		Interval (Days)
					Start	End	
01	16°23′	60°32′	3,024	4,020	May 10, 1986	Oct. 26, 1986	13.0
02	16°18′	60°28′	3,021	4,018	Nov. 19, 1986	May 1, 1987	12.6
03	16°19′	60°28′	3,033	4,010	May 12, 1987	Oct. 21, 1987	12.5
04	16°35′	60°28′	3,039	4,016	Nov. 22, 1987	Oct. 31, 1988	26.5
05	16°24′	60°29′	3,029	4,016	Nov. 20, 1988	Sept. 28, 1989	24.0
06	16°19′	60°31′	3,016	4,013	Jan. 15, 1990	Oct. 15, 1990	21.0
07	16°20′	60°32′	3,039	4,027	Dec. 19, 1990	Oct. 26, 1991	24.0
08	16°19′	60°30′	3,030	4,018	Jan. 16, 1992	Dec. 16, 1992	26.0
09	16°20′	60°19′	2,002	4,018	Dec. 25, 1992	Oct. 11, 1993	23.0
10	16°20′	60°18′	3,041	4,025	Oct. 18, 1993	Oct. 05, 1994	27.0
11	16°13′	60°26′	3,246	4,230	Jan. 15, 1995	Oct. 03, 1995	12.0
13	16°13′	60°19′	3,007	4,041	Apr. 04, 1997	Feb. 02, 1998	12.0
14	15°50′	61°29′	2,991	4,020	May 27, 1998	Aug. 26, 1998	26.0

crushed prior to chemical analysis. Samples severely disturbed, e.g. by malfunctioning of the traps or the activity of swimmers, were ignored.

3.2 Chemical Analysis

Total carbon and nitrogen were determined with a Carlo Erba Nitrogen Analyzer 1500 that measures CO_2 and N_2 in a constant helium flow with a thermal conductivity detector after a catalytic high-temperature combustion of the sample. The reproducibility of the determined total carbon and nitrogen concentration is $\pm 0.05\%$ and $\pm 0.02\%$, respectively. Carbonate carbon concentration was derived from the conductivity change of a sodium hydroxide solution while injecting CO_2 released from the acid-treated sample. This method was performed with a Wösthoff Carmograph 6 and standard deviation of replicate measurements was $\pm 1\%$. The organic carbon concentration was calculated as the difference between total carbon and carbonate carbon concentration. Biogenic opal concentration was determined photometrically after extraction of silicon with a sodium carbonate solution (Mortlock and Froelich, 1989). A more detailed description of these methods is given by Haake et al. (1993). Nitrogen isotopic composition expressed as $\delta^{15}N$ was determined by a gas isotope mass spectrometer (Finnigan MAT 251) equipped with a trapping box and a Carlo Erba Nitrogen Analyzer 1500. The standard deviation of this method was $\pm 0.2\%$ (Schäfer and Ittekkot, 1995).

4 Results and Discussion

The first set of sediment trap data obtained from the Arabian Sea, covering the years 1986 and 1987, showed a strong monsoon-driven seasonality with enhanced fluxes during the NE and SW monsoon (Nair et al., 1989). The 10 years' records on deep ocean fluxes generated subsequently have further confirmed the strong monsoon-driven seasonality (Fig. 2a). In order to produce an average record covering the annual cycle, the time-series data have been converted into bi-weekly means (Fig. 2b). It may be noted that the $\delta^{15}N$ data are available only for the period between 1986 and 1992. The extended time series reveals that fluxes during the peak of the NE monsoon (January/February) can be as low as during the spring inter-monsoon in May (Fig. 2). In January/February, the mixed layer reaches its maximum depth and exceeds the depth of the euphotic zone (Dickey et al., 1998). Accordingly, deep mixing of photoautotrophic organisms initiating light-limiting conditions have been suggested as possible reason for the low organic carbon fluxes during the peak of the NE monsoon (Prahl et al., 2000; Rixen et al., 2002). The relatively high organic carbon fluxes during the early NE monsoon (November/December) correspond with the initial mixed-layer deepening.

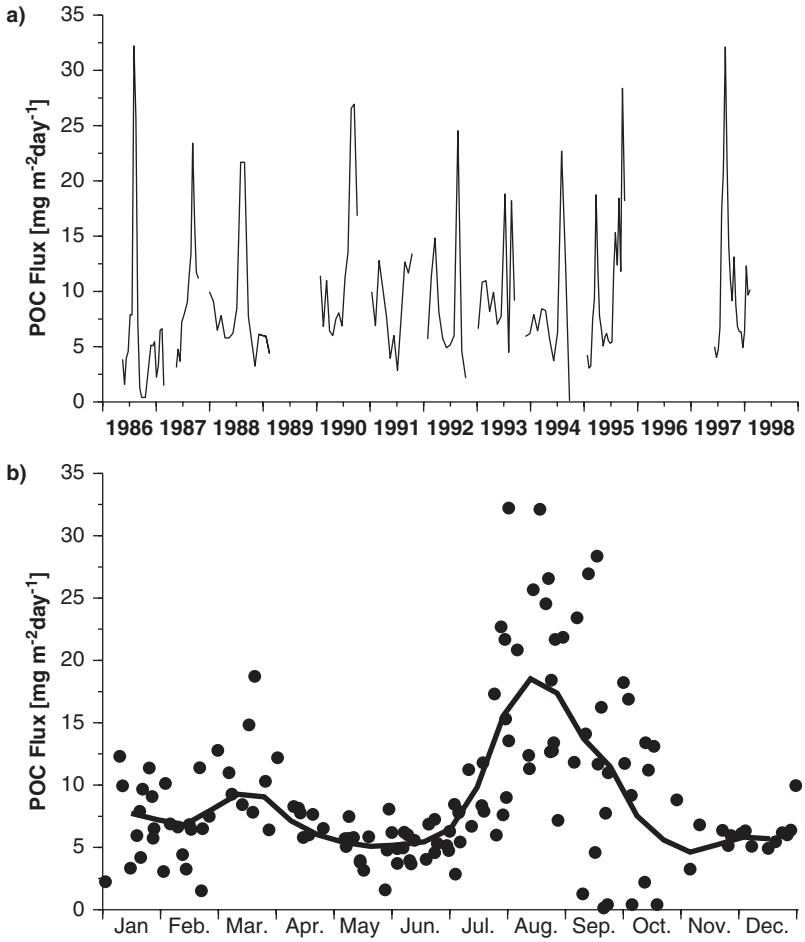

Figure 2: (a) Particulate organic carbon (POC) fluxes measured at 3,000-m water depth in the western Arabian Sea from 1986 to 1998. (b) Same POC fluxes plotted vs. the period of the year during which the sampling took place (black circle). The line indicates the mean bi-weekly POC fluxes during the year.

A second peak of organic carbon fluxes occurs in March/April (late NE monsoon) when the mixed layer shoals and approaches the depth of the euphotic zone (Rixen et al., 2002). Such an interplay between the depth of the mixed layer and the euphotic zone is known from parts of the north Atlantic where the shoaling of the deep winter mixed layer is associated with the development of the spring bloom and the deepening of the shallow summer mixed layer leading to the autumn bloom (Lalli and Parsons, 1993). In the western Arabian Sea, the organic carbon fluxes are higher during spring (late NE monsoon) than during the autumn (early NE monsoon; Fig. 2).

5 Factors Terminating Peak Fluxes during the Late NE and SW Monsoon

Within the framework of JGOFS, profiles of total inorganic nitrogen concentration ($TN = NO_3+NO_2+NH_4$) were measured along a transect from the Oman coast via the trap site WAST into the open southern Arabian Sea (Fig. 1). The TN concentrations averaged for the upper 20 m of the water column along the whole transect are enhanced during the upwelling season (3.6–6.6 $\mu mol\,l^{-1}$) and approach zero during the late NE monsoon (0.12 $\mu mol\,l^{-1}$, Fig. 3a). The mean $\delta^{15}N$ values of the sinking matter decrease during the upwelling season and increase during the late NE monsoon. Since photoautotrophic organisms prefer the uptake of the lighter ^{14}N in comparison to heavier ^{15}N, increasing $\delta^{15}N$ values could reflect nitrogen-limiting condition during plankton growth (Altabet and Francois, 1994). Consequently, increasing $\delta^{15}N$ values in addition to low-TN concentrations suggest a progressive consumption of TN leading to nitrogen-limiting conditions at the end of late NE monsoon. During the following oligotrophic spring inter-monsoon inputs of nitrogen via nitrogen fixation could terminate nitrogen-limiting conditions, but so far it has only been observed in the central and eastern Arabian Sea (Devassy et al., 1978; Capone et al., 1997). However, the decreasing $\delta^{15}N$ values in May/June seem to indicate inputs of recently fixed and thus isotopically light nitrogen that could in part sustain the biological production and the organic carbon export in the WAST (Fig. 3a). During the SW monsoon, decreasing $\delta^{15}N$ values in addition to high TN concentrations imply non-nitrogen limiting conditions, which in turn suggest other factors to be responsible for the decline of the upwelling-driven bloom in the western Arabian Sea.

During the SW and the late NE monsoon, low carbonate/biogenic opal ratios within the exported matter indicate an enhanced share of diatoms in the exported matter (Fig. 3b). Plankton counts during the SW monsoon 1995 and surface ocean nutrient concentrations along the Oman transect show a decline of the contribution of diatoms to the photoautotrophic organisms when the silicate concentration approaches 2 $\mu mol\,l^{-1}$ (Rixen et al., 2005). A silicate concentration of 2 $\mu mol\,l^{-1}$ was identified in other studies (Egge and Aksnes, 1992) as the threshold below which diatoms lose their ecological advantage over other plankton. The effect of nutrient concentration (N) on plankton growth rate (μ) is generally described by a Michaelis–Menton type of kinetics: $\mu = (\mu_{max} \times N)/(K_N+N)$, whereas μ_{max} is the maximum growth rate of plankton and 'K_N' is the half-saturation constant for nutrient uptake (Lalli and Parsons, 1993). This implies that plankton growth rates decrease ($\mu < \mu_{max}$) when the nutrient concentration drops below a certain threshold. The plankton bloom may be terminated when the plankton growth rates fall below the zooplankton grazing rates.

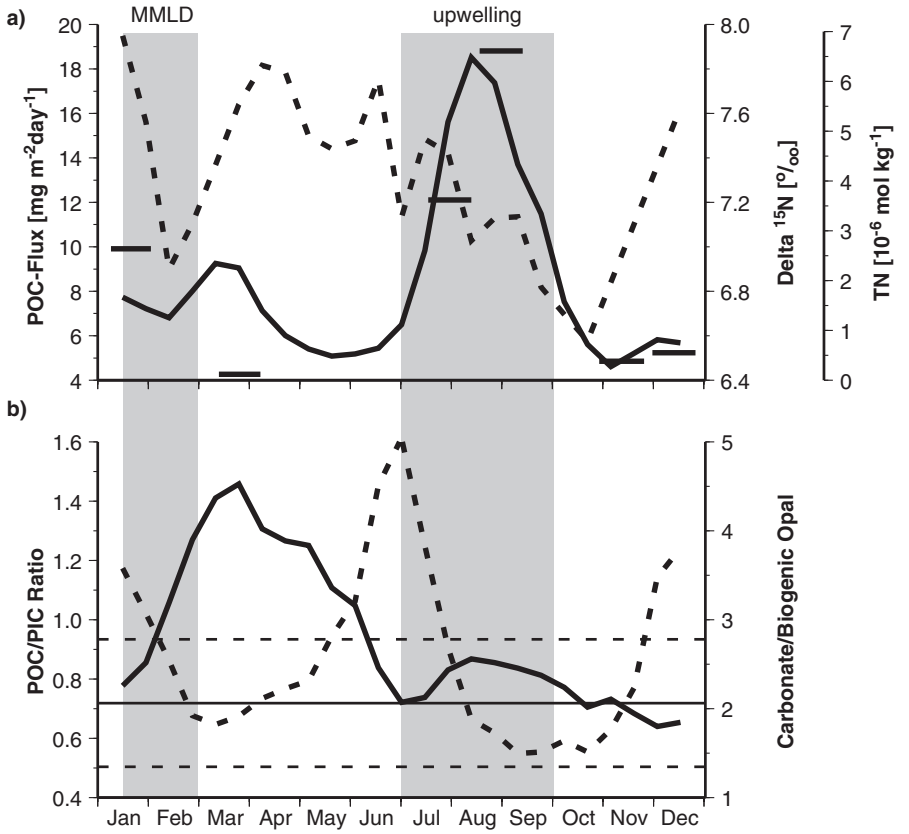

Figure 3: (a) Mean bi-weekly averaged organic carbon fluxes (bold line, see Fig. 2) and δ^{15}N values (broken line) at the station WAST. Mean total inorganic nitrogen (TN) concentrations in the surface water (water depth $<$20m) averaged along the Oman transect (see Fig. 1) for the six US JGOFS cruises ttn 43, 45, 49, 50, 53 and 54 (black horizontal lines; data are obtained from the US JGOFS database). (b) Bi-weekly averaged organic carbon to calcium carbonate carbon (POC/PIC) ratios (bold line) and carbonate to biogenic opal ratios (broken lines). Horizontal lines representing the mean (solid line) and the range (broken line) of POC/PIC ratios obtained from other sediment trap studies in the carbonate-dominated ocean (Klaas and Archer, 2002). The shaded area reveals the periods during which the mixed layer is deepest (MMLD; Dickey et al., 1998) and upwelling occurs along the Oman coast.

In order to study such a system, we developed a small numerical model in which a constant mixed-layer volume is assumed. Diatom growth and zooplankton grazing is calculated as μ (µmol h^{-1}) $= (15 \times N)/(1500+N)$, and grazing $= (20 \times Nd)/(200+Nd)$, respectively, where '$N$' is the silicate concentration in 'µmol l^{-1}'and 'Nd' the diatom biomass in 'µmol Si l^{-1}'. After digestion of soft tissue by zooplankton, biogenic opal (silica) shells are

assumed to be exported into the deep sea as faecal pellets. Owing to vertical mixing, the silica entrainment is set to 1.5 $\mu mol\,l^{-1}$ and upwelling raises the silica concentration to values of 14 $\mu mol\,l^{-1}$ at the coast. The velocity with which the upwelled water advects offshore was set to 0.6 $m\,s^{-1}$ (Rixen et al., 2000a). The model results agree quite well with observations (Fig. 4a, b) and imply that a diminishing diatom bloom can be caused by diatom growth rates falling below zooplankton growth rates when the silica concentration drops below approximately 6 $\mu mol\,l^{-1}$ (Fig. 4c). At silica concentration of 1–2 $\mu mol\,l^{-1}$, characteristic for the oligotrophic inter-monsoon season in the WAST (Rixen et al., 2005), the system reaches a steady state in which silica input via vertical mixing is balanced by biogenic opal export and the diatom growth rate equals the zooplankton grazing rate.

5.1 Seasonal Changes of POC/PIC Ratios

The particulate organic carbon/particulate inorganic carbon (POC/PIC) ratios determined in the sinking matter reveal a generally inverse relationship with carbonate/biogenic opal ratios (Fig. 3), which is in line with the assumption that diatoms out-compete carbonate-producing coccolithophorids (Harrison, 2000; Matsumoto and Sarmiento, 2002). Nevertheless, the POC/PIC ratios are higher by a factor of 1.7 during the late NE than during the SW monsoon although low carbonate/biogenic opal ratios indicate an enhanced contribution of diatoms to the exported matter during both seasons (Fig. 3b, Table 2). Accordingly, the exceptional high POC/PIC ratios during the late NE monsoon seem to be caused by an enhanced contribution of diatoms and additionally of organisms carrying no mineral skeleton. An enhanced share of such soft-tissued organisms to the exported matter explains also the POC/PIC and the carbonate/biogenic opal ratios, which are higher during the oligotrophic inter-monsoon in May and June than during the high-flux period of the SW monsoon. The elevated POC/PIC ratios during the late NE and spring inter-monsoon suggest that the biological pump is even more effective in sequestering atmospheric CO_2 in nitrogen-limited open ocean than in eutrophic systems.

5.2 Comparisons with Other Results from The Northern Indian Ocean

Since it is generally assumed that there are problems with the trapping efficiency at water depths of approximately $<1{,}200$ m (Scholten et al., 2005; Yu et al., 2001), sediment trap results obtained from shallower water depths were excluded from the following discussion. A comparison of sediment trap results obtained from the northern Indian Ocean shows the highest annual mean POC/PIC ratio in the northern Bay of Bengal (1.75; Fig. 5). Within the Bay of Bengal, the POC/PIC ratios decrease from north to south whereas an

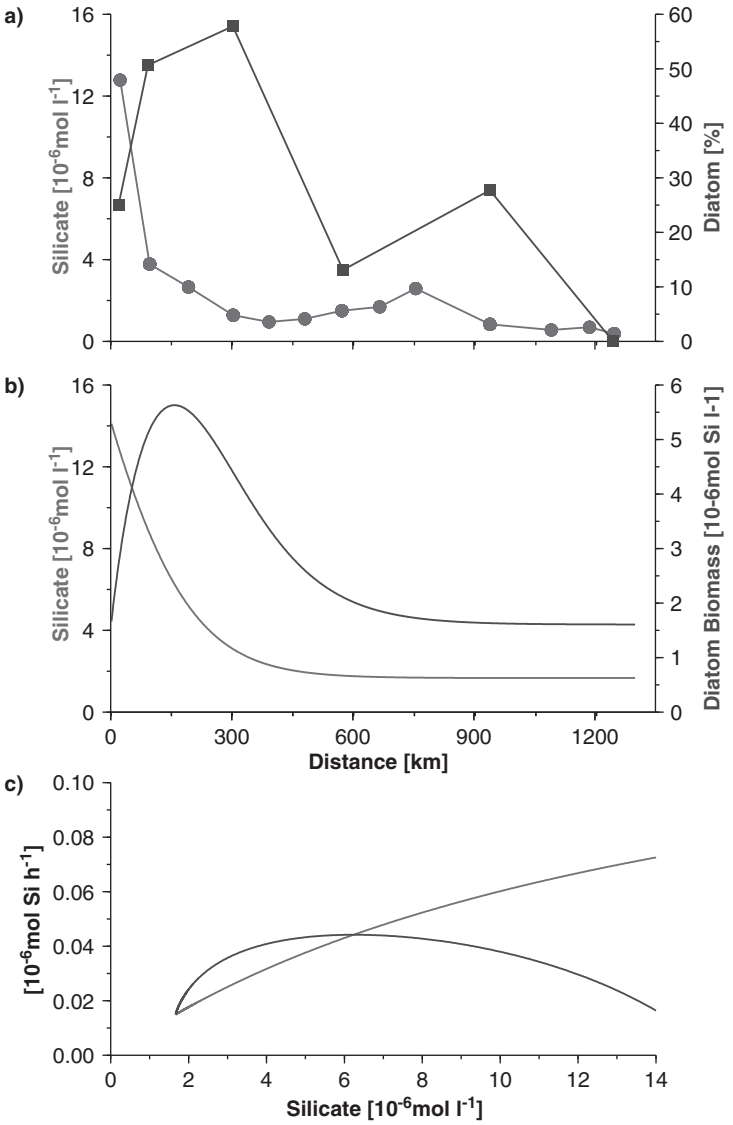

Figure 4: (a) Concentrations of silicate averaged for the upper 20 m of the water column along the transect from the Arabian coast towards the central and southern Arabian Sea, 1,300 km offshore during the SW monsoon of 1995 (compare Fig. 1). Nutrient data have been obtained from the US JGOFS datacentre. The blue line shows the contribution of diatoms to the biomass of photoautotrophic plankton during the same time (Garrison et al., 2000). (b) Diatom biomass (blue line) and silicate concentration derived from a box model that is described in the text. (c) Diatom growth rates (red line) and zooplankton grazing rates (blue line) vs. silicate concentration (data are derived from the model) (For colour version, see Colour Plate Section).

Table 2: Mean late NE and SW monsoon fluxes in the western Arabian Sea averaged for March (NE monsoon) and between July and September (SW monsoon)

Parameter	Late NE monsoon	SW monsoon
POC	9.15	14.41
PIC	6.38	17.38
Carbonate	53.16	144.80
Biogenic opal	28.48	74.79
Carbonate/biogenic opal	1.87	1.94
POC/PIC	1.43	0.83

Note: Units are '$mg\,m^{-2}\,day^{-1}$' except for the ratios that are dimensionless. PIC flux = Carbonate flux × 0.12.

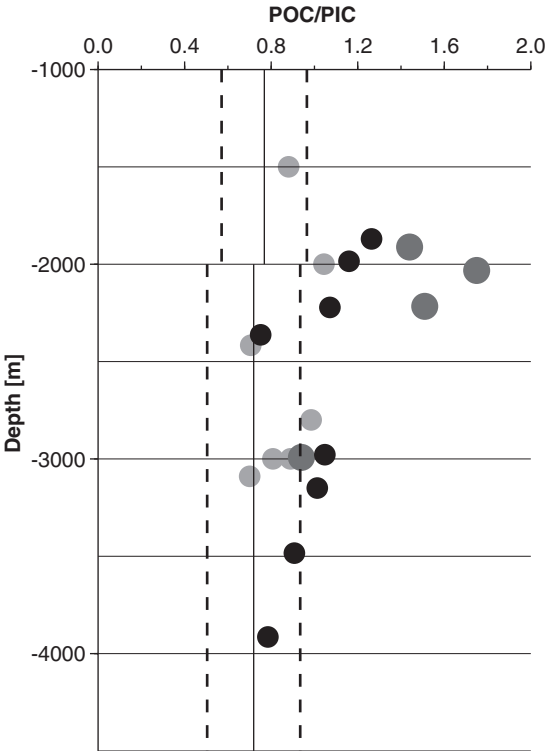

Figure 5: Annual mean POC/PIC ratios vs. water depth. Black circles show results obtained from the US JGOFS sediment trap experiment performed in 1994/1995 (Honjo et al., 1999; Lee et al., 2000), grey circles reveal data derived from the Indo/German sediment trap program in the Arabian Sea (Fig. 1) and those obtained from the Bay of Bengal (Unger et al., 2003) are given in red. Vertical lines representing the mean (solid line) and the range (broken line) of POC/PIC ratios obtained from other sediment trap studies in the carbonate-dominated ocean (Klaas and Archer, 2002) (For colour version, see Colour Plate Section).

increasing salinity in the same direction shows diminishing influence of freshwater in the Bay of Bengal (Fig. 1). Accordingly, it was suggested that river discharges, which are the main marine silica sources (Tréguer et al., 1995), enhance the efficiency of the biological pump by supplying silica from terrestrial sources (Ittekkot et al., 1991).

During the sediment trap experiment in the northern Bay of Bengal, the sampling site was shifted by approximately 2° to the south between 1990 and 1992 because of logistical reasons (Unger et al., 2003). Results from these trap sites were used to fill gaps within the record from the northern site leading to a time series that covers approximately 7 years. The POC/PIC ratios derived from the combined time series shows an inter-annual variation of ±16% exceeding those in the WAST (approximately ±10%). In the northern Bay of Bengal, the highest annual mean POC/PIC ratio was determined in year 1988 (2.15) and the lowest in year 1997 (1.52). The southern oscillation index (SOI: http://www.cpc.ncep.noaa.gov) shows strong La Niña and El Niño conditions during the SW monsoon between (June–September) 1988 and 1997, respectively (Fig. 6). El Niño southern oscillation (ENSO) could, for example, affect the POC/PIC ratios in the northern Bay of Bengal via its influence on precipitation rates in the catchment area

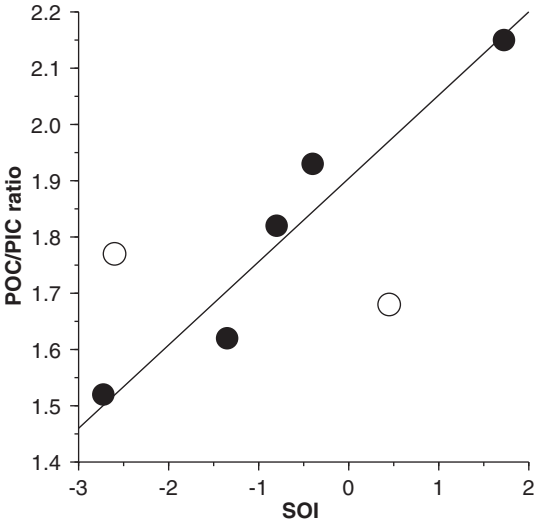

Figure 6: Annual mean POC/PIC ratios obtained from the northern Bay of Bengal at 2,000 m water depth vs. southern oscillation index averaged for the SW monsoon periods of the same year. Sediment trap data are available for years 1988, 1989, 1990, 1991, 1992, 1994 and 1997 (Unger et al., 2003). The open circles indicate the years 1989 and 1994. The solid line represents the regression equation (POC/PIC = 0.15 × SOI+1.91) that excludes the years 1989 and 1994.

of the Ganges–Brahmaputra (Ropelewski and Halpert, 1987) and consequently on the river discharges. Nevertheless, there are 2 years (1989 and 1994) that do not fit into the correlation between the POC/PIC ratios and the SOI (Fig. 6). These exceptions point to other factors of relevance masking the link between ENSO and the efficiency of the biological pump during some years in the Bay of Bengal.

6 Conclusion

The peak organic carbon fluxes in the WAST are driven by upwelling during the SW monsoon and by shoaling of the deep winter mixed layer during the late NE monsoon in March. Although carbonate biogenic opal ratios indicate an enhanced contribution of diatoms to the exported matter during both periods, diatoms seem to dominate the SW monsoon bloom that probably is terminated by the lack of silica. Despite an enhanced share of diatoms to the exported matter, the late NE monsoon bloom appears to be dominated by soft-tissued organisms initiating nitrogen-limiting conditions. The biological pump seems to be more efficient in sequestering CO_2 in nitrogen-limiting open ocean systems than in eutrophic diatom-dominated upwelling systems as indicated by POC/PIC ratios. The highest POC/PIC ratios have been measured in the Bay of Bengal where riverine silica discharges favour diatom blooms. ENSO-influenced riverine silica inputs lead to a more efficient biological pump during stronger La Niña years and vice versa to a weaker biological pump during stronger El Niño years.

Acknowledgements

We thank all scientists, technicians and officers and their crews of the numerous research vessels as well as the national funding agencies who made the Joint Indo/German and the Joint Global Ocean Flux Study possible. Particularly, we thank B. Gaye–Hakke, D. Unger and S.W.A. Naqvi for helpful discussions and the US JGOFS database for providing nutrient data. Furthermore, we are grateful to the Federal German Ministry for Education, Science, Research and Technology (BMBF, Bonn), for financial support of JGOFS-Indik. P. Wessels and W.H.F. Smith are acknowledged for providing the generic mapping tools (GMT).

References

Altabet, M. A., Francois, R., 1994. Sedimentary nitrogen isotopic ratio as a recorder for surface ocean nitrate utilization. Global Biogeochemical Cycles 8 (1), 103–116.

Antoine, D., André, J.-M., Morel, A., 1996. Oceanic primary production – 2. Estimation at global scale from satellite (coastal zone color scanner) chlorophyll. Global Biogeochemical Cycles 10 (1), 57–69.

Archer, D., Winguth, A. M. E., Lea, D., Mahowald, N., 2000. What caused the glacial/interglacial atmospheric pCO_2 cycles?. Reviews of Geophysics 38 (2), 159–189.

Berger, W. H., Keir, R. S., 1984. Glacial–Holocene changes in atmospheric CO_2 and the deep-sea record. In: Hansen, J. E., Takahashi, T. (Eds.), Climate Processes and Climates Sensitivity. American Geophysical Union, Washington, pp. 337–351.

Capone, D. G., Subramaniam, A., Montoya, J. P., Voss, M., Humborg, C., Johansen, A. M., Siefert, R. L., Carpenter, E. J., 1997. An extensive bloom of the N_2-fixing cyanobacterium *Trichodesmium erythraeum* in the central Arabian Sea. Marine Ecology Progress Series 172, 281–292.

Conley, D. J., 2002. Terrestrial ecosystems and the biogeochemical silica cycle. Global Biogeochemical Cycles 16 (4), 68-1–68-8.

Currie, R. I., Fisher, A. E., Hargreaves, P. M., 1973. Arabian Sea Upwelling, Biology of the Indian Ocean. Springer-Verlag, New York, pp.39–52.

Devassy, V. P., Bhattathiri, P. M. A., Qasim, S. Z., 1978. *Trichodesmium* phenomenon. Indian Journal of Marine Sciences 7, 168–186.

Dickey, T., Marra, J., Sigurdson, D. E., Weller, R. A., Kinkade, C. S., Zedler, S. E., Wiggert, J. D., Langdon, C., 1998. Seasonal variability of bio-optical and physical properties in the Arabian Sea: October 1994–October 1995. Deep Sea Research II 45, 2001–2025.

Egge, J. K., Aksnes, D. L., 1992. Silicate as regulating nutrient in phytoplankton competition. Marine Ecology Progress Series 83, 281–289.

Findlater, J., 1977. Observational aspects of the low-level cross-equatorial jet stream of the western Indian Ocean. Pure and Applied Geophysics 115, 1251–1262.

Froelich, P. N., Blanc, V., Mortlock, R. A., Chillrud, S. N., 1992. River fluxes of dissolved silica to the ocean were higher during glacials: Ge/Si in diatoms, rivers, and oceans. Paleoceanography 7 (6), 739–767.

Garrison, D. L., Gowing, M. M., Hughes, M. P., Campbell, L., Caron, D. A., Dennett, M. R., Shalapyonok, A., Olson, R. J., Landry, M. R., Brown, S. L., 2000. Microbial food web structure in the Arabian Sea: a US JGOFS study. Deep Sea Research II 47, 1387–1422.

Haake, B., Ittekkot, V., Rixen, T., Ramaswamy, V., Nair, R. R., Curry, W. B., 1993. Seasonality and interannual variability of particle fluxes to the deep Arabian Sea. Deep Sea Research I 40, 1323–1344.

Harrison, K. G., 2000. Role of increased marine silica input on paleo-pCO_2 levels. Paleoceanography 15 (3), 292–298.

Heinze, C., Maier-Reimer, E., Winn, K., 1991. Glacial pCO_2 reduction by the world ocean: experiments with the Hamburg Carbon Cycle Model. Paleoceanography 6 (4), 395–430.

Honjo, S., Doherty, K. W., 1988. Large aperture time-series sediment traps; design objectives, construction and application. Deep Sea Research 35 (1), 133–149.

Honjo, S., Dymond, J., Prell, W., Ittekkot, V., 1999. Monsoon-controlled export fluxes to the interior of the Arabian Sea. Deep Sea Research II 46 (8–9), 1859–1902.

Ittekkot, V., Nair, R. R., Honjo, S., Ramaswamy, V., Bartsch, M., Manganini, S., Desai, B. N., 1991. Enhanced particle fluxes in Bay of Bengal induced by injection of fresh water. Nature 351, 385–387.

Klaas, C., Archer, D. E., 2002. Association of sinking organic matter with various types of mineral ballast in the deep sea: Implications for the rain ratio. Global Biogeochemical Cycles 16, doi:10.1029/2001GB001765.

Lalli, C. M., Parsons, T. R., 1993. Biological Oceanography: An Introduction. Pergamon Press, Oxford, p. 301.

Lee, C., Hedges, J. I., Wakeham, S. G., Zhu, N., 1992. Effectiveness of various treatments in retarding microbial activity in sediment trap material and their effects on the collection of swimmers. Limnology and Oceanography 37 (1), 117–130.

Lee, C., Murray, D. W., Barber, R. T., Buesseler, K. O., Dymond, J., Hedges, J. I., Honjo, S., Manganini, S. J., Marra, J., 1998. Particulate organic carbon fluxes: compilation of results from the 1995 US JGOFS Arabian Sea Process Study. Deep Sea Research II 45, 2489–2501.

Lee, C., Wakeham, S. G., Hedges, J. I., 2000. Composition and flux of particulate amino acids and chloropigments in equatorial Pacific seawater and sediments. Deep Sea Research Part I: Oceanographic Research Papers 47 (8), 1535–1568.

Ludwig, W., Probst, J.-L., 1996. Predicting the oceanic input of organic carbon by continental erosion. Global Biogeochemical Cycles 10 (1), 23–41.

Matsumoto, K., Sarmiento, J. L., 2002. Silicic acid leakage from the southern ocean: a possible explanation for glacial atmospheric pCO_2. Global Biogeochemical Cycles 16 (3), 5-1–5-23.

Milliman, J. D., Meade, R. H., 1983. World-wide delivery of river sediment to the oceans. The Journal of Geology 91 (1), 1–21.

Milliman, J. D., Quraishee, G. S., Beg, M. A. A., 1984. Sediment discharge from the Indus River to the ocean: past, present and future. In: Haq, B. U., Milliman, J. D. (Eds.), Marine Geology and Oceanography of Arabian Sea and Coastal Pakistan. Van Nostrand Reinhold Company Scientific and Academic Editions, New York, pp. 65–70.

Mortlock, R. A., Froelich, P. N., 1989. A simple method for the rapid determination of biogenic opal in pelagic marine sediments. Deep Sea Research 36 (9), 1415–1426.

Nair, R. R., Ittekkot, V., Manganini, S. J., Ramaswamy, V., Haake, B., Degens, E. T., Desai, B. N., Honjo, S., 1989. Increased particle flux to the deep ocean related to monsoons. Nature 338, 749–751.

Prahl, F. G., Dymond, J., Sparrow, M. A., 2000. Annual biomarker record for export production in the central Arabian Sea. Deep Sea Research II 47 (7–8), 1581–1604.

Ramage, C. S., 1971. Monsoon Meteorology. Academic Press, New York, London.

Ramage, C. S., 1987. Monsoon Climates. In: Oliver, J. E., Fairbridge, R. W. (Eds.), The Encyclopedia of Climatology. Van Nostrand Reinhold Company, New York.

Ramesh Kumar, M. R., Prasad, T. G., 1997. Annual and interannual variation of precipitation over the tropical Indian Ocean. Journal of Geophysical Research 102 (C8), 18519–18527.

Ramesh Kumar, M. R., Schlüssel, P., 1998. Air–sea interaction over the Indian Ocean during the two contrasting monsoon years 1987 and 1988 studied with satellite data. Theoritical and Applied Climatology 60, 219–231.

Rixen, T., Guptha, M. V. S., Ittekkot, V., 2002. Sedimentation. In: Watts, L., Burkill, P. H., Smith, S. (Eds.), Report of the Indian Ocean Synthesis Group on the Arabian Sea Process Study. JGOFS International Project Office, Bergen, pp. 65–73.

Rixen, T., Guptha, M. V. S., Ittekkot, V., 2005. Deep ocean fluxes and their link to surface ocean processes and the biological pump. Progress in Oceanography 65, 240–259.

Rixen, T., Haake, B., Ittekkot, V., Guptha, M. V. S., Nair, R. R., Schlüssel, P., 1996. Coupling between SW monsoon-related surface and deep ocean processes as discerned from continuous particle flux meausurements and correlated satellite data. Journal of Geophysical Research 101, 28569–28582.

Rixen, T., Haake, B., Ittekkot, V., 2000a. Sedimentation in the western Arabian Sea: the role of coastal and open-ocean upwelling. Deep Sea Research II 47, 2155–2178.

Rixen, T., Ittekkot, V., Haake-Gaye, B., Schäfer, P., 2000b. The influence of the SW monsoon on the deep-sea organic carbon cycle in the Holocene. Deep Sea Research II 47, 2629–2651.

Ropelewski, C. F., Halpert, M. S., 1987. Global and regional scale precipitation patterns associated with El Niño/southern oscillation. Monthly Weather Review 115, 1606–1626.

Schäfer, P., Ittekkot, V., 1995. Isotopic biogeochemistry of nitrogen in the northern Indian Ocean. Mitteilungen aus dem Geologisch-Paläontologischen Institut der Universität Hamburg 78, 67–93.

Schäfer, P., Ittekkot, V., Bartsch, M., Nair, R. R., Tiemann, J., 1996. Fresh water influx and particle flux variability in the Bay of Bengal. In: Ittekkot, V., Schafer, P., Honjo, S., Depetris, P. J. (Eds.), Particle Flux in the Ocean. John Wiley & Sons, Chichester, pp. 271–292.

Scholten, J., Fietzke, J., Mangini, A., Stoffers, P., Rixen, T., Gaye-Haake, B., Blanz, T., Ramaswamy, V., Sirocko, F., Schulz, H., Ittekkot, V., 2005.

Radionuclide fluxes in the Arabian Sea: the role of particle composition. Earth and Planetary Science Letters 230, 319–337.

Subramanian, V., Richey, J. E., Abbas, N., 1985. Geochemistry of river basins of India Part II – Preliminary studies on the particulate C and N in the Ganges–Brahmaputra river system. Mitteilungen aus dem Geologisch-Paläontologischen Institut der Universität Hamburg 58, 513–518.

Tréguer, P., Nelson, D. M., Van Bennekom, A. J., DeMaster, D. J., Leynaert, A., Queguiner, B., 1995. The silica balance in the world ocean: A reestimate. Science 268, 375–379.

Unger, D., Ittekkot, V., Schafer, P., Tiemann, J., Reschke, S., 2003. Seasonality and interannual variability of particle fluxes to the deep Bay of Bengal: Influence of riverine input and oceanographic processes. Deep Sea Research Part II: Topical Studies in Oceanography 50 (5), 897–923.

Volk, T., Hoffert, M. I., 1985. The carbon cycle and atmospheric CO_2, natural variation archean to present. In: Sundquits, E. T., Broecker, W. S. (Eds.), The carbon cycle and Atmospheric CO_2: Natural variations Archean to present, AGU, Washington, pp. 99–110.

Yu, E.-F., Francois, R., Bacon, M. P., Honjo, S., Fleer, A. P., Manganini, S. J., Rutgers van der Loeff, M. M., Ittekkot, V., 2001. Trapping efficiency of bottom-tethered sediment traps estimated from the intercepted fluxes of ^{230}Th and ^{231}Pa. Deep Sea Research I 48, 865–889.

Zeebe, R. E., Wolf-Gladrow, D., 2001. CO_2 in Seawater: equilibrium, Kinetics, Isotopes. Elsevier Oceanography Series, 65. Elsevier Science B.V., Amsterdam, p. 346.

Chapter 8

Variability of the Indonesian Throughflow: A Review and Model-to-Data Comparison

Andreas Schiller[1,*], Susan E. Wijffels[1] and Janet Sprintall[2]

[1]*CSIRO Marine and Atmospheric Research, Hobart, TAS 7001, Australia*
[2]*Scripps Institution of Oceanography, La Jolla, CA 92093-0230, USA*

Abstract

Existing observations of ocean temperature, sea level and transport within the Indonesian seas and south-east Indian Ocean are reviewed and compared with a simulation. The dynamical mechanisms by which the Indonesian Throughflow (ITF) interacts with the surrounding oceans in the model and real oceans are discussed. The focus is on the variability on timescales ranging from the intraseasonal (<3 months) to the interannual (a few years). A lagged multiple regression technique is applied to anomalies of sea level from a mean seasonal cycle for observed and modeled fields. The results reveal that the region comprises the intersection of two ocean wave guides where sea level and upper ocean temperature anomalies can be largely understood in terms of Kelvin and Rossby waves generated by remote zonal winds along the Indian and Pacific equators, with local wind forcing appearing to play a minor role in generating interannual variability. Variations in zonal Pacific equatorial winds force a response along the Arafura/Australian shelf break through Pacific equatorial Rossby waves exciting coastally trapped waves off the western tip of Irian Jaya, which propagate westward into the Banda Sea and poleward along the Australian west coast. Equatorial Kelvin waves excited by Indian Ocean winds propagate eastward and scatter into coastal waves along the Sumatra–Java–Lesser Sunda coasts to penetrate the western internal seas of Indonesia. While the model captures the variability generated by the equatorial Indian Ocean winds, its pathway eastward into the Indonesian region is prevented by a dynamically

*Corresponding author.
E-mail address: andreas.schiller@csiro.au (A. Schiller).

Elsevier Oceanography Series 73
Edited by H. Kawahata and Y. Awaya
ISBN: 0-444-52948-9

"wide" Lombok Strait, which carries too much of the main throughflow and allows too little wave energy to pass directly into the Banda Sea. The model response to El Nino-southern oscillation (ENSO) wind changes is too weak as expressed by its sea-level response in the western Pacific. The subsequent transmission of this ENSO signal into the ITF region and along the west coast of Australia is also much weaker in the model than observed. Generally, the model/data comparisons suggest that too little energy gets scattered into the model coastal wave guide. An assessment of whether this difference is a model resolution or model dissipation issue (and they are related) needs further work.

Keywords: Indonesian throughflow; model-to-data comparison; climate variability

1 Introduction

The Indonesian Throughflow (ITF) is an integral part of the global thermohaline circulation and climate system (see Gordon, 2001; Sprintall et al., 2001 for recent overviews), providing a low-latitude pathway for the transfer of warm, low-salinity Pacific waters into the Indian Ocean. The heat and freshwater carried by the ITF impacts the basin budgets of both the Pacific and the Indian Oceans (Bryden and Imawaki, 2001; Wajsowicz and Schneider, 2001; Wijffels et al., 2001). Within the internal Indonesian seas, observations and models indicate that the primary ITF source is north Pacific thermocline water flowing through Makassar Strait (sill depth 650 m) (Fig. 1). Additional ITF contributions of lower thermocline water and deep water masses of direct south Pacific origin are derived through the eastern routes, via the Maluku and Halmahera Seas, with dense water overflow at the Lifamatola Passage (sill depth 1,940 m). The ITF exits into the eastern Indian Ocean through the major passages along the Lesser Sunda Island chain: Ombai Strait (sill depth 3,250 m), Lombok Strait (300 m), and Timor Passage (1,890 m). The complex geography of the region, with multiple narrow constrictions connecting a series of large, deep basins, leads to a circuitous ITF pathway within the Indonesian seas. En route, the Pacific inflow waters are modified due to mixing, upwelling, and air−sea fluxes before export to the Indian Ocean.

In recent years, a number of monitoring programs have measured aspects of the ITF from its Pacific source, through the internal seas, to the exit passages. The programs range from individual year-long mooring deployments in Makassar, Timor, and Ombai Straits, a 3-year shallow pressure gauge array (SPGA) in the exit passages, to decade long expendable bathythermograph (XBT) transects within the Indonesian region and five full-depth hydrographic CTD/ADCP sections between Australia and Indonesia.

In Section 2, we detail the progress toward understanding the mean and time-dependent throughflow dynamics made to date from these recent observations, and discuss some of the still outstanding issues toward a

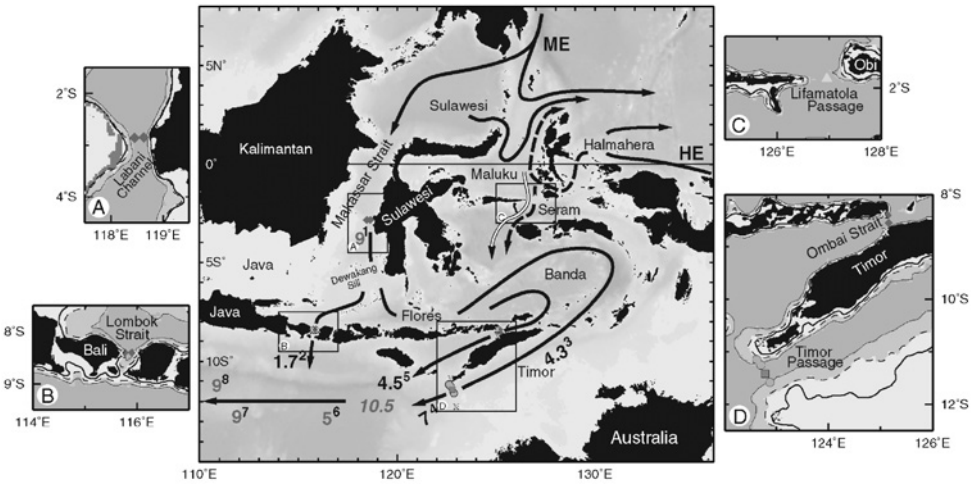

Figure 1: Schematic of Indonesian throughflow pathways (Gordon, 2001; reprinted with permission from Elsevier). The solid arrows represent north Pacific thermocline water; the dashed arrows are south Pacific lower thermocline water. Transports in Sv (10^6 m^3/s) are given in red. The 10.5 Sv in italics is the sum of the flows through the Lesser Sunda passages. ME is the Mindanao Eddy; HE is the Halmahera Eddy. Superscript refers to reference source: 1, Makassar Strait transport in 1997 (Gordon et al., 1999); 2, Lombok Strait (Murray and Arief, 1988; Murray et al., 1990) from January 1985 to January 1986; 3, Timor Passage (between Timor and Australia) measured from March 1992 to April 1993 (Molcard et al., 1996); 4, Timor Passage, between October 1987 and March 1988 (Cresswell et al., 1993); 5, Ombai Strait (north of Timor, between Timor and Alor Island) from December 1995 to December 1996 (Molcard et al., 2001); 6, between Java and Australia from 1983 to 1989 XBT data (Meyers et al., 1995; Meyers, 1996); 7, Upper 470 m of the South Equatorial Current in the eastern Indian Ocean in October 1987 (Quadfasel et al., 1996); 8, Average ITF within the South Equatorial Current defined by five WOCE WHP sections (Gordon et al., 1997). The hollow arrow represents overflow of dense Pacific water across the Lifamatola Passage into the deep Banda Sea, which may amount to about 1 Sv (van Aken et al., 1988). Inserts A–D show the positions of the INSTANT moorings. Insert A: position of the two Makassar Strait inflow moorings (US, red diamond) within Labani Channel. Insert C: position of the Netherland's mooring within the main channel of Lifamatola Passage (yellow triangle). Insert B, D: position of the Sunda moorings in Ombai Strait, Lombok strait, and Timor Passage (US, red diamonds; French, purple square; Australian, green circles). The positions of the shallow pressure gauge array (SPGA) (US, green X). The 100, 500, and 1,000 m isobaths are shown in the inserts (For colour version, see Colour Plate Section).

comprehensive understanding of the dynamics of the ITF and its associated property fluxes. Historic data from moorings, pressure gauges and other stationary measurement systems suggest that large-scale and remotely forced wave interactions play an important role in the dynamics of the ITF. After a brief description in Section 3 of the model and data used here, the large-scale wave dynamics is explored in more detail in Section 4. We compare observed and simulated temperature responses to remote and local wind forcing within the Indonesian region. Section 5 contains a discussion and the conclusions.

2 Velocity and Property Structure of the Throughflow

2.1 Observed Transports through Major Straits of the Indonesian Throughflow

Large-scale observation-based studies (including inverse solutions) reveal significant Pacific export of mass, heat, and freshwater into the Indian Ocean (Piola and Gordon, 1984, 1986; Toole and Raymer, 1985; Wijffels et al., 1992; Toole and Warren, 1993; MacDonald and Wunsch, 1996; Ganachaud et al., 2000; Ganachaud and Wunsch, 2000). The uncertainty in the size of such a warm, fresh throughflow is the dominant source of error in analyses of the basin-wide budgets of heat and freshwater for the Pacific (Wijffels et al., 2001) and Indian Oceans (Robbins and Toole, 1997). Model research reveals dependence of Pacific and Indian Ocean sea-surface temperature (SST) and upper layer heat storage on the throughflow (Hirst and Godfrey, 1993; Verschell et al., 1995; Murtugudde et al., 1998). The Indian and Pacific Oceans would be very different if the ITF were zero (Hirst and Godfrey, 1993, 1994;Maes, 1998; Schneider, 1998; Wajsowicz and Schneider, 2001). Oceanic heat and freshwater fluxes into the Indian Ocean – at the expense of the Pacific – affect atmosphere–ocean coupling with potential impacts on the El Nino-Southern Oscillation (ENSO) and monsoon phenomena (Webster et al. 1998). Saji et al. (1999) found that the cool SST anomalies that lead to a dipole mode of variability in the tropical Indian Ocean first appeared in the vicinity of Lombok Strait in Indonesia. The cold SST anomaly shifts westward as a Rossby wave from the Java and Sumatra Indian Ocean coasts and varies in strength with the phase of ENSO (Susanto et al., 2001).

The ITF source water (North Pacific vs. South Pacific) depends upon land geometry and the tropical Pacific wind fields (Godfrey, 1989; Nof, 1996; Morey et al., 1999; Wajsowicz, 1999; Cane and Molnar, 2001). Observations show that the ITF is composed mostly of North Pacific water flowing through Makassar Strait (Fig. 2; Fine, 1985; Ffield and Gordon, 1992; Gordon, 1995;

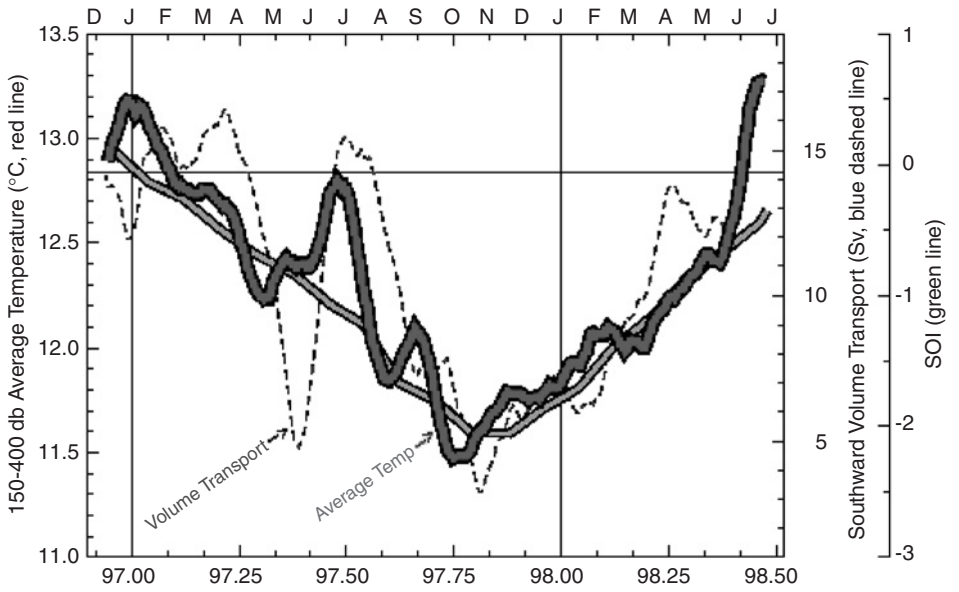

Figure 2: (a) Time series (above) of the average temperature (red) between 150 and 400 db at the MAK-1 mooring (Ffield et al., 2000). The SOI (green) and the Makassar Strait volume transport (blue dashed) are also shown. The data are smoothed by 30-day running averages. (b) Temperature time section constructed from 15 years of Makassar Strait and Flores Sea XBT profiles (Ffield, 2000, personal communication). In the upper panel, the depth of the 22°C XBT isotherm (red) is shown with the SOI (black) highlighting the clear ENSO variability in the XBT temperature data. The data are smoothed by a 1-year running average (For colour version, see Colour Plate Section).

Gordon and Fine, 1996), which is consistent with theory (Wajsowicz, 1996). The 1997 average southward transport in Makassar Strait is 9.3 ± 2.5 Sv, with the highest southward flow occurring at mid to lower thermocline depths (Gordon and Susanto, 1999; Gordon et al., 1999). Warming between the inflow at Makassar and the export into the Indian Ocean is likely a consequence of the impact of mixing and air–sea fluxes within the internal Indonesian seas. While some of the Makassar throughflow exits the Indonesian sea within Lombok Channel (Murray and Arief, 1988), most turns eastward within the Flores Sea to enter the Banda Sea before entering the Indian Ocean via the deeper Ombai Strait and Timor Passage (Meyers et al., 1995; Gordon and Fine, 1996).

The flow in Lombok Strait is well documented, largely due to the Lombok Strait experiment in 1985 (Murray and Arief, 1988; Murray et al., 1990). Flow through the 35-km wide Lombok Strait is restricted by a sill depth of about 300 m at the southern end. From February through May,

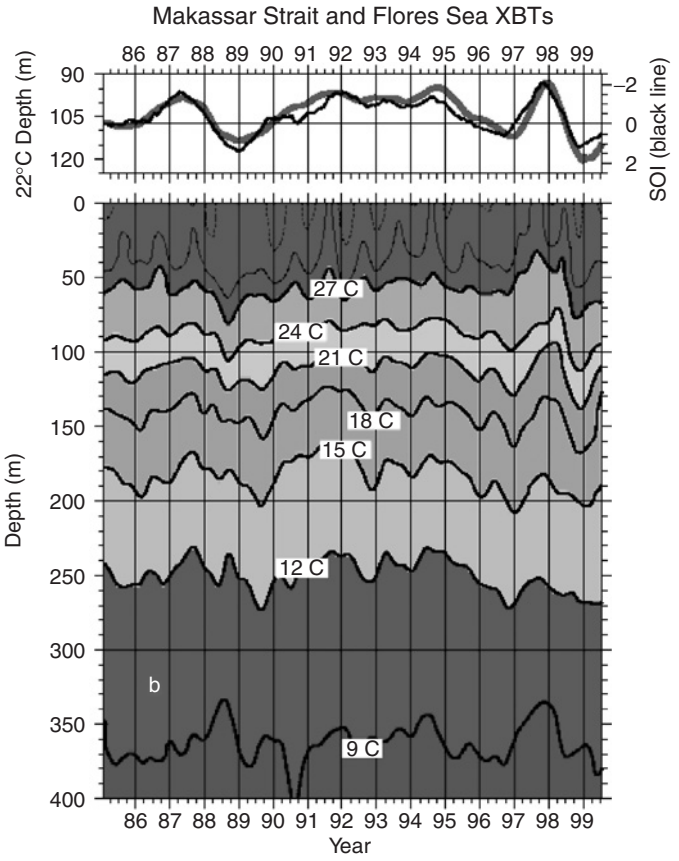

Figure 2 Continued (For colour version, see Colour Plate Section).

transport through Lombok Strait was only 1 Sv southward due to discrete occasions of shallow northward flow, compared to the 4 Sv observed during the southeast monsoon from July through September (Murray and Arief, 1988). Similar periods of northward transport are inferred from changes in the cross-strait pressure gradient measured by the shallow pressure gauges deployed across Lombok Strait from 1996 to 1999 (Hautala et al., 2001). The flow reversals observed in Lombok Strait are likely to be related to the passing of Kelvin waves, forced in the equatorial Indian Ocean (Sprintall et al., 1999, 2000).

Ombai Strait lies between Alor and Timor Islands, and connects the Banda Sea with the Savu Sea (Fig. 1). The strait is 30-km wide, and a recent bathymetric survey by Molcard et al. (2001) suggests a sill depth of 3,250 m. From a single mooring in Ombai Strait, Molcard et al. (2001) suggest a transport range between 4.3 Sv and 5.8 Sv, depending on the

assumed cross-strait shear, with 0.9–1.2 Sv average transport in the upper 100 m.

The Timor Passage is a long, narrow trench that lies between the southeast-oriented coast of Timor and the northern edge of the wide, shallow northwest Australian coastal shelf (Fig. 1). The easternmost sill connecting the Timor Passage with the Banda Sea is 1,250 m, shallower than the 1,890 m western sill connecting the trench with the southeast Indian Ocean. Deployment of two year-long moorings across the western sill have been undertaken on two occasions by the French: a total westward transport of 4.5 ± 1.5 Sv from 120 to 1,050 m in August 1989–September 1990 (Molcard et al., 1994); and 4.3 ± 1 Sv westward from 0 to 1,250 m in March 1992–April 1993 (Molcard et al., 1996). An ADCP repeat survey of Timor Passage in December 1995 (Hautala et al., 2001) suggests that the high-velocity surface core of the throughflow may extend further south than what the Molcard et al. (1996) extrapolation allowed for, which would lead to a much higher total transport through Timor Passage.

2.2 Intraseasonal-to-Interannual Characteristics of the ITF Transport and Property Fluxes

The recent measurements around the Indonesian archipelago revealed an unanticipated richness in the timescales of throughflow variability, from intraseasonal (40–60 days) to interannual (El Niño). The different timescales are evident in all the transport and property fluxes and are likely the result of remote forcing by both the Pacific and Indian Ocean winds, and local forcing within the regional Indonesian seas. Earlier estimates of the mean throughflow were wide ranging (2–22 Sv; Godfrey, 1996) in part because of not only the lack of direct estimates, but also the real variation that can severely alias estimates of the mean if survey periods are not long enough. In fact, the recent estimates from the time series measurements suggest a Makassar Strait inflow transport of 9.3 Sv that is comparable to the transport sum of 10.5 Sv through the passages of the Lesser Sunda Island chain (Fig. 1). However, these mean ITF estimates should be interpreted with some caution as the time series were made at different times and at different periods of the ENSO phase: the Makassar moorings in 1997–1998; the Ombai mooring in 1996; the Timor Passage in 1989–1990 and 1992–1993; and the Lombok Strait in 1985.

Annual changes in the ITF arise from the directionally varying winds associated with the regional monsoon system. During the northwest monsoon from December through March, surface waters flow into the Banda Sea (Wyrtki, 1987), with Ekman downwelling reaching a maximum in February (Gordon and Susanto, 2001). The flow from the Banda Sea toward the

Indian Ocean is strongest from July to September, when flow is enhanced by the local Ekman response to the more intense southeast monsoon (Wyrtki, 1987). Observations from the 3-year pressure gauge data in the Lesser Sunda outflow passages (Chong et al., 2000; Hautala et al., 2001), as well as year-long current meter data in Lombok Strait (Murray and Arief, 1988), Ombai Strait (Molcard et al., 2001) and Timor Passage (Molcard et al., 1994, 1996), find that maximum throughflow occurs during the southeast monsoon period.

Remote wind forcing from the Indian Ocean is responsible for changes in the ITF via the generation of equatorial and coastal Kelvin waves. Anomalous wind bursts in the equatorial Indian Ocean force an equatorial Kelvin wave that, upon impinging the west coast of Sumatra, results in poleward-propagating coastal Kelvin waves. Westerly wind bursts force downwelling Kelvin waves semiannually during the monsoon transitions, nominally in May and November, and intraseasonally in response to the Madden-Julian oscillation. The poleward propagation of the downwelling coastal Kelvin wave raises the sea level along the Indonesian wave guide of Sumatra and the Lesser Sunda islands (Clarke and Liu, 1993, 1994), causes maximum eastward flow of the semiannually reversing South Java current (Quadfasel and Cresswell, 1992), and may temporarily reverse the along-strait pressure gradient within the Lesser Sunda passages. In May 1997, a semiannually forced Kelvin wave resulted in eastward flow of very fresh, warm water in the South Java current (Sprintall et al., 1999), with subsequent northward flow observed up through Lombok Strait and past the mooring in Makassar Strait (Sprintall et al., 2000).

Remote winds in the Pacific Ocean drive large-scale circulation that impacts the ITF on low-frequency, interannual timescales. The weakening of Pacific trade winds that occurs during El Niño, which reduces the pressure gradient between the Pacific Ocean and the Indian Ocean, is thought to be the driving force for the throughflow on long timescales (Wyrtki, 1987). The changes are of the sense that the transport is smaller (larger), and the thermocline is shallower (deeper) during El Niño (La Niña) time periods (Kindle et al., 1989; Bray et al., 1996; Fieux et al., 1996; Gordon and Fine, 1996; Meyers, 1996; Potemra et al., 1997). The high-resolution POP model (Parallel Ocean Program; http://www.climate.lanl.gov/Models/POP/) yields a 12 Sv annual average during La Niña and 4 Sv average during El Niño (Gordon and McClean, 1999). The Arlindo mooring observations within Makassar Strait, which span the entire cycle of the strong 1997/1998 El Niño, find a correlation ($r = 0.73$) between Makassar transport and ENSO (Gordon et al., 1999; though the time series is far too short to say this with assurance). During the El Niño months of December 1997–February 1998, the transport average is 5.1 Sv with a corresponding internal energy "heat" transport of 0.39 pW; while during the La Niña months of December

1996–February 1997, the average is 12.5 Sv, a 2.5-fold difference, with a 0.63 pW heat transport. The Arlindo Makassar Strait time series reveals that the ITF transport is smaller and the thermocline is shallower during El Niño (Fig. 2a; Bray et al., 1996, 1997; Meyers, 1996; Ffield et al., 2000). The correlation between variability in the average thermocline temperature to variability in the southward Makassar transport is $r = 0.67$ (Ffield et al., 2000). Using nearly 15 years of XBT data, Ffield et al. (2000; Fig. 2b2) show that the Makassar upper thermocline temperature is highly correlated with ENSO: 0.77 for the Southern Oscillation Index; –0.80 for NINO3 SST anomaly; and –0.82 for NINO4 SST anomaly. The correlations increase when the ENSO time series are lagged a month or so. Thus the Makassar temperature field, when coupled with the throughflow, transmits equatorial Pacific El Niño and La Niña temperature fluctuations into the Indian Ocean.

In the Lesser Sunda exit passages, the transport variations estimated from the shallow pressure gauges suggest diminished flow through Lombok and Ombai Straits during the ENSO years 1997–1998, with increased flow through Timor Passage (Hautala et al., 2001). This is consistent with a 20-year run of the POCM model (Parallel Ocean Climate Model; http://www.nps.navy.mil/~rtt/POCM_info.html), in which there is stronger flow through Timor Passage and weaker flow through Ombai Strait during ENSO events (Potemra et al., 2002), although the magnitude of the transport changes through the two model straits do not fully compensate each other. This change in the ratio of transport carried through each of the Indonesian passages has been hinted at by the recent measurements, although again, the lack of simultaneous direct measurements in the passages makes interpretation difficult. For example, water mass analysis suggests that during La Niña time periods, when Makassar Strait throughflow is maximum, it appears that additional, albeit small, amounts of north Pacific thermocline water may enter the Banda Sea via the Lifamatola Passage from the Maluku Sea (Gordon and Fine, 1996).

2.3 Storage and Modification of the ITF Waters within the Internal Indonesian Seas

The different monitoring programs within the Indonesian region indicate large differences in peak transport timing between the inflow and outflow straits (Meyers et al., 1995). For example, while Gordon et al. (1999) found maximum transport through Makassar Strait during the northwest monsoon of 1996–1997, flow observed during the SPGA leaving the interior seas for the Indian Ocean was minimum during the same period (Hautala et al., 2001). The phase differences are most likely due to storage in the Banda Sea. Assuming a two-layer ocean, Gordon and Susanto (2001) found that the

Banda Sea surface water divergence, estimated from satellite altimetric data, correlates reasonably well with a 3-month lag of the export of upper ocean water through the Lesser Sunda island exit passages, as estimated by the SPGA. It appears that the Banda Sea acts as a reservoir, filling up and deepening the thermocline during the northwest monsoon. During the more intense southeast monsoon, Ekman flow in the Banda Sea combined with the lower sea level off the south coast of the Lesser Sunda Islands, are more conducive to drawing waters into the Indian Ocean (Wyrtki, 1987). The storage of mass and heat within the internal Indonesian seas will dramatically affect the interpretation of the measurements of the throughflow if made over short timescales.

The Banda Sea is also the primary site for conversion of the ITF profile from Pacific into the distinct Indonesian sea stratification, which is then exported into the Indian Ocean (Ffield and Gordon, 1992). A series of CTD stations from the Arlindo 1993–1994 cruises shows the attenuation and modification of the temperature and salinity profiles from the north Pacific salinity-maximum (100–150 m) and salinity-minimum core layers (250––350 m) with distance from the Makassar Strait (Ilahude and Gordon, 1996). The temperature and salinity stratifications as well as SST are significantly altered by the strong air−sea fluxes, seasonal wind-induced upwelling and large tidal forces within the Banda Sea (Ffield and Gordon, 1992, 1996; Hautala et al., 2001). Besides the vertical mixing, the attenuation of the salinity minimum is also due to the isopycnal injection of the more saline water from the south Pacific that enters the Banda Sea through Lifamatola Passage (Gordon and Fine, 1996; Hautala et al., 1996).

Hence it appears that both the composition and magnitude of the stored waters within the Banda Sea could have a significant impact on the Indian Ocean heat, freshwater and mass budgets. For example, Hautala et al. (2001) suggest that an imposed transport imbalance of 5 Sv, consistent with that determined by Gordon and Susanto (2001) on seasonal timescales, affects the temperature at thermocline depths by about 5°C. Convergences and divergences of this magnitude can have a substantial impact on thermocline stratification, and thus may affect SST by changing the temperature of the water being entrained into the mixed layer. Because of the possibility of different sampling biases in the previous measurements of the inflow and outflow straits, and the relatively short time series, we cannot unambiguously determine transport imbalances into and out of the internal seas as yet. Part of the apparent differences in transport timing between the inflow and outflow straits may be due to the nature of the measurements: the Makassar instruments were largely below 200 m, whereas the SPGA in the outflow straits samples the upper throughflow. Another cause for the difference in peak-to-peak timing between transport through Makassar Strait

and the exit passages may be the contribution to the ITF through the seas and passages directly north of the Banda Sea, the so-called "eastern" route for the ITF.

3 Model-to-Data Comparisons: Method

3.1 Model Configuration

The model used in this study is based on the GFDL MOM3 code (Pacanowski and Griffies, 2000). It is a global model with a horizontal resolution of 0.5° longitude by 0.33° latitude and with 36 vertical levels. The model uses partial bottom cells and has an additional frictional bottom boundary layer as described in Pacanowski and Griffies (2000). The model topography is a smoothed discretization of the observation-based ETOPO5 bottom topography. Horizontal viscosities and diffusivities are calculated by a numerical closure scheme based on the ideas of Smagorinsky, in combination with a biharmonic operator (Griffies and Hallberg, 2000). Vertical mixing of momentum, heat and salt is achieved by applying the hybrid Chen et al. (1994) mixed-layer model, in which strong mixing is assumed to occur within a bulk mixed layer. Below the mixed layer, internal mixing is parameterized by a gradient Richardson number-dependent mixing (Schiller et al., 1998). The third-order quicker scheme was used to solve the advection of tracers (Pacanowski and Griffies, 2000). Wind-stress fields were derived from the weekly ERS1/2 scatterometer wind product as provided by IFREMER (http://www.ifremer.fr/cersat/NEWS/2000/E_030400.HTM, also see Bentamy et al., 1999). Thermohaline surface fluxes (apart from incoming solar shortwave radiation and precipitation) are calculated by coupling the ocean general circulation model (OGCM) to an atmospheric boundary-layer model (Kleeman and Power, 1995; Schiller and Godfrey, 2003). The atmospheric boundary-layer model contains a prognostic equation for near-surface air temperature that is used to calculate surface fluxes of latent heat, sensible heat, and long-wave radiation. This simple atmospheric model is designed for simulating anomalies of ocean–atmosphere feedback processes on intraseasonal-to-interannual timescales; on longer timescales, SST and therefore heat fluxes are determined by nudging toward observations (Reynolds and Smith, 1994). The latter data set is used to calculate a seasonal heat flux climatology to which the intraseasonal-to-interannual anomalies are added. The ocean model was initialized with Levitus data (Boyer and Levitus, 1997) and spun up from rest for eight model years. After this time, the upper oceans in lower and midlatitudes have achieved a thermodynamic equilibrium. Subsequent integrations covered the period from October 1992 to September 2000. Table 1 contains a summary of the model.

Table 1: Summary of the OGCM

Model resolution	$\Delta\lambda = 0.5^\circ$, $\Delta\varphi = 0.33^\circ$, 36 vertical levels plus bottom-boundary layer ($C_D = 3 \times 10^{-3}$)
Advection scheme	Quicker scheme
Horizontal subgrid scale parameterization	(a) Biharmonic mixing for momentum and tracers, Smagorinsky-like scheme for coefficients (Griffies and Hallberg, 2000), Prandtl number = 100 (b) Laplacian mixing with $A_h = A_m = 500\,m^2/s$
Vertical subgrid scale parameterization	Hybrid Chen mixing scheme (Power et al., 1995; Schiller et al., 1998): Niiler–Kraus-like bulk mixed layer near the surface, gradient Richardson number mixing below
Surface forcing	Wind stresses: weekly ERS1/2 scatterometer winds (IFREMER), Surface heat fluxes (latent, sensible, and long-wave) provided by atmospheric boundary-layer model with bulk parameterizations (Kleeman and Power, 1995); solar shortwave radiation: OLR-based within 15° of equator, NCEP elsewhere (Schiller and Godfrey, 2002); precipitation: Xie and Arkin (1997) Spin-up run with nudging to Reynolds and Smith (1994) SST data and Boyer and Levitus (1997) SSS data. Time constant: $\lambda = 1/30$ days
Time steps	Tracer: 600 sec, baroclinic velocity: 600 sec, free surface: 10 sec

3.2 Data Analysis

As part of the TOGA upper ocean observing system, a network of XBT sections was established in 1983–1986 along commercial shipping lines between the western coast of Australia and various ports (Meyers et al., 1995; Meyers, 1996; Wijffels and Meyers, 2004). The lines investigated are detailed in Fig. 3 and are designated: IX1 that is from Fremantle on the southwest coast of Australia to Sunda Strait on the western tip of Java, Indonesia; and PX2 that crosses the Banda Sea just north of the Lesser Sunda island arc. On all lines, Sippican T-4 and T-7 XBTs were dropped roughly every 4 h (~80 nm) from volunteer observing vessels. Sampling has occurred on average at fortnightly frequency along IX1 and monthly frequency on the other lines, though it can be less due to changes in shipping and the time required to re-equip the line. In mid-1986, the probe type changed from Sippican T-4 s to T-7 s and thus after this date, the maximum depth of the profiles collected changed from 450 m to 760 m. The profiles were carefully quality controlled (Bailey et al., 1994); further details can be found in Wijffels and Meyers (2004). Wind stresses applied to observational data to explore wave dynamics were derived from the NCEP reanalysis described by Kalnay et al. (1996) as downloaded from the Climate Diagnostic Center, Boulder, USA. Altimetric sea-level data from AVISO are also used (Le Traon et al., 1998).

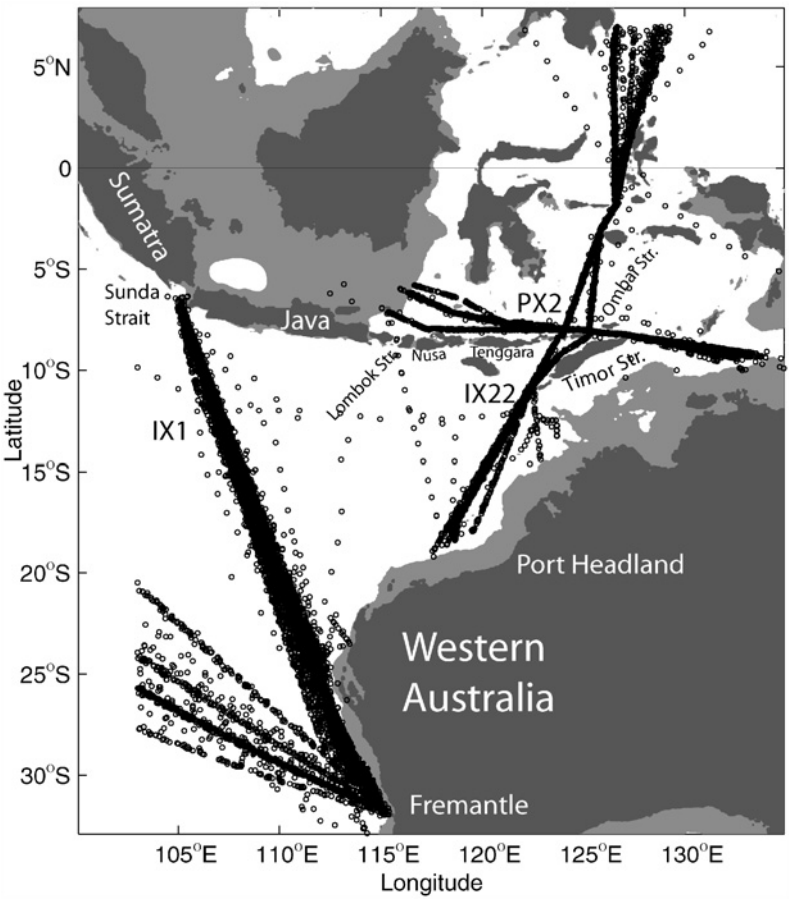

Figure 3: Locations of WOCE XBT profiles used in this study. The names of the primary lines and plots are indicated. Water depths shallower than 200 m are grey shaded.

4 Results

4.1 Temperature Structure in the ITF

Observations from WOCE XBT section IX1 and PX2 (Fig. 3) are compared with model fields, focusing on potential temperature (Sections 4.1 and 4.2) and wave dynamics in the ITF region (Section 4.3). Examples of the mapped observed and simulated temperature from the IX1 and PX2 sections are shown in Figs. 4–7.

Off the Australian coast (Fig. 4), the yearly formation of the seasonal thermocline dominates variability in the upper 150 m (upper 200 m in model). The amplitude of the seasonal cycle of surface temperature is

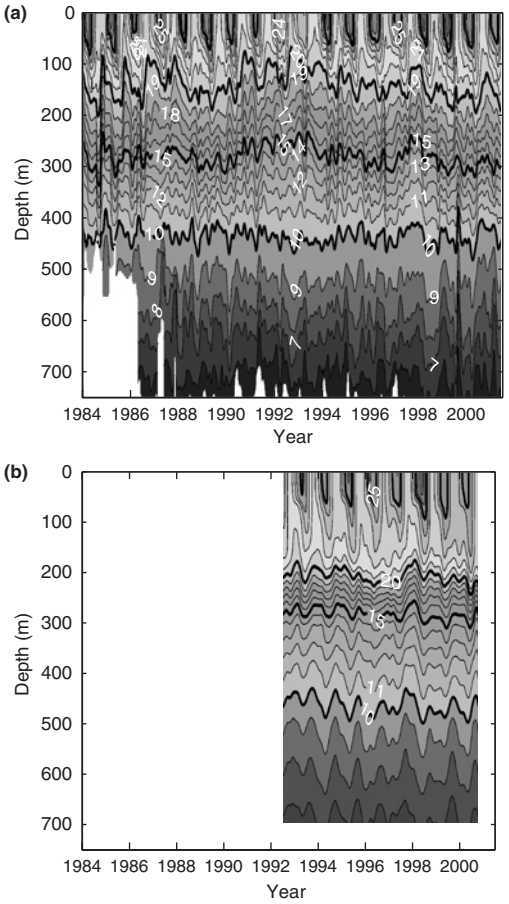

Figure 4: Potential temperature as a function of time and depth along IX1 off the coast of western Australia near 25°S for (a) observations and (b) model (For colour version, see Colour Plate Section).

weaker in the model than in reality, and the waters between the seasonal and permanent thermocline have much lower stratification in the model, possibly indicating a too weak Leeuwin Current (and its associated warm advection of subtropical stratification into the coastal zone). Below this depth (∼150 m), eddy variability is superimposed on a low-frequency modulation of the depth and thickness of the main thermocline. During ENSO years (1986–1987, 1991–1994, and 1997–1998), the thermocline is shallower (closer to the surface), thicker (vertical extent) and surface temperatures are cooler. Although the model reproduces the observed features, the simulated thermocline is too shallow and the ENSO signals are shallower and much weaker than is observed. In particular, the cooling of SST associated with a shallow thermocline, due to lifting and entrainment of cold

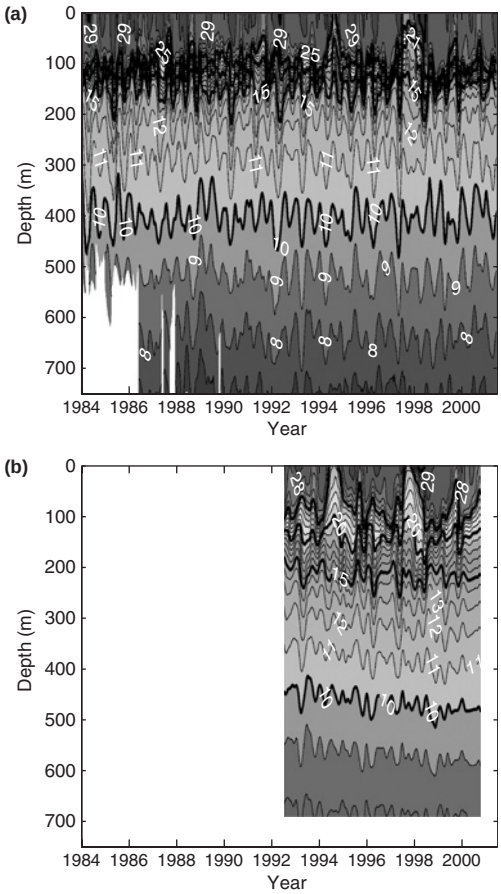

Figure 5: Potential temperature as a function of time and depth along IX1 off the coast of Java at the Sunda Strait for (a) observations and (b) model (For colour version, see Colour Plate Section).

subsurface water, observed in the 1997/1998 El Nino, is not generated in the model.

Off Java, the thermocline is very thin and lies near 100 m with a warm isothermal layer above it (Fig. 5a, b). While generally reproducing these features, the model thermocline is too thick and deep. A seasonal thermocline is almost entirely absent in both model and observations, and instead, the warm surface layer is punctuated by intense upwelling events the largest of which occur in late 1987, 1988, 1989, 1991, 1994, and 1997. These events are present in the model but persist for longer period and have a stronger SST signature than in reality (Fig. 5b). Both model and observations show upward phase propagation of variations at intraseasonal and semiannual timescales.

Temperatures below 150 m (below 200 m in model) undergo semiannual variations remotely wind driven by the Wyrtki Jets (Clarke and Liu, 1993),

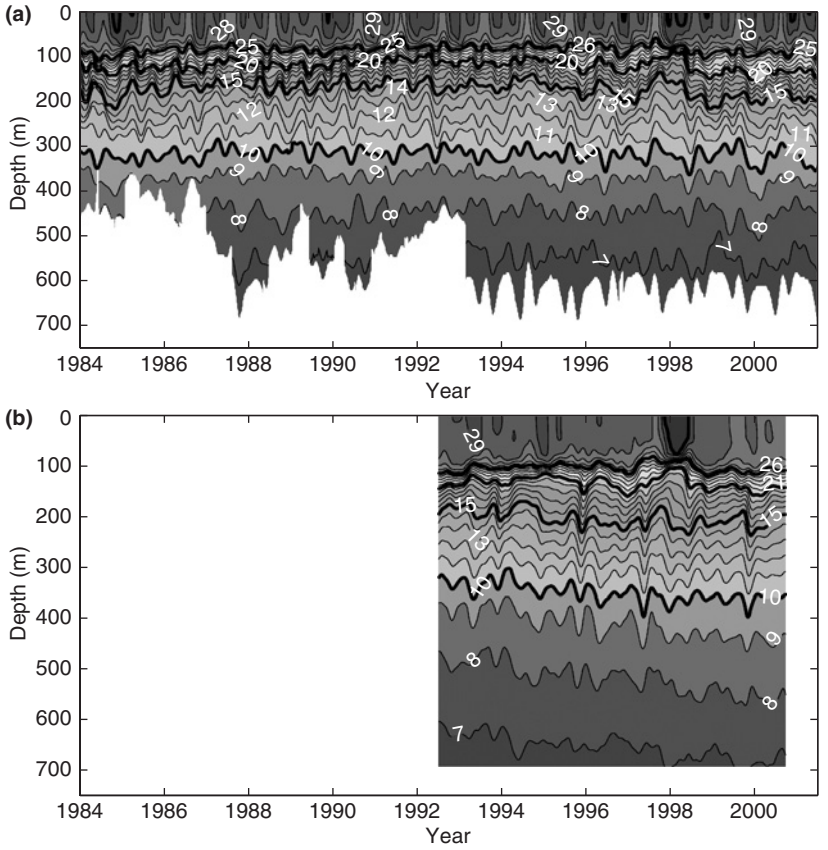

Figure 6: Potential temperature as a function of time and depth along PX2 off the Java shelf break near 116°E for (a) observations and (b) model (For colour version, see Colour Plate Section).

which feature upward vertical phase propagation both in the observations and model, but are weaker in the latter (by about a factor of 2). The semiannual variability attenuates toward the surface, where interannual variability becomes stronger. The 10°C isotherm of the model also reveals a global warming trend that might have been caused by the relatively short spin-up time in the model, which did not allow a dynamic adjustment of the deeper layers of the model.

At the western end of PX2 (Fig. 6), at the Java Sea shelf break, a thin shallow thermocline also exists. Variability in the surface layer is weak, lacking the dramatic variations seen off Java and is dominantly annual and semiannual, while semiannual and lower frequency variations occur at depth. Here, the model simulates the mean temperature structure well. The temperature variability in the surface layer is too weak in the model, but the simulated thermocline events are quite well correlated with the

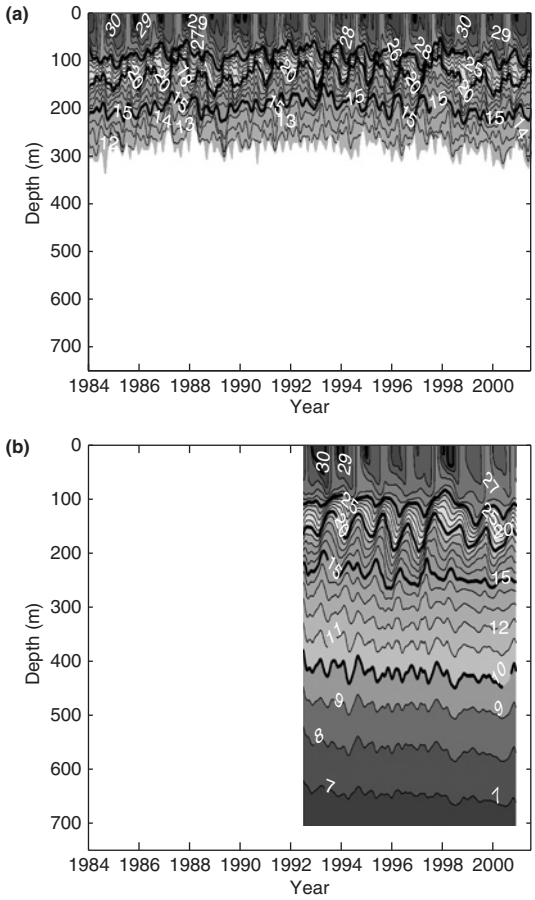

Figure 7: Potential temperature as a function of time and depth along PX2 at the Arafura shelf break near 133°E for (a) observations and (b) model (For colour version, see Colour Plate Section).

observations – note the cooling near 150 m in 1997/1998. Off the Arafura shelf west of Darwin (Fig. 7), a very strong seasonal thermocline forms. Below the seasonal thermocline, the annual period continues to dominate but with striking upward vertical phase propagation, as can be seen in the observations and that is very well simulated by the model.

4.2 Spectral Content of Temperature Variability

To reveal the spatial characteristics of temperature variability along IX1 and PX2, total variance was binned into four broad spectral bands: for periods less than 0.4 years (intraseasonal/mesoscale); periods between 0.4 and 1.1 years (seasonal); periods between 1.1 and 3.2 years (quasi-biennial

(QB) band); and for periods greater than 3.2 years (ENSO band). The model data were detrended prior to calculating the variances. The variance in each spectral band is shown as a percentage of the total mapped variance in Figs. 8 and 9.

Eddy energy is only partially suppressed by the mapping scales used to average the XBT data, and we find that observed intraseasonal energy accounts for typically 10–20% of the total mapped observed temperature variance in two regions along IX1 (Fig. 8a): off the coast of western Australia where the IX1 line intersects the eddy field associated with the Leeuwin Current and between 13°S and 8°S along the axis of the South Equatorial Current, where strong intraseasonal eddies develop as a result of an instability of the current at its seasonal maximum (Feng and Wijffels, 2001). Intraseasonal variability in the model along the Australian coast (Fig. 8e) is less than 10% along most of IX1 with a maximum of about 20% along the coast of Java, which is still significantly weaker than in the observations (up to 40%).

The observed seasonal band (Fig. 8b), which includes both the annual and semiannual frequencies, dominates SST and variability in the seasonal thermocline. The depth penetration of the seasonal thermocline clearly increases to the south along with the strength of the seasonal heating/cooling cycle. This feature is quite accurately reproduced by the model (Fig. 8f). Dominant seasonal variation is also evident in the observations throughout the water column between 12°S and 20°S (Fig. 8b); this is the forced annual Rossby wave described by Masumoto and Meyers (1998), which is primarily driven by local wind-stress curls, and associated Ekman pumping and Rossby wave propagation. Although the model also shows increased seasonal variability between 12°S and 20°S (Fig. 8f), it lacks the coherent signal across the whole latitude band between 12°S and 20°S in the observations.

Off the coast of Java, the relative importance of the observed and simulated seasonal cycle in temperature variability is largest in a narrow region trapped at the coast below 100 m and extending to 750 m (Fig. 8b, f). This signal is in response to the semiannual Kelvin waves excited in the equatorial Indian Ocean. Interestingly, both observed and simulated coastal SST and temperature variability above 100 m off Java largely occur in the QB and ENSO bands (Fig. 8c, d, g, h). Variance in the QB band occurs in the Java mixed layer and upper thermocline and extends further offshore at depth than the seasonal variability (Fig. 8c, g). Off Australia, the simulated and observed ENSO band accounts for 30–40% of the total variability in the upper thermocline.

Along PX2, the observed intraseasonal band has little energy due to the longer averaging times (e-folding scale of 30 days) needed to grid this more sparsely sampled and noisy section (Fig. 9a). Similar to IX1, the model shows weaker than observed intraseasonal variability along this section (Fig. 9d). Seasonal variations dominate observed and, to a lesser extent,

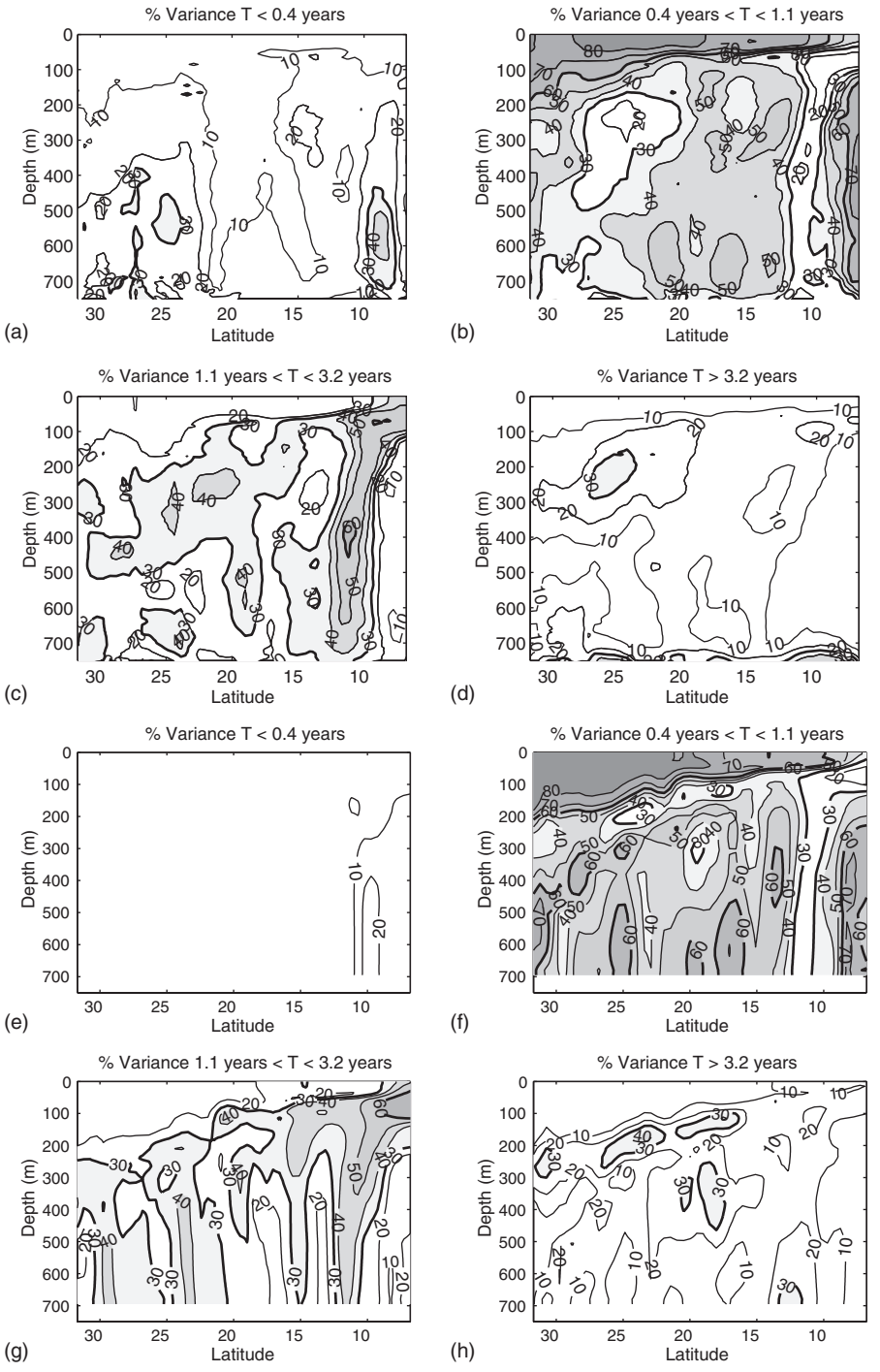

Figure 8: The percentage of mapped temperature variance in four spectral bands along IX1 for observations (upper half) and model (lower half) for 1992–2000 period: (a, e) intraseasonal (periods >0.4 years), (b, f) seasonal (periods between 0.4 and 1.1 years), (c, g) biennial band (periods between 1.1 and 3.2 years), and (d, h) interannual (periods longer than 3.2 years).

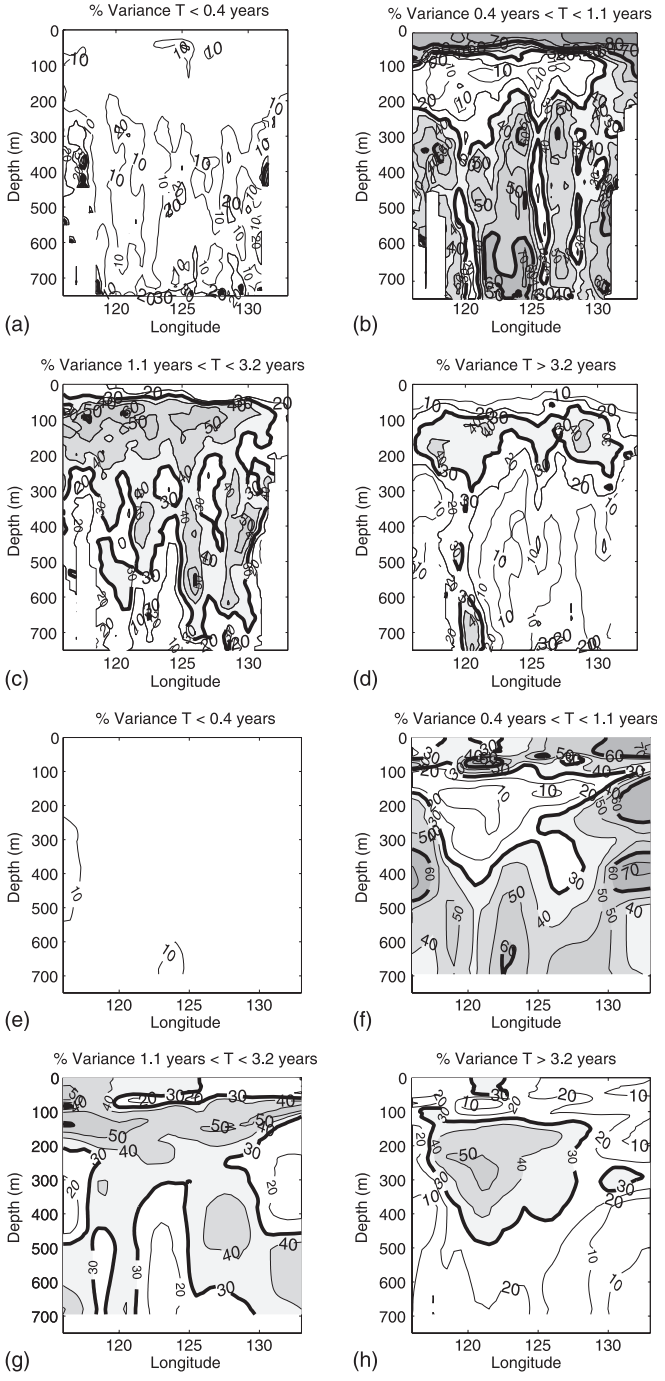

Figure 9: As for Fig. 8, but for PX2.

simulated temperature variability above and below the main thermocline and at the Arafura shelf break (Fig. 9b, f). Both observations and model show a decrease in strength of the seasonal signal in SST from the Arafura to the Java shelf break. Within the thermocline, QB and ENSO band variability dominate (Fig. 9c, d, g, h). The QB variability also contributes significantly below the thermocline. For seasonal and longer timescales the model simulates the observed structures with reasonable accuracy, though the responses occur at deeper depths than observed.

Ray theory explains the results shown in Figs. 5 and 8 where annual and semiannual energy dominates subthermocline depths off Sunda Strait, while ENSO-band variability is confined to the upper thermocline. Simple ray-tracing theory (following Kessler and McCreary, 1993) along the equatorial and coastal wave guides, starting at the thermocline depth of 100 m at 60°E (mid-Indian basin), suggests semiannual energy will dive to below 300 m off Sunda, only to 200 m depth for annual frequencies and barely to 120 m for the ENSO band (5 years). Waves originating at 170°W in the equatorial Pacific can dive to well below 1,000 m for the semiannual, to 300 m for the annual and barely to 130 m for the ENSO band. Thus the upward propagating annual wave seen off the Arafura shelf break (Fig. 7) is remotely forced in the central Pacific. However, a discrepancy in the linear ray theory is the thermocline response off the western Australian coastline, which extends to 300 m depth (Fig. 4), and therefore much deeper than the ray paths suggest was possible. Likely, the energy is following the thermocline as it deepens poleward (Wijffels and Meyers, 2004).

4.3 Wave Guides in the ITF and Their Relation to Remote Wind Forcing

As was shown by Meyers (1996), the interannual variability along IX1 is strongly related to the large-scale wind-stress fields over the Pacific and Indian Oceans. The nature of the relation is qualitatively accounted for by linear wave theory, predicting that equatorial Kelvin and Rossby waves excited by variation in large-scale wind stresses excite coastal waves, which carry the signal to higher latitudes. Here we examine the simulated and observed details of the relationship between these remote wind forcing with sea level and temperature variability in the region at seasonal and longer timescales.

As recognized by Clarke and Liu (1994), the zonal wind stresses along the equator of the Pacific and Indian Oceans are significantly correlated in the ENSO band, such that during ENSO the weakened Pacific Trades are often accompanied by easterly wind anomalies along the Indian Ocean equator. However, while Pacific winds are dominated by the ENSO band, the Indian Ocean winds have much more energy at higher frequencies with spectral peaks near periods of 3 years and between 1 and 2 years. This

higher frequency "signature" of equatorial Indian Ocean winds versus the lower frequency energy of the Pacific winds is crucial in distinguishing the impact of these two sources of remote energy within the Indonesian seas.

To identify the large-scale variations of sea level anomaly (SLA) as a response to wind forcing, a lagged multiple regression is performed at each point of a mapped altimetry data set on wind stresses $\hat{\tau}_I$ (Wijffels and Meyers, 2004):

$$\mathrm{SLA}(t) = a_P[-\hat{\tau}_P(t + L_P)] + a_I\hat{\tau}_I(t + L_I) + a_L\hat{\tau}_L(t + L_L) \quad (1)$$

where the 4-month low-passed seasonal SLA, at time t, is expressed as the sum of three wind indices, $\hat{\tau}_i$, at lag L_i with coefficients a_i. The wind indices used are the zonal wind averaged along the Pacific equator (note the reverse sign, so that positive wind anomalies give positive temperature anomalies); the along path winds on a path extending along the coast from Sunda Strait to the equator and then along the equator to Africa; and a local wind index. These indices – Pacific, Indian and Local – are denoted by P, I, and L, respectively in equation (1). Each wind index had the seasonal cycle removed, was low-pass filtered at 4 months, and normalized before the multiple correlation was performed. Thus coefficients in equation (1) can be interpreted as the sea-level change associated with a single standard deviation change in the wind index.

All possible lags within ± 18 months were searched to find the combination that accounted for the maximum variance at each grid point. Since the wind indices used in equation (1) are normalized, the calculated coefficients are in real physical units (cm). Hence, the response during a peak in the wind index (normalized amplitude of 3) is then given by three times the coefficient plotted. Data used by equation (1) account for up to 90% of 4-month low-passed seasonal anomalies of sea-level height collected since late 1992 throughout the throughflow region and over large parts of the Pacific and Indian Oceans (not shown). We find that various estimates of "local" winds are unable to capture much variance (and hence are not shown). The results based on sea level described below have also been confirmed by results from a similar analysis of the temperature fields along the XBT lines from both the observations and the model. For further details about the method, the reader is referred to Wijffels and Meyers (2004).

Observation-based coefficient and lag of sea level for the Pacific wind index (Fig. 10a, b) show that high sea levels occur in the western Pacific in response to easterly wind anomalies, and much of this signal "leaks" along the New Guinea–Irian Jaya–Australian wave guide down to the southern tip of western Australia, with some suggestion of offshore radiation of energy north of 22°S. Coefficients are large and positive near the west Australian coast. The sense of the multiple correlation is that a large warming and high

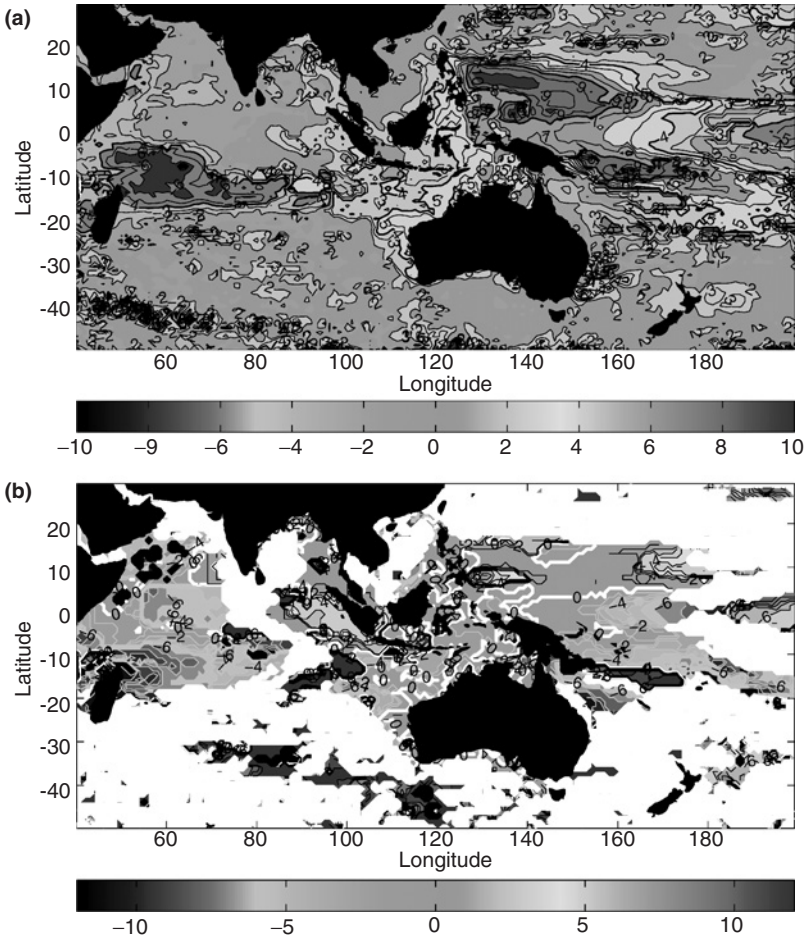

Figure 10a, b: Coefficient in centimeter (top) and lag in months (bottom) of low-frequency anomalies of SSH for Pacific wind index: (a, b) observations and (c, d) model (For colour version, see Colour Plate Section).

sea levels off the western Australian coast are associated with easterly wind anomalies along the Pacific equator, a result obtained previously by Meyers (1996). Downwelling equatorial Rossby waves excited by the wind anomalies in the central and western Pacific propagate westward and excite coastally trapped waves off Papua New Guinea, which then propagate anticlockwise around Australia. Part of this signal also continues around the southwest tip of Australia and along the south coast (obscured by the spatial smoothing in the plot). Lags off western Australia are between 0 and 2 months. In sea level, the maximum lags occur near 18°S.

In the subtropics, the Pacific wind response dies out near 100°E, in agreement with Masumoto and Meyers (1998) and Potemra (2001), who

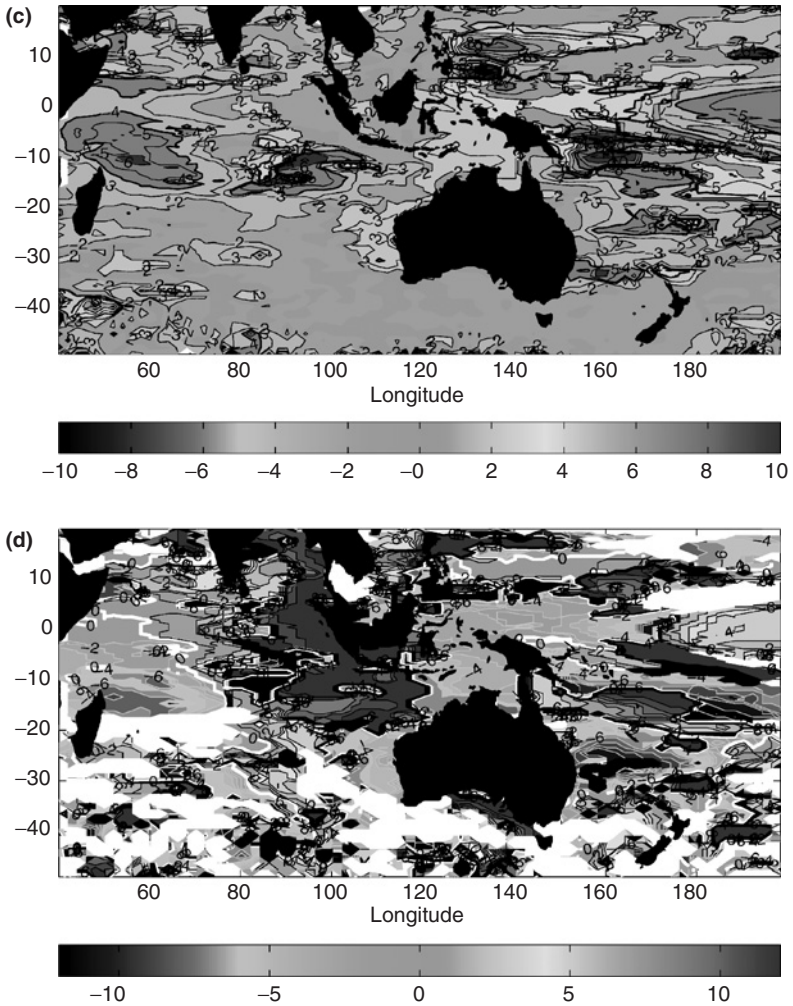

Figure 10c, d Continued (For colour version, see Colour Plate Section).

found that near this longitude, regional Ekman pumping along Rossby wave characteristics begin to dominate over variability originating at the eastern boundary. The simulated correlation pattern looks similar but is significantly weaker in amplitude (Fig. 10c, d). This is particularly visible in small amplitudes in the far western Pacific and also in the weak wave propagation from the Pacific into the Indian Ocean and along the western Australian coastline. The simulated phase lags off western Australia are between 2 and 4 months. This "weak" ENSO response in the model is also confirmed by analysis of its temperature field, showing that the response of the modeled thermocline along the Australian coast to ENSO winds is too diffusive and too deep (Fig. 4).

Interestingly, in both model and observations there is also a strong response to the Pacific winds northeast of Madagascar with lags that suggest a southward propagating response, due to either local wind changes that correlate with ENSO or expressions of later arrivals of Rossby waves at higher latitudes. However, both the relatively short satellite altimetric record and the short model simulation are likely to be dominated by the very large 1997/1998 ENSO event and strong Indian Ocean dipole that occurred during the same years (Saji et al., 1999) – a situation not likely a representative of a longer record.

The simulated response in sea level to Indian Ocean winds agrees well with observation-based results (Fig. 11): westerly wind anomalies

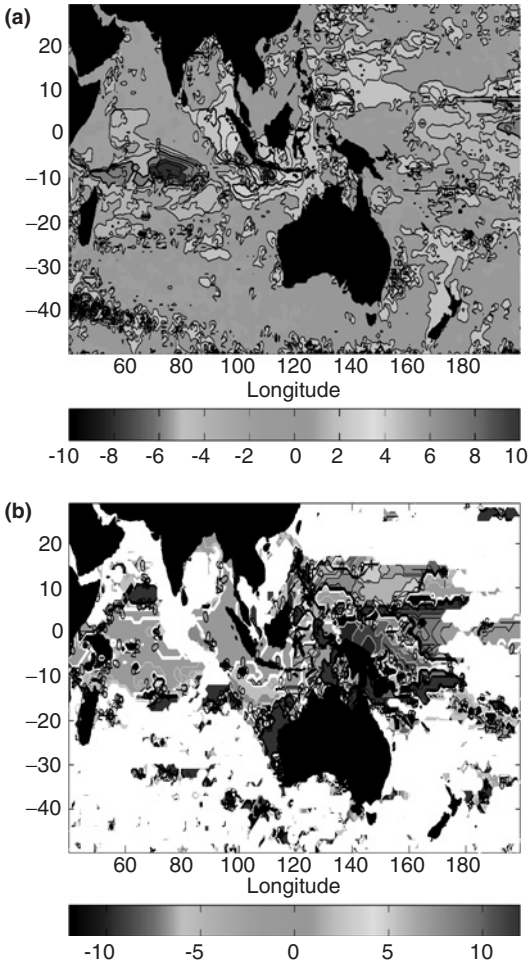

Figure 11a, b: As for Fig. 10, but for the Indian wind index (For colour version, see Colour Plate Section).

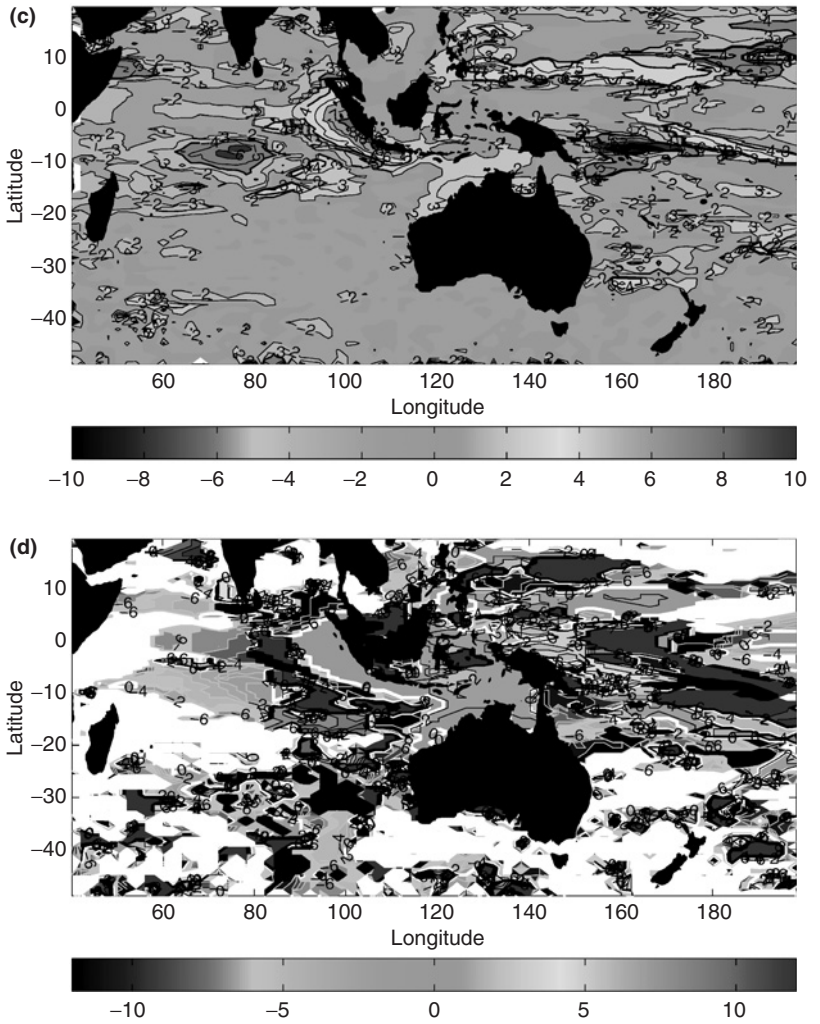

Figure 11c, d Continued (For colour version, see Colour Plate Section).

giving high sea levels in the eastern Indian Ocean equatorial and coastal waveguides. This signal also penetrates into the western portion of the Banda Sea, Savu Sea, and Makassar Strait at near-zero lag. The propagation of the equatorially excited waves around the Bay of Bengal is also evident in the observation-based plot, as is the radiation of energy westward from the eastern boundary off Sumatra and Java. The western and central Indian Ocean response to the equatorial zonal wind anomalies is also evident with lower sea level along 8°S at near zero lag in both model and observations.

Despite the overall quite successful simulation of this response by the model, there are some features that are missing. The radiation of equatorially forced waves around the Bay of Bengal is entirely missing in the model but is

clear in the observations. Also, the response east of Lombok Strait is very weak in the model, unlike in the observations, where much energy is seen to "jump" the strait and reach Ombai Strait near 125°E. In the model, Lombok Strait is known to be too wide and "dynamically slippery." This is apparent in the fact that the bulk of the throughflow transport passes through Lombok in comparison to reality where only 20–30% actually does. Interestingly, despite this, little of the remotely forced wave energy appears to pass through Lombok Strait into the internal seas of the Indonesian archipelago.

5 Discussion and Conclusion

Upper ocean temperature variability within the Indonesian seas and southeast Indian Ocean has been described on the basis of repeat high-quality XBT data collected since 1983. The observations have been compared to results from an eddy-permitting ocean circulation model. Besides strong annual variability in the seasonal thermocline and in the thermoclines off the Arafura and Java shelf breaks in both data sets, interannual variability dominates much of the thermocline variability elsewhere.

Next, a lagged multiple regression technique was performed on the basis of satellite altimetry collected since 1992. The results reveal that interannual sea-level variability in the southeast Indian Ocean and Indonesian seas is largely driven by remote equatorial winds, as predicted by Clarke and Liu (1994). The dominating effect of ENSO, through its modulation of Pacific equatorial winds and associated equatorial Rossby wave response, has been proposed and recognized in a series of studies (Clarke and Liu, 1994; Meyers, 1996; Ffield et al., 2000; Potemra, 2001; Wijffels and Meyers, 2004). The penetrating wave signal is visible in both in the coastal wave guides and as free Rossby waves propagating westward into the southeast Indian Ocean. Equatorial Indian Ocean winds have different timescales than Pacific winds. Indian Ocean wind energy penetrates along the Lesser Sunda island arc and into the internal Indonesian seas, controlling both sea level and thermocline depth along the eastern Java Sea shelf break and within Makassar Strait.

We have identified the presence of many of these features in our ocean circulation model but differences to observations exist in the amplitudes of the signals and, to a lesser extent, also in the phase of the signals. The most significant problem of this model (in common with many other ocean general circulation models) is the deeper than observed thermocline. The near-surface circulation of the ocean is determined by model physics and exterior forcing (surface heat and freshwater fluxes, wind stresses). Both of these components contain errors irrespective of the source of the surface forcing (from observations as used in this study or from an atmospheric circulation

model in a coupled mode), which hampers identification and rectification of model errors. Nevertheless, model errors are the likely cause for the broad-scale overestimate of thermocline depth and associated misrepresentations of water temperature and salinity. A more realistic representation of interior mixing processes is required, and isopycnal mixing might help here.

Another limitation of the model used in this study relates to the moderate resolution ($0.5^\circ \times 0.33^\circ$, 36 vertical levels). This resolution is too coarse to resolve complicated details of currents and water-mass properties in the ITF region. The primary source of vertical mixing for water-mass properties in the Indonesian seas could be internal waves generated by barotropic flow over variable bottom topography as discussed by Ffield and Gordon (1992, 1996). The effect of internal tides and their breaking on vertical mixing has been parameterized in our model by shear-dependent mixing based on a gradient Richardson number and therefore represents a potential source of error in simulating vertical structures.

The relatively weak response to changes in ENSO winds of the model compared to observations is intriguing and requires further investigation. One possible explanation for some of the observed discrepancies could be due to a poorly resolved coastal wave guide in the model. In this region, the remote response to both ENSO and Indian Ocean equatorial wind changes occur outside of the equatorial wave guide. While the response within the wave guide (latitudes approximately $<8^\circ$) is quite well simulated, those outside are not. The signals must travel through coastal wave guides to reach the Ombai Strait, the Bay of Bengal, or the southwestern coast of Australia. We note that these signals are weak in the model, suggesting an unrealistic partition of energy between reflected equatorial waves and coastally trapped waves. Further work is needed to confirm this notion, but it may have implications for where high model resolution is required to resolve these scattering regions.

To help fully resolve the temporal variability and characteristics of the ITF transport and property fluxes, a multiyear comprehensive measurement program is required. A serious shortcoming in previous observational measurement programs within the Indonesian region is the lack of temporal coherence: the data cover different time periods and depths in the different passages of the complex pathways toward the Indian Ocean. This has lead to ambiguity of the mean and variable nature of the ITF, and the transformation of the thermohaline and transport profiles within the interior seas. For this reason, and in keeping with the recommendations stemming from the full community deliberation (OCEANOBS October 1999 meeting in St. Raphael, see Imawaki et al., 1999; Workshop on Sustained Observations for Climate of the Indian Ocean, Perth, November 2000, see http://www.marine.csiro.au/conf/socio/socio.html), an international co-operative effort commenced in August 2003 with deployments of multiyear moorings for

direct throughflow velocity, salinity, and temperature measurements simultaneously in Makassar Strait, Lifamatola Passage, Lombok Strait, Ombai Strait, and Timor Passage (Fig. 1). The program that is called INSTANT (International Nusantara STratification ANd Transport) involves five nations: Australia, France, Indonesia, Netherlands, and USA. INSTANT is designed to provide a time series of ITF transport and property fluxes, and their variability from intraseasonal to annual timescales, along the ITF pathway from the intake of Pacific water at Makassar Strait and Lifamatola Passage to the Lesser Sunda exit channels into the Indian Ocean. The initial deployment of all moorings commenced in August 2003, with redeployment in February 2005, and recovery in July 2006. The resulting simultaneous, multiyear direct measurements in both the inflow and the outflow ITF passages will allow us, for the first time, to unambiguously determine the magnitude of the interocean transport, its properties, and their evolution between the Pacific and the Indian Oceans. Finally, an important outcome of the program will be to recommend an efficient set of ongoing observations that may offer a proxy for a long-term monitoring strategy of the ITF transport and property fluxes.

Acknowledgements

We thank Russell Fiedler for extracting the model data. We also thank S. Nakamato and Y. Michida for their thoughtful comments that helped to improve the manuscript.

References

Bailey, R., Gronell, A., Phillips, H., Tanner, E., Meyers, G., 1994. Quality Co0ntrol Cookbook for XBT Data, Version 1.1. Report Marine Laboratories CSIRO, Australia, No. 221, p. 84.

Bentamy, A., Grimas, N., Quilfen, Y., 1999. Validation of the gridded weekly and monthly wind fields calculated from ERS-1 scatterometer wind observations. Global Atmosphere and Ocean System 6, 373–396.

Boyer, T. P., Levitus, S., 1997. NOAA Atlas NESDIS 11. Objective analysis of temperature and salinity for the world ocean on a 1/4 grid. U.S. Department of Commerce, National Oceanic and Atmospheric Administration, various pagings.

Bray, N. A., Hautala, S., Chong, J., Pariwono, J., 1996. Large scale sea level, thermocline, and wind variations in the Indonesian throughflow region. Journal of Geophysical Research 101, 12239–12254.

Bray, N. A., Wijffels, S. E., Chong, J. C., Fieux, M., Hautala, S., Meyers, G., Morawitz, W. M. L., 1997. Characteristics of the Indo-Pacific throughflow in the eastern Indian Ocean. Geophysical Research Letters 24, 2569–2572.

Bryden, H. L., Imawaki, S., 2001. Ocean heat transport. In: Siedler, G., Church, J., Gould, J. (Eds.), Ocean Circulation and Climate. International Geographic Series., Academic Press, San Francisco, CA, Volume 77, pp. 455–474.

Cane, M., Molnar, P., 2001. Closing of the Indonesian seaway as a precursor for African aridification around 3–4 million years ago. Nature 411, 157–162.

Chen, D., Rothstein, L. M., Busalacchi, A. J., 1994. A hybrid vertical mixing scheme and its application to tropical ocean models. Journal of Physical Oceanography 24, 2156–2179.

Chong, J., Sprintall, J., Hautala, S., Morawitz, W., Bray, N., Pandoe, W., 2000. Shallow throughflow variability in the outflow straits of Indonesia. Geophysical Research Letters 27, 125–128.

Clarke, A. J., Liu, X., 1993. Observations and dynamics of semiannual and annual sea levels near the eastern equatorial Indian Ocean boundary. Journal of Physical Oceanography 23, 386–399.

Clarke, A. J., Liu, X., 1994. Interannual sea level in the northern and eastern Indian Ocean. Journal of Physical Oceanography 24, 1224–1235.

Cresswell, G., Frische, A., Peterson, J., Quadfasel, D., 1993. Circulation in the Timor Sea. Journal of Geophysical Research 98, 14379–14389.

Feng, M., Wijffels, S., 2001. Intraseasonal variability in the south equatorial current of the east Indian Ocean. Journal of Physical Oceanography 22, 265–277.

Ffield, A., Gordon, A., 1992. Vertical mixing in the Indonesian thermocline. Journal of Physical Oceanography 22, 184–195.

Ffield, A., Gordon, A., 1996. Tidal mixing signatures in the Indonesian Seas. Journal of Physical Oceanography 26, 1924–1937.

Ffield, A. L., Vranes, K., Gordon, A. L., Susanto, R. D., Garzoli, S. L., 2000. Temperature variability within Makassar Strait. Geophysical Research Letters 27, 237–240.

Fieux, M., Molcard, R., Ilahude, A. G., 1996. Geostrophic transport of the Pacific–Indian Oceans throughflow. Journal of Geophysical Research 101, 12421–12432.

Fine, R. A., 1985. Direct evidence using tritium data for throughflow from the Pacific into the Indian Ocean. Nature 315, 478–480.

Ganachaud, A., Wunsch, C., 2000. Improved estimates of global ocean circulation, heat transport and mixing from hydrographic data. Nature 408, 453–456.

Ganachaud, A., Wunsch, C., Marotzke, J., Toole, J., 2000. The meridional overturning and large-scale circulation of the Indian Ocean. Journal of Geophysical Research 105, 26117–26134.

Godfrey, J. S., 1989. A Sverdrup model of the depth-integrated flow for the world ocean allowing for island circulations. Geophysical Astrophysical Fluid Dynamics 45, 89–112.

Godfrey, J. S., 1996. The effect of the Indonesian throughflow on ocean circulation and heat exchange with the atmosphere: a review. Journal of Geophysical Research 101, 12217–12238.

Gordon, A. L., 1995. When is "appearance" reality? Indonesian throughflow is in fact primarily derived from North Pacific water masses. Journal of Physical Oceanography 25, 1560–1567.

Gordon, A. L., 2001. Interocean exchange. In: Siedler, G., Church, J., Gould, J. (Eds.), Ocean Circulation and Climate. International Geophysics Series. Academic Press, San Fransisco, CA, Volume 77, Ch. 4.7, pp. 303–314.

Gordon, A., Fine, R., 1996. Pathways of water between the Pacific and Indian Oceans in the Indonesian seas. Nature 379, 146–149.

Gordon, A. L., Ma, S., Olson, D. B., Hacker, P., Ffield, A., Talley, L. D., Wilson, D., Baringer, M., 1997. Advection and diffusion of Indonesian Throughflow water within the Indian Ocean South Equatorial Current. Geophysical Research Letters 24, 2573–2576.

Gordon, A. L., McClean, J., 1999. Thermohaline stratification of the Indonesian seas — model and observations. Journal of Physical Oceanography 29, 198–216.

Gordon, A. L., Susanto, R. D., 1999. Makassar Strait transport: initial estimate based on Arlindo results. Marine Technology Society Journal 32, 34–45.

Gordon, A. L., Susanto, R. D., 2001. Banda Sea surface layer divergence. Ocean Dynamics 52, 2–10.

Gordon, A. L., Susanto, R. D., Ffield, A. L., 1999. Throughflow within Makassar Strait. Geophysical Research Letters 26, 3325–3328.

Griffies, S. M., Hallberg, R. W., 2000. Biharmonic friction with a Smagorinsky-like viscosity for use in large-scale eddy-permitting ocean models. Monthly Weather Review 128, 2935–2946.

Hautala, S. L., Reid, J. L., Bray, N., 1996. The distribution and mixing of Pacific water masses in the Indonesian seas. Journal of Geophysical Research 101, 12375–12389.

Hautala, S. L., Sprintall, J., Potemra, J., Ilahude, A. G., Chong, J. C., Pandoe, W., Bray, N., 2001. Velocity structure and transport of the Indonesian throughflow in the major straits restricting flow into the Indian Ocean. Journal of Geophysical Research 106, 19527–19546.

Hirst, A. C., Godfrey, J. S., 1993. The role of the Indonesian throughflow in a global ocean GCM. Journal of Physical Oceanography 23, 1057–1086.

Hirst, A. C., Godfrey, J. S., 1994. The response to a sudden change in Indonesian throughflow in a global ocean GCM. Journal of Physical Oceanography 24, 1895–1910.

Ilahude, A. G., Gordon, A., 1996. Thermocline stratification within the Indonesian seas. Journal of Geophysical Research 101, 12401–12409.

Imawaki, S., Zenk, W., Wijffels, S., Roemmich, D., Kawabe, M., 1999. Oceanic boundary currents. In: Proceedings of OceanObs99, International conference on the Ocean Observing System for Climate, October 18–22, SaintRaphael, France.

Kalnay, E., Kanamitsu, M., Kistler, R., Collins, W., Deaven, D., Gandin, L., Iredell, M., Saha, S., White, G., Woollen, J., Shu, Y., Chelliah, M.,

Ebisuzaki, W., Higgins, W., Janowiak, J., Mo, K. C., Ropelewski, C., Wang, J., Leetmaa, A., Reynolds, R., Jenne, R., Joseph, D., 1996. The NCEP/NCAR 40-year reanalysis project. Bulletin of the American Meteorological Society 77, 437–471.

Kessler, W. S., McCreary, J. P., 1993. The annual wind-driven Rossby-wave in the subthermocline equatorial Pacific. Journal of Physical Oceanography 23, 1192–1207.

Kindle, J. C., Hurlburt, H. E., Metzger, E. J., 1989. On the seasonal and interannual variability of the Pacific–Indian Ocean throughflow. In: Picaut, J., Lukas, R., Delcroix, T. (Eds.), Western Pacific International Meeting and Workshop on TOGA-COARE. Noumea, New Caledonia, pp. 355–366.

Kleeman, R., Power, S. B., 1995. A simple atmospheric model of surface heat flux for use in ocean modeling studies. Journal of Physical Oceanography 25, 92–105.

Le Traon, P.-Y., Nadal, F., Ducet, N., 1998. An improved mapping method of multisatellite altimeter data. Journal of Atmospheric Oceanic Technology 15, 522–534.

MacDonald, A. M., Wunsch, C., 1996. An estimate of global ocean circulation and heat fluxes. Nature 382, 436–439.

Maes, C., 1998. Estimating the influence of salinity on sea level anomaly in the ocean. Geophysical Research Letters 25, 3551–3554.

Masumoto, Y., Meyers, G., 1998. Forced Rossby waves in the southern tropical Indian Ocean. Journal of Geophysical Research 103, 27589–27602.

Meyers, G., 1996. Variation of Indonesian throughflow and the El Nino – southern oscillation. Journal of Geophysical Research 101, 12255–12263.

Meyers, G., Bailey, R. J., Worby, A. P., 1995. Geostrophic transport of Indonesian throughflow. Deep-Sea Research 42, 1163–1174.

Molcard, R., Fieux, M., Ilahude, A. G., 1996. The Indo-Pacific throughflow in the Timor Passage. Journal of Geophysical Research 101, 12411–12420.

Molcard, R. M., Fieux, M., Swallow, J. C., Ilahude, A. G., Banjarnahor, J., 1994. Low frequency variability of the currents in Indonesian channels. Deep-Sea Research 41, 1643–1661.

Molcard, R. M., Fieux, M., Syamsudin, F., 2001. The throughflow within Ombai Strait. Deep-Sea Research 48, 1237–1253.

Morey, S., Shriver, J., O'Brien, J., 1999. The effects of Halmahera on the Indonesian throughflow. Journal of Geophysical Research 104, 23281–23296.

Murray, S. P., Arief, D., 1988. Throughflow into the Indian Ocean through Lombok Strait, January 1985–January 1986. Nature 333, 444–447.

Murray, S. P., Arief, D., Kindle, J. C., 1990. Characteristics of circulation in an Indonesian archipelago strait from hydrography, current measurements and modeling results. In: Pratt, L. (Ed.), The Physical Oceanography of Sea Straits. Kluwer Academic Publishers, Norwell, MA, pp. 3–23.

Murtugudde, R., Busalacchi, A. J., Beauchamp, J., 1998. Seasonal-to-interannual effects of the Indonesian throughflow on the tropical Indo-Pacific Basin. Journal of Geophysical Research 103, 21425–21441.

Nof, D. 1996. What controls the origin of the Indonesian throughflow? Journal of Geophysical Research 101, 12301–12314.

Pacanowski, R. C., Griffies, S. M., 2000. MOM3.1 Manual. GFDL Technical Report, p. 704.

Piola, A. R., Gordon, A. L., 1984. Pacific and Indian Ocean upper layer salinity budget. Journal of Physical Oceanography 14, 747–753.

Piola, A. R., Gordon, A. L., 1986. On oceanic heat and freshwater fluxes at 30°S. Journal of Physical Oceanography 16, 2184–2190.

Potemra, J. T., 2001. Contribution of equatorial Pacific winds to southern tropical Indian Ocean Rossby waves. Journal of Geophysical Research 106, 2407–2422.

Potemra, J., Hautala, S., Sprintall, J., 2002. Interaction between the Indonesian seas and the Indian Ocean in observations and numerical models. Journal of Physical Oceanography 32, 1838–1854.

Potemra, J. T., Lukas, R., Mitchum, G. T., 1997. Large scale estimation of transport from the Pacific to the Indian Ocean. Journal of Geophysical Research 102, 27795–27812.

Power, S. B., Kleeman, R., Tseitkin, F., Smith, N. R., 1995. BMRC Technical Report on a global version of the GFDL Modular ocean model for ENSO studies, p.18.

Quadfasel, D., Cresswell, G. R., 1992. A note on the seasonal variability of the south Java current. Journal of Geophysical Research 97 (C3), 3685–3688.

Quadfasel, D., Frische, A., Cresswell, G., 1996. The circulation in the source area of the South Equatorial Current in the eastern Indian Ocean. J. Geophys. Res. 101, 12483–12488.

Reynolds, R. W., Smith, T. M., 1994. Improved global sea surface temperature analyses using optimum interpolation. Journal of Climate 7, 929–948.

Robbins, P. E., Toole, J. M., 1997. The dissolved silica budget as a constraint on the meridional overturning circulation of the Indian Ocean. Deep-Sea Research 44, 879–906.

Saji, N. H., Goswami, B. N., Vinayachandran, P. N., Yamagata, T., 1999. A dipole mode in the tropical Indian Ocean. Nature 401, 360–363.

Schneider, N., 1998. The Indonesian throughflow and the global climate system. Journal of Climate 11, 676–689.

Schiller, A., Godfrey, J. S., 2003. Indian Ocean intraseasonal variability in an ocean general circulation model. Journal of Climate 16, 21–39.

Schiller, A., Godfrey, J. S., McIntosh, P. C., Meyers, G., Wijffels, S. E., 1998. Seasonal near-surface dynamics and thermodynamics of the Indian Ocean and Indonesian throughflow, in a global ocean general circulation model. Journal of Physical Oceanography 28, 2288–2312.

Sprintall, J., Chong, J., Syamsudin, F., Morawitz, W., Hautala, S., Bray, N., Wijffels, S., 1999. Dynamics of the South Java current in the Indo-Australian basin. Geophysical Research Letters 26, 2493–2496.

Sprintall, J., Gordon, A., Molcard, R., Ilahude, A. G., Bray, N., Chereskin, T., Cresswell, G., Feng, M., Ffield, A., Fieux, M., Hautala, S., Luick, J., Meyers, G., Potemra, J., Susanto, R. D., Wijffels, S., 2001. The Indonesian throughflow: past, present and future monitoring. SOCIO Meeting, Perth, Nov. 2000.

Sprintall, J., Gordon, A. L., Murtugudde, R., Susanto, R. D., 2000. A semiannual Indian Ocean forced Kelvin wave observed in the Indonesian seas in May 1997. Journal of Geophysical Research 105, 17217–17230.

Susanto, R. D., Gordon, A. L., Zheng, Q., 2001. Upwelling along the coasts of Java and Sumatra, and its relation to ENSO. Geophysical Research Letters 28, 1599–1602.

Toole, J., Raymer, M., 1985. Heat and fresh water budgets of the Indian Ocean revisited. Deep-Sea Research 32, 917–928.

Toole, J. M., Warren, B. A., 1993. A hydrographic section across the subtropical south Indian Ocean. Deep-Sea Research 40, 1973–2019.

van Aken, H. M., Punjanan, J., Saimima, S., 1988. Physical aspects of the flushing of the east Indonesian basins. Netherlands J. Sea Res. 22, 315–339.

Verschell, M., Kindle, J., O'Brien, J., 1995. Effects of Indo-Pacific throughflow on the upper tropical Pacific and Indian Oceans. Journal of Geophysical Research 100, 18409–18420.

Wajsowicz, R. C., 1996. Flow of a western boundary current through multiple straits: an electrical circuit analogy for the Indonesian throughflow and archipelago. Journal of Geophysical Research 101, 12295–12300.

Wajsowicz, R. C., 1999. Variations in gyre closure at the water mass crossroads of the western equatorial Pacific Ocean. Journal of Physical Oceanography 29, 3001–3024.

Wajsowicz, R. C., Schneider, E. K., 2001. The Indonesian throughflow's effect on global climate determined from the COLA coupled climate system. Journal of Climate 14, 3029–3042.

Webster, P., Magana, V., Palmer, T., Shukla, J., Tomas, R., Yanai, M., Yasunari, T., 1998. Monsoons: processes, predictability, and the prospects for prediction. Journal of Geophysical Research 103, 14451–14510.

Wijffels, S., Meyers, G. A., 2004. An intersection of oceanic wave guides: variability in the Indonesian throughflow region. Journal of Physical Oceanography 34, 1232–1253.

Wijffels, S. E., Schmidt, R. W., Bryden, H. L., Stigebrandt, A., 1992. Transport of freshwater by the oceans. Journal of Physical Oceanography 22, 156–162.

Wijffels, S. E., Toole, J. M., Davis, R. E., 2001. Revisiting the south Pacific subtropical circulation: a synthesis of world ocean circulation experiment

observations along 32°S. Journal of Geophysical Research 106, 19481–19513.
Wyrtki, K., 1987. Indonesian throughflow and the associated pressure gradient. Journal of Geophysical Research 92, 12941–12946.
Xie, P., Arkin, P. A., 1997. Global precipitation: a 17-year monthly analysis based on gauge observations, satellite estimates, and numerical model outputs. Bulletin of the American Meteorological Society 78, 2539–2558.

This page intentionally left blank

Chapter 9

Coral Records of the 1990s in the Tropical Northwest Pacific: ENSO, Mass Coral Bleaching, and Global Warming

Atsushi Suzuki[1,*], Michael K. Gagan[2], Hironobu Kan[3], Ahser Edward[4], Fernando P. Siringan[5], Minoru Yoneda[6] and Hodaka Kawahata[1,7,8]

[1]*Geological Survey of Japan, National Institute of Advanced Industrial Science and Technology (AIST), Tsukuba 305-8567, Japan*
[2]*Research School of Earth Sciences, The Australian National University, Canberra, ACT 0200, Australia*
[3]*Faculty of Education, Okayama University, Okayama 700-8530, Japan*
[4]*College of Micronesia, Pohnpei 96941, Federated States of Micronesia*
[5]*National Institute of Geological Sciences, University of the Philippines, Quezon City, Philippines*
[6]*National Institute of Environmental Studies, Tsukuba 305-8506, Japan*
[7]*Ocean Research Institute, The University of Tokyo, Nakano, Tokyo 164-8639, Japan*
[8]*Graduate School of Frontier Sciences, The University of Tokyo, Nakano, Tokyo 164-8639, Japan*

Abstract

The decade of the 1990s was very likely the warmest of the second millennium. The 1990s was also characterized by one of the strongest El Niño-Southern Oscillation (ENSO) events of the twentieth century, which occurred in 1997–1998 and was followed by worldwide mass coral bleaching. In this study, we examined the signal-recording ability of *Porites* spp. corals by comparing high-resolution coral oxygen isotope ($\delta^{18}O$) records from the northwestern Pacific with instrumental records of these profound events of the 1990s. Temporal changes in coral skeletal $\delta^{18}O$ records from Ishigaki Island, Japan, showed good agreement with instrumental records of sea-surface temperature (SST) because the effect of seasonal and interannual variations in salinity on the $\delta^{18}O$ of seawater in that region was relatively small.

*Corresponding author.
E-mail address: a.suzuki@aist.go.jp (A. Suzuki).

Elsevier Oceanography Series 73
Edited by H. Kawahata and Y. Awaya
ISBN: 0-444-52948-9

In the northwestern equatorial Pacific, the cooler SST and relative drought-characterizing El Niño events were particularly well recorded by corals from the Philippines. These conditions were also faithfully recorded as distinct positive anomalies in coral $\delta^{18}O$ records from Chuuk Atoll and Pohnpei Island in Micronesia. Bleached *Porites* spp. corals from Ishigaki Island, as well as corals from Pandora Reef of the Great Barrier Reef, Australia, showed a growth gap, indicating a substantial decrease in skeletogenesis during the 1997–1998 mass bleaching event. At Ishigaki Island and the Pacific side of the Philippine Islands, a decreasing trend in $\delta^{18}O_c$ was found even over the relatively short period between 1980 and 2000 which may indicate an SST rise and/or surface-water freshening related to global warming. Our results demonstrate the potential of coral isotope records to serve as indicators of climatic change in the tropical and subtropical waters of the northwestern Pacific, where the number of coral records is still limited.

Keywords: coral; oxygen isotopes; sea-surface temperature; salinity; ENSO; western Pacific warm pool; climate change

1 Introduction

The Intergovernmental Panel on Climate Change (IPCC) has reported that the 1990s was very likely the warmest decade of the second millennium and that 1998 is the warmest year in the instrumental record (1861–2000) (IPCC, 2001). The report dared to conclude that most of the warming observed over the last 50 years can be attributed to human activities. A very wide range of physical and biological indicators was listed in the report, together with key observed changes attributable to anthropogenic climate perturbations, including a global rise in mean surface temperature, increased El Niño frequency, and frequent coral bleaching. In this regard, sea-surface temperature (SST) is an important indicator of climate change, because the global mean surface temperature is defined as the area-weighted mean of land- and sea-surface temperatures. All three of these indicators, El Niño frequency, coral bleaching, and SST rise, are detectable by analysis of coral skeletal records.

Corals offer rich archives of past climatic variability in tropical and subtropical regions, where instrumental records are limited (Gagan et al., 2000; IPCC, 2001). The oxygen isotopic composition of the coral skeleton ($\delta^{18}O_c$) is a function of both SST and the oxygen isotopic composition of seawater ($\delta^{18}O_w$; McConnaughey, 1989), which relates to salinity (Fairbanks et al., 1997). In oceanic settings where $\delta^{18}O_w$ is constant, coral $\delta^{18}O_c$ records SST variability (e.g., Dunbar et al., 1994; Wellington and Dunbar, 1995; Charles et al., 1997). In contrast, where $\delta^{18}O_w$ variations are large compared with SST changes, coral $\delta^{18}O_c$ records can be used to reconstruct

paleoprecipitation (e.g., Cole et al., 1993; Linsley et al., 1994; Tudhope et al., 1995) and sea-surface salinity (SSS) (Le Bec et al., 2000).

The synchronous ocean–atmospheric phenomenon known as the El Niño-Southern Oscillation (ENSO) appears to occur as a result of an unstable interaction between the ocean and atmosphere and comprises contrasting warm (El Niño) and cold (La Niña) states in the tropical Pacific (Philander, 1990). El Niño was originally recognized as an unusual warming of the normally cool surface waters off the west coast of South America. ENSO-related climate variations in the low latitudes of the Pacific can be recognized as an oscillation between warm–wet and cool–dry conditions. Because the combination of warm and wet or cool and dry conditions serves to increase the amplitude of $\delta^{18}O_c$ variations, coral $\delta^{18}O_c$ records are useful for examining past ENSO frequency and related climate variability (e.g., Cole et al., 1993; Dunbar et al., 1994; Linsley et al., 1994; Wellington and Dunbar, 1995; Tudhope et al., 1995, 2001; McGregor and Gagan, 2004).

Long-term trends in SST in the tropical and subtropical regions have been examined based on temporal variations in skeletal $\delta^{18}O_c$ retrieved from long-lived *Porites* spp. colonies. Gagan et al. (2000) reviewed the latest developments in the use of coral $\delta^{18}O_c$ records for reconstructing tropical climate over the past several centuries. They pointed out several important findings based on published long-term coral $\delta^{18}O_c$ records, including: (1) a warming/freshening trend during the nineteenth and twentieth centuries, (2) a contribution to the shift in $\delta^{18}O_c$ from freshening of the ocean surface too large to neglect, and (3) abrupt, spatially coherent shifts in $\delta^{18}O_c$ values, possibly related to enhanced volcanism and other global climate events. Long records of ocean temperatures from corals are expected to be particularly valuable for improving our knowledge of climate history (Jones et al., 2001).

Coral bleaching has been described in the literature since the beginning of the twentieth century, including an early observation from the Great Barrier Reef (GBR) (Yonge and Nicholls, 1931). Since the late 1970s, however, there have been numerous reports of mass bleaching affecting coral reefs in the Caribbean and elsewhere in the tropics (Glynn, 1984). These recurrent coral-bleaching events may be a response to global warming (Glynn, 1990, 1991). Coral bleaching is commonly linked to unusually high SST, which destroys the symbiotic relationship between the host corals and zooxanthellae (Jokiel and Coles, 1990). During 1997–1998, in particular, severe coral bleaching was reported from many coral reefs in the tropical and subtropical regions of the world. This global-scale coral-bleaching event coincided with one of the strongest El Niño events of the twentieth century and the warmest global temperatures on record (Lough, 2000). Thermal stress and bleaching of corals are reported to reduced calcification and decrease skeletal extension rates (Jokiel and Coles, 1977; Oliver, 1985; Goreau

and Macfarlane, 1990; Leder et al., 1991; Tudhope et al., 1992). Suzuki et al. (2000) also identified a distinct reduction in skeletal growth of a *Porites lutea* coral during the 1997–1998 mass bleaching event in the Ryukyu Islands. However, the effects of bleaching on stable isotope ratios and proxy climate records extracted from coral skeletons have not been fully examined until very recently (Suzuki et al., 2003).

Our purpose here is to demonstrate that long-lived, massive *Porites* spp. corals can provide accurate climatic information suitable for high-resolution paleoclimate reconstructions. We chose to examine corals in the tropical western Pacific because this is an excellent locality for reconstructing both oceanic and atmospheric anomalies associated with ENSO (Gagan et al., 2004). We present high-resolution skeletal $\delta^{18}O_c$ records of *Porites* spp. corals from four sites: Ishigaki Island in southern Japan, Bicol in the Philippines, and Chuuk (Truk) Atoll and Pohnpei Island in Micronesia. The response of coral growth to the 1997–1998 mass-bleaching event was investigated by comparing skeletal $\delta^{18}O_c$ microprofiles for *Porites* corals from Ishigaki Island and Pandora Reef, central GBR. These coral records demonstrate their ability to function as archives of the ENSO phenomenon, coral-bleaching events, and long-term trends in SST.

2 Study Sites: Tropical Northwestern Pacific

The main area sampled for corals in the present study was the tropical northwestern Pacific, where published coral records are still rare compared with other areas in the tropics and subtropics (Fig. 1; Table 1). The study area covers a relatively wide range of latitude, from Pohnpei Island (7°N) in the equatorial Pacific to Ishigaki Island (24°N) in the Kuroshio Current region of the northwestern Pacific.

The western equatorial Pacific is one of the hottest and wettest tropical ocean regions on Earth. The area in which SST is higher than 28 °C is referred to as the western Pacific warm pool (WPWP) (Yan et al., 1992) and more recently as the Indo-Pacific Warm Pool (IPWP), which includes warm areas in the eastern Indian Ocean (Gagan et al., 2004). Climatic variability relating to the ENSO cycle is typically large along the equator. Corals from Micronesian islands located near the northern border of the WPWP, Palau, Chuuk, Pohnpei, and Majuro, lie along an east–west transect at about 7°N latitude, providing a unique opportunity to reconstruct the migration (E–W zonal displacement) and expansion (in total area and N–S breadth) of the WPWP, both seasonally and in response to the interannual ENSO cycle. Seasonal variations in SST and SSS show an east–west trend along this island transect (Fig. 1; Levitus et al., 1994). Annual mean SST increases, and SSS decreases, westward from Majuro to Palau, because Palau is close to the center of the WPWP.

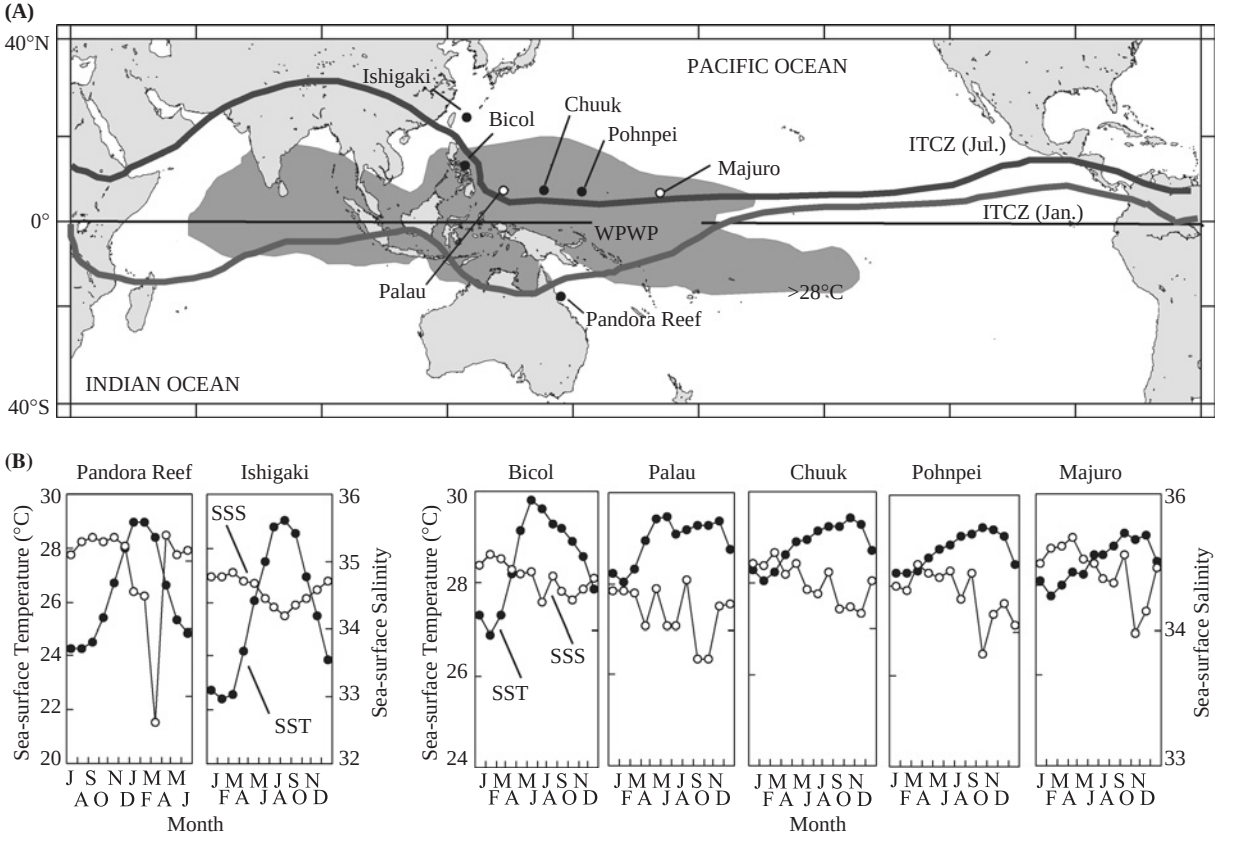

Figure 1: Oceanic settings of study sites in the western Pacific. (A) The location of the western Pacific warm pool (WPWP, mean annual SST > 28 °C) is shown, together with the average position of the Intertropical Convergence Zone (ITCZ) in July and January. (B) Climatological monthly sea-surface temperature (SST), and sea-surface salinity (SSS) at each coral site. The DASILVA SMD94 climatology data (da Silva et al., 1994; http://ingrid.ldeo.columbia.edu/SOURCES/.DASILVA/.SMD94/.climatology/) and data from Levitus et al. (1994) were used for SST and SSS, respectively.

Table 1: *Porites* coral samples examined in this study.

Site	Core id.	Locality		Depth (m MSL)	Date of collection	DASILVA SMD94			Microsampling interval (μm)	Reference
		Lat.	Long			Mean	Max.	Min.		
Micronesia										
Chuuk Atoll	CHU99-01	8°N	152°E	3.9	March 11, 1999	28.8	29.4	28.1	400	This study
Pohnpei Reef	POH99-01	7°N	158°E	1.0	March 15, 1999	28.8	29.3	28.3	400	Inoue et al. (2004)
Philippines										
Bicol	SWGM01-01	13°N	124°E	6	March 2001	28.5	29.8	26.9	400	This study
Ishigaki I., Japan		24°N	124°E			25.7	29.0	22.4		
Urasoko Bay	IU96-07			3.6	November 22, 1996				400	Suzuki et al. (1999)
Shiraho Reef	IS91-06			2	September, 1991					This study
Yasura Channel	IY99-01			0.7	February 2, 1999				200	Suzuki et al. (2003)
Yasura Channel	IY99-02			0.8	February 2, 1999				200	Suzuki et al. (2003)
Great Barrier Reef		19°S	146°E			26.3	28.9	24.2		
Pandora Reef	PAN-1-B			5	January 14, 1999				200	Suzuki et al. (2003)
Pandora Reef	PAN-3			5	January 14, 1999				200	Suzuki et al. (2003)

MSL, mean sea level; SST, sea surface temperature.

Seasonal variation of rainfall in the tropic zone is generally controlled by the position of the Intertropical Convergence Zone (ITCZ; Fig. 1). The ITCZ is an area of low pressure where the northeast and southeast trades meet, and it is characterized by a band of heavy precipitation. On the other hand, interannual variations of SST and rainfall in the western equatorial Pacific are strongly influenced by the ENSO phenomenon (Fig. 2). From the Philippines to Micronesia cooler SSTs and relative drought characterize El Niño events, when the WPWP and the Indonesian low atmospheric pressure system migrate eastward toward the central Pacific. Cooling of SSTs is probably caused by the shallowing of the thermocline as a result of the relaxation of the trade winds across the Pacific basin. Lower than average rainfall in the WPWP area is a result of zonal displacement of convective centers of the Walker circulation during El Niño events.

Two of the four coral sites examined in this study, Bicol (13°N, 124°E), near the southeastern tip of Luzon Island in the Philippines, and Ishigaki Island, one of the Ryukyu Islands in the East China Sea, are located within the path of the warm Kuroshio Current (Fig. 1). Bicol is close to the point where the North Equatorial Current bifurcates, forming the northward flowing Kuroshio and the southward flowing Mindanao Current. Bicol appears to be located near the center of the area of reduced rainfall during El Niño events, but the local SST there shows little correlation with the Southern Oscillation Index (SOI; Trenberth and Hoar, 1996), which is a widely recognized index of ENSO activity (Fig. 2). The seasonal variation in SST increases from the Bicol region northward toward Ishigaki Island (Fig. 1). In terms of interannual variation of SST at Ishigaki Island the majority of the highest SST measurements have been obtained during summers following the onset of El Niño events (warm phase of ENSO), indicating a teleconnection linking Ishigaki SST to ENSO (Suzuki et al., 2000, 2003). Park and Oh (2000) reported a teleconnection pattern between the East China Sea and the equatorial Pacific: SSTs in the East China Sea show significant coherence with SSTs in the Niño 3.4 region (Trenberth, 1997), with a phase lag of 5–9 months. Therefore, the anomalously warm SSTs around the Ryukyus in 1998, which resulted in severe coral bleaching in the area, may have been related to the 1997–1998 El Niño.

3 Materials and Methods

3.1 Micronesia

Vertical cores were retrieved from *Porites* corals at Chuuk Atoll (8°N, 152°E) and Pohnpei Island (7°N, 158°E) of the Federated States of Micronesia (Fig. 1). A 180-cm-long coral core was extracted on March 11–12, 1999 from a *Porites*

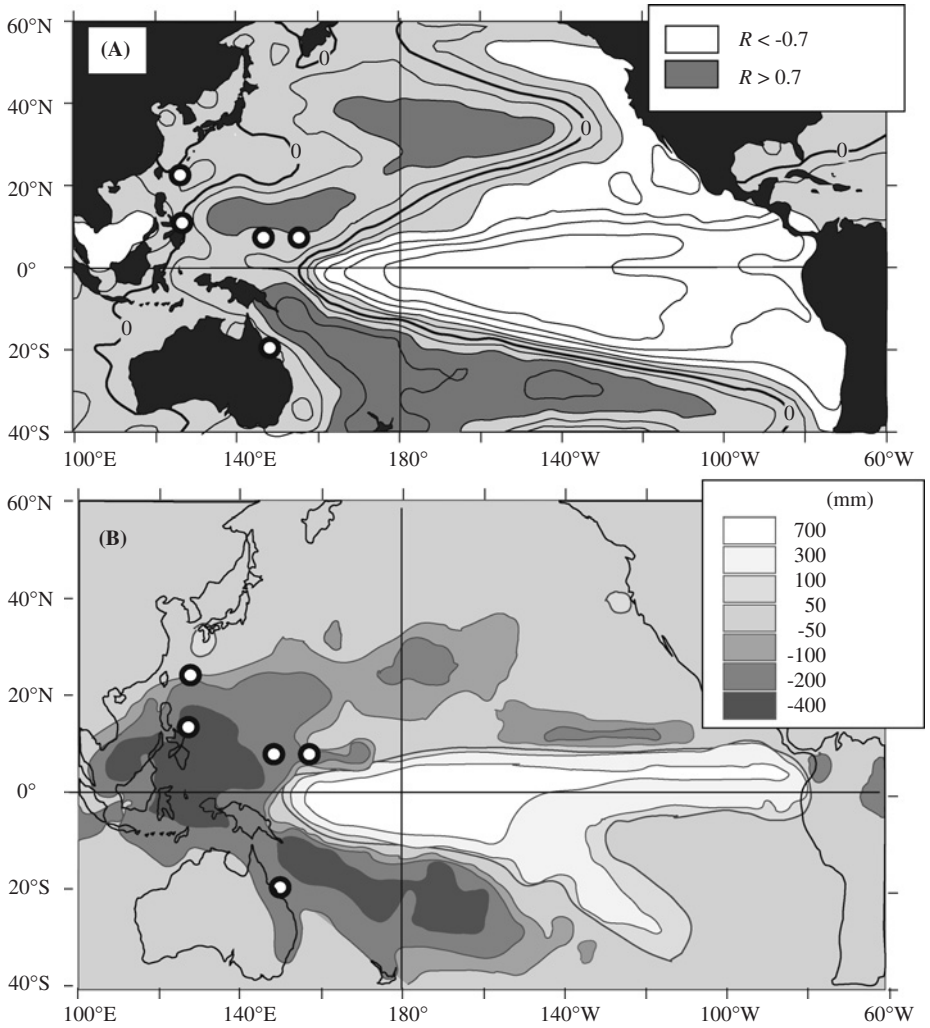

Figure 2: (A) Map of correlations of the smoothed Southern Oscillation Index (SOI; negative Darwin sea-level pressure anomalies) with monthly SST anomalies from 1950 to 1994 (contour interval, 0.1). Magnitudes of regression coefficient (R) exceeding +0.7 and −0.7 are lightly and darkly shaded, respectively. The map is reproduced from Trenberth and Hoar (1996). (B) Pattern of annual precipitation anomalies associated with moderate to strong El Niño events from 1900 to 1998 compared to normal years (after Dai and Wigley, 2000). Locations of sites with coral records discussed in text are shown by circles.

lutea colony at 3.9 m below mean sea level (MSL) in a channel of the outer reef near the Northeast Pass, Chuuk Atoll. The core (sample ID: CHU99-01) was sectioned into 7-mm-thick slabs, which were cleaned with deionized water.

Coral slabs were processed according to the microsampling procedures described by Gagan et al. (1994, 1996, 1998). The microsampling interval was 400 μm along the major growth axis of the core. Measurements of skeletal oxygen isotope ratio ($\delta^{18}O_c$) were carried out on every fourth sample over a distance of about 17 cm downward from the growth surface of the colony, corresponding to a time resolution of about 1 month.

A 97-cm-long coral core (sample ID: POH99-02) was recovered from a *Porites* sp. colony at about 1.0 m below MSL on the coral reef about 2 km offshore of the airport near Kolonia, Pohnpei Island, on March 15, 1999 (Inoue et al., 2004). The same procedures were employed to microsample this core. We also obtained cores from a *Porites* sp. coral in Majuro Atoll's lagoon in 1999, but here we only discuss the result of SST monitoring at Central Shoal, also in the lagoon.

3.2 Bicol, The Philippines

Coring was conducted on a live colony of *Porites* sp. coral off the northern coast of Sawanga, a village in the city of Sorsogon, Bicol (Region V), Philippines (13°N, 124°E; Fig. 1). The coral collection site was near the wide opening of Albay Gulf into the Philippine Sea (western Pacific). The 2.5-m-high colony was growing on a gentle outer reef slope about 6 m below MSL. The core was extracted in March 2001 from the top of the colony (sample ID: SWGM01-01). The microsampling interval was 400 μm along the major growth axis of the core.

3.3 Ishigaki Island, The Ryukyus

Corals were collected from three sites around Ishigaki Island (24°N, 124°E; Fig. 1). A *Porites australiensis* coral (sample ID: IU96-07), growing 3.6 m below MSL in relatively well-flushed conditions, was collected on November 22, 1996 from Urasoko Bay, along the northern coast of the island (Suzuki et al., 1999). Another small coral (*Porites lutea*; sample ID: IS91-06; diameter < 20 cm) was collected from the bottom of a moat (2 m below MSL) in the lee of the fringing reef off the southeast coast (Suzuki et al., 2001).

A *Porites lutea* colony forming a fused complex in a reef channel off Yasura-zaki, in the northern part of Ishigaki Island, became discolored during the 1998 mass bleaching event, but other *Porites* colonies of the fused complex showed no change in color (Suzuki et al., 2003). Vertical coral cores were extracted from the tops of nonbleached (sample ID: IY99-01) and bleached (IY99-02) colonies on February 2, 1999 approximately 6 months after the onset of bleaching in this region.

Coral specimens, except for IU96-07, were microsampled vertically along the major growth axis according to the same method described above. On

average, about 50 samples per annual growth increment were collected. The microsampling of specimen IU96-07 along the major growth axis was conducted using a microdrill with a 0.5-mm-diameter bit, as described by Suzuki et al. (1999).

3.4 Pandora Reef, GBR

To further examine the response of coral calcification to the 1997–1998 mass-bleaching event, several short coral cores (6–13 cm long) were collected from three massive *Porites* spp. colonies at 5 m depth on the seaward side of Pandora Reef, GBR (18°S, 146°E) on January 14, 1999 (Suzuki et al., 2003). We analyzed two cores from the collection of drilled specimens. One core (PAN-1-B) was extracted from the side of a large *Porites lutea* colony. Sample PAN-3 was extracted from the side of a *Porites* cf. *lutea*/*australiensis* colony (~1 m diameter). All coral cores were taken from the sides of the colonies to minimize damage to the colonies from the coring. The microsampling interval for PAN-1-B and PAN-3 was 200 μm along the major growth axis of the cores. Coral bleaching was reported initially at Pandora Reef in March 1998, the end of the austral summer, and 1 month after a large river-runoff event. Thus, the date of sample collection was approximately 9 months after the onset of mass coral bleaching.

3.5 Isotopic Measurements

Stable isotopic analysis of 70–130 μg microsamples from seven coral cores (CHU99-01, POH99-02, SWGM01-01, IY99-01, IY99-02, PAN99-01-B, and PAN99-03) was conducted by reacting the coral aragonite with 100% H_3PO_4 at 90°C in an automated individual-carbonate reaction device (Multiprep, Micromass, Manchester, UK) coupled with a Micromass Optima mass spectrometer at the Geological Survey of Japan, National Institute of Advanced Industrial Science and Technology (AIST) (Suzuki et al., 2000). Carbonate samples for IS91-06 were processed by an automated individual-carbonate reaction (Kiel) device attached to a Finnigan MAT251 mass spectrometer at the Australian National University (Gagan et al., 1994; Suzuki et al., 2001). Coral isotopic data are reported as per million (‰) deviations ($\delta^{18}O_c$) relative to Vienna Peedee Belemnite (V-PDB) (Coplen, 1996). Both mass spectrometers had comparable internal precision for $\delta^{18}O$ (~0.04‰, 1σ). In this study, the oxygen isotope ratios in water ($\delta^{18}O_w$) are also expressed using δ notation, but the reference material is Vienna Standard Mean Ocean Water (V-SMOW; Coplen, 1996).

3.6 Instrumental Records

Several time series of instrumental records of marine parameters were compared with the coral $\delta^{18}O_c$ records. Integrated Global Ocean Services System Products Bulletin, National Meteorological Center (IGOSS NMC) blended ship and satellite data for each 1° square since 1982 were used for the SST time series (Reynolds and Smith, 1994). Because some differences between satellite-based and *in situ* SSTs have been reported in inshore waters (Gagan et al., 1998; Suzuki et al., 1999), we made measurements of SST *in situ* at Chuuk, Pohnpei, Majuro, Bicol, and Ishigaki using TidbiT temperature loggers. The temperature loggers were all attached to the coral colonies from which we extracted skeletal cores, except for that at Majuro Atoll. DASILVA SMD94 climatology data (da Silva et al., 1994), which depict the seasonal and yearly variations of the surface marine atmosphere over the global oceans at the resolution of 1° square, were also used to determine the seasonal variation of SST at coral sites (Fig. 1). *In situ* SSS measurements in the tropical Pacific for 1969–1995 have been compiled and gridded by the Institut de Recherche pour le Développement (IRD) Center in Nouméa, New Caledonia (Delcroix, 1998; http://www.ird.nc/ECOP/), so a monthly SSS time series for the grid between 6°–8°N and 145°–155°E was compared with the Chuuk coral records.

4 Results and Discussion

4.1 Coral $\delta^{18}O$ Record of SST at Ishigaki Island

The *Porites australiensis* colony (IU96-07) in Urasoko Bay, Ishigaki Island, is only 300 m from a long-term daily temperature monitoring station (Yaeyama Station, Japan Sea-Farming Association). Therefore, this coral specimen was considered a good material for the calibration of the skeletal $\delta^{18}O_c$ response to changes in SST (Figs. 3 and 4). Suzuki et al. (1999) proposed the following skeletal $\delta^{18}O_c$–SST relationship (Fig. 5):

$$\delta^{18}O_c(\%) = -0.611 - 0.165T\,(^{\circ}C). \quad (1)$$

The seasonal variation of SST around Ishigaki Island is about 10 °C, and the seasonal salinity change is less than 0.5. Watanabe and Oba (1997) estimated the $\delta^{18}O_w$ variation corresponding to the seasonal salinity change to be 0.1%. Therefore, the effects of seasonal changes in SST on coral $\delta^{18}O_c$ are far greater than the effect of seasonal changes in salinity on $\delta^{18}O_w$; thus, the effect of changes in $\delta^{18}O_w$ on the $\delta^{18}O_c$–SST calibration are negligible.

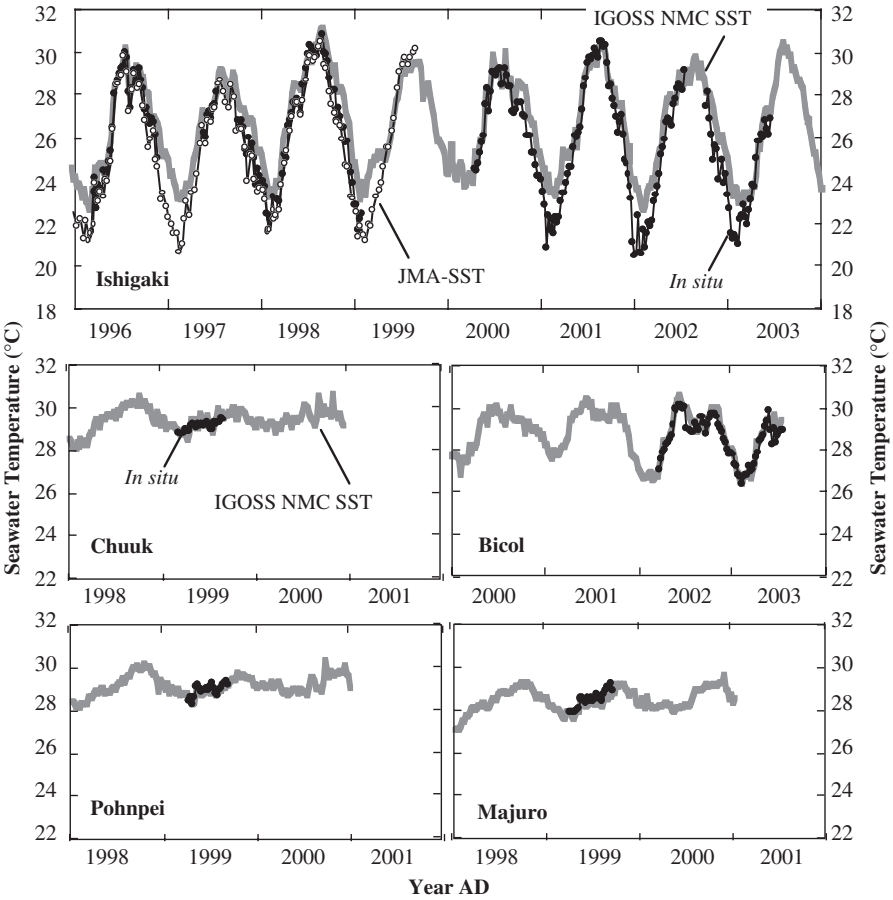

Figure 3: Comparison of satellite-derived SST (IGOSS NMC SST; Reynolds and Smith, 1994) and *in situ* SST measurements at five coral coring sites: Ishigaki Island (Shiraho reef), Bicol (off Sorsogon City), Chuuk Atoll (East Channel), Pohnpei Island (Main Channel), and Majuro Atoll (Central Shoal). Gray lines and black lines with circle lines indicate weekly means of satellite-derived and *in situ* SSTs, respectively. The 10-day mean record at Ishigaki Port derived from a daily observation at 10:00 a.m. local time (black line with open circles) is also shown (Ishigaki-jima Meteorological Observatory, the Japan Meteorological Agency; JMA). At the low latidude Micronesian and Philippine coral sites, *in situ* monitoring of SST showed no differences with IGOSS SSTs, which indicates the accuracy of both measures. However, at the higher latitude of Ishigaki Island, wintertime IGOSS NMC SSTs showed relatively large differences of up to 2 °C with *in situ* SSTs as a result of strong surface cooling.

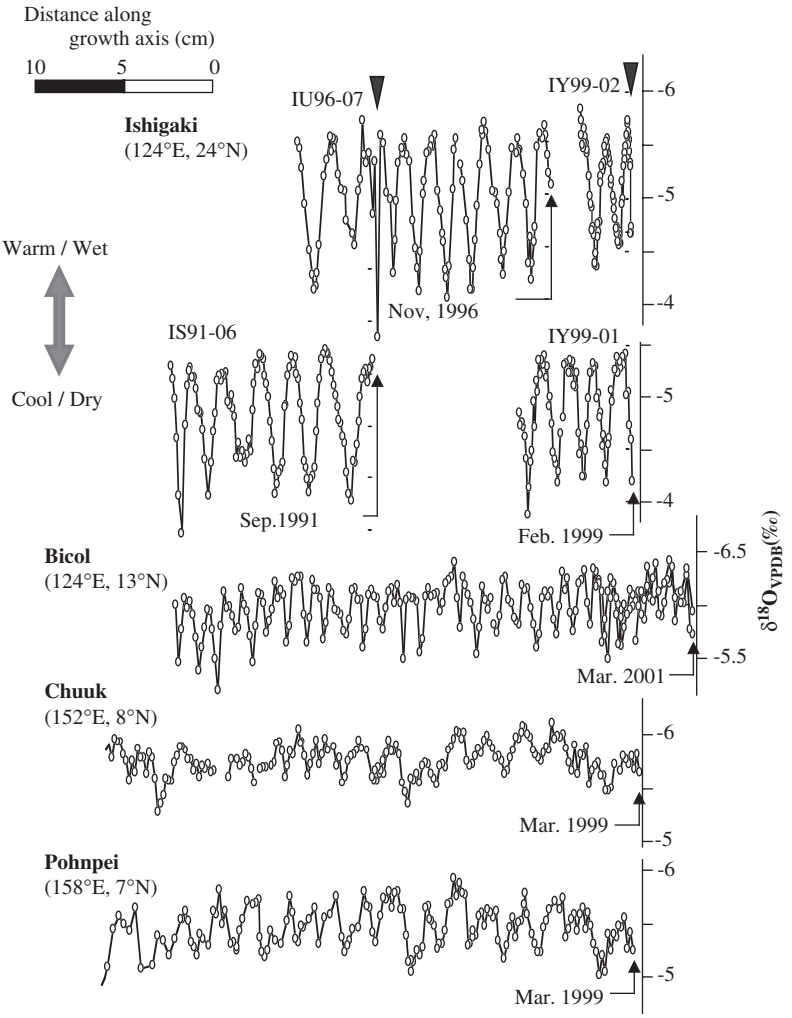

Figure 4: Coral $\delta^{18}O$ records for the western Pacific region covering about 20 years (locations of coral cores are shown in Fig. 1). Black triangles mark positions of growth perturbations in Ishigaki Island corals identified by abrupt shifts in $\delta^{18}O$ profiles. Dates of coral collection are shown with arrows. Details of cores (locality, coral species name, time-span of records) are given in the text.

Suzuki et al. (1999) pointed out that the $\delta^{18}O_c$/SST slope in equation (1) is close to those reported earlier for *Porites* spp. corals from other regions of the Pacific, but differs from that reported by Mitsuguchi et al. (1996) for *Porites lutea* from the east coast of Ishigaki Island (Fig. 5). Suzuki et al. (1999) suggested that the lower frequency of microsampling by Mitsuguchi et al.

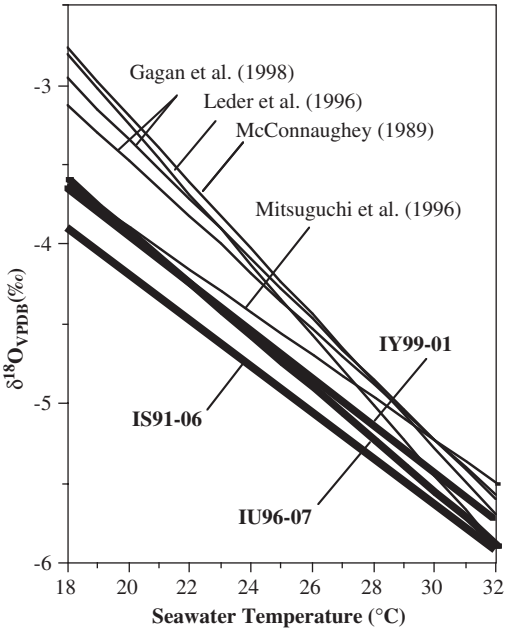

Figure 5: Comparison of the temperature dependence of coral $\delta^{18}O_c$. Bold lines indicate *Porites* spp. coral specimens from Ishigaki Island, southern Ryukyus. Specimen details (sample i.d.,$\delta^{18}O_c$-SST slope, coral species, locality, original reference) are as follows: IS91-06 (-0.140‰ $^{\circ}C^{-1}$, *P. lutea*, Shiraho, this study), IY99-01 (-0.148‰ $^{\circ}C^{-1}$, *P. lutea*, Yasura-zaki, this study), IU96-07 (-0.165‰ $^{\circ}C^{-1}$, *P. australiensis,* Urasoko, Suzuki et al., 1999), and a *Porites* colony (0.134‰ $^{\circ}C^{-1}$, *P. lutea*, Yasura-zaki, Mitsuguchi et al., 1996). The negative displacement of calibration lines for the Ishigaki corals is due to the differences in mean $\delta^{18}O_w$ between Ishigaki Island and the other regions (McConnaughey, 1989; Leder et al., 1991; Gagan et al., 1998; Suzuki et al., 1999, 2001).

(1996) is a possible cause of the difference in the $\delta^{18}O_c$/SST slope relationship between those of Mitsuguchi et al. (1996) and that of Suzuki et al. (1999), because a lower sample frequency would be expected to result in the attenuation of seasonal $\delta^{18}O_c$ signals.

Through multiple deployments of temperature loggers at the coral sites, we found that IGOSS SSTs generally showed excellent agreement with *in situ* temperature records in low-latitude tropical regions, including the Micronesian islands and Bicol (Fig. 3). However, wintertime IGOSS NMC SSTs showed a relatively large difference of up to 2°C with *in situ* SSTs monitored in moats (shallow lagoons) in the subtropical Shiraho and Yasura-zaki areas of Ishigaki Island, suggesting that the utility of satellite-based SSTs for comparison with high-latitude coral records may be limited. On the other hand, SST records from Ishigaki Port collected by the Japan

Meteorological Agency (JMA) showed good agreement with *in situ* SSTs at coral sites around Ishigaki Island. Thus, we analyzed two coral specimens from the Shiraho and Yasura-zaki coral reefs to calibrate the $\delta^{18}O_c$ signal against JMA SSTs collected in Ishigaki Port (Fig. 4). The skeletal $\delta^{18}O_c$–SST relationships obtained for colonies IS91-06 (Shoraho reef) and IY99-01 (Yasura-zaki channel) are shown by equations (2) and (3), respectively:

$$\delta^{18}O_c(‰) = -1.444 - 0.140T(^{\circ}C) \quad (R^2 = 0.99) \tag{2}$$

$$\delta^{18}O_c(‰) = -0.999 - 0.148T\,(^{\circ}C) \quad (R^2 = 0.95) \tag{3}$$

These slopes fall between $-0.134‰\,^{\circ}C^{-1}$ and $-0.165‰\,^{\circ}C^{-1}$ reported by Mitsuguchi et al. (1996) and Suzuki et al. (1999), respectively. Because the microsampling frequency of these two specimens (IS91-06 and IY99-01) was comparable to that of IU96-07 (Suzuki et al., 1999), the smaller slopes obtained for IS91-06 and IY99-01 cannot be attributed to signal attenuation caused by a lower frequency of microsampling. This relatively large variation in the SST–$\delta^{18}O_c$ relationship found at a single island may be related to biological and genetic factors rather than to a difference in microenvironments. Further research, including examination of interspecies differences in the genus *Porites*, is needed to determine the cause of the variation (e.g., Suzuki et al., in press). Keeping these caveats relating to the $\delta^{18}O_c$–SST calibration in mind, we believe that the similarity between the skeletal $\delta^{18}O_c$ profiles and the *in situ* SST time series (Fig. 6) indicates that coral $\delta^{18}O_c$ records can be used as a good proxy for SST in reef settings where the influence of SSS variation on $\delta^{18}O_c$ is negligible.

4.2 ENSO Signals in the Coral $\delta^{18}O$ Record from Micronesia

As expected from seasonal variations in SST and SSS (Fig. 1), annual periodicity was clearly observed in $\delta^{18}O_c$ profiles of the Chuuk and Pohnpei corals (Fig. 4). We employed a coral chronology based on peak matching between skeletal $\delta^{18}O_c$ and instrumental SST with simple linear interpolation; the minima and maxima in the annual $\delta^{18}O_c$ curves were designated as the highest and lowest annual SSTs (Fig. 7). Comparison of the monthly $\delta^{18}O_c$ profile of Chuuk coral CHU99-01 with times series of environmental variables (1980–1999) revealed a modal change in annual $\delta^{18}O_c$ variation relating to the ENSO cycle (Fig. 7). During non-El Niño periods, a combination of warm SSTs and high rainfall in the wet season (June–November) causes coral $\delta^{18}O_c$ values to decrease, whereas the cooler dry season (December–May) produces higher $\delta^{18}O_c$ values. On the other hand, pronounced increases in coral $\delta^{18}O_c$ are evident during El Niño maxima,

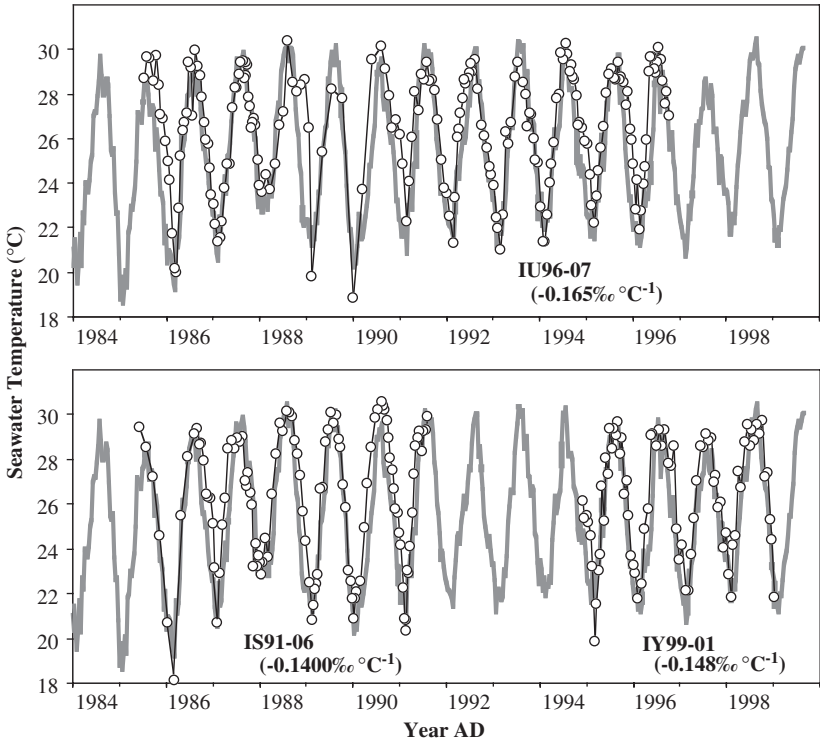

Figure 6: Time-series of instrumental SSTs (gray line) and estimated SST based on coral $\delta^{18}O_c$ records (black line with open circles) from Ishigaki Island, southern Japan. A 10-day mean SST record at Ishigaki Port conducted by the JMA Ishigaki-jima Meteorological Observatory is shown for comparison with the coral $\delta^{18}O_c$ record. SSTs were estimated using equations (1), (2), and (3) for IU96-07, IS91-06, and IY99-01, respectively. The slope of the $\delta^{18}O_c$–SST relationship is shown in each profile. The coral time-series is plotted using linear interpolation between the minima and the maxima of the coral $\delta^{18}O_c$ estimates of SST.

corresponding to cooler SSTs and drought conditions around Chuuk Atoll. Similar climate variations are recorded by the skeletal $\delta^{18}O_c$ of corals living within the WPWP, particularly those from the north coast of Papua New Guinea (Tudhope et al., 1995, 2001; McGregor and Gagan, 2004), North Sulawesi, Indonesia (Moore et al., 1997; Hughen et al., 1999), and Fiji (Le Bec et al., 2000). In detail, the amplitude of the $\delta^{18}O_c$ anomaly corresponds well to El Niño intensity, as indicated by SOI values; the unusually strong El Niño event of 1982–1983, which had widespread ecological and economic impact, shows the largest anomaly in the $\delta^{18}O_c$ profile (Fig. 7).

Coral $\delta^{18}O_c$ values of CHU99-01 showed moderate correlation with both SST and SSS, reflecting that SST and SSS in the region fluctuate with

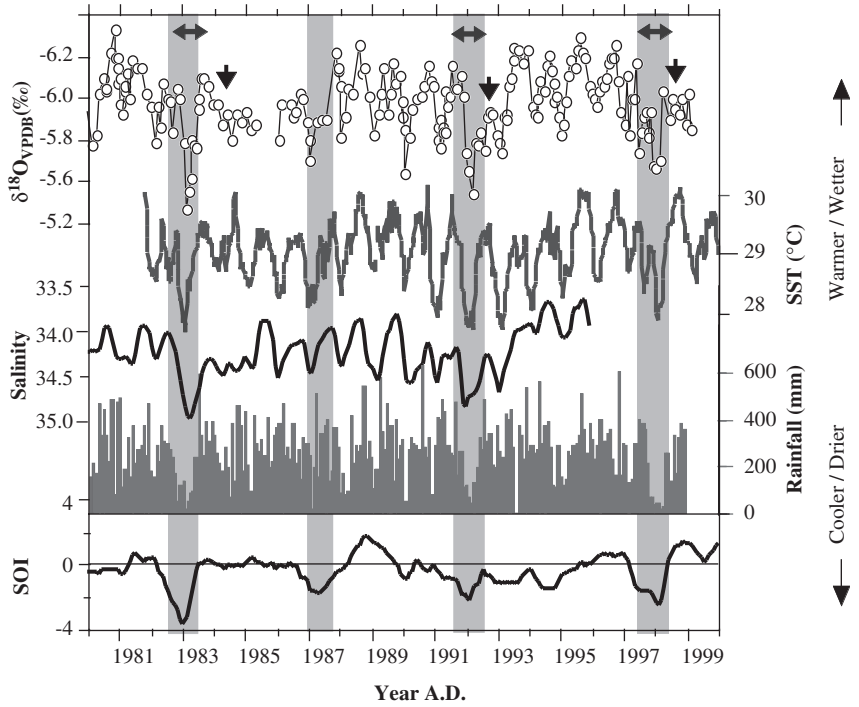

Figure 7: Comparison of skeletal $\delta^{18}O_c$ of the Chuuk coral and instrumental records of climate for the period between 1980–99. Rainfall was observed at a NOAA station (http://lumahai.soest.hawaii.edu/Enso/data/ftp/STATION-RAIN2/chuuk-sum.txt), and the SOI is a standardized sea-level pressure difference (http://ingrid.ldgo.columbia.edu/SOURCES/.Indices/.soi/.standardized/). See text for other data sources. No filter was applied to isotope data. Double arrows indicate the distinct increase in $\delta^{18}O_c$ during El Niño years, while single arrows indicate compression of $\delta^{18}O_c$ curves in the year following the El Niño peak. Note that $\delta^{18}O_c$ and SSS is reverse-plotted so that El Niño-related anomalies vary in the same direction as the other parameters. Time-series of monthly rainfall and SOI are smoothed by a 3-month and 5-month moving average, respectively. El Niño events are shown by shading according to the classification by the NCEP/CPC (http://www.cpc.ncep.noaa.gov/products/analysis_monitoring/ensostuff/ensoyears.html).

comparable amplitude with respect to the coral $\delta^{18}O_c$ signal (Fig. 8). Although when all $\delta^{18}O_c$ data were plotted against SST, the slope of the regression line was different from that of the temperature dependency relationship for coral aragonite (0.13‰–0.18‰ $^{\circ}C^{-1}$; Fig. 8); the discrepancy can be attributed to changes of $\delta^{18}O_W$ in seawater during the ENSO cycle. Coral $\delta^{18}O_c$ values corresponding to El Niño events showed a shift toward higher $\delta^{18}O$ values owing to ^{18}O enrichment of the seawater.

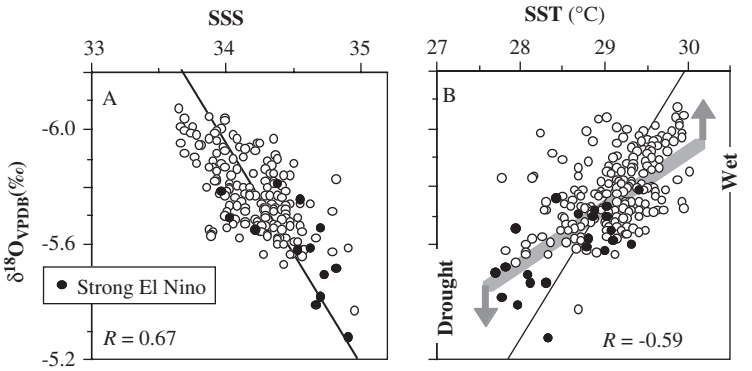

Figure 8: Crossplots of coral $\delta^{18}O_c$ and monthly observations of SSS (A) and SST (B) at Chuuk Atoll. Monthly coral $\delta^{18}O_c$ time-series were resampled using AnalySeries software (Paillard et al., 1996). Months categorized as reflecting strong El Niño conditions by the NCEP/CPC are plotted as closed circles. $SSS = 41.7+1.30\delta^{18}O_c$, $R^2 = 0.35$, $P<0.01$; $SST = 16.9-2.11\ \delta^{18}O_c$, $R^2 = 0.45$, $P<0.01$. The gray bar in panel B represents $\delta^{18}O_c$–SST slope for coral aragonite (-0.13‰ to -0.18‰ $^{\circ}C^{-1}$).

The intra-annual $\delta^{18}O_c$ fluctuations were well recorded by high-resolution microsampling, so the temporal evolution of each El Niño event can be discussed using coral records. El Niño events are usually characterized by initial cooling of SSTs in the tropical western Pacific, followed by lower than average rainfall. A distinct positive shift in $\delta^{18}O_c$ in the year of a strong El Niño event can be attributed to this initial cooling. The skeletal $\delta^{18}O_c$ values for the year following a strong El Niño event do not vary much, suggesting the persistence of cool and/or high-salinity conditions for almost a year (Fig. 7). Although the lower SST can be attributed primarily to the eastward migration of the WPWP during the El Niño event, the shallowing of the thermocline brought about by relaxation of the trade winds across the Pacific basin is also important for surface cooling. High-salinity conditions in the year following a strong El Niño event also appear to be caused by the shallowing of the thermocline, along with the direct effect of the decrease in rainfall locally. Because rainfall and SST data quickly recovered to normal levels just after the El Niño peak, salt advection by the North Equatorial Counter Current and/or subsurface mixing due to transformation of a "barrier layer" (Lukas and Lindstrom, 1991) seems to account for the positive $\delta^{18}O_c$ anomalies in the years following the El Niño peak.

The combination of a positive shift in $\delta^{18}O_c$ followed by compression of the $\delta^{18}O_c$ curve, signals an El Niño event throughout the region because these features were also seen in the Pohnpei Island coral $\delta^{18}O_c$ record (Fig. 4). The

coral $\delta^{18}O_c$ record also shows a potential for quantitative examination of the individual characteristics and temporal evolution of each past El Niño event. Such an examination would improve our understanding of the ENSO cycle, although additional measurements of the skeletal Sr/Ca ratio, an independent proxy for SST, are desirable for a more precise reconstruction. Further $\delta^{18}O_c$ measurements on longer cores would allow us to explore changes in the frequency of El Niño events over the past several centuries and the effect of global warming on the ENSO cycle.

4.3 Skeletal $\delta^{18}O$ Records of Coral Bleaching

Extensive coral bleaching was witnessed in the GBR, Australia, during the austral summer of 1997–1998 and appeared later in the Northern Hemisphere (Wilkinson, 1998). For the first time on record, corals around the Ryukyu Islands, Japan, exhibited severe bleaching which resulted in extensive coral mortality (Fujioka, 1999). The most likely cause of the high-SST event around the Ryukyus in the summer of 1998 was the lack of typhoons in the Ryukyu Islands region (Fujioka, 1999). Low-pressure systems, including tropical typhoons, bring high cloudiness and stimulate vertical mixing of the surface water, which may result in an SST decrease. In the absence of typhoons during the summer of 1998, SST continued to rise because of solar heating during the same year and resulted in an extraordinarily high SST around Ishigaki Island (daily mean SST of 31.5 °C; Fig. 4) which caused the mass bleaching event.

While there has been remarkable progress in understanding the photophysiological processes of coral bleaching (Lesser, 1996; Brown, 1997), less is known about the effect of bleaching on coral skeletogenesis. Moreover, the influence of bleaching on the geochemical composition ($\delta^{18}O$, $\delta^{13}C$, Sr/Ca) of coral skeletons has been controversial. Some studies reported clear changes associated with bleaching events, while in others changes were less evident (Porter et al., 1989; Leder et al., 1991; Alison et al., 1996). However, very fine-resolution sampling is required to detect isotopic changes in the coral skeletons corresponding to brief bleaching events. Recently, Suzuki et al. (2003) introduced a high-resolution skeletal isotope microprofiling technique for examining the skeletal records of coral bleaching (Fig. 9). When this technique was used, bleached corals from Pandora Reef, GBR, and Ishigaki Island, Japan, showed a dramatic decrease in skeletogenesis that was coincident with the worldwide mass coral-bleaching event of 1997–1998. These results indicate that isotopic microprofiling may be the key to identifying gaps in coral growth that are diagnostic of past bleaching events.

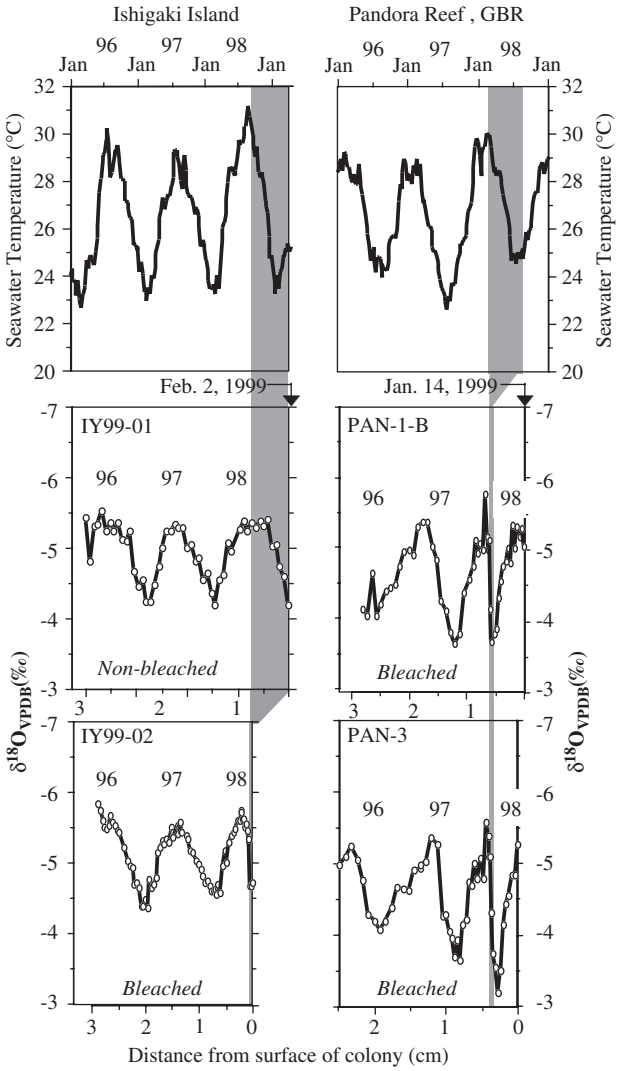

Figure 9: Skeletal $\delta^{18}O_c$ records of *Porites* spp. corals from Ishigaki Island and Pandora Reef, plotted against distance from the surface of the colonies along the microsampling transects. Regional weekly SSTs (IGOSS NMC SSTs) are shown in the top-most panels for comparison with the shape of the coral annual $\delta^{18}O_c$ cycles. The year shown above the $\delta^{18}O_c$ minimum indicates boreal summer for the Ishigaki corals, and austral winter for the Pandora Reef corals. The intervals of growth discontinuity are shown by shaded vertical bars. Data are replotted from Suzuki et al. (2003).

4.4 Recent Decrease in Coral $\delta^{18}O$: An Indication of Global Warming?

Fig. 10 shows coral $\delta^{18}O_c$ time series for the last two decades of the twentieth century for our coral sites in the tropical northwest Pacific. Peak matching between $\delta^{18}O_c$ and instrumental SST with simple interpolation was employed to construct an age model of each coral record. In the Japanese and Philippine coral records, significant decreasing trends in $\delta^{18}O_c$ (-0.24‰ to -0.42‰/10 yr) are evident, even over the relatively short period between 1980 and 2000, which may suggest an SST rise and/or surface-water freshening related to global warming. Any decreasing trend in $\delta^{18}O_c$ recorded by the Micronesian corals may have been masked by the recent large number of ENSO events, which caused local cooling and drought ($\delta^{18}O_c$ increase) during the latter part of the period. Warming or freshening trends have been found generally in coral $\delta^{18}O_c$ records from several sites in the tropical Pacific and Indian oceans (Gagan et al., 2000).

In Fig. 10, coral $\delta^{18}O_c$ curves are also matched to instrumental SSTs based on the $\delta^{18}O_c$–SST relation obtained for each coral site. We have shown that coral records from Micronesia, and possibly the Philippines, are influenced by seawater $\delta^{18}O_w$ variation. Therefore, the coral-based SSTs from these sites should be interpreted as "apparent" SSTs (Gagan et al., 2000) because the influence of seawater $\delta^{18}O_w$ variations is not taken into account. It is also assumed that all changes in $\delta^{18}O_c$ can be attributed to temperature variation, but salinity changes also influence $\delta^{18}O_c$ values. Nevertheless, the general trends in instrumental and coral-derived "apparent" SSTs for each coral site are in good agreement, suggesting that coral records have potential as an SST proxy when discussing long-term trends. High-latitude sites, such as Ishigaki Island, showed a more rapidly increasing SST trend during the last two decades of the twentieth century. Although the long-term instrumental SST data available since 1914 for Ishigaki Port showed a distinct warming trend of 0.12 °C/10 yr throughout the monitoring period (Suzuki et al., 2003), the observed SST increase during the last two decades (0.57 °C/10 yr) is large compared with the earlier part of the century.

Comparison of "apparent" and instrumental SSTs is also a useful tool for identifying El Niño-related drought events in the western Pacific. "Apparent" SSTs during the year 1998 for the Philippine and Micronesian sites were low relative to the actual SSTs (Fig. 10). As discussed previously, the deviation of the Chuuk Atoll $\delta^{18}O_c$ curve from the instrumental SST curve in 1998 can be attributed to increased seawater $\delta^{18}O_w$ (higher salinity), corresponding to the El Niño-induced drought (Fig. 7). The Philippines experience more severe drought conditions compared with the Micronesian islands, as seen in the pattern of annual precipitation anomalies associated

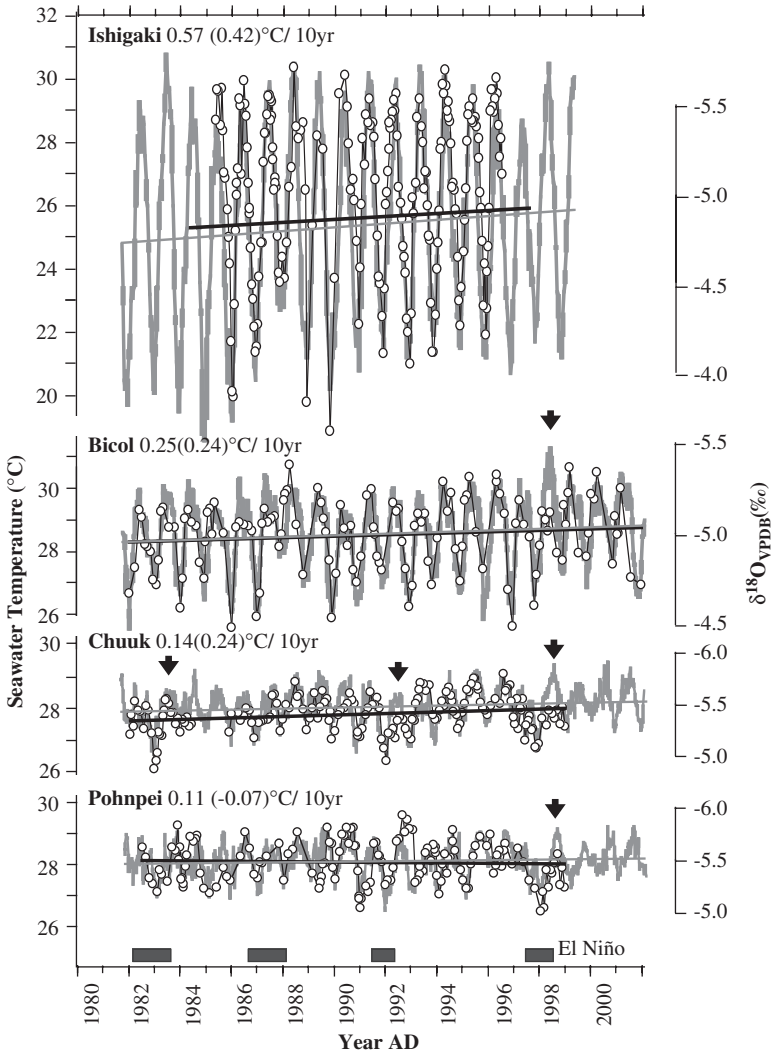

Figure 10: Comparison of instrumental SST (gray curves) and *Porites* coral $\delta^{18}O_c$ values (curves with circles) from Ishigaki Island, Japan; Bicol, Philippines; and Chuuk Atoll and Pohnpei Island, Micronesia, in the northwestern Pacific. Regional weekly SSTs (IGOSS NMC SSTs) are shown for Bicol, Chuuk, and Pohnpe while the 10-day mean SST record of the JMA Ishigaki-jima Meteorological Observatory is shown for Ishigaki Island. Coral $\delta^{18}O_c$ curves are related to "apparent" SSTs based on the $\delta^{18}O_c$–SST relations: Ishigaki (IU96-07), $SST = -1.4-5.57\,\delta^{18}O_c$; Bicol (SWGM01-01), $SST = 0.57-5.58\,\delta^{18}O_c$; Chuuk (CHU99-01), $SST = 8.1-3.60\,\delta^{18}O_c$; and Pohnpei (POH99-02), $SST = 10.3-3.43\,\delta^{18}O_c$. "Apparent" SSTs derived from the coral $\delta^{18}O_c$ values include offsets due to changes in seawater $\delta^{18}O_w$ in each region. The gray and solid lines show simple regressions for

with strong El Niño events (Fig. 2B), and, indeed, coral records from the Philippines showed the largest deviation among the three sites examined.

5 Summary

High-resolution $\delta^{18}O_c$ records from annually banded modern *Porites* spp. corals collected in the tropical northwestern Pacific were used successfully to monitor recent marine climatic events, including the strong El Niño in 1997–1998, severe coral bleaching, and a long-term rise in SST. In the relatively high-latitude region of the western Pacific (Ishigaki Island, Japan), coral $\delta^{18}O_c$ records are a good proxy for SST because of the limited influence from $\delta^{18}O$-depleted rainfall on the $\delta^{18}O_w$ of seawater. In contrast, temporal variations in coral $\delta^{18}O_c$ from the Micronesian islands appeared to be affected by both SST and SSS variations. The temporal pattern of a distinct increase in $\delta^{18}O_c$ followed by compression of the $\delta^{18}O_c$ curve in Micronesian corals is a useful signal for identifying past El Niño events in long coral records from the region. High-resolution isotope microprofiling of bleached corals from Ishigaki Island as well as from Pandora Reef, GBR, allowed us to find a growth gap caused by anomalously warm SSTs related to the 1997–1998 El Niño event. Such a gap in skeletogenesis can be used as an important indicator for reconstructing past bleaching events. At Ishigaki Island and on the Pacific side of the Philippine Islands, a decreasing trend in $\delta^{18}O_c$ was found, even over the relatively short period between 1980 and 2000, which may indicate an SST rise or surface-water freshening related to global warming. Any recent global warming/freshening trend recorded by the Micronesian corals may have been masked by the influence of the recent large number of ENSO events, which cause local cooling and drought toward the end of the record.

Our results are intriguing enough to warrant further data acquisition and attempts at quantitative time-series analysis. This study also demonstrated

---

instrumental and coral-derived "apparent" SSTs, respectively. All isotope data were used for the regression analysis of coral records except for the Ishigaki coral. Only seasonal extremes were used for the regression analysis of the Ishigaki coral because the difference of skeletal extension rate between summer and winter had positive offset on the regression line. Magnitudes of the warming trends between 1981 and 2000 calculated from instrumental SSTs and coral "apparent" SSTs are also shown (the latter in parentheses). Arrows mark times of severe El Niño-related drought in the region. Gray blocks at the bottom represent the periods of El Niño events according to the classification by the NCEP/CPC (http://www.cpc.ncep.noaa.gov/products/analysis_monitoring/ensostuff/ensoyears.html).

that high-resolution coral $\delta^{18}O_c$ records have potential for facilitating studies on the climate of the recent and distant past, including the middle Holocene and earlier interglacial periods, which may provide partial analogs for the future greenhouse Earth.

Acknowledgements

We express our appreciation to Professor Y. Maeda of University of Hyogo for his valuable advice that was essential for the expedition's success. We thank H. Adachi of Geoact Co., Ltd. for coral coring. Coral specimens from Pandora Reef were provided by Dr. K. Fabricius of the Australian Institute of Marine Science. We are also grateful to K. Minoshima, who performed isotopic analyses on coral samples. Assistance in the field was given by S. Akama and M. Yoshino, and assistance in the laboratory by Y. Yoshinaga, I. Yukino, S. Oyamada, H. Muramatsu, and Y. Sato. Coral specimens were identified by R. van Woesik of the University of the Ryukyus. This study was funded by both the Ministry of Education, Sports, Science and Technology (MEXT) of Japan, through the Special Coordination Fund "GCMAPS" program, and the Ministry of the Environment of Japan for a "Study on the increase of sea-surface temperature in the Asian Monsoon region based on coral skeletal climatology," with additional support from the National Institute of Advanced Industrial Science and Technology (AIST).

References

Alison, N., Tudhope, A. W., Fallick, A. E., 1996. Factors influencing the stable carbon and oxygen isotope composition of *Porites lutea* coral skeletons from Phuket, South Thailand. Coral Reefs 14, 43–57.

Brown, B. E., 1997. Coral bleaching: cause and consequences. Coral Reef 16, S129–S138.

Charles, C. D., Hunter, D. E., Fairbanks, R. G., 1997. Interaction between the ENSO and the Asian monsoon in a coral record of tropical climate. Science 277, 925–928.

Cole, J. E., Fairbanks, R. G., Shen, G. T., 1993. Recent variability in the southern oscillation: Isotopic results from a Tarawa Atoll coral. Science 260, 1790–1793.

Coplen, T. B., 1996. New guidelines for reporting stable hydrogen, carbon, and oxygen isotope-ratio data. Geochimica et Cosmochimica Acta 60, 3359–3360.

Dai, A., Wigley, T. M. L., 2000. Global patterns of ENSO-induced precipitation. Geophysical Research Letters 27, 1283–1286.

da Silva, A., Young, A. C., Levitus, S., 1994. Atlas of Surface Marine Data 1994, Volume 1: Algorithms and Procedures. NOAA Atlas NESDIS 6, U.S. Department of Commerce, Washington, D.C.

Delcroix, T., 1998. Observed surface oceanic and atmospheric variability in the tropical Pacific at seasonal and ENSO timescales: A tentative overview. Journal of Geophysical Research 103, 18611–18633.

Dunbar, R. B., Wellington, G. M., Colgan, N. W., Glynn, P. W., 1994. Eastern Pacific climate variability since 1600 A.D.: stable isotopes in Galapagos corals. Paleoceanography 9, 291–315.

Fairbanks, R. G., Evans, M. N., Rubenstone, J. L., Mortlock, R. A., Broad, K., Moore, M. D., Charles, C. D., 1997. Evaluating climate indices and their geochemical proxies measured in corals. Coral Reefs 16, S93–S100.

Fujioka, Y., 1999. Mass destruction of the hermatypic corals during a bleaching event in Ishigaki Island, southwestern Japan. Galaxea, Journal of Japanese Coral Reef Society 1, 41–50.

Gagan, M. K., Ayliffe, L. K., Beck, J. W., Cole, J. E., Druffel, E. R. M., Dunbar, R. B., Schrag, D. P., 2000. New views of tropical paleoclimates from corals. Quaternary Science Reviews 19, 45–64.

Gagan, M. K., Ayliffe, L. K., Hopley, D., Cali, J. A., Mortimer, G. E., Chappell, J., McCulloch, M. T., Head, M. J., 1998. Temperature and surface-ocean water balance of the Mid-Holocene tropical western Pacific. Science 279, 1014–1018.

Gagan, M. K., Chivas, A. R., Isdale, P. J., 1994. High-resolution isotopic records from corals using ocean temperature and mass-spawning chronometers. Earth and Planetary Science Letters 121, 549–558.

Gagan, M. K., Chivas, A. R., Isdale, P. J., 1996. Timing coral-based climatic histories using ^{13}C enrichments driven by synchronized spawning. Geology 24, 1009–1012.

Gagan, M. K., Hendy, E. J., Haberle, S. G., Hantoro, W. S., 2004. Post-glacial evolution of the Indo-Pacific Warm Pool and El Niño-Southern Oscillation. Quaternary International 118–119, 127–143.

Glynn, P. W., 1984. Widespread coral mortality and the 1982/83 El Niño warming event. Environmental Conservation 11, 133–146.

Glynn, P. W., 1990. Coral mortality and disturbances to coral reefs in the tropical eastern Pacific. In: Glynn, P. W. (Ed.), Global Consequences of the 1982–83 El Niño-Southern Oscillation. Elsevier, Amsterdam, pp. 55–67.

Glynn, P. W., 1991. Coral reef bleaching in the 1980s and possible connections with global warming. Trends in Ecology and Evolution 6, 175–179.

Goreau, T., Macfarlane, A. H., 1990. Reduced growth rate of *Montastrea annularis* following the 1987–1988 coral-bleaching event. Coral Reefs 8, 211–215.

Hughen, K. A., Schrag, D. P., Jacobsen, S. B., Hantaro, W., 1999. El Niño during the last interglacial period recorded by a fossil coral from Indonesia. Geophysical Research Letters 26, 3129–3132.

Inoue, M., Suzuki, A., Nohara, M., Kan, H., Edward, A., Kawahata, H., 2004. Coral skeletal tin and copper concentration at Pohnpei, Micronesia: possible index for marine pollution by toxic anti-biofouling paints. Environmental Pollution 129, 399–407.

IPCC. 2001. Contribution of working group I to the third assessment report of the intergovernmental panel on climate change. In: Houghton, J. T., Ding, Y., Griggs, D. J., Noguer, M., van der Linden, P. J., Dai, X., Maskell, K., Johnson, C.A. (Eds.), Climate Change 2001: The Scientific Basis, Cambridge University Press, Cambridge and New York, p. 881.

Jokiel, P. L., Coles, S. L., 1977. Effects of temperature on the mortality and growth of Hawaiian reef corals. Marine Biology 43, 201–208.

Jokiel, P. L., Coles, S. L., 1990. Responses of Hawaiian and other Indo-Pacific reef corals to elevated temperatures. Coral Reefs 8, 155–162.

Jones, P. D., Osborn, T. J., Briffa, K. R., 2001. The evolution of climate over the last millennium. Science 292, 662–667.

Le Bec, N., Juillet-Leclerc, T. A., Delcroix, 2000. A coral $\delta^{18}O$ record of ENSO driven sea surface salinity variability in Fiji (south-western tropical Pacific). Geophysical Research Letters 27, 3897–3900.

Leder, J. J., Szmant, A. M., Swart, P. K., 1991. The effect of prolonged "bleaching" on skeletal banding and stable isotopic composition in *Montastrea annularis*: Preliminary observations. Coral Reefs 10, 19–27.

Lesser, M. P., 1996. Elevated temperatures and ultraviolet radiation cause oxidative stress and inhibit photosynthesis in symbiotic dinoflagellates. Limnology Oceanography 41, 271–283.

Levitus, S., Burgett, R., Boyer, T., 1994. World Ocean Atlas Volume 3: Nutrients, NOAA Atlas NESDIS, 3. U.S. Department of Commerce, Washington, D.C.

Linsley, B. K., Dunbar, R. B., Wellington, G. M., 1994. A coral-based reconstruction of Intertropical Convergence Zone variability over Central America since 1707. Journal of Geophysical Research 99, 9977–9994.

Lough, J. M., 2000. 1997–98: Unprecedented thermal stress to coral reefs?. Geophysical Research Letters 27, 3901–3904.

Lukas, R., Lindstrom, E., 1991. The mixed layer of the western equatorial Pacific Ocean. Journal of Geophysical Research 96, Suppl., 3343–3358.

McConnaughey, T., 1989. ^{13}C and ^{18}O isotopic disequilibrium in biological carbonates: I. Patterns. Geochimica et Cosmochimica Acta 53, 151–162.

McGregor, H. V., Gagan, M. K., 2004. Western Pacific coral $\delta^{18}O$ records of anomalous Holocene variability in the El Niño-Southern Oscillation. Geophysical Research Letters 31, L11204 doi:10.1029/2004GL019972.

Mitsuguchi, T., Matsumoto, E., Abe, O., Uchida, T., Isdale, P. J., 1996. Mg/Ca thermometry in coral skeletons. Science 274, 961–963.

Moore, M. D., Schrag, D. P., Kashgarian, M., 1997. Coral radiocarbon constraints on the source of the Indonesian throughflow. Journal of Geophysical Research 102, 12359–12365.

Oliver, J., 1985. Recurrent seasonal bleaching and mortality of corals on the Great Barrier Reef. Proceedings of 5th International Coral Reef Symposium 4, 201–206.

Paillard, D., Labeyrie, L., Yiou, P., 1996. Macintosh program performs time-series analysis, EOS Trans. AGU 77, 379.

Park, W. S., Oh, I. S., 2000. Interannual and interdecadal variations of sea surface temperature in the East Asian marginal seas. Progress in Oceanography 47, 191–204.

Philander, S. G., 1990. El Niño, La Niña, and the Southern Oscillation. Academic Press, San Diego, p. 289.

Porter, J. W., Fitt, W. K., Spero, H. J., Rogers, C. S., White, M. W., 1989. Bleaching in reef corals: Physiological and stable isotopic responses. Proceedings of National Academy of Science USA 86, 9342–9346.

Reynolds, R. W., Smith, T. M., 1994. Improved global sea surface temperature analyses using optimal interpolation. Journal of Climate 7, 928–948.

Suzuki, A., Yukino, I., Kawahata, H., 1999. Temperature-skeletal $\delta^{18}O$ relationship of *Porites australiensis* from Ishigaki Island, the Ryukyus, Japan. Geochemical Journal 33, 419–428.

Suzuki, A., Kawahata, H., Tanimoto, Y., Tsukamoto, H., Gupta, L. P., Yukino, I., 2000. Skeletal isotopic record of a *Porites* coral during the 1998 mass bleaching event. Geochemical Journal 34, 321–329.

Suzuki, A., Gagan, M. K., De Deckker, P., Omura, A., Yukino, I., Kawahata, H., 2001. Last interglacial coral record of enhanced insolation seasonality and seawater ^{18}O enrichment in the Ryukyu Islands, northwest Pacific. Geophysical Research Letters 28, 3685–3688.

Suzuki, A., Gagan, M. K., Fabricius, K., Isdale, P. J., Yukino, I., Kawahata, H., 2003. Skeletal isotope microprofiles of growth perturbations in *Porites* corals during the 1997–1998 mass bleaching event. Coral Reefs 22, 357–369.

Suzuki, A., Hibino, K., Iwase, A., Kawahata, H., 2005. Intercolony variability of skeletal oxygen and carbon isotope signatures of cultured Porites corals: temperature controlled experiments. Geochimica et Cosmochimica Acta 69, 4453–4462.

Trenberth, K. E., 1997. The definition of El Niño. Bulletin of the American Meteorological Society 78, 2771–2777.

Trenberth, K. E., Hoar, T. J., 1996. The 1990–1995 El Niño-Southern Oscillation event: longest on record. Geophysical Research Letters 23, 57–60.

Tudhope, A. W., Allison, N., Le Tissier, M. D. A., Scoffin, T. P., 1992. Growth characteristics and susceptibility to bleaching in massive *Porites* corals, South Thailand. Proceedings of 7th International Coral Reef Symposium 1, 64–69.

Tudhope, A., Shimmield, G. B., Chiloctt, C. P., Jebb, M., Fallick, A. E., Dalgleish, A. N., 1995. Recent changes in climate in the far western equatorial Pacific and their relationship to the Southern Oscillation: oxygen isotope records from massive corals, Papua New Guinea. Earth and Planetary Science Letters 136, 575–590.

Tudhope, A., Chiloctt, C. P., McCulloch, M. T., Cook, E. R., Chappell, J., Ellam, R. M., Lea, D. W., Lough, J. M., Shimmield, G. B., 2001. Variability in the El Niño-Southern Oscillation through a glacial–interglacial cycle. Science 291, 1512–1517.

Watanabe, T., Oba, T., 1997. High resolution reconstruction of water temperature estimated from oxygen isotopic ratios of a modern *Tridacna* shell based on freezing microtome sampling technique. Chikyukagaku (Geochemistry) (in Japanese with English abstract) 32, 87–95.

Wellington, G. M., Dunbar, R. B., 1995. Stable isotope signature of El Niño-Southern Oscillation events in eastern tropical Pacific reef corals. Coral Reefs 14, 5–25.

Wilkinson, C., 1998. The 1997–1998 mass bleaching event around the world. In: Wilkinson, C. (Ed.), Status of Coral Reefs of the World: 1998. Australian Institute of Marine Science, Townsville, pp. 15–38.

Yan, X.-H., Ho, C.-R., Zheng, Q., Klemas, V., 1992. Temperature and size variabilities of the Western Pacific Warm Pool. Science 258, 1643–1645.

Yonge, C. M., Nicholls, A. G., 1931. Studies on the physiology of corals. IV. The structure, distribution and physiology of the zooxanthellae. Great Barrier Reef Expedition 1928–29. Science Report 1, 135–176.

Chapter 10

Recent Advances in Coral Biomineralization with Implications for Paleo-Climatology: A Brief Overview

Tsuyoshi Watanabe[1,*], Anne Juillet-Leclerc[1], Jean-Pierre Cuif[2], Claire Rollion-Bard[3], Yannicke Dauphin[2] and Stéphanie Reynaud[4]

[1]*Laboratoire de Sciences du Climat et de l'Environnement Laboratoire Mixte CNRS-CEA, Domaine du CNRS, 91198 Gif sur Yvette Cedex, France*
[2]*UMR IDES 8148, Bat. 504, Faculte des Sciences, Universite de Paris XI, 91405 Orsay Cedex, France*
[3]*CRPG-CNRS, BP 20, 15 rue Notre Dame des Pauvres, 54501 Vandoeuvre-lès-Nancy Cédex, France*
[4]*Centre Scientifique de Monaco, Avenue Saint-Martin, 98000 Monaco, Principauté de Monaco*

Abstract

The tropical oceans drive climatic phenomena such as the El Niño-southern oscillation (ENSO) and the Asian–Australian monsoon, which have global scale impacts. In order to understand future climatic developments, it is essential to understand how the tropical climate has developed in the past, on both short and longer timescales. However, good instrumental records are limited to the last few decades. The oxygen isotopic ($\delta^{18}O$) composition and strontium/calcium (Sr/Ca) ratio of massive corals have been widely used as proxies for past changes in sea surface temperature (SST) of the tropical and subtropical oceans, because the geochemistry of the skeleton is believed to vary as a function of several environmental parameters (such as seawater temperature, salinity, light, …). However, recent microanalytical studies have revealed large amplitude variations in Sr/Ca and oxygen isotopic composition in coral skeletons; variations that cannot be ascribed to changes in SST or in salinity. Such micro- and nanometer scale studies of geochemical variations in coral skeletons are still few and somewhat scattered

*Corresponding author.
E-mail address: nabe@mail.sci.hokudai.ac.jp (T. Watanabe).

Elsevier Oceanography Series 73
Edited by H. Kawahata and Y. Awaya
ISBN: 0-444-52948-9

in terms of the species studied and the problems addressed. But collectively they show the great potential for determining chemical variations at length scales of direct relevance to the biomineralization process. For example, it is now possible to measure geochemical variations within the two basic, micrometer-sized building blocks of the coral skeleton: Early mineralization zones (EMZ) and aragonite fibres. Such micro- and nanometer scale observations, in combination with controlled laboratory culturing of corals, hold the promise of yielding important new insights into the various biomineralization processes that may affect the chemical and isotopic composition of the skeletons. One aim of these efforts is to better understand the elemental and isotopic fractionation mechanisms in order to improve the conversion of the geochemical variability into environmental changes.

Keywords: corals; Oxygen isotope; Strontium/Calcium ratio; palaeothermometer; biominelarization

1 Introduction

Accurate estimation of human impacts on climate variability is an important subject, not only for scientists and environmentalists, but also for lawmakers, politicians, and for society in general. In order to predict the effects of anthropogenic activities on the future climate, it is necessary to document how the climate has fluctuated in the past. Instrumental records can extend up to about 150 years (Kaplan et al., 1998), but have limited geographical distribution. Satellite-based temperature surveys of the oceans cover large regions, but high-quality data are limited to the last two decades. On the other hand, the global climate of the last few centuries is known to have been variable and complex, spatially as well as temporally (e.g., Jones and Mann, 2004).

Massive, hermatypic corals are present today in the tropical and subtropical oceans and can be found in a significant fraction of the geologic record dates back to the middle Triassic. These corals potentially provide high-resolution records of climate variability in the tropical oceans that, through ocean-atmosphere interactions, greatly affect the Earth's climate system (Dunbar and Cole, 1999). Paleo-environmental records based on modern corals can go back in time as far as 300–400 years (Quinn et al., 1998; Cobb et al., 2004; Linsley et al., 2004) and the annual density banding of coral skeletons provides an accurate chronology (Knutson et al., 1972; Barnes and Lough, 1993). Thus, corals offer many advantages for climate reconstructions, provided that precise proxies for environmental changes, including sea surface temperature (SST), can be developed. In this paper, we discuss, briefly, recent advances in the use of corals as proxies for past SST variations with special attention to progress made in understanding the effects of biomineralization processes on the chemical and isotopic composition of the coral skeletons.

2 Development and Problems Associated with Coral Paleo-Temperature Proxies

The oxygen isotopic ($\delta^{18}O$) and strontium/calcium (Sr/Ca) ratios of massive coral skeletons have been widely used as proxies for past changes in SST of the tropical and subtropical oceans, because both the geochemical parameters are believed to depend on the temperature of the ambient seawater.

The temperature dependency of the oxygen isotopic composition in inorganically precipitated carbonates was established by Urey (1947), but it was realized early on that the $\delta^{18}O$ of biogenic carbonates reflects a combination of environmental parameters and biological processes, so-called "vital effects" (Urey et al., 1951; Epstein et al., 1953; McConnaughey, 1989). In spite of a biologically induced isotopic disequilibrium with respect to seawater, corals in general provide the best $\delta^{18}O$ paleo-records of ambient SST variations in waters with near constant $\delta^{18}O$, i.e., waters in hydrologic balance (e.g., Leder et al., 1996; Wellington et al., 1996). (Alternatively, corals can provide a record of changes in hydrologic balance in regions where the temperature is nearly constant; e.g., Cole and Fairbanks, 1990). However, seasonal variations in $\delta^{18}O$ of the seawater on the reef are often relatively large (Leder et al., 1996), and in some cases, the effect of seawater $\delta^{18}O$ variations on the $\delta^{18}O$ vs. SST calibration can be quantified (McCulloch et al., 1994; Juillet-Leclerc and Schmidt, 2001). Modern approaches to the construction of $\delta^{18}O$ paleo-environmental records typically involve coring of living coral heads and calibration to (5–10 year) instrumental temperature records obtained in close vicinity to the coral (Stephans et al., 2004).

Temperature dependence of the Sr/Ca ratio in aragonite was demonstrated by Smith et al. (1979). However, initially the analytical errors associated with the analyses of coral Sr/Ca ratios were large ($\pm 2^{\circ}C$, if converted to temperature), limiting the use of the coral Sr/Ca temperature-proxy to localities where temperature variations are significantly larger. Later, Beck et al. (1992) developed isotope dilution and thermal ionization mass spectrometry (TIMS) techniques that allowed the measurement of Sr/Ca ratio with an analytical error corresponding to less than $\pm 0.5^{\circ}C$ for reconstructed SST. In contrast to the isotopic composition of seawater, the Sr/Ca ratio of seawater has been assumed to be essentially constant because of the long residence times of strontium in the ocean (5.1×10^6 yr; Broecker and Peng, 1982). However, more recent observations of the ocean Sr/Ca ratio from different depths and localities raise some doubt about the general validity of this assumption (de Villiers et al., 1994; de Villiers, 1999).

McCulloch et al. (1994) assessed $\delta^{18}O$ fluctuations in seawater by removing the temperature dependency from the $\delta^{18}O$ signal using the calibrated Sr/Ca vs. SST relationship. This method was extended to reconstructions of past sea surface salinity (SSS) (Gagan et al., 1998; Ren et al., 2002) assuming

a linear relationship between the $\delta^{18}O$ of seawater, SSS, and SST. With the development of automated methods for rapid sampling and analyses of carbonate powders, different methods for reconstruction of SST have been applied to a century-long coral records covering most of the tropics (Fig. 1), as well as to climatically important periods in the more distant past, such as the last glacial maximum (e.g., Guilderson et al., 1994), Little Ice Age (Watanabe et al., 2001), and last interglacial warm period (Tudhope et al., 2001). At the same time, it has become clear that coral-based paleo-climatic reconstructions suffer from problems that are not only related to the analytical challenge of obtaining high-quality $\delta^{18}O$ and Sr/Ca data. Fig. 2 shows the large discrepancy among reported modern calibrations both for coral $\delta^{18}O$ (Fig. 2a) and Sr/Ca (Fig. 2b). These discrepancies suggest that simple application of different coral species, localities, and methods can lead to large discrepancies among different reconstructions of past SST (Marshall and McCulloch, 2002; Watanabe et al., 2002).

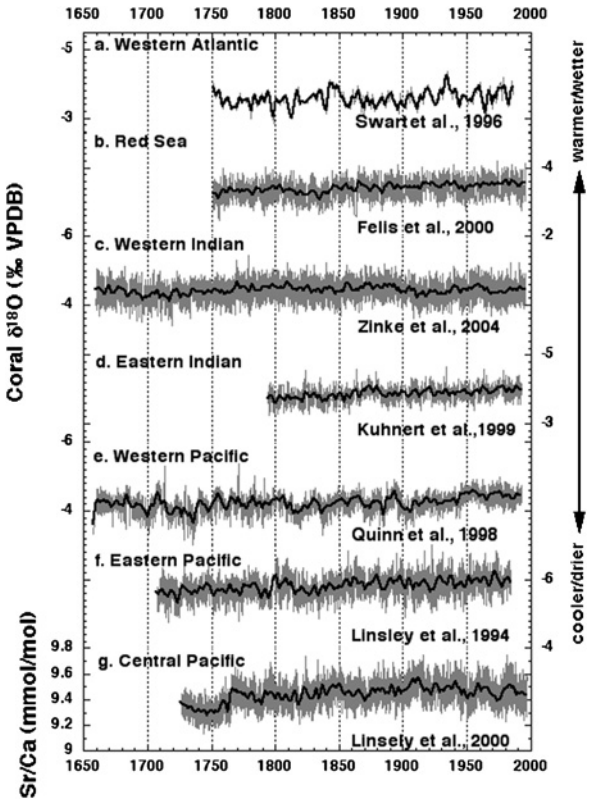

Figure 1: Coral records of $\delta^{18}O$ and Sr/Ca ratio from modern corals. Thick lines represent 5 years running averages. Data are available at the World Data Center for Paleoclimatology (http://www.ngdc.noaa.gov/paleo/corals.html).

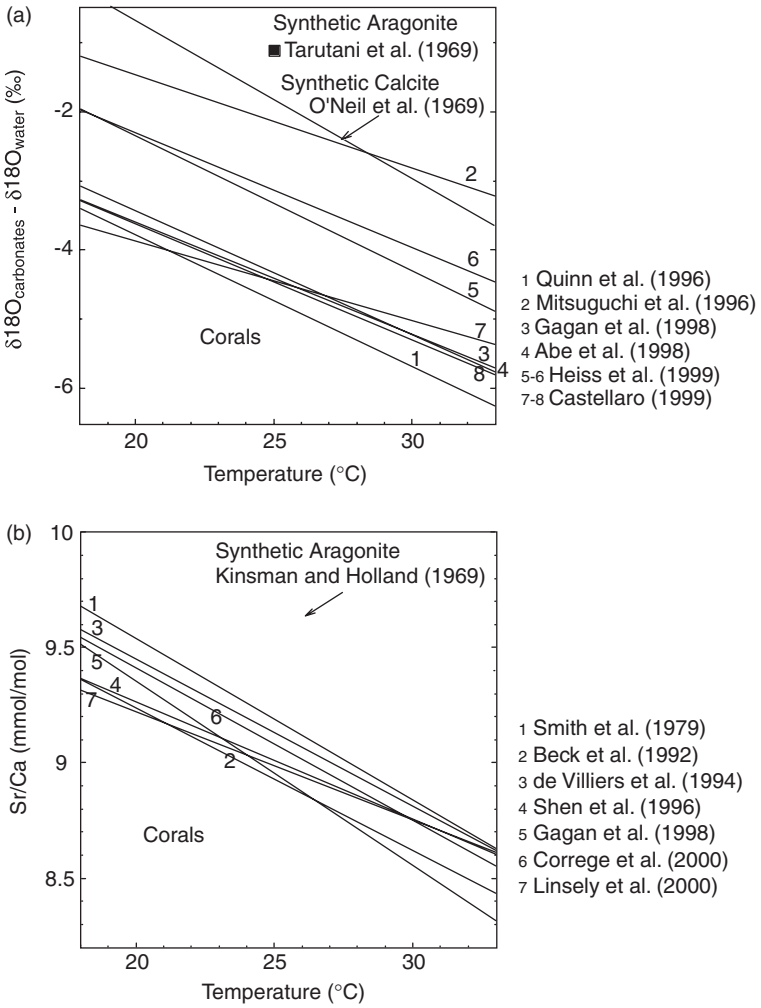

Figure 2: Diagrams showing the disagreement between different calibrations of SST vs. (a) the oxygen isotopic composition in *Porites lutea* and (b) the Sr/Ca ratio in coral *Porites*. Each calibration has been calculated from samples collected along main growth axis, by comparing the geochemical measurement with the SST variability.

3 Biological Sources of Discrepancies in Modern Calibrations

Although biological or "vital" effects are broadly recognized as a source of uncertainty or discrepancy in coral paleo-climatic records relatively little attention has been given to the study of how corals form their skeletons and how, in detail, these biologically induced processes can affect the geochemical

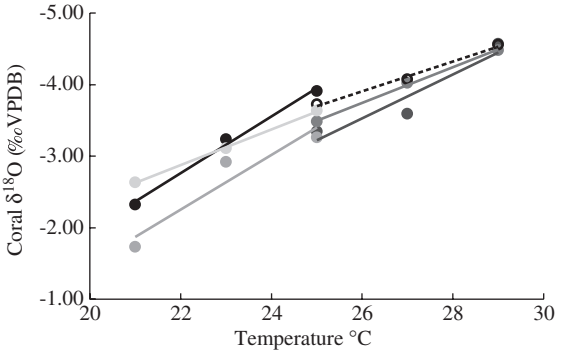

Figure 3: Diagram showing discrepancy between calibrations of SST vs. skeletal $\delta^{18}O$ for five nubbins coming from the same parent colony of *Acropora* sp. cultured by the method of Reynaud-Vaganay et al. (1999). Note that these five nubbins were growing in aquarium under constant condition, except temperature.

composition of the skeletons. For example, the isotopic effect of seawater temperature on skeletal $\delta^{18}O$ has been tested in laboratory by using cultures of corals (Reynaud-Vaganay et al, 1999). Whereas all the nubbins were cultured in the same conditions, in the same aquarium, and originated from one parent colony, their isotopic measurements could be scattered over 1‰ for an identical temperature (Fig. 3). Although oxygen isotopic ratios as well as Sr/Ca ratios often are in disequilibrium with respect to their ambient seawater, the observed elemental and isotopic fractionations are usually treated in the context of thermodynamic equilibrium, modified by kinetic effects associated with the precipitation of the skeleton (McConnaughey, 1989; Gagan et al., 1998; Ren et al., 2002; Adkins et al., 2003). Among geochemists, the widespread idea is that the skeleton is largely produced by simple physiochemical precipitation of calcium carbonate concentrated from seawater. However, from recent studies of coral skeletons, conducted at length scales of relevance to the biomineralization processes, it has become clear that this idea is too simplistic to be right. In the following we briefly discuss recent progress in the study of biologically driven isotopic and trace element variations at the millimeter- to nanometer-length scales. In general, it seems true that we need to understand the coral biomineralization process at the cellular scale, the fundamental-length scale of life, before we can reliably use these structures to draw conclusions about environmental changes on a global scale.

3.1 Geochemical Heterogeneity at the Millimeter-Length Scale

It is well known that even within the same locality, where water chemistry is essentially the same, the use of different coral species can lead to different

SST calibrations, presumably due to biological differences (e.g., Gagan et al., 2000; Marshall and McCulloch, 2002; Watanabe et al., 2002, 2003). Even among the same coral species from the same location, SST calibrations can differ among colonies (Allison, 1996; Wellington et al., 1996; Linsley et al., 1999; Watanabe et al., 2003). Some of these discrepancies can be explained by different sampling resolution, variations in skeletal growth-rate, and small environmental heterogeneities in the reef environment. However, millimeter-scale observations of geochemical heterogeneity within different skeletal elements of the same corallite in a given colony present an additional complication. The aragonitic skeletons of hermatypic corals are comprised of thousands of individual corallites, each with a more or less well defined theca-wall, columellae, septa, and dissepiments (Fig. 4). The theca-wall and columella grow in the vertical direction, the direction for extension. Septa grow vertically and horizontally at the same time, and dissepiments define horizontal layers within each corallite, like floors in a tall building (Barnes and Lough, 1993; Barnes et al., 1995). Differences in growth-direction and growth-rate of each skeletal element could affect the reconstructed climate signals. Land et al. (1975) and Watanabe et al. (2002, 2003) examined the isotopic heterogeneities among different skeletal components

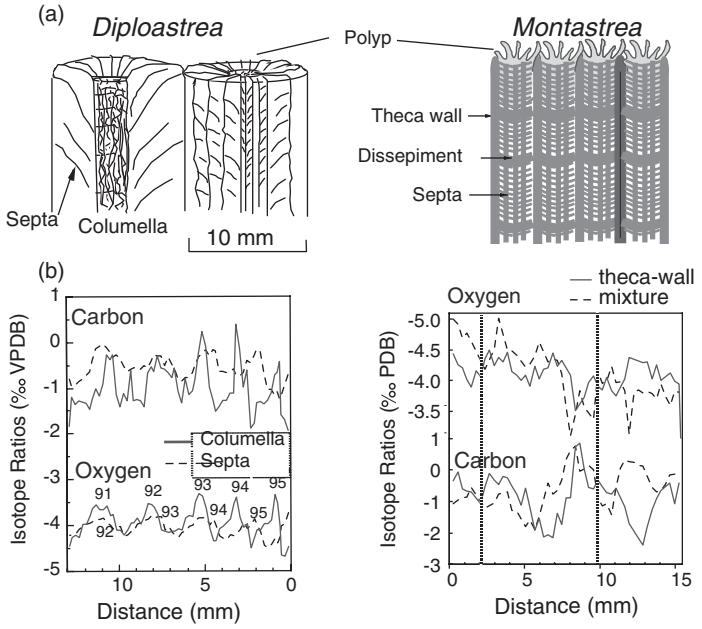

Figure 4: (a) Morphology of coral skeletal structures and (b) millimetre scale heterogeneity in isotopic compositions for different skeletal elements in *Diploastrea* and *Montastrea* (Watanabe et al., 2002, 2003).

using coral species with relatively large corallites and wide intercorallite spacing. The results suggested that there is a rather large difference in the stable isotope chemistry between vertically and horizontally growing skeletal elements. Vertically growing elements, such as the theca-wall, yield a certain stable isotopic signature, but the inclusion of horizontally growing skeletal elements change this signature significantly (Fig. 4). The coral species most commonly used for paleo-climatic reconstructions is *Porites,* which has relatively small corallites (0.5–1 mm) for which it is difficult to sample separately each type of skeletal element using conventional sampling techniques (e.g., dentist drill). On the other hand, a smaller corallite size allows better, more representative average compositions to be obtained. Still, it seems essential to understand the cause of the variable stable isotope signatures in different skeletal components at the millimeter-length scale.

Since late 1990s, microanalytical methods such as Laser ICP–MS and Secondary Ion Mass Spectrometry (SIMS) have been applied more or less systematically for measuring trace element of coral skeletons (Allison, 1996; Hart and Cohen, 1996; Sinclair et al., 1998; Fallon et al., 1999). However, the most striking result of these analyses was the large data scatter, often with amplitudes that were impossible to interpret as the result of changes in environmental conditions.

Two dramatic examples of μm-scale geochemical variations are illustrated in Fig. 5, which show conventional ion microprobe analyses of $\delta^{18}O$ and Sr/Ca ratios in wall segments and septa of the *Porites* skeleton. Both data sets show oscillating variations with amplitudes that are impossible to explain by fluctuations in SST or changes in any other local environmental parameter (Meibom et al., 2003; Rollion-Bard et al., 2003). Indeed, if converted to temperature, the $\delta^{18}O$ and Sr/Ca variations displayed in Fig. 5 would correspond to changes of more than 15°C, which is three times more than the seasonal SST variations at the sites where these corals lived. Similar, but less distinctly oscillating Sr/Ca variations were reported by recent works (e.g., Allison and Finch, 2004; Cohen and Sohn, 2004). The negative isotopic values can only be explained by supposing that coral skeleton is partially deposited according to a kinetic process. The boron isotopic measurements at micrometer scale in the same spots than oxygen analyses (Rollion-Bard et al., 2003) indicate that a variation of one pH unit in good agreement with direct microelectrodes measurements (Al-Horani et al., 2003). In addition, the $\delta^{18}O$ and Sr/Ca oscillations are characterized by an approximately monthly wavelength, which could be caused by biological processes changing in response to the lunar cycle (Meibom et al, 2003). We suggest that the pH controls the $\delta^{18}O$ of the growing carbonate skeleton through the relative fractions of dissolved carbonate species and through the kinetics of their isotope equilibration with water via hydration and hydroxylation.

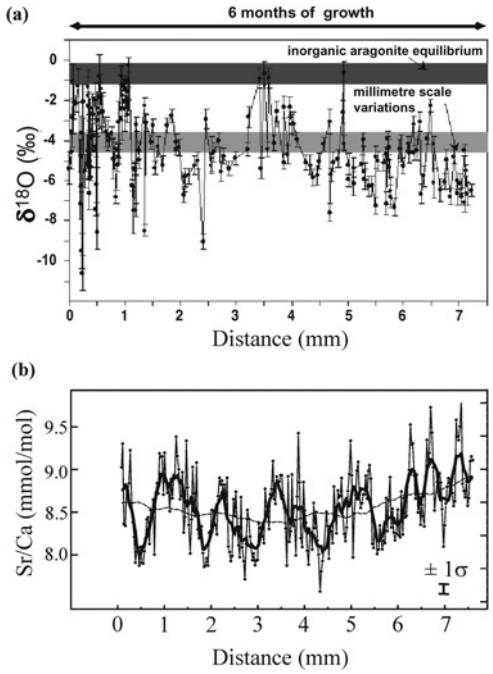

Figure 5: Micro-scale heterogeneity observed in coral *Porites* of $\delta^{18}O$ (a; Rollion-Bard et al., 2003) and of Sr/Ca (b; Meibom et al., 2003) measured by ion microprobe.

3.2 Geochemical Heterogeneities at the Ultra-Structural Level

Fig. 4 illustrates the general morphology of the coral skeleton at the scale of one millimeter. However, in all coral skeletons there is an additional level of structure at the micrometer and nanometer-length scales, which is directly related to the mechanism of skeletal formation – we refer to this as the coral "ultrastructure". Fig. 6 illustrates the ultrastructure of a *Porites* skeleton, but we emphasize that the ultrastructure of all coral skeletons, although species dependent, share the same components and overall architecture. The coral skeleton consists of EMZs, which are small aggregations of nanophase calcium carbonate, embedded in sulfated polysaccharides and other organic molecules. EMZs were previously called as centers of calcification (COC), but "EMZ" has been proposed as better description in the context of the overall growth process (Cuif et al., 2003; Cuif and Dauphin, 2005). EMZs are arranged by the coral in a pattern that reflects the overall morphology of the skeleton. Indeed, one could say that it is the organization of the EMZ (which is completely controlled by the coral) that defines the overall morphology of the skeleton. The EMZs are overgrown by subsequent layers of

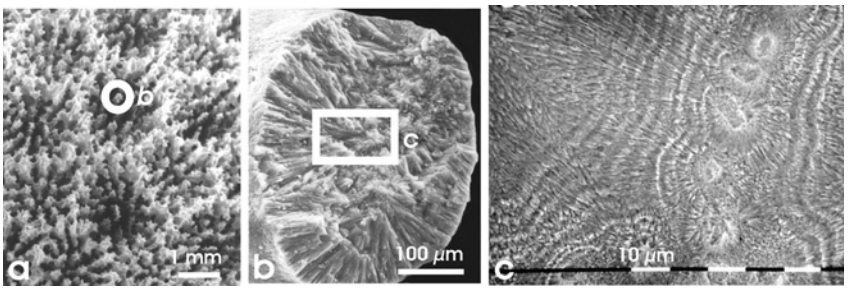

Figure 6: Microstructure of coral skeleton of *Porites* showing different sizes and shapes of the early mineralization zones (EMZ) and fibres. (a) Calice morphology, (b) Radiating fibres, (c) The stepping growth mode of fibres: each biomineralization growth layer is the elemental environment recording unit.

fibrous aragonite that serve to give the skeleton bulk mass and mechanical strength (Fig. 4). Of direct relevance to the utilization of coral skeletons to paleo-climatic reconstructions is the discovery of dramatic geochemical variations at the ultrastructure level.

Using conventional ion microprobe, Cohen et al. (2001) analyzed the Sr/Ca ratio in both EMZ and fibres of *Porites* and found that the Sr/Ca vs. SST relationship differed dramatically for EMZ and aragonite fibres. Cohen et al. (2001) concluded that the Sr/Ca ratio of the aragonite fibres was strongly influenced by biological activity of symbiotic algae during daytime precipitation. In another study, Cohen et al. (2002) compared the Sr/Ca vs. SST relationship between symbiotic and asymbiotic coral colonies of *Astrangia poculata* and found again the Sr/Ca ratio in symbiotic corals to be strongly perturbed from the thermodynamic equilibrium values.

Cuif and Dauphin (1998) observed chemical heterogeneity (strontium, magnesium, and sulfur) between fibres and EMZ in the septa of 15 different coral species. Using synchrotron-based XANES analyses, Cuif et al. (2003) further established that sulfur in the coral skeleton is almost exclusively associated with sulfated polysaccharides, which are highly concentrated in the EMZ, but also present in the fibrous aragonite part of the skeleton, where they display a layered distribution corresponding to the layered organization of the fibres (Fig. 6).

These findings were subsequently extended to other trace elements by Meibom et al. (2004), who reported a distinct zonation of Mg in the coral *Pavona clavus*, again corresponding closely to the layered structure of aragonite fibres (Fig. 7). Meibom et al. (2004) furthermore found the EMZ to be greatly enriched in Mg. Strontium, on the other hand did not show similar banded distributions and it seems that different trace elements have different (metabolic) pathways from the seawater to the coral skeleton.

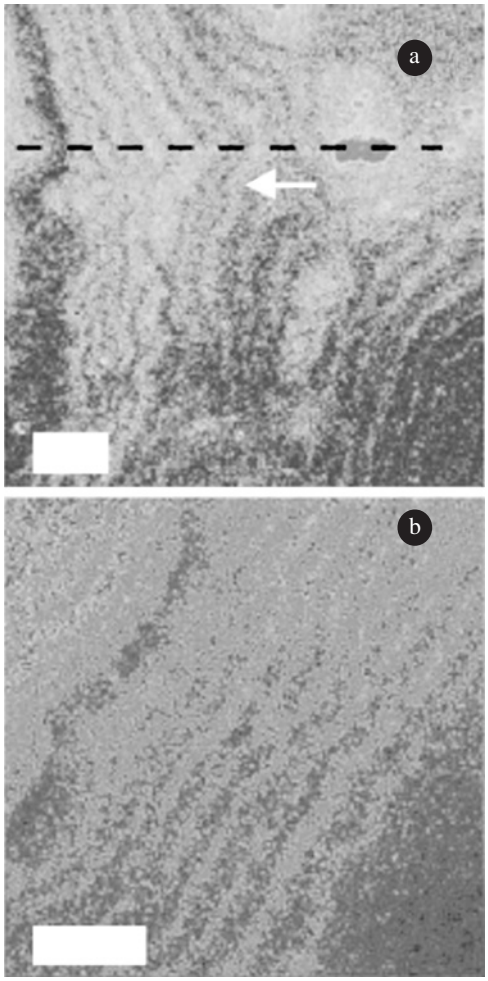

Figure 7: The distribution of Mg in different parts of the *Pavona clavus* skeleton from Meibom et al. (2004). Dark blue colors correspond to relatively low Mg concentrations; green, yellow and red colors correspond to increasingly high Mg concentrations. EMZ have the highest concentration of Mg. Arrow indicates direction of growth. Scale bars are 10 μm (For colour version, see Colour Plate Section).

4 Conclusions

Taken together, the observations described in this brief overview suggest that the distribution of trace elements and stable isotopic composition of hermatypic coral skeletons are strongly affected, if not completely controlled, by biological processes. From a paleo-climatic point of view, the main challenge for the future is to establish the degree to which the SST affects these

biological processes; i.e., how much of the trace element and stable isotope variation can be ascribed to seasonal and interannual SST oscillations and how much other environmental and biological factors affect the skeletal chemistry (Reynaud-Vaganay et al., 1999, 2001; Ferrier-Pagès et al., 2002; Reynaud et al., 2002, 2004). There are strong indications that the degree of biological control and the sensitivity of the coral to variations in SST is species-dependent (Weber and Woodhead, 1972; Weber, 1973). Understanding the coral biomineralization processes in detail has become more important than ever. At the moment, relevant experimental efforts are still somewhat scattered and limited in scope, but the development of new microanalytical techniques, such as the NanoSIMS, enable to precisely measure the recording process in the stepping growth layers and have opened up the field of biomineralization to a new generation of studies that may hold the key to more precise coral-based records of past environmental parameters.

Acknowledgements

We thank Anders Meibom and two anonymous reviewers for valuable comments on our manuscript.

References

Adkins, J. F., Boyle, E. A., Curry, W. B., Lutringer, L., 2003. Stable isotopes in deep-sea corals and a new mechanism for "vital effects". Geochimica et Cosmochemica Acta 67, 1129–1143.

Al-Horani, F. A., Al-Moghrabi, S. M., de Beer, D., 2003. Microsensor study of photosynthesis and calcification in the scleractinian coral, *Galaxea fascicularis*: active internal carbon pool. Journal of Experimental Marine Biology and Ecology 288, 1–15.

Allison, N., 1996. Comparative determinations of trace and minor elements in coral aragonite by ion microprobe analysis with preliminary results from Phuket, southen Thailand. Geochimica et Cosmochimica Acta 60, 3457–3470.

Allison, N., Finch, A. A., 2004. High resolution Sr/Ca records in modern *Porites lobata* corals: effects of skeletal growth rate and architecture. Geochemistry Geophysics Geosystems 5, doi:10.1029/2004GC000696.

Barnes, D. J., Lough, J. M., 1993. On the nature and causes of density banding in massive coral skeletons. Journal of Experimental Marine Biology and Ecology 167, 91–108.

Barnes, D. J., Taylor, R. B., Lough, J. M., 1995. On the inclusion of trace materials into massive coral skeletons. Part II: distortions in skeletal records of annual climate cycles due to growth processes. Journal of Experimental Marine Biology and Ecology 194, 251–275.

Beck, J. W., Edwards, R. L., Ito, E., Taylor, F. W., Recy, J., Rougerie, F., Joannot, P., Henin, C., 1992. Sea-surface temperature from coral skeletal strontium/calcium ratios. Science 257, 644–647.

Broecker, W. S., Peng, T. H., 1982. Tracers in the Sea. Lamont-Doherty Geological Observatory, .

Cobb, K., Charles, C. D., Cheng, H., Edwards, R. L., 2004. El Niño/Southern Oscillation and tropical Pacific climate during the last millennium. Nature 424, 271–276.

Cohen, A. L., Layne, G. D., Hart, S. R., Lobel, P. S., 2001. Kinetic control of skeletal Sr/Ca in a symbiotic coral: Implications for the paleotemperature proxy. Paleoceanography 6, 20–26.

Cohen, A. L., Owens, K. E., Layne, G. D., Shimizu, N., 2002. The effect of algal symbionts on the accuracy of Sr/Ca paleotemperatures from coral. Science 296, 331–333.

Cohen, A., Sohn, R. A., 2004. Tidal modulation of Sr/Ca ratios in a Pacific reef coral. Geophysical Research Letters 31, L16310 doi: 10.1029/2004GL020600.

Cole, J. E., Fairbanks, R. G., 1990. The southern oscillation recorded in the $\delta^{18}O$ of corals from Tarawa Atoll. Paleoceanography 5, 669–683.

Cuif, J. P., Dauphin, Y., 1998. Microstructual and physico-chemical characterization of "centers of calcification" in septa of some recent scleractinian corals. Paläontologische Zeitschrift 72, 257–270.

Cuif, J. P., Dauphin, Y., Douget, J., Salomé, M., Susini, J., 2003. XANES mapping of organic sulfate in three scleractinian coral skeletons. Geochimica et Cosmochimica Acta 67, 75–83.

Cuif, J. P., Dauphin, Y., 2005. The two-step mode of growth in the scleractinian coral skeletons from the micrometer to the overall scale. Journal of Structural Biology 150, 319–331.

de Villiers, S., Shen, G. T., Nelson, B. K., 1994. The Sr/Ca-temperature relationship in coralline aragonite: Iinfluence of variability in (Sr/Ca) seawater and skeletal growth parameters. Geochimica et Cosmochimica Acta 58, 197–208.

de Villiers, S., 1999. Seawater strontium and Sr/Ca variability in the Atlantic and Pacific oceans. Earth and Planetary Science Letters 171, 623–634.

Dunbar, R. B., J. E. Cole, 1999. Annual Records of Tropical Systems (ARTS), 72.

Epstein, S., Buchsbaum, R., Lowenstam, H. A., Urey, H. C., 1953. Revised carbon-water isotopic temperature scale. Bulletin of the Geological Society of America 64, 1315–1356.

Fallon, S. J., McCulloch, M. T., van Woesik, R., Sinclair, D. J., 1999. Corals at their latitudinal limits: laser ablation trace element systematics in *Porites* from Shirigai Bay, Japan. Earth and Planetary Science. Letters 172, 221–238.

Ferrier-Pagès, C., Boisson, F., Allemand, D., Tambuttè, E., 2002. Kinetics of strontium uptake in the scleractinian coral *Stylophora pistillata*. Marine Ecology Progress Series 245, 93–100.

Gagan, M. K., Ayliffe, L. K., Hopley, D., Cali, J. A., Mortimer, G. E., Chappell, J., McCulloch, M. T., Head, M. J., 1998. Temperature and surface-ocean water balance of the mid-Holocene tropical Western Pacific. Science 279, 1014–1018.

Gagan, M. K., Ayliffe, L. K., Beck, J. W., Cole, J. E., Druffel, E. R. M., Dunbar, R. B., Schrag, D. P., 2000. New views of tropical paleoclimates from corals. Quaternary Science Review 19, 45–64.

Guilderson, T. P., Fairbanks, R. G., Rubenstone, J. L., 1994. Tropical temperature variations since 20000 years ago: modulating interhemispheric climate change. Science 263, 663–665.

Hart, S. R., Cohen, A. L., 1996. An ion probe study of annual cycle of Sr/Ca and other trace elements in corals. Geochimica et Cosmochimica Acta 60, 3075–3084.

Jones, P. D., Mann, M. E., 2004, Climate over past millennia, Reviews of Geophysics 42, 2003RG000143.

Juillet-Leclerc, A., Schmidt, G., 2001. A calibration of the oxygen isotope paleothermometer of coral aragonite from *Porites*. Geophysical Research Letters 28 (21), 4135–4138.

Kaplan, A., Cane, M. A., Kushnir, Y., Clement, A. C., 1998. Analysis of global sea surface temperatures 1856–1991. Journal of Geophyscal Research 103, 18,575–18,589.

Knutson, D. W., Buddemeier, R. W., Smith, S. V., 1972. Coral chronometers: Seasonal growth bands in reef corals. Science 177, 270–272.

Land, L. S., Lang, J. C., Barnes, D. J., 1975. Extension rate: a primary control on the isotopic composition of West Indian (Jamaican) scleractinian reef coral skeleton. Marine Biology 33, 221–233.

Leder, J. J., Swart, P. K., Szmart, A. M., Dodge, R. E., 1996. The origin of variations in the isotopic record of scleractinian corals: I. Oxygen. Geochimica et Cosmochimica Acta 60, 2857–2870.

Linsley, B. K., Messier, R. G., Dunbar, R. B., 1999. Assessing between-colony oxygen isotope variability in the coral *Porites lobata* at Clipperton Atoll. Coral Reefs 18 (13), 13–27.

Linsley, B. K., Wellington, G. M., Schrag, D. P., Ren, L., Salinger, M. J., Tudhope, A. W., 2004. Geochemical evidence from corals for changes in the amplitude and spatial pattern of South Pacific interdecadal climate variability over the last 300 years. Climate Dynamics 22, 1–11 doi:10.1007/ 50038200–0364-y.

Marshall, J. F., McCulloch, M. T., 2002. An assessment of the Sr/Ca ratio in shallow water hermatypic corals as a proxy for sea surface temperature. Geochimica et Cosmochimica Acta 66, 3263–3280.

McCulloch, M. T., Gagan, M. K., Mortimer, G. E., Chivas, A. R., Isdale, P. J., 1994. A high-resolution Sr/Ca and $\delta^{18}O$ coral record from the Great Barrier Reef, Australia, and the 1982–1983 El Nino. Geochimica et Cosmochimica Acta 58 (12), 2747–2754.

McConnaughey, T., 1989. ^{13}C and ^{18}O isotopic disequilibrium in biological carbonates: 1.Patterns. Geochimica et Cosmochimica Acta 53, 151–162.

Meibom, A., Stage, M., Wooden, J., Constantz, B. R., Dunbar, R. B., Owen, A., Grumet, N., Bacon, C. R., Chamberlain, P. R., 2003. Monthly strontium/calcium oscillations in symbiotic coral aragonite: Biological effects limiting the precision of the paleotemperature proxy. Geophysical Research Letters 30 1029/2002GL016864.

Meibom, A., Cuif, J. P., Hillion, F., Constantz, B. R., Juillet-Leclerc, A., Dauphin, Y., Watanabe, T., Dunbar, R. B., 2004. Distribution of magnesium in coral skeleton. Geophysical Research Letters 31 doi:10.1029/2004GL021313.

Quinn, T. M., Crowley, T. J., Taylor, F. W., Henin, C., Joannot, P., Yvan, J., 1998. A multicentury sable isotope record from a New Caledonia coral; Interannual and decadal sea surface temperature variability in the southwest Pacific since 1657 A.D. Paleoceanography 13 (4), 412–426.

Ren, L., Linsley, B. K., Wellington, G. M., Schrag, D. P., Hoegh-Guldberg, O., 2002. Deconvolving the $\delta^{18}O$ seawater component from subseasonal coral $\delta^{18}O$ and Sr/Ca at Rarotonga in the southwestern subtropical Pacific for the period 1726 to 1997. Geochimica et Cosmochimics Acta 67, 1609–1621.

Reynaud-Vaganay, S., Gattuso, J. P., Jaubert, J., Juillet-Leclerc, A., 1999. A novel culture technique for scleractinian corals: application to investigate changes in skeletal $\delta^{18}O$ as a function of temperature. Marine Ecology Progress Series 180, 121–130.

Reynaud-Vaganay, S., Juillet-Leclerc, A., Jaubert, J., Gattuso, J. P., 2001. Effect of light on skeletal $\delta^{13}C$ and $\delta^{18}O$, and interaction with photosynthesis, respiration and calcification in two zooxanthellate scleractinian corals. Palaeogeography, Palaeoclimatology, Palaeoecology 175, 393–404.

Reynaud, S., Ferrier-Pagès, C., Sambrotto, R., Juillet-Leclerc, A., Jaubert, J., Gattuso, J. P., 2002. Effect of feeding on the carbon and oxygen isotopic composition in the tissues and skeleton of the zooxanthellate coral *Stylophora pistillata*. Marine Ecology Progress Series 238, 81–89.

Rollion-Bard, C., Chaussidon, M., France-Lanord, C., 2003. pH control on oxygen isotopic composition of symbiotic corals. Earth Planetary Science. Letters 215, 275–288.

Sinclair, D. J., Kinsley, L. P. J., McCulloch, M. T., 1998. High resolution analysis of trace elements in corals by laser ablation ICP-MS. Geochimica et Cosmochimica Acta 62, 1889–1901.

Smith, S. V., Buddemeier, R. W., Redalje, R. C., Houck, J. E., 1979. Strontium-calcium thermometry in coral skeletons. Science 204, 404–407.

Stephans, C. L., Terrence, M., Quinn, T. M., Taylor, F. W. Corrège, T., 2004. Assessing the reproducibility of coral-based climate records Geophysical Research Letters 31, L18210, doi:10.1029/2004GL020343.

Tudhope, A. W., Chilcott, C. P., McCulloch, M. T., Cook, E. R., Chappell, J., Ellam, R. M., Lea, D. W., Lough, J. M., Shimmield, G. B., 2001. Variation in the El Nino-Southern Oscillation through a glacial-interglacial cycle. Science 291, 1511–1517.

Urey, H. C., 1947. The thermodynamic properties of isotopic substances. Journal of the Chemcal Society 562–581.

Urey, H. C., Lowenstam, H. A., Epstein, S., McKinney, C. R., 1951. Measurements of paleotemperatures and temperatures of the upper Cretaceous of England, Denmark and the southeastern United States. Bulletin of the Geological Sociesty of America 62, 399–416.

Watanabe, T., Winter, A., Oba, T., 2001. Seasonal changes in sea surface temperature and salinity during the Little Ice Age in the Caribbean Sea deduced from Mg/Ca and $^{18}O/^{16}O$ ratios in corals. Marine Geology 173, 21–35.

Watanabe, T., Winter, A., Oba, T., Anzai, R., Ishioroshi, H., 2002. Evaluation of accuracy in coral isotope records for environmental proxy. Coral Reefs 21, 169–178.

Watanabe, T., Gagan, M. K., Corrège, T., Scott-Gagan, H., Cowley, J., Hantoro, W. S., 2003. Oxygen isotope systematics in *Diploastrea heliopora*: New coral archive of tropical paleoclimate. Geochimica et Cosmochimica Acta 67, 1349–1358.

Weber, J. N., Woodhead, P. M. J., 1972. Temperature dependence of oxygen-18 concentration in reef coral carbonates. Journal of Geophysical Research 77, 463–473.

Weber, J. N., 1973. Incorporation of strontium into reef coral skeletal carbonate. Geochimica et Cosmochimica Acta 37, 2173–2190.

Wellington, G. M., Dunbar, R. B., Merlen, G., 1996. Calibration of stable oxygen isotope signatures in Galapagos corals. Paleoceanography 11, 467–480.

Chapter 11

Potential Feedback Mechanism Between Phytoplankton and Upper Ocean Circulation with Oceanic Radiative Transfer Processes Influenced by Phytoplankton – Numerical Ocean General Circulation Models and an Analytical Solution

Shoichiro Nakamoto[1,2,3,*], Makoto Kano[3], S. Prasanna Kumar[4], Josef M. Oberhuber[5], Kei Muneyama[6], Kyozo Ueyoshi[7], Bulusu Subrahmanyam[8], Kisaburo Nakata[9], C. Aaron Lai[10] and Robert Frouin[7]

[1]*Dept. of Mechanical System Engineering, Okinawa College of Technology, Henoko, Nago 905-2192, Japan*
[2]*OHTI, OK Bldg., 2-51-10, Honmachi, Nakanoku, Tokyo 162-0012, Japan*
[3]*Physics Department, Tokyo University of Science, 1-3, Tokyo 162-8601, Japan*
[4]*POD, National Institute of Oceanography, Dona Paula, Goa 403004, India*
[5]*DKRZ, Bundesstrasse 55, D-20146 Hamburg, Germany*
[6]*JAMSTEC, 2-15 Natsushima, Yokosuka 237, Japan*
[7]*Scripps Institution of Oceanography, La Jolla, CA 92093, USA*
[8]*Marine Science Program, Dept. of Geology, University of South Calorina, Columbia, SC 29208, USA*
[9]*Ocean Engineering Department, Tokai University, Shimizu, Japan*
[10]*Los Alamos National Laboratory, Los Alamos, NM, USA*

*Corresponding author.
E-mail address: nakamotoocean@aol.com (S. Nakamoto).

Elsevier Oceanography Series 73
Edited by H. Kawahata and Y. Awaya
ISBN: 0-444-52948-9

Abstract

Because of the diversity of the ecosystem in the earth, modeling of such an ecosystem cannot avoid arguing which ecosystem element should be included or excluded. We demonstrated that views of thermodynamics ensuring the flow of solar energy between nonliving things and living things in the oceanic ecosystem as an alternative approach in the modeling of the earth system with life. We showed that marine phytoplankton influence the global pattern of the sea surface temperature, seawater density, and associated flows by heat release to the upper ocean environment. The effect of heat release by phytoplankton on penetrative radiation not only influences directly the vertical structure of seawater density, but also dynamically interacts with surrounding ocean fluids in the equatorial Pacific. Numerical models experiments suggest an active role of phytoplankton in the equatorial ocean dynamics by modifying density and thus providing conditions favorable to phytoplankton growth, i.e., the potential positive feedback mechanism between the ecosystem and the ocean dynamics. A mechanistic model proposed here is simple enough to identify the cause-and-effect relationship of the phytoplankton's active role in the earth system.

Keywords: phytoplankton, oceanic radiative transfer, bio-climate feedbacks

1 Introduction

Earth environmental problems involve feedbacks between the ecosystem and the climate. Concerning global warming, one may assume that potential feedbacks between marine ecosystem and physical processes will increase or decrease the concentration of carbon dioxide in the atmosphere than the sum of the component systems themselves. Because of the complexity of the earth environmental problems in terms of scales in time and space as well as its interconnectivity between multidisciplines in contemporary sciences, providing answers to these questions is an enormous challenge.

The atmosphere and ocean continuously exchange carbon dioxide across sea surface. Within the top hundred meters of seawater, the carbon dioxide is taken up by phytoplankton quite rapidly (Kawabata et al., 2003; Otsuki et al., 2003). Absorption in the lower level of the ocean takes longer because the mixing of the upper ocean water with water at lower level requires up to several hundred years or so. It takes over thousands of years for the deep ocean to complete the same process.

Recent measurements of underwater solar energy absorption spectrum in the northwestern Pacific (see Fig. 3 of Sasaki et al., 2001) showed that living phytoplankton absorbs more light than detritus or other material without life activity do. Siegel and Dickey (1987) demonstrate that the attenuation of visible energy and photosynthetically available radiation (PAR) (Morel, 1978) are primarily functions of chlorophyll pigments. Iturriaga and

Siegel (1989) reported that phytoplankton abundance accounted for 50–70% of the particulate absorption at 440 nm.

Lewis et al. (1990) suggested that variations in the amount of irradiance penetrating through the mixed layer are due to changes in phytoplankton abundance, especially in the Pacific warm pool region. Using TOGA-COARE intensive observation data in January 1992, Siegel et al. (1995) showed that a nearly tripling of mixed-layer phytoplankton following a sustained westerly wind burst resulted in a reduction in the penetrative flux of nearly 6 W m^{-2} in the net solar radiation at 30 m and biologically mediated increase in the mixed-layer radiant heating rate of 0.13 K during the observation period.

By analyzing a three-dimensional numerical model experiment results of Ocean isoPYcnal coordinate (OPYC) general circulation model (Oberhuber, 1993), Nakamoto et al. (2001) showed that surface chlorophyll pigments in the equatorial Pacific not only influence vertical penetration of solar radiation, but also modify geostrophic flows in the Pacific basin scales. They used an empirical relation for a heating rate as a function of depth and of phytoplankton concentration retrieved from the satellite data (Morel and Antoine, 1994).

In their numerical model experiments, the biologically generated geostrophic flows converge toward the equatorial undercurrent (EUC) in the western equatorial Pacific. The water masses converged into the EUC in the west are transported eastward. That induces an upwelling in the eastern equatorial Pacific, and leads to a biomass-related sea surface temperature (SST) anomalies, characterized by water colder than the case without phytoplankton in the ocean (Nakamoto et al., 2001).

Recent model experiments performed by Ueyoshi et al. (2003) using the MIT OGCM with Morel and Antoine's (1994) shortwave penetration scheme and SeaWiFs satellite-measured chloropyhll concentration data produced the results remarkably similar to those described by Nakamoto et al. (2001). In particular, the enhanced EUC and the colder ocean surface region of SST anomalies in the eastern equatorial Pacific were reproduced, indicating ocean dynamical interaction effects of phytoplankton in the equatorial Pacific.

Using coastal zone color scanner (CZCS) satellite-derived chlorophyll concentration data, Murtgudde et al. (2002) conducted ocean general circulation experiments similar to Nakamoto et al. (2000, 2001). Their control runs without phytoplankton were done with the attenuation depth of 17 m and these runs were compared with runs where the attenuation depth was computed from annual mean CZCS data (see the Fig. 1, p. 472 of Murtgudde et al., 2002). They argued that the large region of colder-than-observed SSTs in the eastern equatorial and coastal region is greatly alleviated in their ocean model with CZCS chlorophyll pigment data by stating that the model simulated SST with phytoplankton is as high as 1°C for the cold tongue region compared with the control run without phytoplankton (see Fig. 5a in

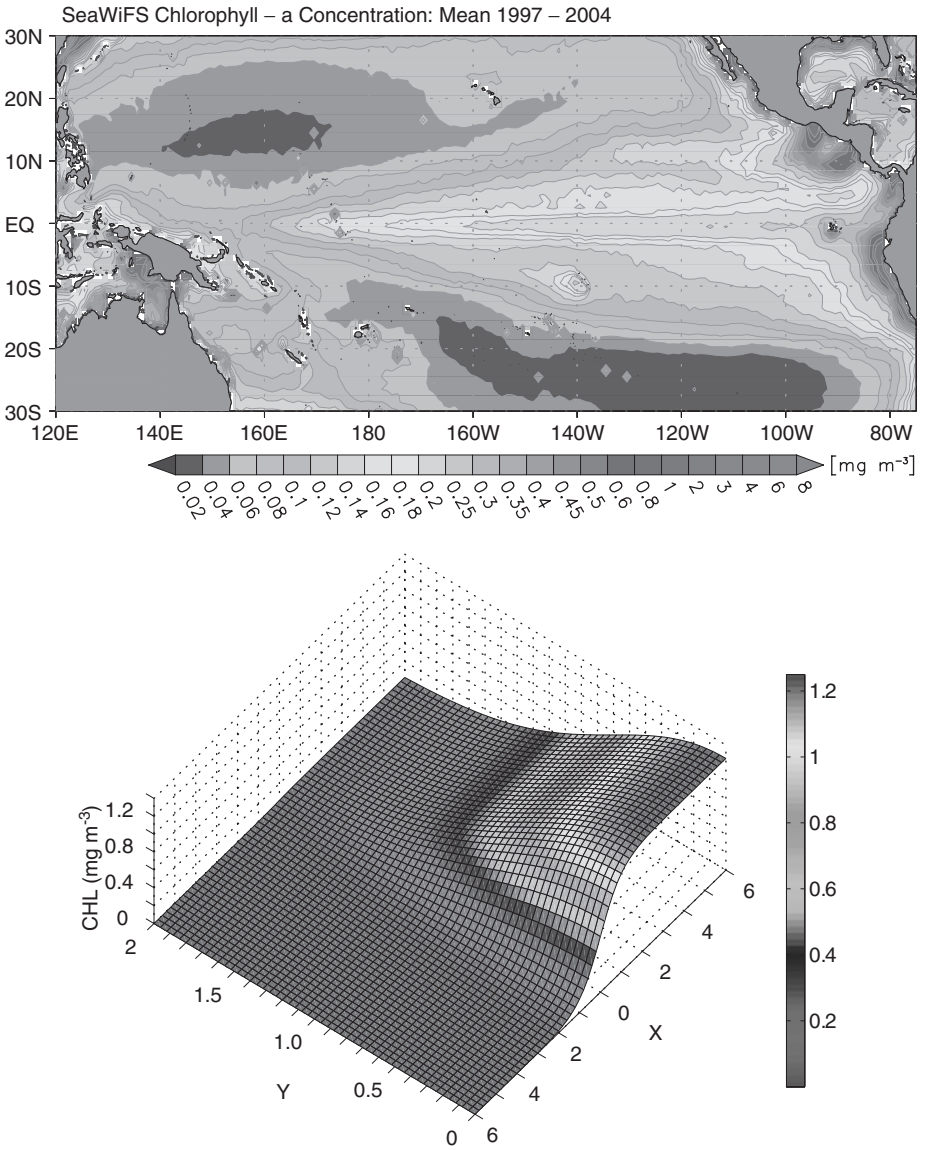

Figure 1: Biomass distribution from SeaWiFS satellite observations and the mathematical distribution function (mg m^{-3}) given by equation (1). The coordinates x and y are normalized by 100 km (For colour version, see Colour Plate Section).

page of Murtgudde et al., 2002). Regarding the process occurring in their ocean model simulations with variable attenuation depths, they speculate that slight warming below the mixed layer with the presence of phytoplankton and the consequent weakening of the stratification leads dynamical

feedbacks as described in their numerical model outputs (see p. 476 of Murtugudde et al., 2002).

Here, it is worth noting that Nakamoto et al. (2000, 2001) and Murtgudde et al. (2002) conducted two different numerical experiments with respect to the process of penetration of solar radiation due to phytoplankton in the upper ocean, i.e., Nakamoto et al. (2001) and Ueyoshi et al. (2003) employed a numerical scheme that allows solar energy shifting toward the ocean surface in the eastern equatorial ocean with phytoplankton, while Murtgudde et al. (2002) employed a numerical scheme allowing solar energy to penetrate deeper into the eastern equatorial subsurface ocean with phytoplankton compared to their control run without phytoplankton.

In this paper, we do not discuss the solar energy penetration process employed by Murtgudde et al. (2002). Instead, we study the hypothesis proposed by Nakamoto et al. (2001) to seek for an analytical approach to verify their bioclimate interaction hypothesis involving living phytoplankton and ocean circulation, by assuming that heat deposition due to phytoplankton occurs in the surface region rather than in the subsurface ocean if phytoplankton concentration is given in the surface part of the ocean.

Question we address here is the following: Why does SST in the eastern equatorial Pacific become cooler in Nakamoto et al. (2001) and Ueyoshi et al. (2003), when phytoplankton is taken into account, despite phytoplankton-traped solar radiation near the ocean surface in Nakamoto et al. (2001) and Ueyoshi et al. (2003)? In order to answer this question, we focus our attention on the geophysical dynamics problem hypothesized by Nakamoto et al. (2001) based on their ocean general circulation model (OGCM) experiment. Now, a new question, "Does the geographical pattern of chlorophyll biomass concentration is the key in the biological interaction with the surrounding seawater in the tropical ocean?" arises. More specifically, we may address the following question: "Do phytoplankton in the equatorial ocean generate subsurface westward-geostrophic currents, which eventually merge into the EUCs in the western equatorial Pacific?"

We illustrate the process via extracting a simple mechanistic model from numerical experiments with OGCMs . The goal of this paper is to motivate earth system modeling from the view of thermodynamics of life in oceanic ecosystem for understanding biological—chemical–physical feedback mechanism essential in the Earth System Sciences (Harte, 2002).

2 Ocean General Circulation Model with Photosynthesis Effects

Chlorophyll can absorb and utilize photons of near ultraviolet and visible wavelengths; therefore, the relevant measure of the underwater light field is

the PAR, which is a broadband quantity integrated from the wavelength of 350 nm to that of 700 nm (Morel, 1978). In Case 1 water, the concentration of phytoplankton is high compared with nonbiogenic particles (Morel and Prieur, 1977). Once the light energy is absorbed by the chlorophyll pigments of phytoplankton or aquatic macrophytes, it is used to generate useful chemical energy in the form of carbohydrate. Since the aquatic plants also contain lipids and nucleic acids, none of which conform closely in their overall composition to glucose, the biosynthesis of these substances requires additional photosynthetically generated reducing power and chemical energy, and so requires additional light quanta per carbon dioxide incorporated (Kirk, 1994). This is why the entropy argument for living phytoplankton is essential in terms of macroscopic heat energy transfer processes between the living system and its environment (Peixoto and Oort, 1992; Nakamoto et al., 2002).

We propose a simple model to provide the essence of Nakamoto et al. (2001) numerical model experiments: The model must contain the radiative transfer mechanism to generate geostrophic currents as seen in the OGCM experiment (Nakamoto et al., 2001). In order to capture the chlorophyll pigment-generated geostrophic current, annually averaged horizontal distribution of chlorophyll pigment concentration is expressed by the following function:

$$B(x,y) = \frac{B_{\max}}{2} \times \left[1 + \tanh\left(\frac{x}{L_x}\right)\right] \times \exp\left(-\frac{y^2}{L_y^2}\right), \tag{1}$$

where the coordinate frame designated by x, y, z is assigned to eastward, northward, and upward, respectively. $B_{\max}$ is the maximum chlorophyll pigment concentration and L_x and L_y are the zonal and meridional length scales for chlorophyll pigment distribution, respectively. The above function $B(x, y)$ (Fig. 1) resembles a typical chlorophyll pigment distribution observed in remotely sensed sea-viewing wide field-of-view sensor (SeaWiFS) data, or a CZCS data (Feldman, 1989) used in the numerical experiments by Nakamoto et al. (2000, 2001).

Given the above surface chlorophyll pigment concentration distribution, how can an attenuation depth of the solar radiation be estimated in the ocean? In general, complex OGCMs employ numerous adjustable parameters that are not directly observable. These models are not falsifiable so that the opportunity to learn from a wrong prediction is short circuited.

The approach we employ here is based on the fact that phytoplankton increase the rapidity of attenuation of light with depth, and in productive waters may do so to such an extent that they become a significant factor limiting their own population growth. The contribution of phytoplankton to the vertical attenuation coefficient of PAR must therefore be taken into

account in any consideration of the extent to which light availability limits primary production in the aquatic biosphere (Kirk, 1994).

Prieur and Sathyendranath (1981) developed a pioneering bio-optical formalism for the spectral absorption coefficient. Their formalism was statistically derived from 90 sets of spectral absorption data taken in various Case 1 waters, and included absorption by phytoplankton pigments, by nonpigmented organic particles derived from deceased phytoplankton, and yellow matter derived from decayed phytoplankton. The contribution of phytoplankton to the total absorption was parameterized in terms of the chlorophyll concentration. The essence of the Prieur and Sathyendranath (1981) formalism is contained in a more recent and simpler variant given by Morel (1991). Statistically derived absorption coefficient values for pure water and for nondimensional chlorophyll-specific absorption coefficient are listed in Table 3.7 of Mobley (1994).

For the averaged vertical attenuation coefficient throughout the euphotic zone, it is assumed that the total vertical attenuation coefficient at a given depth can be regarded as the sum of a set of partial attenuation coefficients, each corresponding to a different component of medium. We make use of a further assumption, namely that the contribution of any component of the medium to the averaged attenuation coefficient is linearly related to the concentration of that components (Kirk, 1994).

A diffuse attenuation coefficient $k(x, y)$ that varies with chlorophyll concentration is thus expressed as a sum of components related to pure water and that due to chlorophyll biomass (Apel, 1987; Kirk, 1994; Mobley, 1994):

$$k(x,y) = k_w + k_c \times B(x,y), \tag{2}$$

$$I(x,y,z) = I_0 \times \exp(k(x,y) \times z), \tag{3}$$

where $k(x, y)$ is the biomass dependent vertically average diffuse attenuation coefficient, k_w is the attenuation coefficient in pure water, k_c is the specific attenuation coefficient due to unit chlorophyll mass, $I_0 = I\ (x, y, 0)$ and $I(x, y, 0)$ are the irradiance just below the surface, respectively.

It is noted that the above formalism is not exactly the same as that used in the numerical OGCM experiment conduced by Nakamoto et al. (2001); however, the physics employed in the above two equations (2) and (3) is simple enough to extract the essence of the radiative transfer mechanism perturbed by phytoplankton concentration, i.e., the solar energy penetration depth becomes smaller with increasing biomass concentration. This means that oceanic phytoplankton traps solar irradiance toward the ocean surface. The implication of the above formalism is that the upper ocean with phytoplankton is optically less transparent than without phytoplankton. The

above formalism is also consistent with recent measurements of the absorption spectrum for solar irradiance in the ocean, which shows significant diminishing of light energy under the existence of phytoplankton (Sasaki et al., 2001): Sasaki's observation of underwater solar radiation represents that living phytoplankton releases more heat energy toward the surrounding waters than the detritus of dead organism does.

In mathematical terms, phytoplankton in the upper part of the ocean localizes the heat source of the heat equation at habitat depth of phytoplankton because living phytoplankton absorb visible energy and convert a small portion of it into glucose during photosynthesis, while releasing the rest of the energy toward the external environment as heat (Nakamoto et al., 2002). These are the physics exhibited in OGCM experiments with the effect of living phytoplankton, i.e., the life activity expressed in radiative energy budget in the upper ocean environment.

In order to describe the heating mechanism of the seawater through radiative transfer process perturbed by living phytoplankton, we employ the following anomalous temperature equation with phytoplankton-induced anomalous heat source:

$$\frac{\partial \theta(x,y,z,t)}{\partial t} = \frac{1}{\rho c_p} \times \frac{\partial I(x,y,z)}{\partial z}, \tag{4}$$

where $\theta(x, y, z, t)$ is the anomalous temperature of the water at a fixed point due to the irradiance perturbation caused by living phytoplankton, ρ is seawater density, and c_p is heat capacity of seawater.

Integrating the above heat equation with respect to time leads,

$$\theta(x,y,z,t) = \frac{I_0 \times t}{\rho c_p} k(x,y) \times \exp(zk(x,y)). \tag{5}$$

Note that the above solution is valid for a vertically averaged attenuation coefficient, $k(x, y)$, which is a function of chlorophyll concentration distribution specified in the equation (1) in this study. As the consequence of the above assumed heat equation, Equation (4), the anomalous temperature increases linearly in time: the temperature perturbation due to phytoplankton biomass is not large enough to induce heat advection influencing the mean heat equation. This model is simple enough to serve as "Fermi approach" as suggested by Harte (2002): The analytical solution for the anomalous temperature rise due to living phytoplankton can be verified or rejected by careful laboratory measurements as well as numerical model experiments. Recently, Ohta and Nakagawa (2003) conducted laboratory experiment to measure photosynthesis efficiency with phytoplankton. They reported that the measured water temperature increased linearly in time, and that 82% of the incoming solar energy was released to the surrounding waters as heat.

Our approach is thus based on the observational fact that most of the solar energy in the visible spectral range is trapped by and released from living phytoplankton to the surrounding waters in the ocean. Thus, less solar radiation penetrates to deeper waters when a high density of phytoplankton exists in the ocean.

3 Feedback Mechanism between Phytoplankton and the Oceanic Environment

Since the perturbation in seawater temperature caused by heat release from living phytoplankton is executed at phytoplankton's dwelling depth, we translate anomalous temperature of seawater into anomalous density of seawater by the following equation:

$$\frac{\partial(\bar{\rho}+\rho)}{\partial\theta} = -\alpha(\bar{\rho}+\rho), \tag{6}$$

where α is the thermal expansion coefficient at fixed salinity and pressure, $\bar{\rho}$ is the background density field neglecting the influence of phytoplankton, ρ is the anomalous density perturbation caused by heat release from living phytoplankton. Note that the background density is independent of the thermal perturbation θ in the above equation.

Solving this equation yields

$$\rho = \bar{\rho} \times [\exp(-\alpha\theta(x,y,z,t)) - 1]. \tag{7}$$

Substituting the anomalous temperature θ into the approximated solution $\rho = -\bar{\rho}\alpha\theta$ yields

$$\rho(x,y,z,t) = -\frac{\alpha I_0 t}{c_p} k(x,y) \times \exp[k(x,y) \times z]. \tag{8}$$

This is the density perturbation caused by the existence of phytoplankton, which causes pressure perturbation due to hydrostatic principles.

Now, we calculate velocity components that are induced by differential heating of water column due to the heat source term generated by spatially inhomogeneous distribution of phytoplankton. The steady state incompressible momentum equations are written as:

$$-fv = -\frac{1}{\rho}\frac{\partial p}{\partial x} + A_v \frac{\partial^2 u}{\partial z^2}, \tag{9a}$$

$$fu = -\frac{1}{\rho}\frac{\partial p}{\partial y} + A_v \frac{\partial^2 v}{\partial z^2}, \tag{9b}$$

$$-\rho g = \frac{\partial p}{\partial z}, \tag{9c}$$

where u and v are the zonal and meridional velocity components, respectively, f is the Coriolis parameter, and A_v is the vertical viscous coefficient of seawater.

In the above equations, the anomalous density $\rho(x, y, z)$ and anomalous pressure $p(x, y, z)$ are perturbations due to phytoplankton biomass, defined at some depths z in the water column. We assume that anomalous pressure by phytoplankton vanishes at ocean surface (z = 0).

Integrating the hydrostatic equation (9c) from the sea surface to the reference depth, we obtain

$$p(x,y,z,t) = -\frac{g\alpha I_0 t}{c_p}\int_z^0 k(x,y) \times \exp(k(x,y) \times \zeta) d\zeta. \tag{10}$$

Our model equations (9a)–(9c) are "mechanistic" in the sense that the process of heat release from space-varying living phytoplankton was replaced with the space-varying water density anomalies. The solar energy penetration scheme in the ocean used in OGCMs was not in such simple exponential formalism; however, the above-employed simple "mechanistic model" (Harte, 2002) is able to mimic the dynamical interaction process between phytoplankton and the surrounding ocean waters to identify the cause-and-effect relationship embedded in more complex OGCMs.

The above Eqs. (9a)–(9c) can be solved analytically. The exact solutions represent phytoplankton-induced geostrophic currents induced in the physical environment. This solution corresponds with those simulated by numerical OGCM experiments (Nakamoto et al., 2001; Miller et al., 2003; Ueyoshi et al., 2003).

After some manipulation, we obtain the general solution for the above mechanistic model:

$$\begin{aligned} u(x,y) = {} & \frac{2A_v}{f\delta_E^2}\exp\left(z/\delta_E\right)\left[b(x,y)\cos\left(z/\delta_E\right) - a(x,y)\sin\left(z/\delta_E\right)\right] \\ & + \frac{\gamma t}{A_v \rho} k(\partial_x k)\exp(zk) \times [P(x,y)k + 2Q(x,y) + zkQ(x,y)] \\ & + \frac{\gamma t}{f\rho} k\left(\partial_y k\right)\exp(zk) \times [R(x,y)k + 2S(x,y) + zkS(x,y)], \end{aligned} \tag{11}$$

and

$$v(x,y) = \exp\left(z/\delta_E\right)\left[a(x,y)\cos\left(z/\delta_E\right) + b(x,y)\sin\left(z/\delta_E\right)\right] + \frac{f\gamma t}{A_v^2\rho}(\partial_x k)\exp(zk)\times[P(x,y)+zQ(x,y)] - \frac{\gamma t}{A_v\rho}\left(\partial_y k\right)\exp(zk)\times[R(x,y)+zS(x,y)], \tag{12}$$

where

$$a(x,y) = -\frac{f\gamma t}{A_v^2\rho}\delta_E\cdot(\partial_x k)\times\left[P(x,y)k + Q(x,y) - \frac{\delta_E^2 k^2}{2}(P(x,y)k+3Q(x,y))\right] - \frac{\gamma t}{f\rho}\delta_E\cdot\left(\partial_y k\right)\times\left[R(x,y)k + S(x,y) - \frac{\delta_E^2 k^2}{2}(R(x,y)k+3S(x,y))\right], \tag{13}$$

$$b(x,y) = -\frac{f\gamma t}{A_v^2\rho}\delta_E\cdot(\partial_x k)\times\left[P(x,y)k + Q(x,y) + \frac{\delta_E^2 k^2}{2}(P(x,y)k + 3Q(x,y))\right] - \frac{\gamma t}{f\rho}\delta_E\cdot\left(\partial_y k\right)\times\left[R(x,y)k + S(x,y) + \frac{\delta_E^2 k^2}{2}(R(x,y)k+3S(x,y))\right], \tag{14}$$

$$P(x,y) = \frac{-\delta_E^5}{\left(D^4+4\right)^2} = 2kQ(x,y) - R(x,y) \tag{15}$$

$$Q(x,y) = \frac{\delta_E^4}{D^4+4} = \frac{S(x,y)}{k^2} \tag{16}$$

$$D = \delta_E \times k, \tag{17}$$

$$\partial_x k = \frac{\partial k}{\partial x}, \tag{18}$$

$$\partial_y k = \frac{\partial k}{\partial y}, \tag{19}$$

$$\gamma = \frac{g\alpha I_0}{C_p}, \tag{20}$$

$$\delta_E = \sqrt{\frac{2A_v}{f}}. \tag{21}$$

Here, we introduce the Ekman layer thickness δ_E, which represents a balance between Coriolis force and eddy friction, analogous to the way of geostrophic balance between Coriolis force and pressure gradient. This

thickness increases with larger values of eddy viscosity, but decreases with large values of Coriolis parameter. It is reminded that the velocity in the Ekman layer thickness approaches the geostrophic velocity while oscillating slightly about that value in the vertical coordinate.

Fig. 2 displays the zonal component of phytoplankton-induced geostrophic current at 100 m depth, when surface chlorophyll concentration is given by equation (1). Note that the coordinate origin of the biomass distribution function, $B(x, y)$, is located on the equator and the length is scaled by 1°. It is seen that the flows are westward in the northern hemisphere, corresponding to the anomalous pressure gradient due to the existence of phytoplankton. Since the chlorophyll concentration distribution function given by equation (1) is symmetric about the equator, phytoplankton-induced geostrophic currents in the southern hemisphere is also westward. Thus, the phytoplankton-induced geostrophic currents are westward in the equatorial region of several degrees north and south of the equator in both the hemispheres.

Fig. 3 displays meridional components of phytoplankton-induced geostrophic currents in the domain near the equator (0.3° N to 1.4° N). It shows the equatorward anomalous currents induced by the anomalous zonal pressure gradient due to the corresponding zonal gradient of phytoplankton concentration given by equation (1). Figs. 2 and 3 represent that phytoplankton-induced geostrophic currents converge toward the equator

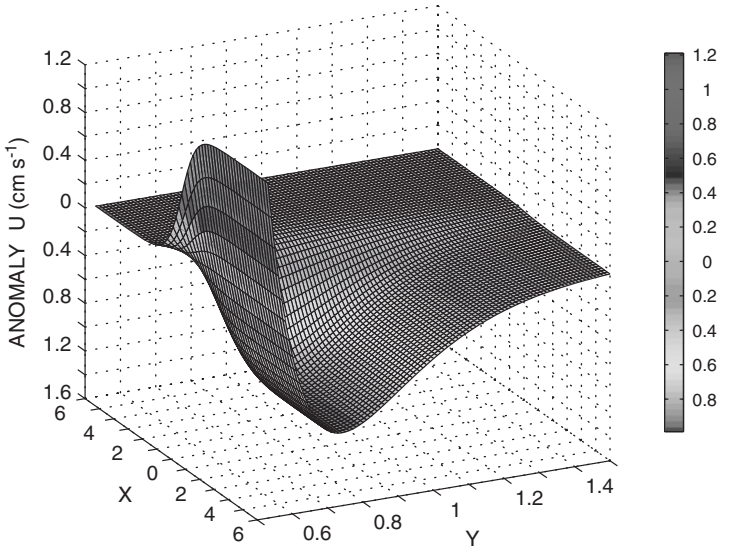

Figure 2: Zonal component of chlorophyll biomass induced southward geostrophic currents (m s^{-1}). The horizontal coordinate origin is located at dateline on the equator and the lengths are scaled by 1°. y coordinate spans 0.5–1.5° N (For colour version, see Colour Plate Section).

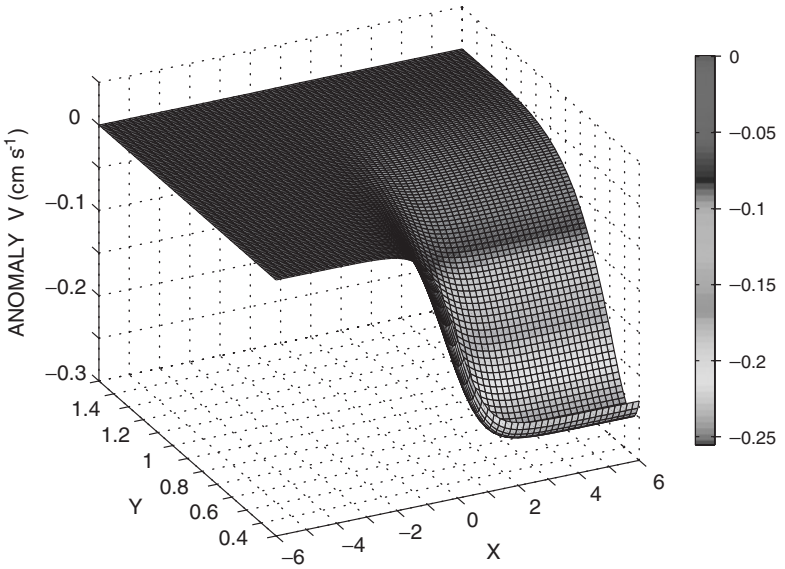

Figure. 3: Meridional component of chlorophyll biomass-induced southward geostrophic currents (m s^{-1}). The horizontal coordinate origin is located at dateline on the equator and the lengths are scaled by 1°. *y* coordinate spans 0.3–1.4° N (For colour version, see Colour Plate Section).

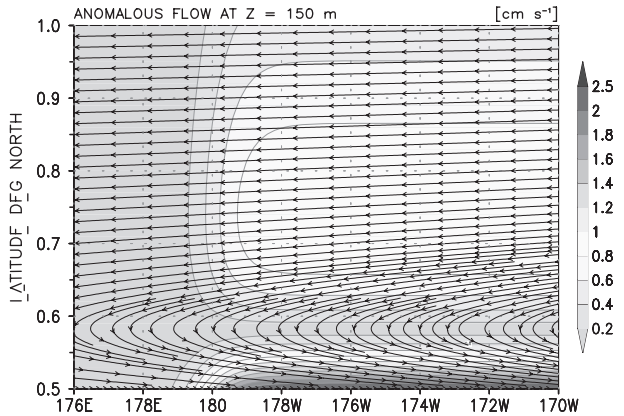

Figure 4: Analytical solutions for biologically generated horizontal current (m s^{-1}) at the depth 100 m (longitude (183–190 E) and latitude (0.5—1 N)) (For colour version, see Colour Plate Section).

where the phytoplankton concentration generates a strong zonal gradient along the equator. Fig. 4 is the longitude–latitude map of the phytoplankton-induced geostrophic currents in (cm sec^{-2}) at the depth of 150 m. It shows that the large water mass off the equator converge toward the equator east

of the dateline along 0.6° N. The large amount of water mass flow back to the east in the equatorial ocean region between 0.6° N and the equator. Since these flows are in geostrophic balance, the flow never crosses the equator due to the singularity of Coriolis parameter on the equator.

Thus, these flows feed the EUCs with biomass-induced subsurface water mass (at the depth of 100 m in our example shown in Fig. 4). These subsurface anomalous flows induced by phytoplankton biomass merge into the EUCs, which are thus strengthened and eventually rise toward the ocean surface in the eastern equatorial Pacific. Thus, the colder waters with rich nutrients rise upward in the eastern equatorial Pacific to feed more nutrients to biomass-rich region, implying positive feedback mechanism between ocean ecosystem and geophysical fluid system in the ocean with life activity. This mechanism corresponds to the hypothesis of phytoplankton-induced EUCs and associated lower temperature surface anomalous spots seen in the previous ocean general circulation experiments (Nakamoto et al., 2001; Miller et al., 2003; Ueyoshi et al., 2003).

4 Discussion and Conclusion

Scientific questions often can be answered after some simplification of the problem and thus can give answers to some aspects only of the full problem. Here, we sought an alternative approach to solve the problems within the earth environmental system by (1) experimenting with a complex OGCM, and then (2) extracting a simple mechanistic model (Harte, 2002) from the view of thermodynamics in the oceanic ecosystem as a whole and solving the mechanistic model analytically. The OGCM experiments involve the dynamical influence of phytoplankton on geophysical fluid with ocean-biological processes embedded. The simple mechanistic model extracts the essence of complexity of thermodynamical interaction between the oceanic ecosystem and the external environmental fluids executed in numerical experiments with OGCMs.

By constructing a mechanistic process model, simple enough to mimic biologically generated anomalous geostrophic currents, we proposed potential feedback mechanism between oceanic phytoplankton and upper tropical equatorial ocean circulation. Since the flow of energy through the boundary is necessary for the balance of entropy for ecosystem as a whole (Tsuchida, 1982; Nakamoto et al., 2002), the feedback mechanism between the ecosystem and its environment is associated with biogeochemical processes involving with photosynthesis, metabolism, and food chain in the entire oceanic ecosystem. The ecosystem in the ocean interact with external physical environment through thermal energy exchange processes.

The OGCM experiments with annual mean chlorophyll pigment concentration demonstrated basin-scale warming of upper ocean in the entire

globe. Biologically generated density gradient and rotating fluids–led dynamical interaction between oceanic living things and external fluid environments. Chlorophyll-dependent variable attenuation of solar radiation in a global circulation model exhibited shallower mixed layer throughout entire oceanic basins (due to more solar radiation energy trapped near the surface) than that of constant attenuation for clear water conditions without phytoplankton (Nakamoto et al., 2001; Ueyoshi et al. 2003). Such mechanism were expressed by simple radiation transfer of solar radiation and the geostrophic dynamics in the equatorial ocean. The two processes (the heat deposition from phytoplankton in the upper part of the ocean and the rotating fluid dynamics in the tropical ocean) play a role of connectivity of the ecosystem and its environment in the ocean, which leads to the enhancement of the EUCs and a colder spot of SST in the eastern equatorial Pacific.

The analytical solution of the simple mechanistic model corresponds with the phytoplankton-induced geostrophic currents hypothesized in the previous OGCM experiments (Nakamoto et al., 2001; Ueyoshi et al., 2003): the analytical solution shows an active role of phytoplankton on density modification and resultant flows that induce seawater conditions favorable to phytoplankton blooming in the eastern equatorial Pacific. Thus, the simple mechanistic model extracting the dynamical interaction of phytoplankton with surrounding water provides a condition of potential feedback mechanism between phytoplankton and upper ocean circulation relevant to basin-scale climate variations (Miller et al., 2003).

We proposed a simple mechanistic model with analytical solutions that extracts thermodynamical aspects of the interaction between ecosystem and its environment in the upper ocean as a whole. Our analytical model is "mechanistic (Harte, 2002)" in the sense that the effect of entropy release as heat from phytoplankton was replaced with the space-varying water density anomalies, because living phytoplankton deposit more heat in the upper ocean than nonliving particulate and resolved materials. Our simple "mechanistic model" was able to mimic and identify the cause-and-result relationship in the oceanic dynamical interaction process between living phytoplankton and ocean water environment as seen in numerical OGCM experiments.

It is worth noting that the choice of the annual averaged chlorophyll pigment concentration in the equation (1) is arbitrary because there was no need to use the exponentially decaying function for the chlorophyll pigment concentration in meridional direction. The essence in this exponentially decaying form exists in the fact that the chlorophyll pigment concentration in the equatorial Pacific decrease as the distance increase from the equator. The penetration of solar irradiance does not necessarily follow an exponential decline with depth. However, the analytical solution obtained in this study extracts the nature of solar radiation energy depositing in the upper

ocean due to the existence of phytoplankton that convert solar energy to chemical energy and heat energy released to the physical environments in the upper ocean. A shallower mixed layer with the existence of phytoplankton is due to the release of biologically generated entropy as heat release to maintain lower entropy for the entire oceanic ecosystem which is surrounded by environmental physical fluids in the ocean.

Acknowledgements

The principal author (S.N.) is supported by the "Study of global carbon cycle and related carbon flux mapping using satellite imagery: Global Carbon Mapping (GCMAP)" program under the Ministry of Education, Culture, Sports, Science and Technology. The idea of the use of satellite-derived chlorophyll pigments data in the radiative transfer process in the OGCM came to our discussion between S.N. and R.F. when S.N. visited the Scripps Institution of Oceanography (SIO) in 1993 under the Memorandum of Understanding (MOU) between SIO and JAMSTEC. Our efforts of using satellite data in the development of the next generation ocean circulation models at JAMSTEC had been receiving continuous encouragements from Mr. Shinichi Ishii, Mr. Shizuo Yamamoto, Mr. Isao Nakanishi, and people involving with NASDA-JAMSTEC-SIO collaboration project (1993–1996) and NASDA-JAMSTEC satellite oceanography collaboration project during the planning period (1993–1995) of climate modeling group at the Earth Observational Research Center (EORC) at NASDA. The hypothesis of phytoplankton-induced geostrophic currents in the equatorial Pacific first came to our mind when S.N. and S.P.K. were puzzled by the anomalous cold spot in the eastern equatorial Pacific seen in our OPYC numerical ocean model simulation results. S.P.K.'s involvements in the JGOFS Arabian Sea observations was extremely instrumental in arriving to our confidence on the simulation results from the mixed layer ocean isoPYcnal-coordinate (OPYC) general circulation model (GCM) in the spring of 1999, resulting in our first collaboration paper (Nakamoto et al., 2000). Our second paper (Nakamoto et al., 2001) was drafted in the summer of 2000 when S.P.K visited the Japan Marine Science and Technology Center (JAMSTEC) under the Project of the Development of the Next Generation OGCM based on the OPYC GCM and the TOGA/TAO-TRITON Network Design Project with the Directors (Dr. Toshiyuki Nakanishi, Mr. Masataka Hishida, and Dr. Masahiro Endoh, each consecutively during the projects period) at JAMSTEC. The present paper is the third collaboration and was first drafted in the summer of 2002 as a part of the collaborative model construction for Carbon cycle mapping planned originally in the early stage of the GCMAP.

Computational assistance from Mr. Ban, Mr. Ishikawa, Mr. Yasui, Ms. Numata were especially helpful in conducting the early stage of the Next Generation Ocean GCM Development Project based on the Ocean isoPYCnal-Coordinate (OPYC) GCM originally developed by J. M. Oberhuber

at the DRZR, Max-Plank Institute for Meteorology. B.S. is supported by NASA/JPL grant no. 961434. R.F. is supported by the National Science Foundation. This is the AESTO/GCMAP contribution No. 1 and the NIO contribution No. 3961.

References

Apel, J. R., 1987. Principles of Ocean Physics, International Geophysics Sereies, Academic Press, San Diego, CA, Vol. 38. p. 634.

Feldman, G. C., 1989. Ocean color: Availability of the global data set. EOS Transplantation 70, 634.

Harte, J., 2002. Toward a synthesis of the Newtonian and Dawinian worldviews. Physics Today 55 (10), 29–34.

Iturriaga, Siegel, 1989. Microphotometric characterization of phytoplankton and detrital absorption in the Sargasso Sea. Limnology Oceanography 34, 1706–1726.

Kawahata, H., Narita, H., Harada, K., Tsunogai, S., Kusakabe, M., 2003. Air-sea gas transfer velocity in stormy winter estimated from radon deficiency. Journal of Oceanography 59, 651–662.

Kirk, J., 1994. Light and Photosynthesis in Aquatic Ecosystems. Cambridge University Press, , p. 509.

Lewis, M., Carr, A. M. E., Feldman, G. C., Esaias, W., McClain, C., 1990. Influence of penetrating solar radiation on the heat budget of the equatorial Pacific ocean. Nature 347, 543–545.

Miller, A. J., Alexander, M. A., Boer, G. J., Chai, F., Denman, K., Erickson III, D. J., Frouin, R., Gabric, A. J., Laws, E. J., Lewis, M. R., Liu, Z., Murtugudde, R., Nakamoto, S., Neilson, D., Norris, J., Ohlnmann, C., Perry, R. I., Schneider, N., Shell, K. M., Timmermann, A., 2003. Potential feedbacks between Pacific Ocean ecosystems and interdecadal climate variations. American Meteorological Society DOI:10.1175/BAMS-84-5-617, 617–633.

Mobley, C. D., 1994. Light and Water–Radioactive transfer in Natural Waters. Academic Press, San Diego, CA, p. 592.

Morel, A., 1978. Available, usable, and stored radiant energy in relation to marine photosynthesis. Deep-Sea Research 25, 673–688.

Morel, A., 1991. Light and marine photosynthesis: A spectral model with geochemical and climatological implications. Prog. Oceanography 26, 263.

Morel, A., Antoine, D., 1994. Heating rate within the upper ocean in relation to its bio-optical state. Journal of Physical Oceanography 24, 1652–1665.

Morel, A., Prieur, L., 1977. Analysis of variations in ocean color. Limnology Oceanography 22 (4), 709.

Murtugudde, R., McClaine, C. R., Lewis, M., Busaracchi, A., 2002. Effect of penetrative radiation on the upper tropical ocean circulation. Journal of Climate 15, 471–487.

Nakamoto, S., Prasanna-Kumar, S., Nakata, K., Shell, K., Frouin, R., Ueyoshi, K., Sammarco, P., Aaron Lai, C., Saito, H., Sato, T., Muneyama,

K., 2002. Themo-physical interaction of ocean ecosystem and geophysical system – for understanding carbon circulation in the ocean. Journal of Advanced Marine Science and Technology Society 8 (1), 35–48.

Nakamoto, S., Prasanna-Kumar, S., Oberhuber, J. M., Ishizaka, J., Muneyama, K., Frouin, R., 2001. Response of the equatorial Pacific to chlorophyll pigment in a mixed layer isopycnal ocean general circulation model. Geophysical Research Letter 28, 2021–2024.

Nakamoto, S., Prasanna-Kumar, S., Oberhuber, J. M., Muneyama, K., Frouin, R., 2000. Chlorophyll modulation of sea surface temperature in the Arabian Sea in a mixed layer isopycnal general circulation model. Geophysical Research Letter 27, 747–750.

Oberhuber, J. M., 1993. Simulation of the Atlantic circulation with a coupled sea ice – mixed layer – isopycnal general circulation model. Part I: Model description. Journal of Physical Oceanography 23, 808–829.

Ohta, Y., Nakagawa, K., 2003. Measuement of light-into-heat conversion efficiency of phytoplankton. 2003 Annual Meeting of the Physical Society of Japan 58 (2), 338.

Otsuki, A., Watanabe, S., Tsunogai, S., 2003. Absorption of atmospheric CO_2 and its transport to the intermediate layer in the Okhotsk Sea. Journal of Oceanography 59, 709–718.

Peixoto, J. P., Oort, A. H., 1992. Physics of Climate. American Institute of Physics, p. 520.

Prieur, L., Sathyendranath, S., 1981. An optical classification of coastal and oceanic waters based on the specific spectral absorption curves of phytoplankton pigments, dissolved organic matter, and other particulate materials. Limnology Oceanography 26 (4), 671–689.

Sasaki, H., Saitoh, S., Kishino, M., 2001. Bio-optical properties of seawater in the western subarctic Gyre and Alaskan Gyre in the subarctic North Pacific and southern Bering Sea during the summer of 1997. Journal of Oceanography 57, 275–284.

Siegel, D. A., Dickey, T. D., 1987. On the parameterization of irradiance for open ocean photo-processes. Journal of Geophysical Research 92, 14648–14662.

Siegel, D. A., Ohlman, J. C., Washburn, L., Bidigare, R. R., Nosse, C. T., Fields, E., Zhous, Y., 1995. Solar radiation, phytoplankton pigments and the radiation heating of the equatorial Pacific warm pool. Journal of Geophysical Research 100, 4885–4891.

Tsuchida, A., 1982. Shigen-Butsurigaku-Nyumon (Introduction to Physics of Natural Resourses). NHK Books, Tokyo, p. 231, ISBN4-14-001423-7.

Ueyoshi, K., Stamer, D., Nakamoto, S., Subrahamanyam, B., Prasanna Kumar, S., Muneyama, K., 2003. Sensitivity of the equatorial Pacific Ocean circulation to chlorophyll modulation of penetrative solar irradiance in a GCM. XXIII General Assembly of the International Union of Geodesy and Geophysics IUGG 2003 Scientific Program and Abstracts, Sapporo, Japan, June 30–July 11, 2003, JSP09/11P/B20-002 page B.103.

Chapter 12

Precession and ENSO-Like Variability in the Equatorial Indo-Pacific Ocean

Luc Beaufort*

CEREGE, CNRS-Université Aix-Marseille III, Domaine de l'Arbois, BP 80 13545 Aix en Provence Cedex 04, France

Abstract

Since 900,000 years the 100- and 41-kyr cycles of the ice volume dominate most of the climatic parameters. Exception occurs in the tropics, where some records exhibit stronger precession cycles. Primary productivity is one of these parameters. Late pleistocene quantitative changes in nannoplankton communities preserved in eight deep-sea cores are used to monitor primary productivity along the equator in the Indian and Pacific oceans. The precession-controlled changes, significantly present in these cores, are discussed here in detail. Primary production (PP) is highest during high precession times in most of the records, and during low precession time in the western Pacific warm pool (WPWP). The opposite response of the WPWP corresponds to the rocking of the east–west thermocline slope of the Indo-Pacific that strongly affects PP. These balance movements of the thermocline slope are linked to processes similar to the southern oscillation phenomenon but on a longer time scale and are labelled ENSO-like. The precession-induced ENSO-like variability precedes changes in the oxygen isotopic ratio, which indicates that it is not the result of ice sheet fluctuations. On the reverse, because deglaciations occur during the transition caused by the onset of El Niño-like phases that produce great transport of heat to the high latitudes, ENSO-like variability could be at the origin of late pleistocene deglaciations. The stack of all these PP records shows that the glacial PP was 50% (3.5 Giga ton of carbon) higher than the interglacials in the equatorial Indo-Pacific ocean.

*Corresponding author.
E-mail address: beaufort@cerege.fr (L. Beaufort).

Elsevier Oceanography Series 73
Edited by H. Kawahata and Y. Awaya
ISBN: 0-444-52948-9

Keywords: primary productivity; precession; ENSO-like; Pleistocene; coccolithophorides

1 Introduction

The Milankovitch theory of climate suggests that the oscillations of the 65°N summer solstice insolation induce ice volume variations, which in turn produce global climatic variations. Ice volume variations not only display the 23-kyr cycle (precession) and the 41-kyr cycle (obliquity), which are characteristic of orbitally driven insolation changes, but also show a 100-kyr cycle, which is the strongest of the upper pleistocene cycles and may correspond to the non-linear response of ice volume to the precession cycles (Imbrie et al., 1993). Most of the paleoclimatic records related to global climates show a strong 100-kyr component. In contrast, some low-latitude paleoclimatic proxies show variability strongly dominated by precession. Molfino and McIntyre (1990) and Pokras and Mix (1987) explained the dominance of precession in the tropical Atlantic records as caused by the influence of precessional changes on trade winds and the African monsoon. Beaufort et al. (1997) documented that PP, and thus wind dynamics in the equatorial Indian Ocean, varied independently of global ice volume. In precession frequency band, an advance of 3,000 years was also observed for tropical primary production (PP) (Beaufort et al., 1997, 1999, 2001), for index of rain in the Amazonian basin (Harris and Mix, 1999) and for tropical sea surface temperature (SST) (Schneider et al., 1997; Lea et al., 2000), for East Asian monsoon dynamics (Wang et al., 1999) and for Indonesian biomass burning (Beaufort et al., 2003).

Climatic variables at higher latitudes in the southern Hemisphere appear to lead to variations in the volume of the Northern Ice-Sheet (Imbrie et al., 1993; Blunier et al., 1998; Shackleton, 2000). Imbrie et al. (1993) suggested that those records that lead ice volume could respond to an even earlier cooling in the Norwegian Sea. This hypothesis would not explain the dominance of precession in tropical records. Another explanation could be that some climatic proxies behave independently of ice volume (and even could lead to ice volume variation). Shackleton (2000) suggested that ice volume was lagging in CO_2 because ice sheets were responding to the global carbon budget dynamics (instead of the reverse as previously thought) but did not give any mechanism to explain the CO_2 dynamics.

I suggest here that the strong precession response of the tropical ocean, triggered through an ENSO-like forcing, is responsible for the advance of the tropical climate variability ahead of the ice volume. I base my demonstration on results from PP estimates from eight areas of the tropical Indian and Pacific (TIP) oceans for the last 180 kyr.

2 Methods

2.1 Coccoliths as Paleoproductivity Markers

The coccolithophores are phytoplanktons that are widespread and abundant in the world's oceans. As photosynthetic organisms they must remain within the photic zone, with most species at a depth of 0–80 m. This part of the photic zone is often depleted in nutrients and the productivity is highest just above the nutricline. When the ocean is strongly stratified and the nutricline is too deep in the photic zone, the PP is low. Some species (e.g. *Florisphaera profunda*, *Gladiolithus* spp. and *Algirosphaera* spp.) that are adapted to low-light environment are commonly found between 80 and 180 m (Okada and Honjo, 1973). These taxa thrive when the nutricline is deep, because the light penetration increases at low productvity. The relative abundance of *F. profunda* (the most abundant of the three deep-living taxa) may serve to monitor the depth of the nutricline (Molfino and McIntyre, 1990). A high relative abundance of *F. profunda* indicates a deep nutricline and a low productivity in the shallow waters (and the reverse) (Fig. 1).

The *F. profunda* index (%Fp) has been calibrated using data on the percentage of *F. profunda* (Fp) in a total of 400 counted coccolith (total coccoliths = TC) in 96 core top samples from a large variety of environments in the Indian Ocean (Beaufort et al., 1997). In this paper all counts have been realized by the same micropalaeontologist except for a core in Sulu Sea. This index (%Fp = 100 × Fp/TC) was correlated to the estimate of averaged annual PP based on a compilation of 12 years' of satellite observations with the Coastal Zone Colour Scanner (CZCS) (Antoine et al., 1995). We tested various equations to determine the best fit of the distribution of Fp% versus PP, using the least squares method. The most significant correlation ($r = 0.94$) was found for the equation PP = 617–(279 log[%Fp+3]) (Beaufort et al., 1997) (Fig. 1).

2.2 Wind Stress and Primary Production

Wind stress plays an important role in controlling PPs in the oceans because it can break stratification of the open ocean bringing nutrients to the upper part of the photic zone, inducing an increase in PP. This relation between wind and PP in the Indian Ocean has been demonstrated by a sediment-traps study (Nair et al., 1989) that shows that the flux of organogenic material increases in September and October, a couple of months after the height of the monsoon. This indicates that peaks in PP closely follow strong wind activity. Pronounced seasonal response of PP from wind strength can be identified by comparing PP estimates from satellite imagery with seasonal wind stress data from COADS data sets; e.g., in the western Indian

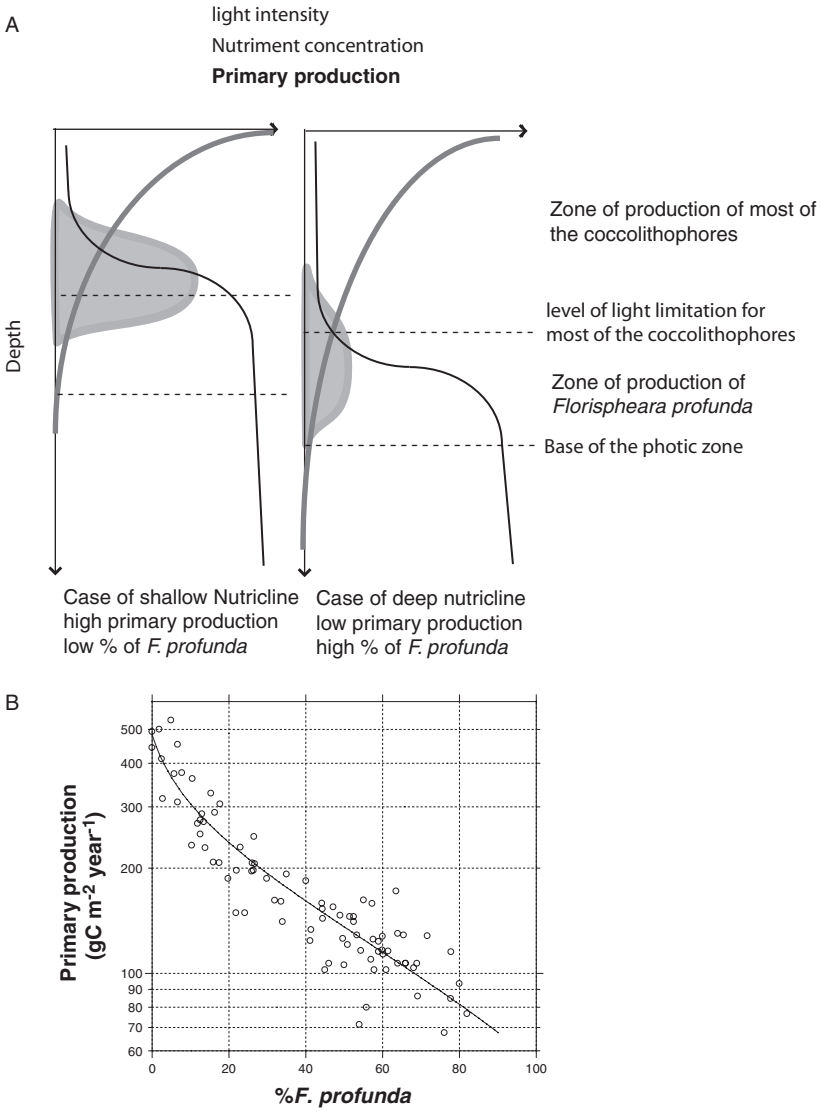

Figure 1: (A) Schematic representation of the influence of the depth of nutricline on the percentage of *Florispheara profunda* in coccolithophore assemblages. Black curve represents the amount of nutriments through depth in the photic zone; the grey curve, the amount of light; and the filled area the primary production. The dotted lines are levels of light limitation for most of the coccolithophores (shallow) and *F. profunda* deep. Two cases are shown: left is with a shallow nutricline, right with a deep nutricline. (B) Relationship between the percentage of *F. profunda* in 94 core top samples from the Indian Ocean (Beaufort et al., 1997) and primary production estimated from satellite imagery (Antoine et al., 1995). The line corresponds to the equation $PP = 617-(279 \log[\%Fp+3])$ which represent the best fit with a correlation ($r = 0.94$).

Ocean (Beaufort et al., 1999), Central Indian Ocean (Beaufort et al., 1997) and Sulu Sea (de Garidel-Thoron et al., 2001).

2.3 Thermocline and PP

In the equatorial Pacific, most of the time, the tropical trade winds transport surface waters westwards (Philander, 1983). This deepens the thermocline in the western Pacific where warm surface waters pile up against the Australian and Asian continents; the PP is consequently low. During El Niño years, the collapse of the trade winds produces a shoaling of the thermocline permitting PP at a higher rate than usual. Therefore in the WPWP, the relation between PP and wind is reversing than in the rest of the equatorial Pacific.

3 Material

The coccolithophore community preserved in eight deep-sea cores taken from the TIP oceans, have been analysed (Beaufort et al., 2001) (Table 1; Fig. 2). A precise chronology was obtained by tuning oxygen isotope records from foraminifera in most of the cores to the SPECMAP stacked record (Imbrie et al., 1984) so that our sampling achieves a temporal resolution of 0.7–3 kyr. The eight records span the last 180 kyr.

Table 1: Position, depth and stratigraphic resolution achieved foraminifera species used for $\delta^{18}O$ analysis, reference for the stratigraphy

Core	Acron.	Lat. N	Long	Depth (m)	Resol. (kyr)	Strati.	Ref.
TY93-929	T29	13°42	53°15E	2490	1.7	*N. dutertrei*	Rostek et al., 1997
MD90949	M49	2°05	76°07E	3700	2.8	*G. rubber*	Beaufort et al., 1999
MD90963	M63	5°O3	73°53E	2446	2.0	*G. rubber*	Bassinot et al., 1994
MD972141	M41	8°47	121°17E	3633	0.3	*G. rubber*	Oppo et al., 2003
MD971240	M40	2°2	141°0E	2347	1.9	G. rubber	de Garidel-Thoron et al., 2005
MD972138	M38	–1°25	146°14E	1912	1.7	*G. rubber*	Beaufort et al., 2001
W84-14GC	W84	0°57	138°57W	4287	2.5	*C. wullerstortfi.*	Jasper et al., 1994
RC13-110	R13	0°06	95°65W	3621	2.4	*C. wullerstortfi.*	Pisias and Mix, 1997

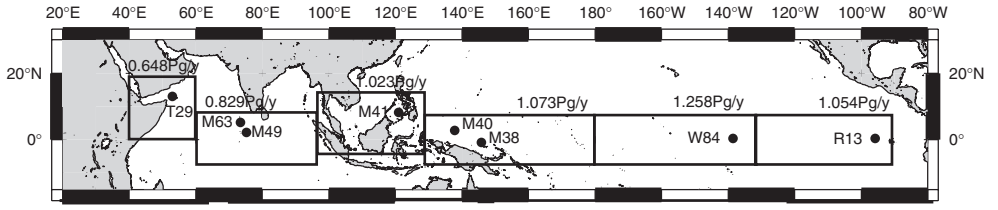

Figure 2: Location of the cores used in this study. The squares represent the area used in preparing the stack of primary production shown in Fig. 8. The numbers in the square are the total integrated primary production in the area (from Antoine et al., 1995).

4 Primary Production Variability along the Equatorial Indo-Pacific

4.1 The Gulf of Aden and the Summer Monsoon

The most prominent climatic feature of the Indian Ocean is the monsoon. Winds blow from the south–west during the boreal summer season and from the north–east during the boreal winter season. The monsoon is strongest on the western part of the Indian Ocean and the Arabian Sea.

Core TY93-929 (T29) shows that PP increases generally with precession cycle (Fig. 3). Most of the models and data from cores north of this position show a reversed pattern (Prell, 1984; Clemens et al., 1991; Anderson and Prell, 1993; Emeis et al., 1995; Reichart et al., 1998; Schulz et al., 1998; Schulte et al., 1999; Altabet et al., 2002). *Florisphaera profunda* is not the only productivity proxy that shows that trend: Corg and alkenone concentration vary in parallel to the PP reconstituted in the same core (Rostek et al., 1994). That latter work suggests that PP dynamics observed is related to the winter monsoon. However, the summer monsoon has a dominant effect on PP. A supposed lower PP related to the lower LGM summer monsoon (Prell et al., 1980) could not have been compensated by the small increase in PP due to a more intense winter monsoon. More likely, PP dynamics observed in core T29 is related to the precession influence of the migration of the low-levels Finlater jets (Beaufort, 1996). These middle-altitudes winds, closely related to the monsoon, migrate from the south to north during the onset of the summer Indian monsoon (Wyrtki, 1973; Hastenrath et al., 1993). Their path could be modified by seasonal insolation and deflected to the south east along the equator during maximum precession (Beaufort, 1996). This is confirmed by results of ocean/atmosphere-coupled models that indicate that during maximum precession, monsoon winds and rains were located to the south in the Indian Ocean (De Noblet

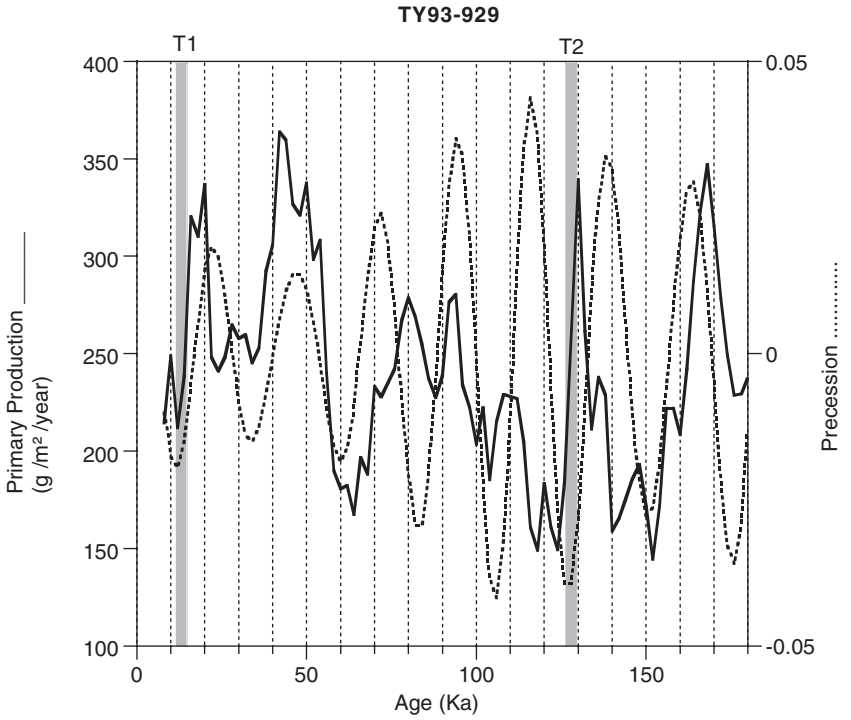

Figure 3: Variations of primary production estimates in Core TY93-939 (solid line) compared with precession (Laskar, 1990) (doted line). Vertical lines represent Termination I and II.

et al., 1996). That could be also described in terms of stronger Indian Ocean Dipole (Webster and Palmer, 1997; Saji et al., 1999) and this is described in Section 4.2. The T29 PP record exhibits the same variability as those established from cores located to the south, close to Soccotra Island (Caulet et al., 1992; Vénec-Peyré et al., 1995; Beaufort et al., 2001).

For some peaks, the relation between PP and precession is not perfect and a shift of up to 5 kyr can be observed (Fig. 3). This can be attributed to (1) stratigraphic uncertainty, or (2) the existence of other processes influencing PP or (3) a phase modulation of the precession cycle by a glacial/interglacial condition (Beaufort et al., 2001, 2003).

4.2 Central Indian Ocean and the Indian Dipole

In the central equatorial Indian Ocean (CEIO) winds are weak during monsoon seasons. In spring and autumn the Indian Ocean wind pattern becomes zonal when the intertropical Convergence Zone (ITCZ) crosses the equator. CEIO winds are consequently stronger during spring and autumn.

In both seasons CEIO winds blow from the west as a response to the pressure gradient between western Indian Ocean (highs), and the Indonesian tropical warm pool (lows). In the CEIO, a strong jet-like current flows to the east in response to the westerlies, causing the thermocline to rise in the west and become deeper in the east (Wyrtki, 1973). The westerlies represent the Indian Ocean part of the "Walker circulation" – the large-scale west-east circulation in the tropical ocean associated with convection (Bjerkness, 1969). The southern oscillation (SO) characterizes the interannual variations of the Walker circulation. The strength of the equatorial Indian westerlies is naturally related to the SO (Reverdin et al., 1986; Hastenrath et al., 1993). This has been further evidenced by Webster et al.(1999) who clearly showed the reversal in wind pattern in the CEIO during the 1997 El Nino event. Saji et al. (1999) call that climatic feature the Indian dipole.

The cores MD90-0963 and MD90-0949 are placed ideally at the centre of that climatic feature and can serve to monitor the Indian dipole of the past. Estimate of past PP in both cores show a strong influence of precession. It has been shown that the PP structure in core MD90-0963 varies independently of ice volume variation for the past 902 kyr in phase with the late winter insolation at low latitude and in advance of 3,000 year with $\delta^{18}O$ (Beaufort et al., 1997), therefore in phase with the PP estimates of the Aden Gulf core and with precession. Fig. 4 clearly shows this increase in PP during precession maxima in the two cores. Precession is the dominant paleoclimatic feature in that area.

4.3 The Sulu Sea and the East Asian Winter Monsoon

The main feature governing the Sulu Sea climates is the East Asian monsoon. Although most of the rain falls into the Sulu Sea during the summer monsoon, the winter monsoon brings the strongest winds (Beaufort et al., 2003). The East Asian monsoon results from the difference in potential heating between the WPWP and the Asian continent. During the boreal winter, the main heating source is located in the ocean. The latent heat release associated with intense convective precipitation fuels meridional circulation. Tropical convection in the western equatorial Pacific is connected to the descending branch over the Siberian region, forming a strong local Hadley cell in the East Asian region (Zhang et al., 1997). The East Asian winter monsoon (EAWM) winds in the Sulu Sea result from the merging of the northerly East Asian monsoon with the Pacific trade winds over the South China Sea (McGregor and Nieuwolt, 1998).

Owing to those strong winds that are able to break the upper oceanic stratification, it is during the winter monsoon that the PP is highest, nowadays (de Garidel-Thoron et al., 2001). Past estimates of PP in core MD97-2141 show that PP follows closely the glacial/interglacial variation

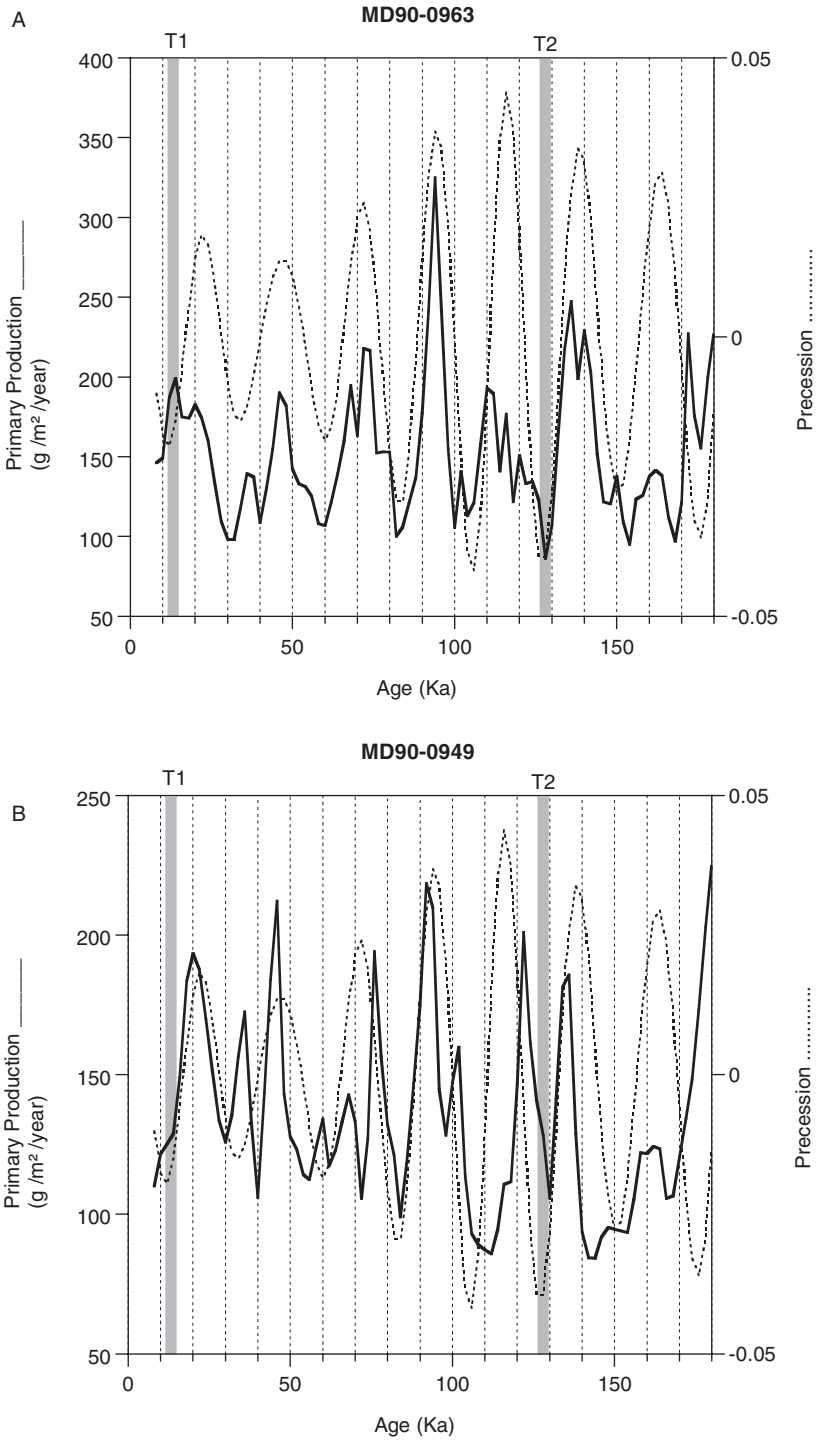

Figure 4: Variations of primary production estimates (solid line) in Core MD900963 (upper panel) and Core MD900949 (lower panel) compared with precession (Laskar, 1990) (doted line). Vertical lines represent Termination I and II.

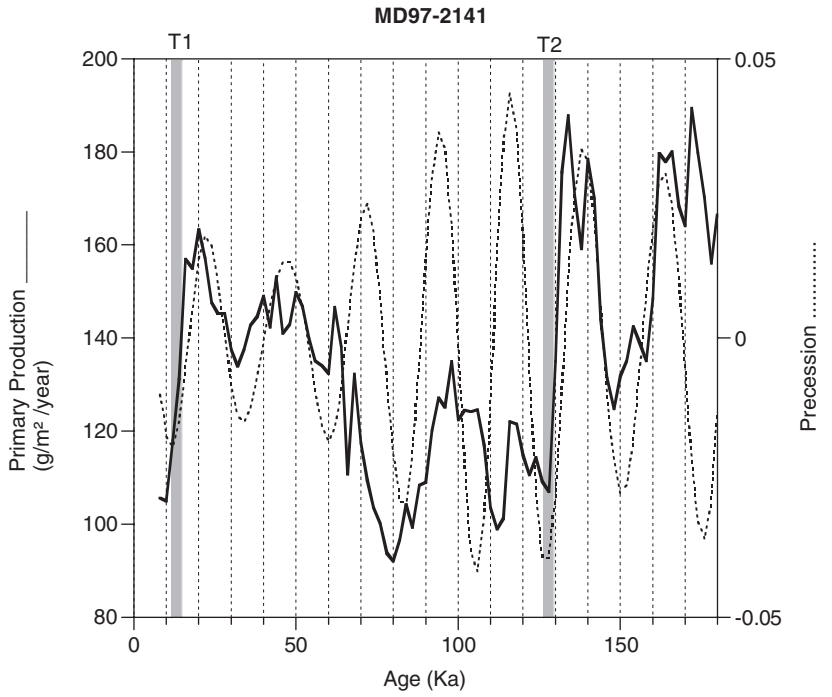

Figure 5: Variations of primary production estimates in Core MD972141 (solid line) compared with precession (Laskar, 1990) (doted line). Vertical lines represent Termination I and II.

closely as evidenced by the strong 100- and 40-kyr cycles and the resemblance with $\delta^{18}O$ record obtained at the same location (de Garidel-Thoron et al., 2001). These cycles represent the influence of the high latitudes of Siberian area on EAWM. Precession cycles are also present. They are in phase with the precession and precede $\delta^{18}O$ by about 3,000 yr (Beaufort et al., 2001, 2003; Fig. 5). Therefore the precessional cycle observed in this core is again in phase with the Indian Ocean records described above, although other orbital frequencies (41 and 100 kyr) are also strongly influential here (Beaufort et al., 2003).

4.4 The Eastern and Central Equatorial Pacific

The eastern equatorial Pacific is characterized by the strongest open ocean welling up on earth. It results from the strength of the equatorial current flowing to the west, pushed by the equatorial easterly winds. Cold waters coming from the southern Pacific as well as from below feed this surface current. The new nutrients, provided to the photic zone, sustain an intense

PP. During El Niño years, the decline of the easterlies provokes a collapse of the oceanic upwelling.

Cores W84-14GC and RC13-110 are located below the path of the oceanic upwelling and they can monitor its strength through time. Fig. 6 shows that precession is not strong in these two records, which are dominated by 100- and 41-kyr cycles. This implies strong influence of global climatic variations and high latitudes. This is certainly related to the direct link of this upwelling to the high southern latitudes via the Humbolt current. PP variability in the precession band is still visible and appears to be again in phase with precession in both records.

4.5 The Western Pacific Warm Pool

This oceanic area, located north of New Guinea, is characterized today by having small seasonal variability in SST: always superior to 28°C. It is the highest annual SST in the ocean. The thermocline is deep (200 m) due to Equatorial Easterlies that push a bulge of warm water in that area. The seasonal variability here is much less than the interannual variability (Longhurst, 1998). During El Niño years the easterlies weaken, inducing a shoaling of the thermocline. That helps to sustain higher PP than usual.

Cores MD97-2138 and MD97-2140 are both located in the WPWP. The two PP records show an opposition with precession, which is opposite to all the other records described in Fig. 7. However, PP dynamics exhibit some difference between Termination 2 and Termination 1, which implies that precession is not the only driving force for PP long–term variability in that area.

4.6 Phase of PP and Precession

Up to now I mention that was high PP during high precession. In detail, all these records exhibit a shift of about 3 kyr between PP and maximum precession. This can be seen clearly on a phase diagram resulting from cross-spectral analysis (Fig. 8). Also, the advance of PP over $\delta^{18}O$ is shown to be statistically significant.

4.7 Assessment of the Equatorial Indo-Pacific Primary Production

In order to put in perspective how different areas contribute to the total PP of the equatorial Indo-Pacific, I designed six areas inspired from the oceanic biomes of (Longhurst, 1998). These areas are represented by the squares in Fig. 2. For each of these areas, the total amount of yearly primary production (TYPP) has been estimated using the map of PP estimates from satellite

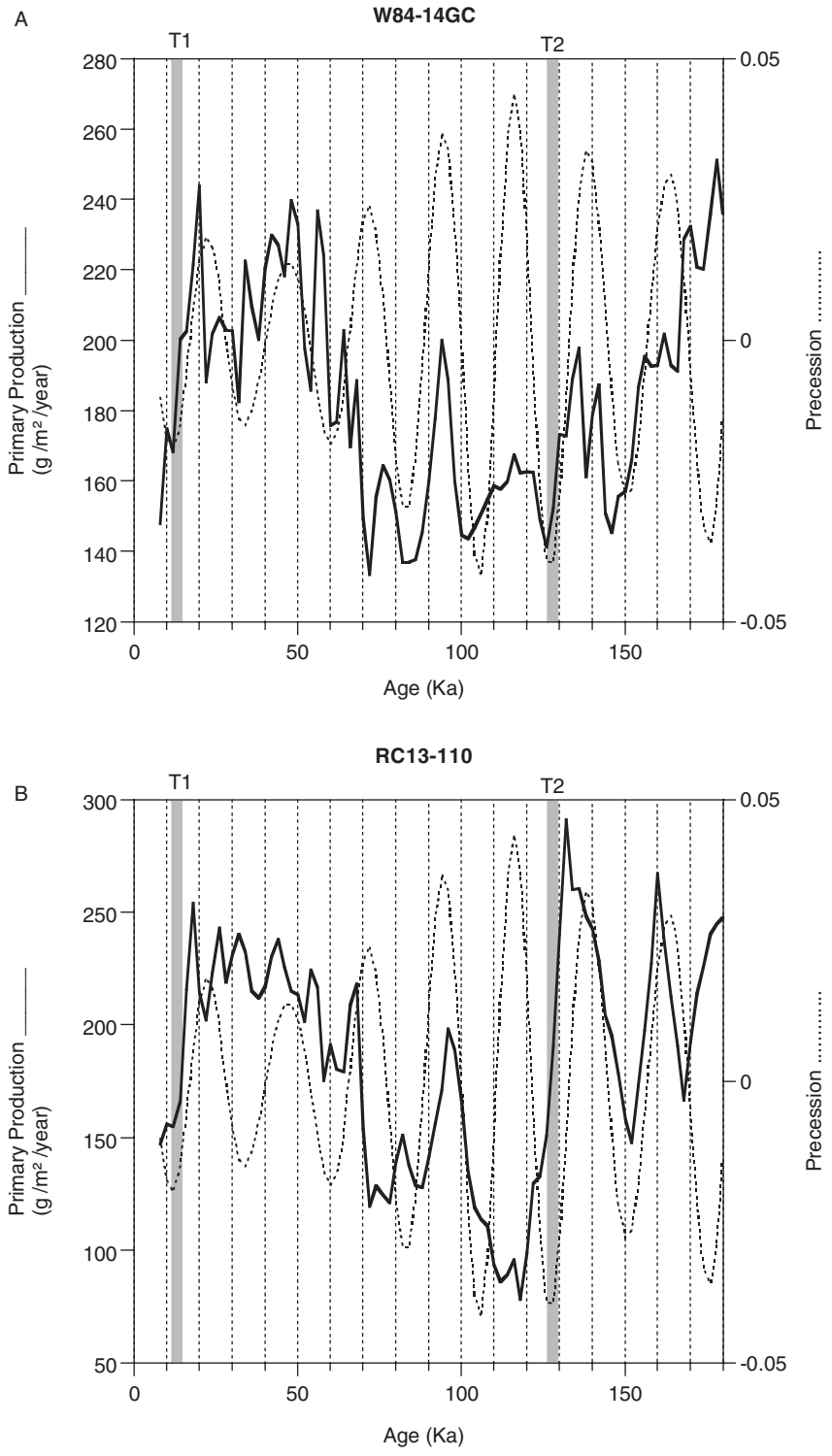

Figure 6: Variations of primary production estimates (solid line) in Core W84-14GC (upper panel) and Core RC13-110 (lower panel) compared with precession (Laskar, 1990) (doted line). Vertical lines represent Termination I and II.

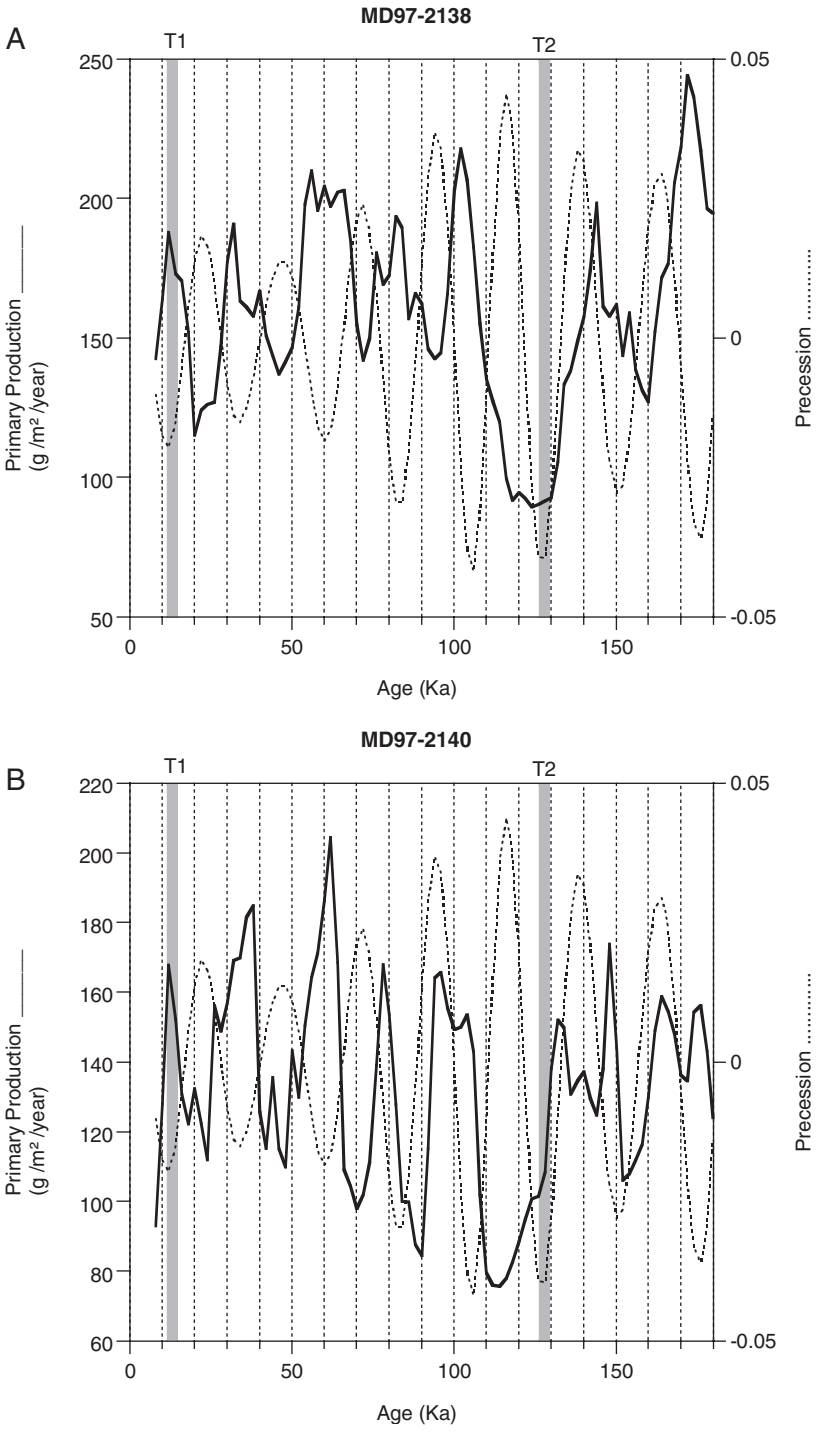

Figure 7: Variations of primary production estimates (solid line) in Core MD972138 (upper panel) and Core MD972140 (lower panel) compared with precession (Laskar, 1990) (doted line). Vertical lines represent Termination I and II.

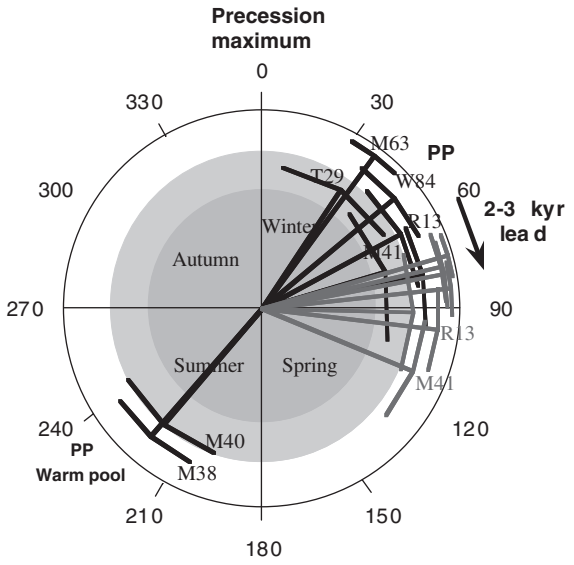

Figure 8: Phase wheel diagram established using cross-Blackman–Tukey spectral analysis between all the PP and (black lines), $\delta^{18}O$ (grey lines) records and precession. A phase wheel can be read as a watch, time running clockwise, the "needles" make a full turn in 23 kyr; their size is proportional to their coherency. The inner grey circles represent the 80% (dark) and 90% (light) confidence level on coherency. The bars at the end of the "needles" represent the confidence (band width) of the phase. Because precession is season related, the different seasons are given inside the diagram.

imagery (Antoine et al., 1995). For each record ofPP, its average Holocene PP (PPh) value has been subtracted from all the PP values (PPs). These new values have been divided by the variance of the original record (PPv), and then multiplied by the total PP of the zone in which the records have been taken.

The new record of variations of total yearly production of each area (TYPPa) is given by the following equation:

$$\mathrm{TYPPs} = \mathrm{TYPP} \times \mathrm{PPv} \times (\mathrm{PPs} - \mathrm{PPh})$$

In two areas two cores were studied. This was the case for Cores M49, M63, M40 and M38. The mean of cores M49 and M63, and M40 and M38 were used for the calculations presented above.

The sum of all the six different TYPPs provides the first estimate of the total yearly production of the low-latitude Indo-Pacific Ocean for the last

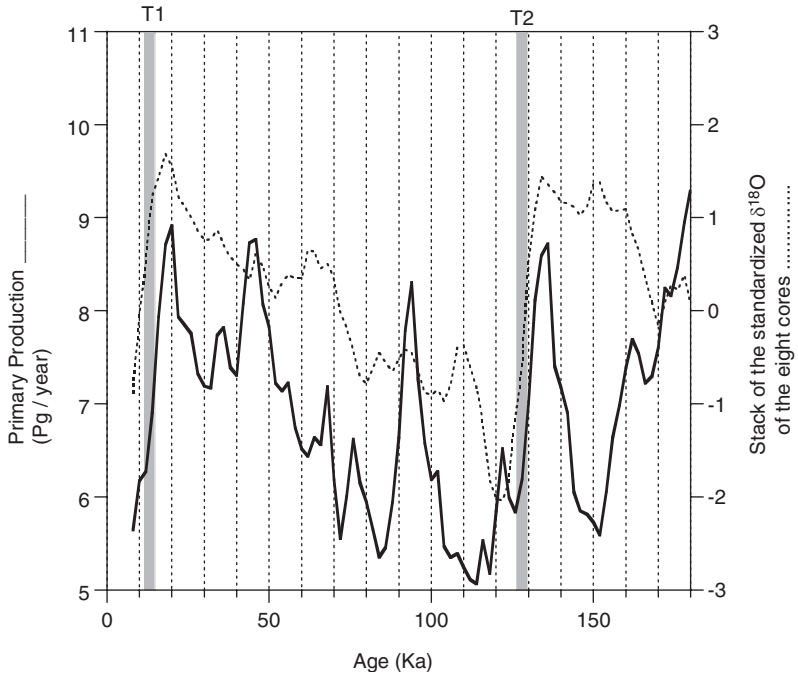

Figure 9: Record of low-latitude Indo-Pacific primary production in Pg of carbon per year derived by adding the weighted variability of the different records. The weighing factor corresponds to the annual production of the area (see Fig. 2) where the core has been retrieved (solid line). The dotted line is the $\delta^{18}O$ stack of the cores used in that study.

180 kyr (Fig. 9). The importance of precession is clearly visible, but one cycle is missing at 115 kyr. This shows the strong weight of the eastern Pacific in that reconstruction, for which the precession cycle is not strongly marked. The obliquity signal is also strongly present. That figure shows the advance of PP on the $\delta^{18}O$ stack. The glacial/interglacial difference is of 3.5 Pg (= 3.5 Giga tons) of carbon, which represents an increase of 50% of productivity of that area during the glacial time (MIS 2 and 6) versus interglacial time (MIS 1 and 5).

5 Discussion

5.1 ENSO-Like Variability

A striking feature of these records is that they are in phase with precession in most (5 of 6) of the studied areas and in opposite phase with precession in the WPWP. The only explanation of this opposition results from a change in

the variability of the thermocline. The thermocline depth, which has a strong influence on oceanic PP, evolves in the WPWP in opposition to the rest of the IPO. This evolution is equivalent to that observed in the modern Pacific Ocean during an ENSO cycle. During maximum precession (high insolation at the end of the boreal winter), strong tropical trade winds transport surface waters westwards in the Pacific. This lifts the thermocline along the equator in the central and eastern Pacific, but deepens the thermocline in the western Pacific where warm surface waters pile up against the Australian and Asian continents. In the Indian Ocean, an analogous pattern exists but with a shallow thermocline in the west (the Somalian upwelling) and a deep thermocline in the east (strong Indian Ocean dipole). When precession is low, trade winds relax, and the basin wide slope of the thermocline changes intensely. The thermocline rises in the western Pacific and in the eastern Indian Ocean, whereas it deepens on the other sides of these two basins. ENSO-like variability is therefore defined as an oceanographic/atmospheric phenomenon equivalent to the ENSO but acting at a much longer time scale.

5.2 Precession and ENSO-Like

Clement et al. (1999) described a strong link between ENSO and precession. The seasonal warming of the Pacific is a key factor in that theory. They used the model of Zebiak and Cane (1987), which has been demonstrated to predict relatively well the recent ENSO intensities. The important season for insolation is autumn. The results presented here show a strong phase with precession (winter/summer), and a lag by 5,000 yr the prediction of Clement et al. (1999). This lag can be attributed to erroneous date of the SPECMAP stack, as radiometric dating point out (e.g. Henderson and Slowey, 2000). Another possibility is that, although predictable for the present, the model of Zebiak and Cane (1987) is not directly applicable for the past with the same phase. For example, the IPSL-CM2 coupled ocean–atmosphere model (Braconnot et al., 2000) run for three precession configurations (123, 115 and 110 kyr) predicts for the oceanic continent and the WPWP low precipitation at 123 kyr and high precipitation at 110 kyr (Braconnot and Marti, 2003). Clement et al. (1999) predict more frequent and strong La Niña at 123 kyr and more frequent and strong El Niño at 110 kyr, which is completely opposite to the IPSL-CM2 model. The seasonal phasing in the model is critical and creates apparent discrepancies. Also, minima and maxima precession simulations by ECBilt, a global fully coupled atmosphere/ocean/sea-ice climate model (Tuenter et al., 2003), show that winds in the central Indian ocean blow stronger during high precession times, in complete agreement with PP results. Therefore I conclude that it is likely that a phase shift of a few thousand years has to be considered for the Clement et al.

(1999) reconstruction of ENSO-like variability, and that the absolute chronology bias is not needed to explain that shift as suggested by Beaufort et al. (2001).

Difference in the annual movement of a convective maximum appears to play an important role in interannual variability (Meehl, 1987, 1993). The warm-pool area experiences strong convection, which provides a large part of the energy necessary for the Walker circulation (e.g. Graham and Barnett, 1987). This annual cycle is opposite on each side of the Indian and Pacific oceans. The maximum of convection occurs during the boreal winter, a period that coincides with the maximum in positive SST anomaly (Lau et al., 1994). The convection is minimum in the warm pool in summer. Thus, the warm pool exhibits a strong annual cycle with contrasted winter and summer. In February, convection is maximum during strong years (strong SOI) and minimum in weak years (weak SOI and El Nino) (Salby and Hendon, 1994). Above a critical sea surface temperature of 27.5°C, insolation becomes a determining factor in warming the mixed layer and creating strong evaporation (Graham and Barnett, 1987). These migrations of the convection cells or inter-tropical convergence zone (ITCZ) are observed in paleoclimate records (Haug et al.; 2001, Koutavas et al., 2002). With precession maxima, when equatorial area receives maximum insolation in winter, and minimum in August, the annual cycle of convection along the equator is accentuated, strong years occur frequently and the temperature gradient is the maximum.

De Noblet et al. (1996) used an atmospheric general circulation model (AGCM) to check the sensitivity of summer monsoons to variations in insolation. The tested periods were 126, 115 and 6 ka. The study shows clearly that 115 ka ago (hint: maximum of PP occurs at 114 ka in our study) the convection was strong in the western Pacific whereas at 126 ka no convective activity was simulated for the same area. Winds were more zonal at 115 ka and meridian at 126 and 6 ka (strong monsoon). The wind and convective activity migrated from the continent (e.g. India) where they are high during strong monsoon years (6 and 126 ka), towards the ocean (e.g. CEIO) during weak monsoon periods (115 ka). Sediment records presented here confirm these simulation results.

5.3 Advance of 3,000 Years

As discussed, many low latitude records appear in advance to glacial cycles. Lea et al. (2000) showed that the equatorial Pacific SST varied in phase with Vostok δD temperatures, a correspondence in favour of the climatic importance of the equatorial ocean for global climatic variations. The reason of the timing of the equatorial SST variability is not clearly understood. Here I propose that this timing is related to precession-induced ENSO-like

variability. ENSO has a significant effect on the exchange of heat between low and high latitudes (Molnar and Cane, 2002; Philander and Fedorov, 2003). During La Niña periods, high latitudes lose heat in favour of low latitudes whereas during El Niños it is the reverse, with heat gaining polewards (Philander and Fedorov, 2003). The shift from "La Niña-like" to "El Niño-like" occurs 3,000 years before the deglaciation, suggesting that the transfer of heat from low to high latitude induced the beginning of the deglaciation.

Acknowledgements

This work has been supported by CNRS-INSU, as a contribution to the ECLIPSE programme. The support of the French Polar Institute (IPEV formerly IFRTP) is gratefully acknowledged for coring on Marion Dufresne. I thank Noëlle Buchet for her invaluable technical help and two anonymous reviewers for their useful comments and corrections.

References

Altabet, M. A., Higginson, M. J., Murray, D. W., 2002. The effect of millennial-scale changes in Arabian Sea denitrification on atmospheric CO2. Nature 415, 159–162.

Anderson, D. M., Prell, W. L., 1993. A 300 kyr record of upwelling off Oman during the late Quaternary: Evidence of the Asian Southwest monsoon. Paleoceanography 8 (2), 193–208.

Antoine, D., André, J.-M., Morel, A., 1995. Oceanic primary production 2. Estimation at global scale from satellite (coastal zone color scanner) chlorophyll. Global Biogeochemical Cycles 10 (1), 57–69.

Bassinot, F. C., Labeyrie, L. D., Vincent, E., Quidelleur, X., Shackleton, N. J., Lancelot, Y., 1994. The astronomical theory of climate and the age of the Brunhes-Matuyama magnetic reversal. Earth and Planetary Science Letters 126, 91–108.

Beaufort, L., 1996. Dynamics of the monsoon in the Equatorial Indian Ocean over the last 260,000 years. Quaternary International 31, 13–18.

Beaufort, L., Bassinot, F. C., Vincent, E., 1999. Primary production response to orbitally induced variations of the Southern Oscillation in the Equatorial Indian Ocean. In: Abrantes, F., Mix, A. C. (Eds.), Reconstructing Ocean History: A Window into the Future. Kluwer Academic/Plenum, New York, pp. 245–272.

Beaufort, L., de Garidel Thoron, T., Mix, A. C., Pisias, N. G., 2001. ENSO-like forcing on oceanic primary production during the late Pleistocene. Science 293 (5539), 2440–2444.

Beaufort, L., de Garidel-Thoron, T., Linsley, B., Oppo, D., Buchet, N., 2003. Continental biomass burning and oceanic primary production estimates in the Sulu Sea over the last 380 kyr and the East Asian monsoon dynamics. Marine Geology 201 (1–3), 53–65.

Beaufort, L., Lancelot, Y., Camberlin, P., Cayre, O., Vincent, E., Bassinot, F., Labeyrie, L., 1997. Insolation cycles as a major control of the Equatorial Indian Ocean primary production. Science 278, 1451–1454.

Bjerkness, J., 1969. Atmospheric teleconnections from the equatorial Pacific. Monthly Weather Research 97, 163–172.

Blunier, T., Chappellaz, J., Schwander, J., Dällenbach, Stauffer, B., Stocker, T. F., Raynaud, D., Jouzel, J., Clausen, H. B., Hammer, C. U., Johnsen, S. L., 1998. Asynchrony of Antarctic and Greenland climate change during the last glacial period. Nature 394, 739–743.

Braconnot, P., Marti, O., 2003. Impact of precession on monsoon characteristics from coupled ocean atmosphere experiments: changes in Indian monsoon and Indian ocean climatology. Marine Geology 201, 23–34.

Braconnot, P., Marti, O., Joussaume, S., Leclainche, Y., 2000. Ocean feedback in response to 6-kyr before present insolation. Journal of Climate 13, 1537–1553.

Caulet, J.-P., Vénec-Peyré, M.-T., Vergnaud-Grazzini, C., Nigrini, C., 1992. Variation of South Somalian upwelling during the last 160 ka: Radiolarian and foraminifera records in core MD 85674. In: Summerhayes, C. P., Prell, W. L., Emeis, K. C. (Eds.), Upwelling Systems: Evolution since the Early Miocene. Geological Society Special Publication, London, pp. 379–389.

Clemens, S., Prell, W. L., Murray, D., Shimmield, G., Weedon, G., 1991. Forcing mechanisms of the Indian Ocean monsoon. Nature 353, 720–725.

Clement, A. C., Seager, R., Cane, M. A., 1999. Orbital controls on the El Nino/Southern Osciallation and the tropical climate. Paleoceanography 14 (4), 441–456.

de Garidel-Thoron, T., Beaufort, L., Linsley, B. K., Dannenmann, S., 2001. Millennial-scale dynamics of the East Asian winter monsoon during the last 200,000 years. Paleoceanography 16, 1–12.

de Garidel-Thoron, T., Rosenthal, Y., Bassinot, F. C., Beaufort, L., 2005. Stable sea surface temperatures in the western Pacific warm pool over the past 1.75 million years. Nature 433, 294–298.

De Noblet, N., Braconnot, P., Joussaume, S., Masson, V., 1996. Sensitivity of simulated Asian and African summer monsoons to orbitally induced variations in insolation 126, 115 and 6 kBP. Climate Dynamics 12 (9), 589–603.

Emeis, K.-C., Anderson, D. M., Doose, H., Kroon, D., Schulz-Bull, D., 1995. Sea-surface temperature and the history of monsoon upwelling in the Northwest Arabian Sea during the last 500,000 years. Quaternary Research 43, 355–361.

Graham, N. E., Barnett, T. P., 1987. Sea surface temperature, surface wind divergence, and convection over tropical oceans. Science 238 (4827), 657–659.

Harris, S. E., Mix, A. C., 1999. Pleistocene precipitation balance in the Amazon Basin reocorded in deep sea sediments. Quaternary Research 51, 14–26.

Hastenrath, S., Nicklis, A., Greischar, L., 1993. Atmospheric-Hydrospheric mechanisms of climate anomalies in the western Equatorial Indian Ocean. Journal of Geophysical Research 98, 20219–20235.

Haug, G. H., Hughen, K. A., Sigman, D. M., Peterson, L. C., Röhl, U., 2001. Southward migration of the intertropical convergence zone through the holocene. Science 293, 1304–1308.

Henderson, G. M., Slowey, N. C., 2000. Evidence from U-Th dating against northern hemisphere forcing of the penultimate deglaciation. Nature 404, 61–66.

Imbrie, I., Berger, A., Boyle, E. A., Clemens, S. C., Duffy, A., Howard, W. R., Kukla, G., Kutzbach, J., Martinson, D. G., Mclntyre, A., Mix, A. C., Molfino, B., Morley, J. J., Peterson, L. C., Pisias, N. G., Prell, W. L., Raymo, M. E., Shackleton, N. J., Toggweier, J. R., 1993. On the structure and origin of major glaciation cycles2: the 100,000-year cycle. Paleoceanography 8 (6), 699–736.

Imbrie, J., Hays, J. D., Martinson, D. G., Mclntyre, A., Mix, A. C., Morley, J. J., Pisias, N. G., Prell, W. L., Shackleton, N. J., 1984. The orbital theory of Pleistocene climate: Support from a revised chronology of the marine $\delta^{18}O$ record. In: Berger, A. L., Imbrie, J., Hays, J. D., Kulka, G., Saltzman, B. (Eds.), Milankovitch and Climate, Part 1. D. Reidel, Dordrecht, The Netherlands, pp. 269–305.

Jasper, J. P., Hayes, J. M., Mix, A. C., Prahl, F. G., 1994. Photosynthetic fractionation of 13C and concentrations of dissolved CO_2 in the central equatorial Pacific during the last 255,000 years. Paleoceanography 9 (6), 781–798.

Koutavas, A., Lynch-Stieglitz, J., Marchitto, T. M. Jr., Sachs, J. P., 2002. El Nino–Like pattern in Ice Age Tropical Pacific sea surface temperature. Science 297, 226–230.

Laskar, J., 1990. The chaotic motion of the solar system: a numerical estimate of the chaotic zones. Icarus 88, 266–291.

Lau, K.-M., Sheu, P.-J., Kang, I.-S., 1994. Multiscale low-frequency circulation modes in the global atmosphere. Journal of the Atmospheric Sciences 51 (9), 1169–1193.

Lea, D. W., Pak, D. K., Spero, H. J., 2000. Climate impact of late quaternary Equatorial Pacific sea surface temperature variations. Science 289, 1719–1724.

Longhurst, A., 1998. Ecological Geography of the Sea, 1. Academic Press, San Diego, 398 pp.

McGregor, G. R., Nieuwolt, S., 1998. Tropical Climatology. J. Wiley, Chichester, p. 339.

Meehl, G. A., 1987. The annual cycle and interanual vaiability in the tropical Pacific and Indian Ocean regions. Monthly Weather Review 115, 25–70.
Meehl, G. A., 1993. A cupled air-sea biennial mechanism in the Tropical Indian and Pacific regions: role of the ocean. Journal of Climate 6, 31–41.
Molfino, B., McIntyre, A., 1990. Precessional forcing of the nutricline dynamics in the Equatorial Atlantic. Science 249, 766–769.
Molnar, P., Cane, M., 2002. El Niño's tropical climate and teleconnections as a blueprin for Ice-Age climate. Paleoceanography 17 (2), 1021.
Nair, R. R., Ittekkot, V., Manganini, S. J., Ramaswamy, V., Haake, B., Degens, E. T., Desai, B. N., Honjo, S., 1989. Increased particle flux to the deep ocean related to monsoons. Nature 338, 749–751.
Okada, H., Honjo, S., 1973. The distribution of oceanic coccolithophorids in the Pacific. Deep-Sea Research 20 (4), 355–374.
Oppo, D. W., Linsley, B. K., Rosenthal, Y., Dannenmann, S., Beaufort, L., 2003. Orbital and suborbital climate variability in the Sulu Sea western tropical Pacific. Geochemical Geophysical Geosystems 4 (1), 1001.
Philander, G., Fedorov, A. V., 2003. Role of tropics in changing the response to Milankovich forcing some three million years ago. Paleoceanography 18 (2), 1045.
Philander, S. G. H., 1983. El Niño Southern Oscillation phenomena. Nature 302, 295–301.
Pisias, N. G., Mix, A. C., 1997. Spatial and temporal oceanographic variability of the eastern equatorial Pacific during the late Pleistocene: evidence from radiolaria microfossils. Paleoceanography 12 (3), 381–393.
Pokras, E. M., Mix, A., 1987. Earth's precession cycle and Quaternary climatic change in tropical Africa. Nature 326 (6112), 486–487.
Prell, W. L., 1984. Monsoonal climate of the Arabian Sea during the late Quaternary: a response to changing solar radiation. In: Berger, A. L., Imbrie, J., Hays, J. D., Kukla, G., Saltzman, B. (Eds.), Milankovitch and Climate, Part 1. D. Reidel, Dordrecht, The Neatherlands, pp. 349–366.
Prell, W. L., Hutson, W. H., Williams, D. F., Bé, A. W. H., Geitzenauer, K., Molfino, B., 1980. Surface circulation of the Indian Ocean during the last glacial maximum, approximately 18.000 yr B.P. Quaternary Research 14, 309–336.
Reichart, G. J., Lourens, L. J., Zachariasse, W. J., 1998. Temporal variability in the northern Arabian sea oxygen minimum zone (OMZ) during the last 225,000 years. Paleoceanography 13 (6), 607–621.
Reverdin, G., Cadet, D. L., Gutzler, D., 1986. Interannual displacement of convection and surface circulation of the equatorial Indian Ocean. Quarterly Journal – Royal Meteorological Society 112, 43–67.
Rostek, F., Bard, E., Beaufort, L., Sonzogni, C., Ganssen, G., 1997. Sea surface temperature and productivity records for the past 240 kyr in the Arabian Sea. Deep-Sea Research Part II 44 (6–7), 1461–1480.
Rostek, F., Ruhland, G., Bassinot, F. C., Beaufort, L., Müller, P. J., Bard, E., 1994. Fluctuations of the Indian monsoon regime during the last 170,000

years: evidence from sea surface temperature, salinity and organic carbon records. In: Desbois, M., Désalamand (Eds.), Global Precipitations and Climate Changes. NATO ASI Series I., pp. 27–51.
Saji, N. H., Goswami, B. N., Vinayachandran, P. N., Yamagata, T., 1999. A dipole mode in the tropical Indian Ocean. Nature 401, 360–363.
Salby, M. L., Hendon, H. H., 1994. Intraseasonal behavior of clouds, temperature, and Motion in the tropics. Journal of the Atmospheric Sciences 51 (15), 2207–2224.
Schneider, R. R., Price, B., Müller, P. J., Kroon, D., Alexander, I., 1997. Monsoon related variations in Zaïre (Congo) sediment load and influence of fluvial silicate supply on marine productvity in the east equatorial Atlantic during the last 200,000 years. Paleoceanography 12 (3), 463–481.
Schulte, S., Rostek, F., Bard, E., Rullkötter, J., Marchal, O., 1999. Variations of oxygen-minimum and primary productivity recorded in sediments of the Arabian Sea. Earth and Planetary Science Letters 173, 205–221.
Schulz, H., von Rad, U., Erienkeuser, H., 1998. Correlation between Arabian Sea and Greenland climate oscillations of the past 110,000 years. Nature 393, 54–57.
Shackleton, N. J., 2000. The 100,000-year ice-age cycle identified and found to lag temperature, carbon dioxide, and orbital eccentricity. Science 289, 1897–1902.
Tuenter, E., Weber, S. L., Hilgen, F. J., Lourens, L. J., 2003. The response of the African summer monsoon to remote and local forcing due to precession and obliquity. Global and Planetary Change 36, 219–235.
Vénec-Peyré, M.-T., Caulet, J.-P., Vergnaud Grazzini, C., 1995. Paleohydrogrphic changes in the Somali Basin (5°N pwelling and equatorial areas) during the last 160 kyr, based on correspondence analysis of foraminiferal and radiolarian assemblages. Paleoceanography 10 (3), 473–491.
Wang, L., Sarnthein, M., Erlenkeuser, H., Grimalt, J., Grootes, P., Heilig, S., Ivanova, E., Kienast, M., Pelejero, C., Pflaumann, U., 1999. East Asian monsoon climate during the late Pleistocene: high-resolution sediment records from the South China Sea. Marine Geology 156 (1–4), 245–284.
Webster, P. J., Moore, A. M., Loschnigg, J. P., Leben, R. R., 1999. Coupled ocean-atmosphere dynamics in the Indian Ocean during 1997–98. Nature 401, 356–360.
Webster, P. J., Palmer, T. N., 1997. The past and the future of El Niño. Nature 390, 562–564.
Wyrtki, K., 1973. An Equatorial Jet in the Indian Ocean. Science 181, 1331–1338.
Zebiak, S. E., Cane, M. A., 1987. A model El Niño-Southern Oscillation. Monthly Weather Review 115, 2262–2278.
Zhang, Y., et al., 1997. East Asian winter monsoon: results from eight AMIP models. Climate Dynamics 13 (11), 797–820.

Chapter 13

Methods of Estimating Plant Productivity and CO_2 Flux in Agro-Ecosystems – Liking Measurements, Process Models, and Remotely Sensed Information

Yoshio Inoue[1,*] and Albert Olioso[2]

[1]*National Institute for Agro-Environmental Sciences, Tsukuba, Ibaraki 305-8604, Japan*
[2]*INRA, Climat, Sol et Environnement, 84914 Avignon Cedex 9, France*

Abstract

Since both net primary production (NPP) and net ecosystem productivity (NEP) are the time-integrated values of CO_2 exchange at the interface of plant, ecosystem, and atmosphere, continuous measurements of CO_2 fluxes using methods such as eddy covariance may be the most direct and accurate approach. However, the geospatial assessment of key variables such as plant productivity and CO_2 flux is essential because terrestrial ecosystems are quite heterogeneous. Remotely sensed information plays a crucial role for scaling up such ecosystem variables obtained by point measurements. Biophysical and ecophysiological process models have also an important role in the assessment and prediction of plant productivity and carbon flux, since they dynamically change interacting with many environmental variables. Despite the significant potential of these two methods, they both have limitations in ecological and ecophysiological applications; thus, synergistic linkage between the two methods is required. This chapter overviews the recent advancements in remote sensing of ecophysiological variables as a basis for such applications, and conducts methodological investigations on the synergy between remote sensing and process modeling based on some

*Corresponding author.
E-mail address: yinoue@affrc.go.jp (Y. Inoue).

Elsevier Oceanography Series 73
Edited by H. Kawahata and Y. Awaya
ISBN: 0-444-52948-9

case studies. A case study based on airborne remote sensing data demonstrates the normalized difference vegetation index (NDVI) among various vegetation indices and may be useful enough for approximate assessment of plant productivity at an ecosystem scale. Another case study also shows that the soil surface CO_2 flux (SSF_{CO_2}) is most closely related to the remotely sensed soil surface temperature, while air temperature is less well correlated and soil temperature and soil water content are poorly correlated. Remotely sensed surface temperature will provide useful information for investigation of CO_2 transfer processes near the soil surface, as well as for quantitative assessment of ecosystem surface CO_2 flux (ESF_{CO_2}). It is clearly shown that a synergy of remote sensing and a soil–vegetation–atmospheric transfer (SVAT) model; parameterization of the model with remote sensing signatures is promising for estimating important ecosystem variables such as biomass growth and ecosystem CO_2 flux. This approach allows the effective use of infrequent and multisource remote sensing data.

Keywords: dynamic simulation; eddy covariance method; NPP; NEP; process model; SVAT model; vegetation index

1 Introduction

The function of terrestrial vegetation in the global carbon cycle is well recognized; the net primary production (NPP) is the major part of carbon flux at the interface between the atmosphere and terrestrial ecosystems such as agricultural fields and forests. However, the quantitative dynamics of plant productivity and CO_2 flux between atmosphere and terrestrial ecosystems remains elusive (Keeling et al., 1996; Schimel et al., 2000). Most ecological investigations and assessments are based on site-specific measurements assuming that they are representative of the area of interests, which often cause serious errors (Kicklighter et al., 1994). The continuous measurements of CO_2 fluxes using methods such as eddy covariance or chamber methods may be the most direct and accurate approach for assessment of net ecosystem productivity (NEP). However, such site-specific observations of CO_2 flux have to be generalized by means of process modeling for geospatial and dynamic assessment.

Therefore, it is crucial to use remote sensing information and numerical process models for more quantitative and mechanistic assessment of those important ecosystem variables since the terrestrial ecosystems and their environments are both heterogeneous and dynamically changing.

A great number of studies have been conducted to relate the remotely sensed spectral signatures to biomass, leaf area index (LAI), vegetation coverage, and the fraction of absorbed photosynthetically active radiation (fAPAR), which will be overviewed later. One of the newest approaches is to use a hyperspectral reflectance index, which is based on photochemical processes in chloroplast. It may be directly related to the photosynthetic capacity of

vegetation (Peñuelas and Inoue, 2000). On the contrary, the soil CO_2 flux from vegetated land surfaces has been little related to remotely sensed information yet. It is still needed to explore significant relationships between remotely sensed signatures and biophysical ecosystem variables at various scales. One of the most attractive aspects of numerical process modeling is to describe the interactions between soil, plant, and atmosphere quantitatively as well as to predict the ecosystem functioning under different conditions.

Nevertheless, these powerful methods have some limitations in ecological and geophysical applications. Remote sensing observations are basically instantaneous, and require biophysical interpretations. Models require a number of input data, but they are often unavailable at geospatial basis. These limitations hamper operational and reliable assessments. Therefore, the synergistic linkage of these two methods seems most promising by facilitating and compensating each other. The use of fAPAR in a simple mechanistic model (e.g., Monteith, 1977) is one of the most conventional approaches for rough assessment of NPP at various scales using remote sensing (e.g., Potter et al., 1993; Maisongrande et al., 1995; Ruimy et al., 1996; Veroustraete et al., 1996). Both optical and microwave information is useful for estimating the aboveground characteristics of vegetation such as LAI and biomass. However, far more accurate, dynamic, and comprehensive methods are desirable for both scientific and operational purposes.

Thus, in this chapter, we first overview the state-of-the-art in remote sensing of ecophysiological variables. Second, we discuss the possible linkages between remote sensing and process-based modeling in estimating plant productivity and ecosystem CO_2 flux. Third, we investigate the relationship between remotely sensed signature and soil surface CO_2 flux (SSF_{CO_2}). Fourth, the performance of synergy between remote sensing and biophysical and ecophysiological models is examined on the basis of some case studies. All case studies are based on comprehensive data set of soil, plant, atmospheric, and remote sensing measurements.

2 Remote Sensing of Ecophysiological Parameters as Related to Plant Productivity and Carbon Cycle

Remote sensing methods have a number of advantages in monitoring vegetation and environmental conditions, since useful signatures can be remotely detected at wide-area, nondestructive, and real-time bases. Sensor technology allows invisible signals between near-infrared and microwave wavelengths to be detected from a distance. Fig. 1 shows the typical reflectance spectra in solar domain for various components of agro-ecosystem surfaces. It is clearly

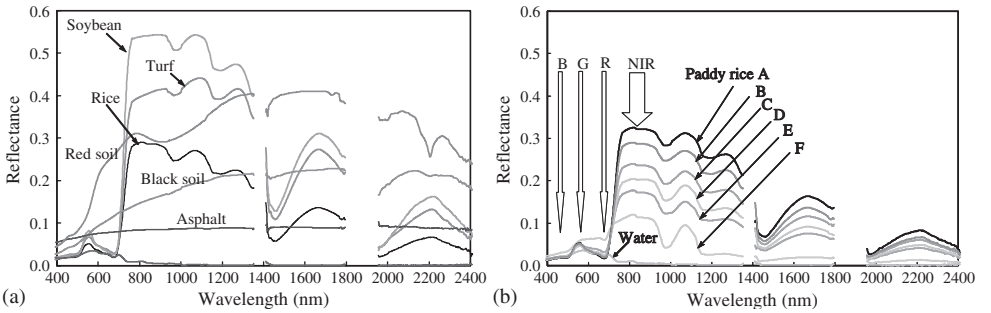

Figure 1: Typical reflectance spectra for agro-ecosystem surfaces (a), and for paddy fields with different biomass (b). Abbreviations B, G, R, and NIR mean blue, green, red, and near-infrared wavelengths, respectively. Biomass of rice paddies decreased in order from A to F (For colour version, see Colour Plate Section).

shown that each object has unique reflectance spectra, and reflectance signatures at specific wavelengths are strongly related to biophysical properties of targets such as green biomass. Hence, remotely sensed data have been used for a variety of agricultural and ecological applications, such as yield prediction, stress detection, monitoring of leaf area and biomass growth, disease diagnosis, and so forth. Relationship between remotely sensed signatures and ecophysiological variables are useful basis for geospatial assessment of plant productivity and CO_2 flux.

2.1 Biomass, Leaf Area Index, and Fraction of Absorbed Photosynthetically Active Radiation

Voluminous papers have reported significant relations between remotely sensed spectral signatures and biomass, LAI, vegetation coverage, and the fAPAR for various plant species. The most common approach involves an empirical regression between those variables and vegetation indices that use a small number of spectral bands. The simple ratio of reflectance at near-infrared and red wavelengths ($\rho_{\mathrm{NIR}}/\rho_{\mathrm{Red}}$), and the normalized difference vegetation index (NDVI: $[\rho_{\mathrm{NIR}}-\rho_{\mathrm{Red}}]/[\rho_{\mathrm{NIR}}+\rho_{\mathrm{Red}}]$) are often used, but also a variety of vegetation indices have been proposed for more reliable and wider application of such semiempirical relations as discussed in Section 4. Since vegetation indices are affected by both plant and measurement conditions, field validation studies for various plant species, locations, and environmental conditions are needed to derive robust semiempirical relations (e.g., in relation with fAPAR; Daughtry et al., 1983; Steinmetz et al., 1990; Inoue and Iwasaki, 1991; Pinter et al., 1993). Despite obvious limitations, spectral indices are simple and useful if they are used within a range of validation.

Since microwave signatures are not affected by cloudy conditions, synthetic aperture radar (SAR) is a powerful sensor, especially in monsoon Asia. A number of reports have shown that the microwave backscattering coefficient correlates with biomass and LAI (Ulaby et al., 1984; Bouman and Hoekman, 1993; Le Toan et al., 1997), although experimental results and the interpretation of microwave backscatter information have not always been consistent, presumably because the microwave backscatter from vegetated surfaces is affected by several factors, including plant biomass, structure, and soil moisture and roughness (Brisco and Brown, 1998). A recent comprehensive study based on season-long daily measurements using a multifrequency, multipolarization, and multiangular sensing system showed consistent relations of the backscattering coefficients with biomass and LAI for a rice canopy (Inoue et al., 2002). It was clearly shown that C and L bands were most effective in estimating LAI and above-ground biomass, respectively.

2.2 Photosynthesis, Transpiration, and Physiological Stress Response

Since transpiration is an important part of a plant leaf's energy budget, remotely sensed leaf or canopy temperatures provide useful information about transpiration and, consequently, stomatal behavior. A number of experimental studies have shown that leaf and canopy temperatures have significant relationship with transpiration, stomatal conductance, and photosynthesis (Jackson et al., 1981). Using infrared thermal imagery, Inoue (1990) clearly demonstrated that canopy temperature responds sensitively to stomatal conductance, transpiration, and photosynthetic rates. The mean surface temperature in the water-stressed canopy was consistently higher than in the nonstressed one, which was closely linked with physiological depression. Any physiological depression caused by water deficiency, disease, insects, or other matters related to stomatal conductance and transpiration can be detected by remotely sensed canopy temperature (Nilsson, 1991). Nevertheless, the applicability of canopy temperature alone is limited, because it is also affected by air temperature, solar radiation, vapor pressure deficit, and wind speed. Thus, the first simple approaches for wider applicability involved canopy–air temperature differences, such as stress–degree–days and the crop water stress index (CWSI), which further incorporated the effect of vapor pressure deficit (Jackson et al., 1981). The CWSI was designed to express the degree of water stress as a number between 0 (no stress) and 1 (severe stress). The operational applicability of CWSI has been evidenced by commercial instruments and several application studies using airborne and space-borne thermal imagery (Moran and Jackson, 1991). A widely used approach, often using AVHRR data, considers

the "simplified relationship," which was proposed by Seguin and Itier (1983) to relate linearly evapotranspiration to the difference between surface temperature and air temperature. Another simple approach relating canopy temperature together with a vegetation index to canopy transpiration has been proposed for estimating plant stress conditions (Moran et al., 1994; Inoue and Moran, 1997). The other combinations of remotely sensed information and process-based modeling are discussed in detail in the Section 2.3.

Vegetation indices have also been related semiempirically to stomatal conductance and photosynthesis (e.g., Sellers, 1987). Another interesting approach involves the use of hyperspectral signatures to estimate photosynthetic activity directly; one such signature is chlorophyll fluorescence, which can be remotely induced and detected (e.g., Méthy et al., 1994). Chlorophyll fluorescence in the red and near-infrared regions may be a good indicator of the capacity of photosynthetic electron transport, because fluorescence is emitted mainly from photosystem II(PSII). However, no relation between fluorescence, gross photosynthesis, and photosynthetically active radiation (PAR) intensity has been established (Rosema et al., 1998). Yet another approach is to use the spectral reflectance at a wavelength of approximately 530 nm, which is related to both the photosynthetic efficiency (photosynthesis/incident photon flux density) and the relative increase of zeaxanthin in the xanthophylls cycle pool to avoid photoinhibition (e.g., Filella et al., 1996). A high correlation between the normalized reflectance at 531 nm and CO_2 uptake has been found at the canopy scale (Peñuelas and Inoue, 2000). This relation may be useful for remote and direct estimation of photosynthetic activity.

2.3 Water, Chlorophyll, and Nitrogen Contents

Water and nitrogen are the major constraints for plant productivity. Since water has a specific absorption spectrum, reflectance spectra relate to water content or to relative water content (RWC), especially in shortwave infrared spectral regions (e.g., Thomas et al., 1971; Inoue et al., 1993). Reflectance at 1,430 and 1,910 nm, the strong absorption bands of water, and at 1,650 and 1,200 nm was well correlated with leaf water content and RWC. The first derivative at 1,121 nm and the spectral shift at approximately 2,010 nm were also closely related to leaf water status (Inoue et al., 1993). The ratio of reflectance at 970 nm (ρ970) to ρ900 was closely correlated with the water condition at leaf and canopy scales (Peñuelas and Inoue, 1999). Plant pigments, such as chlorophyll and carotenoids, also have specific absorption spectra, which play essential roles in the photochemical cycle in plant leaves (Inoue and Peñuelas, 2001). Since the chlorophyll strongly absorbs red light and reflects green, the reflectance at 675 and 550 nm can be used to determine chlorophyll content. Reflectance at these wavelengths is also used to

estimate nitrogen stress, which is highly correlated with the chlorophyll content of green leaves. The position of the maximum slope in the increase of reflectance from red to near-infrared was found to shift toward blue with decreasing chlorophyll content (Filella and Peñuelas, 1994). Inada (1985) showed that the spectral reflectance ratio $\rho 800/\rho 550$ is the most effective index for estimating the leaf chlorophyll content of rice. However, $\rho 800/\rho 550$ was effective at a canopy scale only when measurements were taken at an oblique viewing angle under cloudy (diffusive light) conditions (Takebe et al., 1990); canopy nitrogen content correlated poorly with $\rho 800/\rho 550$ when it was measured at an angle perpendicular to the canopy (Inoue et al., 1998, 2002).

The total nitrogen content of a canopy can be estimated using visible and near-infrared wavelengths such as $\rho 480$, $\rho 620$, and $\rho 840$ (Shibayama and Akiyama, 1986), and estimates can also be improved by using shortwave infrared wavelengths, such as $\rho 1{,}650$ and $\rho 2{,}200$ (Inoue et al., 1998). Based on their simulation study, Daughtry et al. (2000) proposed that the slope of $\rho_{\mathrm{NIR}}/\rho_{\mathrm{Green}}$ regressed on $\rho_{\mathrm{NIR}}/\rho_{\mathrm{Red}}$ and is useful for estimating leaf chlorophyll concentration at a canopy scale. Yoder and Pettigrew-Crosby (1995) reported that $\rho 2{,}132$ contributes significantly to estimation of nitrogen in maple seedlings, and suggested that the spectral region between 2,000 and 2,200 nm s generally useful for this purpose, although exactly how useful it may be remains unclear, especially at the canopy scale. The great contribution of this spectral region is probably because the synthesis and decomposition of enzymes and relative increases in lignin and cellulose are coupled with plant growth, nitrogen supply, and senescence. However, further detailed analyses based on hyperspectral measurements are needed to clarify this contribution. The spectral region from 2,000 to 2,200 nm is also closely related to plant litter cover on the soil surface due to the cellulose absorption feature at 2,100 nm (Nagler et al., 2003), which may be applied to quantitative assessment of plant litter.

3 Methodology of Synergizing Remotely Sensed Information and Biophysical and Ecophysiological Process Models

The advantage of remote sensing is that signatures over broad electromagnetic domains can be detected on remote/nondestructive, wide area, or real-time bases, while the surrounding issue is that measurements are usually instantaneous, directional, and infrequent, and must be converted to biophysically meaningful variables. Conversely, the advantage of process modeling is that numerical models can take account of multiple variables, and can provide dynamic simulations as well as predictions under imaginary

situations, while the issue is that experimental determination of model parameters and model validation are not easy, and that it is tedious or impossible to gather the necessary input data. Hence, one of the most promising approaches for effective monitoring and accurate prediction of plant production processes is the synergy of remote sensing and process models, which can reinforce each other.

A variety of approaches for relating remotely sensed signatures to plant and ecosystem variables are summarized in Fig. 2(a). One of the most widely used approaches is the simple regression of target variables on remotely sensed signatures, such as spectral reflectance, thermal temperature, and microwave backscattering coefficients (Fig. 2A). Several of these relations are reviewed in Section 2.

Nevertheless, physical processes such as spectral reflection, thermal emission, and scattering should be taken into account to extend the applicability and to improve the accuracy of relations between remotely sensed signatures and target variables. The first type of models to be linked with remotely sensed signatures are radiative transfer models, which represent physical processes such as spectral reflectance/absorption, thermal emission, and microwave scattering. Examples of such models in the optical domain are BRDF (bidirectional reflectance distribution function) models, which can take into account sun angle, sensor angle, and some other spectral parameters (Qi et al., 1995). Detailed approaches may include the effect of the complex architecture of plant stands, such as the presence of stems, fruit organs (Weiss et al., 2001) as well as the 3D distribution of canopy elements such as tree crowns and bushes (Gastellu-Etchegorry et al., 1999). The reflectance model SAIL is a well-known process model in the optical domain for plant canopy (Verhoef, 1984). Optical reflectance model at a leaf scale such as PROSPECT (Jacquemoud and Baret, 1990) and LIBERTY (Dawson et al., 1998) have been developed for broad and coniferous leaves, respectively. Remotely sensed signatures can be related more systematically to ecophysiological plant variables by inverting these models (see, for examples, recent studies by Combal et al. (2003)). For the thermal domain, the energy budget model and mass and energy transfer models are essential for describing thermal emission (Olioso et al., 1999). The backscattering process of microwaves by a plant canopy can also be described by some scattering models (Attema and Ulaby, 1978; Prevot et al., 1993; Wigneron et al., 1999), which take account of soil, plant, and sensor conditions such as LAI, leaf size, plant moisture, soil moisture, roughness, and incident angle. Plant ecophysiological variables can be estimated by inverting the model, based on the remotely sensed signatures (Fig. 2B).

Another type of process models to be linked with remote sensing information are the canopy functioning models, such as the energy budget model, plant growth model, and the soil–vegetation–atmospheric transfer (SVAT) model. The leaf or canopy temperature is determined as a part of the energy budget in

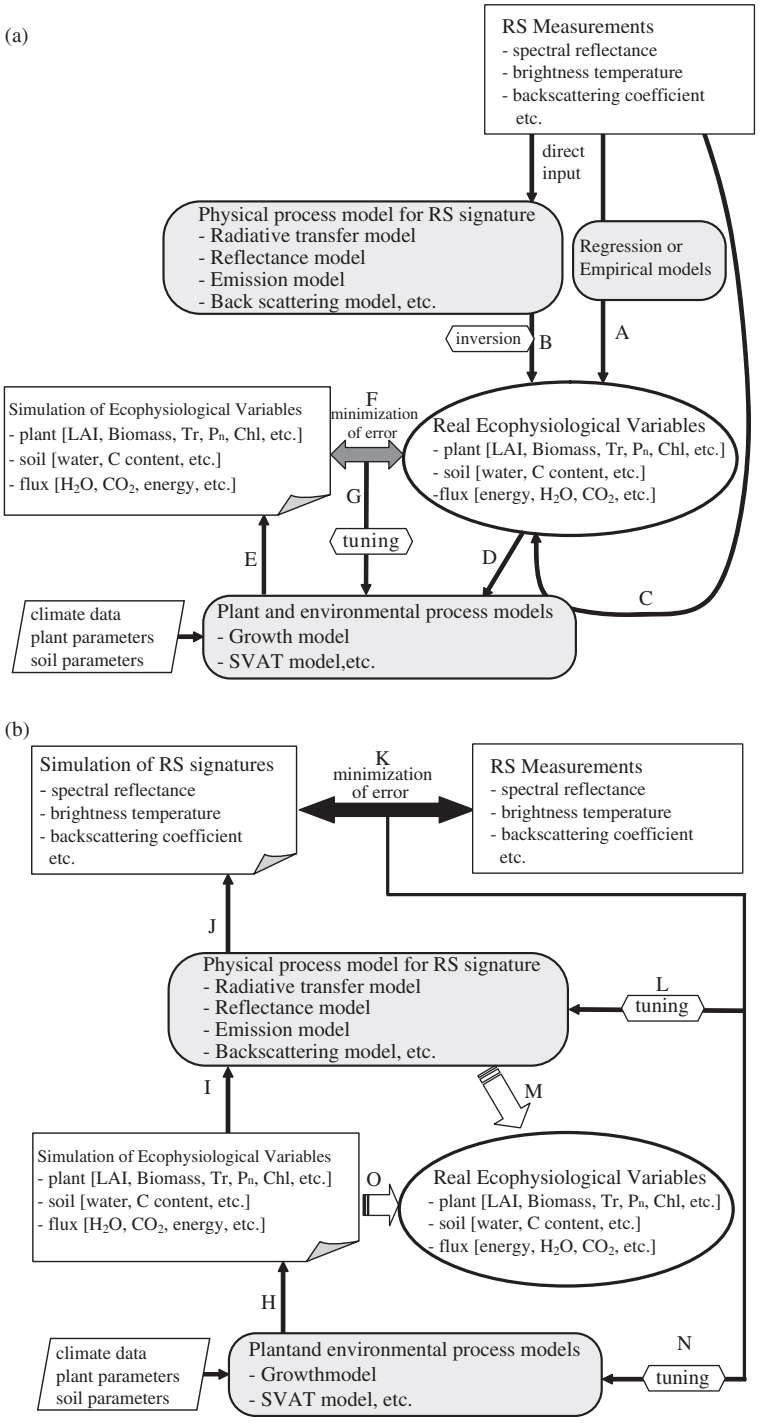

Figure 2: Synergistic linkage of remote sensing with biophysical and ecophysiological process models for estimation of ecophysiological variables. RS: remote sensing; LAI: leaf area index; Tr: transpiration; P_n: photosynthesis; Chl: chlorophyll content; SVAT: soil–vegetation–atmosphere transfer.

the soil–plant–atmosphere system, where energy, water, CO_2, and ecophysiological conditions all fluctuate. Hence, temperature data from infrared imagery provides more quantitative and reliable information when they are used as inputs into ecophysiological models or stress indices (Fig. 2C). Inoue (1987) and Inoue et al. (1990a, b) estimated leaf transpiration and stomatal resistance remotely, using infrared leaf temperatures. Canopy transpiration has been well estimated by a combination of remotely sensed canopy temperatures and an energy- and mass-transfer model under various soil–water conditions (Inoue et al., 1994).

Canopy functioning models can simulate plant growth or fluxes in vegetated surfaces dynamically using meteorological inputs without remote sensing data (Fig. 2E). In addition, these functioning process models can utilize remotely sensed signatures (Fig. 2C), or plant parameters estimated by remote sensing (Fig. 2D), as inputs; they can also be calibrated using remote sensing information to provide more realistic estimates (Fig. 2F, G). Further deep linkage between remote sensing and models is presented in Fig. 2(b). Remote sensing signatures can be simulated by radiative transfer models using output from the functioning models (Fig. 2H–J). The remotely sensed measurements are then compared with simulated signatures to fine-tune the functioning models so that they can simulate more realistic signatures (Fig. 2K–N), which in turn yield more realistic estimates of ecophysiological variables (Fig. 2M, O). Maas (1988) and Bouman (1992) conducted the first practical studies of this type of synergy. They showed the need for within-season calibration of simulation models, and demonstrated that this method effectively reduced model complexity, simplified input requirements, and made the model more operational. This synergistic approach may be a practical and effective method for linking instantaneous remote sensing data with continuous growth simulation, because process models are based on biological foundations and yield robust patterns of growth and development. This approach has an advantage over the direct use of remotely sensed data as inputs and the use of correlations between accumulated remotely sensed indices (e.g., ΣNDVI) and productivity, because both the latter two require frequent remote sensing observations (e.g., Wiegand et al., 1986).

In general, there are two levels of synergy for this approach; one approach uses remote sensing data to estimate a few key plant variables (e.g., LAI and evapotranspiration), which are then used to recalibrate the model (e.g., Moran et al., 1995) (Fig. 2B or A with EFG). This first approach can utilize a wide range of vegetation indices, regression models, and model inversions to estimate plant variables such as LAI and above-ground biomass, which can then be used to recalibrate simulation models. This recalibration may be done by tuning model parameters, so that simulated variables such as LAI are in agreements with their remote sensing estimates. Another possibility may be to simply correct the time course of simulated variables by

reinitializing the model each time remote sensing estimates are available (Olioso et al., 2002).

Another approach is to use the outputs of a plant growth model, such as LAI and leaf-angle distribution (LAD), to calculate the radiative features (e.g., spectral reflectance and microwave backscatter) of the plant canopy by using a radiation transfer model such as SAIL (Verhoef, 1984; Olioso et al., 2001; Weiss et al., 2001). Then, simulated and measured radiative features are compared to recalibrate the plant growth model (Bouman, 1992; Clevers et al., 1994; Olioso et al., 2002) (Fig. 2H–K, N, O). This second approach would be more attractive, provided a plant model is able to produce the output of several geometrical and spectral variables for a canopy that are required by radiation transfer models, and also that the spectral model is well calibrated to yield accurate spectral features of the canopy. To simulate canopy reflectance, Moulin et al. (1998) used the output LAI from a growth model for sugar beet (SUCROS) as the input to a canopy reflectance model (SAIL). The parameters of SUCROS were then optimized to minimize the difference between the simulated and measured reflectance. This approach proved useful for predicting sugar beet production at a regional scale. The recalibration approach may be more robust and operational than others, because the process model can provide some normal simulation results based on weather and plant inputs, and because intermittent or infrequent remote-sensing observations can be used efficiently to adjust the model parameters and to rerun the simulations using modified parameters. The tuning of model parameters is usually based on iterative optimization toward the minimized residual difference between observed and simulated data (Moulin et al., 1998; Olioso et al., 2002).

4 A Simple Method for Estimating NPP Using Remotely Sensed Information as Input

4.1 Theoretical Background

In terrestrial ecosystems, photosynthesis by vegetation is the major sink of atmospheric CO_2, while microbial respiration is the major source of CO_2 into the atmosphere. Since these two processes behave independently under changing environmental conditions, it is ideal to estimate both the net photosynthesis and the microbial respiration separately at high temporal and geospatial resolution for quantitative assessment of carbon budget. Nevertheless, this has never been realized to date even with the state of art in ecological, geo-scientific, and mathematical achievements.

Thus, for the moment, the NPP and net ecosystem production (NEP) are of the major concern in the context of the terrestrial carbon budget. These

two variables are assumed to represent the long-term carbon budget for the above ecophysiological processes. The NPP is defined as the time-integrated value of net photosynthesis A_n (= Gross photosynthesis A_g – Respiration R_v). The NEP is defined as the time-integrated value of A_g – microbial respiration R_m. The term for integration is usually 1 year. One of the most preliminary and tedious methods to estimate NPP is to weigh the above- and underground plant biomass as well as litter based on sampling method. Sampling of fine root may be the most difficult procedures. Change of carbon content in the soil has to be measured at the same time for NEP estimation.

In the long history of agricultural sciences, plant ecophysiological processes, i.e., the interactions of plant, soil, and atmosphere have been intensively studied for efficient production of high-quality products. A number of growth models have been proposed for better understanding of these interactions and for dynamic simulation of plant growth under changing soil and atmospheric conditions (e.g., Penning de Vries and van Laar, 1982; Hanks and Ritchie, 1991; Brisson et al., 1998). Therefore, these scientific achievements can be applied to the assessment of NPP. Since the photosynthesis is driven by the light energy, the light absorption processes within a canopy has been investigated in detail (Monsi and Saeki, 1953). Meanwhile, a simple but robust relationship between crop dry matter (DM) production and PAR intercepted or absorbed by the crop canopy has been reported (Shibles and Weber, 1966; Monteith, 1977; Gallaghter and Biscoe, 1978). On the basis of this simple linear relationship, NPP can roughly be expressed by a simple model as follows:

$$\mathrm{NPP} = \mathrm{RUE} \times \mathrm{APAR} = \mathrm{RUE} \times \mathrm{fAPAR} \times \mathrm{PAR} \tag{1}$$

where PAR is the photosynthetically active radiation, APAR the PAR absorbed by a canopy, RUE the radiation use efficiency (conversion coefficient of absorbed PAR to DM), and fAPAR the fraction of APAR to PAR, respectively. The fAPAR has long been expressed as a function of LAI in plant growth models,

$$\mathrm{fAPAR} = 1 - r - (1 - r_0)\exp[-(1 - m)k\mathrm{LAI}]) \tag{2}$$

where r and r_0 are the reflectance of canopy and soil background, respectively; m is the scattering coefficient; and k the extinction coefficient of the canopy to shortwave solar radiation. This relationship is still commonly used in a number of growth simulation models.

On the other hand, remote sensing studies have provided a significant relationship between the spectral reflectance by optical remote sensing and above-ground green biomass or LAI (e.g., Tucker et al., 1983; Asrar et al., 1985; Shibayama and Akiyama, 1989; Inoue et al., 2000). Since chlorophyll

pigments strongly absorb red light and reflect/transmit near infrared light, simple spectral indices using these two reflectance values (ρ_{Red} and ρ_{NIR}, respectively) have a near-linear relationship with the light intercepted or absorbed by plant canopies (e.g., Daughtry et al., 1983; Asrar, 1989; Baret and Guyot, 1991). It is further investigated that such spectral indices would be more useful than LAI (Inoue et al., 1998). The normalized difference vegetation index,

$$\mathrm{NDVI} = \frac{\rho_{\mathrm{NIR}} - \rho_{\mathrm{Red}}}{\rho_{\mathrm{NIR}} + \rho_{\mathrm{Red}}} \tag{3}$$

is one of the most commonly used spectral indices, while a variety of vegetation indices VI have been proposed for more reliable and wider application of such semiempirical relations (e.g., Huete, 1988; Qi et al., 1994; Govaerts et al., 1999; Haboudane et al., 2002).

By replacing the equation (2) with equation (3),

$$\mathrm{fAPAR} = \mathrm{aVI} \tag{4}$$

NPP can be expressed by,

$$\mathrm{NPP} = \mathrm{RUE} \times \mathrm{APAR} = \mathrm{aRUE} \times \mathrm{VI} \times \mathrm{PAR} \tag{5}$$

where a is the proportionality constant.

The theoretical foundation of VIs has been well examined (e.g., Asrar, 1989; Baret and Guyot, 1991; Myneni et al., 1995; Qi, 2001).

Despite obvious limitations, equation (4) is widely used for NPP estimation using remote sensing data since the spectral indices are simple and useful if they are used within a range of validation. Since vegetation indices are affected by both plant and measurement conditions, field validation studies for various plant species, locations, and environmental conditions are needed to derive useful and robust semiempirical relations (e.g., in relation with fAPAR; Daughtry et al., 1983; Steinmetz et al., 1990; Inoue and Iwasaki, 1991; Pinter et al., 1993). In this approach, one should be careful about the validation of RUE and its sensitivity to the other environmental conditions.

4.2 Estimating NPP at an Ecosystem Scale based on fAPAR from Remotely Sensed Information – A Case Study

A comparative study on the relationship between the fAPAR of various plant canopies and seven vegetation indices was conducted based on airborne remote sensing data (Inoue et al., 2001). During this experiment, well-calibrated

airborne optical measurements at fine spatial resolution were obtained simultaneously with ground-based hyperspectral and detailed plant measurements. This may be a useful case study that investigates the realistic relationship between vegetation indices and fAPAR, since there are few experimental studies at an ecosystem or landscape scales based on accurate ground-based data and airborne remote sensing data.

4.2.1 Experimental Site

An experimental study was conducted in agricultural fields at the National Agricultural Research Center (Tsukuba, Japan; 36°01′N, 140°07′E, 25 m above sea level) and surrounding farmland areas. The size of the whole area was approximately 60 km^2, where a wide range of crop fields (rice, soybean, corn, peanut, etc.) and natural vegetation areas (tree, turf grass, bush, etc.) were included.

4.2.2 Airborne and Ground-Based Remote Sensing Measurements

An airborne multispectral scanner (AZM, Nakanihon-kouku, Co. Inc., Japan) was used for remote sensing of the study area. Airborne spectral images were taken at eleven optical bands (474, 553, 656, 675, 848, 1,089, 1,193, 1,623, 2,044, 2,135, and 2,207 nm) and one thermal band (9.3 μm) from the altitude of 1,000 m around midday. The spatial resolution on the ground was 1.25 m. The digital images were converted to reflectance images using calibration sources. No atmospheric correction was made because the sky condition was perfectly clear and humidity was low (49%). Ground-based hyperspectral reflectance and surface temperatures were measured using a portable radiometer (FS-FR1000, ASD, USA) and infrared thermometers (Model4000, Everest Inc., USA), respectively. The reflectance spectra (380–2,500 nm, 1 nm resolution) were taken over more than 50 different uniform target areas including rice, soybean, corn, grassland, turf, vegetables, bare soil, asphalt, concrete, water pond, river, etc. Infrared surface temperatures were measured for 10 different uniform targets (bare soils, rice canopies, water pond, asphalt, concrete, etc.). Emissivity was assumed to be 0.98 for all targets. Temperature data for the time window of airborne observation were averaged and used for calibration.

4.2.3 Measurements of fAPAR and Plant Parameters

Plant data such as LAI and biomass were estimated from destructive measurements based on plant sampling. The LAI was measured using an optical leaf area meter (AAM8, Hayashi-denkoh Co. Ltd., Japan) for green leaves only. Wet and dry biomass was measured for green leaves, stems, roots, and senescent plant parts, respectively.

The fAPAR was estimated from the budget of four components of the photosynthetic photon flux density (PPFD) measurements, i.e., downward and upward over and below canopies. These PPFD values were measured using a meter-long PPFD sensor (LI-191SA, Li-Cor Inc., USA) several times, and were averaged so that they were representative for each canopy. The fAPAR data were taken at near the time of remotely sensing measurements; these data were not daily average values of fAPAR, but the instantaneous values near midday. It is well known that the value of fAPAR is not consistent during a day but relatively high near sunrise and sunset periods; nevertheless, the midday fAPAR may be representative enough for the daily average of fAPAR, because they are highly correlated with each other due to extremely low solar radiation during those periods of low sun elevation.

4.2.4 Estimating fAPAR and Plant Productivity from Spectral Indices

From the data for 107 different canopies, a close linear relationship was obtained between the fraction of intercepted radiation by a plant canopy (fIPAR) and fAPAR:

$$\text{fAPAR} = 0.954\text{fIPAR} \quad r^2 = 0.997(n = 107) \tag{6}$$

These two parameters are both often used in simple process models, but it should be noted that the fIPAR is smaller than fAPAR by 5%.

The relationship of fAPAR with the seven different vegetation indices, NDVI, RVI, SAVI (Huete, 1988), MSAVI (Qi et al., 1994), WDVI (Clevers, 1989), GEMI (Pinty and Verstraete, 1992), and EVI (Huete et al., 1999) was compared. Definitions for VIs are as follows:

$$\text{RVI} = \frac{\rho_{\text{NIR}}}{\rho_{\text{Red}}} \tag{7}$$

$$\text{SAVI} = (1 + L)\frac{\rho_{\text{NIR}} - \rho_{\text{Red}}}{\rho_{\text{NIR}} + \rho_{\text{Red}} + L} \quad L = 0.5 \tag{8}$$

$$\text{MSAVI} = (1 + L)\frac{\rho_{\text{NIR}} - \rho_{\text{Red}}}{\rho_{\text{NIR}} + \rho_{\text{Red}} + L} \tag{9}$$

with a optimized value of L

$$\text{WDVI} = \alpha\rho_{\text{NIR}} - \rho_{\text{Red}} \quad \alpha = \text{coefficient} \tag{10}$$

$$\text{GEMI} = \eta(1 - 0.25\eta) - \frac{\rho_{\text{Red}} - 0.125}{1 - \rho_{\text{Red}}} \tag{11}$$

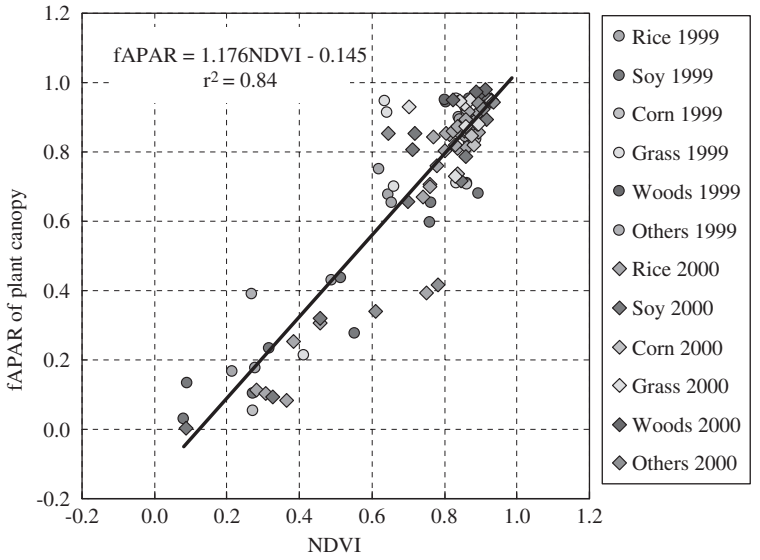

Figure 3: Relationship between fAPAR of various plant canopies and vegetation index NDVI derived from airborne remote sensing images (For colour version, see Colour Plate Section).

$$\eta = \frac{[2(\rho_{\mathrm{NIR}}^2 - \rho_{\mathrm{Red}}^2) + 1.5\rho_{\mathrm{NIR}} + 0.5\rho_{\mathrm{Red}}]}{(\rho_{\mathrm{NIR}} + \rho_{\mathrm{Red}} + 0.5)}$$

$$\mathrm{EVI} = 2.0\frac{\rho_{\mathrm{NIR}} - \rho_{\mathrm{Red}}}{1 + \rho_{\mathrm{NIR}} + 6\rho_{\mathrm{Red}} - 7.5\rho_{\mathrm{Blue}}} \tag{12}$$

The fAPAR was best correlated with NDVI (Fig. 3), which was of better linearity than the other VIs; RVI ($r^2 = 0.55$), SAVI ($r^2 = 0.73$), MSAVI ($r^2 = 0.62$), WDVI ($r^2 = 0.61$), GEMI ($r^2 = 0.67$), and EVI ($r^2 = 0.68$). The regression equation for NDVI,

$$\mathrm{fAPAR} = 1.176\mathrm{NDVI} - 0.145 \quad r^2 = 0.84 \tag{13}$$

agreed well with the following theoretically derived equation (Myneni and Williams, 1994),

$$\mathrm{fAPAR} = 1.164\mathrm{NDVI} - 0.143. \tag{14}$$

Since the regression equation (13) was derived from a data set for 2 years and for a wide range of plant canopies including crops, vegetables, and woods, it will be a useful basis for various applications. The deviation of individual data points from the regression line, i.e., error of the estimations is large in some cases, but this is the inherent limitation to this simple approach, which uses only two spectral wavelengths.

On the basis of this equation, a fine resolution map of fAPAR was generated (Inoue et al., 2001), from which plant productivity could be estimated at the landscape scale using measured RUE and PAR data. Since the daily global solar radiation can be estimated from satellite imagery (GMS) at 5-km resolution, it is possible to estimate daily productivity for specific biomes or areas. During the midsummer growing season, typical values of the fAPAR for uniform areas of rice-paddies, upland-crops, and urban zone were 0.3, 0.25, and 0.1, respectively. It is noticeable that the regional average of fAPAR for the typical and uniform rice areas was not more than 0.3, while it was 0.8–0.9 for rice canopies with nearly maximum LAI on the same day. The amount of carbon fixed into the area of rice-paddies, upland-crops, and urban areas was estimated to be 2.8, 2.4, and 1.0 $C\,g\,m^{-2}\,day^{-1}$. For example, on a clear-sky day with the global solar radiation (RAD) of 25 $MJ\,m^{-2}\,day^{-1}$, assuming that RUE is 2.66 $gDM\,MJ^{-1}_{APAR}$, PAR is 0.45 of RAD, and carbon content is 0.449 of plant DM, respectively. The values for cropped areas are comparable with typical values for crop species such as 300–400 $gC\,m^{-2}\,y^{-1}$ (Goudriaan et al., 2001).

During the same experiment, the soil carbon content in agricultural fields was found to be highly correlated with spectral reflectance at 480 and 560 nm ($r^2 = 0.63$; range of carbon content: 0.20–0.61% DM) based on the same data set. This result suggests that the annual change in the soil carbon content may be estimated from remotely sensed spectral reflectance. Nevertheless, further research is needed for more accurate and robust estimation.

5 Measurement of Ecosystem CO_2 Flux as Related to Remotely Sensed Information – A Case Study

Continuous measurement of ecosystem CO_2 flux leads the most direct estimation of CO_2 exchange at the interface between ecosystem and atmosphere. Both NPP and NEP are also estimated as time-integrated values of the CO_2 flux. Hence, a number of scientists are continuing on-site measurements of CO_2 flux in various types of ecosystems using up-to-date instrumentations such as the eddy covariance method (e.g., Dugas, 1993; Miyata et al., 2000; Widén, 2002). Since the ecosystem CO_2 flux measured by eddy covariance method consists of net photosynthesis and microbial respiration that behave independently, microbial CO_2 flux from the soil surface has to be estimated separately. The SSF_{CO_2} has been measured by various types of chambers (e.g., Norman et al., 1997). Yet, the separation of CO_2 from plant root and soil remains one of the most difficult tasks to date.

Anyhow, there is no doubt that such point measurements under some environmental conditions have to be representative of the ecosystem, as well as to be generalized for wider applications.

Thus, the continuous measurements of CO_2 flux and their linkage with process modeling and remote sensing may be the most promising approach for geospatial and dynamic estimation of CO_2 exchange between ecosystems and atmosphere. Such approach may be investigated only with a comprehensive data set of soil, plant, and atmospheric variables as well as concurrent flux and remote sensing measurements as in the following case study. Hereafter, we designate the CO_2 flux at the interface between the atmosphere and ecosystem as ESF_{CO_2} (ecosystem surface CO_2 flux), which is equivalent to the SSF_{CO_2} (soil surface CO_2 flux) under bare soil conditions. By definition, the SSF_{CO_2} consists of respiration of plant roots and microorganisms under vegetated conditions. We avoid using the conventional term "soil respiration" since it includes respiration of both soil microorganisms and plant roots under vegetated conditions.

5.1 Acquisition of a Comprehensive Data Set

5.1.1 Experimental Site

An experimental study has been conducted in agricultural fields at the National Agricultural Research Center (Tsukuba, Japan; 36°01′N, 140°07′E, 25 m above sea level) from 1995 to 2002. Two flat and uniform 4-ha fields were used, which were surrounded by the similar type of cropped fields under different management conditions. The soil was a humic volcanic ash soil Andisol, which belongs to the Hydric Hapludands and is the major cultivated soil for upland crops in Japan. The field capacity and wilting point for the top 20-cm layer were estimated to be $0.44\,m^3\,m^{-3}$ (-6 kPa) and $0.275\,m^3\,m^{-3}$ (-1.5 MPa), respectively. The mean carbon and nitrogen contents of the topsoil (0–5 cm) were estimated to be 3.7% and 0.31%, respectively. Each field has been used with the cropping pattern (soybean (*Glycine max* L. Merr.)–rapeseed (*Brassica napus* L.)–forage corn (*Zea mays* L.)–wheat (*Triticum* spp.)) for every 2 year. We mainly used the data set from 1996 to 1998 for this particular analysis. The annual mean air temperature and annual total rainfall were 13.3°C (1996), 13.6°C (1997), and 14.9°C (1998), and 1,032 mm (1996), 972 mm (1997), and 1,536 mm (1998), respectively.

5.1.2 CO_2 Flux Measurements

The CO_2 flux over the field (ESF_{CO_2} or SSF_{CO_2}) was measured by the eddy covariance method. The method has been widely used for the measurement of CO_2, water vapor, and sensible heat fluxes over plant canopies (Leuning and Judd, 1996). We used an open-path eddy covariance system, the main

components of which were a 3D sonic anemometer, a fast response infrared gas analyzer, and a data logger. The sonic anemometer was used for measuring the fluctuations of three components of wind speed, and virtual temperature, while the fluctuations in CO_2 and water vapor concentrations were measured by the gas analyzer. Both sensors were of 10-Hz time resolution. A pair of sonic anemometer and gas analyzer–model DA600 (Kaijo Co., Japan) with path length of 20 cm and model E009A (Advanet Inc., Japan) with 20 cm–was used for 1995–1998 period. These sensors were installed at the central part of the field so that the height of the open path was at 1.5 m above the ground. The horizontal distance between the open paths of sonic anemometer and gas analyzer was 15 cm. Data were recorded to the data logger CR23X (Campbell Scientific Inc., USA), and CO_2 flux as well as H_2O and sensible heat fluxes were calculated from the covariance between vertical wind speed and each components for every 20 min. The CO_2 flux derived from the covariance was corrected based on the method described in Webb et al. (1980). All CO_2 flux data are defined as positive when they are coming from the surfaces toward the atmosphere. Owing to inherent limitations of the eddy covariance method, such data obtained under rainy conditions, and calm conditions (average wind speed at 20 min basis $< 0.3\,\mathrm{m\,sec^{-1}}$) were eliminated, and hourly average values were calculated for the analyses.

5.1.3 Remote Sensing Measurements

Surface temperatures of the field were measured remotely using three infrared thermometers (Model4000, Everest Inc.). One of them was installed at the height of 3 m, and the other two were attached to booms, the height of which was adjustable. Their height was fixed to 1.5 m during bare soil conditions, but adjusted so that plant leaves were targeted during cropped periods. All three sensors were set at nadir-looking angle during bare soil periods. The field of view of sensors was 15°. The emissivity was assumed to be 0.98, since the emissivity of the plants and soil was in the range of 0.95–0.99 (Olioso, 1995). Data from the infrared thermometers were acquired by the data logger at 1-sec rate and averaged for every 20 min.

Spectral reflectance measurements were periodically obtained over the ecosystem using a hyperspectral radiometer and a hand-held radiometer. The hyperspectral one (FSFR1000, ASD) covered the wavelength range from 350 to 2,500 nm at 1 nm resolution. The hand-held radiometer (Opto-Research, Co. Ltd., Japan) was equipped with seven bands from the visible to short-wave infrared wavelength regions (560, 660, 830, 1,100, 1,200, 1,650, and 2,200 nm). Spectral observations were made from a height of 2 m above the canopy at the nadir-looking angle. The reflectance factor was calculated as a relative value to the reflectance of a $BaSO_4$ standard panel, which was

coated with Kodak Analytical Standard White Reflectance Coating (♯6080) to about 1.0 mm thickness (Inoue et al., 1998). The white panel was calibrated using the commercial reference board, Spectralon (Labsphere, USA).

5.1.4 Micrometeorological and Plant Measurements

Air temperature and relative humidity were measured using a probe HMP45C (Campbell Scientific Inc.), which contains a platinum resistance temperature detector and a capacitive relative humidity sensor. Wind speed was measured using a three-cup anemometer model 03001 (Campbell Scientific Inc.). Incident and reflected solar radiations were measured by pyranometer CM3 (Kipp & Zonen, the Netherlands). Net radiation was measured by three sensors: Q6 (REBS Inc., USA), CG3, and NR-Lite (Kipp & Zonen). Photosynthetically active photon flux density was measured by a quantum sensor LI-190SB (Li-Cor Inc.). Soil heat flux was measured by two heat flux plates PHF-01 (REBS Inc.). Soil temperature was measured by an averaging thermocouple probe TCAV (Campbell Scientific Inc.), which was installed at depths of 5 and 10 cm below the soil surface. Volumetric soil water content was measured using TDR probes (CS615, Campbell Scientific Inc.) for the soil layers at the depths of 10, 20, and 30 cm at 20 min intervals.

Plant height, wet and dry biomass, and LAI were determined about every 10 days by destructive sampling. Sampled plants were divided into stems, green leaves, roots, and dead parts. The green leaf area was measured by an area-meter AAM8 (Hayashi-denkoh Co. Ltd.).

5.2 Dynamics of CO_2 Flux Over Agricultural Field

Fig. 4 shows the typical seasonal changes of ESF_{CO_2} and plant growth during the soybean cropping and postcropping periods in 3 years. The ESF_{CO_2} consists of photosynthesis and respiration of plant and microbial respiration. The SSF_{CO_2} represents the respiration of microorganisms alone during the bare soil periods, while it includes root respiration under vegetated conditions. During the early period with low LAI values, the ESF_{CO_2} was positive and the patterns of diurnal change were similar to those during the postcropping period (bare soil conditions). The diurnal pattern of ESF_{CO_2} during some selected periods is shown in Fig. 5. The diurnal trend was apparently synchronized with those of solar radiation and air temperature. On the Contrary, for the growth period with high LAI, the ESF_{CO_2} showed negative values due to CO2 uptake by plant photosynthesis during the daytime, while it was positive during the nighttime. These measurements were comparable with those in previous reports (e.g., Curtin et al., 2000), and the trend of dynamic change seemed to reasonably represent the underlying mechanisms involved in the emission and uptake of CO2.

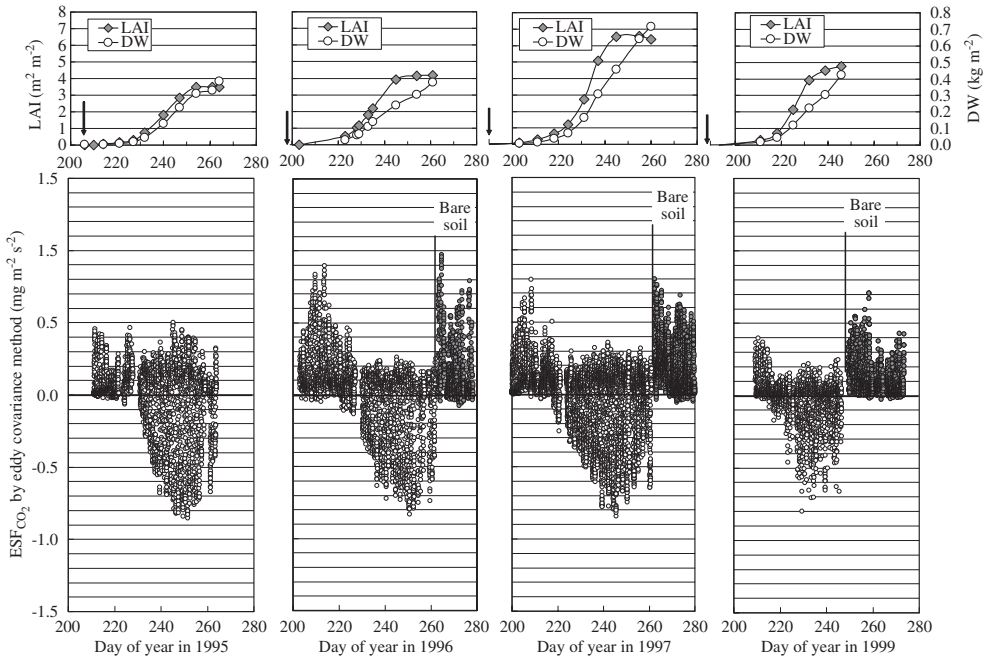

Figure 4: Seasonal change of net ecosystem exchange of CO_2 flux (ESF_{CO_2}) and crop growth variables; leaf area index (LAI) and dry biomass (DW). Examples are from soybean cropping periods in year 1995, 1996, 1997, and 1999. Vertical arrows indicate the time of seeding.

5.3 Soil CO_2 Efflux and Remotely Sensed Surface Temperature

As described in the previous section, CO_2 efflux from the soil surface has been expressed as a function of soil temperature, soil moisture, or air temperature (Grant and Rochette, 1994; Maisongrande et al., 1995; Nakadai et al., 1996). Nevertheless, since the activity of soil microorganisms is related to temperature, water, oxygen, and organic matter in the soil (Paul and Clark, 1989), it may be related to remotely sensed data in the optical, thermal, or microwave domains via information on the color, temperature, and water content of the soil, as well as on vegetation coverage. The present experimental study (Inoue et al., 2004) can be the first to report that remote sensing information may be used directly to estimate the SSF_{CO_2}.

Since it has been one of the important issues to quantify the dynamics of the SSF_{CO_2}, this study first focused on the relationship between remotely sensed information and the ESF_{CO_2} under bare soil conditions (= SSF_{CO_2}). The relationship of the SSF_{CO_2} with air temperature, soil temperature, soil water content, and remotely sensed surface temperature were investigated based on their hourly average data (Fig. 6). Soil temperatures for the 5–10-cm

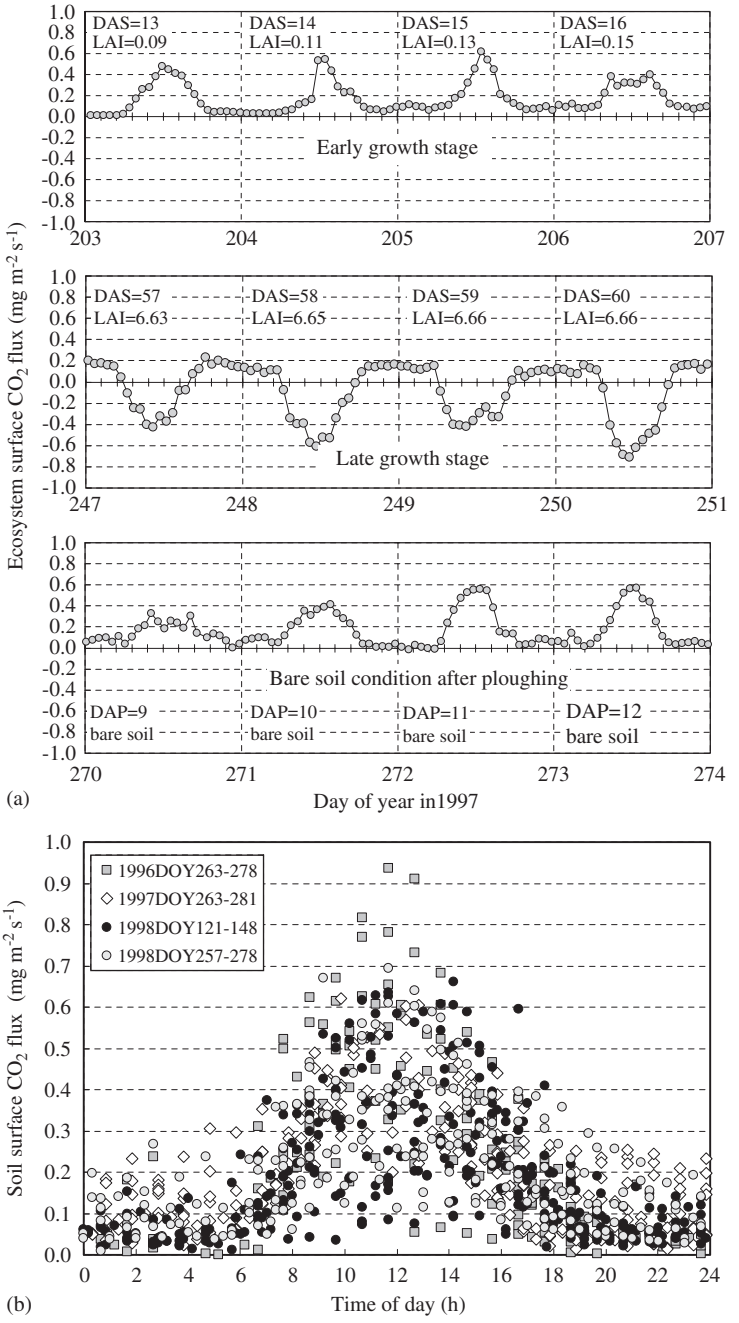

Figure 5: Typical time course changes of ecosystem surface CO_2 flux (ESF_{CO_2}) over soybean canopy and bare field estimated by eddy covariance method (a). Soil surface CO_2 flux (SSF_{CO_2}) under bare soil conditions is indicated in the time of day axis (b). DAS, DAP, and LAI are days after seeding, days after ploughing, and leaf area index, respectively (Inoue et al., 2004) (For colour version, see Colour Plate Section).

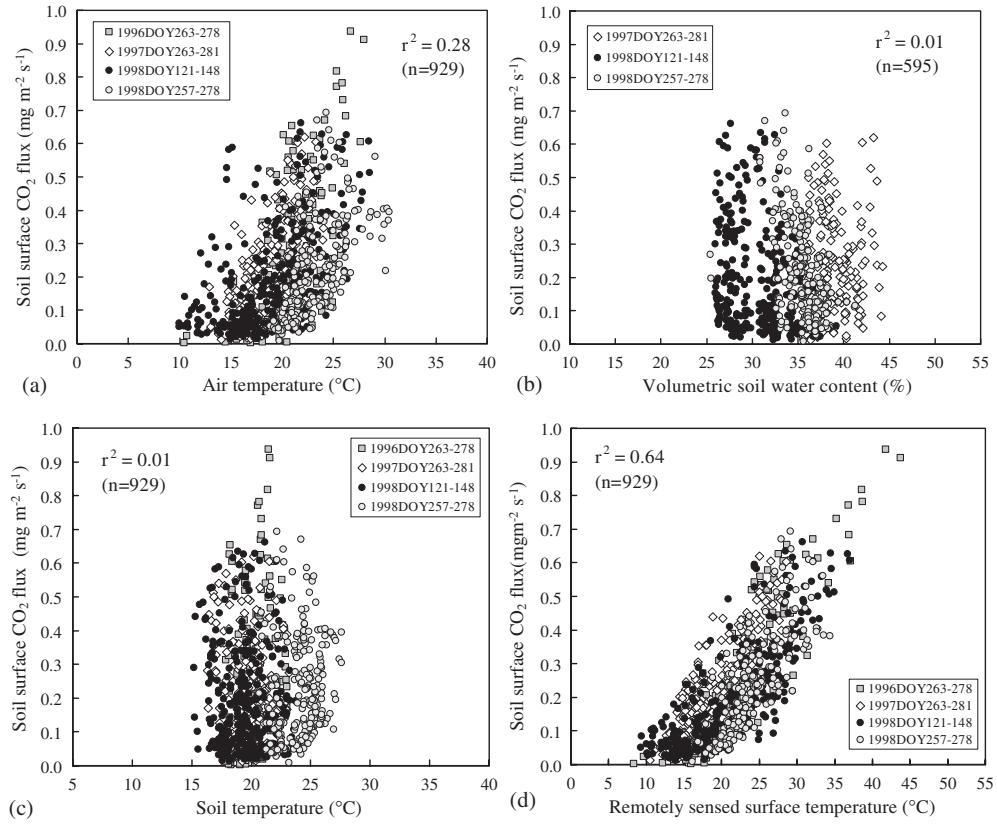

Figure 6: Relationship of SSF_{CO_2} under bare soil conditions with (a) air temperature, (b) soil water content of the top 10-cm layer, (c) soil temperature at depth of 5–10 cm, and (d) remotely sensed surface temperature. Number of data for (b) was less than for the others because less availability of soil moisture measurements (Inoue et al., 2004).

layer obtained by the averaging thermocouple probe, averaged temperatures from the three infrared thermometers, and volumetric soil water contents measured by the TDR probe for the depth of 10 cm were used for the analysis. Correlation coefficients are indicated in Fig. 6 for reference since no specific curve was inferred from the data points. The remotely sensed surface temperature had the highest correlation coefficient ($r^2 = 0.64$; $n = 929$) with the SSF_{CO_2} flux over the soil surface. The next highest was air temperature ($r^2 = 0.28$), and the other two had poor correlation ($r^2 = 0.01$). The effect of soil moisture on microorganism respiration or SSF_{CO_2} has been reported to be positive or negative, but there was no obvious relationship in the range of our data set likewise in some previous reports (Wagai et al., 1998). The effect of soil moisture may be obscured presumably because of two contrary roles in

the activity of soil microorganisms; soil moisture is required as it provides the soluble part of organic matter to microorganisms, but increasing moisture may have a negative effect on oxygen availability for microorganisms in the soil pore space (Paul and Clark, 1989).

It was obvious that the SSF_{CO_2} changes dynamically during a day due to microenvironment such as soil and atmospheric conditions, which may be most clearly detected by remotely sensed surface temperature. On the Contrary, the effect of soil moisture and soil temperature on the SSF_{CO_2} was not significant in our analysis, presumably because the analysis was based on hourly data while they changed much slower than air and soil surface temperature. In general, the time response is fastest in the soil surface temperature and getting slower in air temperature, soil temperature, and soil water content in this order. Therefore, soil temperature and soil water content might be better correlated with the SSF_{CO_2} in long-term comparisons (e.g. Nakadai et al., 1996). The time response of SSF_{CO_2} depends upon the reaction rate of microorganisms to temperature, moisture, and oxygen concentrations in the soil, as well as upon the physical processes of CO_2 transfer through the soil pore. The key factors in the physical processes are the differential of CO_2 concentration between the atmosphere and soil pore, as well as the differential of air pressure between them. The pressure differential is affected by air temperatures near the soil surface and within the soil, wind speed (especially, gustiness), rainfall, and soil compaction. Under open field conditions, these conditions all affect the dynamic change of SSF_{CO_2}, which must be the major reason for the data scatters in figures. Nevertheless, the high correlation between soil surface temperature and SSF_{CO_2} suggests that the CO_2 transfer from the soil surface is strongly related to the surface temperature of the soil, presumably due to the changes in microbial activity, air temperature in the soil pore near the surface, and turbulent conditions adjacent to the soil surface. Daily or monthly averages of soil temperature (or air temperature) are sometimes used for rough estimation of SSF_{CO_2} at regional or global scales (e.g. Potter et al., 1993; Maisongrande et al., 1995). However, information on the dynamic change of SSF_{CO_2} at high temporal resolution is useful for more mechanistic understanding of the biophysical processes in the field, as well as for more accurate estimation of ESF_{CO_2} using dynamic simulation models such as SVAT models (Olioso et al., 2001) where the temporal resolution is often shorter than 1 h.

Although the SSF_{CO_2} depends on several environmental and soil-related parameters as discussed previously, it is well known that temperature is the dominant factor determining the activity of microorganisms, and it was obvious that the soil surface temperature is most highly correlated with the SSF_{CO_2}. Hence, we applied the following Q_{10} function for more generalized

understanding and prediction:

$$SSF_{CO_2} = aQ_{10}^{(T_{IR}-20)/10} - b \tag{15}$$

where SSF_{CO_2} is the CO_2 flux over the soil surface, Q_{10} is the temperature coefficient, T_{IR} is the remotely sensed surface temperature (°C), and a and b are parameters, respectively. The SSF_{CO_2} was better estimated by the Q_{10} function from the remotely sensed surface temperature ($r^2 = 0.66$, RMSE = 0.098) than by the single correlation (Fig. 7). The Q_{10} coefficient was estimated to be 1.47, which was between the values for the physical and biochemical reactions. The critical temperature at which the SSF_{CO_2} approached zero was estimated to be 10.0°C, which may be an apparent lowest limit for the microbial activity. Some part of variation should also be caused by experimental errors in both flux and temperature measurements. Nevertheless, a large number of data from different seasons and years show that the equation represents a robust relationship between the remotely sensed surface temperature and the SSF_{CO_2} under bare soil conditions. From a theoretical point of view, the contents of both moisture and organic matter in the soil would affect the SSF_{CO_2}, which may be incorporated in the Q_{10} and the two parameters (a and b). We attempted to include the effect of soil water content in these coefficients, but no significant improvement was obtained in the estimation of SSF_{CO_2}.

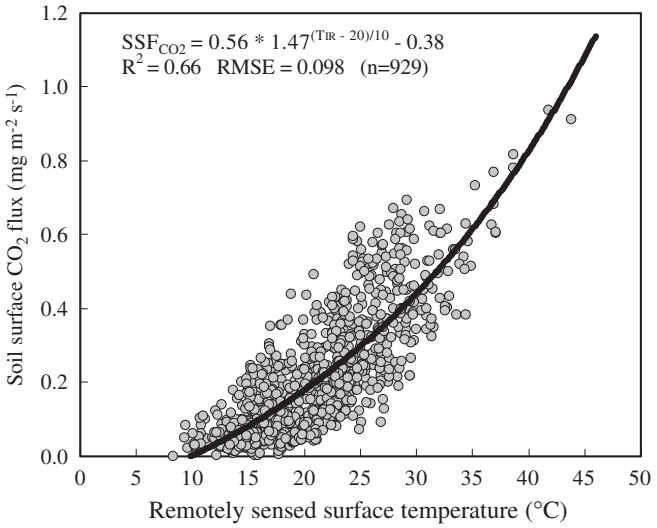

Figure 7: Relationship between soil surface CO_2 flux (SSF_{CO_2}) under bare soil conditions and remotely sensed surface temperature expressed by a Q_{10} function (Inoue et al., 2004).

It is straightforward to estimate the soil surface temperature directly by remote sensing under bare or sparely vegetated conditions, but vegetation coverage may have to be known at the same time for wide area applications. For this purpose, optical remote sensing data may be used; the average value of NDVI for bare soil surfaces was 0.178 with a standard deviation of 0.027, while it exceeded 0.5 even at a low value of LAI such as 0.5. Therefore, it may be possible to clearly detect bare (or sparsely vegetated) areas by optical remote sensing.

6 Predicting Dynamic Change of Biomass and Ecosystem CO_2 Flux based on Synergy of Remotely Sensed Data and A SVAT Model

6.1 The SVAT Model

We used a SVAT model, ISBA–Ags (Calvet et al., 1998). The original version of the 0model, ISBA (interactions between soil, biosphere and atmosphere) was developed at Météo-France for being implemented as a land-surface scheme in atmospheric weather forecast model and GCM (Noilhan and Mahfouf, 1996). This model solves the surface energy balance and the soil water balance at a 5-min time step. The soil is described by one bulk reservoir corresponding to the maximum root zone (including a thin surface layer and regardless to actual root development). The main surface variables simulated by the model are the surface temperature, the soil moisture in the root zone, and the energy fluxes. The ISBA–Ags has incorporated a physiological submodel to describe photosynthesis and its coupling with stomatal resistance at the leaf level, by adding three parameters; leaf life expectancy, effective biomass per unit leaf area, and a mesophyll conductance. The stomatal conductance is expressed as a function of radiation, temperature, vapor-pressure deficit, and soil moisture. The model requires meteorological variables, albedo, minimum stomatal resistance, LAI and vegetation height, soil texture, wilting point, and field capacity. The computed net vegetation assimilation is used to feed a simple growth submodel and to predict the density of the vegetation cover. Thus, the model is able to simulate water budget, energy and mass fluxes (CO_2, sensible and latent heat fluxes, etc.), and LAI in response to changes in the environmental conditions (precipitation, irrigation, water storage of the soil moisture in the root-zone, atmospheric CO_2 concentration, etc.).

The model was carefully parameterized with various data sets of comprehensive soil, plant, and meteorological measurements. We further combined the quantitative relationships between canopy surface temperature and SSF_{CO_2} with the model (Inoue et al., 2003). We assumed that the surface

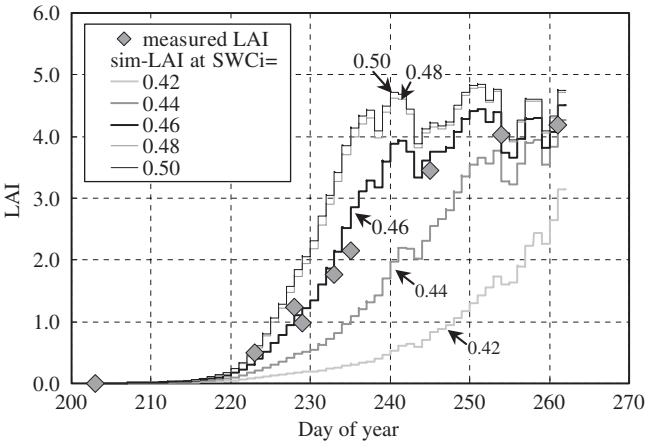

Figure 8: Simulation results of the SVAT model at different values of initial soil water content (SWCi).

temperature can be used for estimating SSF_{CO_2} not only under bare or sparsely vegetated conditions but also under densely vegetated plant conditions because the soil surface temperatures get closer to the canopy temperature accordingly with increasing vegetation coverage.

The performance of the model was excellent provided all necessary inputs and parameters were available; however, the simulation results by the coupled model proved to be sensitive to the input variables such as initial soil water content (Fig. 8), while the soil moisture condition is one of the most important but difficult input variables to be estimated at regional scales. That is, simulation results by the model alone are subject to uncertainty if the thorough set of input data is unavailable.

6.2 Performance of the Synergy

The information on vegetation coverage or LAI is essential for estimating both energy and CO_2 fluxes from a plant canopy. We derived an intimate relationship between LAI and NDVI from our experimental data for over 6 years (Fig. 9). The relationship was consistent and robust for the years. The effects of the other plant conditions (leaf angle, etc.) and measuring configurations (sun elevation, etc.) on the relationship were also examined using a canopy reflectance model SAIL+PROSPECT (Jacquemoud, 1993), which indicated the reliability of the relationship. We incorporated this relationship between NDVI and LAI into the SVAT model so that remote sensing measurements can be used in the parameterization process. It was confirmed that NDVI values could be accurately simulated as long as the SVAT model was well calibrated. Consequently, the coupled model was able

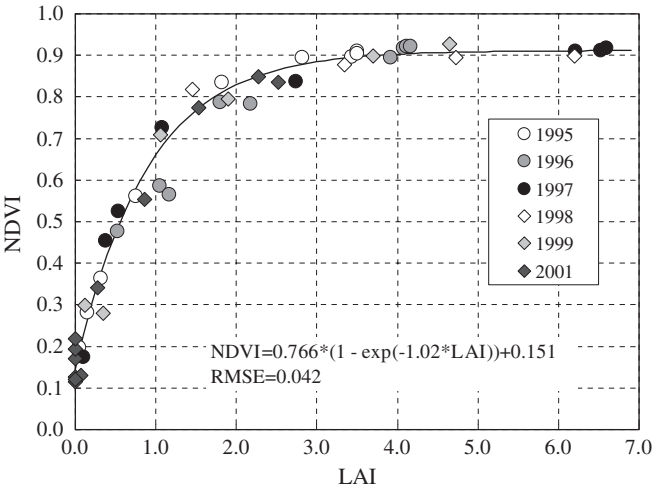

Figure 9: Relationship between leaf area index and spectral index NDVI in soybean canopies.

to simulate the surface temperature, NDVI as well as all components of ecosystem CO_2 fluxes and biomass growth.

As discussed in previous Section 6.1, the parameterization, that is, tuning of a process model with remotely sensed data is probably the most effective approach to utilize infrequent and multisource remote sensing data for estimating the dynamics of various ecosystem components (Olioso et al., 2002; Inoue, 2003). The optimization procedures of the SVAT model using the remotely sensed data are shown in Fig. 10. The structure of the SVAT model is also schematically indicated. Remotely sensed signatures in optical, thermal, and microwave domains are to be used to drive this parameterization procedure. Fig. 11 shows an example result of parameterization where the error between measured and simulated NDVI values was minimized through iterative optimization of the initial soil moisture content; the NDVI is the key parameter for optimization in this case. The initial soil moisture content was assumed to be unknown since it is not routinely available but one of the most important input data to properly run the SVAT model. After parameterization, the NDVI was best simulated with the initial soil moisture of 0.456, which was nearly equal to the independently measured value of soil moisture, 0.46. The dynamic changes in SSF_{CO_2}, net photosynthesis, and their sum ESF_{CO_2}, as well as the plant growth were also simulated for the entire growth period. Seasonal changes of LAI and DM production agreed well with those by destructive measurements. Simulated values of net photosynthesis showed reasonable diurnal and seasonal changes during the entire period. The simulated ESF_{CO_2} was in good agreement with the independent measurements of ESF_{CO_2} by the eddy covariance method during both early and

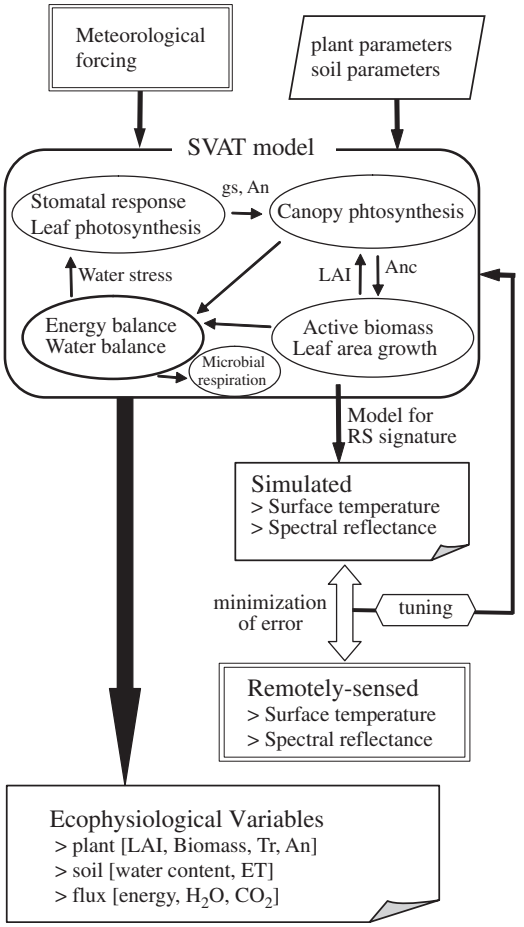

Figure 10: Structure of the SVAT model and the procedure for parameterization of the model using remotely sensed signature. The final output results (bottom) can be derived after tuning through iterative optimization of parameter or state variables. LAI: leaf area index; gs: stomatal conductance; An: leaf net photosynthesis; Anc: canopy net photosynthesis; Tr: transpiration; ET: Evapotranspiration; RS: remote sensing.

late growth stages. Simulation results of canopy transpiration and evapotranspiration also agreed well with those measurements by stem heat balance method and eddy covariance method, respectively. Furthermore, the simulated and measured canopy surface temperatures agreed quite well each other, which suggests that remotely sensed canopy temperature will also be used for calibration of the SVAT model instead of optical measurements. Optimization trials with various sets of remote sensing measurements suggested that a set of only a few remote sensing measurements could have a significant effect on improvement of simulation results.

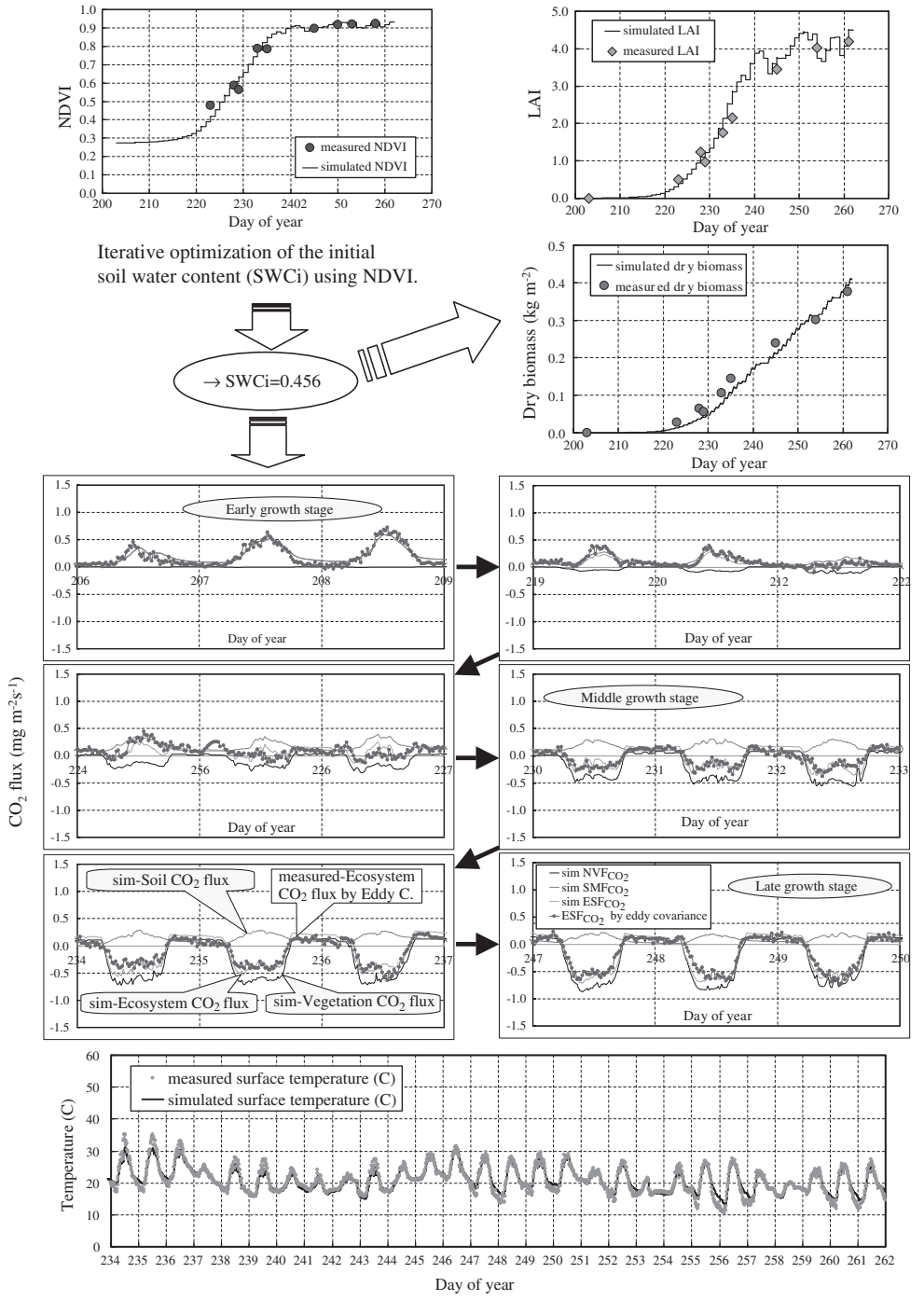

Figure 11: Dynamic change of ecosystem CO_2 (ESF_{CO_2}) flux estimated by the synergy of remote sensing and process model – a case study for soybean field. NVF_{CO_2}: net vegetation CO_2 flux; SMF_{CO_2}: soil microbial CO_2 flux (For colour version, see Colour Plate Section).

7 Conclusions

Three decades of remote sensing studies have found a range of significant relationships between remotely sensed information and ecophysiological variables. The spectral indices such as NDVI, based on only two wavelengths, are quite simple but useful for geospatial applications. A case study based on airborne remote sensing data demonstrated that the NDVI among various VIs might be useful enough for a rough assessment of plant productivity at fine spatial resolution.

Up-to-date investigations on remote sensing signatures from hyperspectral and microwave sensors are providing new findings that may be used for estimation of plant photosynthesis, pigments, chemical components, canopy geometry, etc., although some of them need further investigation or validation. Our study also showed a significant relationship between remotely sensed surface temperature and SSF_{CO_2}. This may extend the opportunities for applications of remotely sensed surface temperature to investigations of CO_2 transfer processes near the soil surface, as well as to quantitative assessment of ESF_{CO_2}.

Our case study clearly demonstrated that a synergy of remote sensing data and a SVAT model was effective for estimating important ecosystem variables such as biomass growth, water, and ecosystem CO_2 fluxes. Simulated ESF_{CO_2} agreed nicely with those measured by eddy covariance method, while simulated biomass agreed well with independent measurements. A set of only a few remote sensing measurements had a significant effect on improvement of simulation results. Remotely sensed surface temperature as well as spectral reflectance may be useful to effectively tune the process-based model. This synergistic approach may be suitable especially in utilizing infrequent remote sensing data for dynamic estimation of biophysical functioning of the ecosystems. Another advantage for this approach is that a wide range of remotely sensed signatures in optical, thermal and microwave domains can be used to drive this parameterization procedure. It is strongly recommended to include remote sensing measurements in agricultural, ecological, and geophysical field experiments.

References

Asrar, G., Kanemasu, E. T., Jackson, R. D., Pinter, P. J.Jr., 1985. Estimation of total above-ground phytomass production using remotely sensed data. Remote Sensing of Environment 17, 211–220.

Asrar, G., (Ed.), 1989. Estimation of plant-canopy attributes from spectral reflectance measurements. In: Theory and Application of Optical Remote Sensing. Wiley Interscience, New York, pp. 1–733.

Attema, E. P. W., Ulaby, F. T., 1978. Vegetation modeled as a water cloud. Radio Science 13, 357–364.

Baret, F., Guyot, G., 1991. Potentials and limits of vegetation indices for LAI and APAR assessment. Remote Sensing of Environment 35, 161–173.

Bouman, B. A. M., 1992. Linking physical remote sensing model with crop growth simulation models, applied for sugar beet. International Journal of Remote Sensing 13, 2565–2581.

Bouman, B. A. M., Hoekman, D. H., 1993. Multi-temporal, multi-frequency radar measurements of agricultural crops during the Agriscatt-88 campaign in the Netherlands. International Journal of Remote Sensing 14, 1595–1614.

Brisco, B., Brown, R. J., 1998. Agricultural applications with radar. In: Henderson, F. M., Lewis, A. J. (Eds.), Principles and Applications in Imaging Radar. John Wiley & Sons, Inc., New York, pp. 381–406.

Brisson, N., Mary, B., Ripoche, D., Jeuffroy, M. H., Ruget, F., Nicoullaud, B., Gate, P., Devienne-Barret, F., Antonioletti, R., Durr, C., Richard, G., Beaudoin, N., Recous, S., Tayot, X., Plenet, D., Cellier, P., Machet, J. M., Meynard, J. M., Delecolle, R., 1998. STICS: A generic model for the simulation of crops and their water and nitrogen balances. I. Theory and parameterization applied to wheat and corn. Agronomie 18, 311–346.

Calvet, J. C., Noihan, J., Roujean, J. L., Bessemoulin, P., Cabelguenne, M., Olioso, A., Wigneron, J. P., 1998. An interactive vegetation SVAT model tested against data from six contrasting sites. Agricultural and Forest Meteorology 92, 73–95.

Clevers, J. G. P. W., 1989. The application of a weighted infrared-red vegetation index for estimating leaf area index. Remote Sensing of Environment 29, 25–37.

Clevers, J. G. P. W., Buker, C., van Leeuwen, H. J. C., Bouman, B. A. M., 1994. A framework for monitoring crop growth by combining directional and spectral remote sensing information. Remote Sensing of Environment 50, 161–170.

Combal, B., Baret, F., Weiss, M., Trubuil, A., Mace, D., Pragnere, A., Myneni, R., Knyazikhin, Y., Wang, L., 2003. Retrieval of canopy biophysical variables from bidirectional reflectance using prior information to solve the ill-posed inverse problem. Remote Sensing of Environment 84, 1–15.

Curtin, D., Wang, H., Selles, F., McConkey, B. G., Campbell, C. A., 2000. Tillage effects on carbon fluxes in continuous wheat and fallow-wheat rotations. Soil Science Society of American Journal 64, 2080–2086.

Daughtry, C. S. T., Gallo, K. P., Bauer, M. E., 1983. Spectral estimates of solar radiation intercepted by corn canopies. Agronomy Journal 75, 527–531.

Daughtry, C. S. T., Walthall, C. L., Kim, M. S., de Colstoun, E. B., McMurtrey, J. E.III, 2000. Estimating corn leaf chlorophyll concentration from leaf and canopy reflectance. Remote Sensing of Environment 74, 229–239.

Dawson, T. P., Curran, P. J., Plummer, S. E., 1998. LIBERTY – Modeling the effects of leaf biochemical concentration on reflectance spectra. Remote Sensing of Environment 65, 50–60.

Dugas, W. A., 1993. Micrometeorological and chamber measurements of CO_2 flux from bare soil. Agricultural and Forest Meteorology 67, 115–128.

Filella, I., Amano, T., Araus, J. L., Peñuelas, J., 1996. Relationship between photosynthetic radiation-use efficiency of barley canopies and the photochemical reflectance index (PRI). Physiologia Plantarum 96, 211–216.

Filella, I., Peñuelas, J., 1994. The red edge position and shape as indicators of plant chlorophyll content, biomass and hydric status. International Journal of Remote Sensing 7, 1459–1470.

Gallaghter, N. J., Biscoe, P. V., 1978. Radiation absorption, growth and yield of cereals. Journal of Agricultural Sciences 91, 47–60.

Gastellu-Etchegorry, J. P., Guillevic, P., Zagolski, F., Demarez, V., Trichon, V., Deering, D., Leroy, M., 1999. Modeling BRF and radiation regime of boreal and tropical forests. I. BRF. Remote Sensing of Environment 68, 281–316.

Goudriaan, J., Groot, J. J., Utihol, P. W. J., 2001. Productivity of agroecosystems. In: Roy, J., Saugier, B., Mooney, H. A. (Eds.), Terrestrial Global Productivity. Academic Press, New York, pp. 301–313.

Govaerts, Y. M., Verstraete, M. M., Pinty, B., Gobron, N., 1999. Designing optimal spectral indices: a feasibility and proof of concept study. International Journal of Remote Sensing 20, 1853–1873.

Grant, R. F., Rochette, P., 1994. Soil microbial respiration at different water potentials and temperatures; theory and mathematical modeling. Soil Science Society of America Journal 58, 1681–1690.

Haboudane, D., Miller, J. R., Trembaly, N., Zarco-Tejada, P. J., Dextraze, L., 2002. Integrated narrow-band vegetation indices for prediction of crop chlorophyll content for application to precision agriculture. Remote Sensing of Environment 81, 416–426.

Hanks, J., J. T. Ritchie (Eds.), 1991, Modeling Plant and Soil Systems. American Society of Agronomy, Madison Wisconsin.

Huete, A. R., 1988. A soil-adjusted vegetation index (SAVI). Remote Sensing of Environment 25, 295–309.

Huete, A. R., Justice, C., van Leeuwen, W., 1999. MODIS Vegetation Index, MODIS algorithm theoretical basis document, NASA Goddard space flight center, Greenbelt.

Inada, K., 1985. Spectral ratio of reflectance for estimating chlorophyll content of leaf. Japanese Journal of Crop Science 54, 261–265.

Inoue, Y., 1987. Remote-monitoring of the physiological and ecological status of crops. III. Estimating remotely the transpiration in corn canopy by means of multi-sensing of infrared canopy temperature and micrometeorological data. Japanese Journal of Crop Science 56, 337–344.

Inoue, Y., 1990. Remote detection of physiological depression in crop plants with infrared thermal imagery. Japanese Journal of Crop Science 59, 762–768.

Inoue, Y., 2003. Synergy of remote sensing and modeling for estimating ecophysiological processes in plant production. Plant Production Science 6, 3–16.

Inoue, Y., Iwasaki, K., 1991. Spectral estimation of radiation absorptance and leaf area index in corn canopies as affected by canopy architecture and growth stage. Japanese Journal of Crop Science 60, 578–580.

Inoue, Y., Kimball, B. A., Jackson, R. D., Pinter, P. J.Jr., Reginato, R. J., 1990a. Remote estimation of leaf transpiration rate and stomatal resistance based on infrared thermometry. Agricultural and Forest Meteorology 51, 21–33.

Inoue, Y., Kimball, B. A., Mauney, J. R., Jackson, R. D., Pinter, P. J.Jr., Reginato, R. J., 1990b. Stomatal behavior and relationship between photosynthesis and transpiration in field-grown cotton as affected by CO_2 enrichment. Japanese Journal of Crop Science 59, 510–517.

Inoue, Y., Kurosu, T., Maeno, H., Uratsuka, S., Kozu, T., Dabrowska-Zielinska, K., Qi, J., 2002. Season-long daily measurements of multi-frequency (Ka, Ku, X, C, and L) and full-polarization backscatter signatures over paddy-rice field and their relationship with biological variables. Remote Sensing of Environment 81, 194–204.

Inoue, Y., Moran, M. S., 1997. A simplified method for remote sensing of daily canopy transpiration – A case study with direct measurements of canopy transpiration in soybean canopies. International Journal of Remote Sensing 18, 139–152.

Inoue, Y., Moran, M. S., Horie, T., 1998. Analysis of spectral measurements in rice paddies for predicting rice growth and yield based on a simple crop simulation model. Plant Production Science 1, 269–279.

Inoue, Y., Morinaga, S., Shibayama, M., 1993. Non-destructive estimation of water status of intact crop leaves based on spectral reflectance measurements. Japanese Journal of Crop Science 62, 462–469.

Inoue, Y., Morinaga, S., Tomita, A., 2000. A blimp-based remote sensing system for low-altitude monitoring of plant variables: a preliminary experiment for agricultural and ecological applications. International Journal of Remote Sensing 21, 379–385.

Inoue, Y., Olioso, A., Choi, W., 2003. Dynamic change of CO_2 flux over agricultural ecosystem and its relationship with remotely sensed thermal and optical signatures. Proceedings of the International Geoscience and Remote Sensing Symposium (IGARSS) 2003, Toulouse, France, V: 3251–3253.

Inoue, Y., Olioso, A., Choi, W., 2004. Dynamic change of CO_2 flux over bare soil field and its relationship with remotely sensed surface temperature. International Journal of Remote Sensing 25, 1881–1892.

Inoue, Y., Olioso, A., Moran, M. S., Qi, J., Choi, W., 2001. Remote sensing of photosynthetic capacity of vegetation-estimating productivity related parameters based on airborne spectral measurements. Proceeding of the 31st Conference of Journal of Remote Sensing Society of Japan, pp. 239–242.

Inoue, Y., Peñuelas, J., 2001. An AOTF-based hyperspectral imaging system for field use in ecophysiological and agricultural applications. International Journal of Remote Sensing 22, 3883–3888.

Inoue, Y., Sakuratani, T., Shibayama, M., Morinaga, S., 1994. Remote and real-time sensing of canopy transpiration and conductance – Comparison of remote and stem flow gauge methods in soybean canopies as affected by soil water status. Japanese Journal of Crop Science 63, 664–670.

Jackson, R. D., Idso, S. B., Reginato, R. J., Pinter, P. J.Jr., 1981. Canopy temperature as a crop water stress indicator. Water Resources Research 17, 1133–1138.

Jacquemoud, S., Baret, F., 1990. PROSPECT: A model of leaf optical properties spectra. Remote Sensing of Environment 34, 75–91.

Jacquemoud, S., 1993. Inversion of the PROSPECT+SAIL canopy reflectance model from AVIRIS equivalent spectra: Theoretical study. Remote Sensing of Environment 44, 281–292.

Keeling, R. F., Piper, S. C., Heimann, M., 1996. Global and hemispheric CO_2 sinks deduced from changes in atmospheric O_2 concentration. Nature 6579, 218–221.

Kicklighter, D. W., Melillo, J. M., Peterjohn, W. T., Rastetter, E. B., McGuire, A. D., Steudler, P. A., 1994. Aspects of spatial and temporal aggregation in estimating regional carbon dioxide fluxes from temperate forest soils. Journal of Geophysical Research 99 (D1), 1303–1315.

Le Toan, T., Ribbes, F., Wang, L., Floury, N., Ding, K., Kong, J., Fujita, M., Kurosu, T., 1997. Rice crop mapping and monitoring using ERS-1 data based on experiment and modeling results. IEEE Transactions on Geoscience and Remote Sensing 35, 41–56.

Leuning, R., Judd, M. J., 1996. The relative merits of open- and closed-path analyses for measurements of eddy fluxes. Global Change Biology 2, 241–253.

Maas, S. J., 1988. Use of remotely-sensed information in agricultural crop growth models. Ecological Modeling 41, 247–268.

Maisongrande, P., Ruimy, A., Dedieu, G., Saugier, B., 1995. Monitoring seasonal and interannual variations of gross primary productivity, net primary productivity and net ecosystem productivity using a diagnostic model and remotely-sensed data. Tellus 47B, 178–190.

Méthy, M., Olioso, A., Trabaud, L., 1994. Chlorophyll fluorescence as a tool for management of plant resources. Remote Sensing of Environment 47, 2–9.

Miyata, A., Leuning, R., Denmead, O. T., Kim, J., Harazono, Y., 2000. Carbon dioxide and methane fluxes from an intermittently flooded paddy field. Agricultural and Forest Meteorology 102, 287–303.

Monsi, M., Saeki, T., 1953. Uber den lichtfactor in den pflanzengesellshaften und seine bedeutung fur dir stoffproduktion. Japanese Journal of Botany 14, 22–52.

Monteith, J. L., 1977. Climate and the efficiency of crop production in Britain. Philosophical Transactions of Royal Society of London 281, 277–294.

Moran, M. S., Clarke, T. R., Inoue, Y., Vidal, A., 1994. Estimating crop water deficit using the relation between surface–air temperature and spectral vegetation index. Remote Sensing of Environment 49, 246–263.

Moran, M. S., Jackson, R. D., 1991. Assessing the spatial distribution of evapotranspiration using remotely sensed inputs. Journal of Environmental Quality 20, 725–737.

Moran, M. S., Maas, S. J., Pinter, P. J.Jr., 1995. Combining remote sensing and modeling for estimating surface evaporation and biomass production. Remote Sensing Review 12, 335–353.

Moulin, S., Bondeau, A., Delecolle, R., 1998. Combining agricultural crop models and satellite observations: From field to regional scales. International Journal of Remote Sensing 19, 1021–1036.

Myneni, E. B., Williams, D. L., 1994. On the relationship between FAPAR and NDVI. Remote Sensing of Environment 49, 200–211.

Myneni, R. B., Maggion, S., Iaquinta, J., Privette, J. L., Gobron, N., Pinty, B., Kimes, D. S., Verstraete, M. M., Williams, D. L., 1995. Optical remote sensing of vegetation: modeling, caveats and algorithms. Remote Sensing of Environment 51, 169–188.

Nagler, P. L., Inoue, Y., Glenn, E. P., Russ, A. L., Daughtry, C. S. T., 2003. Cellulose absorption index (CAI) to quantify mixed soil-plant litter scenes. Remote Sensing of Environment 87, 310–325.

Nakadai, T., Koizumi, H., Bekku, Y., Totsuka, T., 1996. Carbon dioxide evolution of an upland rice and barley, double cropping field in central Japan. Ecological Research 11, 217–227.

Nilsson, H. E., 1991. Hand-held radiometry and IR-thermography of plant diseases in field plot experiments. International Journal of Remote Sensing 12, 545–557.

Noilhan, J., Mahfouf, J.-F., 1996. The ISBA land surface parameterization scheme. Global Planetary Changes 13, 145–159.

Norman, J. M., Kucharik, C. J., Gower, S. T., Baldocchi, D. D., Crill, P. M., Rayment, M., Savage, K., Striegl, R. G., 1997. A comparison of six methods for measuring soil-surface carbon dioxide fluxes. Journal of Geophysical Research 102, 28771–28777.

Olioso, A., 1995. Estimating the difference between brightness and surface temperatures for a vegetal canopy. Agricultural and Forest Meteorology 72, 237–242.

Olioso, A., Chauki, H., Courault, D., Wigneron, J. P., 1999. Estimation of evapotranspiration and photosynthesis by assimilation of remote sensing data into SVAT models. Remote Sensing of Environment 68, 341–356.

Olioso, A., Inoue, Y., Demarty, J., Wigneron, J. P., Braud, I., Ortega-Farias, S., Lecharpentier, P., Ottle, C., Calvet, J.-C., Brisson, N., 2002. Assimilation of remote sensing data into crop simulation models and SVAT models. Proceedings on International Symposium on Recent Advances in Quantitative Remote Sensing 1, 329–338.

Olioso, A., Inoue, Y., Wigneron, J. P., Ortega-Farias, S., Lecharpentier, P., Parde, M., Calvet, J. C., Inizan, O., 2001. Using a coupled crop-SVAT model to assess crop canopy processes from remote sensing data. Proceedings of the International Geoscience and Remote Sensing Symposium (IGARSS) 2001, VII, pp. 3006–3011.

Paul, E. A., Clark, F. E., 1989. Soil Microbiology and Biochemistry. Academic Press, New York, USA.

Penning de Vries, F. W. T., H. H. van Laar (Eds.), 1982, Simulation of plant growth and crop production. Pudoc, Wageningen.

Peñuelas, J., Inoue, Y., 1999. Reflectance indices indicative of changes in water and pigment content of peanut and wheat leaves. Photosynthetica 36, 355–360.

Peñuelas, J., Inoue, Y., 2000. Reflectance assessment of canopy CO_2 uptake. International Journal of Remote Sensing 21, 3353–3356.

Pinter, P. J.Jr., Kimball, B. A., Mauney, J. R., Hendrey, G. R., Lewin, K. F., Nagy, J., 1993. Effects of free-air carbon dioxide enrichment on PAR absorption and conversion efficiency by cotton. Agricultural and Forest Meteorology 70, 209–230.

Pinty, B., Verstraete, M. M., 1992. GEMI: A non-linear index to monitor global vegetation from satellites. Vegetatio 101, 15–20.

Potter, C. P., Randerson, J. T., Field, C. B., Matson, P. A., Vitousek, P. M., Mooney, H. A., Klooster, S. A., 1993. Terrestrial ecosystem production: a process model based on global satellite and surface data. Global Biogeochemical Cycles 7, 811–841.

Prevot, L., Campion, I., Guyot, G., 1993. Estimating surface soil moisture and leaf area index of a wheat canopy using a dual-frequency (C and X bands) scatterometer. Remote Sensing of Environment 46, 331–339.

Qi, J., 2001. Interpretation of spectral vegetation indices and their relationship with biophysical variables. Proceedings of the NIAES-STA International Workshop Crop Monitoring and Prediction at Regional Scales, 127–139.

Qi, J., Cabot, F., Moran, M. S., Dedieu, G., 1995. Biophysical parameter estimations using multidirectional spectral measurements. Remote Sensing of Environment 54, 71–83.

Qi, J., Chehbouni, A., Huete, A. R., Kerr, Y., Sorooshian, S., 1994. A modified soil adjusted vegetation index (MSAVI). Remote Sensing of Environment 48, 119–126.

Rosema, A., Snel, J. F. H., Zahn, H., Buurmeijer, W. F., Van Hove, L. W. A., 1998. The relation between laser-induced chlorophyll fluorescence and photosynthesis. Remote Sensing of Environment 65, 143–154.

Ruimy, A., Dedieu, G., Saugier, B., 1996. TURC: A diagnostic model of continental gross primary productivity and net primary productivity. Global Biogeochemical Cycles 10, 269–285.

Schimel, D. S., Melillo, J., Tian, H., McGuire, A. D., Kicklighter, D., Kittel, D., Rosenbloom, N., Running, S., Thornton, P., Ojima, D., Parton, W., Kelly, R., Sykes, M., Neilson, R., Rizzo, B., 2000. Contribution of increasing CO_2 and climate to carbon storage by ecosystems in the United States. Science 287, 2004–2006.

Seguin, B., Itier, B., 1983. Using midday surface temperature to estimate daily evapotranspiration from satellite thermal IR data. International Journal of Remote Sensing 4, 371–383.

Sellers, P. J., 1987. Canopy reflectance, photosynthesis and transpiration. II. The role biophysics in the linearity of their interdependence. Remote Sensing of Environment 21, 143–183.

Shibayama, M., Akiyama, T., 1986. A spectroradiometer for field use. VII. Radiometric estimation of nitrogen levels in filed rice canopies. Japanese Journal of Crop Science 55, 433–438.

Shibayama, M., Akiyama, T., 1989. Seasonal visible, near-infrared and mid-infrared spectra of rice canopies in relation to LAI and above-ground dry phytomass. Remote Sensing of Environment 27, 119–127.

Shibles, R. M., Weber, C. R., 1966. Interception of solar radiation and dry matter production by various soybean planting patterns. Crop Science 6, 55–59.

Steinmetz, S., Guerif, M., Delecolle, R., Baret, F., 1990. Spectral estimates of the absorbed photosynthetically active radiation and light-use efficiency of a winter wheat crop subjected to nitrogen and water deficiencies. International Journal of Remote Sensing 11, 1797–1808.

Takebe, M., Yoneyama, T., Inada, K., Murakami, T., 1990. Spectral reflectance of rice canopy for estimating crop nitrogen status. Plant and Soil 122, 295–297.

Thomas, J. R., Namken, J. L., Oerther, G. F., Brown, R. G., 1971. Estimating leaf water content by reflectance measurements. Agronomy Journal 63, 845–847.

Tucker, C. J., Vanpraet, C., Boerwinkel, E., Gaston, A., 1983. Satellite remote sensing of total dry matter production in the Senegalese Sahel. Remote Sensing of Environment 13, 461–474.

Ulaby, F. T., Allen, C. T., Eger, G., Kanemasu, E. T., 1984. Relating the microwave backscattering coefficient to leaf area index. Remote Sensing of Environment 14, 113–133.

Verhoef, W., 1984. Light scattering by leaf layers with application to canopy reflectance modeling: the SAIL model. Remote Sensing of Environment 16, 125–141.

Veroustraete, F., Patyn, J., Myneni, R. B., 1996. Estimating net ecosystem exchange of carbon using the normalized difference vegetation index and an ecosystem model. Remote Sensing of Environment 58, 115–130.

Wagai, R., Brye, K. R., Gower, S. T., Norman, J. M., Bundy, L. G., 1998. Land use and environmental factors influencing soil surface CO_2 flux and microbial biomass in natural and managed ecosystems in southern Wisconsin. Soil Biology and Biochemistry 30, 1501–1509.

Webb, E. K., Pearman, G. I., Leuning, R., 1980. Correction for flux measurements for density effects due to heat and water vapor transfer. Quarterly Journal of Royal Meteorological Society 106, 85–100.

Weiss, M., Troufleau, D., Baret, F., Chauki, H., Prevot, L., Olioso, A., Bruguier, N., Brisson, N., 2001. Coupling canopy functioning and radiative transfer models for remote sensing data assimilation. Agricultural and Forest Meteorology 108, 113–128.

Widén, B., 2002. Seasonal variation in forest-floor CO_2 exchange in a Swedish coniferous forest. Agricultural and Forest Meteorology 111, 283–297.

Wiegand, C. L., Richardson, A. J., Jackson, R. D., Pinter, P. J.Jr., Aase, J. K., Smika, D. E., Lautenschlager, L. F., McMurtrey, J. E.III, 1986. Development of agrometeorological crop model inputs from remotely sensed information. IEEE Transactions on Geoscience and Remote Sensing GE 24 (1), 90–97.

Wigneron, J.-P., Ferrazzoli, P., Calvet, J.-C., Kerr, Y., Bertuzzi, P., 1999. A parametric study on passive and active microwave observations over a soybean crop. IEEE Transactions on Geoscience and Remote Sensing 37, 2728–2733.

Yoder, B. J., Pettigrew-Crosby, R. E., 1995. Predicting nitrogen and chlorophyll content and concentrations form reflectance spectra (400–2500 nm) at leaf and canopy scales. Remote Sensing of Environment 53, 199–211.

This page intentionally left blank

Chapter 14

Absorption of Photosynthetically Active Radiation, Dry-matter Production, and Light-use Efficiency of Terrestrial Vegetation: A Global Model Simulation

Akihiko Ito[1,2,*] and Takehisa Oikawa[3]

[1]*Frontier Research Center for Global Change, Japan Agency for Marine-Earth Science and Technology, 3173-25 Showa-machi, Kanazawa-ku, Yokohama, Kanagawa 236-0001, Japan*
[2]*National Institute for Environmental Studies, Onogawa 16–2, Tsukuba, Ibaraki 305–8506, Japan*
[3]*Institute of Biological Sciences, University of Tsukuba, Tennoh-dai 1-1-1, Tsukuba, Ibaraki 305-8572, Japan*

Abstract

Light-use efficiency (*LUE*, carbon assimilation per unit light absorption) is a key parameter for global mapping of the terrestrial carbon cycle by remote sensing and modeling approaches. We simulated the terrestrial carbon cycle with a process-based model (Sim-CYCLE) to capture the spatial and temporal distributions of light absorption, photosynthetic carbon assimilation, and light-use efficiency. The global simulation was conducted for the years 1901–2000 at a spatial resolution of $0.5^\circ \times 0.5^\circ$. For the years 1981–2000, the global annual gross primary production (*GPP*) and net primary production (*NPP*) were estimated as 130.7 and 62.5 Pg y^{-1}, respectively, at the cost of absorbed photosynthetically active radiation (*APAR*) of 185.6×10^{21} J y^{-1}. We calculated the global average *LUEs* for *GPP* and *NPP* as 0.70 and 0.34 g C MJ^{-1}, respectively. The long-term simulation implied that global *LUE* has increased from 0.66 and 0.32 g C MJ^{-1} in the 1900s, because elevated atmospheric CO_2

*Corresponding author.
E-mail address: itoh@nies.go.jp (A. Ito).

Elsevier Oceanography Series 73
Edited by H. Kawahata and Y. Awaya
ISBN: 0-444-52948-9

concentration has had a fertilization effect on terrestrial vegetation. Seasonal and latitudinal changes in *APAR*, *GPP*/*NPP*, and *LUE* were analyzed. The estimated *LUE* (for *GPP*) differed among biomes, from 1.0 g C MJ^{-1} for tropical rain forest to 0.34 g C MJ^{-1} for cool semi-desert scrub. These model results will be useful for future combination with the remote-sensing approach to achieve a more realistic mapping of the terrestrial carbon cycle.

Keywords: carbon cycle; global change; land-surface process; model analysis; vegetation productivity

1 Introduction

Climatic warming and its ramifications are among the most urgent issues regarding global environmental change. Because the carbon budget of the terrestrial ecosystem is likely to affect the progress of climatic warming, extensive research has been conducted on efforts to elucidate carbon dynamics (i.e., flows and pools) in a wide variety of terrestrial ecosystems (Running et al., 1999). Currently, the total storage of organic carbon in terrestrial ecosystems (about 2,000 Pg C [1 Pg = 10^{15} g]) is nearly three times as large as the amount of carbon present (about 760 Pg C) in atmospheric carbon dioxide (CO_2) and methane, both of which are major greenhouse gases. In addition, the annual gross carbon exchange between the atmosphere and the terrestrial ecosystems (about 120 Pg C y^{-1}) is one of the largest carbon flows in the global bio-geochemical carbon cycle (IPCC, 2001).

However, because of environmental diversity and human impact, the land surface is so heterogeneous that our ability to quantify the terrestrial carbon budget over a broad scale is far from sufficient. For example, many boreal forests undergo frequent wildfires of various intensities and extents, leading to obvious horizontal heterogeneity in net CO_2 exchange and carbon storage. The spatial scale of disturbances (m^2 to km^2) is too small to be incorporated explicitly into regional ecosystem carbon cycle models, whose mesh size is typically thousands of square kilometers. On the other hand, recent progress in remote-sensing techniques is expected to permit higher resolution mapping (m^2 to km^2) of terrestrial ecosystems in terms of their structure and function. Thus, collaborations between modeling and remote sensing will be an effective and inevitable way to achieve high-resolution mapping and analysis.

Most remote-sensing approaches concerning terrestrial functions, especially carbon assimilation and biomass production, are based on a simple relationship between the absorbed energy of photosynthetically active radiation (*APAR*) and the gross primary production (*GPP*) or net primary

production (*NPP*) (Kumar and Monteith, 1981):

$$GPP = LUE_{(GPP)} \times APAR \tag{1a}$$

$$NPP = LUE_{(NPP)} \times APAR \tag{1b}$$

The conversion coefficient represents the light-use efficiency (*LUE*) of terrestrial vegetation. There are many empirical algorithms to estimate *APAR* or its fraction (*fAPAR*) from observed optical information (spectra of reflection), which are usually represented by several vegetation indices such as the normalized difference vegetation index (NDVI) (Ruimy et al., 1994). Moreover, many models have been developed to estimate transfer, attenuation, penetration, and absorption of radiation within canopy (Myneni, 1991; Asrar et al., 1992). On the other hand, *LUE* is not only determined by physical factors, but also affected by a multitude of physiological properties; consequently, *LUE* differs among different plant types and varies with environmental conditions (Runyon et al., 1994; Turner et al., 2003). Accordingly, the parameterization of *LUE* is still a challenge for remote-sensing researchers, plant ecologists, and micro- and agro-meteorologists (Haxeltine and Prentice, 1996). Physiologically, *LUE* is termed as the quantum yield that corresponds to the initial slope of the light-photosynthesis curve. It is known to increase with increasing ambient CO_2 level and decreasing temperature, and to differ between C_3 and C_4 plants. Hence, physiological *LUE* depends on both – gain by assimilation (carboxylation) and loss by photorespiration (oxygenation). For agro-meteorology and remote-sensing studies, *LUE* is usually defined as the ratio of *NPP* to absorbed PAR energy, and is then regulated by additional complex factors specific to the canopy scale (Asner et al., 1998).

This study addresses *APAR, GPP*/*NPP*, and *LUE* on a global scale with a process-based model of the terrestrial ecosystem that considers remote-sensing applications. Recently, several studies have attempted to derive global terrestrial productivity from the *APAR–NPP* relationship (equation (1b), since satellite observations provide broad, periodic, and equally accurate data about the land surface (Potter et al., 1993; Prince and Goward, 1995; Ruimy et al., 1996; Goetz and Prince, 1999). However, in these studies, *LUE* is parameterized in rather simplified manners: e.g., with a biome-specific constant and as an empirical function of environmental variables. Ruimy et al. (1999) compared 12 global models and concluded that differences in *LUE* parameterization resulted in a significant uncertainty in estimation results. In this study, *APAR* and *GPP*/*NPP* were explicitly simulated with a model that included ecophysiological relationships, using time-series climate data from 1901 to 2000. Next, latitudinal, biome-specific,

seasonal, and interannual aspects of *LUE* were analyzed, which may carry implications for remote-sensing studies assessing vegetation activity.

2 Methods

2.1 Canopy Absorption of PAR

Absorption of instantaneous photosynthetically active radiation (*APAR*, $\mathrm{W\,m^{-2}}$) is calculated by the Lambert–Beer law (Monsi and Saeki, 1953):

$$APAR = PAR_{\mathrm{sfc}}(1.0 - \alpha)\{1.0 - \exp(-K_a \times LAI)\} \tag{2}$$

where K_a is the attenuation coefficient, α the biome-specific canopy reflectance, and *LAI* the leaf-area index estimated by the terrestrial ecosystem model (based on foliage biomass and specific leaf area). For the calculation of PAR_{sfc}, see the Appendix. Here, K_a is parameterized as a function of biome type and solar height angle φ:

$$K_a = \frac{K_{a0}}{\sin(\varphi)} \tag{3}$$

where K_{a0} is the value of the coefficient when the sun is at the zenith. In general, grass species (monocots), which have erect leaves, have lower K_{a0} (about 0.45), whereas dicotyledonous herb species and tree species have higher K_{a0} (about 0.55). Assuming that the daily variation in irradiance may be adequately approximated by a sine-square function of time, we can easily estimate the daily *APAR* ($\mathrm{MJ\ m^{-2}\ day^{-1}}$) as follows:

$$APAR_{(\mathrm{daily})} = 0.5 \times 10^{-6} \times DL \times APAR_{(\mathrm{midday})} \tag{4}$$

where *DL* is the day length (seconds).

2.2 Carbon Cycle

A simulation model, Carbon cYCle in Land Ecosystems (Sim-CYCLE), which is a process-based terrestrial model (overview in Table 1; for more details, see Ito and Oikawa, 2002), is globally applied to the simulation of vegetation productivity. In the model, the ecosystem structure is simplified into a six-compartment system (atmosphere, foliage, stem, root, litter, and humus), while 16 carbon flows represent ecosystem dynamics (growth, mortality, and reproduction) (Fig. 1).

Net primary production (*NPP*, $\mathrm{g\,C\,m^{-2}\,day^{-1}}$ or $\mathrm{y^{-1}}$) is defined as the amount of plant dry-matter production during a given period, and is

Table 1: Brief description of the processes in Sim-CYCLE (see Ito and Oikawa (2002) for details)

Process	Synopsis	Environmental dependence	Key parameters
PAR/*PPFD*	Iqbals's empirical model: diffused radiation and direct radiation are separated	Latitude, season, cloudiness	–
Net radiation	Albedo model for short-wave radiation, and empirical model for long-wave radiation.	*VPD*, surface temperature, cloudiness	Albedo, snow cover
Evapotranspiration	Penman-Monteith model is used for potential evapotranspiration, limited by available water (soil moisture and precipitation)	Temperature, wind, soil water, precipitation, *VPD*	Canopy conductance
Photosynthesis	Empirical single-leaf gas exchange is scaled up to canopy scale, based on the Monsi-Saeki theory	Temperature, soil water, *PPFD*, day-length, atmospheric CO_2	Quantum yield, light-saturated photosynthetic rate, *LAI*, light attenuation coefficient
Respiration	Two-component model (growth and maintenance) with exponential temperature response for maintenance respiration	Temperature	Specific respiration rate, temperature coefficient (Q_{10})
Allocation	Theoretically optimal *LAI* determines allocation to leaf. Allometric shoot-root proportion is considered	Indirectly on photosynthesis and leaf phenology	Optimum *LAI*, root/shoot ratio
Litterfall	Constant senescence rate and seasonal deciduousness	Temperature, precipitation (leaf phenology)	Specific mortality
Decomposition	Two-layer model (dependent on soil moisture and temperature)	Soil moisture, soil temperature	Specific decomposition rate

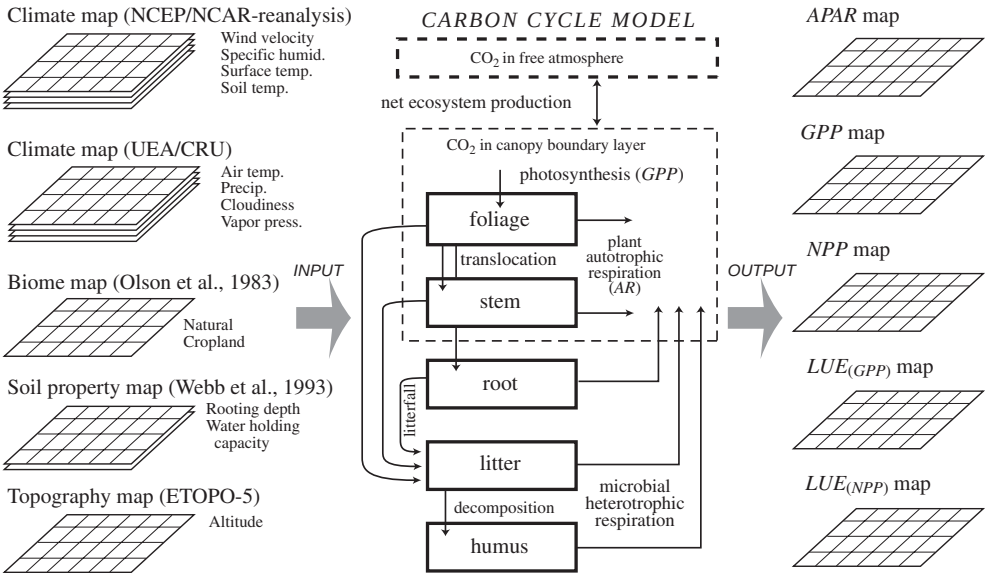

Figure 1: Operational flow of the model simulation, including schematic diagram of the carbon cycle in the terrestrial ecosystem (For colour version, see Colour Plate Section).

calculated by the CO_2 budget:

$$NPP = GPP - AR \tag{5}$$

where *GPP* is gross photosynthetic production and *AR* the autotrophic respiration. *GPP* responds to irradiance, ambient CO_2 level, temperature, vapor pressure deficit, and soil water content, while *AR* is composed of maintenance and construction components that depend on temperature and biomass growth rate, respectively.

The estimation of *GPP* is based on a method that uses Monsi–Saeki theory, by which ecophysiological findings at the single-leaf level are scaled up to the canopy level (Monsi et al., 1973; Terashima and Hikosaka, 1995). Single-leaf *LUE* (apparent quantum yield, mol CO_2 mol^{-1} photon) is defined as a constant for C_4 plants and as a variable for C_3 plants:

$$LUE_{(C_4\text{leaf})} = 0.05 \tag{6}$$

$$LUE_{(C_3\ \text{leaf})} = 0.05 \times fT_{(LUE)} \times fC_{i(LUE)} \tag{7}$$

$$fT_{(LUE)} = \frac{52.0 - T}{3.5 + 0.75(52.0 - T)} \tag{8}$$

$$fC_{i(LUE)} = \frac{C_i}{90.0 + 0.6C_i} \tag{9}$$

where T is leaf temperature (°C) and C_i the intercellular CO_2 concentration (ppmv), estimated by the stomatal gas exchange module of Sim-CYCLE. Thus, a cooler and/or higher CO_2 condition leads to a higher *LUE* for C_3 leaves owing to reduced photorespiration. The single-leaf photosynthetic rate (A, μmol CO_2 m^{-2} s^{-1}) is approximated by a rectangular hyperbolic curve:

$$A = \frac{PPFD \times LUE \times A_{sat}}{PPFD \times LUE + A_{sat}} \tag{10}$$

where *PPFD* is the photosynthetic photon flux density (μmol photons $m^{-2} s^{-1}$, see the Appendix) and A_{sat} is the light-saturated photosynthetic rate, which is a function of the intercellular CO_2 level, temperature, and soil water availability. Based on Fick's first law of gas diffusion, intercellular CO_2 concentration (C_i) is calculated as follows:

$$A = g_s(C_a - C_i) \tag{11}$$

where C_a is the ambient CO_2 level (ppmv) and g_s the stomatal CO_2 conductance (mmol CO_2 $m^{-s} s^{-1}$). Because A, g_s, and C_i are interdependent, they are obtained by a numerical method, that is, iterative calculation. Finally, to obtain the *GPP*, the single-leaf rate A is analytically integrated over the leaf-area index, taking light attenuation (equation (2)) into account:

$$GPP = \rho \int^{LAI} AdF \tag{12}$$

where ρ is a unit conversion coefficient (from μmol CO_2 to g C). Furthermore, by integrating *GPP* in equation (12)or the day length, we can obtain a formula for the daily *GPP* (see Ito and Oikawa, 2002).

Autotrophic respiration (*AR*) consists of maintenance (AR_M) and construction (AR_C) components, both of which are calculated for three plant compartments (leaf, stem, and root), separately. AR_M represents the maintenance cost of standing biomass:

$$AR_M = SAR_M \times W \times fT_{(AR)} \tag{13}$$

$$fT_{(AR)} = Q_{10}^{(T-15)/10} \tag{14}$$

where SAR_M is the specific respiration rate (g g^{-1} day^{-1}), W the standing biomass (g), T the temperature (°C), and Q_{10} a coefficient of temperature dependence. Typically, AR_M doubles for every 10°C temperature rise (i.e., Q_{10} = about 2.0); here, seasonal acclimatization of Q_{10} is additionally taken into account (see Ito and Oikawa, 2002). AR_C represents the construction

cost of new tissues from photosynthate and is proportional to the translocation rate (TL, g C m^{-2} day^{-1}):

$$AR_C = \frac{SAR_C \times TL}{(1 + SAR_C)} \tag{15}$$

where SAR_C is the specific respiration ($g\,g^{-1}$): high for leaves (about 0.5), low for stems (about 0.2), and intermediate for roots (about 0.35).

2.3 Light-use Efficiency

Canopy light-use efficiency (LUE, g C MJ^{-1}) is directly calculated from the estimated $APAR$ and productivities:

$$LUE_{(GPP)} = \frac{GPP}{APAR\ (\text{daily})} \tag{16}$$

$$LUE_{(NPP)} = \frac{NPP}{APAR\ (\text{daily})} \tag{17}$$

The canopy-scale LUE is generally lower than that of single leaves (equations (6,7)), because of the light saturation of sunny leaves and respiratory loss by non-assimilative organs (in the case of NPP). The *APAR–GPP/NPP* relationships is analyzed later.

2.4 Data and Simulation

Global simulation is performed at a spatial resolution of $0.5^\circ \times 0.5^\circ$ in longitude and latitude (58,772 grid points). The vegetation distribution is based on Olson's actual biome map (Olson et al., 1983), with a correction for the distribution of deciduous needle-leaved forest by ancillary data, in which global land-cover is classified into 32 vegetation types (Table 2) and ice sheet. At present, land-use conversion from natural vegetation to cropland is not considered. Altitude and soil properties (water-holding capacity and rooting depth) are characterized by ETOPO5 and NASA/GISS datasets (Webb et al., 1993), respectively.

The long-term mean climate condition is defined by the 38-year average (1961–1998) of the US National Centers for Environmental Prediction and the US National Center for Atmospheric Research (NCEP/NCAR) reanalysis dataset (Kistler et al., 2001) in terms of cloudiness, air temperature and humidity, precipitation, ground temperature, and wind velocity. Under the contemporary climate condition, the carbon cycle model is stabilized by iterative calculation (200–2000 years) to obtain an equilibrium state; that is, the annual net-carbon budget is balanced everywhere. Then, time-series

Table 2: Category, area, absorbed PAR (*APAR*), productivity (*GPP* and *NPP*), and light-use efficiency ($LUE_{(GPP)}$ and $LUE_{(NPP)}$) of 32 biome types, averaged over 1981–2000

		Area (10^6 km^2)	*APAR*[1]		*GPP*[2]			*NPP*[2]		
			Total	Density	Total	Density	*LUE*	Total	Density	*LUE*
1	Tropical and subtropical evergreen forest	10.4	21.5	2.6	22.0	2,107	1.02	10.9	1049	0.51
2	Tropical montane forest	1.2	2.5	2.7	2.2	1,868	0.87	1.1	961	0.45
3	Tropical and subtropical dry forest	4.7	9.9	2.9	7.3	1,547	0.74	3.7	777	0.37
4	Mid-latitude mixed woods	3.5	6.2	2.2	4.0	1,139	0.65	2.3	648	0.37
5	Mid-latitude broad-leaved forest	1.5	2.7	2.3	1.5	981	0.54	0.8	558	0.31
6	Semiarid wood or low forest	0.9	2.1	3.1	0.8	847	0.37	0.3	348	0.15
7	Coniferous forest	3.5	6.0	2.0	3.6	1,034	0.60	2.1	613	0.36
8	Southern taiga	1.6	2.4	1.8	1.1	663	0.43	0.6	393	0.26
9	Main boreal taiga (evergreen)	3.4	4.7	1.6	2.8	817	0.60	1.7	499	0.36
10	Main boreal taiga (deciduous)	2.1	2.7	1.6	1.5	716	0.56	1.0	465	0.36
11	Northern taiga (evergreen)	2.7	3.5	1.6	1.7	607	0.47	1.0	371	0.29
12	Northern taiga (deciduous)	1.6	1.7	1.5	0.9	532	0.51	0.6	349	0.34
13	Second growth woods	5.2	9.4	2.3	6.1	1185	0.65	2.9	566	0.31
14	Second growth fields	4.1	4.6	2.4	3.8	936	0.83	1.7	419	0.37
15	Succulent and thorn woods	4.0	6.2	3.0	5.2	1310	0.84	2.2	546	0.35
16	Tropical savanna, woodland	6.7	11.1	2.8	10.7	1590	0.96	4.4	658	0.40
17	Mediterranean-type dry woods	3.6	4.5	2.9	2.9	797	0.64	1.3	363	0.29
18	Heath and Moorland	0.1	0.2	2.2	0.1	748	0.74	0.1	337	0.33
19	Warm or hot shrub and grassland	17.3	18.0	2.8	14.9	863	0.83	6.3	361	0.35
20	Tibetan meadow, Siberian highland	0.8	1.2	2.2	0.4	482	0.35	0.2	262	0.19
21	Tundra	9.9	11.6	1.7	5.0	502	0.43	2.8	281	0.24
22	Wooded tundra	1.7	2.1	1.6	0.9	521	0.43	0.5	298	0.25
23	Warm or hot wetlands	1.6	3.1	2.7	2.3	1463	0.75	1.0	612	0.31
24	Cool bog and mire	1.0	1.3	1.8	0.6	660	0.49	0.3	356	0.26
25	Shore and hinterlands	1.0	1.9	2.5	1.2	1178	0.64	0.5	529	0.29
26	Cool semi-desert scrub	2.0	3.1	2.3	1.1	525	0.34	0.6	275	0.18
27	Non-polar desert	11.1	7.6	3.1	4.2	380	0.55	1.8	159	0.23
28	Non-polar sand desert	5.2	3.3	3.1	1.8	349	0.55	0.7	143	0.22
29	Paddyland	2.0	3.8	2.6	3.2	1636	0.85	1.3	670	0.35
30	Cool croplands	3.0	4.0	2.0	2.5	850	0.63	1.3	439	0.33
31	Warm croplands	13.2	20.8	2.5	13.4	1,014	0.64	6.0	450	0.29
32	Irrigated	1.6	2.1	2.8	1.1	668	0.50	0.5	286	0.21
	Total	132.3	185.6		130.7		0.70	62.5		0.34

[1]Total in 10^{21} J, density in 10^9 J (GJ) m^{-2}.
[2]Total in Pg C yr^{-1}, density in g C m^{-2} yr^{-1}, *LUE* in g C MJ^{-1}.

climate data of the University of East Anglia, Climate Research Unit (New et al., 2002) are used to simulate a transient state of the monthly carbon budget for the period from 1901 to 2000. During the experimental period, the model accounts for temporal variations in temperature, precipitation, and cloudiness, as well as the atmospheric CO_2 concentration (Keeling and Whorf, 2002). Here, however, more emphasis will be placed on the average state of vegetation productivity (between 1980s and 1990s), rather than interannual variability.

3 Results

3.1 Global Features

The carbon cycle of terrestrial ecosystems from 1901 to 2000 was simulated with Sim-CYCLE (Fig. 2). In the 1980s and 1990s, the annual average *GPP* and *NPP* were estimated to be 130.7 and 62.5 Pg C y^{-1}, respectively. Plant biomass and soil organic carbon were estimated as 481 and 1429 Pg C, respectively. However, during the 20th century, *GPP*, *NPP*, and plant biomass were estimated to have increased gradually, as atmospheric CO_2 concentration increased (Fig. 2). The temporal change in soil-carbon storage was slightly complicated, in that it decreased from the 1930s to the 1950s and then increased again from the 1960s to the 1970s. The magnitude of the soil-carbon change (about 10 Pg C) was one-third of the variation of plant biomass, and was mostly determined by the climatic variation, especially in temperature (e.g., the global mean temperature was higher in the 1930s and 1940s than in the 1920s and 1960s). On average, terrestrial vegetation received 330.4×10^{21} J of PAR, of which 56.2% (185.6×10^{21} J) was absorbed by canopy. Accordingly, the average *LUE*s for *GPP* and *NPP* were readily calculated as 0.70 and 0.34 g C MJ^{-1}, respectively. Fig. 2 shows that the estimated mean *LUE*s have gradually increased, with a small magnitude of interannual variability, although the total *APAR* has also increased. This implies that the elevated atmospheric CO_2 concentration (and to some extent climatic change) resulted in higher photosynthetic light-use efficiencies, through the CO_2 fertilization effect.

Fig. 3 shows the estimated distributions of annual *APAR*, *GPP*, and $LUE_{(GPP)}$, averaged over the 1980s and 1990s. Apparently, more PAR was absorbed by tropical and subtropical forests, except for some cloudy ones, leading to higher photosynthetic productivity. In these forests, the humid climate allows them to sustain a higher leaf area index, which absorbs a large fraction of incident solar radiation. Table 2 summarizes biome-specific aspects with respect to light-use efficiency. For example, on average, tropical rain forest absorbed 2600 MJ m^{-2} of PAR and assimilated 2107 g C m^{-2} of

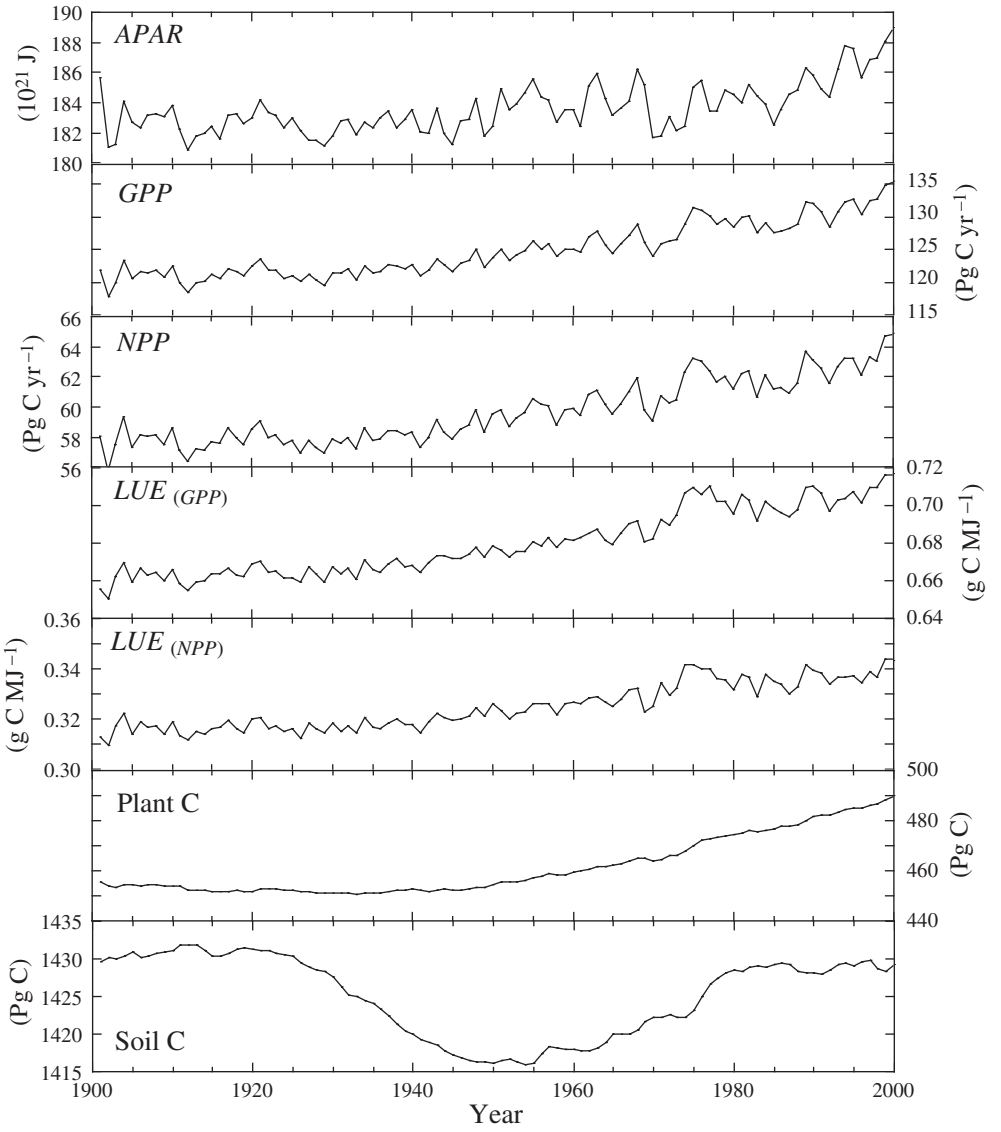

Figure 2: Interannual changes in the estimated global terrestrial processes, from 1901 to 2000: absorbed photosynthetically active radiation (*APAR*), gross primary production (*GPP*), net primary production (*NPP*), light-use efficiency (*LUE*) of *GPP* and *NPP*, and plant and soil-carbon storage.

atmospheric CO_2, annually. Because of optimal temperature and moisture conditions, the tropical rain forest showed the highest *LUE* (1.02 g C MJ^{-1} for *GPP*) among the biomes. On the other hand, cooler biomes (e.g., tundra and cool semi-desert scrub) showed lower *LUE*s (0.35 g C MJ^{-1}) because of insufficient warmth. In spite of dryness, tropical savanna showed higher *LUE*

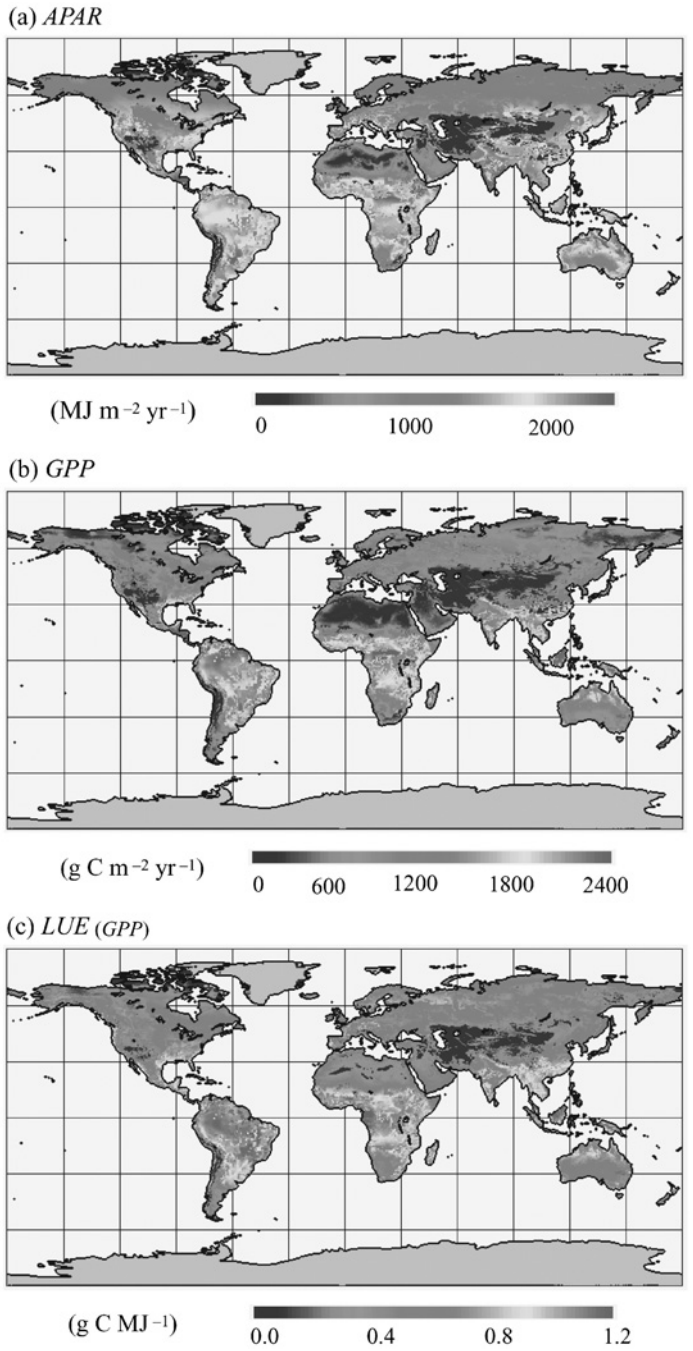

Figure 3: Estimated global distributions of (a) *APAR*, (b) *GPP*, and (c) $LUE_{(GPP)}$, averaged from 1981 to 2000 (For colour version, see Colour Plate Section).

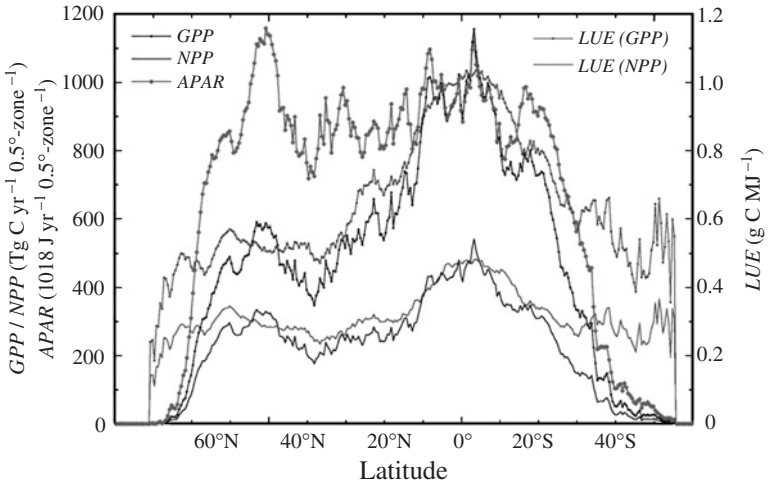

Figure 4: Latitudinal distributions of absorbed PAR (*APAR*), productivities (*GPP* and *NPP*), and light-use efficiencies ($LUE_{(GPP)}$ and $LUE_{(NPP)}$), averaged from 1981 to 2000 (For colour version, see Colour Plate Section).

($0.96\,\mathrm{g\,C\,MJ^{-1}}$ for *GPP*) because of the dominance of C_4 grass species. Fig. 4 shows the estimated latitudinal distributions of *APAR*, *GPP*/*NPP*, and *LUE*. The land area between 60°N and 20°S absorbed a comparable amount of PAR, although there are differences in land area and incident irradiance. The latitudinal distribution of *GPP* and *NPP* shows two peaks: one around 50°N and the other around the equator. Lower productivity in northern middle latitudes (around 30°N) was attributable to a broad area of arid and infertile ecosystems. The latitudinal distribution of *LUE* was mostly similar to that of productivity, except in the northernmost and southernmost areas. Specifically, warm and humid ecosystems around the equator show higher *LUE*, especially for *GPP*. However, smaller differences among latitudes were found for the *LUE* of *NPP*, because larger respiratory consumption of tropical forests offsets a part of the higher photosynthetic efficiency. Table 3 summarizes the latitudinal features for every 30° latitudinal zone. Apparently, the southern low (0–30°S), northern low (0–30°N), and northern-middle (30–60°N) zones absorbed comparable amounts of *PAR*, about 53×10^{21} J y^{-1}, although the incident *PAR* was different among the three zones. The southern and northern low zones accounted for nearly 70% of the photosynthetic CO_2 assimilation by the terrestrial biosphere, with a higher *LUE* than other zones. In contrast, the northern-middle and high zones accounted for nearly 60% of the total carbon storage (1080 Pg C out of 1910 Pg C), and there was a clear difference in the carbon cycle regime between the low- and high-latitudinal zones.

It is seen from Fig. 5 that *APAR*, *GPP*, and *LUE* changed roughly in parallel seasonally because, in general, higher incident radiation leads to

Table 3: Summary of the simulation result for each of the 30°-zones, averaged over 1981–2000

	Land area (10^6 km^2)	*PAR* (10^{21} J yr^{-1})	*APAR* (10^{21} J yr^{-1})	*GPP* (Pg C)	$LUE_{(GPP)}$ (g C MJ^{-1})	*NPP* (Pg C)	$LUE_{(NPP)}$ (g C MJ^{-1})	Plant C (Pg C)	Soil C (Pg C)
90–60°N	15.2	22.2	15.9	7.9	0.50	4.8	0.30	35	382
60–30°N	46.0	103.7	54.7	28.5	0.52	15.4	0.28	104	559
30–0°N	36.6	109.3	54.4	44.0	0.81	19.4	0.36	156	213
0–30°S	29.0	80.7	52.3	45.4	0.87	20.5	0.39	174	227
30–60°S	5.5	14.4	8.3	4.9	0.59	2.4	0.29	12	48
Total	132.3	330.4	185.6	130.7	0.70	62.5	0.34	481	1,429

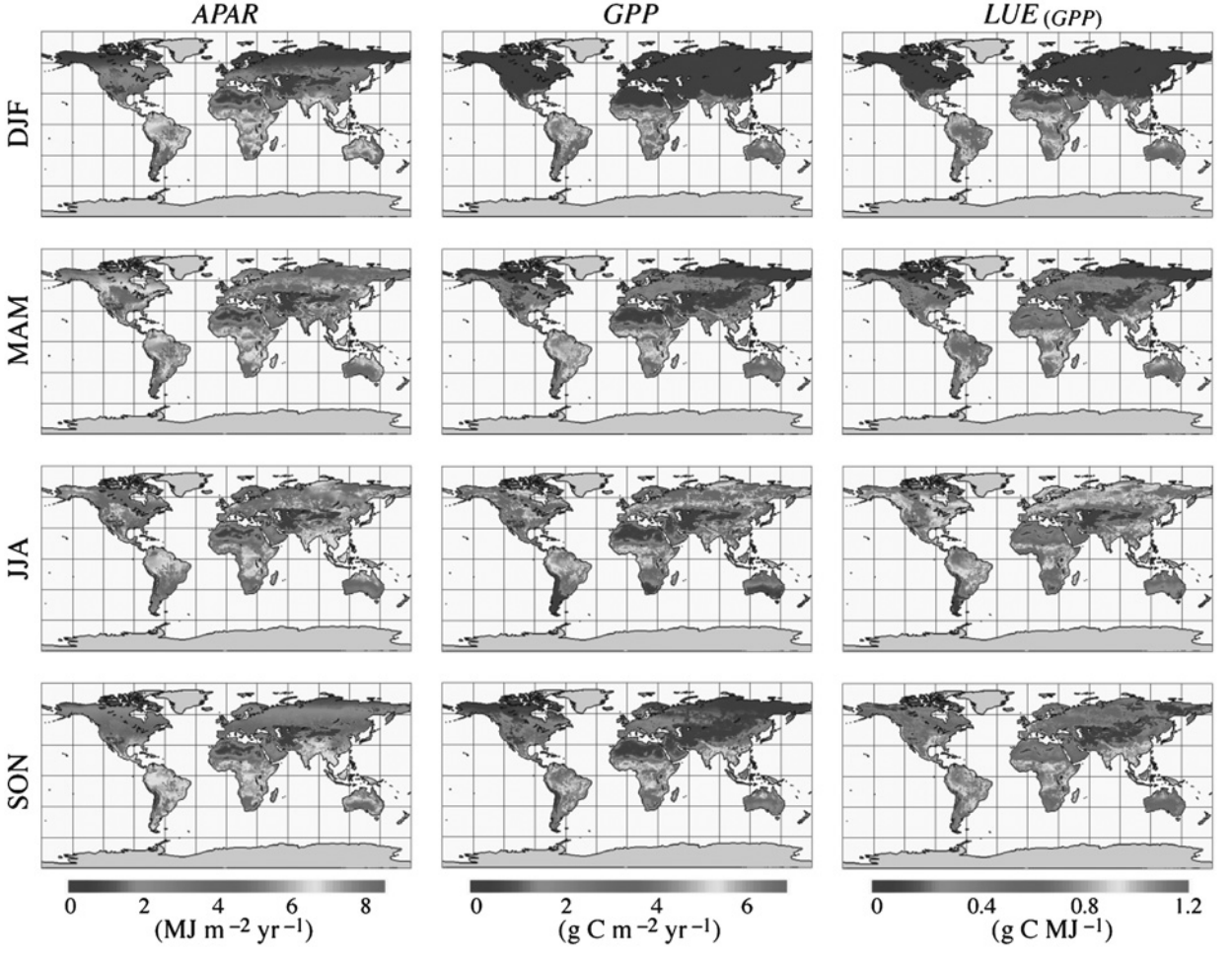

Figure 5: Seasonal change in the estimated global distributions of *APAR*, *GPP*, and $LUE_{(GPP)}$, averaged from 1981 to 2000: DJF (December, January, and February), MAM (March, April, and May), JJA (June, July, and August), and SON (September, October, and November), averaged from 1981 to 2000 (For colour version, see Colour Plate Section).

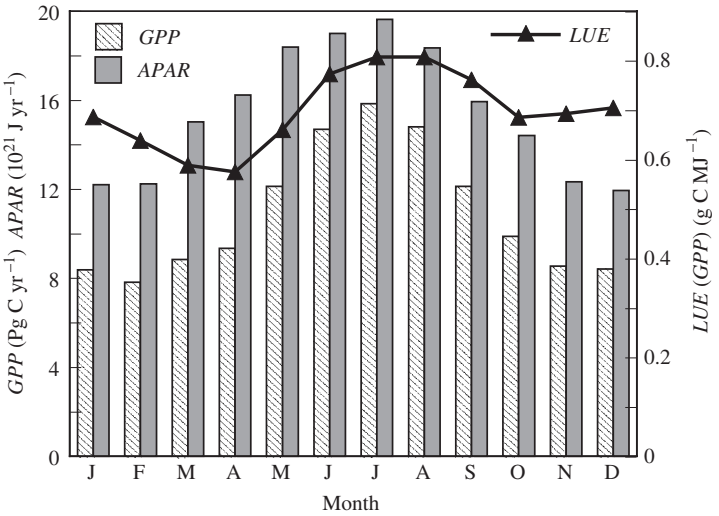

Figure 6: Seasonal change in the global total *APAR*, *GPP*, and $LUE_{(GPP)}$, averaged from 1981 to 2000.

warmer conditions that enable plants to photosynthesize with a higher light-use efficiency. Higher *LUE*s occurred in tropical rain forests all year round and in temperate and boreal forests in their growing season (e.g., June, July, and August [JJA in Fig. 5] in northern taiga). In tropical, temperate, and boreal deciduous forests, *APAR* and *LUE* differed drastically between the dormancy and growing period, reflecting their clear leaf phenology. In arid regions, however, water limitation inhibits plants from expanding leaf area and utilizing solar energy for photosynthesis all year. Fig. 6 indicates that globally, *APAR* and *GPP* (and also *NPP*, not shown) changed almost in parallel seasonally, but the global average *LUE* showed a considerable degree of seasonal change (0.575–0.807 g C MJ^{-1} for *GPP* and 0.260–0.420 g C MJ^{-1} for *NPP*).

3.2 Grid-by-Grid Correlation

Annual *APAR* and *GPP/NPP* are correlated in a grid-by-grid manner, as shown in Fig. 7. A single line does not represent the relationship, although there is a positive correlation between absorbed PAR and productivity ($r^2 = 0.69$ for *GPP* and 0.68 for *NPP*). This is simply because the *LUE* by Sim-CYCLE is not homogeneous over the terrestrial biosphere. Fig. 8 shows the seasonal change in the *APAR–GPP* relationship (similar for *APAR–NPP*, not shown); the correlation coefficient is highest in DJF ($r^2 = 0.79$) and lowest in MAM ($r^2 = 0.38$). The lowest correlation coefficient in MAM coincides with lower *LUE*s in the same period (see Fig. 6). Additionally, *LUE*s for *GPP* and *NPP* were correlated with the productivities (Fig. 9), showing

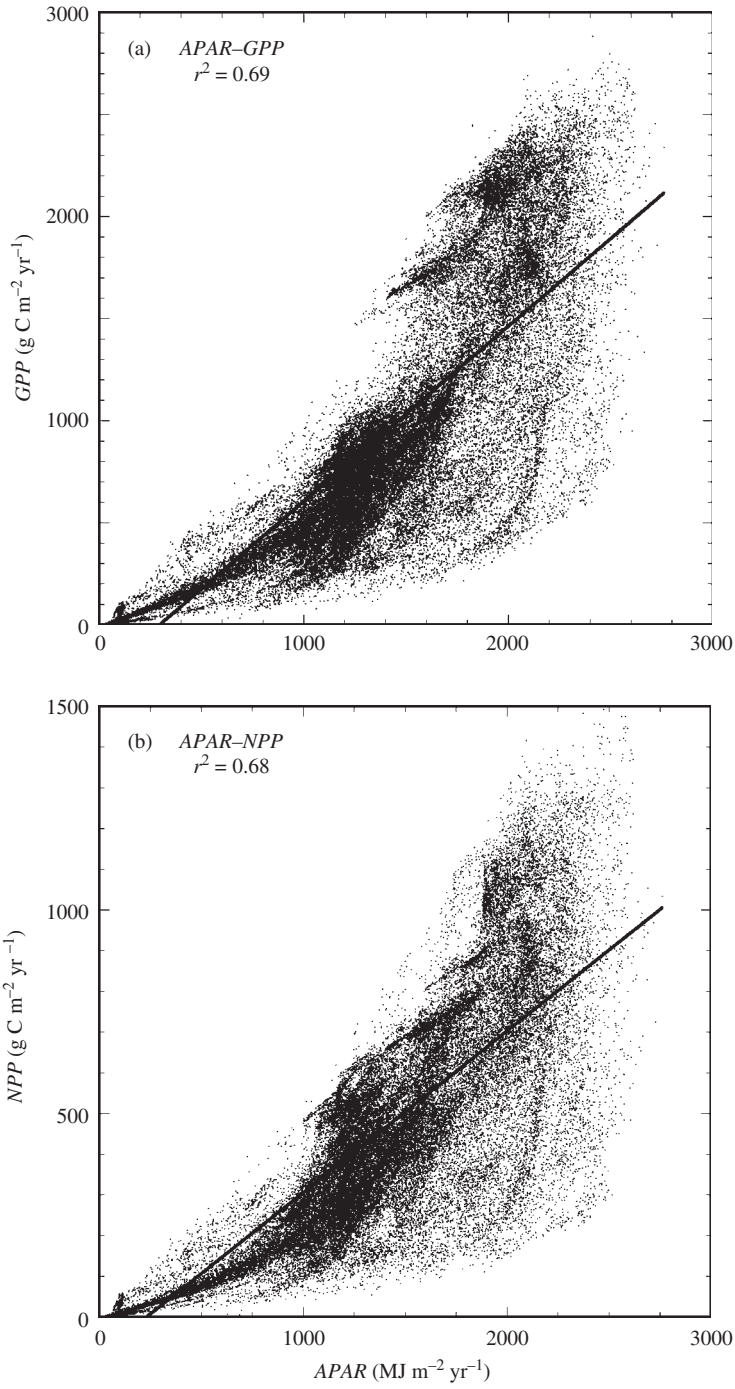

Figure 7: Correlation between annual absorbed energy (*APAR*) and CO_2 assimilation rate (*GPP* and *NPP*) for each of the $0.5^\circ \times 0.5^\circ$grids ($n = 58\ 772$).

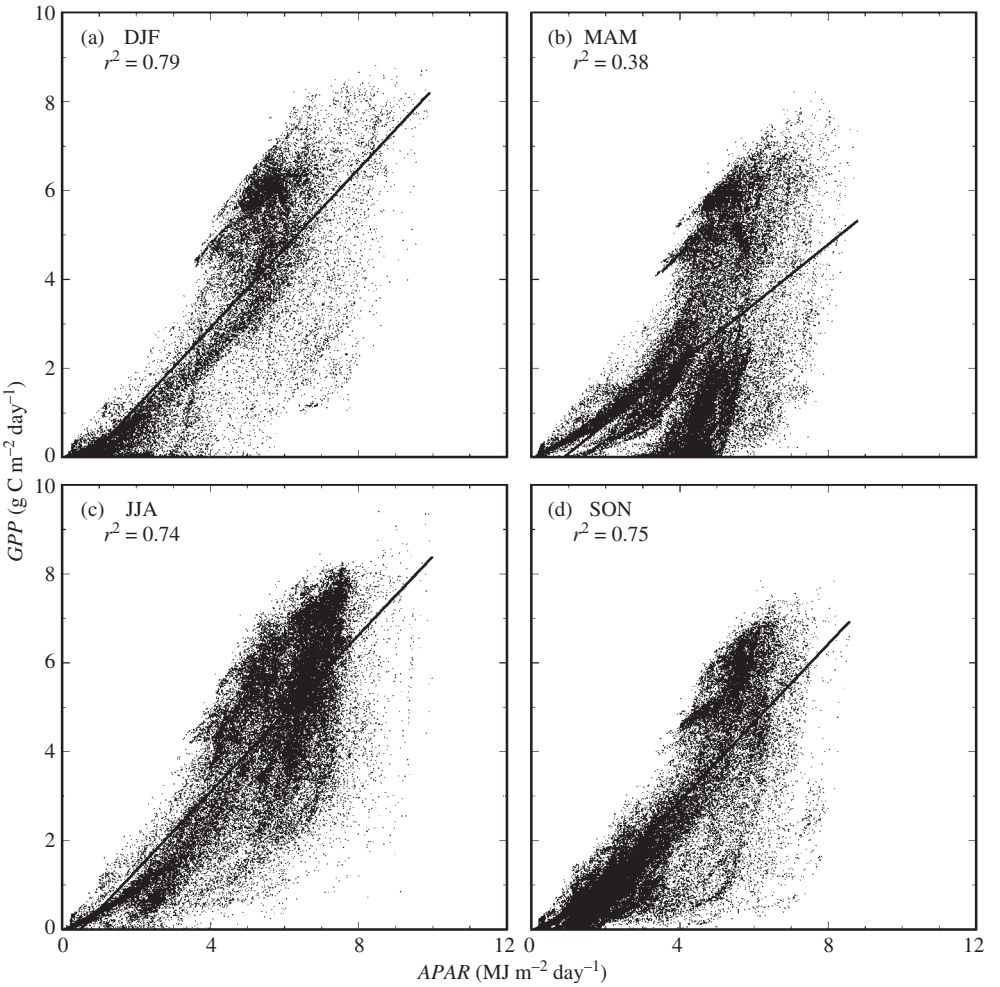

Figure 8: Same as Fig. 7, but showing the seasonal change in the *APAR–GPP* relationship.

considerably higher correlation coefficients ($r^2 = 0.81$ for GPP and 0.75 for *NPP*). Again, this relationship indicates that higher productivities are attributable to higher light-use efficiency, as well as higher incident PAR. Compared with a similar correlation analysis with 12 global models by Ruimy et al. (1999), Sim-CYCLE showed a moderate degree of correlation between *APAR* and *NPP* ($r^2 = 0.26$–0.98 among the 12 models) and a high correlation between *LUE* and *NPP* ($r^2 = 0.06$–0.71). The behavior of Sim-CYCLE is relatively close to that of process-based models such as the Frankfurt Biosphere Model, rather than that of remote-sensing-based models. Such a correlation analysis and model intercomparison are apparently effective in clarifying the characteristics of the models.

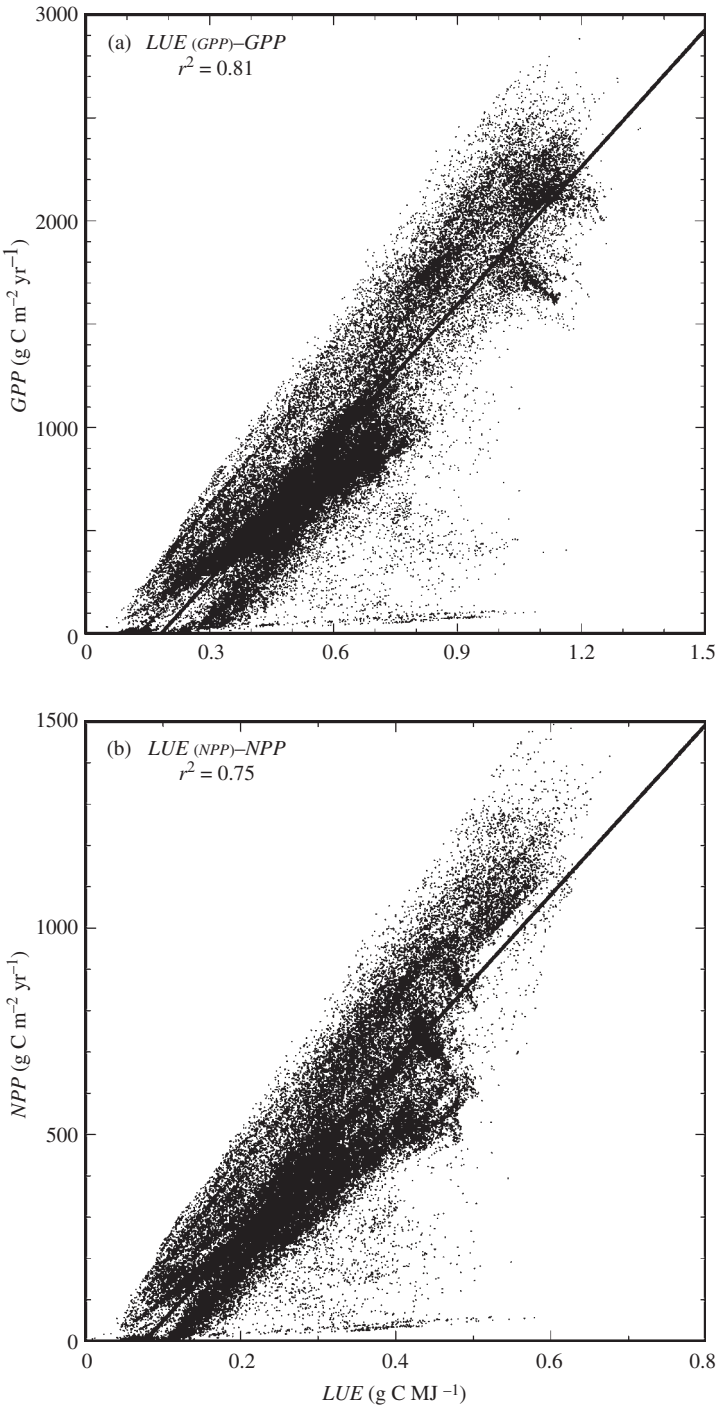

Figure 9: Correlation between *LUE* and productivity, for *GPP* (top) and *NPP* (bottom).

4 Discussion

4.1 Comparison with Other Studies

The estimated global features are difficult to validate with observational evidence but can be compared with several former model studies. Many models have estimated that the global annual *NPP* is about $54.9 \pm 10.6\,\mathrm{Pg\,C\,y^{-1}}$ (Cramer et al., 1999), comparable with the estimation by Sim-CYCLE ($62.5\,\mathrm{Pg\,C\,y^{-1}}$). Ruimy et al. (1999) analyzed the estimated *APAR* and *NPP* with 12 models and calculated that the global average $LUE_{(NPP)}$ was $0.427 \pm 0.126\,\mathrm{g\ C\ MJ^{-1}}$; again, the estimation of Sim-CYCLE ($0.34\,\mathrm{g\,C\,MJ^{-1}}$) fell within the range of the other 12 models. The latitudinal distributions of *APAR*, *NPP*, and *LUE* (Fig. 4) were also consistent with the analysis of Ruimy et al. (1999), which shows a close relationship between *APAR* and *NPP*. On the other hand, there are few comparable studies that examine the interannual (Fig. 2) and seasonal changes (Fig. 6) in *LUE*, although long-term and interannual variability in *APAR*, *GPP/NPP*, and *LUE* should be challenging issues in regards to the function of terrestrial ecosystems under a changing environment. Indeed, several empirical studies suggest that global terrestrial productivity is increasing, probably because of atmospheric CO_2 increase and ongoing climatic change (Nemani et al., 2003). Alterations in PAR absorption (due to land-use changes and biological changes in leaf greenness) are detectable by the remote-sensing approach, while alterations in *LUE* (due to physiological responses) are difficult to determine observationally, highlighting the importance of the modeling approach.

4.2 Higher Resolution Mapping

In forthcoming studies, the modeling approach will be more intimately linked with the remote-sensing approach in order to accomplish a higher-resolution mapping of the global carbon cycle. At present, *NPP* mapping on a continental scale is being accomplished at a spatial resolution of 1 km (Hicke et al., 2002; Matsushita and Tamura, 2002) on the basis of satellite remote-sensing data such as the NDVI by NOAA/AVHRR and MODIS. Recent developments in computer technology allow us to deal with greater amounts of data, so it will not be impossible to perform process-based models (e.g., Sim-CYCLE) at such a high resolution. Compared with remote-sensing-based carbon cycle models (e.g., CASA by Potter et al. (1993); GLO-PEM by Prince and Goward (1995); TURC by Ruimy et al. (1996)), process-based models are less accurate (diagnostic) but more predictive (prognostic). For example, a process-based model is preferable for simulating underground processes (e.g., decomposition and soil-root interaction).

Hence, the two approaches should work in a complementary manner rather than being exclusive. However, in spite of much effort (e.g., by IGBP Data and Information Services), basic datasets to capture the heterogeneity of the land surface are still under development (DeFries et al., 2000; Zheng et al., 2000; Masson et al., 2003). Along with advancements in spatial resolution, parameterization of sub-grid-scale heterogeneity is required in order to include the effect of disturbances (e.g., wildfires and pest outbreaks). For example, fire-prone ecosystems such as tropical savanna and inner boreal forest suffer from fires once every few decades (i.e., a few percent of area annually), leading to significant suppression of biomass and soil-carbon pools. The situation is even more severe for human land-use conversion and management, which are especially important for mapping in the Asian region. Therefore, further studies are needed to achieve high-accuracy mapping of the terrestrial carbon cycle, which is applicable for carbon accounting and management planning, as well as for the quantification of the global carbon cycle.

Acknowledgements

The climate data by the University of East Anglia, Climate Research Unit were provided by T. Mitchell, Tyndall Centre for Climate Change Research, UK.

Appendix: How Incident *PAR* and *PPFD* is Estimated in this Study

The global distribution of photosynthetically active radiation (PAR, wavelength 400–700 nm) is estimated on the basis of some geometric and empirical relationships (Iqbal, 1983). First, the downward solar radiation at the top of the atmosphere (S_{top}, $\mathrm{W\,m^{-2}}$) is calculated as follows:

$$S_{top} = S_0 \times \left(\frac{d}{d_0}\right)^2 \times \cos(\theta) \tag{A1}$$

where S_0 is the solar constant ($1365\,\mathrm{W\,m^{-2}}$), θ the zenith angle, d the distance between the sun and the earth, and d_0 the annual average of d. The zenith angle θ is calculated geometrically as follows:

$$\theta = a\cos(\sin(\delta) \times \sin(\phi) + \cos(\delta) \times \cos(\phi) \times \cos(h)) \tag{A2}$$

where δ is the solar declination angle (+23.4° to –23.4°), ϕ is the latitude (+90° to –90°), and h is the hour angle from culmination ($\pm 15°$ per hour).

Empirically, δ and $(d/d_0)^2$ are approximated as:

$$\begin{aligned}\delta = 180/\pi\{&0.006918 - 0.399912 \times \cos(\Gamma) \\ &+ 0.070257 \times \sin(\Gamma) - 0.006758 \times \cos(2\Gamma) \\ &+ 0.000907 \times \sin(2\Gamma) - 0.002697 \times \cos(3\Gamma) + 0.00148 \times \sin(3\Gamma)\}\end{aligned} \tag{A3}$$

$$\begin{aligned}\left(\frac{d}{d_0}\right)^2 = &1.000110 + 0.034221 \times \cos(\Gamma) \\ &+ 0.001280 \times \sin(\Gamma) + 0.000719 \times \cos(2\Gamma) \\ &+ 0.000077 \times \sin(2\Gamma)\end{aligned} \tag{A4}$$

$$\Gamma = 360\left(\frac{\imath}{365}\right) \tag{A5}$$

where $\imath$ is the day-number from the beginning of year. Solar radiation at the land surface (S_{sfc}), attenuated in passing through the atmosphere, is estimated by an empirical function of cloudiness (C, 0 to 1):

$$S_{sfc} = S_{top}(0.8964 - 0.5392C) \tag{A6}$$

This relationship was derived from the NCEP/NCAR reanalysis data, by correlating S_{sfc} and S_{top} globally (Ito, unpublished data). To estimate PAR, the surface solar radiation was separated into diffused (D_{sfc}) and direct beam (B_{sfc}) fractions, again in an empirical manner:

$$D_{sfc} = S_{sfc}\left(\frac{0.958 - 0.982S_{sfc}}{S_{top}}\right) \tag{A7}$$

$$B_{sfc} = S_{sfc} - D_{sfc} \tag{A8}$$

Finally, PAR at the land surface (PAR_{sfc}, $\mathrm{W\,m^{-2}}$) and photon flux density ($PPFD_{sfc}$, μmol photon $\mathrm{m^{-2}\,s^{-1}}$) at the land surface are estimated:

$$PAR_{sfc} = 0.43 \times B_{sfc} + 0.57 \times D_{sfc} \tag{A9}$$

$$PPFD_{sfc} = 0.43 \times K_b \times B_{sfc} + 0.57 \times K_d \times D_{sfc} \tag{A10}$$

where K_b (= 4.6) and K_d (= 4.2) are conversion coefficients for beam and diffused radiation, respectively. Note that the empirical relationships adopted in the PAR estimation method can be revised on the basis of new observational results.

References

Asner, G. P., Wessman, C. A., Archer, S., 1998. Scale dependence of absorption of photosynthetically active radiation in terrestrial ecosystems. Ecological Applications 8, 1003–1021.

Asrar, G., Myneni, R. B., Choudhury, B. J., 1992. Spatial heterogeneity in vegetation canopies and remote sensing of absorbed photosynthetically active radiation: A modeling study. Remote Sensing of Environment 41, 85–103.

Cramer, W., Kicklighter, D. W., Bondeau, A., Moore, B. I., Churkina, G., Nemry, B., Ruimy, A., Schloss, A. L.Potsdam NPP model intercomparison participants, 1999. Comparing global NPP models of terrestrial net primary productivity (NPP): Overview and key results. Global Change Biology 5 (Suppl.1), 1–15.

DeFries, R. S., Hansen, M. C., Townshend, J. R. G., Jenetos, A. C., Loveland, T. R., 2000. A new global 1-km dataset of percentage tree cover derived from remote sensing. Global Change Biology 6, 247–254.

Goetz, S. J., Prince, S. D., 1999. Modelling terrestrial carbon exchange and storage: Evidence and implications of functional convergence in light-use efficiency. Advances in Ecological Research 28, 57–92.

Haxeltine, A., Prentice, I. C., 1996. A general model for the light-use efficiency of primary production. Functional Ecology 10, 551–561.

Hicke, J. A., Asner, G. P., Randerson, J. T., Tucker, C., Los, S., Birdsey, R., Jenkins, J. C., Field, C., 2002. Trend in North American net primary productivity derived from satellite observations, 1982–1998. Global Biogeochemical Cycles 16, doi 10.1029/2001GB001550.

Intergovernmental Panel on Climate Change (IPCC), 2001. Climate Change 2001: The Scientific Basis. Cambridge University Press, Cambridge, p. 892.

Iqbal, M., 1983. An introduction to solar radiation. Academic Press, Toronto, p. 390.

Ito, A., Oikawa, T., 2002. A simulation model of the Carbon Cycle in Land Ecosystems (Sim-CYCLE): A description based on dry-matter production theory and plot-scale validation. Ecological Modelling 151, 147–179.

Keeling, C. D., Whorf, T. P., 2002. Atmospheric CO_2 concentrations–Mauna Loa Observatory, Hawaii, 1958-2001. NDP001, Oak Ridge National Laboratory, Oak Ridge.

Kistler, R., Kalnay, E., Collins, W., Saha, S., White, G., Woollen, J., Chelliah, M., Ebisuzaki, W., Kanamitsu, M., Kousky, V., van den Dool, H., Jenne, R., Fiorino, M., 2001. The NCEP-NCAR 50-year reanalysis: Monthly means CD-ROM and documentation. Bulletin of the American Meteorological Society 82, 247–267.

Kumar, M., Monteith, J. L., 1981. Remote sensing of crop growth. In: Smith, H. (Ed.), Plants and Daylight Spectrum. Academic Press, New York, pp. 133–144.

Masson, V., Champeaux, J.-L., Chauvin, F., Meriguet, C., Lacaze, R., 2003. A global database of land surface parameters at 1-km resolution in meteorological and climate models. Journal of Climate 16, 1261–1282.

Matsushita, B., Tamura, M., 2002. Integrating remotely sensed data with an ecosystem model to estimate net primary productivity in East Asia. Remote Sensing of Environment 81, 58–66.

Monsi, M., Saeki, T., 1953. Über den Lichtfaktor in den Pfanzengesellschaften und seine Bedeutung für die Stoffproduktion. Japanese Journal of Botany 14, 22–52.

Monsi, M., Uchijima, Z., Oikawa, T., 1973. Structure of foliage canopies and photosynthesis. Annual Review of Ecology and Systematics 4, 301–327.

Myneni, R. B., 1991. Modeling radiative transfer and photosynthesis in three-dimensional vegetation canopies. Agricultural and Forest Meteorology 55, 323–344.

Nemani, R. R., Keeling, C. D., Hashimoto, H., Jolly, W. M., Piper, S. C., Tucker, C. J., Myneni, R. B., Running, S. W., 2003. Climate-driven increases in global terrestrial net primary production from 1982 to 1999. Science 300, 1560–1563.

New, M., Lister, D., Hulme, M., Makin, I., 2002. A high-resolution data set of surface climate over global land areas. Climate Research 21, 1–25.

Olson, J. S., Watts, J. A., Allison, L. J., 1983. Carbon in live vegetation of major world ecosystems. ORNL-5862, Oak Ridge National Laboratory.

Potter, C. S., Randerson, J. T., Field, C. B., Matson, P. A., Vitousek, P. M., Mooney, H. A., Klooster, S. A., 1993. Terrestrial ecosystem production: a process model based on global satellite and surface data. Global Biogeochemical Cycles 7, 811–841.

Prince, S. D., Goward, S. N., 1995. Global primary production: A remote sensing approach. Journal of Biogeography 22, 815–835.

Ruimy, A., Dedieu, G., Saugier, B., 1996. TURC: a diagnostic model of continental gross primary productivity and net primary productivity. Global Biogeochemical Cycles 10, 269–285.

Ruimy, A., Kergoat, L., Bondeau, A.Potsdam NPP model intercomparison participants, 1999. Comparing global NPP models of terrestrial net primary productivity (NPP): Analysis of differences in light absorption and light-use efficiency. Global Change Biology 5 (Suppl. 1), 56–64.

Ruimy, A., Saugier, B., Dedieu, G., 1994. Methodology for the estimation of terrestrial net primary production from remotely sensed data. Journal of Geophysical Research 99, 5263–5283.

Running, S. W., Baldocchi, D. D., Turner, D. P., Gower, S. T., Bakwin, P. S., Hibbard, K. A., 1999. A global terrestrial monitoring network integrating tower fluxes, flask sampling, ecosystem modeling and EOS satellite data. Remote Sensing of Environment 99, 108–127.

Runyon, J., Waring, R. H., Goward, S. N., Welles, J. M., 1994. Environmental limits on net primary production and light-use efficiency across the Oregon transect. Ecological Applications 4, 226–237.

Terashima, I., Hikosaka, K., 1995. Comparative ecophysiology of leaf and canopy photosynthesis. Plant, Cell and Environment 18, 1111–1128.

Turner, D. P., Urbanski, S., Bremer, D., Wofsy, S. C., Meyers, T., Gower, S. T., Gregory, M., 2003. A cross-biome comparison of daily light use efficiency for gross primary production. Global Change Biology 9, 383–395.

Webb, R. S., Rosenzweig, C. E., Levine, E. R., 1993. Specifying land surface characteristics in general circulation models: Soil profile data set and derived water-holding capacities. Global Biogeochemical Cycles 7, 97–108.

Zheng, X., Dickinson, R. E., Walker, A., Shaikh, M., DeFries, R. S., Qi, J., 2000. Derivation and evaluation of global 1-km fractional cover data for land monitoring. Journal of Applied Meteorology 39, 826–839.

This page intentionally left blank

Chapter 15

Terrestrial Net Primary Production (NPP) Estimation Using NOAA Satellite Imagery: Inter-annual Changes between 1982 and 1999

Yoshio Awaya[1,*], Eiji Kodani[2] and Dafang Zhuang[3]

[1]*Forestry and Forest Products Research Institute, 1 Matsunosato, Tsukuba, Iberaki 305-8687, Japan*
[2]*Shikoku Research Center, Forestry and Forest Products Research Institute, 2-915 Asakura-Nishi, Kohchi 780-8077, Japan*
[3]*Institute of Geographical Sciences and Natural Resources Research, Chinese Academy of Sciences, Anwai, Beijing 100101, P. R. China*

Abstract

The light use efficiency (LUE) approach using the normalized difference vegetation index (NDVI) is the simplest method to estimate terrestrial net primary production (NPP). A simple LUE-based model, which used LUEs of plants, solar radiation, NDVI and stress functions for soil water and air temperature, was applied to estimate global terrestrial NPP between 1982 and 1999. NDVI images were computed using channels 1 and 2 of the Advanced Very High Resolution Radiometer (AVHRR) produced by the Pathfinder AVHRR LAND (PAL) datasets, after a simple radiometric correction. Anomalies in time series of global average monthly NDVI of the original PAL data, which were probably caused by volcanic ashes exposed in the atmosphere by huge eruptions such as Pinatubo, were successfully reduced in the computed NDVI. The solar radiation, air temperature and soil water of NCEP/NCAR Reanalysis data were also used for the NPP estimation. LUEs were determined based on the maximum photosynthetic rate in the literature for 17 land cover types of the IGBP-DIS classification. NPP was also computed using a constant LUE for the global vegetation to

*Corresponding author.
E-mail address: awaya@ffpri.affrc.go.jp (Y. Awaya).

Elsevier Oceanography Series 73
Edited by H. Kawahata and Y. Awaya
ISBN: 0-444-52948-9

understand the effects of multiple LUE-settings. As a result, global NPP was estimated at between 58.5 and 62.6 petagram (Pg) carbon in 1983 and 1998, respectively, for the multiple LUE-settings and between 51.0 and 54.8 Pg carbon in 1983 and 1991, respectively, for the constant LUE-setting. NPP increased about 0.1 Pg carbon annually ($P<0.1$) for the case of multiple LUE-settings and about 0.08 Pg carbon annually (not significant) for the case of constant LUE-setting. Carbon absorption by the terrestrial ecosystems in 1980s and 1990s are reported in a literature (Kalnay et al., 1996) based on an analysis of atmospheric CO_2 concentration. The rate of change in carbon absorption observed in that study is similar to that of NPP by our estimation. Inter-annual changes in NPP varied from region to region. Most clear long-term increasing or decreasing trends of NPP appeared in semiarid areas. The inter-annual changes in NDVI seemed to relate most clearly to the inter-annual NPP changes in these areas among parameters used for the NPP estimation, which were NDVI, average monthly air temperature, volumetric soil water content and solar radiation.

Keywords: AVHRR; NDVI; net primary production; inter-annual change; light use efficiency

1 Introduction

The concentration of atmospheric carbon dioxide (CO_2), a greenhouse gas, is increasing steadily. Global mean air temperature seems to have increased greatly since the 1910s, in coincidence with the increases in the concentrations of greenhouse gasses (Houghton et al., 2001). Therefore, there is an urgent need to reduce the amount of atmospheric CO_2 as well as to understand the carbon storage and balance in terrestrial ecosystems throughout the world. If global climate changes, the net primary production (NPP), which is a measure of the amount of atmospheric CO_2 absorbed by vegetation, would suffer as a result of the changing climate (Houghton et al., 2001). Estimation of NPP is essential for evaluating the global carbon balance, and for understanding the effects of climate change on vegetation.

The normalized difference vegetation index (NDVI) of the Advanced Very High Resolution Radiometer (AVHRR) on NOAA satellites has been used for regional and global vegetation studies (*e.g.* Tucker et al., 1984; Justice et al., 1985; Box et al., 1989). NDVI shows seasonal vegetation changes clearly and is useful for vegetation analysis such as vegetation cover and type mapping. However, there are some problems to be solved for reliable analysis. For example, aging of satellite sensors, which causes degradation of sensitivity, necessitates post-launch calibration of the sensor (Slater et al., 1987; Rao and Chen, 1995). Atmospheric correction is a common problem for visible and near-infrared radiometer data. Although data processing is designed to overcome these problems (Smith et al., 1997), some effects remain in the NDVI images of the Pathfinder AVHRR LAND (PAL) dataset (Smith et al., 1997; Young and Anyamba, 1999).

NPP has been mapped on a global scale using NDVI images accompanied by simple models (Potter et al., 1993; Ruimy et al., 1994; Prince and Goward, 1995; Malmström et al., 1997; Awaya et al., 2004). There is a great advantage in using NDVI, since NDVI images show the terrestrial vegetation status such as leaf area index (LAI) (Asrar et al., 1984; Chen et al., 2002), fraction of photosynthetically active radiation (fAPAR) (Asrar et al., 1984; Myneni and Williams, 1994) and so on. These NPP models are based on the fact that dry matter (net) production is proportional to the amount of light absorbed by vegetation (Monteith, 1972). Such models, referred to as the light use efficiency (LUE)-based models, are also used to estimate daily and annual NPP using images of the Moderate Resolution Imaging Spectroradiometer (MODIS) of the Terra and Aqua satellites (Running et al., 1999). As described in the MODIS NPP algorithm document, many factors influence vegetation production, and MODIS NPP algorithm is based on some factors including temperature and water vapour deficit. To make inter-annual monitoring of NPP possible, it is essential to have not only a reasonable NPP model but also satellite data corrections. Various methods of calibration were prepared for MODIS including pre- and post-launch calibrations (Butler and Barnes, 1998). On the other hand, the radiometric accuracy of PAL data is inadequate as described by Smith et al. (1997). However, Awaya et al. (2004) demonstrated a method to reduced errors in PAL images caused by inadequate correction. They estimated global NPP between 1988 and 1993 using a simple LUE-based model with corrected NDVI and grid meteorological data. Their model takes into account the effects of air temperature and soil water content to estimate vegetation production. This study aims to understand inter-annual variations of global NPP between 1982 and 1999 based on the method of Awaya et al. (2004).

2 Data and Methods

2.1 Materials

Monthly PAL images of channels 1 and 2 (ch1 and ch2), which record the red (0.58–0.68 μm) and near-infrared (NIR, 0.73–1.10 μm) wavelength, respectively, by AVHRR sensors, were used to compute NDVI after simple intensity corrections as described below. Monthly NDVI of PAL data, which were produced by the PAL project using the AVHRR data, were compared with the corrected NDVI to understand the effects of simple intensity corrections. Because PAL data for 1994 were incomplete, they were omitted in this study. PAL data were in the Interrupted Goode Homolosine equal area projection having an 8-km grid (Smith et al., 1997).

NDVI was computed as follows:

$$NDVI = (\rho_{ch2} - \rho_{ch1})/(\rho_{ch2} + \rho_{ch1}) \quad (1)$$

where ρ_{ch1} and ρ_{ch2} are reflectance factors of ch1 and ch2, respectively.

Grid meteorological data of the average air temperature at 2 m (T), the downward solar radiation at the surface (SR) and the fraction of volumetric soil moisture data at 10 cm below the soil surface (SW) were used to estimate global NPP with the NDVI images. These data, T, SW and SR, were supplied by the National Center for Environmental Prediction and the National Center for Atmospheric Research (NCEP/NCAR reanalysis monthly data). T was expressed in degree Celsius and SR was expressed in joules (joule $s^{-1} m^{-2}$) in the analysis. The NCEP/NCAR reanalysis monthly data were stored as grid data of approximately 1.9 degrees in resolution on a longitude and latitude coordinate system (Kalnay et al., 1996).

The IGBP-DIS global land-cover data set was used to identify vegetation types, and NPP was estimated by allocating an individual LUE to each vegetation type. The IGBP-type map, which was the simplest vegetation type map in the IGBP-DIS data set, was used, since LUE data were insufficient for other maps. The IGBP-DIS land-cover data was stored in the Interrupted Goode Homolosine equal area projection having 1 km grid (Loveland et al., 2000).

The PAL images, the NCEP/NCAR reanalysis monthly data and the IGBP-DIS land cover data were re-projected onto a longitude and latitude coordinate system having a 0.072 degree grid, the nearest neighbour resampling was applied to the PAL images and the IGBP-DIS land cover data, and the bi-linear resampling was applied to the NCEP/NCAR reanalysis monthly data.

2.2 Intensity Correction

The data obtained in the period between 1988 and 1990 in the middle of the NPP analysis period were selected as a standard, because the atmosphere seemed to be clear globally during these years based on inter-annual changes of global average ch1 intensity and atmospheric turbidity (Meteorological Agency of Japan, 1999). During this period, there were no effects of ash from volcanic eruptions such as the eruption of Mt. El Chichon in Mexico in 1982 and the eruption of Mt. Pinatubo in the Philippines in 1991.

Since seasonal spectral variations of plants were larger in ch2 than in ch1, different intensity correction procedures were applied to ch1 and ch2. The averages of ch1 and ch2 in 1988, 1989 and 1990 were computed for each pixel and each month as the standards (ch1s and ch2s, respectively). To determine the equations for the intensity corrections, regressions between

the standards and original images of ch1 and ch2 (ch1t and ch2t, respectively) were computed as follows (Awaya et al., 2004).

2.2.1 Channel 1

A regression line, which crossed a point with reflectance factor of 50% for both ch1s and ch1t, was calculated for each month using pixels, which were sampled in the area between 40°N and 35°S (hereafter, standard area), as follows:

$$\rho_{\mathrm{ch1t}} = a_{\mathrm{ch1}} \times (\rho_{\mathrm{ch1s}} - 50) + 50 \tag{2}$$

where ρ_{ch1s} and ρ_{ch1t} are reflectance factors (%) of the standard and original images, respectively, and a_{ch1} is the regression slope.

2.2.2 Channel 2

Spatial and temporal standard deviation (SD) in a moving window of 3 by 3 pixels was computed for each monthly image set, which consisted of 17 channels of the same month from the images between 1982 and 1999. The maximum SD among 12 images (months) was selected for each pixel in the standard area. Pixels with a maximum SD less than 3.6% were chosen as unchanged pixels. Relationships were analysed between reflectance factors of ch2 s (ρ_{ch2s}(%)) and reflectance factors of original images (ρ_{ch2t}(%)) using the selected pixels by a linear regression method as follows:

$$\rho_{\mathrm{ch2t}} = a_{\mathrm{ch2}} \times \rho_{\mathrm{ch2s}} + b_{\mathrm{ch2}} \tag{3}$$

where a_{ch2} and b_{ch2} are the slope and intercept of the regression, respectively.

2.2.3 Normalized Difference Vegetation Index

Reflectance factors of ch1 and ch2 were computed using the results of the regression analysis as follows:

$$\rho_{\mathrm{cor}} = (\rho_{\mathrm{org}} - b)/a \tag{4}$$

where a is a_{ch1} or a_{ch2} for ch1 or ch2, respectively. b is $50 \times (1 - a_{\mathrm{ch1}})/a_{\mathrm{ch1}}$ or b_{ch2} for ch1 or ch2, respectively. ρ_{cor} is the corrected reflectance factors (%) of ch1 or ch2, and ρ_{org} is the original reflectance factors (%) of ch1 or ch2.

The normalized difference vegetation index (NDVI) was computed using equation (1) (corrected NDVI) and the corrected reflectance factors of ch1 and ch2. Averages of the original and the corrected ch1, ch2 and NDVI were computed in the standard area for each month, and inter-annual changes of all PAL parameters were compared to check the results of the intensity correction.

Biomass burning, air pollution and desert dust are other sources of aerosols and have a strong influence on atmospheric optical depth (Eck et al., 1999) on a regional scale. For example, biomass burning occurs at all times of the year and in many regions of the globe (Dwyer et al., 1998). However, our atmospheric correction doesn't take into account the effects of regional biomass burning, air pollution and desert dust. Our omission of these effects is expected to cause errors in NDVI correction on a regional scale.

2.3 NPP Estimation

2.3.1 Model

Numerous studies are based on the following two findings. NPP can be obtained from the product of absorbed light and LUE of plants (Monteith, 1972), and NDVI is proportional to fAPAR (Asrar et al., 1984). Based on the first finding, NPP is expressed as the product of fAPAR, PAR and LUE (ε) (equation (5)). The second finding allows fAPAR to be expressed as a linear equation of NDVI with offset value close to zero (equation (6)):

$$\mathrm{NPP} = \varepsilon \times \mathrm{fAPAR} \times \mathrm{PAR} \tag{5}$$

$$\mathrm{fAPAR} = a \times \mathrm{NDVI} + c \tag{6}$$

Combining equations (5) and (6), equation (7) was derived to estimate NPP as the product of NDVI, ε and PAR, and was used in this study. Taking into account air temperature effects and water stress, NPP is expressed numerically as follows (Awaya et al., 2004):

$$\mathrm{NPP} = \Sigma(\mathrm{f(T)} \times \mathrm{f(SW)} \times \varepsilon'(\mathrm{v}) \times \mathrm{NDVI} \times \mathrm{SR}) \tag{7}$$

where T is air temperature (°C) and SW is volumetric soil water content (fraction). f(T) and f(SW) are responses of photosynthesis to T and SW, respectively. SR is approximately twice PAR. ε'(v) (g DW MJ^{-1}) is LUE for vegetation type v and was determined for NDVI and SR.

The photosynthetic rate is highest at the leaf temperature, at which leaves experience commonly on sunny days during growing season (Chapin III et al., 2002). The leaf temperature is the optimum temperature for photosynthesis. However, T was obtained from monthly average air temperatures, including data for sunny, cloudy and rainy days. It was necessary to determine the optimum air temperatures of plants (OPTM) using T, which was similar to leaf temperature at the highest photosynthetic rate. Therefore, it was assumed that OPTM were average air temperatures over the warmer part of the growing season, when the air temperature was greater than or equal to 10 degrees C (°C) in all parts of the land. This calculation gives higher average air temperature than that during growing season, and

may give closer air temperature on sunny days during growing season. A function for the air temperature multiplier was determined according to the air temperature response curves of the tree species' photosynthesis (Semikhatova et al., 1992) by modifying the Gauss distribution curve as follows:

$$f(T) = 1/(\text{sqrt}(2\pi) \times 10) \times \exp(-1/8 \times ((T - OTMP)/10)^4) \quad (8)$$

Since one pixel of PAL data covers about 64 km^2, various species with different photosynthetic capacities must grow within an area of each pixel. Therefore, the optimum-temperature range was set broader than that of single species. It was assumed that f(T) is dependent only on OTMP due to the uncertainty of responses for various species.

Vegetation growth suffers seriously as a result of soil water deficit and low air humidity. Therefore a soil water stress function was considered to reduce errors in NPP estimation in arid and semiarid areas. Although the response of vegetation to soil water deficit is complicated and varies by soil type and species (Kozlowski and Keller, 1966), only loam soil and mesophytes were considered. Since photosynthetic rate changes linearly against soil water content in low SW (Maruyama and Toyama, 1987; Larcher, 2003), a linear multiplier f(SW) was determined as follows based on the literature (Larcher, 2003) when SW is less than 0.2. The f(SW) was applied in areas where NDVI was less than 0.42:

$$f(SW) = (SW - 0.12)/0.08 \quad (9)$$

f(SW) was set to 0 when SW is less than 0.12 (permanent wilting point). Since stress is small in high SW (Maruyama and Toyama, 1987; Larcher, 2003), the stress was neglected and f(SW) was set to 1 when SW was over 0.2.

2.3.2 LUE Setting and NPP Estimation

Because LUE depends on the vegetation type (Gower et al., 1999), different ε' values were used for different vegetation types, which were defined in the IGBP-DIS land cover map. The maximum photosynthetic rate is nearly proportional to the maximum relative growth rate (Chapin III et al., 2002), which is NPP during ideal environmental conditions for vegetation growth. Area-based photosynthetic capacity is a good measure of the photosynthetic rate per unit available light (Chapin III et al., 2002). Therefore, we assumed that the maximum photosynthetic rate was an indicator of LUE and proportional to LUE among ecosystems. Deciduous temperate forests, which have a medium photosynthetic rate among global natural vegetation (Larcher, 2003), were selected as the standard to determine $\varepsilon'(v)$. A constant LUE was determined at first for global vegetation by a linear regression analysis using the climatic potential NPP and the products of NDVI and

SR (Awaya et al., 2004). The climatic potential NPP is computed only taking into account the climatic conditions for plant growth, and was computed using the Chikugo model (Uchijima and Seino, 1985) in this study.

The constant LUE was calculated as 0.494 g DW MJ^{-1} for net production. This value was assumed to be the LUE of deciduous temperate forest. LUEs ($\varepsilon'(\upsilon)$) of other ecosystems of 17 IGBP-DIS types were calculated by multiplying the above value by the ratio of the maximum photosynthetic rate of the ecosystem to deciduous temperate forest (multiple LUEs, Table 1). Since natural vegetation has longer leafy periods than crops, mixture of natural vegetation in crop fields within a pixel (mixture pixel or mixel) causes an apparent longer leafy period than that of pure crops. It results in greater NDVI in mixels than that in pixels of pure crops in seedling stage. Therefore, the LUEs were averaged with weights, which were one for crops and two for others, for mixed vegetation types with crops to reduce the effect of leafy periods.

Global NPP was estimated using equation (7) using T, SW, SR and the corrected NDVI for the period between 1982 and 1999. Kanda et al. (2002) used 10°C as a threshold of effective cumulative air temperature to estimate plant growth in Japan. *Poa* spp. starts leaf extension at about 10°C in the lower Alps in Austria (Fitter and Hay, 2002). Thus, 10°C would be a reasonable choice of the cold air temperature limit for plant growth in the temperate zones. We assumed 10°C is the average of the cold air temperature limit for terrestrial vegetation growth. The cold limit of growth temperature

Table 1: Weights for LUE setting

Categories	Weight
Evergreen needleleaf forest	0.35
Evergreen broadleaf forest	0.70
Deciduous needleleaf forest	0.74
Deciduous broadleaf forest	1.00
Mixed forest	0.68
Closed shrublands	0.58
Open shrublands	0.58
Woody savannas	1.75
Savannas	1.75
Grasslands	0.85
Permanent wetlands	0.47
Croplands	1.78
Urban and built-up	0.35
Cropland/natural vegetation mosai	1.03
Snow and ice	0.00
Barren or sparsley vegetated	1.65
Water bodies	0.00

depends on species, area and environment, and is not easy to determine on a global scale. Therefore, for this study, NPP was computed for months with air temperatures greater than or equal to 10°C. NPP was also estimated using the constant LUE (0.494 g DW MJ^{-1}) for all vegetation, and the two results were compared.

2.3.3 Inter-annual Variation Analysis

The total global NPP was calculated for each year by weighting areas of each vegetation type using the multiple LUEs and a constant LUE. Inter-annual changes of global NPP were examined by a scattergram and a linear regression analysis for both LUE setting cases. Regional distribution patterns of NPP were examined visually. The rate of NPP change was computed by a linear regression analysis for each pixel after averaging NPP by a local moving window of 11 by 11 pixels for the multiple-LUE-setting case. The primary purpose of applying 11 by 11 pixel moving window was to reduce effects of noise and to identify local inter-annual trends. Regional variations in the rate of NPP change, i.e. the variations in the slopes of regressions in the regional scale, were checked. Training areas were selected in areas with the greatest NPP increase and decrease, and average values of T, SR, SW and NDVI were computed for the training areas. Inter-annual trends of these averages were depicted with scattergrams.

3 Results and Discussion

3.1 Intensity Correction

Pixels with lower and higher reflectance factors in the red and the near-infrared channels, respectively, give higher NDVI values, which result in higher NPP estimation in equation (5). Therefore it is very important to adjust image intensity at lower reflectance factors of ch1. The reason why setting the regressions, which cross 50% of reflectance factor, was to keep better intensity adjustment in dark pixels to make NPP estimation more accurate. This method will reduce the effect of misregistration of pixels and mixels caused by a coarse resolution since the coefficients of determination were between 0.821 and 0.972 for ch1 ($P<0.01$). For the case of ch2, it is important to adjust intensity of dense vegetation pixels with higher reflectance factors. Since differences of reflectance factors are great among land cover and vegetation types, effects of misregistration and mixels are serious in the regression analysis. We selected spatially and temporary homogeneous areas for the regression analysis to reduce these effects. As a result, the coefficients of determination were between 0.899 and 0.980 for ch2 ($P<0.01$).

These high values suggest that the pixels were sampled appropriately, and that the regression lines provided reliable intensity corrections.

Inter-annual changes of the averages were compared between the original and the corrected imagery. The averages of ch1, ch2 and NDVI of original data clearly changed with season (Figs. 1a, 2a and 3a). However, there were some exceptions to this pattern. For the case of ch1, there were a clear drop of the average from mid-1983 until early 1985, and a clear rise followed by another clear drop from the middle of 1991 until the end of 1993. The former and latter anomalies were caused probably by the eruption of Mt. El Chichon and Mt. Pinatubo, respectively. Atmospheric turbidity or optical thickness increased after these volcanic eruptions (Meteorological Agency of Japan, 1999), and this probably caused errors in atmospheric corrections during the PAL data processing.

The average reflectance factors of the original ch2 data shifted up at the end of 1984 and 1988, and dropped remarkably in 1995. These changes agreed with replacements of NOAA satellites (Kramer, 2002), and suggested poor calibration of each AVHRR sensor. Above all, reflectance factors of the original ch2 increased from 1989 until 1994 before a change of NOAA satellite (Kramer, 2002), and the reflectance factors dropped suddenly after the

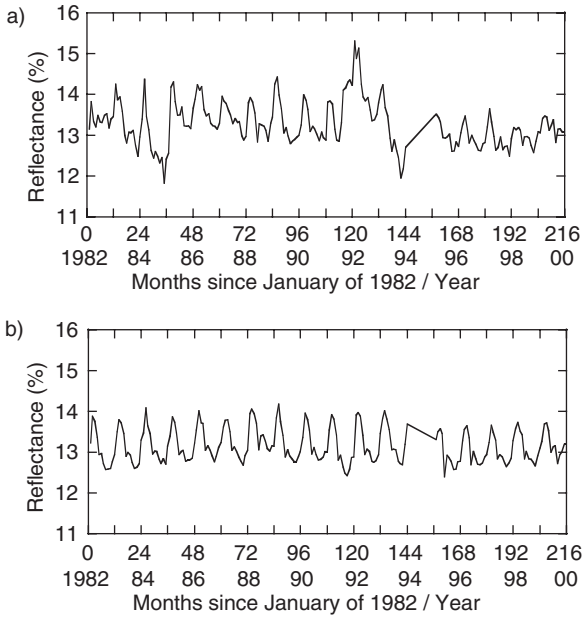

Figure 1: Changes in average reflectance in the standard area (channel 1). Averages within areas between 40°N and 35°S were computed. (a) Original PAL data, (b) the corrected data. Anomalies were observed clearly in the original PAL data, while the anomalies were removed after the correction.

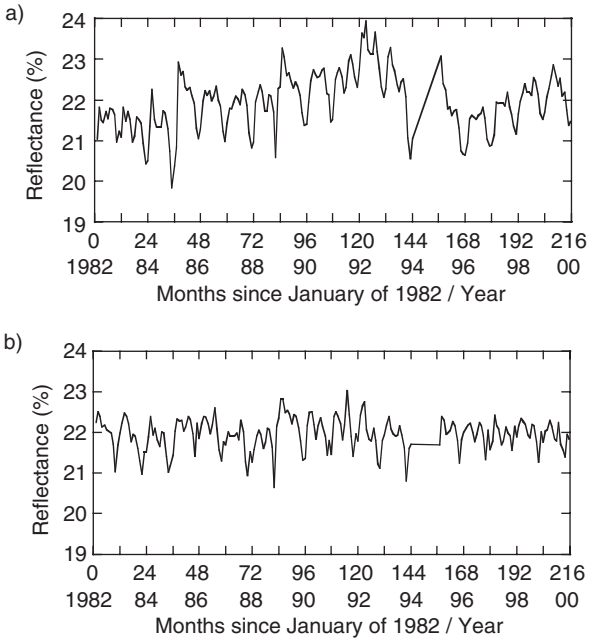

Figure 2: Changes of average reflectance in the standard area (channel 2). Averages within areas between 40°N and 35°S were computed. (a) Original PAL data, (b) the corrected data. The reflectance shifted up in 1985 and 1989, and the reflectance was increasing gradually. The reflectance dropped in 1993 suddenly and increased again after a change of NOAA satellite at the end of 1994. Similar anomalies with channel 1 also appeared in (a). On the other hand, the anomalies were removed after the correction.

change. Then the intensity increased again after 1995. The same trend with ch1 appeared in late 1984 and 1993 in ch2, namely, a clear drop followed by a clear increase followed by another clear drop. These inter-annual trends suggested that the quality of the original ch1 and ch2 images was unreliable, and that the original NDVI, which was computed using the original ch1 and ch2, was also unreliable. As a result, the original NDVI showed a trend that was opposite to that observed in the original ch1 and ch2 in 1984 and between 1992 and 1993. We pointed out that the original NDVI tended to increase since 1982, although there were many uncertainties in the PAL data processing.

On the other hand, inter-annual change patterns of the corrected ch1, ch2 and NDVI were cyclic (Figs. 1b, 2b and 3b). Global vegetation conditions during the study periods were unclear, however, there was no report about a severe vegetation damage on a global scale. Vegetation probably grew as usual in most parts of the world during the study period. Thus, the corrected results were probably reasonable. On the other hand, it should be noted that

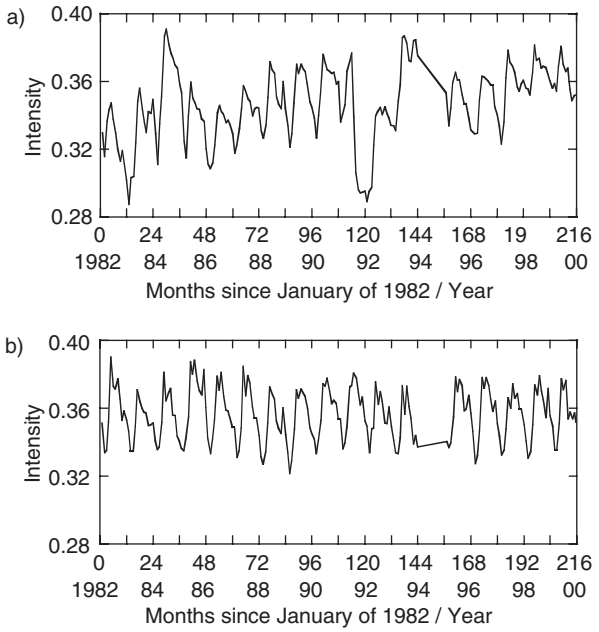

Figure 3: Changes of average intensity in the standard area (NDVI). Averages within areas between 40°N and 35°S were computed. (a) Original PAL data, (b) the corrected data. Opposite trends of anomalies with channel 1 and channel 2 appeared in the original NDVI. The anomalies were removed after the correction.

plants change their spectra greatly season after season in the near-infrared wavelength (Awaya and Tanaka, 1996, 1999; Kodani et al., 2002). There is a risk that the seasonal spectral changes interfere with the correction of ch2, although we sampled spectrally stable pixels for the correction.

3.2 Light Use Efficiency Setting

The PAL data were produced using the Global Area Coverage (GAC) data of AVHRR (Smith et al., 1997). One GAC pixel is an average of sampled 4 pixels within pixels of five columns and three lines of the original AVHRR data (Townshend and Justice, 1986). This means that one GAC pixel may not represent the most common land cover of the area covered by original 5 by 3 pixels. Some GAC pixels are arranged in a coordinate system having 8 km grid in the PAL data, and the pixel with maximum NDVI during a month is chosen for the monthly compositions. Therefore, the PAL data are temporal and spatial mixtures of different ground objects and vegetation species, and it is difficult to determine the appropriate LUE for each pixel. Even though the IGBP-DIS vegetation map consisted of basic plant types

based on plant physiognomy (Running et al., 1994a; Loveland et al., 2000), the compositions of the plant species in the pixels varied. This suggests that using LUEs, which were measured in the field in the literature (e.g. Gower et al., 1999), would not be appropriate without adjustments. Therefore, Awaya et al. (2004) used a constant LUE, which was determined by analysing the relationship between the climatic potential NPP and the sums of products of NDVI multiplied by SR. On the other hand, the plant species distributions show clear geographical gradients. Thus, it is necessary to take into account both the geographical gradient of species and spatiotemporal mixture of various species in the pixels. Therefore, the constant LUE of 0.494 g DW MJ^{-1} was supposed to be an average LUE of global natural vegetation for the PAL data, and was used as a standard of LUE computation in this study (Table 1). Owing to the nature of the GAC data, the appropriateness of the LUE-setting is unclear.

3.3 NPP Estimation

3.3.1 Inter-annual Change

The highest and the lowest annual global NPP were 58.3 and 62.6 petagram (Pg) carbon in 1983 and 1998, respectively, for the multiple LUE-setting case. For the case of the constant LUE-setting, the highest and the lowest NPP were 51.0 and 54.8 Pg carbon in 1983 and 1991, respectively (Fig. 4). The constant LUE-setting case was about 12% lower than the multiple

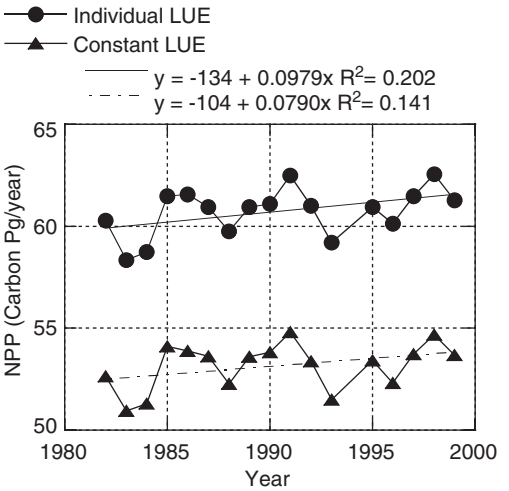

Figure 4: Inter-annual changes in global NPP. The results of multiple and a constant LUE-settings were compared. NPP of a constant LUE case was about 8% smaller than the case of multiple LUE-setting. The slopes of the regression lines show the annual rate of NPP increase.

LUE-setting case. This shows that the LUE control has a big influence on NPP estimation. The IPCC working group I cites 2 NPP estimations, which are 59.9 and 62.6 Pg carbon per year, in the latest report (Houghton et al., 2001). These values were similar to the NPPs estimated by the multiple LUE settings, but greater than NPPs estimated by the constant LUE setting. Intensive validation would be necessary to know the actual terrestrial NPP distribution.

Although the atmospheric CO_2 concentration is increasing steadily, its rate of increase varies from month to month. The rate of increase appears to be influenced by the CO_2 uptakes of terrestrial and ocean ecosystems. Therefore, the rate of changes in CO_2 concentration (hereafter, CO_2 change rate) may show a similar inter-annual pattern to NPP. According to the atmospheric CO_2 measurements, the CO_2 change rate was greater in 1983, early 1988, early 1994 and early 1998 than in other periods. On the other hand, the rate was smallest in early 1992, and was smaller in early 1990, 1996 and 1999 than in other periods (Meteorological Agency of Japan, 1999, 2002). A greater CO_2 change rate in these periods than in other periods suggests less uptake of CO_2 by ecosystems (smaller NPP), and a smaller change rate suggests the opposite. Valleys of NPP appeared in 1982, 1983, 1988, 1993 and 1996, and peaks appeared in 1985, 1986, 1991 and 1998 (Fig. 4). Although the cases of 1996 and 1998 didn't agree with the atmospheric CO_2 change rate, our NPP estimation closely resembled to the inter-annual change trend of the atmospheric CO_2.

The regression coefficients in Fig. 4 suggest that global NPP was increasing about 0.1 Pg annually ($P<0.1$) for the case of multiple LUE-settings and about 0.08 Pg carbon annually (not significant) for the case of constant LUE-setting. These results mean that global NPP increased about 3% during 20 years in the 1980s and 1990s. The carbon fixation by the terrestrial ecosystem was estimated at -0.2 ± 0.7 per year in the 1980s and -1.4 ± 0.7 Pg per year in the 1990s by atmospheric CO_2 analysis (Houghton et al., 2001). This suggests that carbon fixation by terrestrial ecosystem was increasing roughly 0.12 Pg annually, and our NPP estimation showed a similar result especially for the case of multiple LUE-settings. Though our estimates of global NPP seem to be reasonable, the accuracy of the corrected PAL and NCEP/NCAR data should be validated carefully to make more accurate NPP estimation possible.

3.3.2 Regional Distribution

NPP was very small in the arid areas (the Sahara, the Gobi and Western Australia), high mountains (the Himalayas, the Tibet plateau, the Andes and the Rockies) and latitudes higher than 60° north as reported in the literature (Chapin III et al., 2002; Larcher, 2003). NPP was obviously

greater in Europe than other areas in the same latitudes, and NPP was greater in the coastal regions than inland in low latitudes. NPP appeared to be high in agricultural areas in the eastern USA, eastern China and Europe (Fig. 5). The greatest NPP appeared not in the tropical forests but in the tropical deciduous forests or savannas. The tropical rain forests have the greatest NPP and the savannas have about a half the tropical rain forests according to the literature (Chapin III et al., 2002; Larcher, 2003). Thus our results were different from those obtained in previous ecological studies for subtropical and tropical vegetation for the case of multiple LUE setting. However, the constant LUE approach gave monthly NPP maps with more

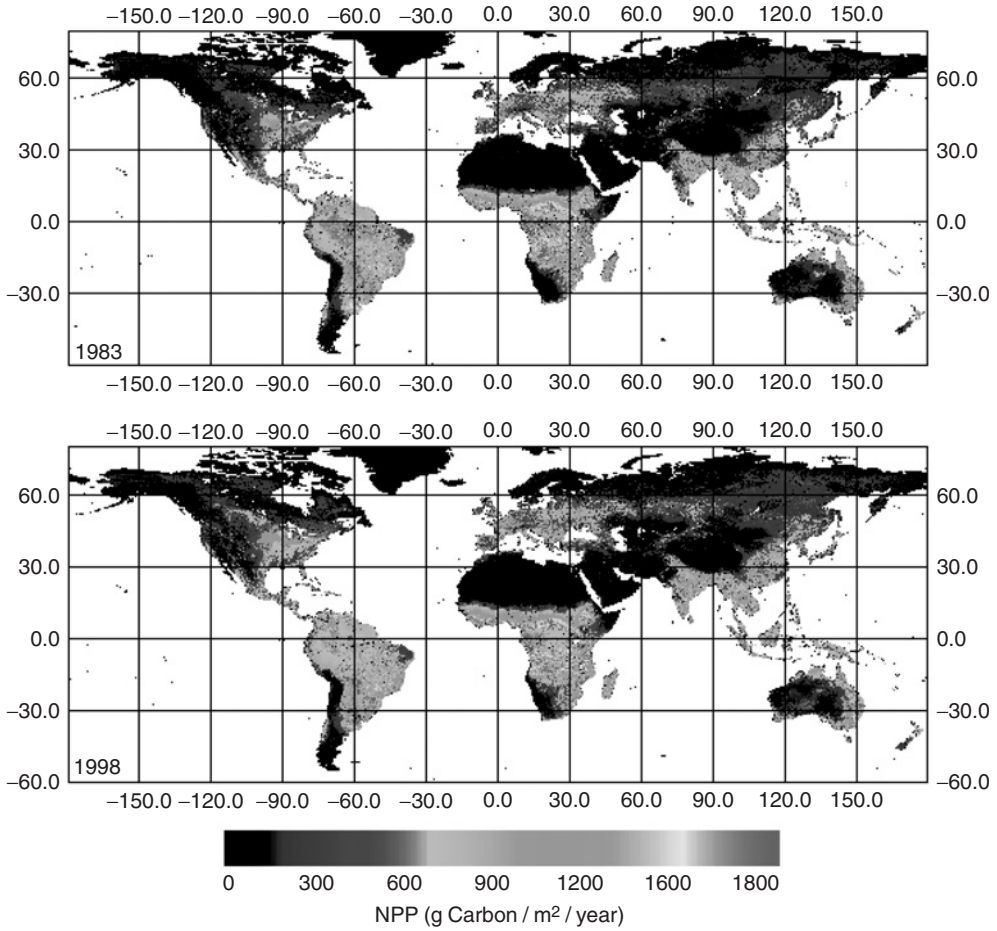

Figure 5: The results of NPP estimation by the multiple LUE settings. The minimum appeared in 1983 (above), and the maximum appeared in 1998 (below). The greatest NPP appeared in tropical deciduous forest or savannas. (for colour version; see Colour Plate Section)

similar seasonal changes to NPP maps by ecological models in Cramer et al. (1999). The geographical distribution of NPP obtained by the constant LUE approach was more similar to that obtained by an ecological model (Ito and Oikawa, 2002) than that obtained by the multiple LUE settings (Fig. 5). Although the LUEs were based on the eco-physiological knowledge, the results seemed less reasonable than the constant LUE. An appropriate LUE-setting method for the PAL data should be developed to make more precise estimation possible as described previously.

3.3.3 Regional Variation of Inter-annual Changes

The inter-annual change rates of NPP varied region by region. However, NPP appeared to be increasing in many parts of the world (Fig. 6). Myneni et al. (1997) reported that plant growth was increasing between 1981 and 1990 due to lengthening of the active growing season, and the greatest increase existed between 45°N and 70°N based on an analysis of NDVI images. Although our analysis showed a great NPP increase in East Europe, the rate was not the highest. The greatest rate of increase appeared in southern India (12°N, 79°E) and in south-western Australia (28.5°S, 125.5°E). On the other hand, the greatest rate of decrease appeared in Bolivia (19.5°S, 60°W) and in the Southern Angola (14.5°S, 20.5°E). Inter-annual changes in T, SW, SR and the corrected NDVI were checked in these four areas. No clear trend was

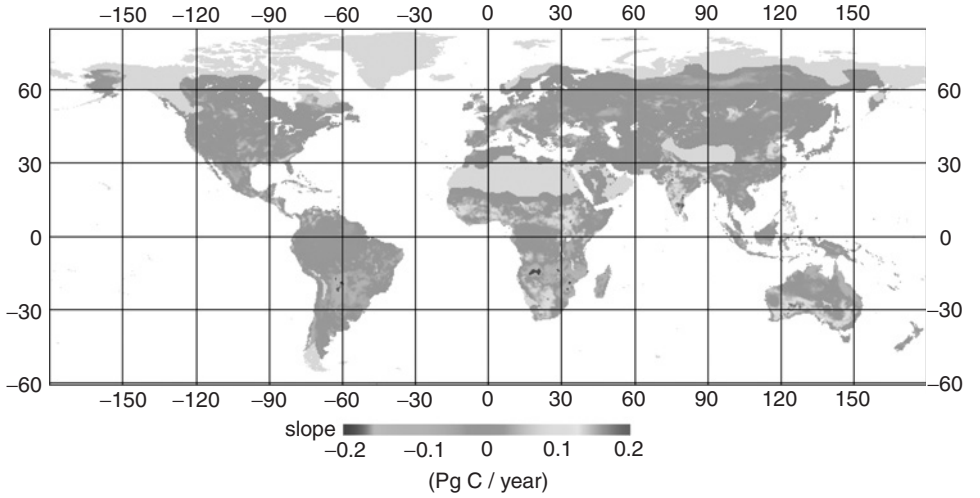

Figure 6: Regional changes of NPP. The rate of NPP change in each region was estimated by a linear regression analysis for the results of the multiple LUE-setting for 17 vegetation classes. Clear increases and decreases of NPP were detected in some areas around semiarid zones. Grey areas show extremely low NPP and were omitted in the regression analysis. (for colour version; see Colour Plate Section)

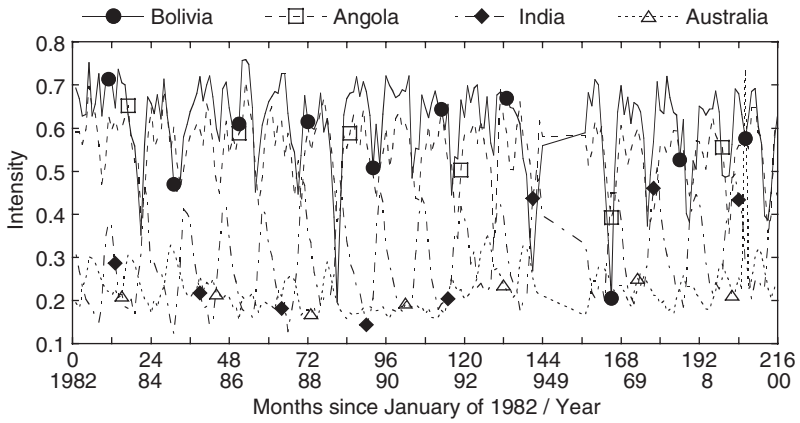

Figure 7: Inter-annual changes of NDVI in areas with the greatest rate of change of NPP. NDVI decreased consistently in Bolivia and Angola, but increased slightly in India.

observed in the NCEP/NCAR parameters except for SW and T in Angola. However, NDVI has tended to decrease in Bolivia and Angola, and has tended to increase in India (Fig. 7). Long-term trends in NDVI seemed to have a strong influence in the regional variations of inter-annual NPP changes, although no clear relationship between NPP and the parameters was found in south-western Australia. The greatest NPP changes appeared in semiarid areas where precipitation changes have significant impacts on vegetation growth. The data in Fig. 6 suggest that changing precipitation patterns have had a greater impact in semiarid areas than an impact in boreal areas by increasing air temperature on vegetation growth. Although NDVI values are also affected by factors such as land cover change, biomass burning and so on, the NDVI images appear to show the effect of changing precipitation patterns on vegetation growth in semiarid areas, which was unclear in the reanalysis data. Therefore, NDVI appears to be a good indicator of global change in vegetation.

4 Conclusion

An LUE-based NPP estimation model, which used NDVI data in the Pathfinder AVHRR Land (PAL) dataset, solar radiation, air temperature, and soil water content, was applied to estimate global NPP and to analyse annual and regional variations of NPP.

A regression-based intensity correction method was applied to PAL data of ch1 and ch2, and NDVI was computed using these data. Anomalies in monthly global average in the original ch1, ch2 and NDVI data were greatly

reduced by the correction. The correction results seemed to be reliable according to the evaluation of NPP inter-annual change trends. However, regional events such as biomass burning, small volcanic eruptions, and yellow wind, cause regional anomalies in the PAL images, and our intensity adjustment method cannot remove these regional anomalies.

Since the NPP estimation was greatly influenced by LUE, it will be necessary to develop a method to determine reliable LUEs for temporal and spatial mixels of PAL data. Our NPP estimation showed that global NPP was increasing between 1982 and 1999. The rate of NPP increase was similar with the rate of carbon absorption by terrestrial ecosystems based on atmospheric CO_2 measurements (Houghton et al., 2001). Our results demonstrate that PAL images after accurate radiometric corrections can give reliable estimations of changes in NPP. We conclude that the corrections of PAL data were successful in reducing anomalies caused by huge volcanic eruptions on a global scale, and that the NPP estimation was reasonable.

The inter-annual NPP changes were different in different regions. The regional differences seemed to be caused mainly by inter-annual variation of NDVI according to our analysis. The greatest NPP changes appeared in semiarid areas. This suggests that precipitation changes have a great impact on terrestrial NPP, which is a major component of the carbon budget. Precipitation changes in semiarid areas should have a greater impact on NPP than an increase air temperature in boreal areas.

The Terra satellite was launched in December 1999 and observations using MODIS were started. The MODIS data should greatly improve the accuracy of global vegetation analysis based on the original mission concepts (Running et al. 1994b) by overcoming the problems in AVHRR data analyses. However, the AVHRR data, which have been recorded since the 1970s, are important records of terrestrial vegetation. A proper correction of the AVHRR data will make analyses of global vegetation status in the last two decades reliable. Therefore, the AVHRR data are still very important to understand climatic impacts on terrestrial ecosystems under ongoing global change.

Acknowledgements

This study was supported by the research project ‘Global Carbon Cycle and the Related Global Mapping Based on Satellite Imagery’ operated by the former Science and Technology Agency of Japan, currently Ministry of Education, Culture, Sports, Science and Technology. The authors thank members of the project for meaningful discussions to improve our study. The authors also thank Miss Tae Toba for summarizing the reference data.

References

Asrar, G., Fuchs, M., Kanemasu, E. T., Hatfield, J. L., 1984. Estimating absorbed photosynthetic radiation and leaf area index from spectral reflectance in wheat. Agronomy Journal 76, 300–306.

Awaya, Y., Tanaka, N., 1996. Successional and seasonal pattern of spruce spectra: as a basis of forest monitoring. In: Proceedings for the 26th International Symposium on Remote Sensing of Environment, 25–29 March 1996, Vancouver: ISRSE & CRSS, pp. 142–146.

Awaya, Y., Tanaka, N., 1999. Seasonal spectral changes in cool temperate forests: An analysis using Landsat TM images. Journal of the Japan Society of Photogrammetry and Remote Sensing 38 (4), 35–46 (in Japanese with an English abstract).

Awaya, Y., Kodani, E., Tanaka, K., Liu, J., Zhuang, D., Meng, Y., 2004. Estimation of the global net primary productivity using NOAA images and meteorological data: Changes between 1988 and 1993. International Journal of Remote Sensing 25 (9), 1597–1613.

Butler, J. J., Barnes, R. A., 1998. Calibration Strategy for the Earth Observing System(EOS)-AM1 Platform. IEEE Transactions on Geoscience and Remote Sensing 36 (4), 1056–1061.

Box, E. O., Holben, B. N., Kalb, V., 1989. Accuracy of the AVHRR vegetation index as a predictor of biomass, primary productivity and net CO_2 flux. Vegetatio 80, 71–89.

Chapin III, F. S., Matson, P. A., Mooney, H. A., 2002. Principles of Terrestrial Ecosystem Ecology. Springer, New York, pp. 105–122.

Chen, J. M., Pavlic, G., Brown, L., Cihlar, J., Leblanc, S. G., White, H. P., Hall, R. J., Peddle, D. R., King, D. J., Trofymow, J. A., Swift, E., Van der Sanden, J., Pellikka, P. K. E., 2002. Derivation and validation of Canada-wide coarse-resolution leaf area index maps using high-resolution satellite imagery and ground measurements. Remote Sensing of Environment 80, 165–184.

Cramer, W., Kicklighter, D. W., Bondeau, A., Moore III, B., Churkina, G., Nemry, B., Ruimy, A., Schloss, A. L.the participants of the Potsdam NPP Model Intercomparison, 1999. Comparing global models of terrestrial net primary productivity (NPP): Overview and key results. Global Change Biology 5 (Suppl. 1), 1–15.

Dwyer, E., Gregoire, J. M., Malingreau, J. P., 1998. A global analysis of vegetation fires using satellite images: Spatial and temporal dynamics. Ambio 27 (3), 175–181.

Eck, T. F., Holben, B. N., Reid, J. S., Dubovik, O., Smirnov, A., O'Neill, N. T., Slutsker, I., Kinne, S., 1999. Wavelength dependence of the optical depth of biomass burning, urban, and desert dust aerosols. Journal of Geophysical Research 104 (D24), 31333–31349.

Fitter, A., Hay, R., 2002. Environmental Physiology of Plants3rd edn . Academic Press, London, pp. 211–224.

Gower, S. T., Kucharik, C. J., Norman, J. M., 1999. Direct and indirect estimation of leaf area index, fAPAR, and net primary production of terrestrial ecosystems. Remote Sensing of Environment 70, 29–51.

Houghton, J. H., Y. Ding, D. J. Grigss, M. Noguer, P. J. van der Linden, D. Xiaosu (Eds.), 2001, Climate Change 2001: The Scientific Basis. Cambridge University Press, Cambridgepp. 99–237.

Ito, A., Oikawa, T., 2002. A simulation model of the carbon cycle in land ecosystems (Sim-CYCLE): A description based on dry-matter production theory and plot-scale validation. Ecological Modelling 151, 143–176.

Justice, C. O., Townshend, J. R. G., Holben, B. N., Tucker, K., 1985. Analysis of the phenology of global vegetation using meteorological satellite data. International Journal of Remote Sensing 6 (8), 1271–1318.

Kalnay, E., Kanamitsu, M., Kistler, R., Collins, W., Deaven, D., Gandin, L., Iredell, M., Saha, S., White, G., Woollen, J., Zhu, Y., Chelliah, M., Ebisuzaki, W., Higgins, W., Janowiak, J., Mo, K. C., Ropelewski, C., Wang, J., Leetmaa, A., Reynolds, R., Jenne, R., Joseph, D., 1996. The NCEP/NCAR 40-year reanalysis project. Bulletin of the American Meteorological Society 77 (3), 437–471.

Kanda, E., Torigoe, Y., Kobayashi, T., 2002. A simple model to predict the development of rice panicles using the effective air temperature. Japanese Journal of Crop Science 71, 394–402.

Kodani, E., Awaya, Y., Tanaka, K., Matsumura, N., 2002. Seasonal patterns of canopy structure, biochemistry and spectral reflectance in a broad-leaved deciduous *Fagus crenata* canopy. Forest Ecology and Management 167, 233–249.

Kramer, H. J., 2002. Observation of the Earth and its Environment4th edn . Springer, Berlin, pp.730–742.

Larcher, W., 2003. Physiological Plant Ecology4th edn . Springer-Verlag, Berlin, pp.100–104.

Loveland, T. R., Reed, B. C., Brown, J. F., Ohlen, D. O., Zhu, Z., Yang, L., Merchant, J. W., 2000. Development of a global land cover characteristics database and IGBP DISCover from 1 km AVHRR data. International Journal of Remote Sensing 21 (6&7), 1303–1330.

Malmström, C. M., Tompson, M. V., Juday, G. P., Los, S. O., Randerson, J. T., Field, C. B., 1997. Interannual variation in global-scale net primary production: testing model estimates. Global Biogeochemical Cycles 11, 367–392.

Maruyama, K., Toyama, Y., 1987. Effect of water stress on photosynthesis and transpiration in three tall trees. Journal of Japanese Forest Society 69, 165–170.

Meteorological Agency of Japan, 1999. Climatic aberration report '99. Printing Bureau of Ministry of Finance, Tokyo, pp. 63–91. (In Japanese; the title is a tentative translation by the author.)

Meteorological Agency of Japan, 2002. Climate change monitoring report 2002. http://www.data.kishou.go.jp/climate/cpdinfo/monitor/2002/. (In Japanese; the title is a tentative translation by the author.)

Monteith, J. L., 1972. Solar radiation and productivity in tropical ecosystems. Journal of Applied Ecology 9, 747–766.

Myneni, R. B., Williams, D. L., 1994. On the relationship between FAPAR and NDVI. Remote Sensing of Environment 49, 200–211.

Myneni, R. B., Keeling, C. D., Tucker, C. J., Asrar, G., Nemani, R. R., 1997. Increased plant growth in the northern high latitudes from 1981 to 1991. Nature 386 (17), 698–702.

Potter, C. S., Randerson, J. T., Field, C. B., Matson, P. A., Vitousek, P. M., Mooney, H. A., Klooster, S. A., 1993. Terrestrial ecosystem production: A process model based on global satellite and surface data. Global Biogeochemical Cycle 7, 811–841.

Prince, S. D., Goward, S. N., 1995. Global primary production: A remote sensing approach. Journal of Biogeography 22, 815–835.

Rao, C. R. N., Chen, J., 1995. Inter-satellite calibration linkages for visible and near-infrared channels of the Advanced Very High Resolution Radiometer on the NOAA-7, -9, and -11 spacecraft. International Journal of Remote Sensing 16, 1931–1942.

Ruimy, A., Saugier, B., Dedieu, G., 1994. Methodology for the estimation of terrestrial net primary production from remotely sensed data. Journal of Geophysical Research 99, 5263–5283.

Running, S. W., Loveland, T. R., Pierce, L. L., 1994a. A vegetation classification logic based on remote sensing for use in global biogeochemical models. Ambio 23 (1), 77–81.

Running, S. W., Justice, C. O., Salomonsen, V., Hall, D., Barker, J., Kaufman, Y. J., Strahler, A. H., Huete, A. R., Muller, J. P., Vanderbilt, V., Wan, Z. M., Teillet, P. M., Carneggie, D., 1994b. Terrestrial remote sensing science and algorithms planned for EOS/MODIS. International Journal of Remote Sensing 15 (17), 3587–3620.

Running, S. W., Nemani, R., Glassy, J. M., Thornton, P. E., 1999. MODIS daily photosynthesis (PSN) and annual net primary production (NPP) product (MOD17) algorithm theoretical basis document. Available at: http://modis.gsfc.nasa.gov/data/atbd/atbd_mod16.pdf, p. 59.

Semikhatova, O. A., Gerasimenko, T. V., Ivanova, T. I., 1992. Photosynthesis, respiration, and growth of plants in the Soviet Arctic. In: Arctic Ecosystems in a Changing Climate. Academic Press, San Diego, pp. 169–193.

Slater, P. N., Biggar, S. F., Holm, R. G., Jackson, R. D., Mao, Y., Moran, M. S., Palmer, J. M., Yuan, B., 1987. Reflectance- and radiance-based methods for the in-flight absolute calibration of multispectral sensors. Remote Sensing of Environment 22, 11–37.

Smith, P. M., Kalluri, S. N. V., Prince, S. D., Defries, R., 1997. The NOAA/NASA Pathfinder AVHRR 8-km land data set. Photogrammetric Engineering and Remote Sensing 63, 12–13 and 27–32.

Townshend, J. R. G., Justice, C. O., 1986. Analysis of the dynamics of African vegetation using the normalized difference vegetation index. Int. J. Remote Sensing 7 (11), 1435–1445.

Tucker, C. J., Gatlin, J. A., Schneider, S. R., 1984. Monitoring vegetation in the Nile delta with NOAA-6 and NOAA-7 AVHRR imagery. Photogrammetric Engineering and Remote Sensing 50, 53–61.

Uchijima, Z. H., Seino, J., 1985. Agroclimatic evaluation of net primary productivity of natural vegetations (1) Chikugo model for evaluating net primary productivity. Journal of Agricultural Meteorology 40, 343–352.

Young, S. S., Anyamba, A., 1999. Comparison of NOAA/NASA PAL and NOAA GVI data for vegetation change studies over China. Photogrammetric Engineering and Remote Sensing 65, 679–688.

Chapter 16

Global Mapping of Net Primary Production

Haruhisa Shimoda[1,*], Yoshio Awaya[2] and Ichio Asanuma[3]

[1]*Tokai University Research & Information Center, 2-28-4 Tomigaya, Shibuya, Tokyo 151-0063, Japan*
[2]*Forestry and Forest Products Research Institute, 1 Matsunosato, Tsukuba, Ibaraki 305-8687, Japan*
[3]*Tokyo University of Information Sciences, 1200-2, Yato, Wakaba, Chiba 265-8501, Japan*

Abstract

It is a well-known fact that atmospheric greenhouse gases are rapidly increasing within these 100 years, however, the sinks and sources of these gases are not necessarily clarified. Especially, sinks of carbon dioxide, which have the largest effects on global warming, are not evident. Generation of global map of net primary production (NPP) using earth-observing satellite data was performed in the research project named "International joint researches on global mapping of carbon cycle and its advancement" sponsored by the Ministry of Education, Culture, Sports, Science and Technology (MEXT). The results of this mapping project are briefly described in this chapter. The first global NPP maps using satellite data, which cover both ocean and continental ecosystems, have been obtained in this project. These global NPP maps have sufficient accuracy for a primary approximation. However, many problems remain, and various efforts are required to increase the accuracy of the global NPP data.

Keywords: NPP; global NPP; AVHRR; SeaWiFS

1 Introduction

It is a well-known fact that atmospheric greenhouse gases are rapidly increasing within these 100 years, however, the sinks and sources of these gases

*Corresponding author.
E-mail address: smd@keyaki.cc.u-tokai.ac.jp (H. Shimoda).

Elsevier Oceanography Series 73
Edited by H. Kawahata and Y. Awaya
ISBN: 0-444-52948-9

are not necessarily clarified. Especially, sinks of carbon dioxide, which have the largest effects on global warming, are not clearly described. Many researches have been done to clarify those sinks both in the land and the ocean. The difficulties in these researches are that ground-based researches are executed on a local scale and need a long period. For example, researches in forests need at least 10 years for each independent forest to derive meaningful results.

A global map of net primary production (NPP) was produced using earth-observing satellite data in the research project named "International joint researches on global mapping of carbon cycle and its advancement" sponsored by MEXT. The results of this mapping project are briefly described in this chapter.

2 Primary Production

It is necessary to estimate net carbon flux, which shows exchange of carbon dioxide between the ecosystems and atmosphere, in order to identify sinks of carbon dioxide (Field et al., 1998; Battle et al., 2000). However, only NPP maps, which show uptake of carbon dioxide by ecosystems, were generated in this project. The reasons are as follows. Vegetations on land and phytoplankton in the ocean both fix atmospheric carbon dioxide through photosynthesis process. This amount of fixation is called as gross primary production (GPP). After the fixation (mostly in night), vegetations emit carbon dioxide by respiration. NPP is the amount of difference between GPP and R (respiration). This way of retrieving NPP is the same both on land and in the ocean. On the contrary, the induction of net flux (NEP: net ecosystem production) is different between the land and the ocean.

Over land, carbon dioxide is further emitted through soil respirations (Matamala et al., 2003). In order to estimate NEP, amount of these soil respirations should be estimated, but estimation of the soil respiration is rather difficult using satellite data. In the ocean, final carbon dioxide fixations are achieved through sinking of dead phytoplanktons or their consumption zooplankton or fishes. It is also very difficult to estimate the fixation amount from satellite data (Baret and Guyot, 1991). In addition to these biological processes, absorption and emission of carbon dioxide through physical processes exist. It is necessary to know difference of carbon dioxide partial pressures just above and below sea surface to estimate this physical process. However, estimating difference of partial pressures is also difficult from satellite data.

Although the target of this project was set to estimate NPP, not NEP for those reasons above, the NPP maps obtained in this project are far from completeness. Many assumptions accompany the NPP retrieval processes both in the land and the ocean, and further, accurate validations have not

yet been achieved on a global scale. However we suppose that these results are still useful, and advanced and accurate NPP maps would be generated through detailed investigations of our results.

3 Outlines of NPP Estimation

3.1 Methods

Primary production is given by a product of absorbed radiant flux and photosynthetic efficiency. Absorbed radiant flux is given by a product of total radiant flux and absorption coefficient, while photosynthetic efficiency are affected by atmospheric temperature, water supply, nutrient supply, and so on. In the case of primary production estimation using satellite data, total radiant flux is estimated from the satellite data and then photosynthetic efficiency according to each target is determined. The total radiant flux corresponds to photosynthetic active radiation (PAR) and can be obtained from amounts of cloud retrieved from satellite data and solar irradiance at the top of the atmosphere. As for PAR, PAR distribution maps obtained from geostationary satellites are most appropriate, since PAR is an integrated value over a full day and geostationary satellites observe the earth's surface hour by hour. Other parameters, which are required for NPP estimation, are not specific and dependent upon each algorithm.

3.2 Estimation Over Land

Three algorithms were compared to estimate land NPP. In the first algorithm, satellite data were used to estimate light absorption coefficients (fraction of photosynthetical active radiation: fAPAR) and the light use efficiency was fixed in this algorithm. The second algorithm used different light use efficiency according to each vegetation type and satellite data. Light use efficiencies were mainly determined on the basis of published field data. The third algorithm was a process model and did not use satellite data, however, results of this algorithm were used for comparisons. This process model used land cover data and meteorological data as input parameters. After the comparison of first and second algorithms, we decided to use the first algorithm which showed a better result compared to the ground data and the results of process model. The details of this algorithm are described in chapter 15 of this book and Awaya et al. (2004). The second algorithm showed higher values of NPP over agricultural fields. The reason for this overestimate may come from the fact that light use efficiency of agricultural fields was mainly decided by experiments in Japan. Light use efficiency of agricultural fields may differ based upon nutrient fertilization, hence overestimation of NPP occurred in fields in developing countries.

3.3 Estimation in the Ocean

Only one algorithm was used for NPP estimation in the ocean. The most popular algorithm in this field is that given by Behrenfeld and Falkowski (1997). In this algorithm, light use efficiency is given by a 7th order polynomial as a function of sea surface temperature. The coefficients of this polynomial were obtained by a least squares fit to the *in-situ* measurements, however, a 7th order polynomial is rather unnatural to describe natural phenomena. In this project, light use efficiency was given by a function of chlorophyll-a concentration obtained by satellite data considering vertical light attenuation. As a result, light use efficiency was expressed by a 3rd order polynomial of sea surface temperature. The details of this algorithm are described in chapter 4 of this book and Asanuma et al. (2003).

4 Results and Discussions

4.1 Satellite Data Used

NOAA AVHRR Path Finder Land dataset between 1982 and 1998, which are distributed by NOAA only for this period, were applied to calculate the land NPP distribution. On the contrary, in the ocean, SeaWiFs dataset between 1998 and 2002, which are distributed by NASA, were applied to calculate the ocean NPP distribution. We could retrieve the overlapping period of land and ocean NPP map in 1998. The result and discussions for the year of 1998 are described in the following section.

4.2 Global NPP Map

Fig. 1 shows the daily mean of global NPP for each month in 1998, where Fig. 1-(a) to (l), are corresponding to January to December. It should be noted that one largest El-Nino occurred from the end of 1997 to 1998, and these results could be slightly different from other years. On the land, large values of NPP are obtained in tropical rain forests and savanna as well as boreal forests around 50 to 60 degree north. In the ocean, large values are obtained on the continental shelf regions, like the west coast of Africa, the East China Sea, and the west coast of South Africa during phytoplankton bloom. In the eastern equatorial Pacific ocean, which is known as the equatorial upwelling region, a rather high NPP values was observed. Comparisons from Fig. 1(a) to Fig. 1(l) exhibit a large seasonal change on a local scale.

Fig. 2(a) shows a monthly change of zonal mean of NPP. The highest values are obtained in September to October at 10 to 0 degree north. These areas correspond to the northern part of South America, a savanna in Africa, and a part of Indonesia and Malaysia. These seasonal increases of

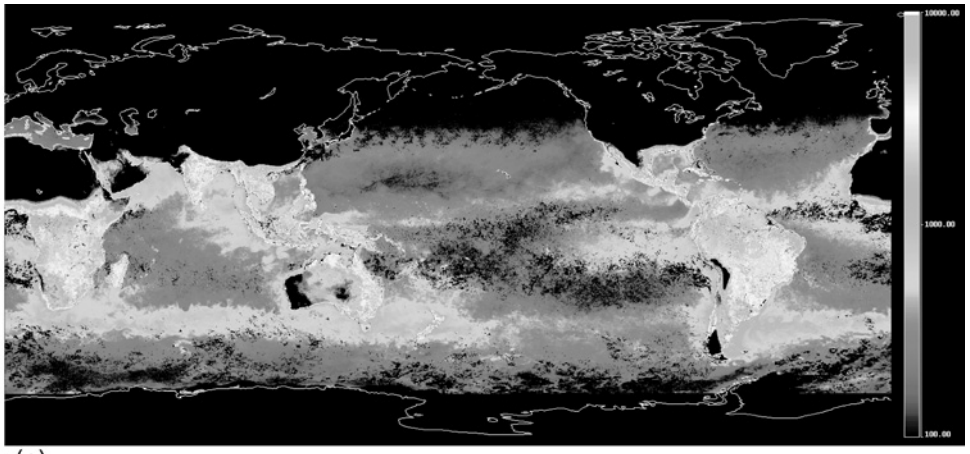

(a)

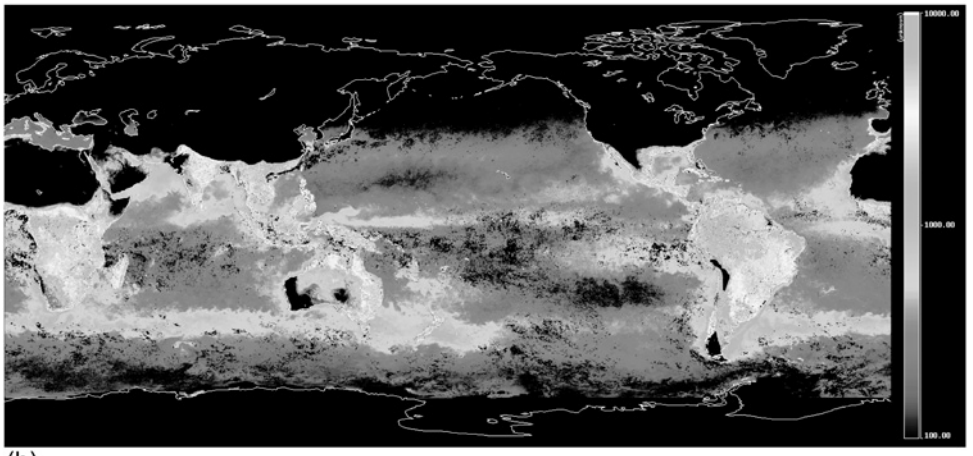

(b)

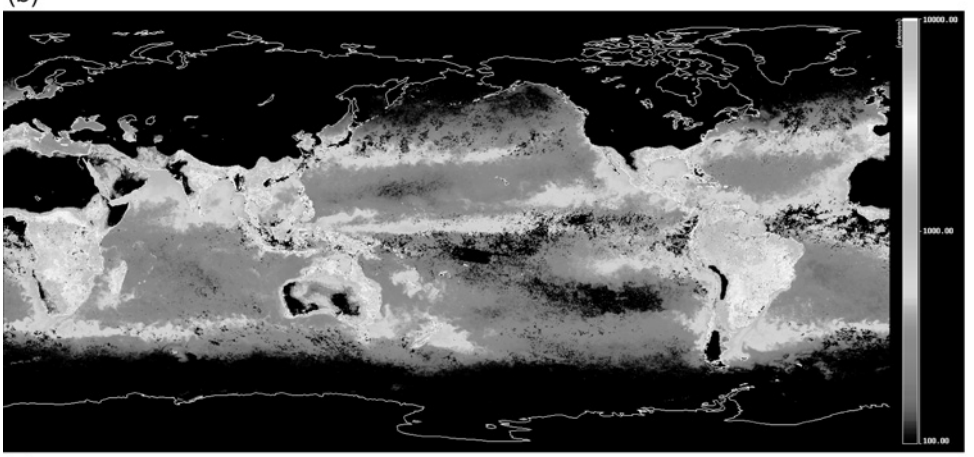

(c)

Figure 1: Global NPP maps in 1998. (a) January, (b) February, (c) March, (d) April, (e) May, (f) June, (g) July, (h) August, (i) September, (j) October, (k) November, (l) December (For colour version, see Colour Plate Section).

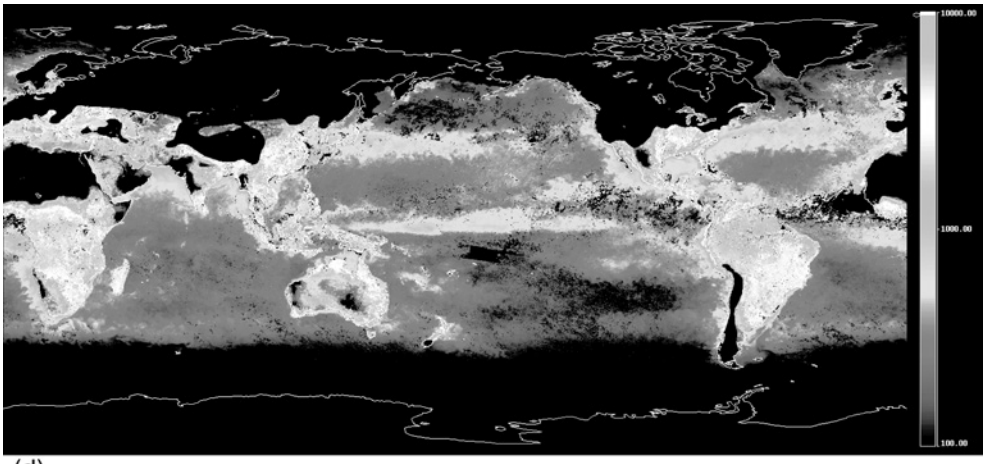

(d)

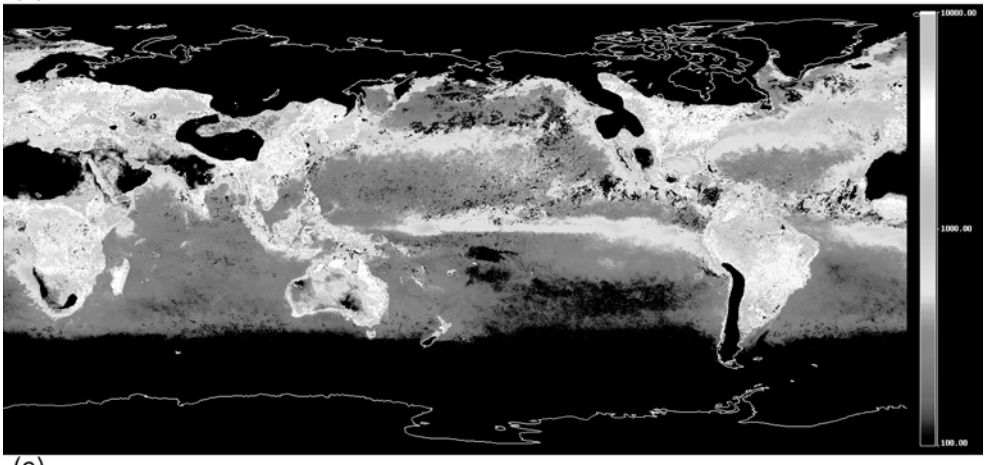

(e)

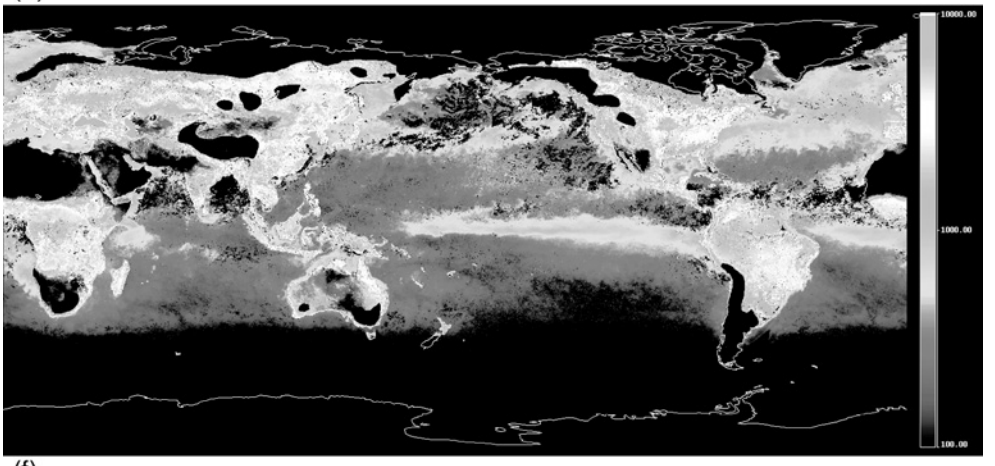

(f)

Figure 1 (Continued)

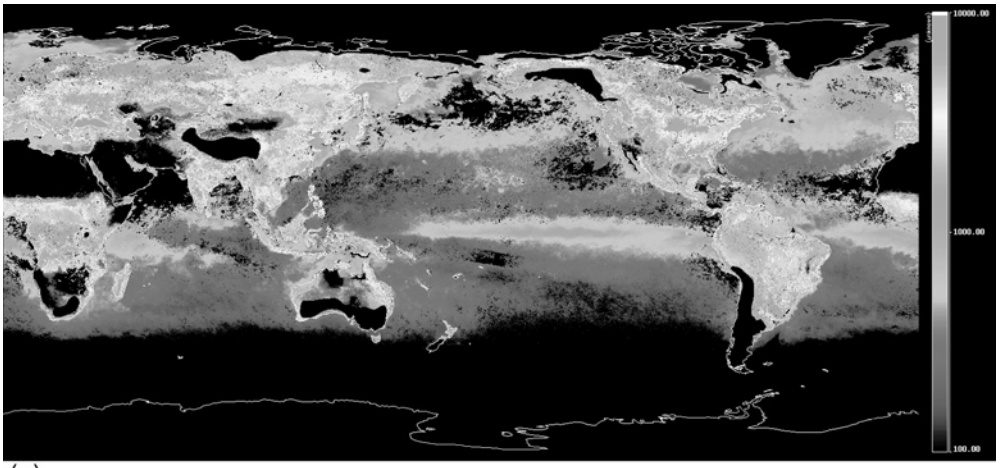

(g)

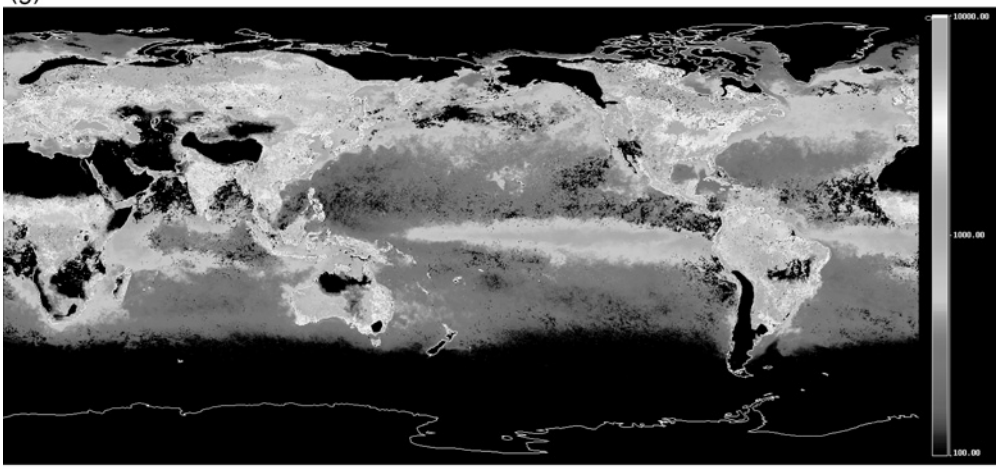

(h)

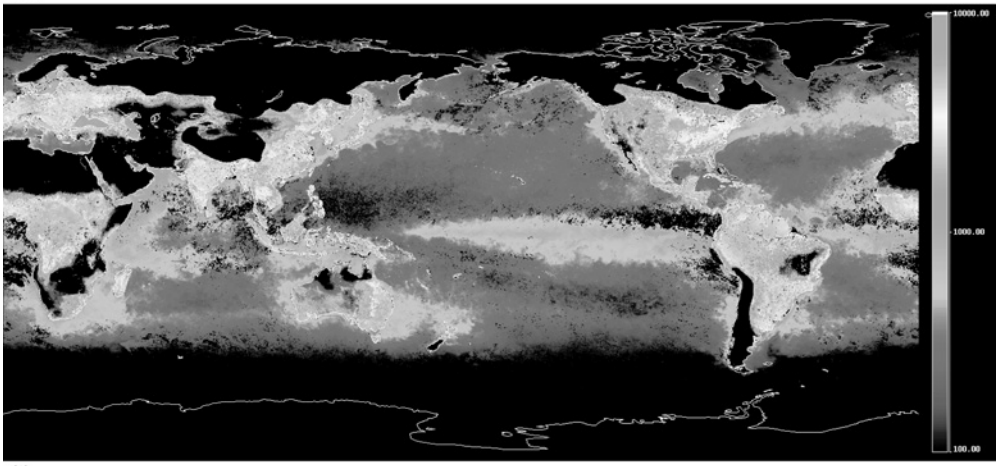

(i)

Figure 1 (Continued)

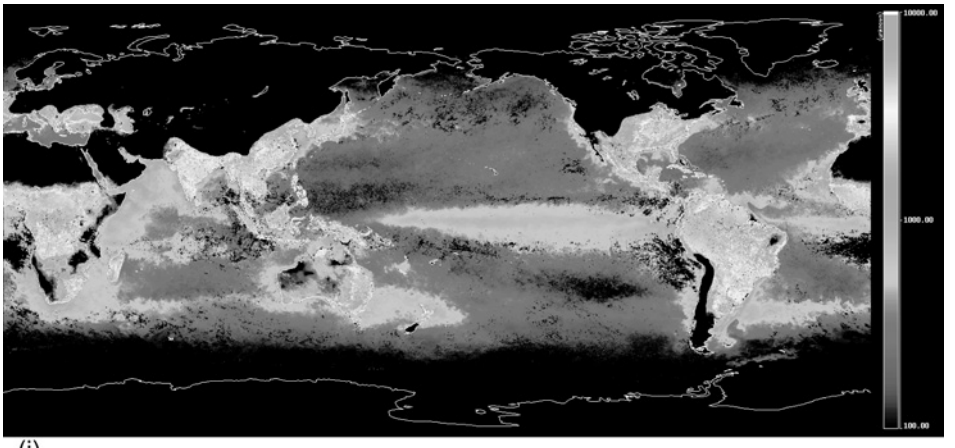

(j)

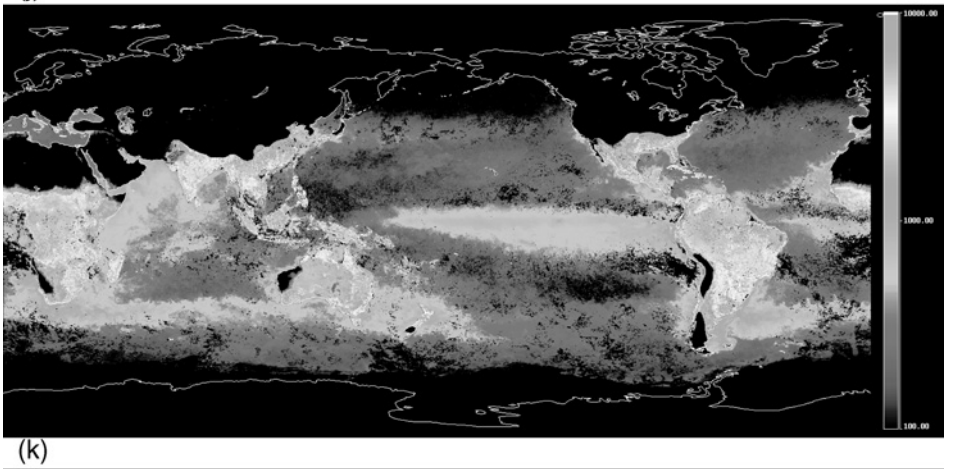

(k)

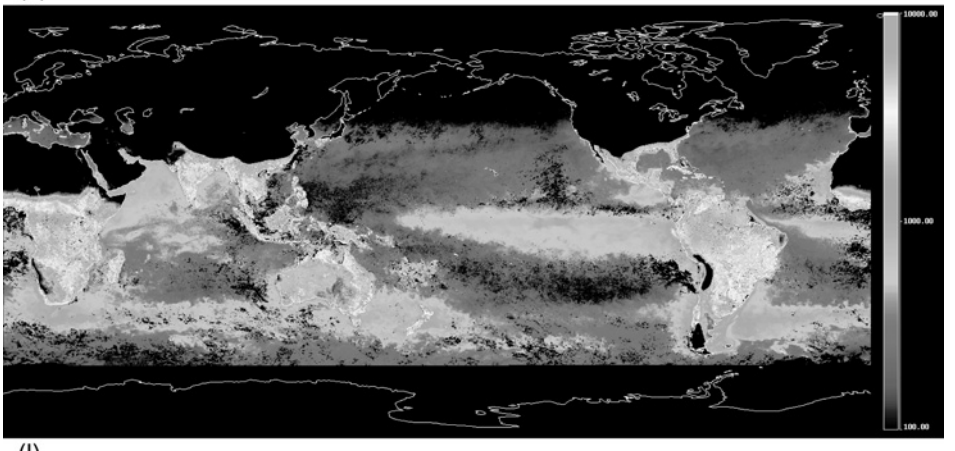

(l)

Figure 1 (Continued)

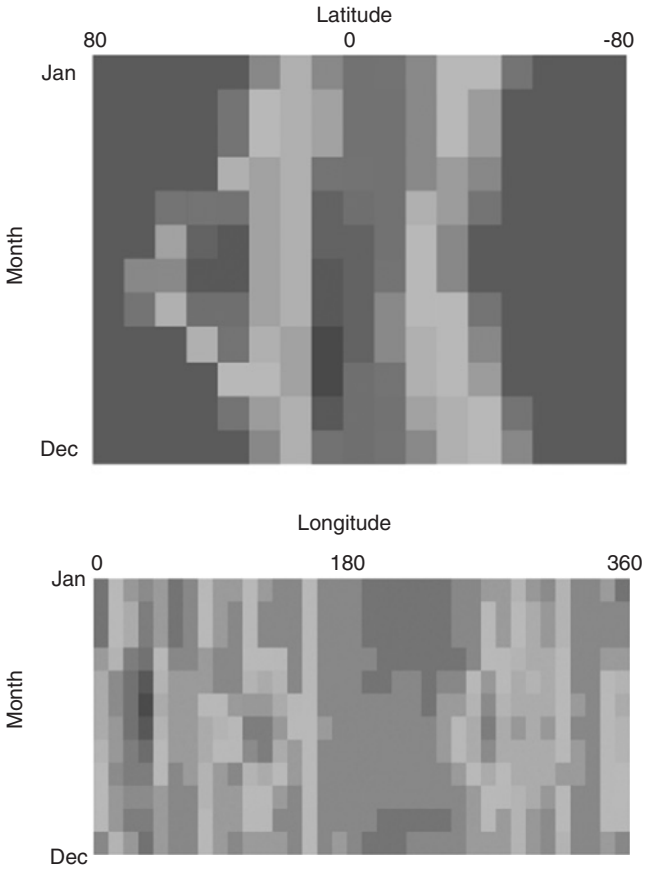

Figure 2: Seasonal change of zonal and meridional mean NPP. (a) Zonal mean. Horizontal axis corresponds to 80−80 degree from north to south and vertical axis corresponds to January to December. (b) Meridional mean. Horizontal axis corresponds to 0–360° eastbound and vertical axis corresponds to January to December (for colour version, see Colour Plate Section).

NPP may correspond to rainy season in these areas. High NPPs are next obtained in June to July at 30–50 degree north. These areas cover most of the large crop field in the North America and the Eurasia, which correspond to agricultural fields and exhibit a distinct seasonal change. In contrast, the regions from 10 to 20 degree north and 0–20 degree south show rather high NPP with very weak seasonal changes, where tropical forests are major contributors with weak seasonal changes.

Fig. 2(b) shows a monthly change of meridional mean of NPP. The highest values are obtained in May to July between 30 and 40 degree east, where the eastern part of Western Europe, some part of savanna, and some part of tropical forests are included. As tropical forests show very weak seasonal

change as discussed in a zonal mean of NPP, the seasonal change observed between 30 and 40 degree may be the result of the change in savanna and agricultural fields in Europe. This seasonal change is also evident between 0 and 30 degree east, where the western part of Europe could be a major contribution. Next high NPP regions are observed from June to August between 100 and 120 degree east, which covers the most of the South Eastern Asia and exhibits high seasonal variations, because of agricultural fields in this region. The North and South America also show high NPP values, which is corresponding to the region between 110 and 40 degrees west. The North America shows high seasonal variations, i.e. high NPPs in May to September. South America, however, shows a small seasonal change because of tropical forests in this region.

However, it should be noted again that NPP in 1998 was influenced by a large El-Nino event. Therefore the Western part of the American continent had high-level precipitations, while Indonesia suffered from drought. Also, NPP in the equatorial Pacific was rather small because of reduction of equatorial upwelling in this zone.

4.3 Validations

As mentioned in the Introduction, validations of these values are extremely difficult in the global scale. In this project, the results were validated using data in China main land for the land products, and the North Western Pacific and the equatorial Pacific Ocean for the ocean products. The details of these experiments are described by Asanuma et al. (2003) and Awaya et al. (2004). A correlation coefficient of 0.7 was derived in the validation of NPP using the surface-based data in both the land and the ocean, which shows some degree of credibility to the results of global NPP maps obtained in this project.

5 Conclusion

The first global NPP maps using satellite data have been obtained in this project. The accuracy of these global NPP maps is sufficient for a first-degree approximation. However, many problems remain, and many efforts are required to increase the accuracy of the global NPP data.

References

Asanuma, I., Nieke, J., Sasaoka, K., Matsumoto, K., Kawano, T., 2003. Optical properties control primary productivity model on the East China

Sea. In: Frouin, R. J. (Ed.), Ocean Remote Sensing and Applications. SPIE, pp. 312–319.

Awaya, Y., Kodani, E., Tanaka, K., Liu, J., Zhuang, D., 2004. Estimation of the global net primary productivity using NOAA images and meteorological data: Changes between 1988 and 1993. International Journal of Remote Sensing 25–29, 1597–1613.

Baret, F., Guyot, G., 1991. Potentials and limits of vegetation indices for LAI and APAR assessment. Remote Sensing of the Environment 35, 161–173.

Battle, M., Bender, M. L., Tans, P. P., White, J. W. C., Ellis, J. T., Conway, T., Francey, R. J., 2000. Global carbon sinks and their variability inferred from atmospheric O_2 and $\delta\ ^{13}C$. Science 287, 2467–2470.

Behrenfeld, M. J., Falkowski, P. G., 1997. Photosynthetic rates derived from satellite based chlorophyll concentration. Limnology and Oceanography 42, 1–20.

Field, C. B., Behrenfeld, M. J., Randerson, J. T., Falkowski, P., 1998. Primary production of the biosphere: Integrating terrestrial and oceanic components. Science 281, 237–240.

Matamala, R., Gonzalez-Meler, M. A., Jastrow, J. D., Norby, R. J., Schlesinger, W. H., 2003. Impacts of fine root turnover on forest NPP and soil C sequestration potential. Science 302, 1385–1387.

This page intentionally left blank

Chapter 17

Slash-and-Burn Agriculture in a Japanese Cedar (*Cryptomeria japonica* D. Don.) Plantation: Effects of Fire on Nutrients and Soil Emissions of Carbon Dioxide

Toshiyuki Ohtsuka[1,*], Wenhong Mo[2], Masaki Uchida[3], Hironori Sako[2] and Hiroshi Koizumi[2]

[1]*Laboratory of Ecology, Ibaraki University, Ibaraki, Japan*
[2]*River Basin Research Center, Gifu University, Gifu, Japan*
[3]*National Institute of Polar Research, Tokyo, Japan*

Abstract

On the temperate coast of central Japan, a unique agroforestry system exists, wherein red turnips (*Brassica rapa* L. var. *glabra* Kitam.) are grown on slash-and-burn sites following the harvesting of mature Japanese cedar (*Cryptomeria japonica* D. Don.) plantations. We studied the effect of fire on nutrient dynamics, soil CO_2 efflux, and microbial biomass at two slash-and-burned sites. Burning, besides raising soil pH from acid to neutral, had an ash-fertilizing effect, reflected by a large increase in soluble P (15.6-fold) and exchangeable cations (Ca, Mg, and K) in the topsoils (0–5 cm). Burning resulted in a 4.8-fold rise in soil NH_4-N because moderate heating of the topsoil induced high microbial activities and, therefore, greater mineralization of soil organic N. On the other hand, there was a pronounced increase in soil CO_2 efflux after burning, which may have resulted from the fire-induced high microbial activity. Thus a significant amount of C was released not only by combustion of litter, but also by decomposition of soil organic matter (SOM). Carbon and nitrogen fluxes during the growth

*Corresponding author.
E-mail address: toshi@mx.ibaraki.ac.jp (T. Ohtsuka).

Elsevier Oceanography Series 73
Edited by H. Kawahata and Y. Awaya
ISBN: 0-444-52948-9

of the turnip crop, however, were small compared to the total stocks of SOM accumulated in the mature cedar plantation (CP) pre-fire. Moreover, soluble P content and pH of the topsoils remained at post-fire levels until the end of the turnip growing season, while the initial increases in soil inorganic N and exchangeable cations returned to pre-fire levels after a single cropping season. We highlight the probable existence of a positive feedback response in carbon sequestration during the fallow due to a higher NPP arising from the modified soil conditions. When estimating the total carbon budget of slash-and-burn agricultural ecosystems, this positive feedback needs to be balanced against the short-term increases in carbon dioxide emissions from litter combustion and fire-induced CO_2 efflux from soils.

Keywords: Cedar plantation; microbial biomass; nutrient dynamics; slash-and-burn agriculture; soil CO_2 efflux

1 Introduction

Slash-and-burn agriculture is a common farming system in tropical regions. Nutrient cycles in forest ecosystems are greatly affected by the burning that is an inherent part of slash-and-burn agriculture. Numerous studies have shown that the burning of forest generates a flush of available soil nutrients (Nye and Greenland, 1960; Ewel et al., 1981; Jordan, 1989; Romanya et al., 1994; Juo and Manu, 1996; Nakano and Miyauchi, 1996). The flush of nutrients is lost through erosion and leaching and is quickly exhausted by growing plants (crops and weeds), which then results in a decline in crop yields (Uhl, 1987; Jordan, 1989). Moreover, ecosystem carbon dynamics are affected by slash-and-burn agriculture because significant amounts of C might be lost by burning in a short time period. Biomass burning, such as natural fire and slash-and-burn agriculture, is considered a large CO_2 source, particularly in the tropics (Tulaphitak et al., 1985b; McNaughton et al., 1998; Hougton, 2000), and thus, net land–atmosphere carbon flux is around zero in the tropics (Schimel et al., 2001).

On the other hand, a number of studies have focused on ecosystem recovery through secondary succession in fallow areas (Tergas and Popenoe, 1971; Toky and Ramakrishnan, 1983; Williams-Linera, 1983; Uhl and Jordan, 1984; Kleinman et al., 1996; Palm et al., 1996; Lawrence and Schlesinger, 2001) and have reported that soil fertility can take from 5 years to more than 10 years of fallow to recover under traditional slash-and-burn agriculture (Nakano, 1978; Reading et al., 1995). While crop yields do indeed decline rapidly in traditional slash-and-burn agricultural areas, net primary productivity (NPP) can increase dramatically after abandonment in fallow (Uhl, 1987).

Slash-and-burn agriculture is on the decline in temperate regions (Kang and Iizumi, 1981; Kamada et al., 1987; Hidaka et al., 1993). However, a unique agroforestry system exists in coastal mountain regions of central

Japan to grow red turnips (*Brassica rapa* L. var. *glabra* Kitam.) and generate a value-added commodity. Under this unique agroforestry system, Japanese cedar (*Cryptomeria japonica* D. Don.) plantation is harvested for timber, the undergrowth and trimmings are burned, and a crop of red turnips is grown. There are some studies of the relationships between nutrient dynamics and microbial activity under slash-and-burn agriculture in temperate regions (Su et al., 1996, 1997). However, few studies from temperate regions have suggested that the short-term losses from carbon pools caused by burning and fire induce change in soil CO_2 efflux (Wüthrich et al., 2002).

Given the paucity of data on carbon and nutrient dynamics under slash-and-burn agriculture, especially in temperate regions, this study sought to clarify the effects of burning on available soil nutrients, soil CO_2 efflux, and microbial biomass. We also discuss the effects of fire on increasing soil emissions of CO_2 under slash-and-burn agriculture as related to changes in soil microbial biomass and nutrient dynamics.

2 Materials and Methods

2.1 Study Sites

The coastal mountain area of Sanpoku Township, Niigata Prefecture in central Japan (38°28′N, 139°36′E) was chosen as the study site. Climatological data were obtained from the nearby Murakami meteorological station (38°14′N, 139°29′E, 10 m a.s.l.). Mean annual air temperature was 12.3°C, with a monthly mean high of 25.1°C in August, and a monthly mean low of 1.3°C in January. Mean annual rainfall was 2,094 mm, with thick snow cover from December to April.

Over 90% of Sanpoku Township is covered by forests: 40% of the area is Japanese cedar plantations (CPs), the remainder being secondary cool-temperate deciduous broadleaf forest. Moreover, agroforestry is common in the mountainous areas of Sanpoku; CPs are regenerated as part of a slash-and-burn agricultural cycle in which red turnips are produced as a value-added commodity. Cedar saplings are replanted to regenerate after only one or two turnip crop. Generally, about 10 ha of clear-felled (CF) CP is burned every year.

2.2 The Slash-and-Burn Sites

2.2.1 Sites Measured in 2001

A 78-year-old CP that had been recently CF for slash-and-burn agriculture (SA01 site) and a nearby intact 80-year-old CP site were selected in 2001. The SA01 and CP sites were on south-facing slopes. Cedar trees at the SA01 site were CF for timber harvest in December 2000, and trimmed branches

and twigs were left on the forest floor. In mid-June 2001, the remaining forest understory was cut and all the slash (trimmed branches from logging and cut understory) was leveled by hand to prepare for the summer burning. In early August 2001, a 10 m × 10 m permanent quadrat, which was divided into 25 2 m × 2 m subplots, was established in a mid-slope position at each site for measuring soil CO_2 efflux and soil nutrients. The slash and litter over the entire SA01 site was burned during the night of 16 August 2001. The permanent quadrat of SA01 site was defined with metal stakes enabling the field investigations to be conducted at exactly the same site before and after burning. Red turnip seeds were sown by direct seeding the day after burning and took several days to germinate to almost 100%. Weeding and thinning were conducted on one or two occasions in September and the turnips were harvested in mid-October.

2.2.2 Sites Measured in 2002

A 70-year-old CP on a west-facing slope about 4 km north-east of the SA01 site was selected in 2002 (SA02 site). The site had been CF for slash-and-burn agriculture in December 2001. The agricultural procedures conducted at the SA02 site were the same as those conducted at the SA01 site, with the slash being burned on the night of 10 August 2002. A 10 m × 10 m permanent quadrat (divided into 25 2 m × 2 m subplots) was set in a mid-slope position of the SA02 site in early August 2002 for soil CO_2 efflux and soil microbial biomass measurements. A 10 m × 2 m quadrat (divided into five 2 m × 2 m subplots) was established about 5 m above the SA02 site and was protected from burning so it could be used as an unburned control CF site.

2.3 Nutrient Pools in Above- and Below-Ground Litters

Prior to the burn at the SA01 site, carbon and nutrient pools in above- and below-ground litters were measured in July 2001. The above-ground dead plant material, principally slash composed of cedar twigs and boughs, was collected within five 1 m × 1 m plots randomly located near the permanent quadrat of the SA01 site. The below-ground component, defined as biomass and necromass of roots in the soil to 0–10 cm depth, was also carefully excavated from the five plots. For each plot, the total fresh weight of above- and below-ground litters and dry weight of oven dried (>48 h at 70°C) subsamples were measured. Total C and N of the dried samples were measured using an NC analyzer (Sumigraph NC-800, Sumika Chemical Analysis Service, Ltd.). The dried samples were digested by nitric acid for chemical analysis. Phosphorus was determined colorimetrically. Potassium, Ca, and Mg were determined by an ICP spectrometer (SPS4000 Plasma Spectrometer, SEIKO Corporation).

2.4 Soil Nutrient Contents

At the CP site, soil samples were taken four times at monthly intervals from August to November 2001. At the SA01 site, soil samples were taken prior to the fire (August 11 and 16), immediately after the fire (August 18 and 20), during crop development (September 14, October 9), and after harvest (November 21). At each sampling date, in the permanent quadrats of both the CP site and the SA01 site, ten soil volumetric cores (100 cm^3) of topsoil beneath the litter (0–5 cm deep) were obtained at randomly located positions. These cores served for the measurement of bulk density and gravimetric soil nutrient contents. Fresh soil samples were used to measure soil pH [soil:water ratio of 1:2.5 (g/g)] and the standing stock of soil inorganic N (NH_4-N and NO_3-N). Inorganic N was extracted by 1.5 M KCl solution and measured colorimetrically. Total C and N contents of dried soil were measured using the NC analyzer. Soluble P in the topsoil was extracted by Truog solution (0.1 N H_2SO_4) and quantified colorimetrically. Exchangeable cations in the topsoils (Ca, Mg, and K) were extracted by 1 M ammonium acetate solution (pH 7.0) and measured by analysis with the ICP spectrometer. Volumetric soil nutrient mass (kg ha^{-1}) was evaluated from the products of gravimetric soil-nutrient content and soil bulk density.

2.5 Soil CO_2 Efflux Measurements

The soil CO_2 efflux was measured using a portable soil respiration system (LI-6400, LI-COR, Lincoln, NE, USA) connected to a soil respiration chamber (LI-6400-09, LI-COR) of 9.5 cm diameter and 991 cm^3 volume. In 2001, the CO_2 efflux was measured at 2 m intervals (i.e., 25 points and each point was at the center of each subplot) of the SA01 and CP sites between 13:00 and 15:00 when the soil surface temperature reached the peak of the day. We measured soil CO_2 effluxes at 1-month intervals from July to November to determine the seasonal changes at both the SA01 and CP sites. To clarify the effects of fire on the soil CO_2 efflux at the SA01 site, we also conducted CO_2 efflux measurements in August on the same days as soil sampling before and after burning. During each measurement, the soil temperature at depths of 1 and 5 cm was measured using a soil temperature probe (Soil Temperature Probe, Type E, LI-COR) and the volumetric soil water content (SWC) at a depth of 0–12 cm was measured using a soil moisture sensor (Hydro Sense, Cambell Scientific Australia). Continuous soil temperature data were recorded at depths of 1 and 5 cm at both the SA01 and CP sites once every 30 min by self-contained temperature loggers (StowAway Tidbit Temperature Logger, Onset Computer Corporation, MA, USA).

In 2002, CO_2 efflux was measured before and after burning at the SA02 site at 2 day intervals (August 9, 10, 14, 16, 18, and 20) and compared to that

of the unburned control CF site (the same methods of measurement were used as in 2001). Soil temperature and SWC were also measured during each measurement using the same methods as in 2001, as were the continuing soil temperature data at depths of 1 and 5 cm for both the SA02 and CF sites.

2.6 Soil Microbial Biomass

There is a close linear relationship between the concentration of adenosine triphosphate (ATP) in soil and the concentration of microbial biomass C over a wide range of soils (Contin et al., 2001). In addition, ATP measurements are more sensitive than fumigation-extraction or fumigation-incubation for measuring low concentrations of microbial biomass (Contin et al., 2001; Castellazzi et al., 2004). Due to the CF management of the SA02 and CF sites, the concentrations of microbial biomass C at these sites were expected to be relatively low, so soil ATP was chosen as a surrogate measure of microbial biomass in the present study.

Soil samples were taken five times, before and after burning (August 9, 12, 14, 16, and 18 in 2002), at the SA02 and CF sites, respectively. At each sampling date, five soil samples were taken by cutting a 10 cm × 10 cm block to a depth of 5 cm.These soil samples were freeze-dried immediately and then carefully broken up to pass a 2 mm mesh sieve and prepared for ATP measurement. Soil ATP was extracted from 1 g soil by 10 ml TCA reagent, a mixture of 0.5 M trichloro-acetic acid and 0.25 M Na_2HPO_4. The extractant was diluted at a rate of 1:100 with AF-2B1 solution (TOA Corporation, Tokyo, Japan), and 100 µl aliquots of the diluted extractant were used to determine the ATP concentration by the fire-fly luciferin-luciferase assay system (AF-70, DKK. TOA Corporation).

3 Results

3.1 Pre-Burning Soil Condition, Organic Matter, and Nutrient Pools

Above-ground plant litter (slash) at the SA01 site totaled 15.2 Mg ha^{-1} (7.5 Mg C ha^{-1} for carbon base), nearly five times the mass of below-ground litter (Table 1). The total N, P, K, Ca, and Mg pools in the litter at the SA01 site, including above- and below-ground parts, were 221.6, 13.6, 22.8, 231.4, and 35.2 kg ha^{-1} respectively.

While soil pH at both sites was acidic, it was significantly lower at the SA01 site than at the CP site (Table 2). Bulk density and total C and N contents of the topsoil (0–5 cm) did not differ significantly between the SA01 and CP sites. The soil inorganic N fractions (NH_4-N and NO_3-N) were nearly

Table 1: Total carbon and nutrient pools in above- and below-ground litters at the pre-burn SA01 site

	Dry mass ($Mg\,ha^{-1}$)		Nutrient mass ($kg\,ha^{-1}$)				
	Dry weight	C base	N	P	K	Ca	Mg
Above-ground	15.2±2.6	7.5±1.3	183.3±31.6	10.6±1.8	14.3±2.5	199.5±34.4	26.6±4.6
Below-ground (0–10 cm)	3.3±1.6	1.4±0.7	38.3±19.0	3.0±1.5	8.5±4.2	31.9±15.9	8.6±4.3
Total	18.5±3.7	8.8±1.7	221.6±43.5	13.6±2.8	22.8±5.7	231.4±43.8	35.3±7.5

Note: Values are mean±one SE ($n = 5$).

Table 2: Properties and nutrient contents of the surface soil (0–5 cm) of the pre-burn SA01 and the CP sites

	SA01 site	CP site
pH	5.6±0.08	$5.8\pm0.03^{*}$
Bulk density ($g\,cm^{-3}$)	0.48±0.05	0.48 ± 0.01^{ns}
Total C (%)	7.72±0.80	6.76 ± 0.15^{ns}
Total N (%)	0.50±0.06	0.42 ± 0.01^{ns}
C/N ratio	15.7±0.19	16.1 ± 0.21^{ns}
Inorganic N ($\mu g\,N\,g^{-1}$)		
NH_4-N	28.6±2.76	$11.0\pm0.56^{***}$
NO_3-N	25.4±3.17	$7.7\pm0.51^{***}$
Soluble P ($\mu g\,P_2O_5\,g^{-1}$)	16.2±2.42	$31.4\pm3.81^{**}$
Exchangeable cations		
Potassium ($\mu mol_C\,g^{-1}$)	19.0±1.73	14.3 ± 1.19^{ns}
Calcium ($\mu mol_C\,g^{-1}$)	174.1±15.13	$231.6\pm5.29^{**}$
Magnesium ($\mu mol_C\,g^{-1}$)	54.5±3.04	$76.0\pm1.06^{***}$

Note: Values are mean±one SE ($n = 10$). Superscript letters indicate the result of *t*-test: $^{*}p \leqq 0.05$; $^{**}p \leqq 0.01$; $^{***}p \leqq 0.001$; ^{ns}not significant.

three-fold greater at the SA01 site than at the CP site. Soluble P and exchangeable cations in the topsoils, except for K, were significantly lower at the SA01 site than at the CP site.

3.2 Effects of Burning and Nutrient Dynamics During the Turnip Crop

The soil pH at the SA01 site was elevated significantly by more than 1 unit (6.7±0.05) soon after burning and remained near neutral throughout the growth of the turnip crop (Fig. 1). During the same period, soil pH at the CP

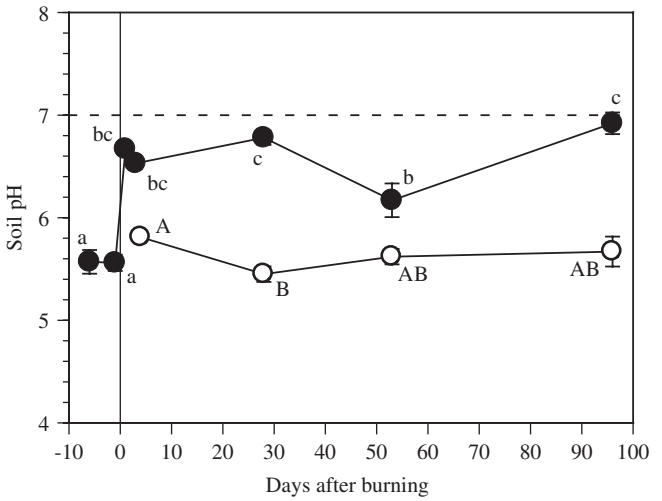

Figure 1: Soil pH levels at the CP site (◦) and at the SA01 site (•). Vertical bars represent ± one SE of the mean ($n = 10$). The SA01 site was burned on 16 August 2001. Superscript letters indicate the results of one-way ANOVA; means with the same letters are not significantly different by Scheffe's test at each site ($p = 0.05$).

site stayed in the range 5.4–5.9. The NH_4-N content of the topsoil at the SA01 site rose significantly from $29 \pm 2.8\,\mu g\,g^{-1}$ before burning to $130 \pm 19.8\,\mu g\,g^{-1}$ the day after burning (Fig. 2a). After this initial increase, the NH_4-N content of the topsoil gradually decreased, reaching pre-burn levels in mid-November ($26 \pm 2.7\,\mu g\,g^{-1}$). In contrast, the pre-burn NO_3-N content of the topsoil ($25 \pm 3.2\,\mu g\,g^{-1}$) remained unchanged after burning ($24 \pm 3.8\,\mu g\,g^{-1}$, Fig. 2b) and then underwent a slow decline, reaching $14 \pm 2.5\,\mu g\,g^{-1}$ by mid-November. Inorganic N content of the topsoil at the CP site, which was initially lower than that at the pre-burn SA01 site, remained constant during the growth of the turnip crop and then rose, especially NO_3-N, in November after the turnips were harvested (Fig. 2b).

At the SA01 site, soluble P content of the topsoil increased 15.6-fold from $16.2 \pm 2.4\,\mu g\ P_2O_5\,g^{-1}$ before burning to $248.2 \pm 36.5\,\mu g\ P_2O_5\,g^{-1}$ the day after burning (Fig. 3a). Soluble P content of the topsoil decreased in mid-October during crop development, subsequently rising back to the immediate post-fire levels ($256.0 \pm 44.2\,\mu g\ P_2O_5\,g^{-1}$) in mid-November after the turnip harvest. In contrast, soluble P content of the topsoil at the CP site remained constant at a lower level (16.9–$42.1\,\mu g\ P_2O_5\,g^{-1}$) throughout the growing season.

Exchangeable cations in the topsoils at the SA01 site increased significantly after burning: 1.9 ± 0.17 to $4.4 \pm 1.04\,\mu mol_C\,g^{-1}$ for K, 17.4 ± 1.51 to $47.0 \pm 11.68\,\mu mol_C\,g^{-1}$ for Ca, and 5.5 ± 0.30 to $9.1 \pm 1.5\,\mu mol_C\,g^{-1}$ for Mg

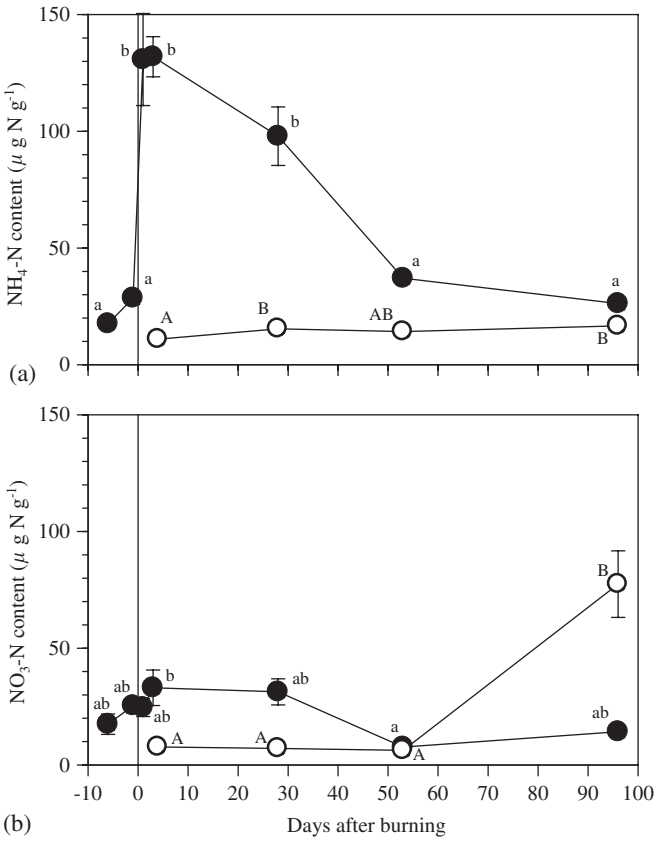

Figure 2: Inorganic N content (μg N g^{-1}) in the surface soil (0–5 cm) at the CP site (◦) and at the SA01 site (•). (a) NH_4-N, (b) NO_3-N. Vertical bars represent ± one SE of the mean ($n = 10$). The SA01 site was burned on 16 August 2001. Superscript letters indicate the results of one-way ANOVA; means with the same letters are not significantly different by Scheffe's test at each site ($p = 0.05$).

(Fig. 3b–d). However, exchangeable cations in the topsoils had decreased within the 2 days following the first post-fire sampling. The concentrations of these exchangeable cations of the topsoils dropped during the period of the turnip crop, reaching levels similar to those at the CP site by mid-November.

3.3 Total Carbon and Nitrogen Contents in the Topsoil

Fig. 4 shows the change in total carbon and nitrogen contents of the topsoils (0–5 cm) over the period of the turnip crop at the SA01 and CP sites. Total

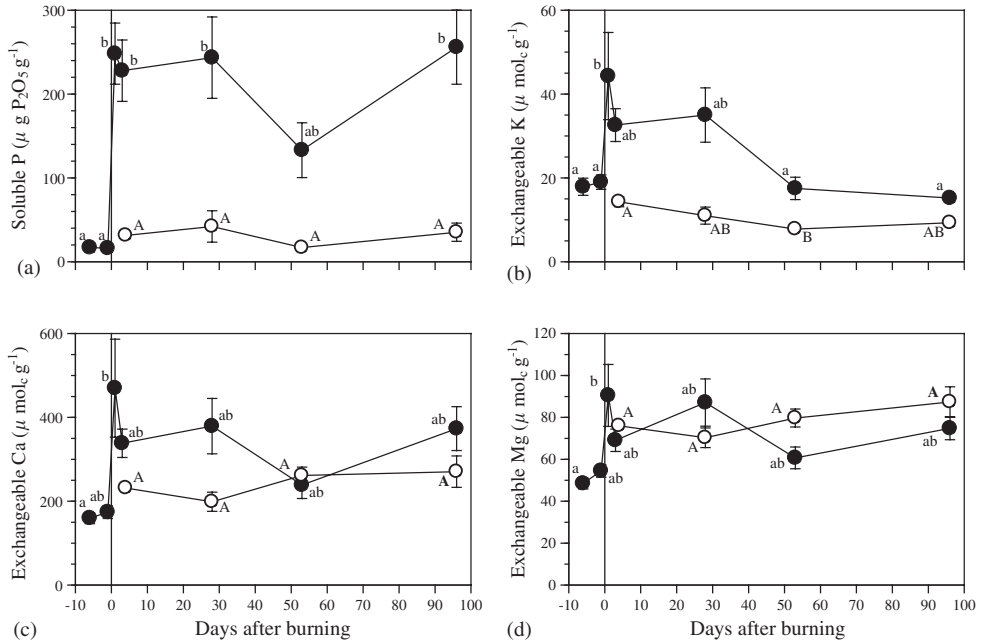

Figure 3: Nutrient contents in the surface soil (0–5 cm) at the CP site (◦) and at the SA01 site (•). (a) Soluble P (μg $P_2O_5\,g^{-1}$), (b) exchangeable K ($\mu mol_C\,g^{-1}$), (c) exchangeable Ca ($\mu mol_C\,g^{-1}$), and (d) exchangeable Mg ($\mu mol_C\,g^{-1}$). Vertical bars represent ± one SE of the mean ($n = 10$). The SA01 site was burned on 16 August 2001. Superscript letters indicate the results of one-way ANOVA; means with the same letters are not significantly different by Scheffe's test at each site ($p = 0.05$).

carbon and nitrogen contents at the SA01 site increased slightly before burning and more the day after burning but then decreased gradually over the crop period, reaching pre-burn levels in mid-November. Total carbon and nitrogen contents at the CP site increased gradually during the same period.

3.4 Effects of Slash-and-Burn on Soil CO_2 Efflux

Soil CO_2 effluxes at the first slash-and-burn site (SA01) were significantly higher than in the 80-year-old CP site in July and August before and after the burning, ranging between 944.6 and 1,196.5 mg $CO_2\,m^{-2}\,h^{-1}$ at the SA01 site and 800.9–904.0 mg $CO_2\,m^{-2}\,h^{-1}$ at the CP site (Fig. 5a). A marked increase in CO_2 efflux was detected after the burning at the SA 01 site. Soil CO_2 efflux values at the SA01 site were similar to those of the CP site from September to November (within the range 231.8–759.6 mg $CO_2\,m^{-2}\,h^{-1}$). Soil temperature at −5 cm fluctuated more at the SA01 site

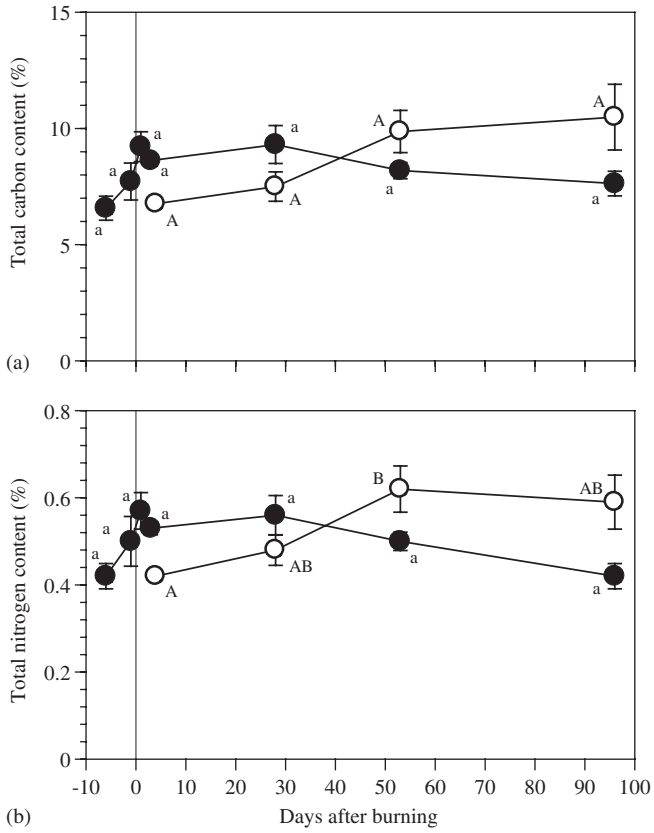

Figure 4: Total carbon (a) and nitrogen (b) contents (% of dry weight) in the surface soil (0–5 cm) at the CP site (◦) and at the SA01 site (•). Vertical bars represent ± one SE of the mean ($n = 10$). The SA01 site was burned on 16 August 2001. Superscript letters indicate the results of one-way ANOVA; means with the same letters are not significantly different by Scheffe's test at each site ($p = 0.05$).

(ca. 10°C difference between daily maximum and minimum) than at the CP site (ca. 2°C difference; Fig. 5b), and mean soil temperature at –5 cm between 13:00 and 15:00 was higher at the SA01 site than at the CP site (data not shown). The break in continuity of soil temperature data at the SA01 site was due to removal of the data logger before the burning. SWC at each CO_2 efflux measuring event showed no significant differences (t-test, $p < 0.05$) between the SA01 and CP sites (ranged between 17.4 and 31.6% at the SA01 site, and 21.1–34.5% at the CP site; Fig. 5c). Fig. 6 shows that the soil CO_2 efflux was significantly correlated with soil temperatures at −5 cm over the measuring period. This indicated that soil temperature was the principal control on seasonal variation in soil CO_2 efflux at both the

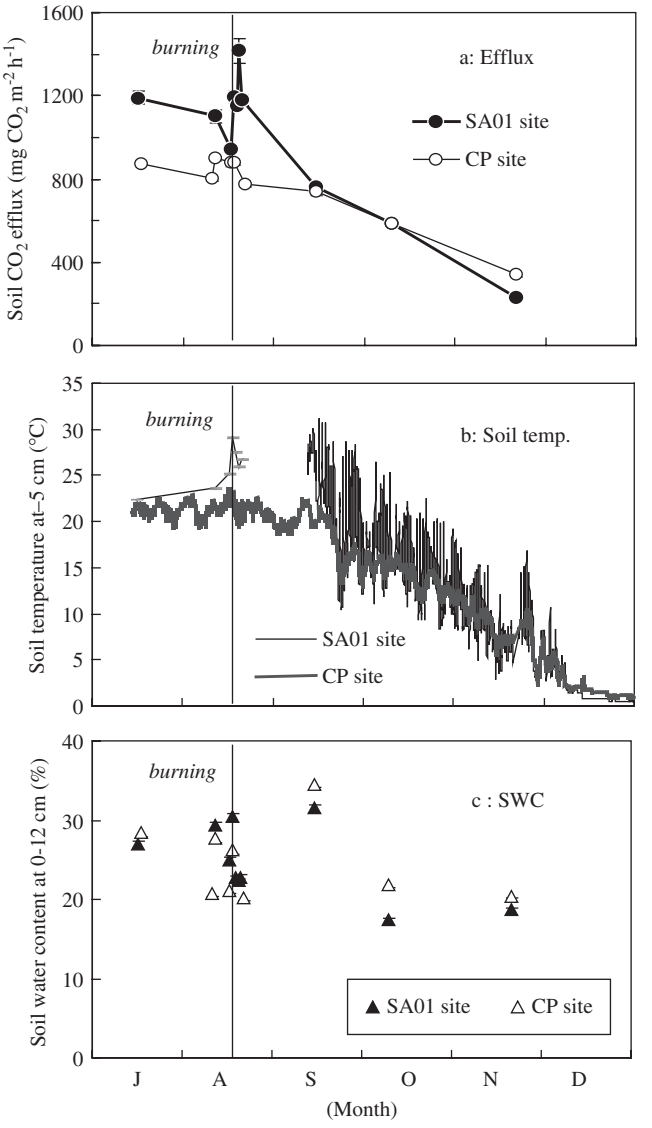

Figure 5: Seasonal changes in (a) soil CO_2 efflux, (b) soil temperature, and (c) soil water content (SWC) for 2001 at the SA01 (•) and CP (◦) sites. Soil temperature at –5 cm was obtained from data recorded continuously every 30 min outside of the CO_2 efflux chambers. SWC over the 0–12 cm depth range was measured inside of the chamber for each efflux measurement. Vertical bars represent $\pm$ one SE of the mean ($n = 25$). The SA01 site was burned on 16 August 2001.

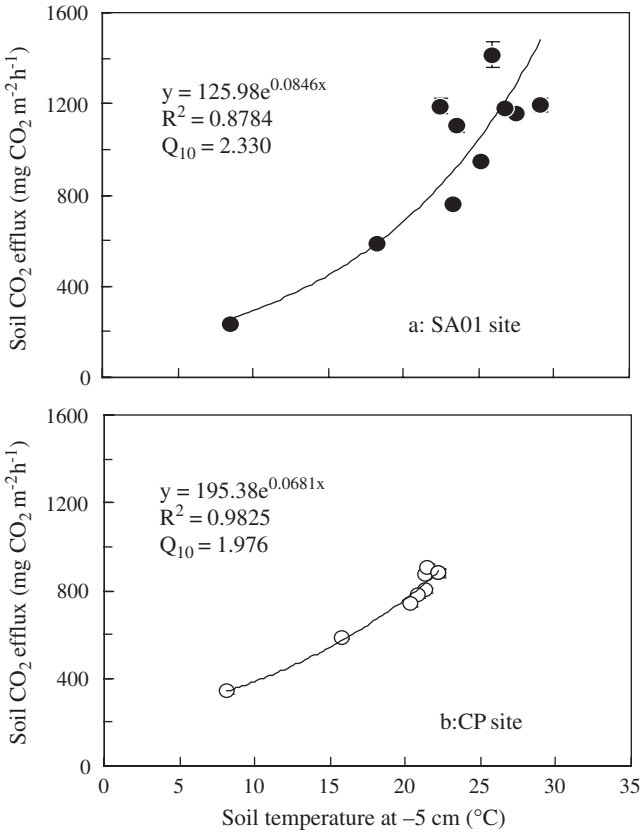

Figure 6: Relationship between soil CO_2 efflux and soil temperature at the SA01 site (a) and the CP site (b) in 2001. Soil temperatures (-5 cm) were measured inside of the chamber just after each efflux measurement. Vertical bars represent $\pm$ one SE of the mean ($n = 25$). The SA01 site was burned on 16 August 2001. The regression lines are significant ($n = 9$, $p < 0.001$ for the SA01 site and $n = 10$, $p < 0.001$ for the CP site).

SA01 and CP sites. The Q_{10} of temperature sensitivity of CO_2 efflux was higher at the SA01 site (2.330) than at the CP site (1.976).

3.5 Effects of Burning on Soil CO_2 Efflux and Microbial Biomass

Changes in soil CO_2 efflux before and after burning at the SA02 site are shown in Fig. 7a, with values from the CF site shown for comparison. Before the burning on August 9 and 10, values of soil CO_2 efflux were slightly higher at the CF site (641.7–744.2 mg $CO_2\,m^{-2}\,h^{-1}$) than at the SA02 site (484.4–543.3 mg $CO_2\,m^{-2}\,h^{-1}$). There was no significant change in soil CO_2

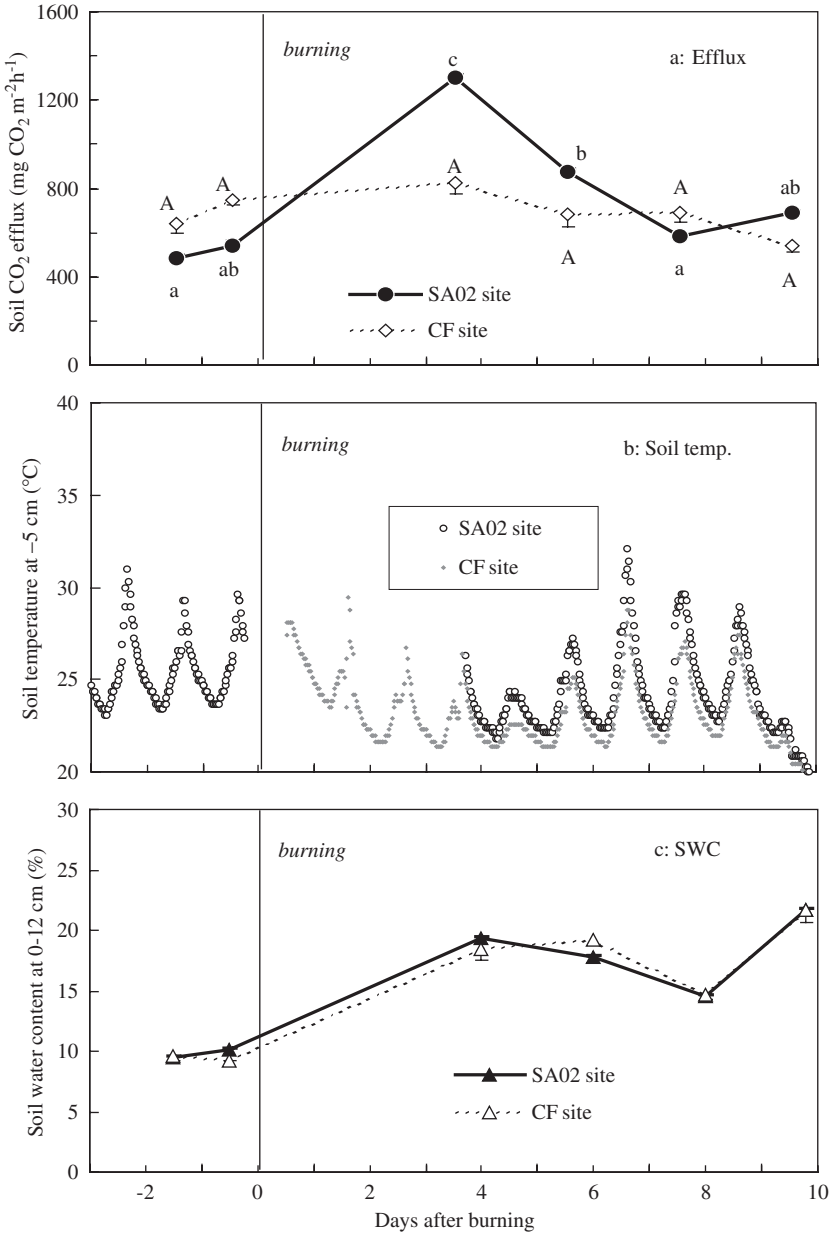

Figure 7: Soil CO_2 efflux (a), soil temperature (b), and SWC (c) at the SA02 and CF sites before and after burning in 2002. Soil temperature at –5 cm was obtained from data recorded continuously every 30 min outside of the CO_2 efflux chambers. SWC over a depth of 0–12 cm was measured inside of the chamber for each efflux measurement. Vertical bars represent ± one SE of the mean ($n = 25$ for the SA02 site and $n = 5$ for the CF site). The SA02 site was burned on 10 August 2002. Superscript letters indicate the results of one-way ANOVA; means with the same letters are not significantly different by Scheffe's test at each site ($p = 0.05$).

efflux at the CF site during August 9–20, and values ranged between 540.5–822.2 mg $CO_2\,m^{-2}\,h^{-1}$. Significant increases in soil CO_2 efflux were detected on August 14 and 16 (four and six days after the burning) at the SA02 site, and CO_2 efflux values were 58 and 28% higher than those at the CF site on August 14 and 16, respectively. However, soil CO_2 effluxes on August 18 and 20 (8 and 10 days after the burning) at the SA02 site decreased to similar levels as those of the CF site (581.2 ± 201.8, 686.4 ± 344.3 mg $CO_2\,m^{-2}\,h^{-1}$ at the SA02 site and 693.3 ± 222.5, 540.5 ± 156.3 mg $CO_2\,m^{-2}\,h^{-1}$ at the CF site). Soil temperature at –5 cm and SWC showed no significant differences (t-test, $p < 0.05$) between the SA02 and CF sites, indicating that the burning may have enhanced soil CO_2 efflux, at least for several days after the burning.

Soil ATP concentrations in the 0–5 cm layer were slightly higher at the CF site than at the SA02 site (Fig. 8). Soil ATP concentration slightly declined in the 2 days after burning at the SA02 site, but had significantly increased by 6 days after burning. On the contrary, there were no significant differences in soil ATP concentrations between 2 and 8 days after burning at the control unburned CF site.

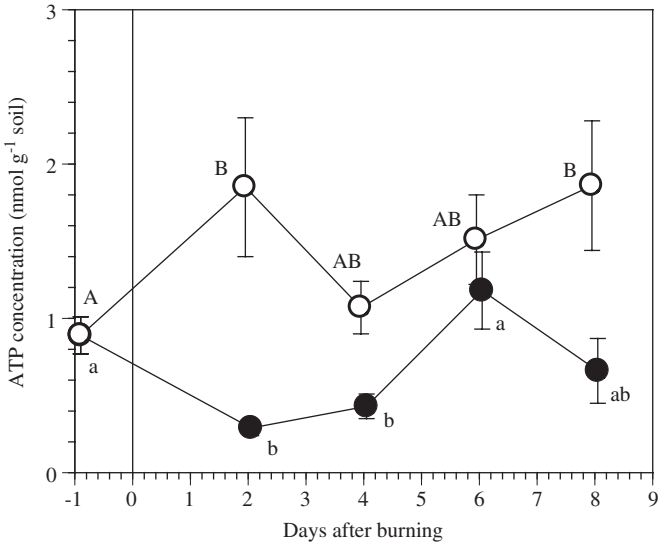

Figure 8: Soil ATP concentration (nmol g^{-1} soil) as a measure of microbial biomass in the surface soil (0–5 cm) at the CF site (◦) and at the SA02 site (•). Vertical bars represent ± one SE of the mean ($n = 5$). The SA02 site was burned on 10 August 2002. Superscript letters indicate the results of one-way ANOVA; means with the same letters are not significantly different by Scheffe's test at each site ($p = 0.05$).

4 Discussion

4.1 Effects of Burning on the Availability of Nutrients of the Topsoil

One of the main advantages of slash-and-burn agriculture for crop growth is the rapid release of mineral nutrients stored in the litter and soil organic matter (SOM). The nutrient most effectively enhanced through burning at this site was phosphorus (Fig. 3a), which is consistent with results reported from a number of studies in tropical regions (Nakano, 1978; Tulaphitak et al., 1985a; Romanya et al., 1994; Juo and Manu, 1996). The exchangeable cations in the topsoils also significantly increased after burning (Fig. 3b–d). Many authors also emphasize the significance of ash-fertilization in raising the levels of these nutrients in soils under shifting cultivation in the tropics (Ewel et al., 1981; Uhl and Jordan, 1984; Nakano and Miyauchi, 1996).

The temperatures needed to volatilize P and exchangeable cations are significantly higher than N (Raison et al., 1985). Phosphorus, for example, is lost by volatilization only when temperatures exceed 360°C (Romanya et al., 1994), whereas available P increases with burning temperature up to 200°C (Andriesse and Koopmans, 1984/1985; Kwari and Batey, 1991). Earlier, during a burn at a nearby site subject to the same agroforestry system, Tsuda et al. (1992) recorded maximum soil temperatures of 185.1°C at the surface, 105.5°C at 2 cm, and 95.7°C at 4 cm depth. Temperatures exceeding 50°C lasted nearly 25 min at the soil surface, 8 min at 2 cm, and 5 min at 4 cm.Therefore, most of the increase in P and exchangeable cations in the topsoils may have come from the ash of the burned surface litter in the current study.

The fire gain of soluble P (volumetric soil nutrient mass on 18 August – that on 16 August = 28.0 kg ha^{-1}) and exchangeable cations in the topsoils were substantially greater than the nutrient pools existing in the pre-burn litter (Table 1, 13.6 kg ha^{-1} for P) at the SA01 site. A similar situation was noted by Kyuma et al. (1985). The cause of this discrepancy was not clear. One of the reasons might be the result of an underestimation of litter pool, since heterogeneously distributed large branches and stumps were not sampled in the current study. Moreover, the fire gain of these nutrients may not be explained by ash-fertilization alone, especially in the case of P. Available P content of the topsoil returned to post-burning level after the harvesting of turnips (Fig. 3a), while exchangeable cations in the topsoils returned to pre-fire levels after a single cropping season (Fig. 3b–d). Therefore, availableP in topsoil increased not only by ash-fertilization but also by mobilization of inorganic and organic P as a result of increased pH (Romanya et al., 1994).

4.2 Nitrogen Dynamics and Microbial Activities

About three-fold increase in the soil inorganic N, especially NH_4-N, after burning has been widely reported from studies of shifting cultivation in the tropics (Nakano, 1978; Kyuma et al., 1985; Reading et al., 1995). One of the main reasons for the flush of soil inorganic N after burning is the release of NH_4^+ from protein-like components of organic nitrogen in litter and soil (Raison, 1979). The fire gain of inorganic N in the topsoil (volumetric soil nutrient mass on 18 August – that on 16 August) was 29.4 kg ha^{-1}, only one seventh of the N pool estimated to exist in the pre-burn litter (Table 1).

Soil inorganic N was gained not only by ash-fertilization but also by enhanced mineralization of the SOM (Stromgaard, 1984; Andriesse and Koopmans, 1987; Singh et al., 1991), despite the fact that heating of the soil may have killed a fraction of the microorganisms in general. The influence of fire on microbial activities depends on site specific differences in fire intensity (Ahlgren and Ahlgren, 1965). Fire intensity differs with litter mass and water contents of litter and soils, which in turn depend on the climate and pre-burning weather and will be heterogeneously distributed within any given site. At a slash-and-burned site located in a temperate climate, for example, Su et al. (1996) reported that the microbial biomass and N mineralization rates were reduced in the subsurface soil layer immediately after burning when soil surface temperature reached more than 400 and 78°C at 5 cm depth. In contrast, in a relatively low temperature burn (40°C at 5 cm depth), microbial biomass was not reduced and N mineralization rate increased immediately after burning (Su et al., 1997). In the present study, microbial biomass was reduced by burning, but did not fall to zero in the topsoils 2 days after burning at the SA02 site (Fig. 8). Moreover, microbial biomass increased quickly in the 6 days after burning. Thus, moderate heating of the topsoil at the SA01 site might have induced high microbial activities soon after burning, and thus resulted in the higher N mineralization rates.

4.3 Responses of Soil CO_2 Efflux and Carbon Dynamics to Fire

Fire-induced increases in microbial activities after burning result in an increase in post-fire soil CO_2 efflux. Some studies have found that there is a pronounced increase in soil CO_2 efflux after burning (Singh et al., 1991; Wüthrich et al., 2002). For example, Wüthrich et al. (2002) examined the effects of fire on soil CO_2 efflux from a sweet chestnut forest in southern Switzerland and demonstrated that the greater post-fire soil CO_2 efflux might have resulted from increased microbial activity and CO_2 release from below the topsoil, and that the enhanced soil CO_2 efflux after a fire could last

for 6 months. They also suggested that large amounts of easily available organic carbon from the remains of plants, animals, and microorganisms in the soil killed by above-ground fire, are rapidly decomposed by microorganisms and significantly enhancing post-fire CO_2 efflux.

The higher Q_{10} value of soil CO_2 efflux at the slash-and-burn (SA01) site compared to the unburned control CP site (Fig. 6) might be explained partly by the enhancing post-fire CO_2 efflux at SA01 site. It has been demonstrated that the Q_{10} function intergrates all processes that influence seasonal soil CO_2 efflux, not only the temperature response of soil CO_2 efflux, but also seasonal changes in respirationary activities induced by changes in root phenology, microbial biomass, and other factors (Mo et al., 2005). Fire-induced increasing in microbial activities resulted in the enhancing post-fire soil CO_2 effluxes and therefore may induce a higher Q_{10} value for the SA01 site compared to the unburned control site.

This enhanced soil CO_2 efflux after burning lasted at least one week in the present study (Fig. 7a), and possibly longer considering that root respiration might greatly decrease at the slash-and-burn site (SA02) because old roots were killed by fire and new roots of the turnip crop were still under developing. On the other hand, root respiration may contribute a large proportion to total soil CO_2 efflux in the unburned control CF site across the whole growing season. By direct measurements of root respiration, it is estimated that root respiration at the slash-and-burn (SA02) site accounted for 43% of total soil CO_2 efflux for the pre-fire period (July 21 to August 10) and decreased to 14% for the post-fire period (August 25 to October 4); whileas soil respiration at the unburned control CF site contributed 43% to the total soil CO_2 efflux for the pre-fire period (July 21 to August 10), and increased to 63% just after burning (August 11 to August 24), and contributed to 66% for the post-fire period (August 25 to October 4) (Sako, unpublished data). Therefore, our results suggested that a significant amount of carbon was released at the slash-and-burn agriculture sites, not only by combustion of litter during the fire, but also by decomposition of SOM following the fire and during the growth of the turnip crop.

However, a decrease in SOM of the topsoil was not detected in this study (Fig. 4). This means that carbon and nitrogen fluxes caused by burning at the slash-and-burn agriculture (SA 01) site was small compared to the total stocks of SOM accumulated in the mature plantation pre-fire. In an experiment at San Carlos, the total stocks of nutrients in the soil did not appear to be as seriously depleted by slash-and-burn as other treatments, such as pasture establishment using bulldozers (Jordan, 1989). In this case, NPP can increase dramatically after abandonment in fallow, while crop yields do indeed decline rapidly in traditional slash-and-burn agricultural areas (Uhl, 1987).

In the current study site, pH and available P content of the topsoil remained at post-fire levels until the end of the turnip crop, while soil inorganic N and exchangeable cations were increased by burning and then returned to pre-fire levels. These soil conditions might result in higher carbon sequestration during the fallow in the slash-and-burn agricultureal sites as a result of the higher NPP, as suggested by Uhl (1987). Therefore, when estimating the total carbon budget of slash-and-burn agricultural ecosystems, the potential for this feedback increase in carbon sequestration should be taken into account in addition to the temporary emissions of carbon dioxide from litter burning and subsequent fire-induced increment in CO_2 efflux. Long-term research on carbon dynamics beyond one annual cycle is needed on slash-and-burn systems to better understand the increase in carbon dioxide emissions from soil after burning and the feedback increase in carbon sequestration during the fallow.

Acknowledgements

We are grateful to the members of River Basin Research Center, Gifu University for their kind cooperation in the field survey. We also thank Ms. Y. Abe, Yamanashi Institute of Environmental Science, for her kind assistance with the laboratory analysis. We express our thanks to the members of the Sanpoku town office, especially Mr. K. Itagaki, who provided the chance to study the slash-and-burn agricultural site and information about the agroforestry system in this town.

References

Ahlgren, I. F., Ahlgren, C. E., 1965. Effects of prescribed burning on soil microorganisms in a Minnesota jack pine forest. Ecology 46, 304–310.

Andriesse, J. P., Koopmans, T. Th., 1984/1985. A monitoring study on nutrient cycles in soils used for shifting cultivation under various climatic conditions in tropical Asia. I. The influence of simulated burning on form and availability of plant nutrients. Agriculture, Ecosystems and Environment 12, 1–16.

Andriesse, J. P., Koopmans, T. Th., 1987. A monitoring study on nutrient cycles in soils used for shifting cultivation under various climatic conditions in tropical Asia. III. The effects of land clearing through burning on fertility level. Agriculture, Ecosystems and Environment 19, 311–332.

Castellazzi, M. S., Brookes, P. C., Jenkinson, D. S., 2004. Distribution of microbial biomass down soil profiles under regenerating woodland. Soil Biology and Biochemistry 36, 1485–1489.

Contin, M., Todd, A., Brooke, P. C., 2001. The ATP concentration in the soil microbial biomass. Soil Biology and Biochemistry 33, 701–704.

Ewel, J., Berish, C., Brown, B., 1981. Slash and burn impacts on a Costa Rican wet forest site. Ecology 62, 816–829.
Hidaka, K., Kamada, M., Fukuda, T., 1993. Some notes on the slash and burn agriculture at Higashi-Iyayama Village in Tokushima Prefecture, Shikoku, Japan. I. Evaluation of cultivation system as the subsistence agriculture. Bulletin of the Tokushima Prefectural Museum 3, 1–24 (in Japanese with English summary).
Hougton, R. A., 2000. A new estimate of global sources and sinks of carbon from land-use change. Eos 81, S281.
Jordan, C. F., 1989. An Amazonian Rain Forest. Man and the biosphere series, Vol. 2. The Parthenon Publishing Group, New Jersey, USA.
Juo, A. S. R., Manu, A., 1996. Chemical dynamics in slash-and-burn agriculture. Agriculture, Ecosystems and Environment 58, 49–60.
Kamada, M., Nakagoshi, N., Takahashi, F., 1987. Effects of burning of germination of viable seeds in a slash and burn agriculture soil. Japanese Journal of Ecology 37, 91–100 (in Japanese with English summary).
Kang, S. J., Iizumi, S., 1981. A historical review on the shifting cultivation and on some studies related to the burned field ecosystem in Korean Peninsula. Ecological Review 19, 237–252.
Kleinman, J. A., Bryant, R. B., Pimentel, D., 1996. Assessing ecological sustainability of slash-and-burn agriculture through soil fertility indicators. Agronomy Journal 88, 122–127.
Kwari, J. D., Batey, T., 1991. Effect of heating on phosphate sorption and availability in some north-east Nigerian soils. Journal of Soil Science 42, 381–388.
Kyuma, K., Tulphitak, T., Pairintra, C., 1985. Changes in soil fertility and tilth under shifting cultivation. I. General description of soil and effect of burning on the soil characteristics. Soil Science and Plant Nutrition 31, 227–238.
Lawrence, D., Schlesinger, W. H., 2001. Changes in soil phosphorus during 200 years of shifting cultivation in Indonesia. Ecology 82, 2769–2780.
McNaughton, S. J., Stronach, N. R. H., Georgiadis, N. J., 1998. Combustion in natural fires and global emissions budgets. Ecological Applications 8, 464–468.
Mo, W., Lee, M.-S., Uchida, M., Inatomi, M., Saigusa, N., Mariko, S., Koizumi, H., 2005. Seasonal and annual variations in soil respiration in a cool-temperate deciduous broad-leaved forest in Japan. Agricultural and Forest Meteorology 134, 81–94.
Nakano, K., 1978. An ecological study of swidden agriculture at a village in northern Thailand. South East Asian Studies 16, 411–446.
Nakano, K., Miyauchi, N., 1996. Changes in physical and chemical properties of surface soil in a swidden and subsequent fallow in a northwestern region of Malaita island, Solomon islands. South Pacific Study 17, 1–20.
Nye, P. H., Greenland, D. J., 1960. The soil under shifting cultivation. Technical Comm. No. 51, Commonwealth Bureau of Soils, Harpenden, Cmmonwealth Agricultural Bureaux, Farnham Royal, Bucks, England.

Palm, C. A., Swift, M. J., Woomer, P. L., 1996. Soil biological dynamics in slash-and-burn agriculture. Agriculture, Ecosystems and Environment 58, 61–74.

Raison, R. J., 1979. Modification of the soil environment by vegetation fires, with particular reference to nitrogen transformations: A review. Plant and Soil 51, 73–108.

Raison, R. J., Khanna, P. J., Woods, P. V., 1985. Mechanisms of element transfer to the atmosphere during vegetation. Canadian Journal of Forest Research 15, 132–140.

Reading, A. J., Thompson, R. D., Millington, A. C., 1995. Humid Tropical Environments. Blackwell, Oxford, UK.

Romanya, J., Khanna, P. K., Raison, R. J., 1994. Effects of slash burning on soil phosphorus fractions and sorption and desorption of phosphorus. Forest Ecology and Management 65, 89–103.

Schimel, D. S., House, J. I., Hibbard, K. A., Bousquest, P., Ciais, P., Peylin, P., Braswell, B. H., Apps, M. J., Baker, D., Bondeau, A., Canadell, J., Churkina, G., Cramer, W., Denning, A. S., Field, C. B., Friedlingstein, P., Goodale, C., Heimann, M., Houghton, R. A., Melillo, J. M., Moore, B.III., Murdiyarso, D., Noble, I., Pacala, S. W., Prentice, I. C., Raupach, M. R., Rayner, P. J., Scholes, R. J., Steffen, W. L., Wirth, C., 2001. Recent patterns and mechanisms of carbon exchange by terrestrial ecosystems. Nature 414, 169–172.

Singh, R. S., Raghubanshi, A. S., Singh, J. S., 1991. Nitrogen-mineralization in dry tropical savanna: effects of burning and grazing. Soil Biology and Biochemistry 23, 269–273.

Stromgaard, P., 1984. The immediate effect of burning and ash-fertilization. Plant and Soil 80, 307–320.

Su, J., Katagiri, S., Kaneko, N., 1997. Short-term changes in soil inorganic nitrogen following a slash-and-burn treatment in a secondary forest of Western Japan – Under low intensity burn. Journal of Japanese Forest Society 79, 37–42 (in Japanese with English summary).

Su, J., Katagiri, S., Kaneko, N., Nagayama, Y., 1996. Soil nitrogen dynamics following a slash-and-burn treatment in a secondary forest of Western Japan – In relation to topography. Journal of Japanese Forest Society 78, 257–265 (in Japanese with English summary).

Tergas, L. E., Popenoe, H. L., 1971. Young secondary vegetation and soil interactions in Izabel, Guatemala. Plant and Soil 34, 675–690.

Toky, O. P., Ramakrishnan, P. S., 1983. Secondary succession following slash and burn agriculture in north-eastern India. II. Nutrient cycling. Journal of Ecology 71, 747–757.

Tsuda, S., Tanaka, M., Kikuchi, T., 1992. Effects of fire on wild plants under slash and burn agriculture. Shinrin-bunka-kenkyu 13, 71–79 (in Japanese with English summary).

Tulaphitak, T., Pairintra, C., Kyuma, K., 1985a. Changes in soil fertility and tilth under shifting cultivation. II. Changes in soil nutrient status. Soil Science and Plant Nutrition 31, 239–249.

Tulaphitak, T., Pairintra, C., Kyuma, K., 1985b. Changes in soil fertility and tilth under shifting cultivation. III. Soil respiration and soil tilth. Soil Science and Plant Nutrition 31, 239–249.
Uhl, C., 1987. Factors controlling succession following slash-and-burn agriculture in Amazonia. Journal of Ecology 75, 377–407.
Uhl, C., Jordan, C. F., 1984. Succession and nutrient dynamics following forest cutting and burning in Amazonia. Ecology 65, 1476–1490.
Williams-Linera, G., 1983. Biomass and nutrient content in two successional stages of tropical wet forest in Uxpanapa, Mexico. Biotropica 15, 275–284.
Wüthrich, C., Schaub, D., Weber, M., Marxer, P., Conedera, M., 2002. Soil respiration and soil microbial biomass after fire in a sweet chestnut forest in southern Switzerland. Catena 48, 201–215.

Chapter 18

Leaf and Shoot Ecophysiological Properties and Their Role in Photosynthetic Carbon gain of Cool-Temperate Deciduous Forest Trees

Hiroyuki Muraoka* **and Hiroshi Koizumi**

Institute for Basin Ecosystem Studies, Gifu University, 1–1 Yanagido, Gifu 501–1193, Japan

Abstract

Plant ecophysiological properties including photosynthetic responses to environmental conditions, canopy geometrical consequences with photosynthetic carbon gain and their seasonality have considerable responsibility to the forest ecosystem carbon fixation. This paper overviews these traits for canopy tree species in a cool-temperate deciduous broadleaved forest of Takayama AsiaFlux site located in central Japan. Two-year measurements of leaf CO_2 gas exchange characteristics for full growing season on canopy tree species, *Betula ermanii* and *Quercus crispula*, revealed that their photosynthetic capacity increases with leaf expansion from late spring (mid-May) to early summer (June) in 2004 or mid-summer (August) in 2003 and decreases in autumn (October). The delayed peak of photosynthetic capacity in 2003 was associated with a prolonged rainy season that year. In contrast, seasonal change of dark respiration was similar between the 2 years; the maximum was observed at the start of leaf expansion and decreased by June when the leaf area matured. Leaf- and shoot- (branch) level photosynthetic and geometrical consequences to canopy carbon gain were examined with a 3D structural–functional model, Y-plant. Simulations with shoots at the canopy top of *Betula* and *Quercus* revealed that steeper leaf angle and higher stomatal conductance of *Betula* contribute to maintaining a high photosynthetic activity by reducing high light stresses, such as heat load and photoinhibition. Comparison of sunlit

*Corresponding author
E-mail address: muraoka@green.gifu–u.ac.jp (H. Muraoka).

Elsevier Oceanography Series 73
Edited by H. Kawahata and Y. Awaya
ISBN: 0-444-52948-9

(canopy top) and shaded (inner canopy) shoots of *Quercus* revealed that the leaf display with small self-shading of shade shoots is effective in receiving light incidence in the light-limited environment, but prolonged sun fleck limits photosynthesis of the shade leaves by increasing temperature and stomatal closure. These ecophysiological considerations of photosynthesis and plant structure would provide us a deeper insight into the mechanistic understanding of the forest ecosystem carbon gain in changing environments.

Keywords: canopy architecture; cool-temperate deciduous broadleaved forest; leaf area index (LAI); phenology; photosynthesis

1 Introduction

There is a growing requirement of plant ecological and physiological understanding on terrestrial ecosystem carbon budget and dynamics since those are the fundamental determinants of the ecosystem function. Photosynthetic productivity of an ecosystem, namely gross primary production (GPP), is mainly governed by leaf area distribution and leaf photosynthesis and their seasonality. As the ecosystem carbon gain is affected by the relationship between leaf ecophysiological characteristics and meteorological environment, which would be largely heterogeneous in space and time and different among the species composing a given ecosystem, an understanding of these traits responsible for the ecosystem carbon gain provides us deeper insight into the ecosystem function and further mechanistic analyses and evaluation of ecosystem-scale observation by flux measurements and satellite remote sensing (Ehleringer and Field, 1993; van Gardingen et al., 1997; Plummer, 2000). Considering the fact that an ecosystem behavior is the integration of individual leaves, shoots (branch) and individual plants of the species forming the ecosystem, revealing small-scale ecophysiological behavior created by leaf photosynthesis and shoot-level properties would provide us basic, but important, characteristics in the process of photosynthetic carbon fixation of the ecosystem, which are necessary to estimate, analyze, and predict the whole ecosystem CO_2 flux of past, present, and future world. This chapter aims at overviewing these traits for canopy tree species in a cool-temperate deciduous broadleaved forest of Takayama Asia-Flux site located in central Japan.

Forest ecosystems have been widely and intensively investigated, as they are potentially large carbon sink. Studies from the viewpoint of such ecosystem function are conducted by plant ecophysiology, meteorological observation, satellite remote sensing, and model analysis (e.g., Field et al., 1995; Baldocchi and Meyers, 1998; Ustin et al., 2004). The common question of these different techniques has been raised for the phenology of canopy leaf area and single leaf photosynthesis (Wilson et al., 2001; Xu and Baldocchi, 2003) since they would determine the seasonality of ecosystem

CO_2 flux, which is responsible for the fluctuation of atmospheric CO_2 concentration as can be recognized in the observation data (IPCC, 2001). In tropical forest and arid ecosystems, rainy/dry seasons have remarkable influences on the leaf area and photosynthetic phenology and hence ecosystem-level carbon gain, while temperature is the major climatic determinant of the phenology in temperate, cool-temperate and high-latitude regions (Larcher, 2001; Chapin et al., 2002). The deciduous forest ecosystems widely distributed in temperate and cool-temperate regions can be characterized by rapid temporal change of leaf biomass and CO_2 gas exchange characteristics (i.e., photosynthesis and respiration) of the plant species composing the forests. Efforts have been made for measuring the seasonal patterns of leaf area index (LAI) and photosynthetic capacity in some recent studies that would contribute to ecosystem-scale models and analysis of the meteorological CO_2 flux data (Wilson et al., 2001; Morecroft et al., 2003; Xu and Baldocchi, 2003).

In Takayama AsiaFlux site in central Japan, CO_2 flux has been measured since 1993 (Yamamoto et al., 1999; Saigusa et al., 2002; Murayama et al., 2003) and ecological process observations such as tree biomass accumulation, soil CO_2 efflux, and plant ecophysiological characteristics have also been conducted to get ecological insights into the ecosystem-scale measurements (e.g., Lee et al., 2003). Recently, model analyses and spectral remote sensing measurements are also being used for mechanistic analyses and continuous observation of the forest ecological characteristics. Among these studies, plant ecophysiological data and understanding are required for scaling the ecosystem function in time and space.

Photosynthetic carbon gain of a canopy is determined by the single leaf photosynthetic traits and canopy geometrical characteristics (Caldwell et al., 1986; Beyschlag and Ryel, 1999; Valladares, 1999). We would come to know that various meteorological environmental conditions such as light (photosynthetically active radiation, PAR), temperature and humidity affect leaf photosynthetic activity via biochemical process and stomatal aperture (Farquhar et al., 1980; Ball et al., 1987; Pearcy et al., 1994; Leuning, 1995). However, what is important in the ecological context is the quantitative evaluation of the consequence of environmental conditions and photosynthetic activity. In a high-light environment at the canopy top, light as energy for photosynthetic reaction exceeds the requirement in midday hours, and such excessive light reduces photosynthetic activity via stomatal closure and photoinhibition (Tenhunen et al., 1984; Ögren and Sjöström, 1990; Osmond, 1994; Muraoka et al., 2000). Understanding the species-specific or functional-type characteristics of the environment–leaf physiological relationship is essential in the mechanistic analysis of ecosystem function.

In addition to the single leaf-level properties, the geometrical (structural) characteristics of shoots, which are the aggregation of single leaves,

are highly responsible for the leaf photosynthetic activity and hence canopy carbon gain (Pearcy and Valladares, 1999; Valladares, 1999). A model estimation of plant photosynthesis at any organ (single leaf, shoot, branch, and stem) without considering the plant structural characteristics would mislead our understanding of canopy photosynthesis via over- or underestimation of light interception by the foliage. Leaf position and orientation in a given canopy affect light interception and energy budget, and hence, photosynthesis and transpiration at various time scales from seconds to season. In a high light environment, excess light interception would reduce photosynthetic activity; therefore, leaf orientation and leaf ecophysiological traits, such as photosynthetic capacity and stomatal opening, should have considerable effects on carbon gain, but these relationships may be different between the canopy species if their successional status and/or ecophysiological responses to light are different (Bazzaz, 1996; Kitao et al., 2000; Valladares et al., 2002). The whole canopy structure also affects the light environment of the leaves emerged in lower part of the canopy. Reduction in light penetration through a canopy creates the gradient of light availability among the shoots across the canopy, and leaves under low light conditions should have different photosynthetic characteristics as compared to those at the canopy top. This phenotypic differentiation has been recognized as "light acclimation" and is suggested to be adaptive by effective utilization of light resource in a canopy (Terashima and Hikosaka, 1995; Niinemets and Valladares, 2004). The different leaf photosynthetic and shoot architectural characteristics between sun and shade environments within a canopy would have different function in canopy carbon gain as well as different environmental constraints on the physiological activity.

This chapter focuses on the plant ecophysiological processes that are responsible for forest canopy photosynthetic carbon gain in a cool-temperate deciduous broadleaved forest, an AsiaFlux study site located in Takayama, central Japan. We will show the seasonal changes of forest canopy LAI and single leaf photosynthetic characteristics by field observations, and the consequences of shoot architecture, leaf photosynthetic, and stomatal conductance characteristics and light environments on photosynthetic carbon gain at shoot (branch) level by a simulation study.

2 Materials and Methods

2.1 Study Site and Plant Species

Field study was taken in a cool-temperate deciduous broadleaved forest (36°08′ N, 137°25′ E, 1420 m a.s.l.) on the northwestern slope of Mt. Norikura, Japan.

In this forest, a 1-ha study plot is situated as the Takayama experimental forest for AsiaFlux research site and Institute for Basin Ecosystem Studies, Gifu University. Annual mean air temperature and precipitation from 1980 to 2002 measured at the field station (about 300 m apart from the study site) are 7.2°C and 2275 mm, respectively. The forest canopy is dominated by *Quercus crispula* (Blume.), *Betula platyphylla* (Sukatchev) var. *japonica* (Hara), and *Betula ermanii* (Cham.), and subcanopy and shrub layers are dominated by *Acer rufinerve* (Sieb. et Zucc.), *Acer distylum* (Sieb. et Zucc.), *Hydrangea paniculata* (Sieb.), and *Viburnum furcatum* (Blume. ex Maxim). The understory is dominated by an evergreen dwarf bamboo *Sasa senanensis* (Fr. Et Sav.) Rehder. Of these species, *Betula ermanii* and *Quercus crispula* were selected for our material tree species (hereafter referred to as *Betula* and *Quercus*, respectively). *Betula* is a pioneer species and has thin crown in the present multispecies deciduous forest, while *Quercus* is a mid-late successional species and has multilayered crown, which often reaches to the shrub layer in the forest. All these deciduous tree species flush their leaves after snowmelt, while second flush (in early summer) can be found in birch with smaller leaf area than the first one.

In the experimental forest, a canopy access tower (10 m × 10 m × 18 m height) was established in winter of 2001 to access the foliage of dominant canopy trees, three *Betula* trees (*ca*. 17–20 m tall) and two *Quercus* trees (*ca*. 12–15 m tall). Leaf gas exchange was measured periodically for several shoots of these canopy species throughout the growing season from late May to late October 2003 and 2004, and shoot architecture was measured in summer 2003.

2.2 Evaluation of Forest Canopy Leaf Area Index

The forest canopy LAI was estimated by hemispherical canopy photographs taken in the forest understory at 14 locations covering the 1-ha plot. Photographs were taken with a digital camera (CoolPix 910, Nikon, Japan) equipped with a fish-eye lens (FC-E8, Nikon, Japan) mounted on a monopod. The camera was carefully leveled by referring to a bubble level. A thin wire was used to indicate south on the photographs. All photographs were taken while the sky was overcast in midday or in late afternoon. The photographs were analyzed with a commercially available software program, HemiView 2.1 (Delta-T Devices, UK). Gap fraction was determined for 160 specific sky sectors on the photographs and sectors within 30° from the zenith were used for the estimation of LAI. Data analyses for the selected area, thus, minimized the influence of trunk shadow and surrounding understory vegetation on upper slope of the observation points, which cover a significant area of the photographs.

2.3 Measurements of Leaf Gas Exchange

Relationship between net photosynthetic rate (A) and leaf intercellular CO_2 concentration (Ci), and dark respiration rate (R) was measured to obtain the leaf gas exchange characteristics. Measurements for three to seven intact leaves in canopy species were taken periodically throughout the growing season using a portable photosynthesis measuring system (LI-6400, Li-Cor, Inc., USA). The A–Ci curves were obtained under constant photosynthetically active photon flux density (PPFD) for light-saturation, air temperature, and leaf to air vapor pressure deficit (VPD, <1 kPa), and the CO_2 concentration entering the leaf chamber (Ca) was changed from 0 to 1000 μ mol CO_2 mol^{-1} air. Value of R was measured under the same air temperature and VPD conditions with A–Ci curves but under Ca of 370 μ mol mol^{-1}. Measurements at the canopy-top were taken in morning hours (0800–1200 h) to avoid possible effects of photoinhibition, heat load, and stomatal closure. Air temperature of the leaf chamber was adjusted to the mean daytime air temperature of about 1 week before each measurement day. Immediately after the gas exchange measurements, index of leaf chlorophyll content (SPAD) was measured (SPAD-502, Minolta, Japan; Markwell et al., 1995). Using thus obtained gas exchange data, maximum carboxylation rate (V_{cmax}) and maximum electron transport rate (J_{max}) were calculated for shoot-level photosynthesis model Y-plant (see below), by using the equations by Farquhar et al. (1980), Harley and Baldocchi (1995), and Medlyn et al. (2002).

2.4 Measurements of Shoot Architecture and Photosynthesis Simulation

Light capture and photosynthesis at the shoot scale were simulated with a 3D canopy architecture model, Y-plant (Pearcy and Yang, 1996; Pearcy et al. 2005). Y-plant simulates light interception and photosynthesis at leaf and shoot levels to study the interactive effects of leaf ecophysiological properties and shoot architecture on plant carbon gain and growth (e.g., Pearcy and Valladares, 1999; Valladares, 1999; Muraoka et al., 2003; Pearcy et al., 2005). In this chapter, we utilized Y-plant to gain an implication of the possible effects of leaf ecophysiology and shoot architecture specific to each species on foliage CO_2 fixation in summer. The calculations of light interception and photosynthesis include the effects of environmental conditions around the shoots, ecophysiological properties of the leaves specific to species and local light environment, and the structural characteristics (size, orientation, and position of single leaves and hence mutual shading of the leaves). Y-plant requires inputs of the angles, azimuths and length of stems (internodes), petioles, and leaves, which construct a shoot. At each node

within the shoot, the internode and petiole angles and azimuths, the angle and azimuth of the leaf surface normal, and the azimuth of the midrib were measured with a compass-protractor (Norman and Campbell, 1989). Leaf, petiole and internode lengths were measured with a ruler and petiole and internode diameters were measured with digital calipers. Coordinates for leaf-blade shape were obtained by tracing representative leaves onto graph paper and then recording the x- and y-coordinates for points on the leaf margins starting at $x = 0$ and $y = 0$ at the point of attachment of the petiole. The leaf shape thus determined was used to reconstruct the measured leaves, whose areas were scaled by leaf length. Measurements of shoot geometrical characteristics were taken for three sunlit shoots of *Betula* and sunlit and shaded shoots of *Quercus*.

Calculation of light incidence was performed assuming open sky for the shoots of *Betula* and sun shoots of *Quercus*, while hemispherical photographs were used for the shade shoots of *Quercus*. The measured shoots of *Betula* and *Quercus* were rotated in azimuth angle of +90°, +180°, and +270° by Y-plant to simulate the different azimuth of whole shoot and treated as replications to examine the possible range of light interception for the shoots. For the shade shoots of *Quercus*, light interception and photosynthesis were estimated for three shoots (not rotated) under the above 12 hemispherical photographs taken at a height of 3.5 m above ground. These hemispherical photographs were analyzed with HemiView 2.1 software. The photographs having 160 sky sections were used to estimate diffuse and direct PPFD on the individual leaves in Y-plant, using the SOC (standard overcast sky) algorithm to calculate the distribution of light over the sky. In the computation of absorbed PPFD by the leaves, we assumed the leaf absorptance and transmittance of 0.85 and 0.10, respectively, for both *Betula* and *Quercus*. The calculation of photosynthesis given below is based on this absorbed PPFD.

The latest version of Y-plant contains photosynthesis (Farquhar et al., 1980), stomatal conductance for water vapor (g_{sw}), (Ball et al., 1987) and leaf energy balance models to calculate the leaf CO_2 gas exchange, stomatal conductance, and transpiration rate by incorporating the interactive effects of irradiance, temperature, and relative humidity/VPD (Baldocchi, 1994; Valladares and Pearcy, 1999). The recent changes of Y-plant involve the use of stomatal conductance model by Ball et al. (1987) and flexible settings of temperature dependency of V_{cmax} and J_{max}, which were different from our previous study simulating the shoot-level photosynthesis (Muraoka and Koizumi, 2005). These changes made more realistic estimates of photosynthetic rate under high light conditions. Calculation of photosynthetic rate requires light-saturated rate of gross photosynthesis (A_{gmax}) at Ca of $370\,\mu\,mol\,mol^{-1}$, dark respiration (R), apparent quantum yield (α, set at 0.06), and convexity factor (θ, set at 0.8) of light-photosynthetic curve, V_{cmax}

and J_{max} at temperature optimum (set at 303 K). Combined model of photosynthesis and stomatal conductance (g_{sw}) was used to simulate both g_{sw} and photosynthetic rate as

$$g_{sw} = g_0 + a\,A\,hs/Cs \tag{1}$$

where a and g_0 are constants and were set at 8.48 and 0.243 for *Betula*, and 10.33 and 0.096 for *Quercus*, respectively; according to the empirical data, hs is relative humidity and Cs is CO_2 concentration at leaf surface. In Y-plant, the above-combined model of photosynthesis and stomatal conductance was used primarily to calculate the photosynthetic rate at light saturation and the current intercellular CO_2 pressure and leaf temperature (A_{max}), and then it was applied to the light response of photosynthetic rate modeled by Thornley (1976) as

$$A = \frac{\alpha I + A_{max} - \sqrt{(\alpha I + A_{max})^2 - 4\theta\alpha I A_{max}}}{2\theta} - R \tag{2}$$

Maximum PPFD in open sky (about 2400 μmol m^{-2} s^{-1} at horizontal plane), maximum and minimum air temperatures and water vapor pressure for the simulations were determined referring to the meteorological data obtained at the canopy tower. In the simulations, two sets of minimum and maximum air temperatures, 15–20 °C and 15–28 °C were applied. Ambient CO_2 concentration was set at 370 μmol mol^{-1} and relative humidity at 80%. The photosynthesis and stomatal conductance submodels of Y-plant output the net photosynthetic rate and stomatal conductance at the sunlit and shaded parts of a single leaf, and then the values were integrated with sunlit and shaded leaf area for net photosynthetic rate of an entire single leaf. The light interception and net photosynthesis of the shoots were obtained by integrating the values for single leaves, and divided by total leaf area for each shoot.

In addition to these gas exchange calculations, Y-plant can give outputs of photosynthetic rate only calculated by light incidence using the model of Thornley (1976). Comparison of photosynthetic carbon gain between those calculated by above-combined model of photosynthesis-stomatal conductance and the solely light-dependent model (equation (2)) provides us to examine the stomatal and temperature limitation of photosynthesis. Moreover, the latest version of Y-plant calculates the influence of photoinhibition on photosynthesis (Pearcy et al. 2005; Valladares et al. 2005). This photoinhibition model is based on the findings of Ögren and Sjöström (1990) and Werner et al. (2001) that reduction of photosystem II photochemistry

(Fv/Fm) is affected by weighted PPFD dose for the previous 6 h of the target time of the day. In Y-plant, Fv/Fm was estimated as a function of PPFD dose, and the magnitude of reduction from predawn value (0.8) was then multiplied to α and θ of photosynthetic light response curve shown above. Thus, we can obtain the photoinhibited photosynthetic rate. Comparison of photosynthetic rate estimated by the combined photosynthesis-stomatal conductance model and that by this photoinhibition model provides us to evaluate the photoinhibitory limitation of photosynthesis in a sunny high light environment.

3 Results and Discussion

3.1 Seasonal Changes of Forest Canopy Properties

3.1.1 Leaf Area Index

Two-year measurements of LAI by using the hemispherical photography analysis showed remarkable changes in LAI over the growing season of deciduous canopy tree species (Fig. 1a). The low values of about 1.0 at the beginning and end of the season reflect the projected area of branches. LAI increased with increasing single leaf area expansion (data not shown) and reached the maximum in mid-June (DOY of about 170) in both 2003 and 2004. LAI remained constant by early October, and then decreased with leaf senescence and fall. Both increasing and decreasing rate of LAI were slightly different between the two years. These differences might be caused by the yearly variation of meteorological conditions including precipitation and air temperature. Further measurements for several years are necessary to analyze this fluctuation, and this would be one of the important ecological determinants of the seasonality of ecosystem carbon gain and its yearly variation (Yamamoto et al., 1999; Saigusa et al., 2002).

With these seasonal changes in LAI, light penetration into forest understory, which was expressed as diffuse light transmittance (= 1–FPAR (fraction of PAR absorbed by canopy)) estimated from the hemispherical canopy photographs, decreased during the period of leaf area expansion from May to June, remained constant until early October, and increased with leaf fall in autumn (Fig. 1b). The maximum diffuse light transmittance of about 0.5–0.6 was observed at the beginning and at the end of growing season, and the minimum of about 0.11–0.15 was observed in summer. The seasonal change of understory light environment affects considerably the photosynthetic rate of evergreen dwarf bamboo and deciduous shrub trees, whose leaf expansions begin earlier than the canopy trees (H. Muraoka, unpublished observation).

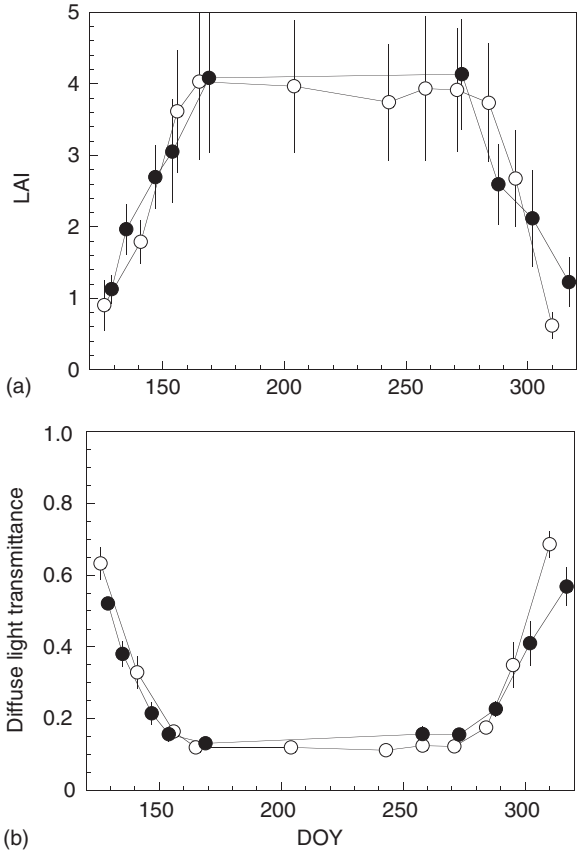

Figure 1: Seasonal changes of leaf area index (LAI) (a) and diffuse light transmittance to understory (b) for 2 years (2003, open circle; 2004, solid circle) in a cool-temperate deciduous broadleaved forest. Mean $\pm$ SD for 14 locations within a 1-ha study plot are shown.

3.1.2 Leaf Physiological Characteristics

Photosynthetic rate at light saturation (A_{max}), dark respiration (R), and index of chlorophyll concentration (SPAD) showed remarkable seasonal changes in the two deciduous broadleaved tree species of *Betula* and *Quercus* (Fig. 2). Although the apparent patterns of leaf physiological characteristics were similar between the sunlit (canopy top) and shaded (inner canopy) leaves of *Quercus*, A_{max} and R were higher in sunlit leaves throughout the growing seasons, indicating that this deciduous broadleaf tree changes the photosynthetic characteristics along the gradient of local light environment in its canopy (see also Niinemets and Tenhunen, 1997; Niinemets and Valladares, 2004).

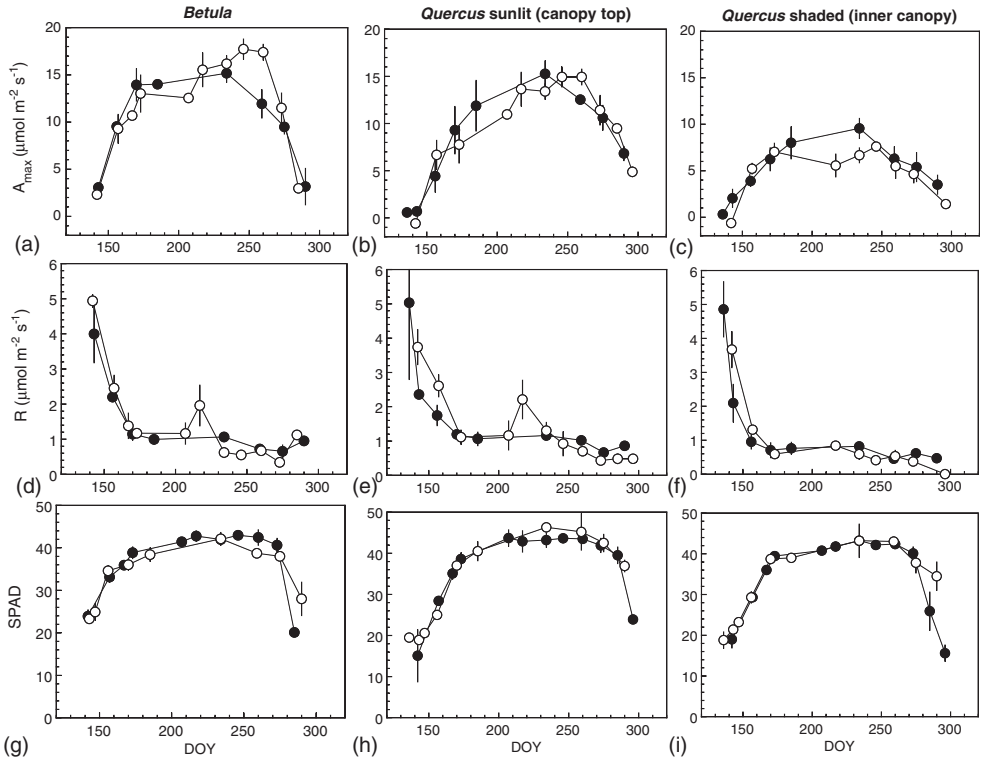

Figure 2: Seasonal changes of single leaf photosynthetic characteristics in *Betula ermanii* (left column), sunlit leaves (center column), and shaded leaves (right column) of *Quercus crispula* for 2 years (2003, open circle; 2004, solid circle). Light-saturated photosynthetic rate (A_{max}; a–c), dark respiration rate (R; d–f), and index of chlorophyll concentration (SPAD; g–i) for three to seven sample leaves (mean $\pm$ SD) are shown.

At the beginning of the growing season, A_{max} and SPAD were the lowest and R was the highest. Then A_{max} and SPAD increased rapidly until their maximum in early summer and remained high values during the summer, and decreased in autumn. On the other hand, R decreased rapidly until the leaf area maturation at DOY of 170, and remained relatively constant until the leaf senescence. The increase of A_{max} and SPAD at the first phase of the phenology indicates the physiological growth of leaf biochemistry (Grassi and Magnani, 2005; Grassi et al., 2005), while the high R in this phase indicates the construction costs for leaf anatomy and expansion of leaf area (Miyazawa and Terashima, 2001).

The initiation of decline was different between A_{max} and SPAD, suggesting the different senescence schedule or responses to autumn climate between the components responsible for photochemistry and carbon fixation

involved in the photosynthetic reaction. Our previous analyses for V_{cmax} and J_{max} using the data obtained throughout the growing season showed that the ratio of J_{max} to V_{cmax} changes seasonally; the ratio was higher at the beginning and the end of the season (Muraoka and Koizumi, 2005). Such tendency has also been reported in some studies (Hikosaka et al., 1999; Wilson et al., 2000, 2001; Xu and Baldocchi, 2003; Onoda et al., 2005), and it can be argued that the seasonal change of J_{max}/V_{cmax} reflect the shift of nitrogen allocation within a leaf so as to have an efficient photosynthetic resource utilization under changing temperature conditions.

The 2-year measurements of these leaf physiological characteristics revealed the existence of year-to-year variation as was also observed in LAI. The most remarkable difference was found for A_{max} of *Betula* and sun leaves of *Quercus* in mid-summer (Fig. 2). In 2003, A_{max} of *Betula* and *Quercus* reached the maximum in late summer (late August to early September), while A_{max} of *Betula* reached the maximum in early summer (mid-June), but A_{max} of *Quercus* in mid-summer (mid-August). This seasonality in A_{max} and its yearly variation would no doubt affect the photosynthetic productivity of the forest ecosystem.

These differences in leaf physiological phenology would involve two different reasons: the leaf ontogenetic characteristics of the two tree species and the yearly variation of climate conditions. *Betula* is recognized to be a pioneer species characterized by its high photosynthetic activity under high light conditions (Koike, 1988). The rapid leaf morphological and physiological development of this species would highly contribute to the high growth rate. On the other hand, *Quercus* is recognized to be a mid-late successional species, which has tough leaves (Koike, 1988). The rates of leaf anatomical and physiological developments have been suggested to be related to the leaf thickness or leaf mass area ratio (LMA); the thicker or tougher the leaves, the slower the rate of physiological development (fulfilment of biochemical components) as compared to the anatomical development (Miyazawa et al., 1998). This perspective is thought to be adaptive in ecological sense since mid-late successional species have to grow in a resource-limited environment of forest understory during the juvenile stages. Therefore, the cost–benefit relationships, which are determined by costs for leaf construction and herbivory and benefit by photosynthesis for these species, should be more severe than the species in resource-rich environment (Mooney and Gulmon, 1982; Miyazawa et al., 1998).

The yearly difference of the developmental rate of A_{max} in both *Betula* and *Quercus* might reflect the difference of climate conditions in early to mid summer. In 2003, the rainy season was irregularly prolonged as compared to the other years, while the climate condition in 2004 was relatively regular. Since leaf physiological development and photosynthetic capacity (A_{max}) are constrained by light incidence (Niinemets et al., 2004), the shortage of light

incidence by the long rainy season might have inhibited the growth of leaf biochemistry in 2003. If this is true, it gives us insight into the relationship between morphological (leaf area) and physiological (photosynthesis) developments and climate conditions, since such information would be important in modeling ecosystem function such as canopy photosynthesis.

The different phenology in leaf area and physiological development of trees composing the forest further lead to the different developmental rate of canopy LAI and photosynthetic capacity; the earlier development of LAI as compared to leaf photosynthetic capacity, and rapid decrease in respiration rate during leaf area development (Figs. 1 and 2). These results (Figs. 1 and 2) and other reports (Wilson et al., 2001; Morecroft et al., 2003; Xu and Baldocchi, 2003) strongly indicate that the photosynthetic productivity of the deciduous forest canopy should be evaluated by considering the different patterns of these plant characteristics; if one assumes that in the ecosystem-scale model the photosynthetic capacity (A_{max} or V_{cmax}) is constant throughout the growing season while LAI changes seasonally, the estimated photosynthetic productivity must be overestimated considerably (Ito et al., 2006).

3.2 Branch Architecture and Photosynthetic Carbon Gain at the Canopy Top

3.2.1 Diurnal Patterns of Plant Ecophysiological Performance

Three-dimensional shoot architectures of *Betula* and *Quercus* (for sun and shade branches) were measured and reconstructed with a structural–functional model, Y-plant (Fig. 3). Leaf angle of the shoots were different among the tree species or growth light environment, i.e., $65.0 \pm 12.2^{\circ}$ for *Betula* (mean $\pm$ SD for 40 leaves from three shoots), $31.5 \pm 12.1^{\circ}$ for sunlit (56 leaves), and $24.5 \pm 12.8^{\circ}$ for shaded (62 leaves) shoots of *Quercus*. Reflecting the differences in leaf angle and length of petiole, self-shading in *Betula* shoots was smaller than those of *Quercus* shoots, and projected leaf area to the light source (the sun) in midday hours is reduced in *Betula*, which would be effective in avoiding high light stresses and realizing moderate light interception . The leaf display was different between the sunlit and shaded shoots of *Quercus*, suggesting that the species changes its shoot architecture by responding to the local light environment within its canopy, as well as leaf photosynthetic characteristics. Leaf arrangement was flatter and self-shading was smaller in shaded shoots (Fig. 3). These characteristics in shaded shoots are effective in receiving light incidence in the light-limited environment of inner canopy and understory positions (Niinemets, 1998).

Figs. 4 and 5 show the diurnal patterns of the relationships between temperature regimes, stomatal conductance (g_{sw}), photoinhibition,

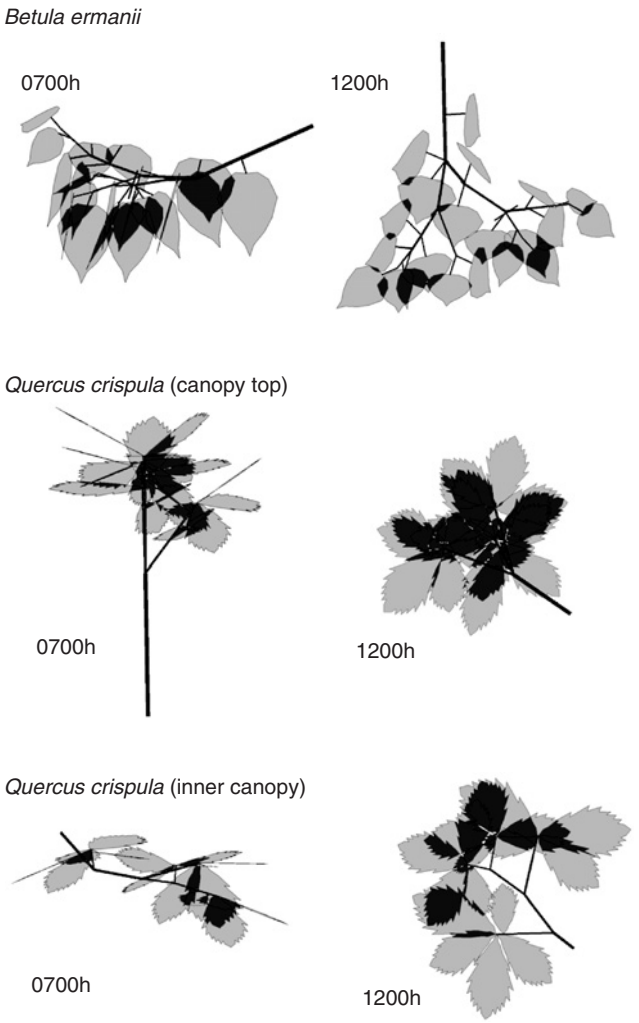

Figure 3: Architectures of a shoot of *Betula*, sunlit and shaded shoots of *Quercus* reconstructed by a simulation program Y-plant. The structures were reconstructed on the basis of the measured geometrical parameters (see text). Images indicate the views from sun angle in early morning (0700 hr) and noon (1200 hr). The darker areas of the shoots indicate self-shading.

photosynthetic rate (A), and light utilization efficiency (LUE = A/absorbed PPFD) for *Betula* and *Quercus* in a high light environment based on simulation results by Y-plant. Owing to the steep leaf angles and resulting small projection of leaf area to the sun in *Betula*, light absorption on the leaf area basis was largely reduced as compared to that for horizontal plane

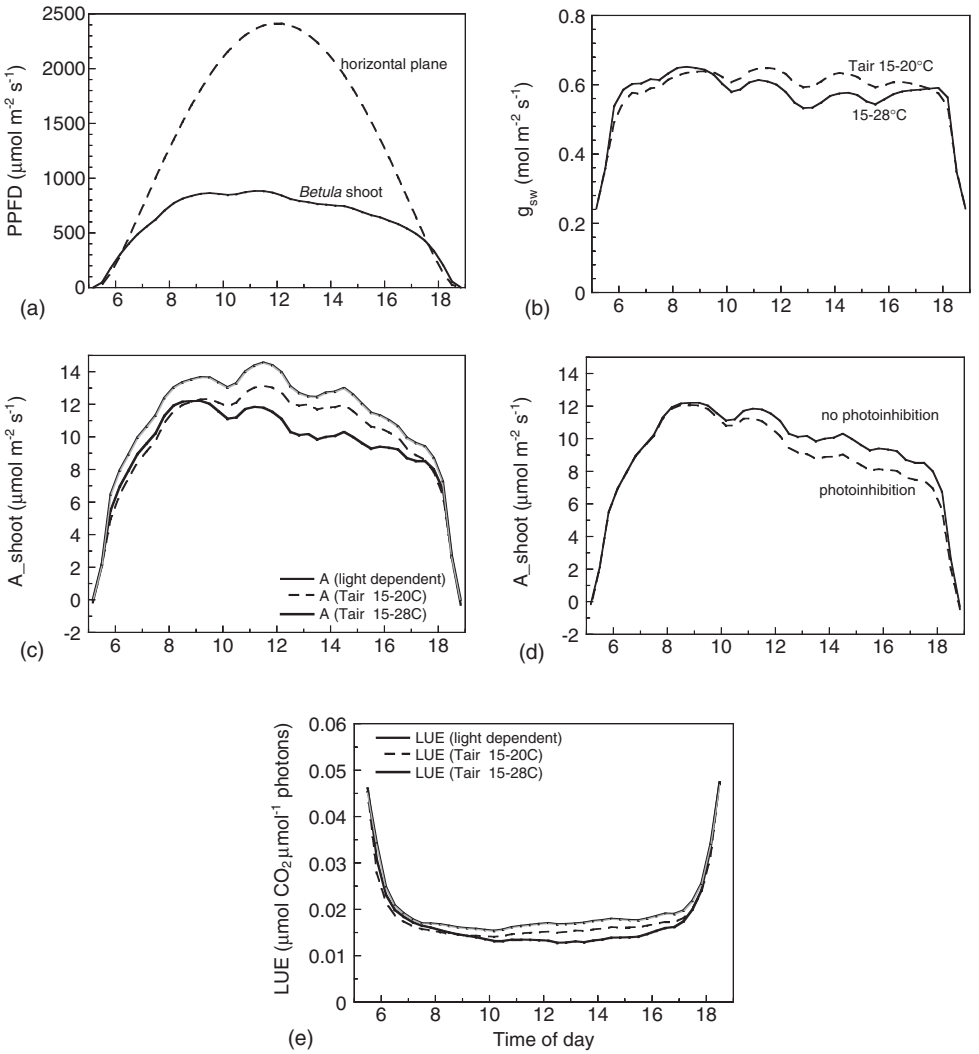

Figure 4: Example diurnal course of simulated light interception (a) stomatal conductance to water vapor (b) photosynthetic rate as a function of light incidence and temperature (c) photosynthetic rate with and without photoinhibition (d) and light utilization efficiency (LUE) and (e) of a shoot of *Betula*. Light interception, stomatal conductance, and photosynthetic rate are expressed on the basis of leaf area averaged over the sample shoot. Photosynthetic rate shown in (c) were calculated by solely light dependence (gray line) or by considering the temperature dependence of photosynthetic reaction and stomatal conductance to vapor pressure under two air temperature conditions (Tair; minimum–maximum of 15–20 °C, dotted line; and 15–28 °C, bold line). LUE shown in (e) were calculated from the data on (a) and (c).

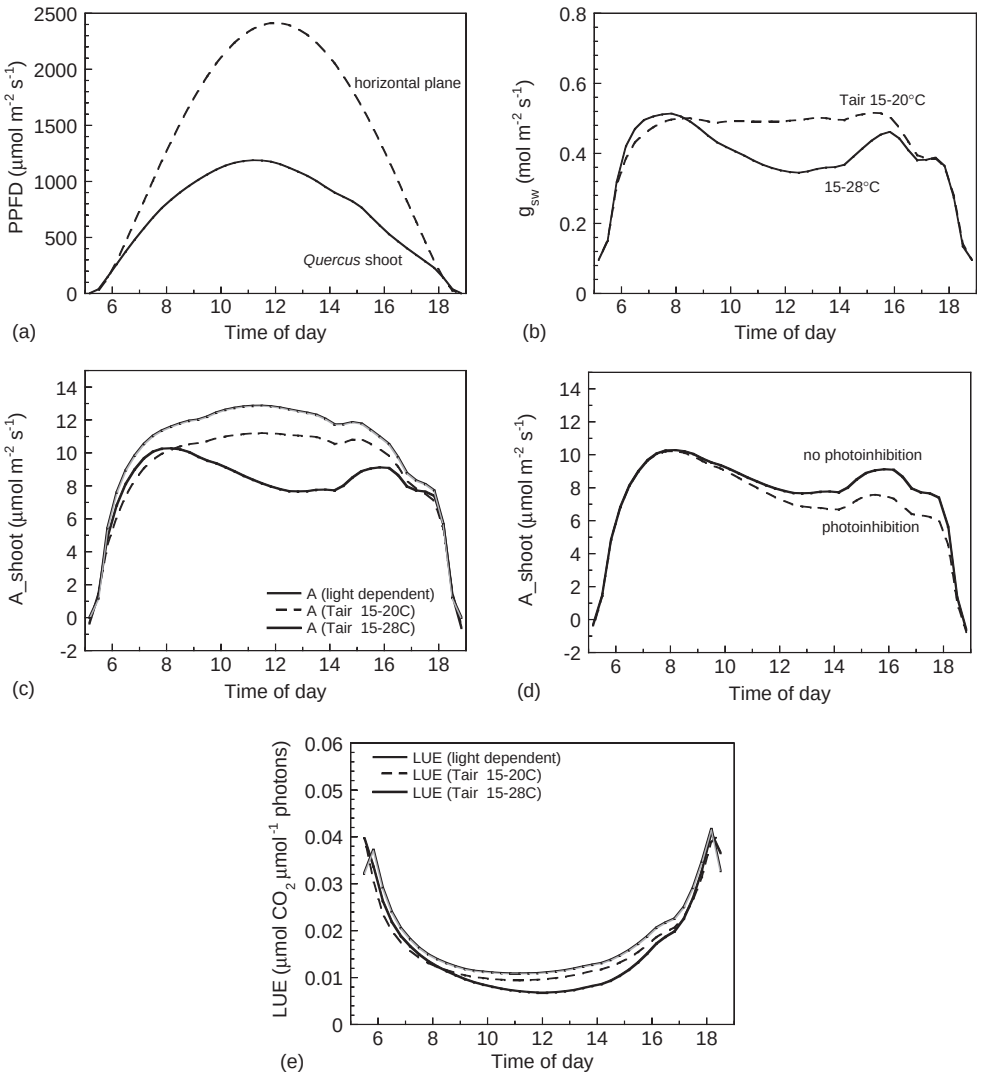

Figure 5: Example diurnal course of simulated light interception (a), stomatal conductance to water vapor (b), photosynthetic rate solely light dependent (gray line) and or by considering the temperature dependence of photosynthetic reaction and stomatal conductance to vapor pressure under two air temperature conditions (Tair; minimum–maximum of 15–20 °C, dotted line; and 15–28 °C, bold line) (c), photosynthetic rate with and without photoinhibition (d) and light utilization efficiency (e) of a sunlit shoot of *Quercus*.

(Fig. 4a). Different daily maximum air temperature (20 and 28 °C) led different maximum leaf temperature of about 20.5 and 28.5 °C, respectively. Consequently, g_{sw} and A, and hence LUE was reduced by this rising leaf temperature: A was the highest in a case that was estimated solely from light absorption, and was reduced by incorporating the temperature and stomatal effects on photosynthetic rate (Figs. 4c, e; daily values will be shown below). The reduced g_{sw} and A at midday hours are called "midday depression", and would have considerable limitation to the daily photosynthetic carbon gain in high light environments. Daily accumulation of light absorption (PPFD dose) led to decline in Fv/Fm at midday hours with minimum of 0.64 and hence reduction of photosynthetic carbon gain in afternoon hours (Fig. 4d).

In the sun shoot of *Quercus* (Fig. 5), the maximum leaf temperatures were higher than *Betula*, about 23.5 °C at air temperature of 20 °C, and 30.5 °C at 28 °C. These higher leaf temperatures of *Quercus* than *Betula* were induced by the smaller leaf angles and resulting large projection leaf area to the sun in midday hours that receive larger amount of light in midday hours (Fig. 5). The high leaf temperature led to considerable reduction of g_{sw} and hence A and LUE in *Quercus* (Figs. 5b, c, e). Also in *Quercus*, exposure of the leaves to direct sun light led to reduction of Fv/Fm to the minimum of 0.60 in afternoon and that photoinhibition reduced A (Fig. 5d).

3.2.2 Effects of Shoot Architecture and Stomatal Closure on Daily Photosynthesis

Daily integrated values of light absorption, photosynthesis, and photosynthetic limitation by stomatal closure and photoinhibition are shown in Fig. 6. To clarify the effects of shoot architecture (leaf angle and self-shading) on the plant performance, simulation results for virtual plants with horizontal and non-self-shaded leaves are also shown. In horizontal leaves with no self-shading, they can receive 58.0 mol photons $m^{-2}\,day^{-1}$ of PAR (expressed as daily PPFD: $PPFD_{day}$) under a clear open sky of a sunny day. But this $PPFD_{day}$ was reduced to $28.9 \pm 3.5\,mol\,m^{-2}\,day^{-1}$ in *Betula* or 35.4 ± 3.1 in *Quercus* shoots. These reductions were due to the variation of leaf angle within the shoots and self-shading among the leaves.

The high $PPFD_{day}$ in horizontal leaves led to high daily photosynthesis (A_{day}) than those for shoot-level performance in all cases of calculation of photosynthesis, i.e., solely light dependent, including stomatal effects and photoinhibition in both *Betula* and *Quercus* (Figs. 6a, b, c). Owing to the interception of full sunlight throughout the day, horizontal leaves had higher leaf temperature by 2 °C and lower Fv/Fm (*ca.* 0.4) than the leaves along the actual shoot architecture (Fv/Fm of *ca.* 0.6–0.65): these high light stresses led to larger stomatal and temperature limitation (= reduction of

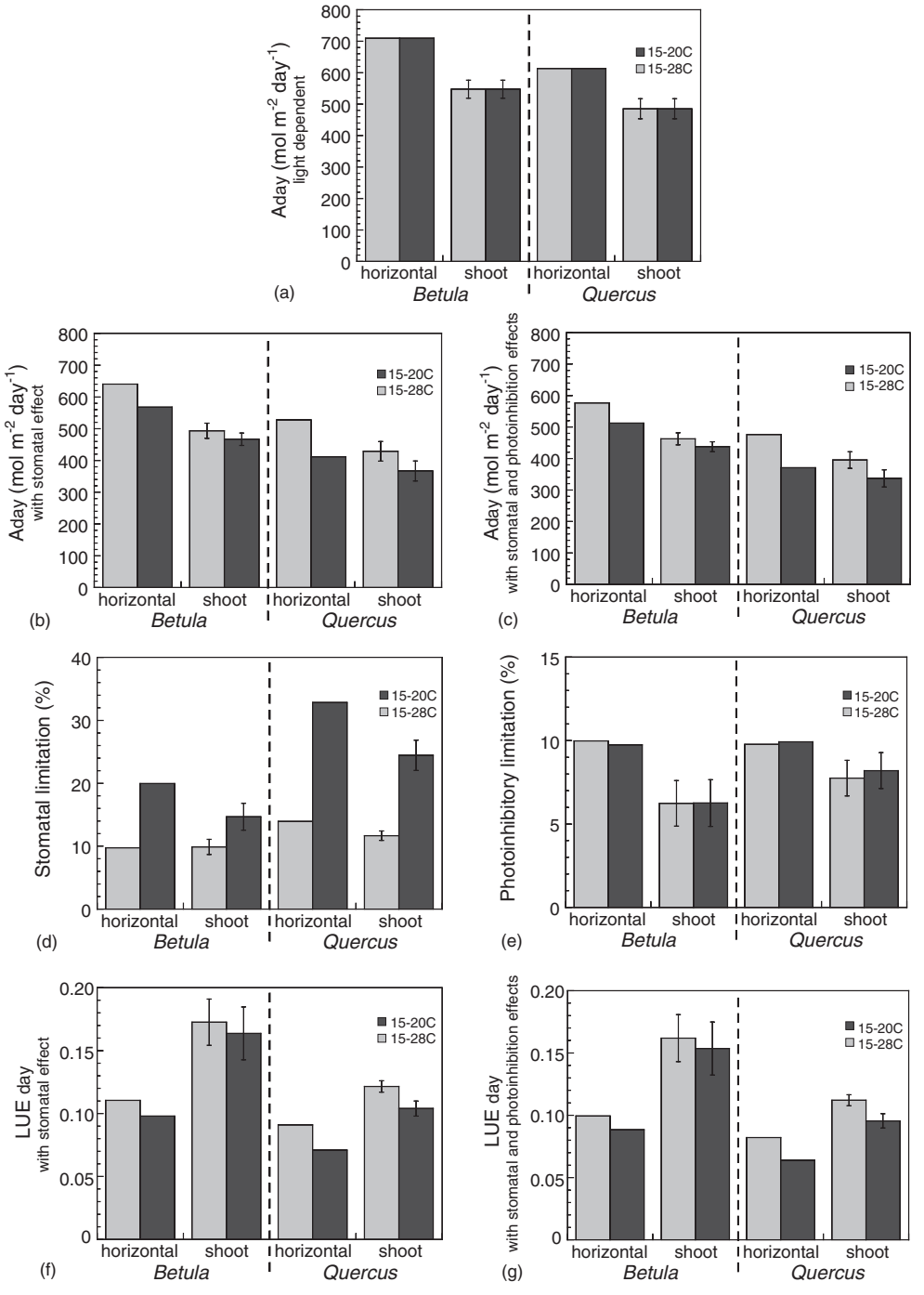
Aday (mol m-2 day-1) light dependent
Aday (mol m-2 day-1) with stomatal effect
Aday (mol m-2 day-1) with stomatal and photoinhibition effects
Stomatal limitation (%)
Photoinhibitory limitation (%)
LUE day with stomatal effect
LUE day with stomatal and photoinhibition effects
15-20C
15-28C
horizontal
shoot
Betula
Quercus
(a)
(b)
(c)
(d)
(e)
(f)
(g)

A_{day} as compared to light-dependent A_{day}; Fig. 6d) and/or photoinhibitory limitation (= reduction of A_{day} as compared to stomatal and temperature-limited photosynthesis; Fig. 6e) of photosynthesis. In horizontal leaves of *Betula*, stomatal and temperature limitation of A_{day} was 9.7 and 20.0% for air temperature regimes of 15–20 and 15–28°C, respectively, while those for actual shoots were 9.9 and 14.7%. In *Quercus*, stomatal limitation of horizontal leaves were 13.9 and 32.8% for the two air temperature regimes, while those for actual shoots were 11.7 and 24.4%, respectively. These results indicate important aspects in canopy photosynthesis that (1) stomatal limitation has quantitatively remarkable effect on daily photosynthetic carbon gain for plants in high light and high air temperature (and VPD) environments, and (2) leaf angles and foliage geometry affect estimation of canopy photosynthesis considerably.

LUE was dependent on the shoot architecture (leaf orientation) and tree species (Fig. 6f, g). LUE was higher in leaves having their natural orientation along the shoot than in horizontal leaves, and higher in *Betula* than in *Quercus*. These results were caused by the balance between light interception and photosynthesis, which were affected by leaf angle and photosynthetic activity under high light. Thus use of LUE term in ecosystem-scale models (e.g., Running et al., 2004) requires the ecophysiological understanding of these consequences for accurate and reliable estimates.

The larger midday depression of g_{sw} and A in *Quercus* than *Betula* can be attributed to the smaller leaf angles and lower g_0. As shown in Figs. 4a and 5a, the difference in leaf angles and hence shoot architecture, i.e., projected leaf area to the sun (Fig. 3), led to different light absorption with higher maximum PPFD in *Quercus*. This led to higher leaf temperature and transpirational load. Stomatas are suggested to close by responding to the transpirational load (Mott and Parkhurst 1991), and therefore the higher leaf temperature could induce stomatal closure more remarkably in *Quercus*

Figure 6: Daily integrated performance of *Betula* and *Quercus* shoots under high light conditions with two air temperature regimes (minimum–maximum of 15–20 °C, light gray bar; and 15–28 °C, solid bar). Daily photosynthesis (A_{day}) solely light dependent (a), temperature and stomatal dependent (b), and including the effect of photoinhibition on photosynthesis (c), stomatal limitation (d), and photoinhibitory limitation (e) to photosynthesis, and daily light utilization efficiency in which A_{day} was temperature and stomatal dependent (f) and photoinhibitory limited (g). For each tree species, "horizontal" indicates the calculated data for a model shoot with horizontal leaves with no self-shading and "shoot" indicates the data for the measured architectures (mean $\pm$ SD of three shoots $\times$ four azimuth angles). Note that A_{day} solely light dependent (a) are not different between the temperature regimes.

(Fig. 4b vs. 5b). Moreover, midday g_{sw} is highly dependent on g_0 (equation (1)). *Quercus* leaves have lower g_0 of 0.096 mol m^{-2} s^{-1} as compared to that of *Betula* (0.243 mol m^{-2} s^{-1}). The lower g_0 would contribute to the conservative use of water but highly limits CO_2 transfer into leaves via stomatal pore. On the other hand, the higher g_0 and g_{sw} in *Betula* would be effective in CO_2 transfer as well as transpirational leaf cooling, which should be important in this pioneer species.

3.2.3 Effects of Shoot Architecture and Photoinhibition on Daily Photosynthesis

The smaller leaf angle also led to larger photoinhibitory limitation on photosynthesis (Fig. 6e). Photoinhibition due to accumulated light interception reduced A_{day} by 9–10% in horizontal leaves in both tree species, while it was 6% in *Betula* shoots and 10% in *Quercus* shoots. Reduction of photosynthesis by rising leaf temperature, stomatal closure, and photoinhibition decreased daily LUE from 0.19 to 0.15 in *Betula* and from 0.14 to 0.10 in *Quercus* shoots, as compared to the case of solely light-dependent photosynthesis (Fig. 6(g). Our estimates of the impact of photoinhibition on daily shoot carbon gain agree with previous studies that showed 2–10% reduction in broadleaved tree species (Ögren and Sjöström, 1990; Werner et al., 2001; Pearcy et al., 2005; Valladares et al., 2005). The different photoinhibitory limitation on A_{day} between horizontal leaves and actual shoot leaves can be attributed to two reasons: effect of leaf angle itself and self-shading. Steeper leaf angle contributes to reducing light interception, especially excessive high light of midday that is not necessary for saturating photosynthetic rate. Self-shading can also avoid excess high light and heat load in midday hours and the photosynthesis at shaded part of the leaves might contribute to the whole shoot carbon gain even under high light stresses (Valladares and Pearcy, 1999; Valladares et al. 2005).

In both *Betula* and *Quercus*, the difference of temperature conditions did not affect the influence of photoinhibition on photosynthesis, since the present model estimates photoinhibition only from the light absorption. In general, the magnitude of photoinhibition can be influenced by the capacity and activity of photosynthetic and other physiological dissipation of absorbed photons (Osmond, 1994); the lower the photosynthetic activity in midday hours, the larger the photoinhibition since photosynthesis has the largest capacity of energy dissipation, but midday depression of g_{sw} reduces the photosynthetic utilization of absorbed photons (e.g., Osmond and Grace, 1995; Muraoka et al., 2000). Further quantitative evaluation of these effects on canopy photosynthesis should be progressed.

These simulation studies on two canopy tree species with different leaf physiology and shoot architecture provided the species-specific differences in consequences of plant ecophysiology and microenvironment on

photosynthetic carbon gain. Although these two species can be grouped into one category of vegetation as "broadleaved deciduous trees" in satellite remote sensing observations and regional to global-scale models, we should keep in mind that trees with different successional status would perform differently in terms of photosynthetic response to multiple environment at the canopy top, and that the relative dominance of trees with different successional status in a given forest type would have considerable effect on the ecosystem behavior.

3.3 Light Environment and Branch Photosynthesis at Inner Canopy

Light environment for the shade shoots of *Quercus* on a sunny day is characterized by the temporal fluctuation of diffuse light with low PPFD and sun fleck with high PPFD (Fig. 7a). Light interception in the leaves along the shoot was reduced (6.4 ± 1.9 mol photons m^{-2} day^{-1}; mean $\pm$ SD for three shoots $\times 12$ light environments) as compared to that at horizontal plane

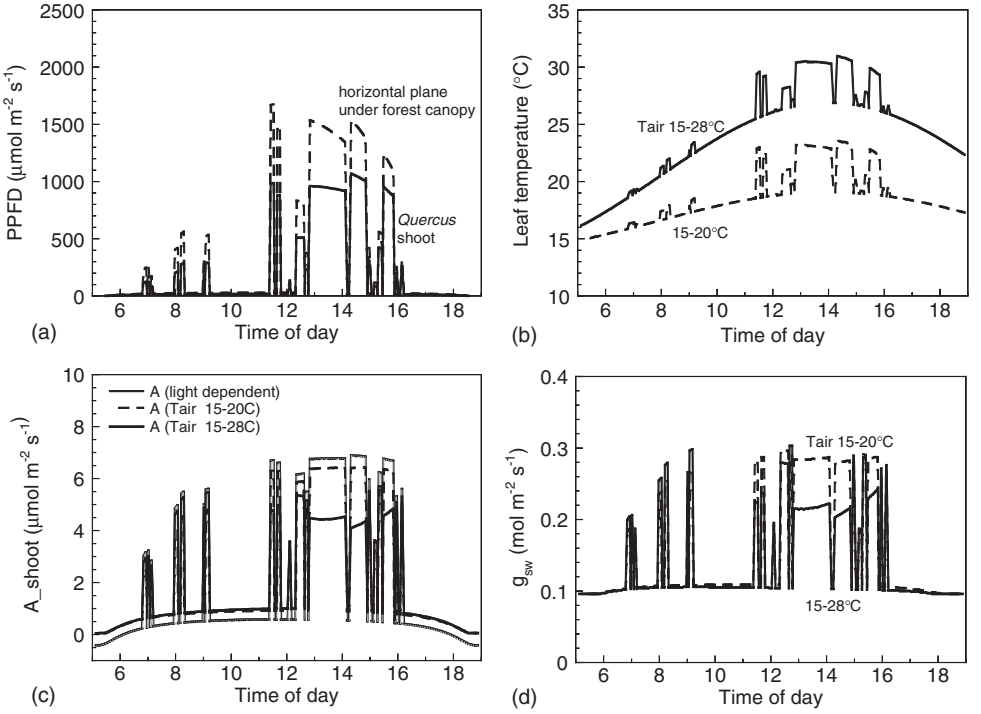

Figure 7: Example diurnal course of light interception (a), leaf temperature (b), photosynthetic rate (c), and stomatal conductance to water vapor (d) in a shaded shoot of *Quercus*.

($9.3 \pm 2.8\,\mathrm{mol\,m^{-2}\,day^{-1}}$), due to various leaf angles and self-shading (but smaller than the sun shoots). According to the diurnal changes in light interception, leaf temperature changed in fluctuated manner with maximum of about 23 and 31 °C for the two air temperature regimes; the maximum leaf temperature was observed when the leaves were receiving sun flecks (Fig. 7b). The g_{sw} and A tracked the fluctuated changes of light interception, but higher temperature condition reduced both g_{sw} and A especially during midday hours, when the light incidence and leaf temperature were maximum throughout the daytime (Figs. 7c, d).

A_{day} of the horizontal and not self-shaded leaves was 119.1 ± 20.0 and $115.3 \pm 19.1\,\mathrm{mmol\,m^{-2}\,day^{-1}}$ under the two temperature regimes of 15–20 °C and 15–28 °C, respectively. At shoot level, A_{day} was 90.9 ± 16.5 and $88.7 \pm 15.3\,\mathrm{mmol\,m^{-2}\,day^{-1}}$, respectively. Increasing temperature led only to 2.4% reduction in A_{day}, while transpirational water loss increased by about 20% (data not shown). Calculation of photosynthetic rate solely dependent on light interception (equation (2)) underestimated A at diffuse light incidence (Fig. 7c), and this difference accounted for 7 to 50% underestimation of A_{day} in a case of 15–20 °C regime (data not shown). This might be partly due to the temperature effects on respiration and photosynthetic processes calculations during the diffuse light with lower temperature than under sun flecks.

4 Conclusion

This chapter demonstrated the seasonality of canopy LAI and single leaf photosynthetic and respiratory capacity in dominant canopy tree species, and the consequences of branch architecture, light environment at canopy top and inner canopy, and photosynthesis in a cool-temperate deciduous broadleaved forest in Japan. The former perspectives determine the potential of forest photosynthetic productivity, and the latter are responsible for the instantaneous and daily photosynthetic productivity. The recent requirements for the mechanistic and quantitative understanding of the carbon budget in forest ecosystems are of great importance in our understanding of ecosystem function from a regional to global scale. The present study, though it is relatively in fine scale within the ecosystem, would suggest the necessity of investment of our research resources and challenge of scaling from leaf and canopy ecophysiology to ecosystem behavior (see also Ehleringer and Field 1993; van Gardingen et al., 1997; Running et al., 2004; Ustin et al., 2004).

The ecosystem carbon cycle studies tend to focus on the budget of photosynthetic carbon fixation and respiratory release of CO_2, but as the recent reports suggest the mechanisms of the carbon cycle and budget, i.e.,

interaction of meteorological environments and plant ecophysiology, promise to provide fundamental information for the analyses and prediction of past and future ecosystem function and its relationship with the regional and global climate. Intensive and integrated research on the consequences of plant ecological and physiological perspectives, and scaling analyses have the central role in telling us what we should know on the ecosystem function and dynamics.

Acknowledgements

We thank Professor R. W. Pearcy of UC Davis (USA) for his kind support for our use of Y-plant. Thanks are also due to Dr. S. Yamamoto, Dr. N. Saigusa, and Dr. S. Murayama of National Institute of Advanced Industrial Science and Technology and Dr. K. Nishida of University of Tsukuba for their encouragements and discussions.

References

Baldocchi, D. D., 1994. An analytical solution for coupled leaf photosynthesis and stomatal conductance models. Tree Physiology 14, 1069–1079.

Baldocchi, D. D., Meyers, T., 1998. On using eco-physiological, micrometeorological and biogeochemical theory to evaluate carbon dioxide, water vapor and trace gas fluxes over vegetation: A perspective. Agricultural and Forest Meteorology 90, 1–25.

Ball, J. T., Woodrow, I. E., Berry, J. A., 1987. A model predicting stomatal conductance and its contribution to the control of photosynthesis under different environmental conditions. Progress in Photosynthesis Research 4, 221–224.

Bazzaz, F. A., 1996. Plants in Changing Environments. Cambridge University Press, Cambridge.

Beyschlag, W., Ryel, R., 1999. Canopy photosynthesis modeling. In: Pugnaire, F. I., Valladares, F. (Eds.), Handbook of Functional Plant Ecology. Marcel Dekker Inc., New York, Basel, pp. 771–804.

Caldwell, M. M., Meister, H. P., Tenhunen, J. D., Lange, O. L., 1986. Canopy structure, light microclimate and leaf gas exchange of *Quercus coccifera* L. in a Portuguese macchia: Measurements in different canopy layer and simulations with a canopy model. Trees 1, 25–41.

Chapin, F. S.III., Matson, P. A., Mooney, H. A., 2002. Principles of Terrestrial Ecosystem Ecology. Springer-Verlag, New York.

Ehleringer, J. R., Field, C. B., 1993. Scaling Physiological Processes: Leaf to Globe. Academic Press, London.

Farquhar, G. D., von Caemmerer, S., Berry, J. A., 1980. A biochemical model of photosynthetic CO_2 assimilation in leaves of C_3 species. Planta 149, 78–90.

Field, C. B., Randerson, J. T., Malmstrom, C. M., 1995. Global net primary production: Combining ecology and remote sensing. Remote Sensing of Environment 51, 74–88.

Grassi, G., Magnani, F., 2005. Stomatal, mesophyll conductance and biochemical limitations to photosynthesis as affected by drought and leaf ontogeny in ash and oak trees. Plant, Cell and Environment 28, 824–849.

Grassi, G., Vicinelli, E., Ponti, F., Cantoni, L., Magnani, F., 2005. Seasonal and interannual variability of photosynthetic capacity in relation to leaf nitrogen in a deciduous forest plantation in northern Italy. Tree Physiology 25, 349–360.

Harley, P. C., Baldocchi, D. D., 1995. Scaling carbon dioxide and water vapour exchange from leaf to canopy on a deciduous forest: I. Leaf model parameterization. Plant, Cell and Environment 18, 1146–1156.

Hikosaka, K., Murakami, A., Hirose, T., 1999. Balancing carboxylation and regeneration of ribulose–1,5–bisphosphate in leaf photosynthesis: Temperature acclimation of an evergreen tree, *Quercus myesinaefolia*. Plant, Cell and Environment 22, 841–849.

Intergovernmental Panel on Climate Change (IPCC), 2001. Climate Change 2001: Impacts, Adaptation, and Vulnerability. McCarthy, J. J., Canziani, O. F., Leary, N. A., Dokken, D. J., White, K. S. (Eds.), Cambridge University Press, Cambridge.

Ito, A., Muraoka, H., Koizumi, H., Saigusa, N., Murayama, S., Yamamoto, S., 2006. Seasonal variation in leaf properties and ecosystem carbon budget in a cool-temperate deciduous broadleaved forest: Simulation analysis at Takayama site. Japan. Ecological Research 21, 137–149.

Kitao, K., Lei, T. T., Koike, T., Tobita, H., Maruyama, Y., 2000. Susceptibility to photoinhibition of three deciduous broadleaf tree species with different successional traits raised under various light regimes. Plant, Cell and Environment 23, 81–89.

Koike, T., 1988. Leaf structure and photosynthetic performance as related to the forest succession of deciduous broadleaved trees. Plant Species Biology 3, 77–87.

Larcher, W., 2001. Physiological Plant Ecology. Springer-Verlag, Berlin, Heidelberg.

Lee, M., Nakane, K., Nakatsubo, T., Koizumi, H., 2003. Seasonal changes in the contribution of root respiration to total soil respiration in a cool-temperate deciduous forest. Plant and Soil 255, 311–318.

Leuning, R., 1995. A critical appraisal of a combined stomatal-photosynthesis model for C_3 plants. Plant, Cell and Environment 18, 39–355.

Markwell, J., Osterman, J. C., Mitchell, J. L., 1995. Calibration of the Minolta SPAD-502 leaf chlorophyll meter. Photosynthesis Research 46, 467–472.

Medlyn, B. E., Dreyer, E., Ellsworth, D., Forstreuter, M., Harley, P. C., Kirschbaum, M. U. F., Le Roux, X., Montpied, P., Strassemeyer, J., Walcroft, A., Wang, K., Loustau, D., 2002. Temperature response of

parameters of a biochemically based model of photosynthesis II: A review of experimental data. Plant, Cell and Environment 25, 1167–1179.
Miyazawa, S., Satomi, S., Terashima, I., 1998. Slow leaf development of evergreen broad-leaved tree species in Japanese warm temperate forests. Annals of Botany 82, 859–869.
Miyazawa, S., Terashima, I., 2001. Slow development of leaf photosynthesis in an evergreen broadleaved tree, *Castanopsis sieboldii*: Relationships between leaf anatomical characteristics and photosynthetic rate. Plant, Cell and Environment 24, 279–291.
Mooney, H. A., Gulmon, S. L., 1982. Constraints on leaf structure and function in response to herbivory. BioScience 32, 198–206.
Morecroft, M. D., Stokes, V. J., Morison, J. I. L., 2003. Seasonal changes in the photosynthetic capacity of canopy oak (*Quercus robur*) leaves: The impact of slow development on annual carbon uptake. International Journal of Biometeorology 47, 221–226.
Mott, K. A., Parkhurst, D. F., 1991. Stomatal responses to humidity in air and helox. Plant, Cell and Environment 14, 509–515.
Muraoka, H., Tang, Y., Terashima, I., Koizumi, H., Washitani, I., 2000. Contributions of diffusional limitation, photoinhibition and photorespiration to midday depression of photosynthesis in *Arisaema heterophyllum* in the natural high light. Plant, Cell and Environment 23, 235–250.
Muraoka, H., Koizumi, H., Pearcy, R. W., 2003. Leaf display and photosynthesis of tree seedlings in a cool-temperate deciduous broadleaf forest understory. Oecologia 135, 500–509.
Muraoka, H., Koizumi, H., 2005. Photosynthetic and structural characteristics of canopy and shrub trees in a cool-temperate deciduous broadleaved forest: implication to the ecosystem carbon gain. Agricultural and Forest Meteorology 134, 39–59.
Murayama, S., Saigusa, N., Chan, D., Yamamoto, S., Kondo, H., Eguchi, Y., 2003. Temporal variations of atmospheric CO_2 concentration in a temperate deciduous forest in central Japan. Tellus 55B, 232–243.
Niinemets, Ü., Tenhunen, J. D., 1997. A model separating leaf structural and physiological effects on carbon gain along light gradients for the shade-tolerant species *Acer saccharum*. Plant, Cell and Environment 20, 845–866.
Niinemets, Ü., 1998. Adjustment of foliage structure and function to a canopy light gradient in two co-exsiting deciduous trees: Variability in leaf inclination angles in relation to petiole morphology. Trees – structure and function 12, 446–451.
Niinemets, Ü., Valladares, F., 2004. Photosynthetic acclimation to simultaneous and interacting environmental stresses along natural light gradients: optimality and constraints. Plant Biology 6, 254–268.
Niinemets, Ü., Kull, O., Tenhunen, J. D., 2004. Within-canopy variation in the rate of development of photosynthetic capacity is proportional to integrated quantum flux density in temperate deciduous trees. Plant, Cell and Environment 27, 293–313.

Norman, J. M., Campbell, G. S., 1989. Canopy structure. In: Pearcy, R. W., Ehleringer, J., Mooney, H. A., Rundel, P. W. (Eds.), Plant Physiological Ecology: Field Methods and Instruction. Chapman and Hall, London, pp. 301–325.

Ögren, E., Sjöström, M., 1990. Estimation of the effect of photoinhibition on the carbon gain in leaves of a willow canopy. Planta 181, 560–567.

Onoda, Y., Hikosaka, K., Hirose, T., 2005. Seasonal change in the balance between capacities of RuBP carboxylation and RuBP regeneration affects CO_2 response of photosynthesis in *Poligonum cuspidatum*. Journal of Experimental Botany 56, 755–763.

Osmond, C. B., 1994. What is photoinhibition? Some insights from comparisons of shade and sun plants. In: Baker, N. R., Bowyer, J. R. (Eds.), Photoinhibition of Photosynthesis from Molecular Mechanisms to the Field. BIOS Scientific Publishers Limited, Oxford, pp. 1–24.

Osmond, C. B., Grace, S. C., 1995. Perspectives on photoinhibition and photorespiration in the field: Quintessential inefficiencies of the light and dark reactions of photosynthesis?. Journal of Experimental Botany 46, 1351–1362.

Pearcy, R. W., Valladares, F., 1999. Resource acquisition by plants: the role of crown architecture. In: Press, M. C., Scholes, J. D., Barker, M. G. (Eds.), Physiological Plant Ecology. Blackwell Scientific Publication, London, pp. 45–66.

Pearcy, R. W., Yang, W., 1996. A three-dimensional crown architecture model for assessment of light capture and carbon gain by understory plants. Oecologia 108, 1–12.

Pearcy, R. W., Chazdon, R. L., Gross, L. J., Mott, K. A., 1994. Photosynthetic utilization of sunflecks: A temporally patchy resource on a time scale of seconds to minutes. In: Caldwell, M. M., Pearcy, R. W. (Eds.), Exploitation of Environmental Heterogeneity by Plants: Ecophysiological Processes above and below ground. Academic Press, San Diego, pp. 175–208.

Pearcy, R. W., Muraoka, H., Valladares, F., 2005. Crown architecture in sun and shade environments: assessing function and trade-offs with a three-dimensional simulation model. New Phytologist 166, 791–800.

Plummer, S. E., 2000. Perspectives on combining ecological process models and remotely sensed data. Ecological Modelling 129, 169–186.

Running, S. W., Nemani, R. R., Heinsch, F. A., Zhao, M., Reeves, M., Hashimoto, H., 2004. A continuous satellite-derived measure of global terrestrial primary production. BioScience 54, 547–560.

Saigusa, N., Yamamoto, S., Murayama, S., Kondo, H., Nishimura, N., 2002. Gross primary production and net ecosystem exchange of a cool-temperate deciduous forest estimated by the eddy covariance method. Agricultural and Forest Meteorology 112, 203–215.

Tenhunen, J. D., Lange, O. L., Geble, J., Beyschjag, W., Weber, J. A., 1984. Changes in photosynthetic capacity, carboxylation efficiency, and CO_2 compensation point associated with midday stomatal closure and midday

depression of net CO_2 exchange of leaves of *Quercus suber*. Planta 162, 193–203.
Terashima, I., Hikosaka, K., 1995. Comparative ecophysiology of leaf and canopy photosynthesis. Plant, Cell and Environment 18, 1111–1118.
Thornley, J. H. M., 1976. Mathematical Models in Plant Physiology. Academic Press, London.
Ustin, S. L., Roberts, D. A., Gamon, J. A., Asner, G. P., Green, R. O., 2004. Using imaging spectroscopy to study ecosystem processes and properties. BioScience 54, 523–534.
Valladares, F., 1999. Architecture, ecology, and evolution of plant crowns. In: Pugnaire, F. I., Valladares, F. (Eds.), Handbook of Functional Plant Ecology. Marcel Dekker Inc., New York, Basel, pp. 121–194.
Valladares, F., Pearcy, R. W., 1999. The geometry of light interception by shoots of *Heteromeles arbutifolia*: Morphological and physiological consequences for individual leaves. Oecologia 121, 171–182.
Valladares, F., Chico, J. M., Aranda, I., Balaguer, L., Dizengremal, P., Manrique, E., Dreyer, E., 2002. The greater seedling high-light tolerance of *Quercus robur* over *Fagus sylvatica* is inked to a greater physiological plasticity. Trees –structure and function 13, 395–403.
Valladares, F., Dobarro, I., Sánchez-Gómez, D., Pearcy, R. W., 2005. Photoinhibition and drought in Mediterranean woody saplings: scaling effects and interactions in sun and shade phenotypes. Journal of Experimental Botany 56, 483–494.
van Gardingen, P. R., Foody, G. M., Curran, P. J., 1997. Scaling-Up from Cell to Landscape. Cambridge University Press, Cambridge.
Werner, C., Ryel, R. J., Correia, O., Beyschlag, W., 2001. Effects of photoinhibition on whole-plant carbon gain assessed with a photosynthesis model. Plant, Cell and Environment 24, 27–40.
Wilson, K. B., Baldocchi, D. D., Hanson, P. J., 2000. Spatial and seasonal variability of photosynthetic parameters and their relationship to leaf nitrogen in a deciduous forest. Tree Physiology 20, 565–578.
Wilson, K. B., Baldocchi, D. D., Hanson, P. J., 2001. Leaf age affects the seasonal pattern of photosynthetic capacity and net ecosystem exchange of carbon in a deciduous forest. Plant, Cell and Environment 24, 571–583.
Xu, L., Baldocchi, D. D., 2003. Seasonal trends in photosynthetic parameters and stomatal conductance of blue oak (*Quercus douglasii*) under prolonged summer drought and high temperature. Tree Physiology 23, 865–877.
Yamamoto, S., Murayama, S., Saigusa, N., Kondo, H., 1999. Seasonal and inter-annual variation of CO_2 flux between a temperate forest and the atmosphere in Japan. Tellus 51B, 402–413.

This page intentionally left blank

Chapter 19

Seasonal Variations in CH_4 Uptake and CO_2 Emission by a Japanese Temperate Deciduous Forest Soil

Yusuke Oe[1] and Shigeru Mariko[2,*]

[1]*Graduate School of Life and Environmental Sciences, University of Tsukuba, Tsukuba 305-8572, Japan*
[2]*Institute of Biological Sciences, University of Tsukuba, Tsukuba 305-8572, Japan*

Abstract

We measured seasonal variations in soil CH_4 uptake and CO_2 emission for three consecutive years in a cool-temperate, deciduous forest in Japan. The fluxes were measured by the static closed-chamber technique during the growing season and by the gas concentration-gradient technique during winter under snow cover. The measured rates of CH_4 uptake and CO_2 emission showed marked seasonal variations that were correlated with soil temperatures rather than with volumetric soil water content. The $Q_{10\ (10\text{–}20^{\circ}C)}$ value of the CH_4 uptake rates was 1.7, which is higher than that of other temperate forests, and that of the CO_2 emission rates was 3.4 and 4.4 for soil temperatures at 0 and 5 cm depths, respectively. No significant relationship was found between soil moisture and rates of CH_4 uptake or CO_2 emission because of the narrow range of the measured soil water content (15–31% v/v). From June 2002 to May 2003, the estimated annual CH_4 uptake and CO_2 emission were 1.53 and 451 g C y^{-1}, respectively. When compared with CH_4 uptake rates of temperate deciduous forests worldwide ($n = 17$), CH_4 uptake rates by Japanese deciduous forest soils are at the high end of the range of reported values. This Japanese temperate forest soil is a strong CH_4 sink. CH_4 oxidation by methanotrophs accounted for 0.4% of the annual soil CO_2 emission. The fluxes through the snowpack composed 14% of the annual CH_4 uptake and 11% of the annual CO_2 emission.

*Corresponding author
E-mail address: marikos@sakura.cc.tsukuba.ac.jp (S. Mariko).

Elsevier Oceanography Series 73
Edited by H. Kawahata and Y. Awaya
ISBN: 0-444-52948-9

Keywords: soil CH_4 flux; soil CO_2 flux; soil temperature; soil water content; temporal variation

1 Introduction

Soil, the second largest carbon pool in the world, stores 1,500 Pg C, about three times as much carbon as is stored as terrestrial biomass carbon (Winkler et al., 1996). Because the soil carbon balance is considered to play a significant role in global carbon dynamics, there is worldwide concern regarding soil CO_2 emission and its effect on our environment. Therefore, a better understanding and quantification of the soil processes that contribute to the global carbon cycle are needed. In the natural biospheric carbon cycle, soil respiration is the major route by which photosynthetically assimilated carbon returns to the atmosphere. Studies on seasonal variation in soil CO_2 emission are important for elucidating the environmental factors that underlie decomposition of organic carbon stored in the soils. However, few studies have been done in snowy regions, although some researchers have reported that measurement of winter soil CO_2 emission is indispensable (Sommerfeld et al., 1993; Mariko et al., 1994, 2000).

As one of the main greenhouse gases, CH_4 accounts for 14% of global warming, with a global warming potential (GWP) 21 times that of CO_2 (IPCC, 2001). Researchers who study carbon budgets in wetlands have paid close attention to both CH_4 and CO_2 fluxes. It is well documented that carbon exchanges of both CO_2 and CH_4 between anaerobic soils and the atmosphere are primarily driven by gas transport mediated by aquatic macrophytes, and that the CH_4 flux greatly influences the soil carbon balance (Brix et al., 2001; Whiting and Chanton, 2001). Recent studies of carbon fluxes in upland ecosystems have focused on CH_4 oxidation in aerobic soils, which are a unique sink for atmospheric CH_4. The uptake of atmospheric CH_4 by aerobic soils is catalyzed by CH_4-oxidizing bacteria (methanotrophs). Methanotrophs are found in the uppermost mineral layers of soils, and their CH_4 oxidation pathway produces CO_2, which is emitted to the atmosphere (Harriss et al., 1982; Hanson and Hanson, 1996). The soils of temperate grasslands and forests have been estimated to oxidize 0.36–1.92 mg CH_4 m^{-2} d^{-1} (Smith et al., 2000). The measured soil CO_2 flux is thus composed in part of CO_2 emitted through CH_4 oxidation by methanotrophs. Therefore, CH_4 oxidation in soils must, to some extent, lead to the underestimation of the carbon loss from the respiratory processes of plant roots and the decomposition of soil organic matter by heterotrophic microbes such as saprophytic fungi in soil. However, there have been few quantitative studies of the contribution of CH_4 oxidation to CO_2 emission from aerobic soils in terrestrial ecosystems. More detailed studies of the soil CH_4 flux are needed to precisely assess the soil carbon

dynamics in various types of terrestrial ecosystems because available measurements of the soil CH_4 flux lack the temporal resolution necessary for understanding the environmental factors that control CH_4 oxidation and the annual contribution of CO_2 produced by CH_4 oxidation to soil CO_2 emissions.

We measured seasonal variations in soil CH_4 uptake and CO_2 emission in a cool-temperate, secondary deciduous forest for three consecutive years. Long-term fluxes were measured periodically year-round, by the static closed-chamber technique during the growing season and by the gas concentration-gradient technique during winter when the soil surface was snow-covered. We then investigated how soil temperature and water content controlled the seasonality of CH_4 and CO_2 fluxes and how and why empirically derived Q_{10} values tended to vary across seasons and soil layers. We also studied the relationship between CH_4 and CO_2 fluxes, assessed the annual contribution of CO_2 produced by CH_4 oxidation to soil CO_2 emissions, and examined the characteristics of soil CO_2 emissions in the study forest in relation to the annual amount of litterfall carbon.

2 Materials and Methods

2.1 Site Description

The study site was a cool-temperate deciduous forest located on the gently sloping (30°) terrain at the Sugadaira Montane Research Center (SMRC; 36°36′N 138°21′E, 1,300 m a.s.l.), University of Tsukuba, Nagano Prefecture, central Honshu, Japan (Fig. 1). The mean annual temperature and precipitation over the last 30 years, recorded by the SMRC meteorological station, were 6.3°C and 1210 mm, respectively. The monthly mean air temperature during the study period (2002–2004) ranged from –10°C in January to 20°C in July or August, and the annual mean air temperature was 6.5, 6.3, and 7.2°C in 2002, 2003, and 2004, respectively (Fig. 2). Daily precipitation data showed no long-term dry period during the study period. Heavy rain events occurred in early summer in 2002 and early summer and autumn in 2004, but none were recorded in 2003. Annual precipitation was 1438, 1236, and 1648 mm in 2002, 2003, and 2004, respectively. Thus, 2004 was a hot, rainy year. The forest floor was covered continuously by snowpack from December to mid-April each year (the maximum snowpack depth of 120 cm was recorded on 5 March, 2003).

The study forest is a 50-year-old secondary (coppice) forest dominated by *Quercus crispula* with *Betula platyphylla* var. *japonica* being subdominant. The tree density in the canopy layer is 2,000 shoots ha^{-1}, and there is little understory vegetation. The soil is a dark-colored, humic Andosol. The soil profile is composed of an O horizon (<3 cm thick), an A horizon (40–50-cm

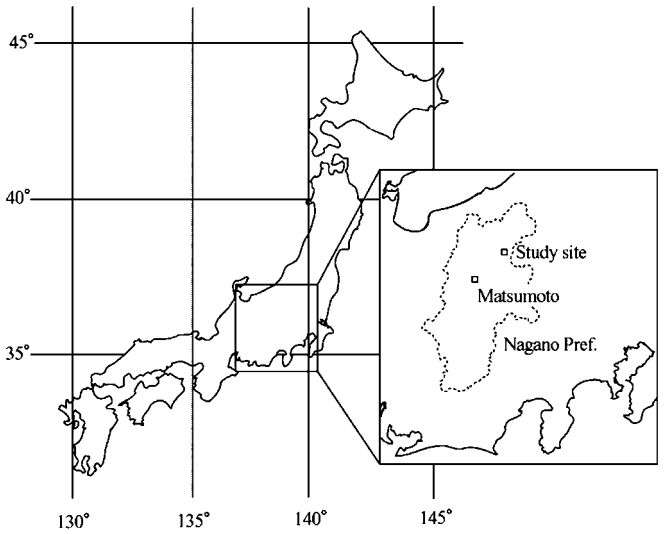

Figure 1: Location of the study site in Nagano Prefecture, Japan.

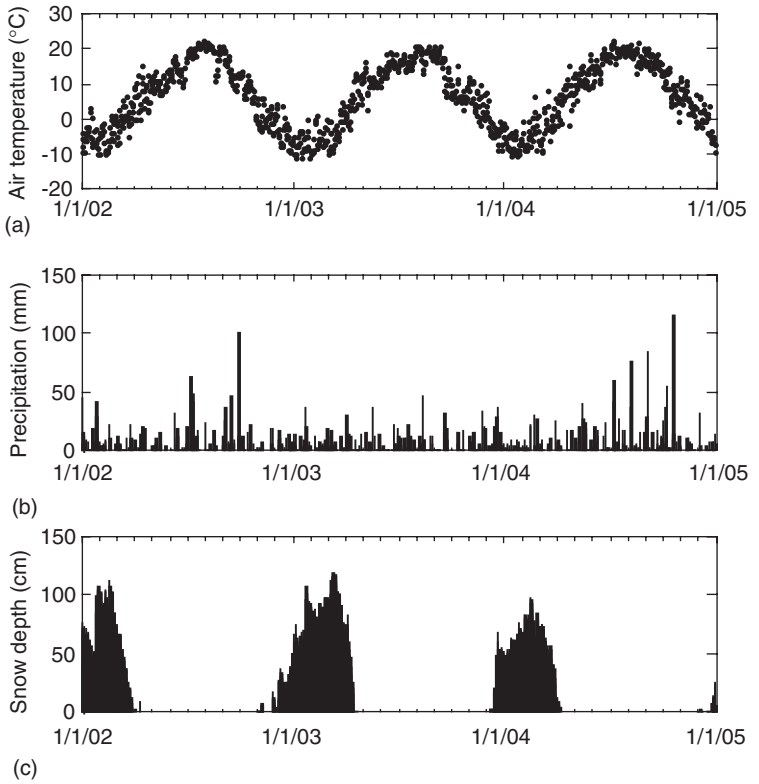

Figure 2: Seasonal variations in daily mean air temperature (a), daily precipitation (b), and snow depth (c) during the study period (2002–2004).

thick), and a B horizon (deeper than 50 cm). Physicochemical analyses were carried out for litter and mineral soil. A 20×20 cm area of litter was sampled at three sites in November 2004, after all leaves had fallen. The litter on the forest floor contained 0.3 kg C m^{-2}. Three soil cores of 100 ml were collected at the depths of 0–10, 10–20, and 20–30 cm in the A horizon in August 2004. Bulk density decreased from 0.33 to 0.23 g cm^{-3} with increasing soil depth. At 0–10 cm air-filled porosity was 80% and pH was 5.2. The total carbon and nitrogen contents, respectively, of the study forest soil were 15 and 0.93% for 0–10 cm, 13 and 0.76% for 10–20 cm, and 9 and 0.56% for 20–30 cm. The concentrations of NH_4^+–N and NO_3^-–N were 29.1 and 2.83 μg N g^{-1}dw, respectively.

2.2 Measurement of CH_4 and CO_2 Fluxes

Between February 2002 and November 2004, CH_4 uptake and CO_2 emission fluxes were measured by the static closed-chamber method during the growing season (late April–November) and by the gas concentration gradient method during winter when the soil surface was snow-covered (Mariko et al., 1994). The flux measurements were made at nine points arranged in a lattice within a 10×10 m plot in the study forest between 10:00 and 14:00 hours (local time). The soil temperatures recorded every 30 min, showed no clear diel cycle, and they varied within 1°C at 5 cm depth. Therefore, soil temperatures measured at the time of the flux measurements should be close to the daily average. The measured CH_4 and CO_2 fluxes are thus reasonable estimates of the daily average.

Nine closed chambers were installed within the soil to a depth of 5 cm, one at each of the lattice points. Each closed chamber comprised two parts: a 15-cm-tall PVC cylinder (21 cm diameter) and a lid. All aboveground parts of the vegetation inside the chamber were removed before measurement began. The cylinder was sealed by a lid in which a rubber-capped, blood-collection-type needle had been inserted, and then air inside the closed chamber was aspirated out through the needle into an evacuated 5-ml vial four times, after 0.5, 5, 10, and 15 min. The concentrations of CH_4 and CO_2 were determined using a gas chromatograph equipped with a packed column (Porapak Q, 80/100) and a flame ionization detector for CH_4 and a thermal conductivity detector for CO_2 (model GC-390B, GL Science Inc., Tokyo, Japan).

The gas flux was calculated with the following equation:

$$F = (V/A)(\Delta C/\Delta t) \tag{1}$$

where F is the gas flux (mg m^{-2} h^{-1}), V the volume of air within the chamber (m^3), A the area of soil within the chamber (m^2), and $\Delta C/\Delta t$ the rate of

increase or decrease of the gas concentration in the air within the chamber. The measured CH_4 concentration decreased linearly with time, whereas the measured CO_2 concentration increased linearly (data not shown).

Flux measurements during the snowpack period were made by the gas concentration-gradient technique. The flux through the snowpack was calculated by Fick's law:

$$F = -aD_{\mathrm{p}}(\Delta C/\Delta z), \tag{2}$$

where F is the gas flux, a is a constant for unit conversion, D_{p} the diffusion coefficient, and $\Delta C/\Delta z$ the gas concentration gradient between the snow surface and depth z. D_{p} is controlled by the *in situ* air temperature and pressure and is estimated with equation (3):

$$D_{\mathrm{p}} = D_0(S)(T/273)^n 1013/P\theta\lambda \tag{3}$$

$D_0(S)$ is the diffusion coefficient in the ideal state, 0.22 for CH_4 and 0.135 for CO_2; n is 1.71 for CO_2 and 1.82 for CH_4 (Striegl et al., 1993); θ is the porosity of the snow; and λ is the tortuosity factor for the snow. We used a λ value of 0.69, following Sommerfeld et al. (1993). The CH_4 concentration in the snowpack decreased with increasing distance from the snow's surface, whereas the CO_2 concentration increased (data not shown).

2.3 Litterfall Measurements

Litterfall was collected by 16 litter traps (60 cm in diameter, 1 m in height), which were arranged as a lattice within a 20×20 m plot that included the flux measurement plot. The litterfall stored inside the litter traps was collected seven times between May 2003 and April 2004, oven-dried at 80°C, and weighed. We used an NC analyzer to determine the carbon content of the litterfall (Sumigraph NC-900, Sumika Chemical Analysis Service, Ltd., Tokyo, Japan) to measure the input of carbon to the soil.

2.4 Soil Temperature and Water Content

At the time of each flux measurement, the volumetric soil water content (SWC) in the uppermost A horizon was gravimetrically determined with a TDR soil moisture sensor (Hydrosense CS620, Campbell Scientific, Inc., Logan, UT, USA) with two 12-cm-long probes, and soil temperatures of 0 and 5 cm depths were measured with a portable thermometer. Soil temperatures were also monitored at the same depths at five of the nine flux-measurement points every 30 min using thermo-recorders (model TR-71 s, T&D Co. Ltd., Nagano, Japan) between July 2002 and June 2004.

2.5 Statistical Analysis

Data sets were tested for normal distribution by the Kolmogorov–Smirnov test. Simple linear regression analyses were used to examine the relationship between CH_4 and CO_2 fluxes and soil environmental parameters (soil temperature and soil water content) over the 3 years. Explanatory variables were arcsine-transformed when necessary to obtain the best fit of the seasonal trend line with the data.

3 Results

3.1 Soil Temperature and Water Content

Soil temperatures at 0 and 5 cm depth, determined at the time of the flux measurements, showed clear seasonal changes (Fig. 3). The maximum soil temperature was reached between July and September, and the minimum during the snowpack season; most winter soil temperatures were higher than 0°C because of the thermal insulation provided by the snowpack. The temperature was slightly higher at the soil surface than at 5 cm depth during the growing season, but it was slightly lower at the surface during the snowpack season. The volumetric soil water content at the time of the flux measurements ranged from 15 to 35% and was not apparently related to daily precipitation.

3.2 CH_4 Uptake and CO_2 Emission

The measured soil CH_4 uptake indicated that the soil of our study forest oxidized atmospheric CH_4 (Fig. 3). Methane uptake showed a seasonal variation with maximum uptake rates of 200–300 $\mu g\, CH_4\, m^{-2}\, h^{-1}$ between July and September and minimum rates of 20–50 $\mu g\, CH_4\, m^{-2}\, h^{-1}$ during the snowpack season. The seasonal pattern was similar over the 3 years. The methane uptake rate was linearly related to soil temperature at both 0 cm ($R^2 = 0.782$; $P < 0.001$) and 5 cm ($R^2 = 0.630$; $P < 0.001$) depth, but not to soil water content ($R^2 = 0.222$; $P > 0.05$) (Fig. 4). The apparent $Q_{10\ (10–20°C)}$ (temperature coefficient) for CH_4 uptake was 1.7 for soil temperatures at both depths.

The CO_2 emission rate increased from April (when the snowpack melted) to August (midsummer), and then decreased (winter) (Fig. 3). The maximum CO_2 emission rate was 603 $mg\, CO_2\, m^{-2}\, h^{-1}$ on 30 July 2002, and the minimum was 21 $mg\, CO_2\, m^{-2}\, h^{-1}$ on 21 February 2002. During the snowpack season, the CO_2 emission rate was less than 50 $mg\, CO_2\, m^{-2}\, h^{-1}$. Seasonal variation in the CO_2 emission rate could be expressed as a simple exponential function of soil temperature at 0 cm ($R^2 = 0.794$;

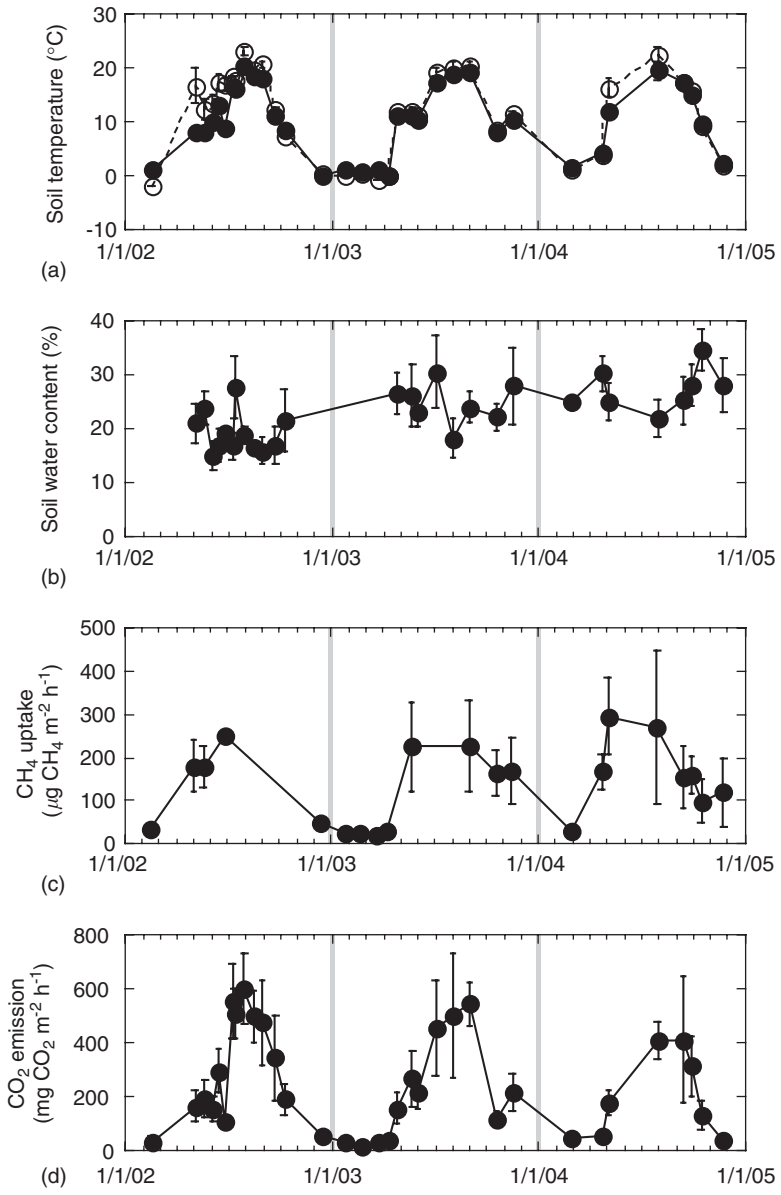

Figure 3: Seasonal variations in soil temperature ((a) open circles and broken line for 0 cm depth and closed circles and solid line for 5 cm depth), volumetric soil water content (b), CH_4 uptake rate (c), and CO_2 emission rate (d) during the study period. Each point represents the mean $\pm$ SD (vertical bars) of the data from the nine chambers used for flux measurements. Soil temperature and water content were measured at these nine points at the same time as the fluxes were measured.

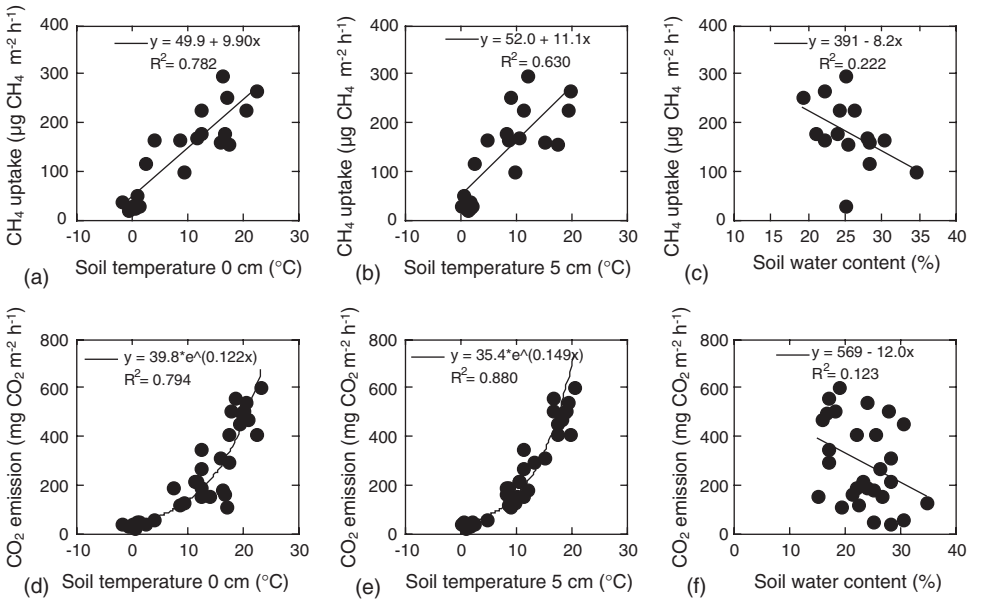

Figure 4: Mean CH_4 uptake and CO_2 emission rates in relation to soil temperature and volumetric soil water content. CH_4 uptake versus soil temperature at 0 cm (a) and 5 cm (b) depth and soil water content (c); CO_2 emission versus soil temperature at 0 cm (d) and 5 cm (e) depth and soil water content (f).

$P < 0.001$) and 5 cm ($R^2 = 0.880$; $P < 0.001$) depth (Fig. 4). There was no relationship between the CO_2 emission rate and volumetric soil water content ($R^2 = 0.123$; $P > 0.05$). The Q_{10} values for CO_2 emission were 3.4 for soil temperatures at 0 cm depth and 4.4 for soil temperatures at 5 cm depth.

The relationship between the CH_4 uptake rate and the CO_2 emission rate was linear and positive ($R^2 = 0.509$; $P < 0.05$) for CO_2 emission rates $< 150\,\text{mg}\,CO_2\,\text{m}^{-2}\,\text{h}^{-1}$ (Fig. 5), obtained from late autumn to early spring. However, during the rest of the year, when the CO_2 emission rate was $> 150\,\text{mg}\,CO_2\,\text{m}^{-2}\,\text{h}^{-1}$, there was no significant relationship between the two rates ($R^2 = 0.005$; $P > 0.05$).

3.3 Litterfall

The annual litterfall was $140\,\text{g}\,\text{C}\,\text{m}^{-2}\,\text{y}^{-1}$ (Fig. 6). Litterfall peaked in autumn (September–October); 76% of the total annual litterfall fell during this period. A small peak occurred in May, but in winter litterfall was extremely small.

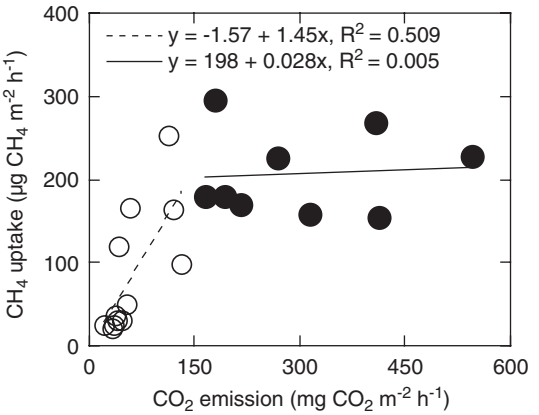

Figure 5: Relationship between CO_2 emission rate and CH_4 uptake rate. Each point represents the mean of the measurements in the nine chambers. Error bars are eliminated for clarity. Open circles and broken fitting line represent a CO_2 emission rate $< 150\,\mathrm{mg\,CO_2\,m^{-2}\,h^{-1}}$; closed circles and solid fitting line represent a CO_2 emission rate $> 150\,\mathrm{mg\,CO_2\,m^{-2}\,h^{-1}}$.

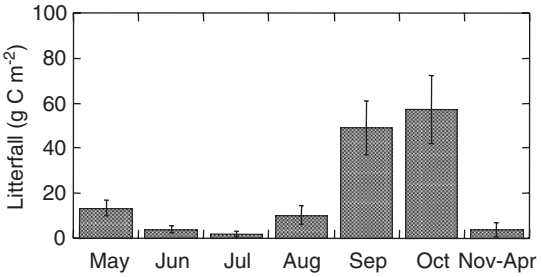

Figure 6: Seasonal variation in litterfall, determined at 16 points from May 2003 to April 2004. Vertical bars represent the SD. The litterfall was estimated to contribute $140\,\mathrm{g\,C\,m^{-2}\,y^{-1}}$.

4 Discussion

In general, temporal variations in the rates of CH_4 uptake and CO_2 emission are regulated by soil variables, for example, temperature, water content, carbon content, NH_4^+ concentration, porosity, and pH. The variables showing the most effect are soil temperature and moisture, which influence both microbial metabolism and gas diffusion in soils. The CH_4 uptake and CO_2 emission values we obtained from this temperate deciduous forest soil varied seasonally and correlated with soil temperature rather than with volumetric soil water content. A similar marked temperature dependence

has been reported previously (Peterjohn et al., 1994; Dobbie and Smith, 1996; Priemé and Christensen, 1997; Saari et al., 1998).

4.1 CH_4 Uptake

The temperate deciduous forest soil that we studied oxidized atmospheric CH_4 over three consecutive years. The mean annual CH_4 uptake between 2002 and 2004 was estimated to be 1.53 g CH_4–C m^{-2}, based on the relationship between the CH_4 uptake rate and the continuously measured soil temperature at 0 cm depth (best-fit equation: $y = 49.9+9.90x$). The daily average CH_4 uptake rate measured during three consecutive years was 5.59 mg CH_4 m^{-2} d^{-1}. This value is 3.5–7 times the averaged rates measured in temperate forests of the United States and Germany (Castro et al., 1995), and the mode of the frequency distribution of measurements in the world's forests (Smith et al., 2000). CH_4 uptake rates in Japanese deciduous forest soils typically are at the higher end of the reported range of CH_4 uptake rates (Fig. 7) in comparison with data from temperate deciduous forests worldwide ($n = 17$). It has been well documented that CH_4 oxidation in forest soils is negatively affected by increased availability of N; the addition of ammonium and nitrate equivalent to more than 16.8 μg NH_4^+–N g^{-1} dw reduced CH_4 oxidation in an incubated soil (Priemé and Christensen, 1997). However, although NH_4^+ concentrations of 10–30 μg NH_4^+–N g^{-1} dw have been measured in Japanese soils (Ishizuka et al., 2000; this study), CH_4 uptake rates do not seem to have been limited by the higher N availability in Japanese forests.

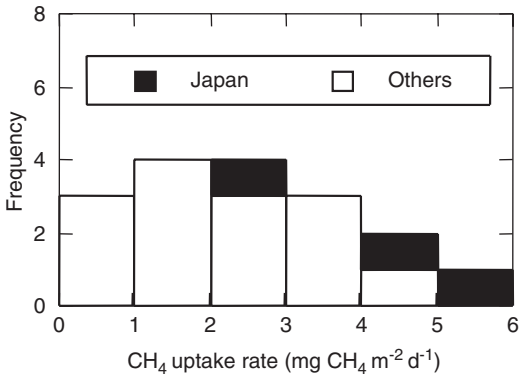

Figure 7: Frequency distribution of CH_4 uptake rates in temperate deciduous forests of the world (*in situ* studies of longer than 7 months' duration, including summer and winter). Black, Japan; white, other countries (literature values). Data sources: Keller et al., 1983; Born et al., 1990; Crill, 1991; Bowden et al., 1993; Dörr et al., 1993; Castro et al., 1995; Peterjohn et al., 1994; Dobbie and Smith, 1996; Ishizuka et al., 2000; Borken et al., 2003; Price et al., 2003; and Merino et al., 2004.

Recent studies in other parts of the world have also reported CH_4 uptake rates close to the top of the range. For instance, Butterbach-Bahl et al. (2002) found that CH_4 uptake in a German Scots pine forest ranged from 140 to 165 $\mu g\, CH_4\, m^{-2}\, h^{-1}$. Price et al. (2003) reported extremely high CH_4 uptake rates of 81 $\mu g\, CH_4\, m^{-2}\, h^{-1}$ in winter and 192 $\mu g\, CH_4\, m^{-2}\, h^{-1}$ in summer in an old-growth mountain beech (*Northofagus solandri*) forest in New Zealand. The magnitude of CH_4 uptake in Japanese forest soils is comparable to these values. We and other Japanese researchers (Tamai et al., 2003) believe that temperate deciduous forests in Japan are a hot spot with respect to the rate of CH_4 uptake. If hot spots of CH_4 uptake are not appropriately assessed, the strength of the global methane sink will be underestimated.

The high CH_4 uptake rates in Japanese forests may be due to high air-filled porosity. Porosity is a key factor controlling the transport of atmospheric CH_4 into the soil. High porosity results in a large gas diffusion coefficient (see equations (2) and (3)). In fact, hot spots of CH_4 uptake are characterized by high porosity values at soil depths of 0–10 cm in both Japan (43–80%; Ishizuka et al., 2000; this study) and New Zealand (84–89%; Price et al., 2003). It is also possible that populations of methanotrophs with high oxidizing activity are present in the soils at the high-uptake sites. Further research is needed to clarify this possibility.

Similar patterns of seasonal variation in CH_4 uptake rates have been observed in other forests (Born et al., 1990; Ishizuka et al., 2000; Price et al., 2003; Tamai et al., 2003). A simple linear regression model showed that soil temperatures at 0 and 5 cm depth accounted for 63% and 78%, respectively, of the seasonal variation in CH_4 uptake rates. The apparent $Q_{10\ (10\text{–}20^\circ C)}$ of our temperate forest was 1.7 for soil temperatures at 0 and 5 cm depths. This Q_{10} is high compared with that of other temperate forests (Born et al., 1990; Crill, 1991; King and Adamsen, 1992; Priemé and Christensen, 1997). The high CH_4 uptake rate may be responsible for the high Q_{10} value. Temperature may affect CH_4 uptake by causing changes in methanotrophic activity and CH_4 diffusion into the soil (Crill, 1991; King and Adamsen, 1992). *In situ* and soil core studies by Priemé and Christensen (1997) revealed that temperature directly affects CH_4 oxidation through its impact on enzymatic processes and CH_4 diffusion. Smith et al. (2000) argued that the inherently low CH_4 concentrations in soil air contribute to low Q_{10} values, because the half-saturation constant (K_m) of the key enzyme, MMO (methane monooxygenase), in the CH_4 oxidation pathway is 3 μM, which is higher than the atmospheric CH_4 concentration of 4.5 nM (Hanson and Hanson, 1996).

Soil core studies have demonstrated that CH_4 oxidation activity is greatest in the uppermost mineral layers (Crill, 1991; Saari et al., 1998), and it is low in the litter of the O horizon. Although the upper organic layers of the A horizon are exposed directly to atmospheric CH_4, they may be unsuitable for the growth or activity of methanotrophs. Wang and Ineson (2003) argued

that, in the upper organic layers, the (i) high fluctuation of temperature and moisture or (ii) high concentration of inorganic N, resulting either from mineralized NH_4^+ or from N deposition, drives methanotrophs to the deeper layers. Low CH_4 uptake rates in deep mineral layers (B and C horizons) are due to poor CH_4 transport. In this study, the stronger temperature dependence on soil temperature at 0 cm depth, the top of the A horizon, implies that the highest oxidation potential is in the uppermost mineral soil.

Soil moisture exerts a dominant limiting effect on CH_4 uptake in many temperate forest soils. Castro et al. (1995) found that 78% of the CH_4 uptake rate in temperate forest soils could be explained by soil moisture. The rate of CH_4 diffusion is important if a strong sink for CH_4 oxidation is present within the soil, because CH_4 has to diffuse down through the soil (Whalen et al., 1991). Czepiel et al. (1995) found that the optimum soil water content for CH_4 oxidation ranged from 30 to 51% (w/w) in woodland soils. In the soil of our study forest, the range of variation in the measured soil water content was small (15–31%) during the year, thus masking the effect of soil moisture on CH_4 uptake.

4.2 CO_2 Emission

The seasonal CO_2 emission in our study forest soil strongly depended on soil temperature. The Q_{10} values (3.4 and 4.4) were higher than the global median of 2.4 reported by Raich and Schlesinger (1992). However, this global median is based on data measured by soda lime techniques, which were previously the most commonly used techniques. Soda lime techniques may overestimate CO_2 emission rates during cold periods and underestimate them during warm periods (Davidson et al., 1998). Consequently, soda lime techniques would underestimate Q_{10} values. Modern chamber-based measurements, with which accurate GC and NDIR analyzers are used, have yielded relatively high Q_{10} values of 3.4–5.6 for soil temperatures at 4–8 cm depth in temperate mixed hardwood forests (Davidson et al., 1998) and of 4.2 for soil temperatures at 2 cm depth in European beech forests (Janssens and Pilegaard, 2003). These Q_{10} values are comparable to those obtained in this study.

Soil core studies have shown that the temperature sensitivity of CO_2 emission varies with increasing temperature. Q_{10} values tend to be high at low temperatures and low at high temperatures (Lloyd and Taylor, 1994; Winkler et al., 1996; Fang and Moncrieff, 2001). In our *in situ* measurements, the Q_{10} values were 1.9 during the warm season (soil temperature at 5 cm depth $\geq 15^{\circ}$C) and 5.8 during the cold season ($< 15^{\circ}$C). In cool-temperate deciduous forests in Japan, high levels of fine root production occur in spring, and the production of new roots with high respiratory activity enhances CO_2 emission from the soil in spring (Lee et al., 2003; Mo et al., 2005). Increased

root production may thus be responsible for the high Q_{10} value in the cold season, which includes spring.

Soil moisture affects both the respiratory activity of microbes and roots and gas transport through the soil. Davidson et al. (1998) found a rapid decrease in soil CO_2 emission rates at a soil water content of less than 12% (v/v) and a moderate decline at values larger than 12%. Xu and Qi (2001) also reported that, at soil moisture lower than 14%, the CO_2 flux rate was reduced. Thus, CO_2 emission rates are significantly inhibited by soil water content only when it is low (dry soil) or very high (wet soil). Between these two extremes, moisture content has no obvious effect on CO_2 emission. At our study site, no significant effect of soil moisture on CO_2 emission was found because the measured soil water content was within the narrow range of 15–35%, which is close to the optimum for CO_2 emission.

The mean annual CO_2 emission over two consecutive years (July 2002–June 2003) was estimated to be 451 g CO_2–C m^{-2}, based on the relationship between the continuously monitored soil temperature at 5 cm depth and the CO_2 emission rate (best-fit equation: $y = 35.4\ \exp(0.149x)$). This value is lower than that measured in another Japanese 50-year-old deciduous forest (dominant species, *Q. crispula* and *Betula ermanii*) on the slope of Mt. Norikura, where an understory of *Sasa senanensis* is well developed (Lee et al., 2002: 754 and 849 g C m^{-2} y^{-1}). The dominant tree species, soil, and climate of the two forests are similar, but little understory vegetation has developed in our study forest. Therefore, one possible explanation for the lower CO_2 emission in our forest could be a smaller amount of organic carbon input (litterfall) from understory vegetation to the soil than in the forest on Mt. Norikura. Comparison of litter carbon content between the two forests supports this possibility: litter carbon in our study forest (0.3 kg C m^{-2}) was one-fifth that in the forest on Mt. Norikura (Jia et al., 2002).

Davidson et al. (2002) reviewed the relationships between annual aboveground litterfall carbon (g C m^{-2} y^{-1}) and annual CO_2 emission (g C m^{-2} y^{-1}) in various types of mature and young forests in the Ameriflux database, and reported that the following relationships were significant:

$$Rs(\text{mature forests}) = 287 + 2.80L \tag{4}$$

$$Rs(\text{young forests}) = 139 + 4.16L \tag{5}$$

where Rs is the annual CO_2 emission (g C m^{-2} y^{-1}) and L the annual aboveground litterfall (g C m^{-2} y^{-1}).

The equations for the mature and young forests are significantly different. The slope (regression coefficient) for the young forests is steeper than that for the mature forests (Davidson et al., 2002). The difference between

the two forests may indicate that root respiration or decomposition of root litter contributes more than decomposition of aboveground litter to the soil CO_2 emission in mature forests. The annual litterfall and CO_2 emission data in this study is at the lower limit of the 95% confidence interval for the mature-forest equation, and it is outside the 95% confidence interval for the young-forest equation. Thus, our middle-aged coppice forest is approaching a balanced soil carbon budget with the soil carbon dynamics characteristics of a mature forest.

4.3 CH_4 Uptake vs. CO_2 Emission

We found a positive linear correlation between CH_4 uptake rates and CO_2 emission rates for CO_2 emission rates between 0 and 150 mg CO_2 m^{-2} h^{-1} but no correlation for higher CO_2 emission rates. This two-phase pattern can be understood by considering the different effects of soil temperature on CH_4 uptake and CO_2 emission rates. First, a linear increase in the CH_4 emission rate in combination with an exponential increase in the CO_2 emission rate with respect to temperature yields an increasing phase when CO_2 emission is low and a plateau phase when CO_2 emission is high. Second, a mechanistic explanation is also possible. The high activity of heterotrophic microbes in summer consumes a relatively large amount of the O_2 in soil air, and the reduced O_2 concentration would result in competition for O_2 between CH_4-oxidizing and CO_2-producing processes. A stricter O_2 dependence is found for CH_4 oxidation, which requires two molecules of O_2 for oxidation from CH_4 to CO_2, whereas catabolism of organic matter by heterotrophic microbes and roots uses one O_2 molecule to produce one CO_2 molecule. The activity of methanotrophs might thus be restricted by the larger requirement for O_2, an effect that might be marked in wet soils, where thick water films can inhibit the mass flow of soil air and diffusion of O_2.

Methanotrophs oxidize CH_4 as their sole substrate. Soil CO_2 emission derived from CH_4 oxidation by methanotrophs accounted for approximately 0.4% of total soil CO_2 emission in this study. As the GWP of CH_4 is 21 times that of CO_2 (IPCC, 2001), CH_4 oxidation by methanotrophs, by converting CH_4 to CO_2, offsets 7.8% of the global warming effect of CO_2 emitted from the soil. Consequently, CH_4 oxidation in soil plays an important role in carbon dynamics and lessens the global warming.

4.4 CH_4 Uptake and CO_2 Emission during the Snowpack Season

The deep layer of snow during the winter insulates the soil from very low air temperatures. The thermally insulated soil can consume atmospheric CH_4 and produce CO_2. We measured CH_4 uptake rates of 20–30 μg CH_4 m^{-2} h^{-1}

and CO_2 emission rates of 10–20 mg CO_2 m^{-2} h^{-1} through the snowpack. These results are in accordance with previous results from *in situ* measurements in temperate forest soils (Castro et al., 1995; Priemé and Christensen, 1997; Mariko et al., 2000). The winter flux accounted for 14 and 11% of the total annual CH_4 uptake and CO_2 emission, respectively. Thus, winter CH_4 uptake and CO_2 emission are not negligible and contribute considerably to the annual carbon fluxes. In the Northern Hemisphere, about 50% of the land area is covered by snow in winter (Barry, 1992). Therefore, the snow-surface flux is of crucial importance in evaluating the precise global carbon balance in ecosystems that experience a winter snowpack.

Better correlations of CO_2 emission rates with soil surface temperatures are obtained in cold ecosystems. In subarctic peatland and tundra ecosystems, both diurnal and seasonal trends in net ecosystem CO_2 emissions are correlated with changes in soil temperature close to the soil surface (Oechel and Vourlitis, 1995; Silvola et al., 1996), where the rate of decomposition of organic matter by microorganisms is higher than in the subsurface. At our snowy site, when the data for the entire year are considered, the CO_2 emission rate was most strongly correlated with the temperature at 5 cm depth, in the A horizon, rather than with the surface temperature, indicating that the subsurface temperature is a better predictor of winter CO_2 emission rates in this snowy region.

Acknowledgements

We thank Professor I. Hayasi and Professor T. Oikawa, University of Tsukuba, for their encouragement and support during the study period. We also acknowledge the members of Terrestrial Ecosystem Laboratory, University of Tsukuba, for their help. This study was performed as part of the “GCMAPS program” (Global Carbon Cycle and Related Mapping Based on Satellite Imagery) sponsored by the Ministry of Education, Culture, Sports, Science and Technology of Japan.

References

Barry, R. G., 1992. Climate–ice interactions. In: Nierenberg, W. A. (Ed.), Encyclopedia of Earth System Science. . Academic Press, San Diego, Vol. 1, pp. 517–524.

Borken, W., Xu, Y.-J., Beese, F., 2003. Conversion of hardwood forests to spruce and pine plantations strongly reduced soil methane sink in Germany. Global Change Biology 9, 956–966.

Born, M., Dörr, H., Levin, I., 1990. Methane consumption in aerated soils of the temperate zone. Tellus 42B, 2–8.

Bowden, R. D., Castro, M. S., Melillo, J. M., Steudler, P. A., Aber, J. D., 1993. Fluxes of greenhouse gases between soils and the atmosphere in a temperate forest following a simulated hurricane blowdown. Biogeochemistry 21, 61–71.

Brix, H., Sorrell, B. K., Lorenzen, B., 2001. Are *Phragmites*-dominated wetlands a net source or net sink of greenhouse gas?. Aquatic Botany 69, 313–324.

Butterbach-Bahl, K., Breuer, L., Gasche, R., Willibald, G., Papen, H., 2002. Exchange of trace gases between soils and the atmosphere in Scots pine forest ecosystems of the northeastern German lowlands 1. Fluxes of N_2O, NO/NO_2 and CH_4 at forest sites with different N-deposition. Forest Ecology and Management 167, 123–134.

Castro, M. S., Steudler, P. A., Melillo, J. M., 1995. Factors controlling atmospheric methane consumption by temperate forest soils. Global Biogeochemical Cycles 9, 1–10.

Crill, P. M., 1991. Seasonal patterns of methane uptake and carbon dioxide release by a temperate woodland soil. Global Biogeochemical Cycles 5, 319–334.

Czepiel, P. M., Crill, P. M., Harriss, R. C., 1995. Environmental factors influencing the variability of methane oxidation in temperate zone soils. Journal of Geophysical Research 100, 9359–9364.

Davidson, E. A., Belk, E., Boone, R. D., 1998. Soil water content and temperature as independent or confounded factors controlling soil respiration in a temperate mixed hardwood forest. Global Change Biology 4, 217–227.

Davidson, E. A., Savage, K., Bolstad, P., Clark, D. A., Curtis, P. S., Ellsworth, D. S., Hanson, P. J., Law, B. E., Luo, Y., Pregitzer, K. S., Randolph, J. C., Zak, D., 2002. Belowground carbon allocation in forests estimated from litterfall and IRGA-based soil respiration measurements. Agricultural and Forest Meteorology 113, 39–51.

Dobbie, K. E., Smith, K. A., 1996. Comparison of CH_4 oxidation rates in woodland, arable and set aside soils. Soil Biology and Biochemistry 28, 1357–1365.

Dörr, H., Katruff, L., Levin, I., 1993. Soil texture parameterization of the methane uptake in aerated soils. Chemosphere 26, 697–713.

Fang, C., Moncrieff, J. B., 2001. The dependence of soil CO_2 efflux on temperature. Soil Biology and Biochemistry 33, 155–165.

Hanson, R. S., Hanson, T. E., 1996. Methanotrophic bacteria. Microbiology Review 60, 439–471.

Harriss, R. C., Sebacher, D. I., Day, F. P., 1982. Methane flux in the Great Dismal Swamp. Nature 297, 673–674.

IPCC (Intergovernmental Panel on Climate Change), 2001. Climate Change 2001: The Scientific Basis. Cambridge University Press, Cambridge, UK.

Ishizuka, S., Sakata, T., Ishizuka, K., 2000. Methane oxidation in Japanese forest soils. Soil Biology and Biochemistry 32, 769–777.

Janssens, I. A., Pilegaard, K., 2003. Large seasonal changes in Q_{10} of soil respiration in a beech forest. Global Change Biology 9, 911–918.

Jia S., Akiyama T., Koizumi H., 2002. Carbon dynamics in a cool-temperate broad-leaved forest soil. II. Estimation of ecosystem carbon based on in situ detailed measurements. JASS 18, 26–35 (in Japanese with English summary).

Keller, M., Goreu, T. J., Wofsy, S. C., Kaplan, W. A., McElroy, M. B., 1983. Production of nitrous oxide and consumption of methane by forest soils. Geophysical Research Letters 10, 1156–1159.

King, G. M., Adamsen, A. P. S., 1992. Effect of temperature on methane consumption in a forest soil and in pure cultures of the methanotroph *Methylomonas rubra*. Applied Environmental Microbiology 58, 2758–2763.

Lee, M.-S., Nakane, K., Nakatsubo, T., Mo, W. H., Koizumi, H., 2002. Effects of rainfall events on soil CO_2 flux in a cool-temperate deciduous broad-leaved forest. Ecological Research 17, 401–409.

Lee, M.-S., Nakane, K., Nakatsubo, T., Koizumi, H., 2003. Seasonal changes in the contribution of root respiration in a cool-temperate deciduous forest. Plant and Soil 255, 311–318.

Lloyd, J., Taylor, J. A., 1994. On the temperature dependence of soil respiration. Functional Ecology 8, 315–323.

Mariko, S., Bekku, Y., Koizumi, H., 1994. Efflux of carbon dioxide from snow-covered forest floors. Ecological Research 9, 343–350.

Mariko, S., Nishimura, N., Mo, W., Matsui, Y., Kibe, T., Koizumi, H., 2000. Winter CO_2 flux from soil and snow surfaces in a cool-temperate deciduous forest, Japan. Ecological Research 15, 363–372.

Merino, A., Pérez-Batallón, P., Macías, F., 2004. Responses of soil organic matter and greenhouse gas fluxes to soil management and land use changes in a humid temperate region of southern Europe. Soil Biology and Biochemistry 36, 917–925.

Mo, W., Lee, M.-S., Uchida, M., Inatomi, M., Saigusa, N., Mariko, S., Koizumi, H., 2005. Seasonal and annual variations in soil respiration in a cool-temperate deciduous broad-leaved forest in Japan. Agricultural and Forest Meteorology 30, 81–94.

Oechel, W. C., Vourlitis, G., 1995. Effects of global change on carbon storage in cold soils. In: Lal, R., Kimble, J., Levine, E., Stewart, B. A. (Eds.), Advances in Soil Science: Soils and Global Change. Lewis Publishers, Tokyo, pp. 117–129.

Peterjohn, W. T., Mellilo, J. M., Steudler, P. A., Newkirk, K. M., 1994. Responses of trace gas fluxes and N availability to experimentally elevated soil temperatures. Ecology Applied 4, 617–625.

Price, S. J., Sherlock, R. R., Kelliher, F. M., McSeven, T. M., Tate, K. R., Condron, F. M., 2003. Pristine New Zealand forest soil is a strong methane sink. Global Change Biology 10, 16–26.

Priemé, A., Christensen, S., 1997. Seasonal and spatial variation of methane oxidation in a Danish spruce forest. Soil Biology and Biochemistry 29, 1165–1172.

Raich, J. W., Schlesinger, W. H., 1992. The global carbon dioxide flux in soil respiration and its relationship to vegetation and climate. Tellus 44B, 81–99.

Saari, A., Heiskanen, J., Martikainen, P. J., 1998. Effect of the organic horizon on methane oxidation and uptake in soil of a boreal Scots pine forest. FEMS Microbiology Ecology 26, 245–255.

Silvola, J., Alm, J., Ahlholm, U., Nykanen, H., Martikainen, P. J., 1996. CO_2 fluxes from peat in mires under varying temperature and moisture conditions. Journal of Ecology 84, 219–228.

Smith, K. A., Dobbie, K. E., Ball, B. C., Bakken, L. R., Sitaula, B. K., Hansen, S., Brumme, R., Borken, W., Christensen, S., Priemé, A., Fowler, D., Macdonald, J. A., Skiba, U., Klemedtsson, L., Kasimir-Klemedtsson, A., Degorska, A., Orlanski, P., 2000. Oxidation of atmospheric methane in Northern European soils, comparison with other ecosystems, and uncertainties in the global terrestrial sink. Global Change Biology 6, 791–803.

Sommerfeld, R. A., Mosier, A. R., Musselan, R. C., 1993. CO_2, CH_4, N_2O flux through a Wyoming snowpack and implication for global budgets. Nature 361, 140–142.

Tamai, N., Takenaka, C., Ishuzuka, S., Tezuka, T., 2003. Methane flux and regulatory variables in soil of three equal-aged Japanese cypress (*Chamaecyparis obtusa*) forests in central Japan. Soil Biology and Biochemistry 35, 633–641.

Wang, Z.-P., Ineson, P., 2003. Methane oxidation in a temperature coniferous forest soil: effects of inorganic N. Soil Biology and Biochemistry 35, 427–433.

Whalen, S. C., Reeburgh, W. S., Sandbeck, K. A., 1991. Rapid methane oxidation in a landfill cover soil. Applied Environmental Microbiology 56, 3405–3411.

Whiting, G. L., Chanton, J. P., 2001. Greenhouse carbon balance of wetlands: methane emission versus carbon sequestration. Tellus B 53, 521–528.

Winkler, J. P., Cherry, R. S., Schlesinger, W. H., 1996. The Q_{10} relationship of microbial respiration in a temperate forest soil. Soil Biology and Biochemistry 28, 1067–1072.

Xu, M., Qi, Y., 2001. Spatial and seasonal variations of Q_{10} determined by soil respiration measurements at a Sierra Nevadan forest. Global Biogeochemical Cycles 15, 687–696.

This page intentionally left blank

Index

Colour Plate Section

This page intentionally left blank

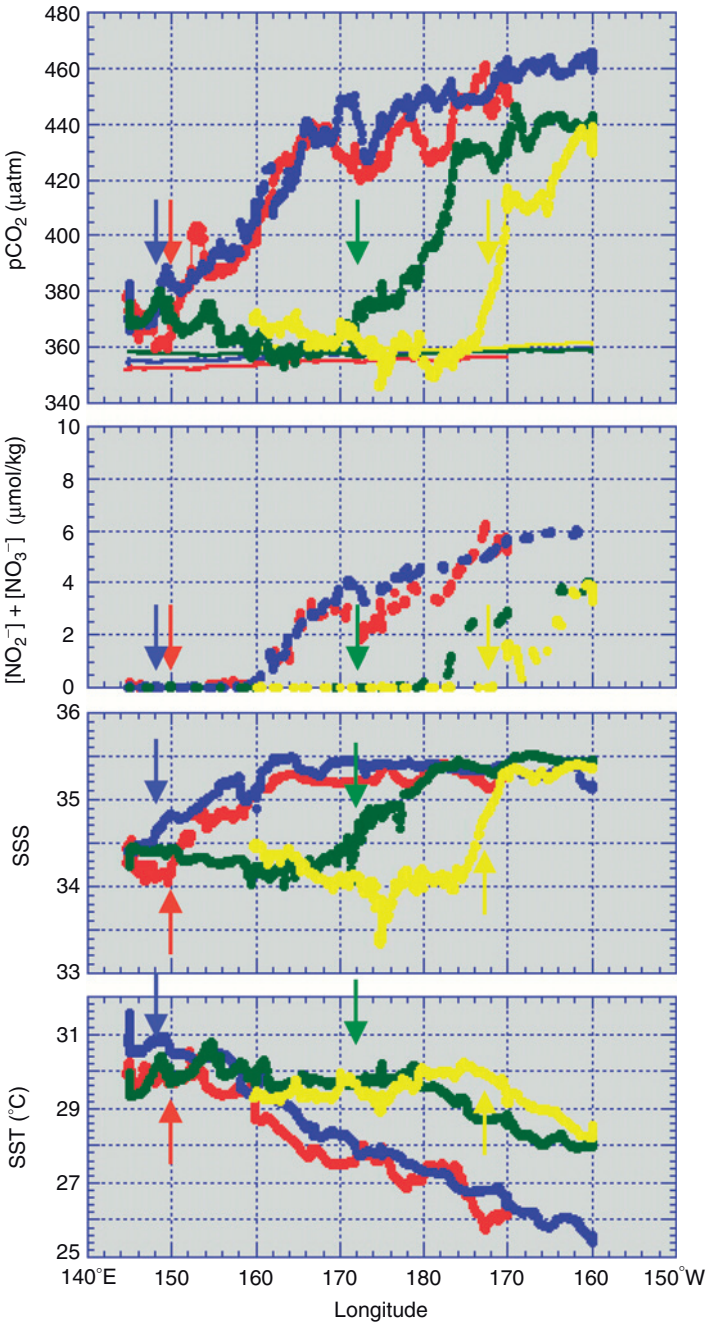

Plate 1.2: Longitudinal distributions of pCO_2^{sw}, pCO_2^{air}, $[NO_2^-]$+$[NO_3^-]$, SSS and SST along the equator in October/December 1999 (red), January/March 2001 (blue), January/March 2002 (green) and November 2002/March 2003 (yellow). In the upper panel, the thick line shows pCO_2^{sw} and the thin line pCO_2^{air}. Arrows show the boundary between the HNLC region and western Pacific warm pool.

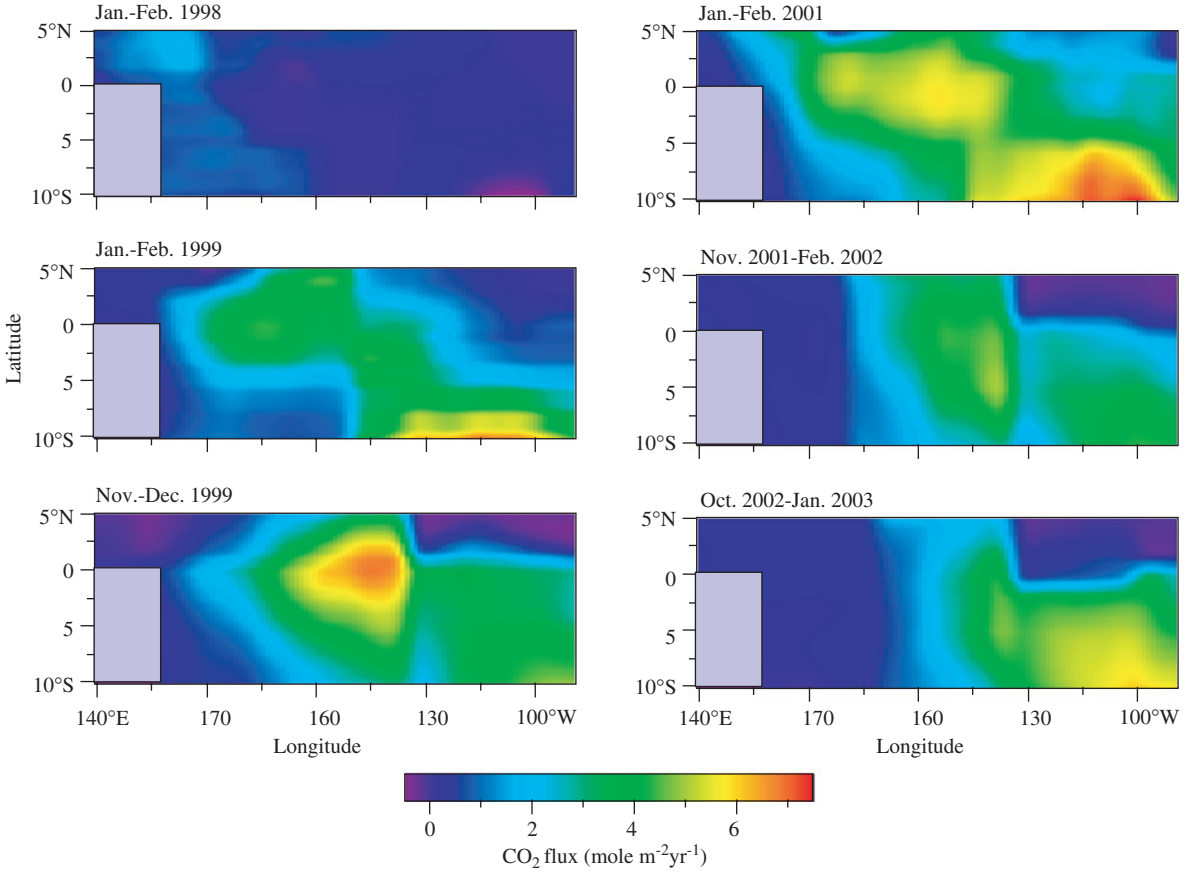

Plate 1.10: The distribution of CO_2 flux in the equatorial Pacific in January/February 1998, January/February 1999, November/December 1999, January/February 2001, November 2001/February 2002, and October 2002/January 2003.

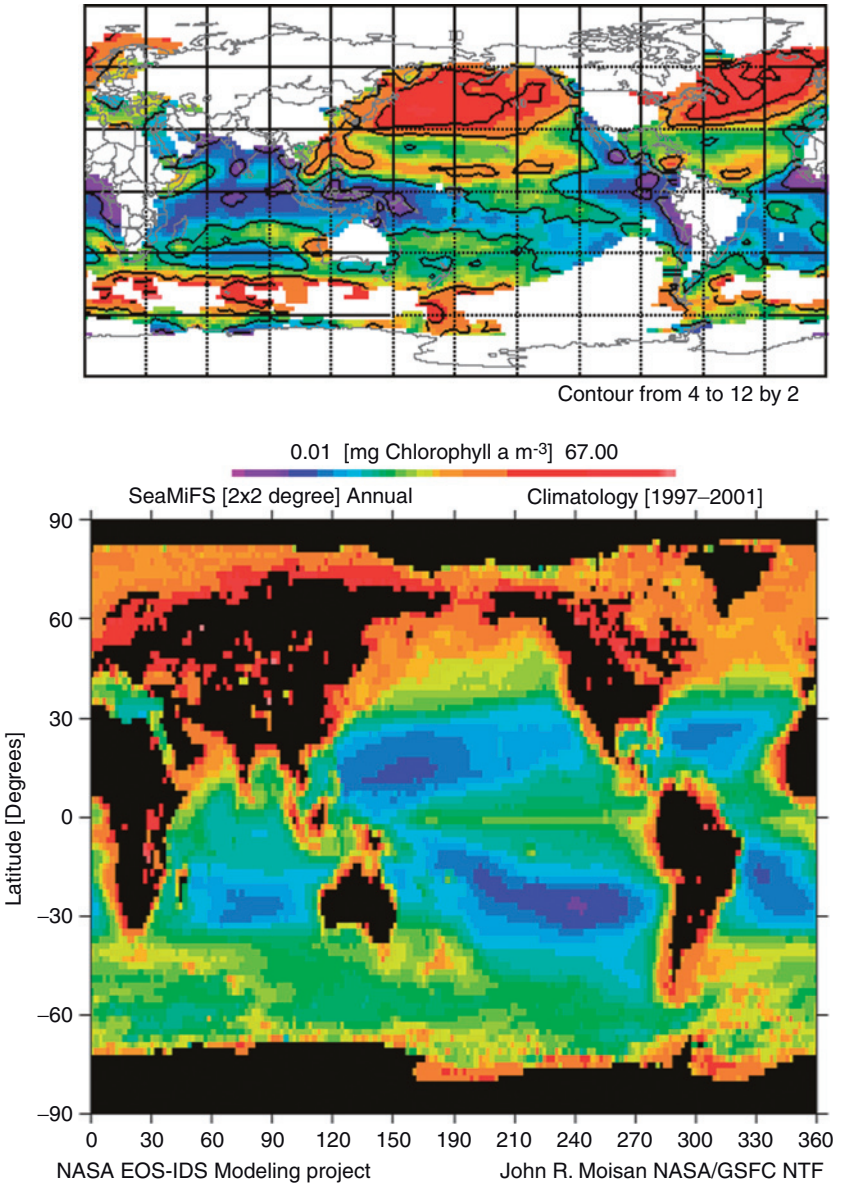

Plate 2.2: (a) January mean of Oberhuber atlas surface wind field. Note the low wind speeds near the equatorial Pacific and Indian Ocean regions. (b) SeaWiFS annual mean 2 $\times$ 2 degree binned climatology. Note the high chlorophyll values in the eastern equatorial Pacific.

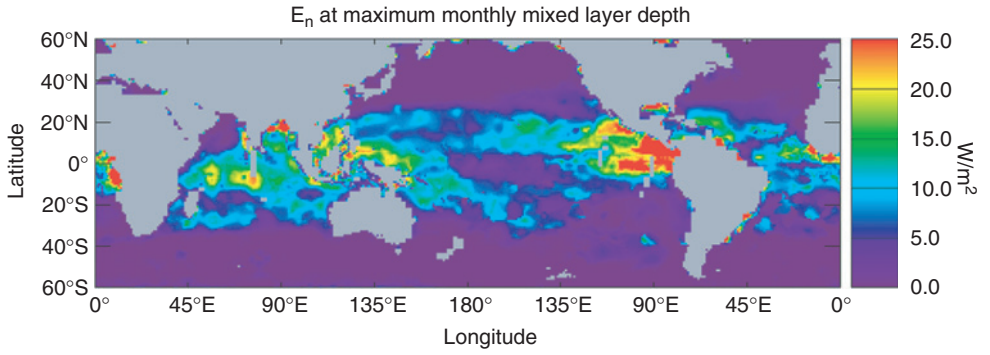

Plate 2.3: Modeled climatological values of the net solar flux at the base of the deepest monthly mixed layer (W m^{-1} m^{-1}). Values correspond to solar fluxes entering the permanent pycnocline. Largest values exist where the deepest monthly mixed layer and chlorophyll concentration are low and solar flux is high. From Ohlmann et al. (1996).

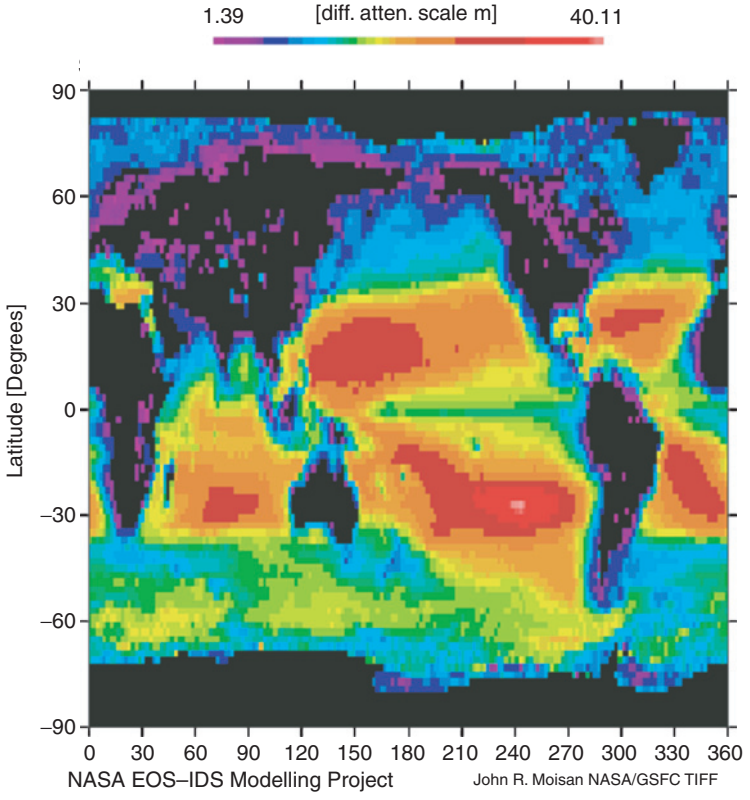

Plate 2.4: The 2×2 degree annual mean SeaWiFS-derived diffuse attenuation coefficient [m-1] field for PAR.

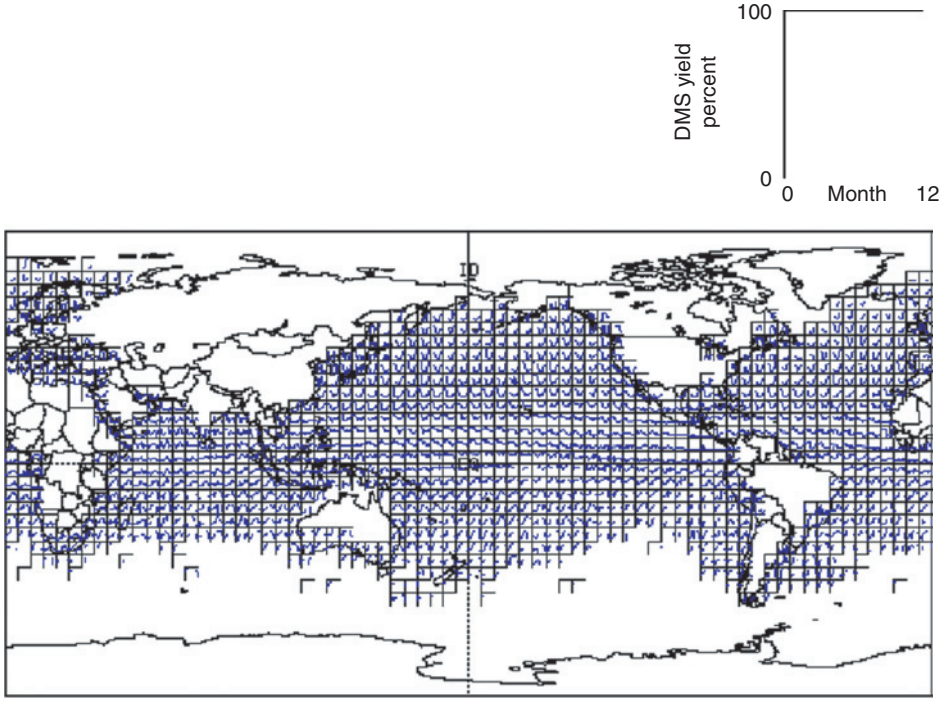

Plate 2.5: DMS percent yield climatologies estimated using observed MLD climatologies from the NODC XBT data set and the Simo and Pedrós-Alló (1999) DMS yield relationship.

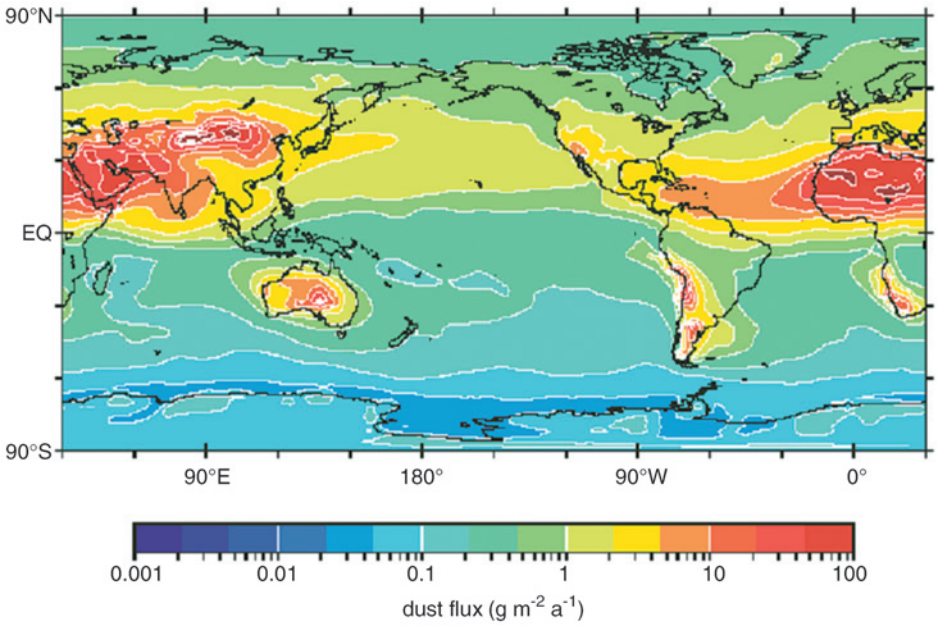

Plate 2.7: Contemporary annual mean dust deposition rate (Ginoux et al., 2001).

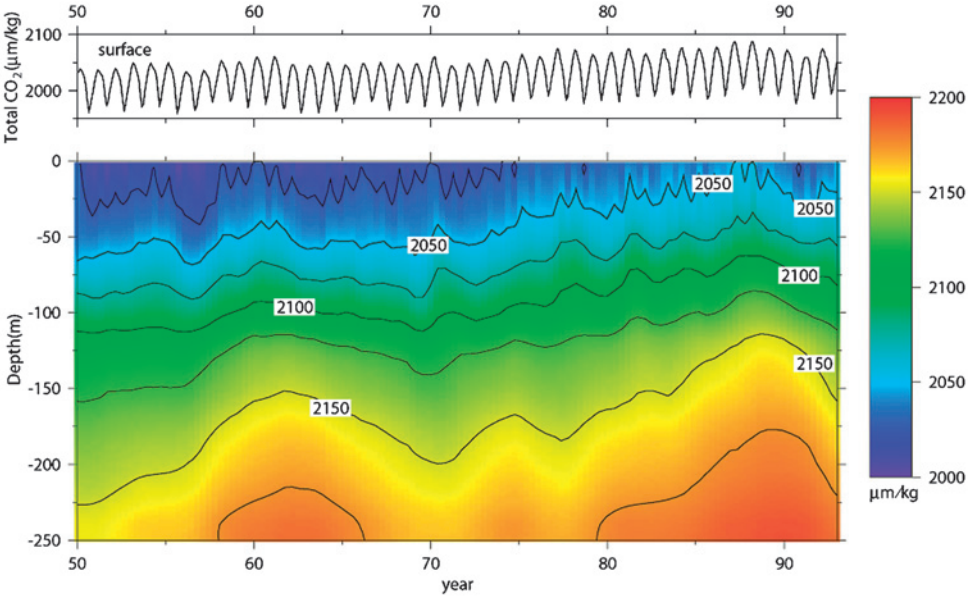

Plate 2.10: Time series of TCO_2 (unit: $\mu mol\,kg^{-1}$) in central north Pacific (35°–45° N, 170°–150° W). Top panel shows the time series of surface TCO_2 concentration. The lower panel shows the vertical profile of modeled TCO_2 concentration from the surface to 250 m. The contour interval is 25 $\mu mol\,kg^{-1}$.

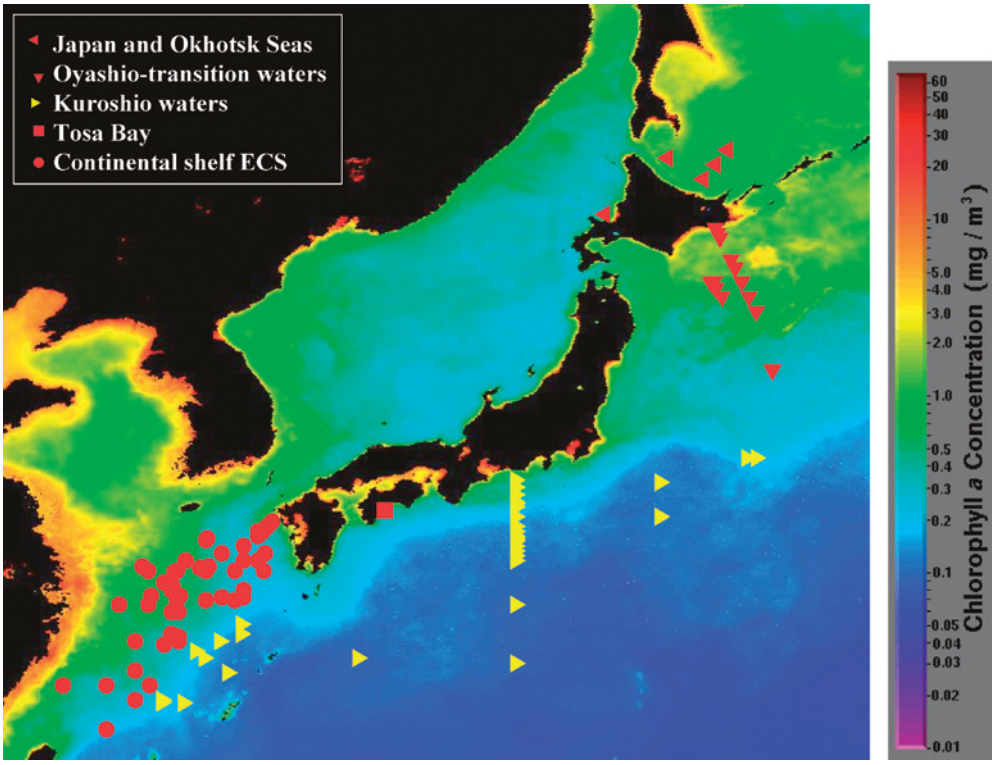

Plate 3.1: Measuring sites for primary production using a ^{13}C spiked incubation for 24 hours in Japan and Okhotsk Seas, Oyashio-transition waters, Kuroshio waters, Tosa Bay, and continental shelf waters in the East China Sea overlaid on an annual mean of chlorophyll a in 2002 derived from SeaWiFS (http://www.seawifs.gsfc.nasa.gov/cgi/level3.pl/).

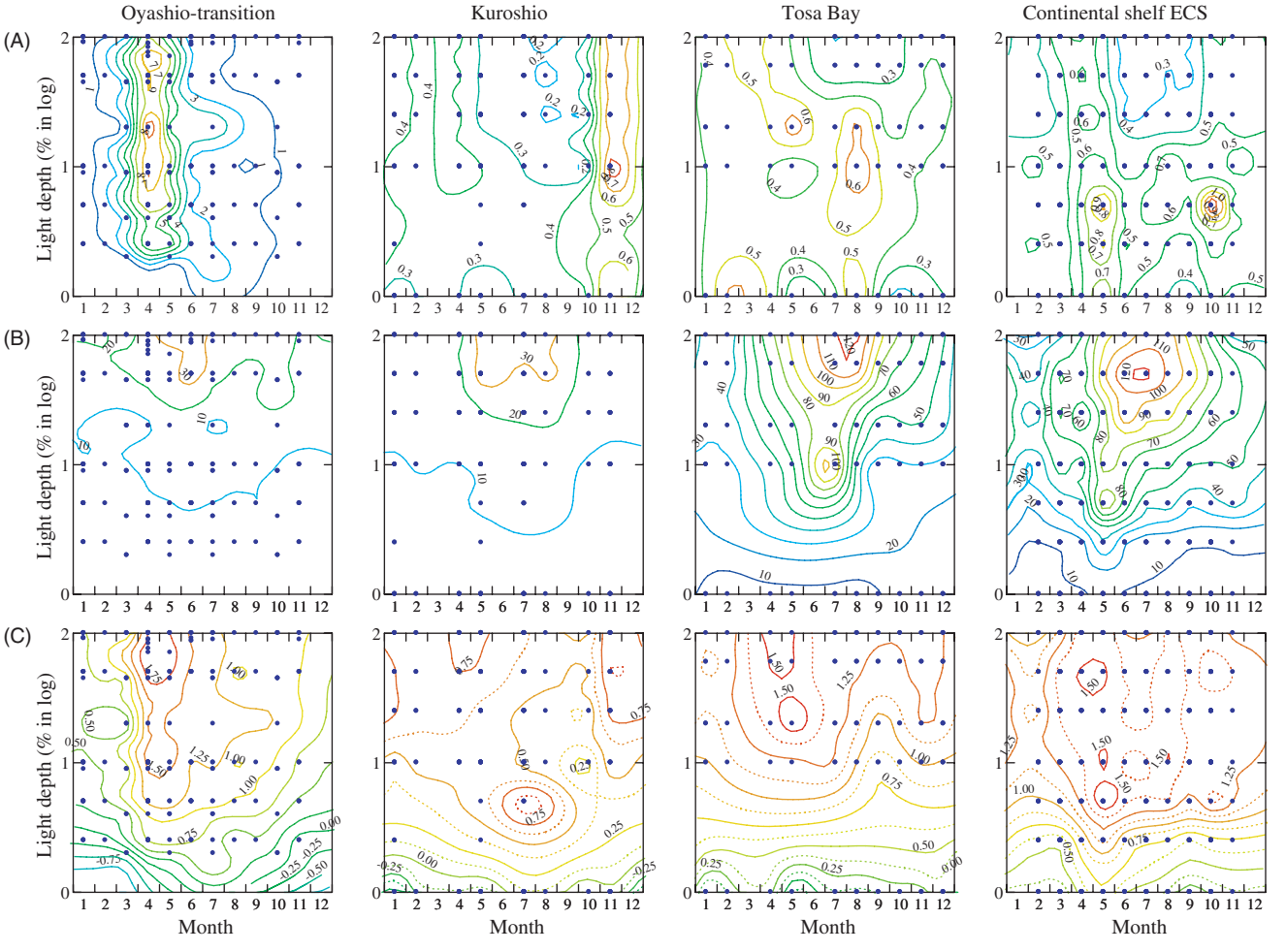

Plate 3.4: Seasonal change in vertical profile of (A) chlorophyll *a* concentration in μg/l, (B) biomass normalized primary production in mgC/mgChl/day, and (C) primary production in $\log_{10}$ (mgC/m^3/day) in the euphotic zone of light depth (% in $\log_{10}$) of Oyashio-transition waters, Kuroshio waters, Tosa Bay, and continental shelf waters of the East China Sea.

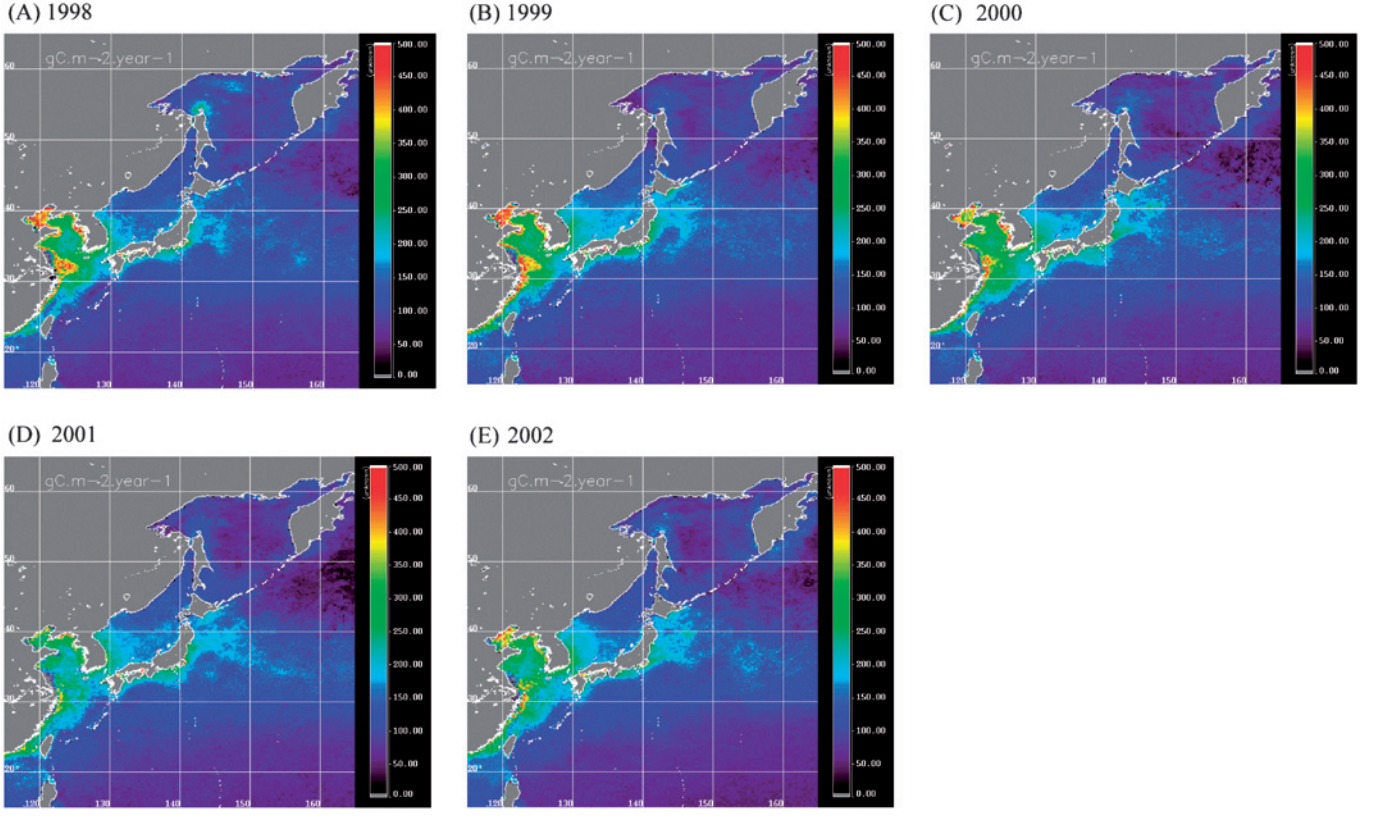

Plate 3.8: Maps of annual primary production (gC/m^2/year) from 1998 to 2002 produced according to Asanuma (2006).

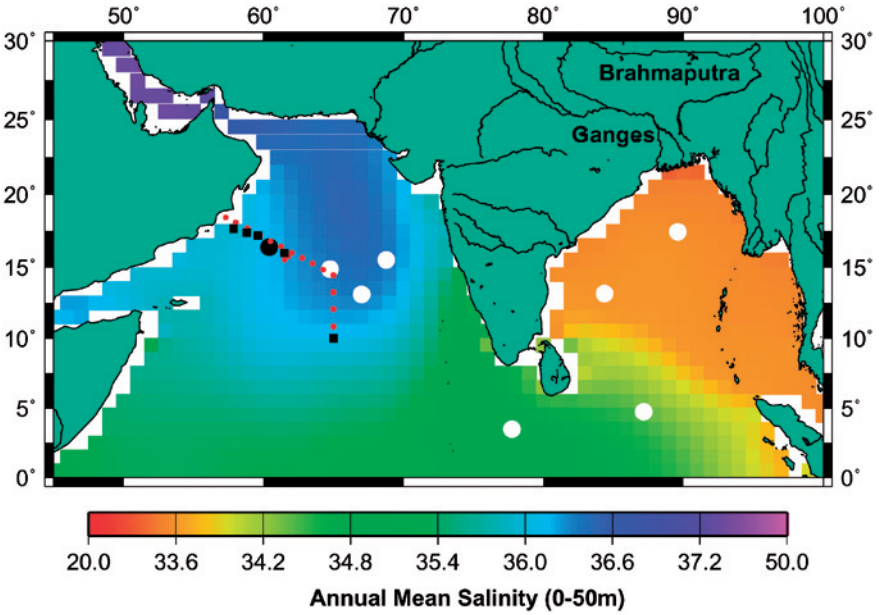

Plate 7.1: Map of the northern Indian Ocean showing the mean annual salinity averaged for the upper 50 m of the water column (Data: World Ocean Atlas, 1998, http://www.cdc.noaa.gov/cdc/data.woa98.html). Black circles show the long-term sediment trap site in the western Arabian Sea (WAST). White circles and black squares indicate the other joint Indo/ German and the US JGOFS sediment trap sites, respectively. US JGOFS water sampling sites are shown by the red circles.

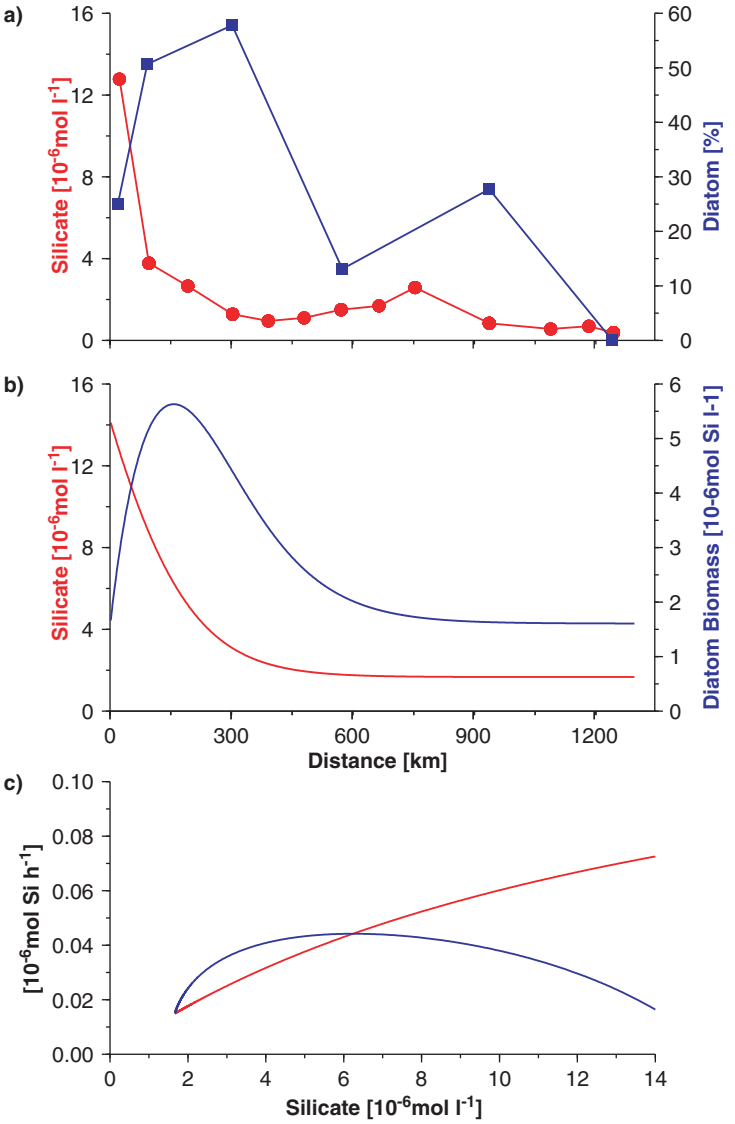

Plate 7.4: (a) Concentrations of silicate averaged for the upper 20 m of the water column along the transect from the Arabian coast towards the central and southern Arabian Sea, 1,300 km offshore during the SW monsoon of 1995 (compare Fig. 1). Nutrient data have been obtained from the US JGOFS datacentre. The blue line shows the contribution of diatoms to the biomass of photoautotrophic plankton during the same time (Garrison et al., 2000). (b) Diatom biomass (blue line) and silicate concentration derived from a box model that is described in the text. (c) Diatom growth rates (red line) and zooplankton grazing rates (blue line) vs. silicate concentration (data are derived from the model).

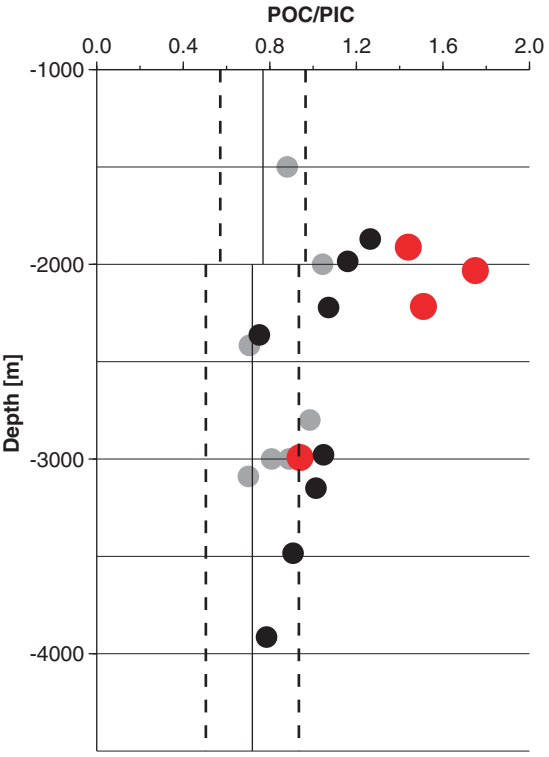

Plate 7.5: Annual mean POC/PIC ratios vs. water depth. Black circles show results obtained from the US JGOFS sediment trap experiment performed in 1994/1995 (Honjo et al., 1999; Lee et al., 2000), grey circles reveal data derived from the Indo/German sediment trap program in the Arabian Sea (Fig. 1) and those obtained from the Bay of Bengal (Unger et al., 2003) are given in red. Vertical lines representing the mean (solid line) and the range (broken line) of POC/PIC ratios obtained from other sediment trap studies in the carbonate-dominated ocean (Klaas and Archer, 2002).

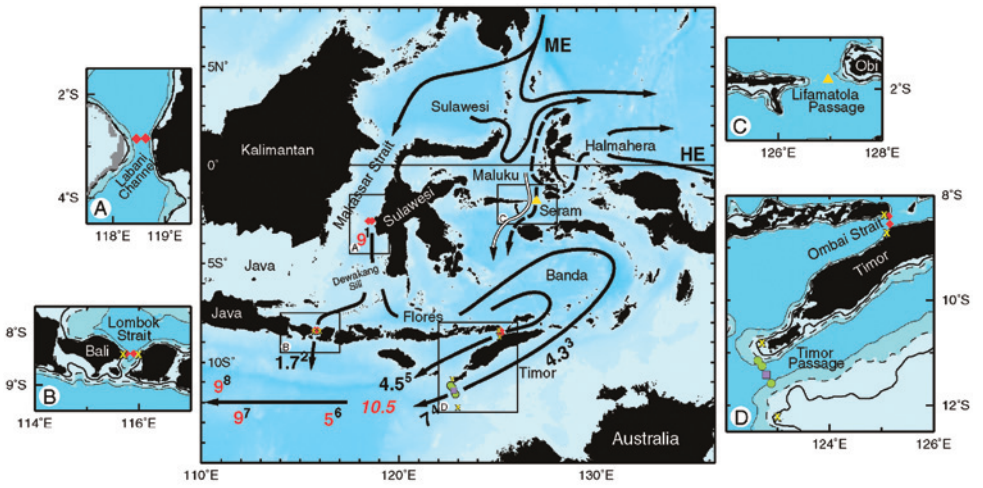

Plate 8.1: Schematic of Indonesian throughflow pathways (Gordon, 2001; reprinted with permission from Elsevier). The solid arrows represent north Pacific thermocline water; the dashed arrows are south Pacific lower thermocline water. Transports in Sv ($10^6\,m^3/s$) are given in red. The 10.5 Sv in italics is the sum of the flows through the Lesser Sunda passages. ME is the Mindanao Eddy; HE is the Halmahera Eddy. Superscript refers to reference source: 1, Makassar Strait transport in 1997 (Gordon et al., 1999); 2, Lombok Strait (Murray and Arief, 1988; Murray et al., 1990) from January 1985 to January 1986; 3, Timor Passage (between Timor and Australia) measured from March 1992 to April 1993 (Molcard et al., 1996); 4, Timor Passage, between October 1987 and March 1988 (Cresswell et al., 1993); 5, Ombai Strait (north of Timor, between Timor and Alor Island) from December 1995 to December 1996 (Molcard et al., 2001); 6, between Java and Australia from 1983 to 1989 XBT data (Meyers et al., 1995; Meyers, 1996); 7, Upper 470 m of the South Equatorial Current in the eastern Indian Ocean in October 1987 (Quadfasel et al., 1996); 8, Average ITF within the South Equatorial Current defined by five WOCE WHP sections (Gordon et al., 1997). The hollow arrow represents overflow of dense Pacific water across the Lifamatola Passage into the deep Banda Sea, which may amount to about 1 Sv (van Aken et al., 1988). Inserts A–D show the positions of the INSTANT moorings. Insert A: position of the two Makassar Strait inflow moorings (US, red diamond) within Labani Channel. Insert C: position of the Netherland's mooring within the main channel of Lifamatola Passage (yellow triangle). Insert B, D: position of the Sunda moorings in Ombai Strait, Lombok strait, and Timor Passage (US, red diamonds; French, purple square; Australian, green circles). The positions of the shallow pressure gauge array (SPGA) (US, green X). The 100, 500, and 1,000 m isobaths are shown in the inserts.

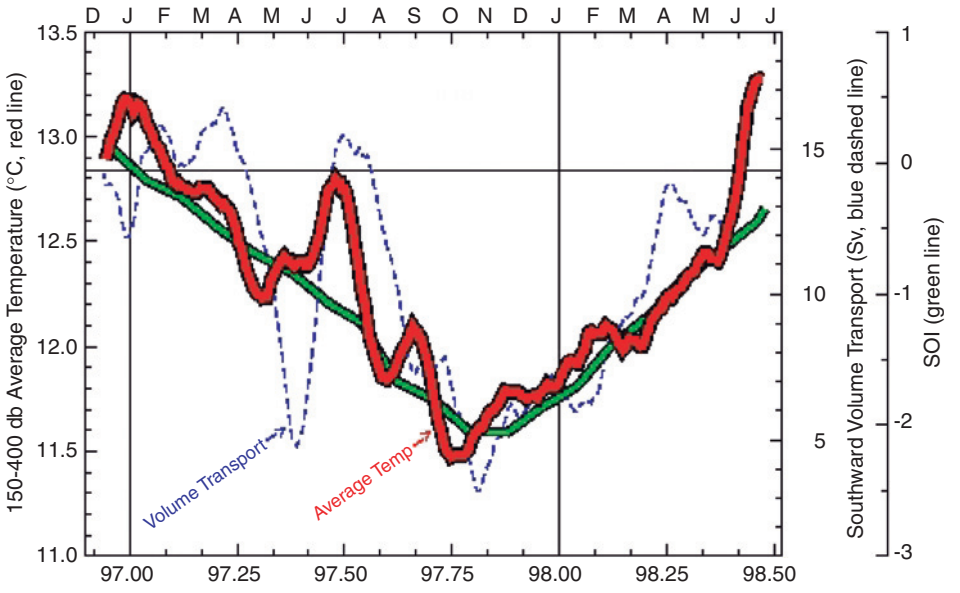

Plate 8.2: (a) Time series (above) of the average temperature (red) between 150 and 400 db at the MAK-1 mooring (Ffield et al., 2000). The SOI (green) and the Makassar Strait volume transport (blue dashed) are also shown. The data are smoothed by 30-day running averages. (b) Temperature time section constructed from 15 years of Makassar Strait and Flores Sea XBT profiles (Ffield, 2000, personal communication). In the upper panel, the depth of the 22°C XBT isotherm (red) is shown with the SOI (black) highlighting the clear ENSO variability in the XBT temperature data. The data are smoothed by a 1-year running average.

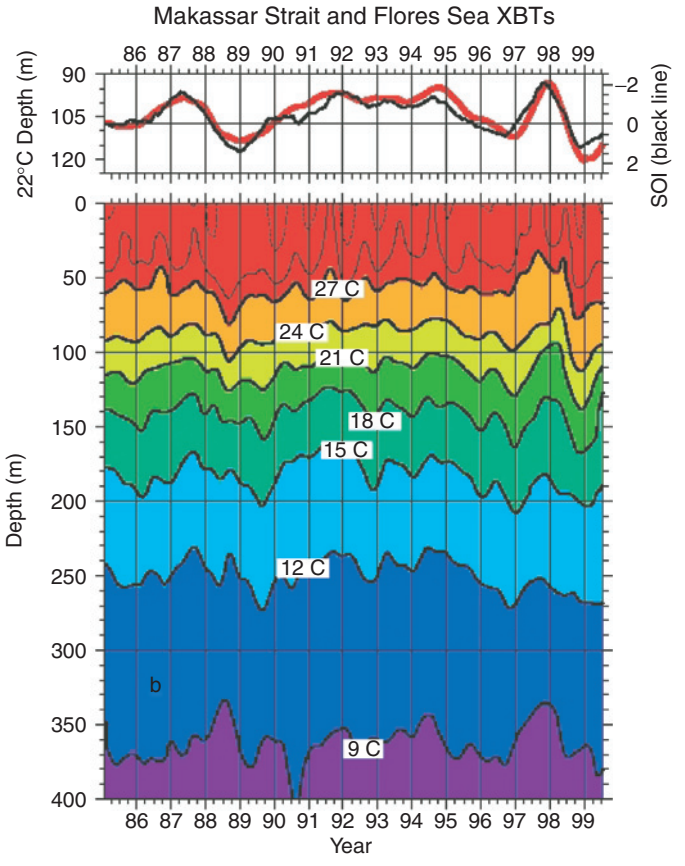

Plate 8.2: Continued.

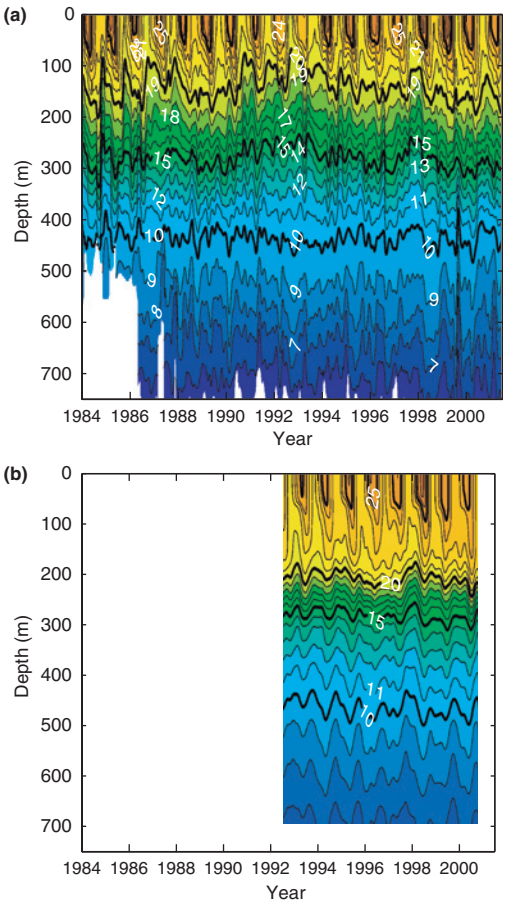

Plate 8.4: Potential temperature as a function of time and depth along IX1 off the coast of western Australia near 25°S for (a) observations and (b) model.

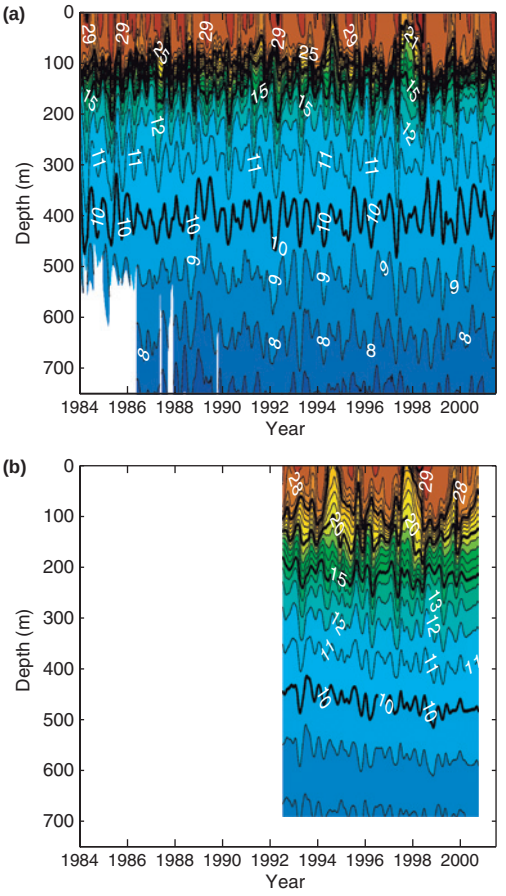

Plate 8.5: Potential temperature as a function of time and depth along IX1 off the coast of Java at the Sunda Strait for (a) observations and (b) model.

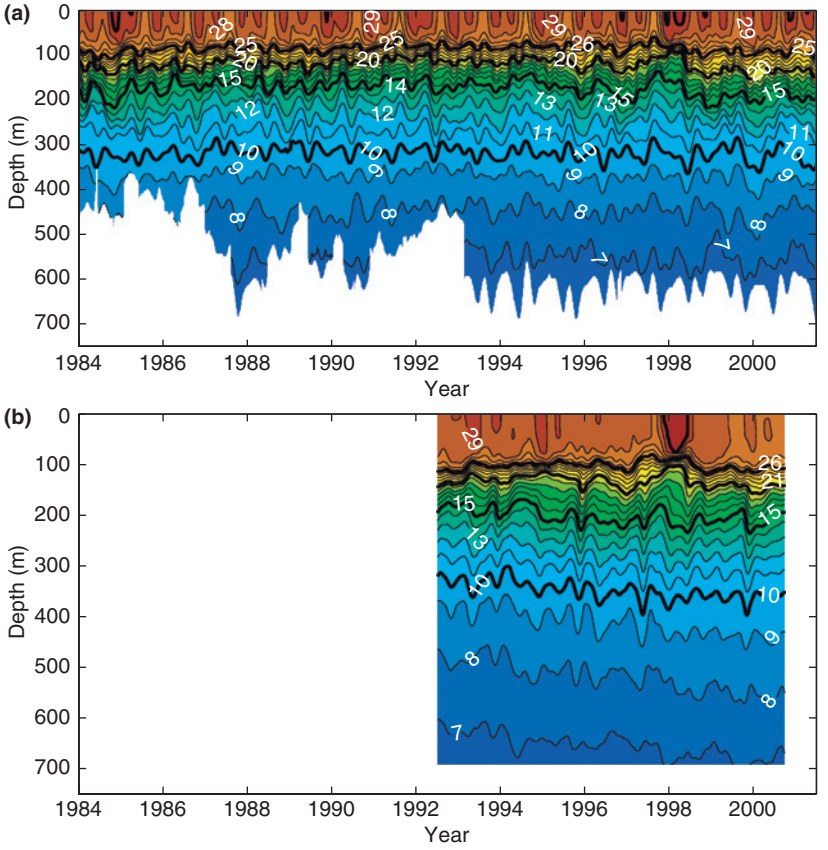

Plate 8.6: Potential temperature as a function of time and depth along PX2 off the Java shelf break near 116°E for (a) observations and (b) model.

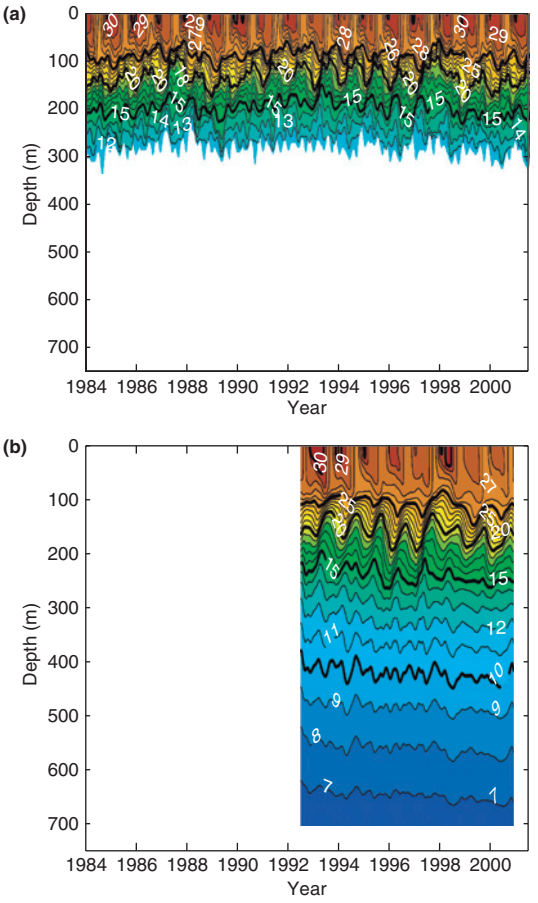

Plate 8.7: Potential temperature as a function of time and depth along PX2 at the Arafura shelf break near 133°E for (a) observations and (b) model.

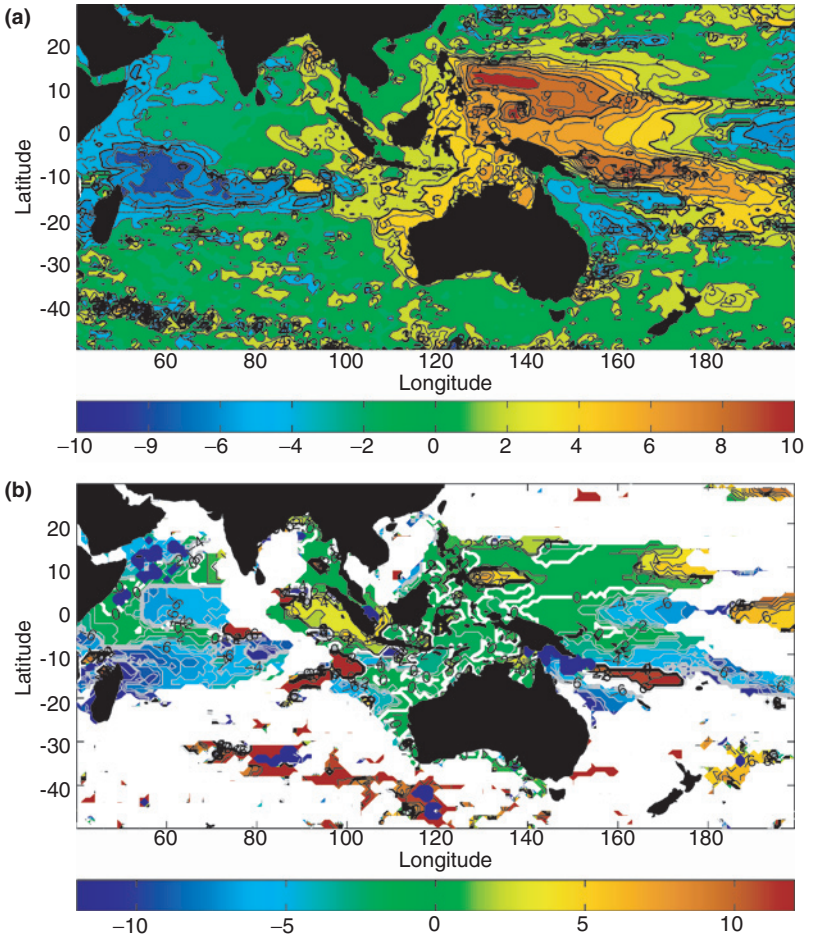

Plate 8.10a, b: Coefficient in centimeter (top) and lag in months (bottom) of low-frequency anomalies of SSH for Pacific wind index: (a, b) observations and (c, d) model.

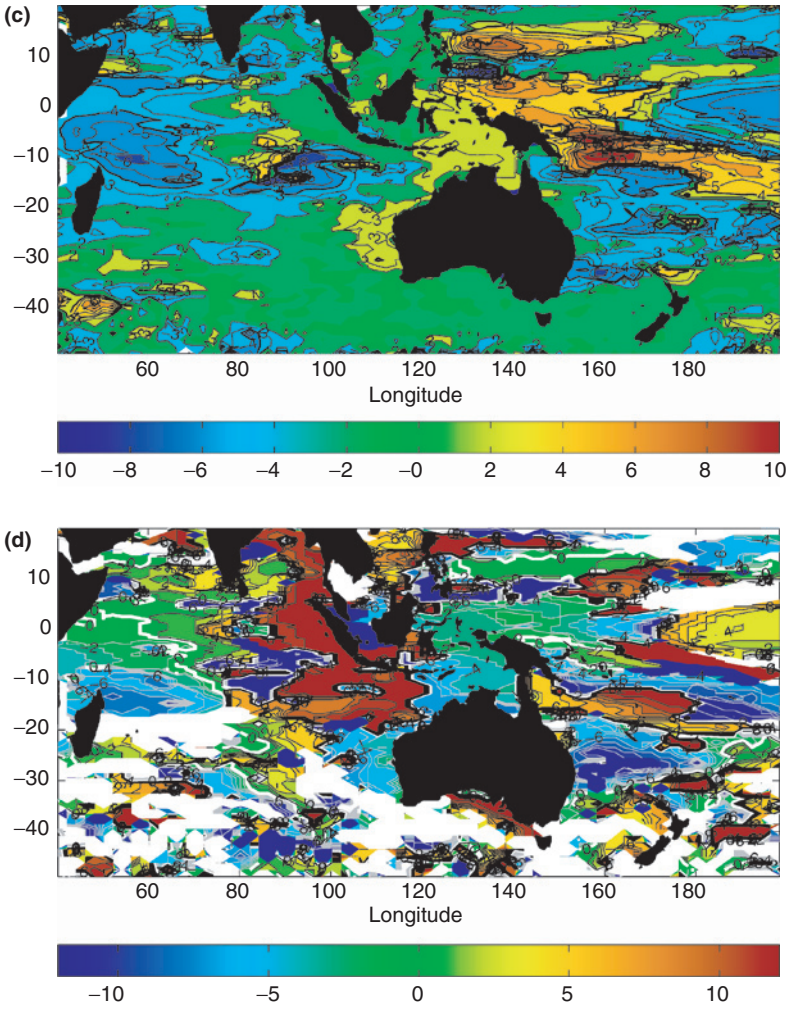

Plate 8.10c, d: Continued.

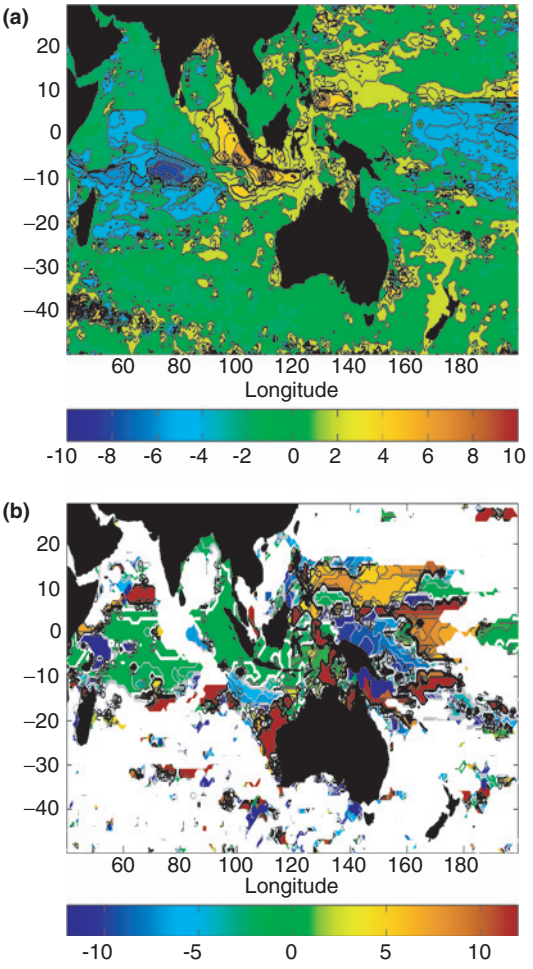

Plate 8.11a, b: As for Fig. 10, but for the Indian wind index.

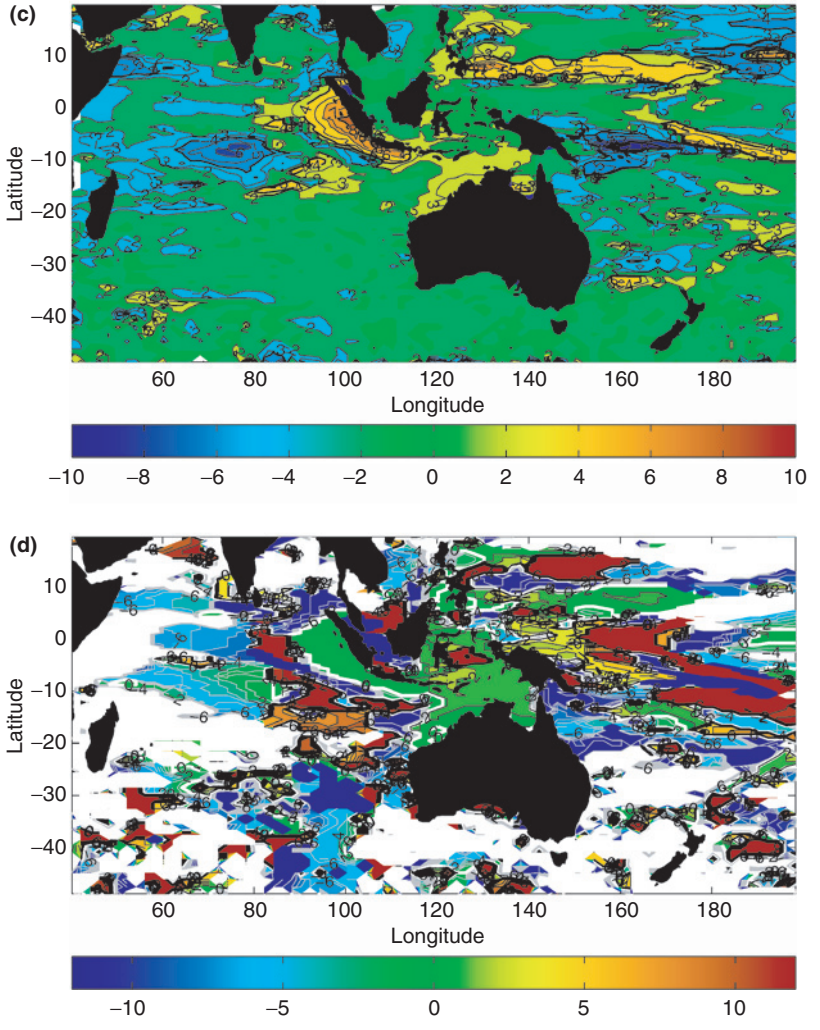

Plate 8.11c, d: Continued.

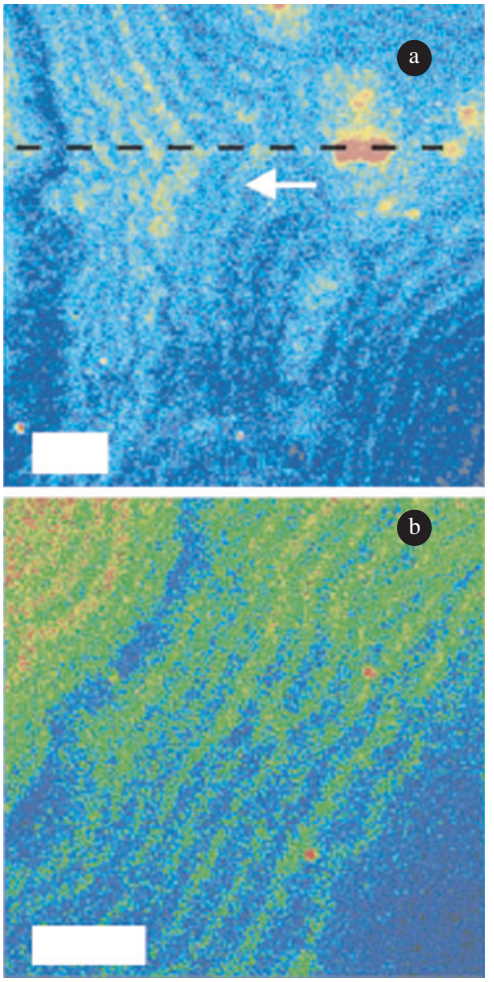

Plate 10.7: The distribution of Mg in different parts of the *Pavona clavus* skeleton from Meibom et al. (2004). Dark blue colors correspond to relatively low Mg concentrations; green, yellow and red colors correspond to increasingly high Mg concentrations. EMZ have the highest concentration of Mg. Arrow indicates direction of growth. Scale bars are 10 μm.

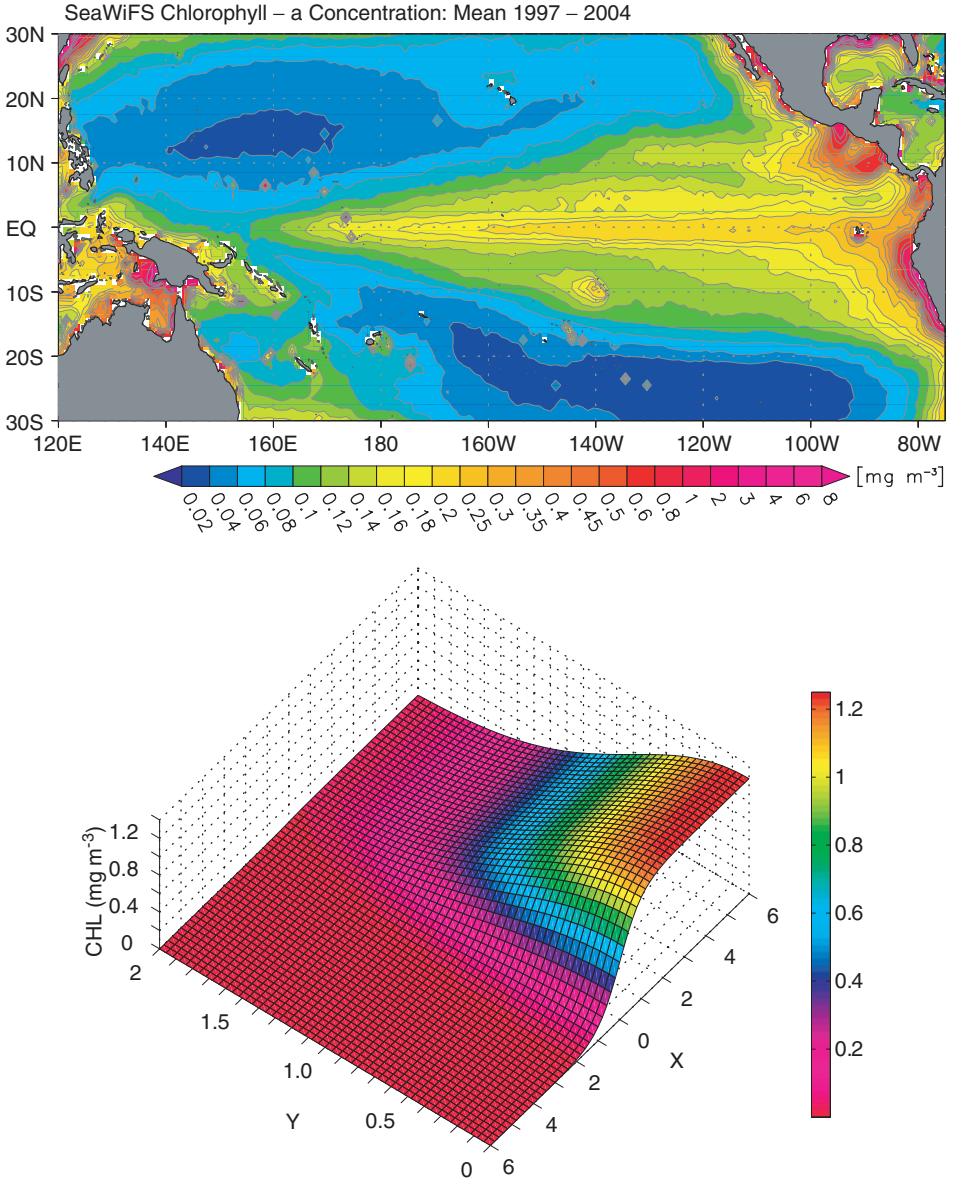

Plate 11.1: Biomass distribution from SeaWiFS satellite observations and the mathematical distribution function (mg m^{-3}) given by equation (1). The coordinates x and y are normalized by 100 km.

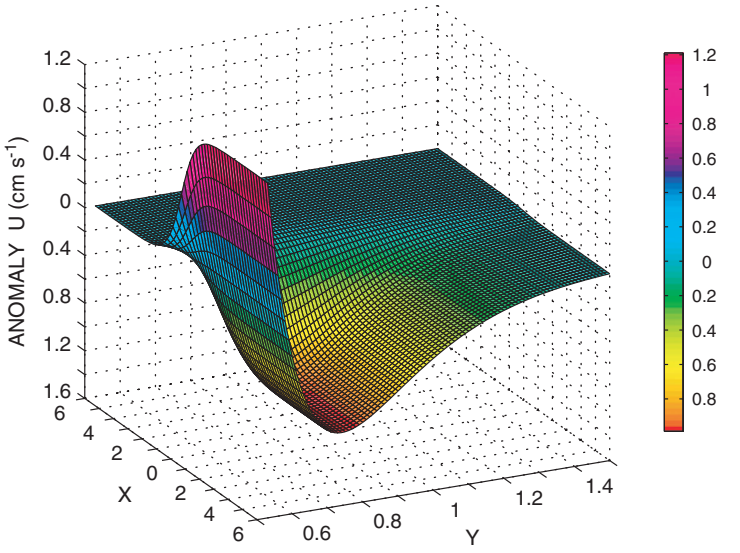

Plate 11.2: Zonal component of chlorophyll biomass induced southward geostrophic currents (m s^{-1}). The horizontal coordinate origin is located at dateline on the equator and the lengths are scaled by 1°. *y* coordinate spans 0.5–1.5° N.

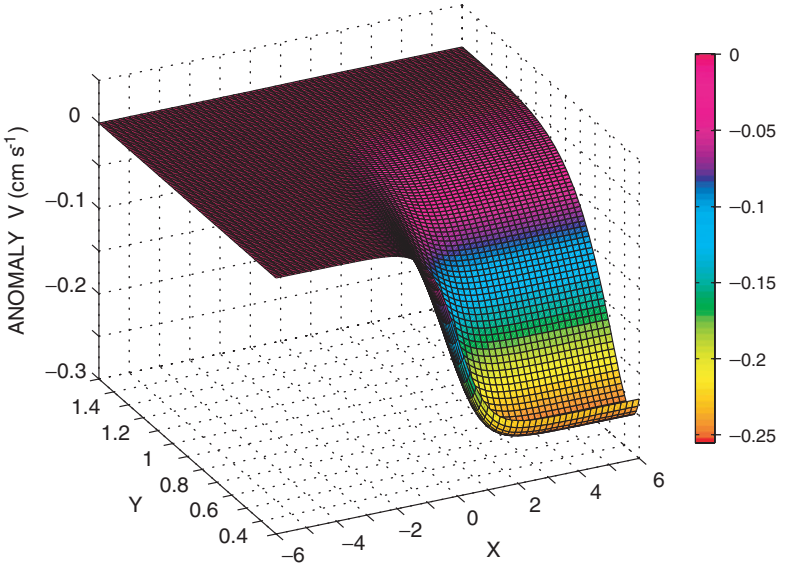

Plate. 11.3: Meridional component of chlorophyll biomass-induced southward geostrophic currents (m s^{-1}). The horizontal coordinate origin is located at dateline on the equator and the lengths are scaled by 1°. *y* coordinate spans 0.3–1.4° N.

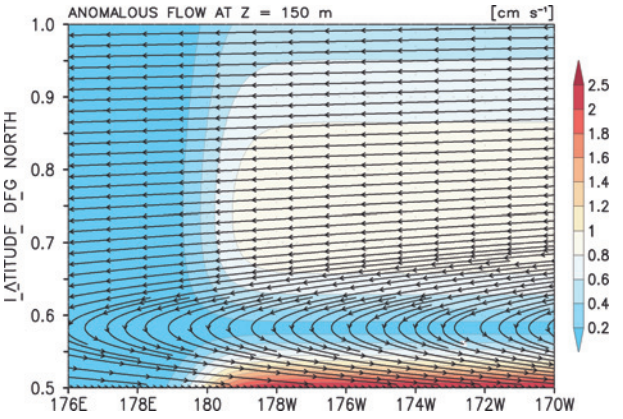

Plate 11.4: Analytical solutions for biologically generated horizontal current (m s^{-1}) at the depth 100 m (longitude (183–190 E) and latitude (0.5—1 N)).

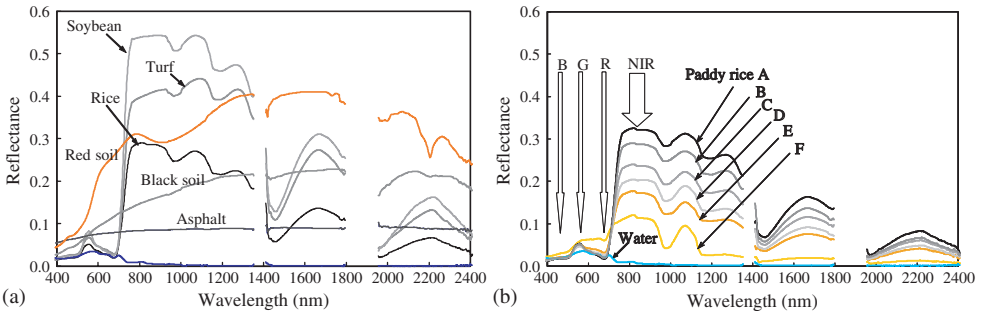

Plate 13.1: Typical reflectance spectra for agro-ecosystem surfaces (a), and for paddy fields with different biomass (b). Abbreviations B, G, R, and NIR mean blue, green, red, and near-infrared wavelengths, respectively. Biomass of rice paddies decreased in order from A to F.

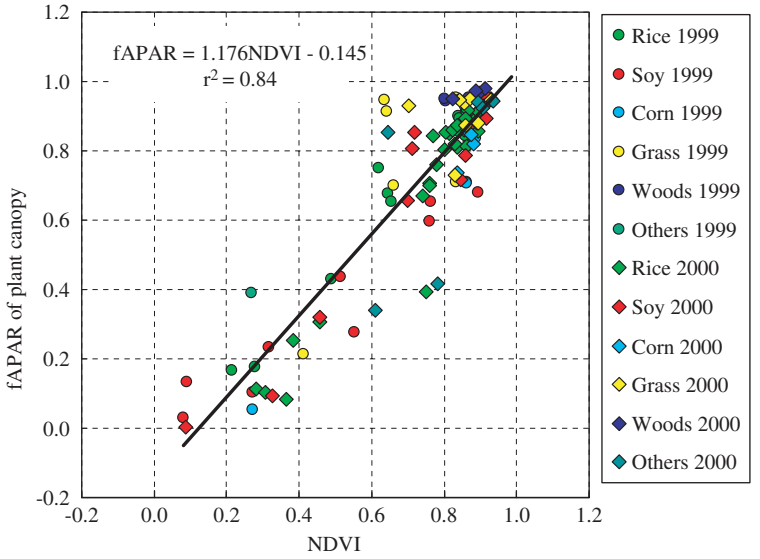

Plate 13.3: Relationship between fAPAR of various plant canopies and vegetation index NDVI derived from airborne remote sensing images.

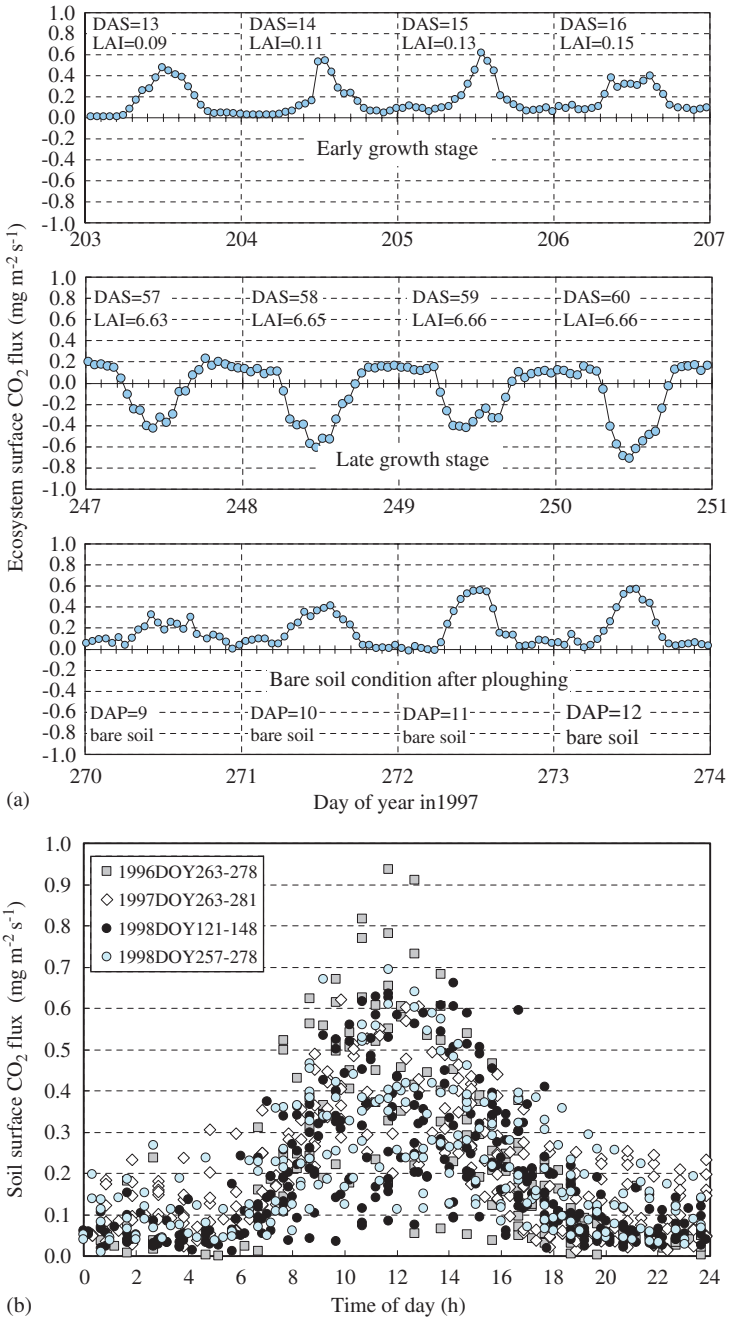

Plate 13.5: Typical time course changes of ecosystem surface CO_2 flux (ESF_{CO_2}) over soybean canopy and bare field estimated by eddy covariance method (a). Soil surface CO_2 flux (SSF_{CO_2}) under bare soil conditions is indicated in the time of day axis (b). DAS, DAP, and LAI are days after seeding, days after ploughing, and leaf area index, respectively (Inoue et al., 2004).

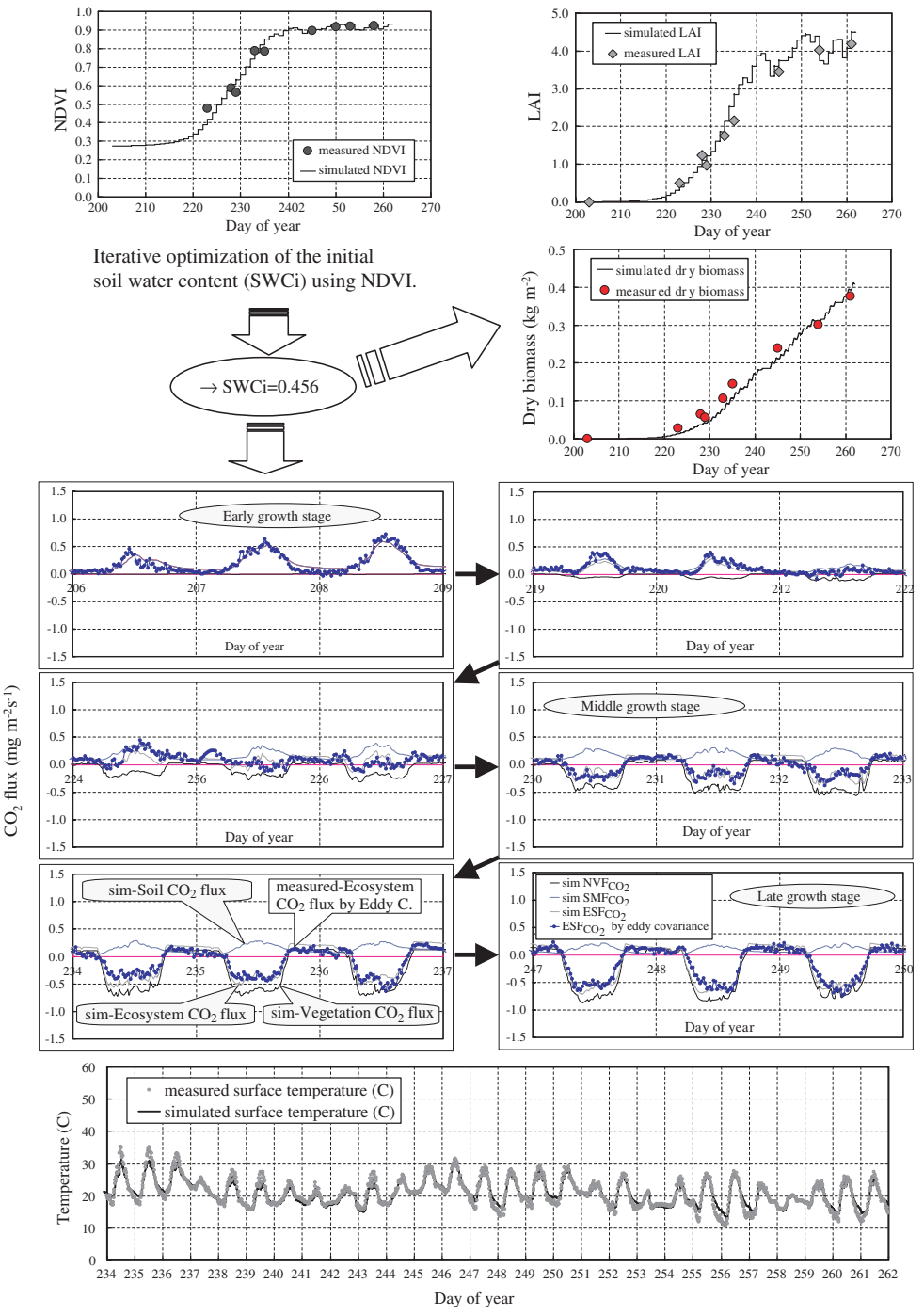

Plate 13.11: Dynamic change of ecosystem CO_2 (ESF_{CO_2}) flux estimated by the synergy of remote sensing and process model – a case study for soybean field. NVF_{CO_2}: net vegetation CO_2 flux; SMF_{CO_2}: soil microbial CO_2 flux.

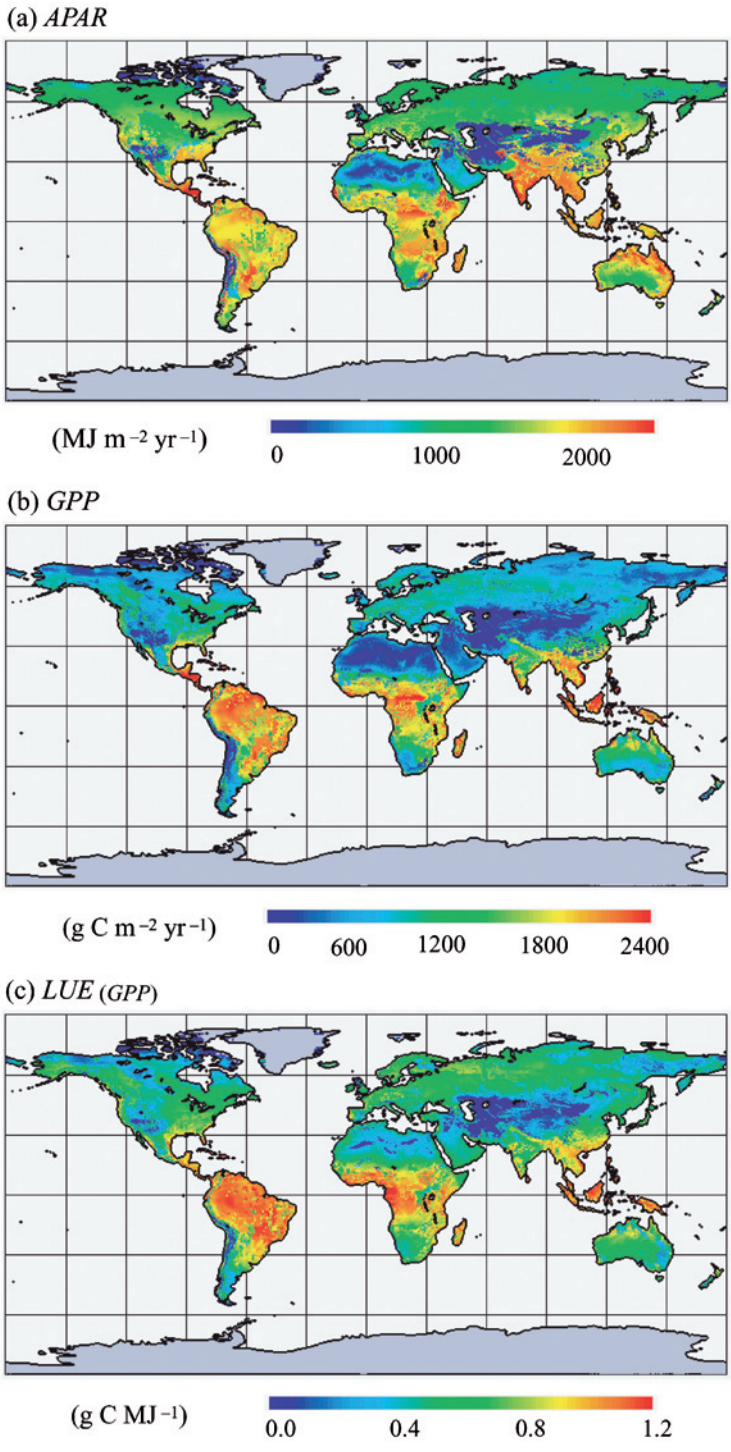

Plate 14.3: Estimated global distributions of (a) *APAR*, (b) *GPP*, and (c) $LUE_{(GPP)}$, averaged from 1981 to 2000.

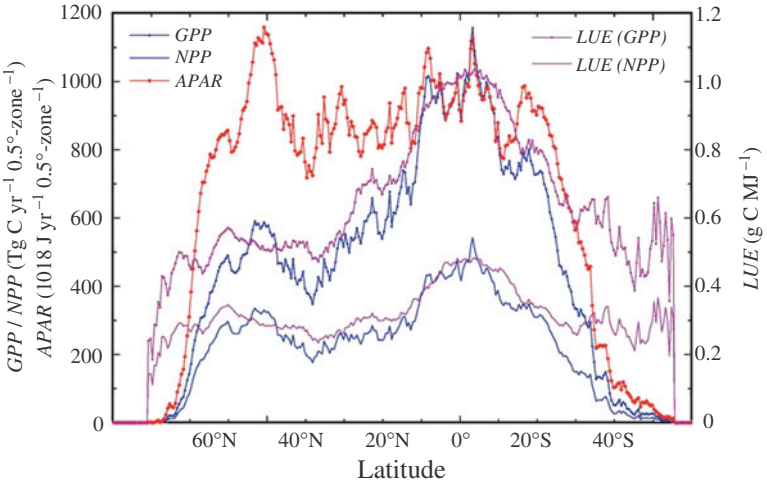

Plate 14.4: Latitudinal distributions of absorbed PAR (*APAR*), productivities (*GPP* and *NPP*), and light-use efficiencies ($LUE_{(GPP)}$ and $LUE_{(NPP)}$), averaged from 1981 to 2000.

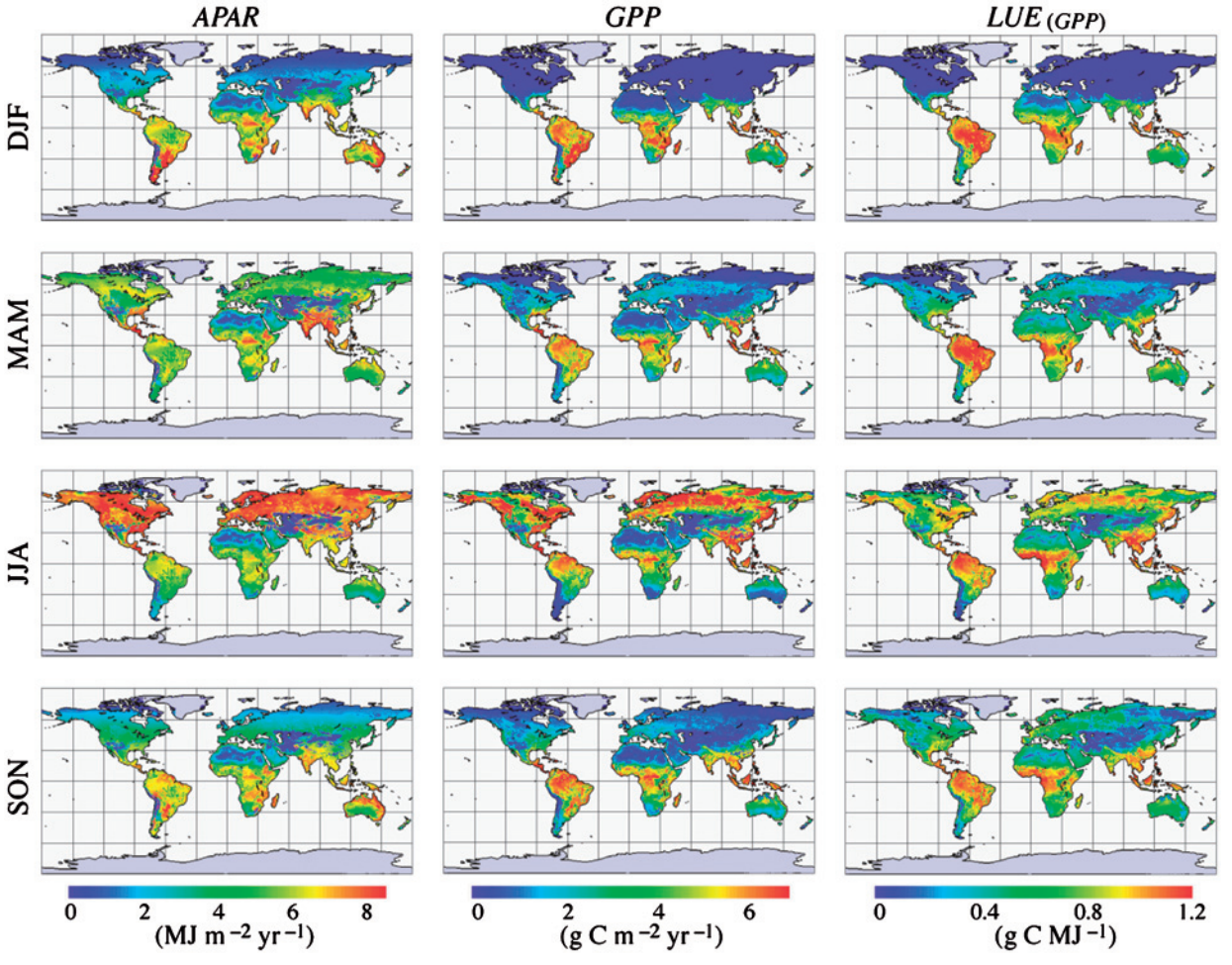

Plate 14.5: Seasonal change in the estimated global distributions of *APAR*, *GPP*, and $LUE_{(GPP)}$, averaged from 1981 to 2000: DJF (December, January, and February), MAM (March, April, and May), JJA (June, July, and August), and SON (September, October, and November), averaged from 1981 to 2000.

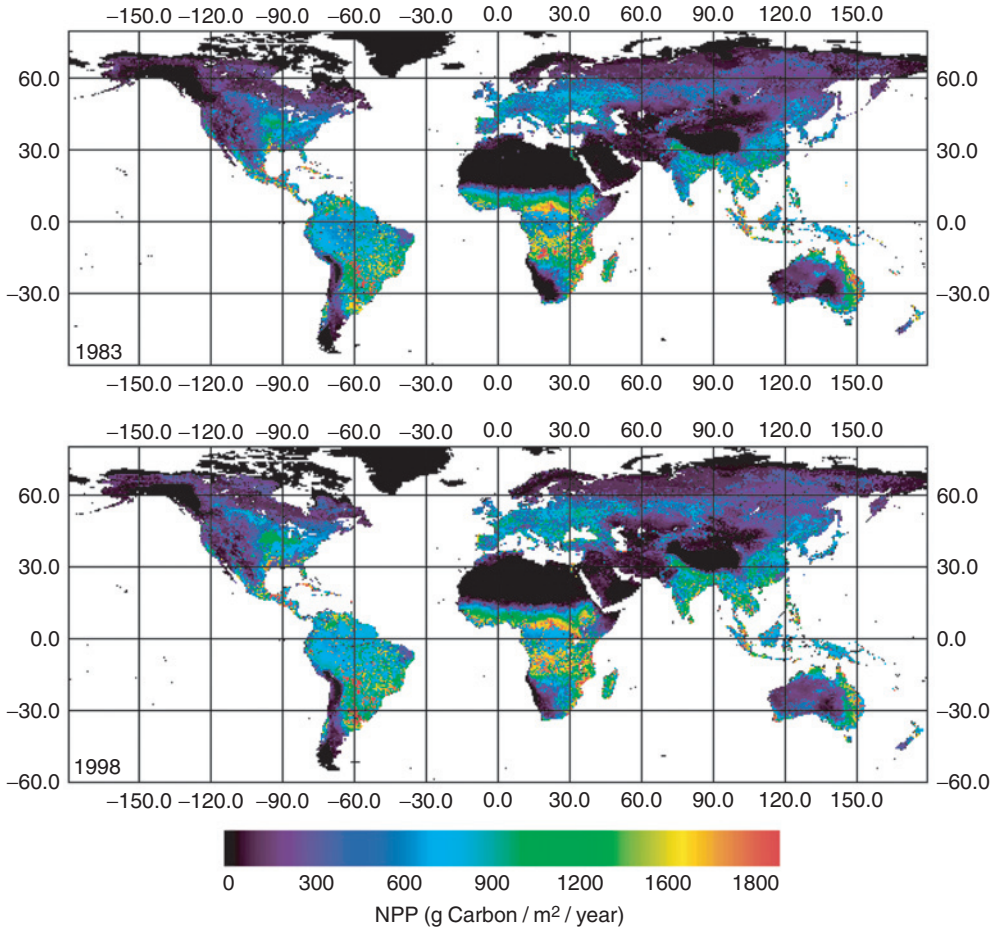

Plate 15.5: The results of NPP estimation by the multiple LUE settings. The minimum appeared in 1983 (above), and the maximum appeared in 1998 (below). The greatest NPP appeared in tropical deciduous forest or savannas.

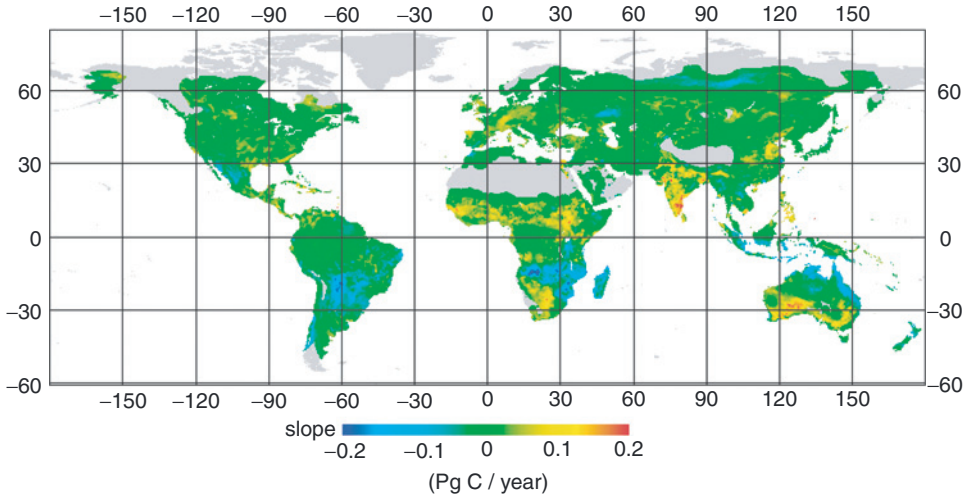

Plate 15.6: Regional changes of NPP. The rate of NPP change in each region was estimated by a linear regression analysis for the results of the multiple LUE-setting for 17 vegetation classes. Clear increases and decreases of NPP were detected in some areas around semiarid zones. Grey areas show extremely low NPP and were omitted in the regression analysis.

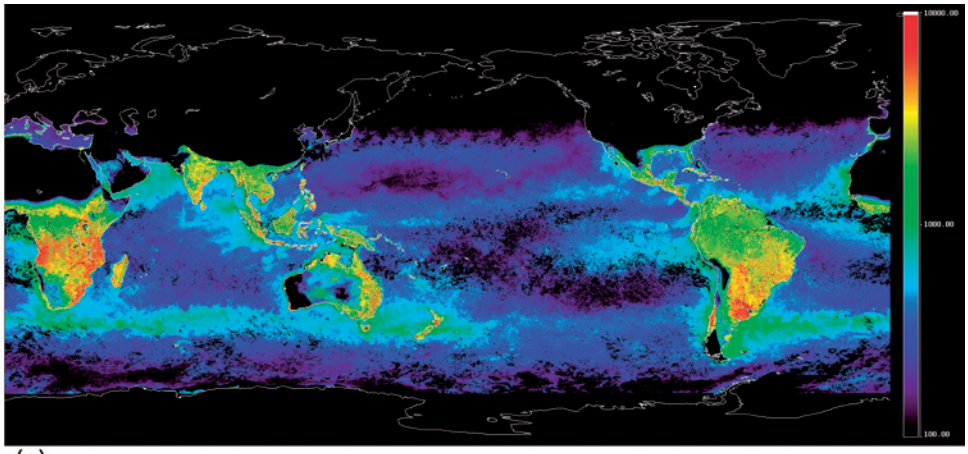

(a)

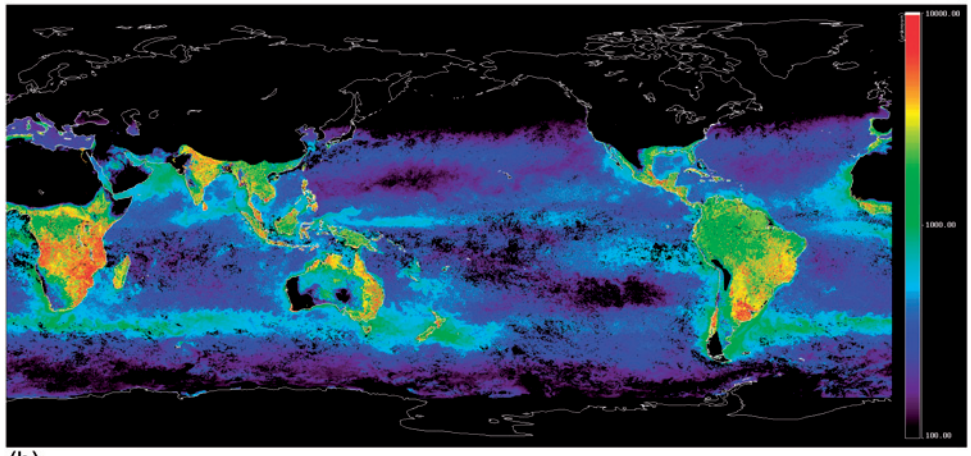

(b)

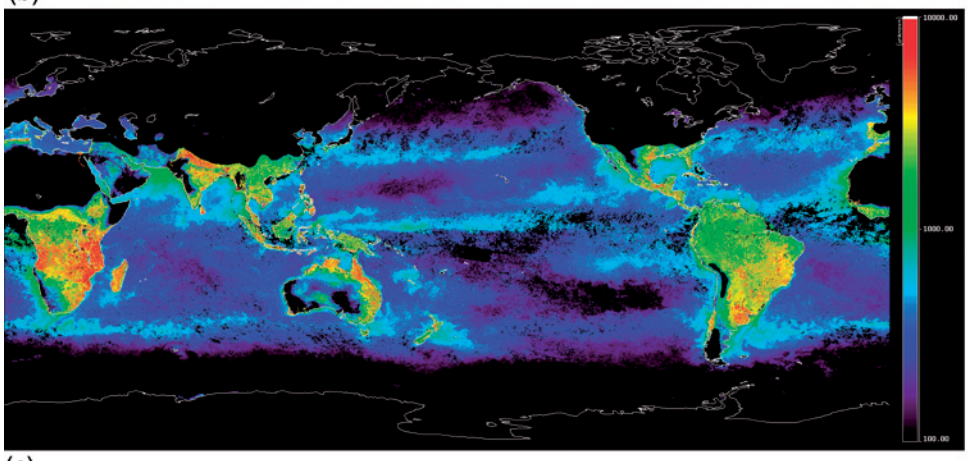

(c)

Plate 16.1: Global NPP maps in 1998. (a) January, (b) February, (c) March, (d) April, (e) May, (f) June, (g) July, (h) August, (i) September, (j) October, (k) November, (l) December.

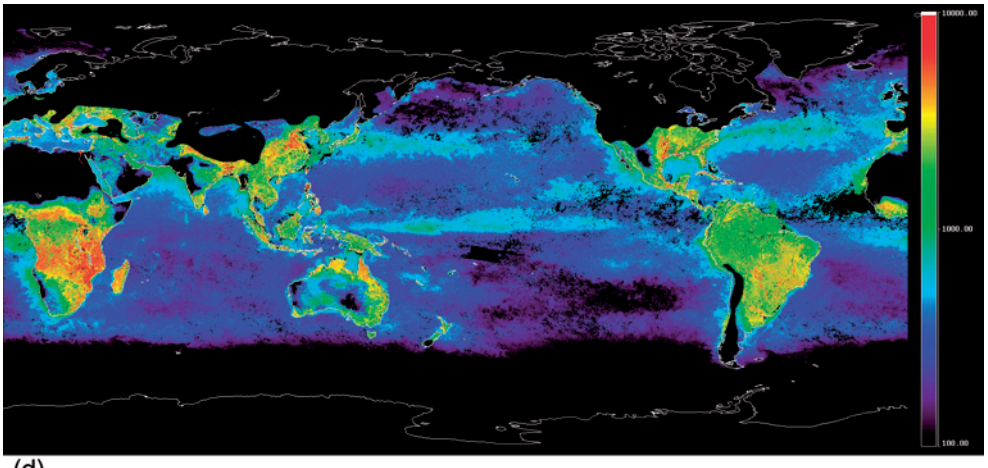

(d)

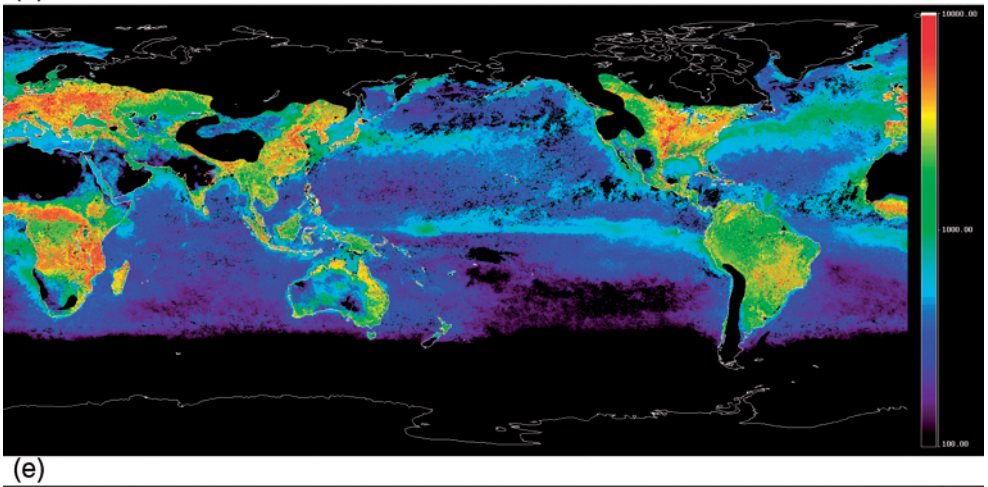

(e)

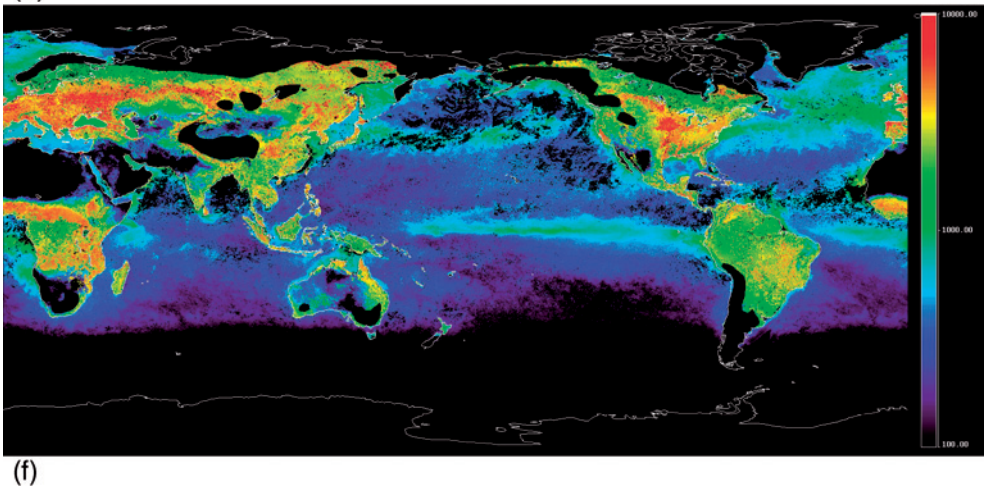

(f)

Plate 16.1: (Continued)

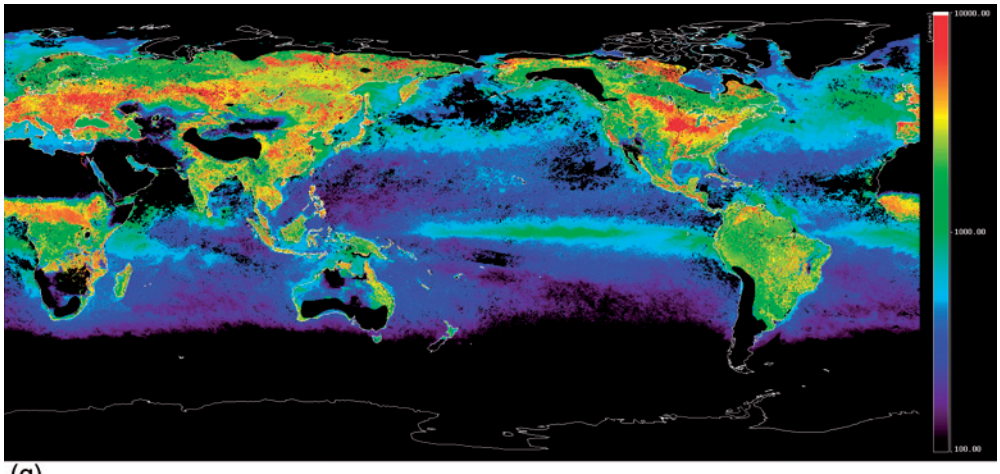

(g)

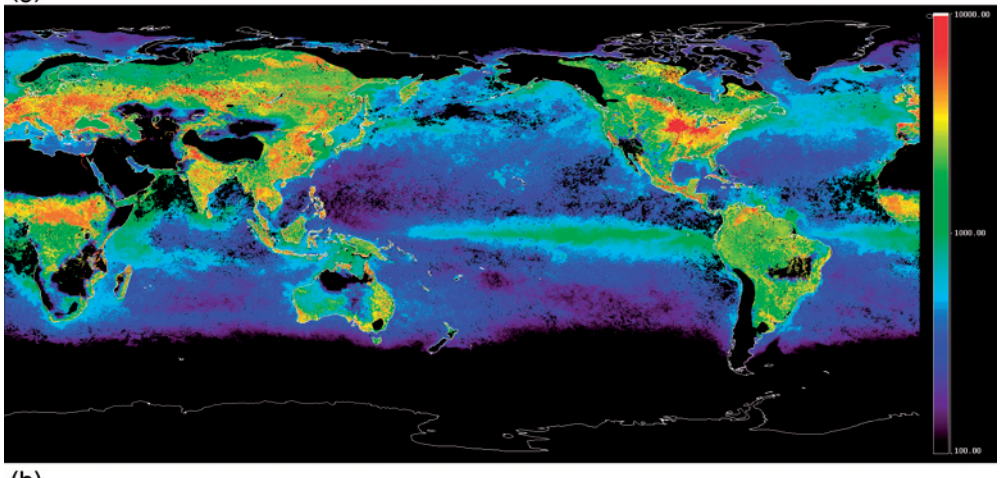

(h)

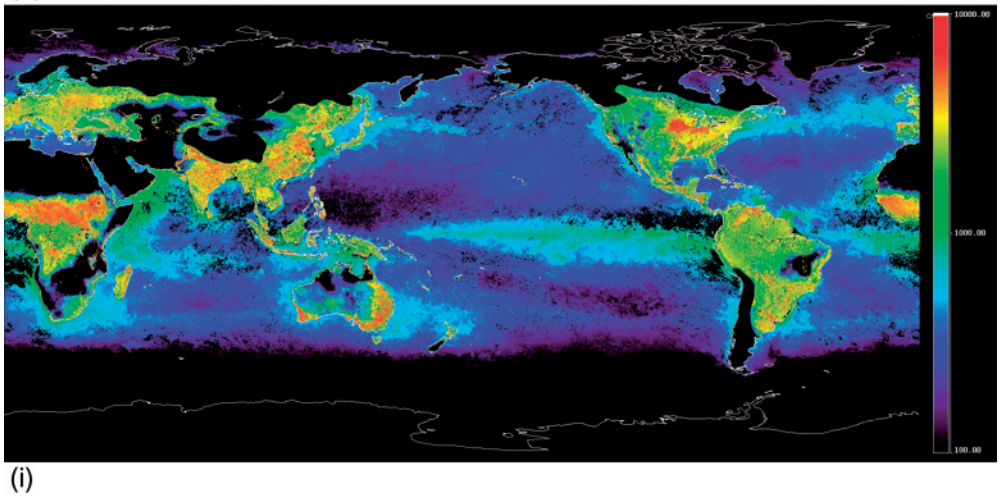

(i)

Plate 16.1: (Continued)

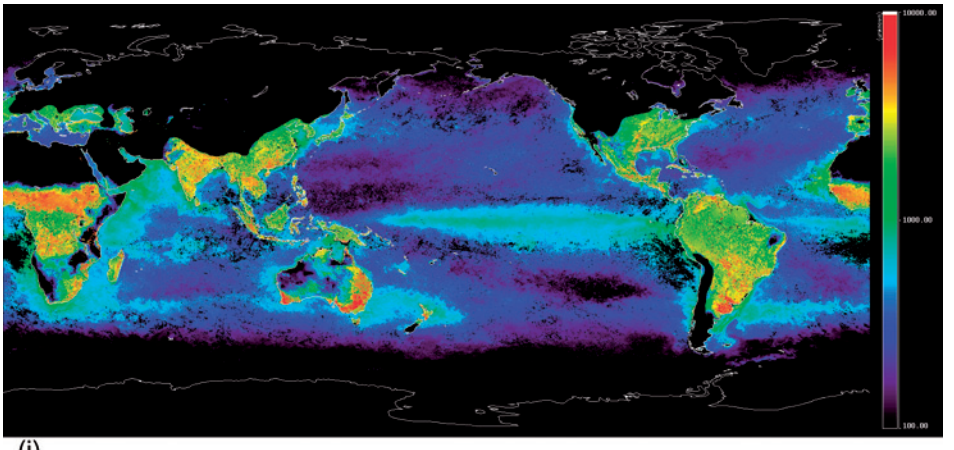

(j)

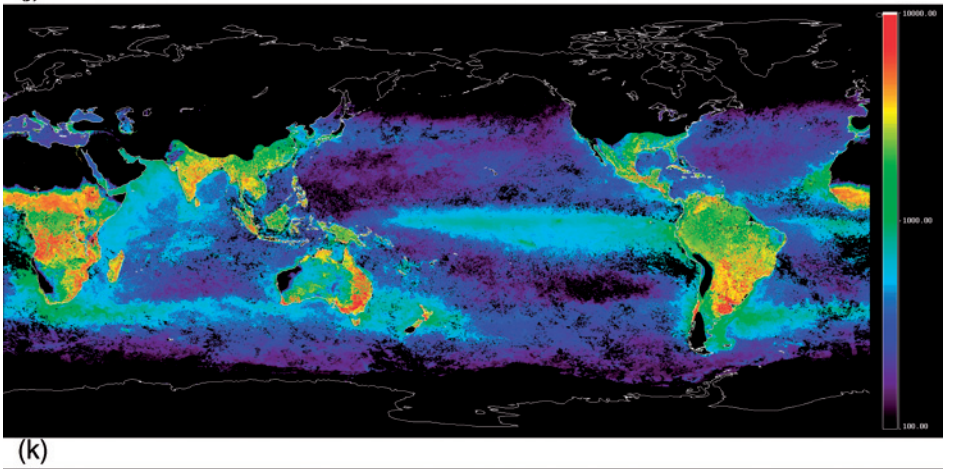

(k)

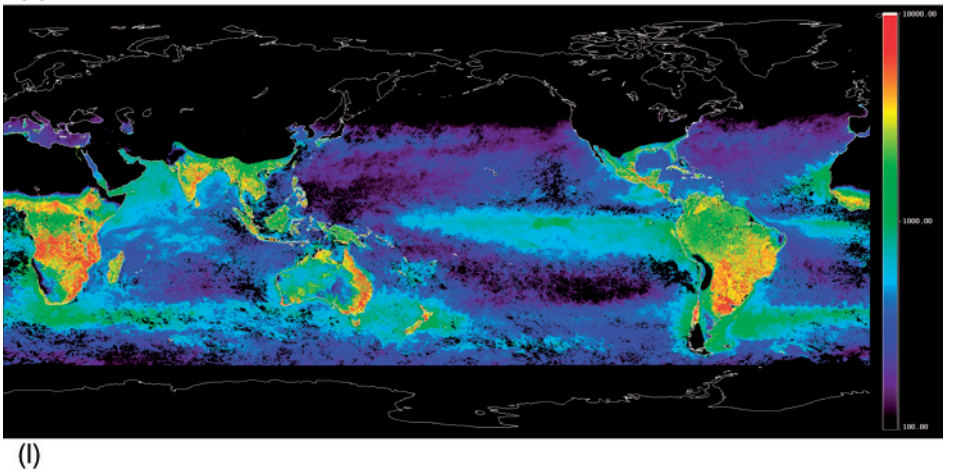

(l)

Plate 16.1: (Continued)

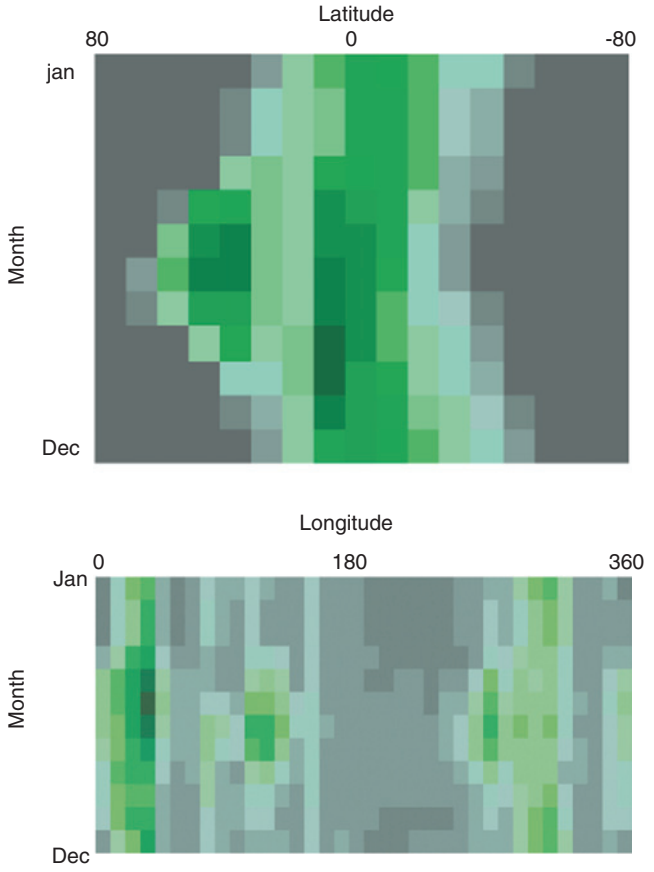

Plate 16.2: Seasonal change of zonal and meridional mean NPP. (a) Zonal mean. Horizontal axis corresponds to 80−80 degree from north to south and vertical axis corresponds to January to December. (b) Meridional mean. Horizontal axis corresponds to 0–360° eastbound and vertical axis corresponds to January to December.

This page intentionally left blank